

*Femtochemistry*. Edited by Frans C. De Schryver, Steven De Feyter, and Gerd Schweitzer  
Copyright © 2001 Wiley-VCH Verlag GmbH  
ISBNs: 3-527-30259-X (Hardback); 3-527-60018-3 (Electronic)

**Femtochemistry**

*Edited by Frans C. De Schryver,  
Steven De Feyter, and Gerd Schweitzer*

## ***Other Titels of Interest***

Berson, Jerome A.

### **Chemical Creativity**

**Ideas from the Work of Woodward, Hückel, Meerwein, and Others**

1999. Softcover

ISBN 3-527-29754-5

Keinan, Ehud / Schechter, Israel (Eds.)

### **Chemistry for the 21st Century**

2000. Softcover

ISBN 3-527-30235-2

Olah, George A.

### **A Life of Magic Chemistry**

2001. Hardcover

ISBN 0-471-15743-0

Quadbeck-Seeger, Hans-Jürgen (Ed.)

Faust, Rüdiger / Knaus, Günter /

Siemeling, Ulrich

### **World Records in Chemistry**

1999. Softcover

ISBN 3-527-29574-7

Roesky, Herbert W. / Möckel, Klaus

### **Chemical Curiosities**

**Spectacular Experiments and Inspired Quotes**

1996. Hardcover

ISBN 3-527-29414-7

*Femtochemistry*. Edited by Frans C. De Schryver, Steven De Feyter, and Gerd Schweitzer  
Copyright © 2001 Wiley-VCH Verlag GmbH  
ISBNs: 3-527-30259-X (Hardback); 3-527-60018-3 (Electronic)

# Femtochemistry

*Edited by*  
*Frans C. De Schryver, Steven De Feyter,*  
*and Gerd Schweitzer*

*With the Nobel Lecture*  
*of A. Zewail*

 **WILEY-VCH**

Weinheim – New-York – Chichester – Brisbane – Singapore – Toronto

**Editor**

**Prof. Dr. Frans C. De Schryver**

**Dr. Steven De Feyter**

**Dr. Gerd Schweitzer**

Department of Chemistry  
Katholieke Universiteit Leuven  
Celestijnenlaan 200 F  
B-3001 Heverlee  
Belgium

■ This book was carefully produced. Nevertheless, authors, editors, and publisher do not warrant the information contained therein to be free of errors. Readers are advised to keep in mind that statements, data, illustrations, procedural details or other items may inadvertently be inaccurate.

**Library of Congress Card No.**

applied for

**British Library Cataloguing-in-Publication Data**

A catalogue record for this book is available from the British Library.

**Die Deutsche Bibliothek – CIP Cataloguing-in-Publication Data**

A catalogue record for this publication is available from Die Deutsche Bibliothek

© 2001 WILEY-VCH GmbH, Weinheim, Germany

All rights reserved (including those of translation in other languages). No part of this book may be reproduced in any form – by photoprinting, microfilm, or any other means – nor transmitted or translated into a machine language without written permission from the publisher. Registered names, trademarks, etc. used in this book, even when not specifically marked as such, are not to be considered unprotected by law.

Printed in the Federal Republic of Germany

Printed on acid-free paper

**Composition** Kühn & Weyh, Freiburg  
**Printing** betz-druck GmbH, Darmstadt  
**Bookbinding** Osswald & Co., Neustadt (Weinstraße)

**ISBN** 3-527-30259-X



## Contents

**Preface** XV

**List of Contributors** XVII

<b>1</b>	<b>Femtochemistry: Atomic-Scale Dynamics of the Chemical Bond Using Ultrafast Lasers (Nobel Lecture)</b>	<b>1</b>
	<i>Ahmed H. Zewail</i>	
1.1	Prologue	1
1.2	Dynamics and Arrow of Time	10
1.2.1	Origins—From Kinetics To Dynamics	10
1.2.1.1	The Arrhenius Seminal Contribution	10
1.2.1.2	The London, Eyring, and Polanyi Contributions	11
1.2.1.3	The Transition State and its Definition	12
1.2.1.4	The Transition State and its Spectroscopy	14
1.2.2	The Arrow of Time	14
1.3	Femtochemistry: Development of the Field	17
1.3.1	The Early Years of Coherence	17
1.3.1.1	New Techniques for Molecules	17
1.3.1.2	The Optical Analogue of NMR Spectroscopy: Controlling the Phase	21
1.3.2	The Marriage with Molecular Beams	22
1.3.2.1	The Anthracene Discovery: A Paradigm Shift	23
1.3.2.2	The Successful 036 Laboratory	25
1.3.2.3	Changing A Dogma: Development of RCS	27
1.3.3	The Transition to the Sub-Picosecond Regime	29
1.3.3.1	A New Beam Machine: Pump-Probe Mass Spectrometry	29
1.3.3.2	The First Experiment on ICN: Sub-picosecond Resolution	30
1.3.4	The Femtosecond Dream	32
1.3.4.2	The Classic Femtosecond Discovery in ICN	32
1.3.4.3	The NaI Discovery: A Paradigm for the Field	35
1.3.4.4	The Saddle-Point Transition State	38
1.3.4.5	The Uncertainty Principle Paradox	40
1.3.4.6	Bimolecular Bond Making and Bond Breaking: Bernstein's Passion	41

1.3.4.7	Ultrafast Electron Diffraction	43
1.3.4.8	Clusters, Dense Fluids and Liquids, and New Generations of FEMTOLANDS	43
1.3.4.9	Theoretical Femtochemistry	44
1.3.4.10	Experimental Femtochemistry	46
1.3.5	Femtocopia—Examples from Caltech	50
1.3.5.1	Elementary Reactions and Transition States	50
1.3.5.2	Organic Chemistry	50
1.3.5.3	Electron and Proton Transfer	50
1.3.5.4	Inorganic and Atmospheric Chemistry	52
1.3.5.5	The Mesoscopic Phase: Clusters and Nanostructures	54
1.3.5.6	The Condensed Phase: Dense Fluids, Liquids, and Polymers	54
1.3.6	Opportunities for the Future	57
1.3.6.1	Transient Structures from Ultrafast Electron Diffraction	57
1.3.6.2	Reaction Control	58
1.3.6.3	Biological Dynamics	62
1.4	Impact and Concepts—A Retrospective	65
1.4.1	Time Resolution—Reaching the Transition-State Limit	65
1.4.2	Atomic-Scale Resolution	66
1.4.3	Generality of the Approach	66
1.4.4	Some Concepts	67
1.4.4.1	Resonance (Nonequilibrium Dynamics)	67
1.4.4.2	Coherence (Single-Molecule-Type Dynamics)	68
1.4.4.3	Transition Structures (Landscape Dynamics)	69
1.4.4.4	Reduced Space (Directed Dynamics)	69
1.5	Epilogue	70
1.6	Appendix	72
1.6.1	A Primer for Femtoscopy, Coherence and Atoms in Motion	72
1.6.1.1	Pump–Probe Femtoscopy	72
1.6.1.2	Coherence and Atomic Motion	73
<b>2</b>	<b>Transition State Theory and Reaction Dynamics – An Overview</b>	<b>87</b>
	<i>Ward H. Thompson, Philip M. Kiefer, and James T. Hynes</i>	
2.1	Introduction	87
2.2	Crossing the Transition State in Solution	88
2.3	Acid–Base Proton-Transfer Reactions in Solution	89
2.4	Wave-Packet Evolution for Proton-Transfer Reactions	92
<b>3</b>	<b>Organic Femtochemistry: Diradicals, Theory and Experiments</b>	<b>97</b>
	<i>Steven De Feyter, Eric W.-G. Diau, and Ahmed H. Zewail</i>	
3.1	Introduction	97
3.2	Experimental	97
3.3	Tetramethylene, Trimethylene, and the Constrained Diradical[6]	99

3.3.1	Theoretical: PES and Reaction Pathways	99
3.3.2	Tetramethylene: Dynamical Time Scales and Stereochemistry	101
3.3.3	The Constrained Diradical and Trimethylene	104
3.3.4	PES, IVR, and Entropy Effects	104
3.4	Diradicals as Intermediates in Norrish Type-II Reactions	106
3.5	Conclusion	111
<b>4</b>	<b>The Coulomb Explosion Imaging Method and Excited-State Proton-Transfer Reactions</b>	<b>113</b>
	<i>Eric S. Wisniewski, Jason R. Stairs, Daniel E. Folmer, and A. Welford Castleman, Jr.</i>	
4.1	Introduction	113
4.2	Experimental Techniques	116
4.2.1	Femtosecond Laser System and Amplification	116
4.2.2	Pump-Probe and Coulomb Explosion Imaging	116
4.3	Results and Discussion	117
4.3.1	Coulomb Explosion Imaging Method	117
4.3.2	Hydration of 7-Azaindole	125
4.4	Conclusions	129
<b>5</b>	<b>Femtosecond Dynamics at Conical Intersections</b>	<b>133</b>
	<i>Wolfgang Domcke</i>	
5.1	Introduction	133
5.2	Modeling of Conical Intersections	135
5.3	Time-Dependent Quantum Wave-Packet and Reduced-Density-Matrix Dynamics	138
5.4	Aspects of Ultrafast Dynamics at Conical Intersections	139
<b>6</b>	<b>Femtosecond Spectroscopy of Molecular Caging: Quantum and Classical Approaches</b>	<b>147</b>
	<i>Vladimir A. Ermoshin, Volker Engel, and Christoph Meier</i>	
6.1	Introduction	147
6.2	Quantum Treatment	148
6.3	Classical Treatment	150
6.4	I <sub>2</sub> /Ar Caging	150
6.5	Summary	153
<b>7</b>	<b>Ultrafast Geometrical Relaxation in Polydiacetylene Induced by Sub-5-fs Pulses</b>	<b>155</b>
	<i>Takayoshi Kobayashi</i>	
7.1	Introduction	155
7.2	Experimental	156

7.3	Results and Discussion	157
7.4	Conclusion	166
<b>8</b>	<b>Ultrafast Probing and Control of Molecular Dynamics: Beyond the Pump-Probe Method</b>	<b>169</b>
	<i>Marcos Dantus</i>	
8.1	Introduction	169
8.2	Four-Wave Mixing Techniques	170
8.2.1	Differences Between the Pump-Probe Method and Four-Wave Mixing	170
8.2.2	Off-Resonance FWM	171
8.2.3	On-Resonance FWM	172
8.2.3.1	Controlling Ground or Excited-State Observation	173
8.2.3.2	Inhomogeneous Broadening and Photon-Echo Measurements	174
8.3	Experimental Methods	175
8.4	Results	177
8.4.1	Off-Resonance Measurements	178
8.4.2	Resonance Measurements	179
8.4.3	Coherent Control with FWM	182
8.5	Discussion	183
8.5.1	Off-Resonance FWM and Time-Resolved Measurements of Ground-State Dynamics	183
8.5.2	Resonance FWM, Ground and Excited-State Dynamics	184
<b>9</b>	<b>Quantum Control of Ultrafast Laser-Driven Isomerization Reactions: Proton Transfer and Selective Preparation Of Enantiomers</b>	<b>189</b>
	<i>Nadja Došlić, Yuichi Fujimura, Leticia González, Kunihito Hoki, Dominik Kröner, Oliver Kühn, Jörn Manz, and Yuki Yoshi Ohtsuki</i>	
9.1	Introduction	189
9.2	Laser Preparation of Pure Enantiomers	190
9.3	Proton Transfer	193
9.4	Conclusions	197
<b>10</b>	<b>Controlling the Vibration and Dissociation Dynamics in Small Molecules and Clusters</b>	<b>199</b>
	<i>Štefan Vajda and Ludger Wöste</i>	
10.1	Introduction	199
10.2	The Choice of the Molecular Systems	200
10.3	Experimental Set-Up	204
10.3.1	Molecular Beam and Laser Systems	204
10.3.2	Pulse Shaping	205
10.3.2.1	Simple Pulse Shaping: Generation of Linearly Chirped Pulses	205
10.3.2.2	Active Feedback Optimization: Search for System-Specific Tailor-Made Pulses	205

10.4	Experimental Results and Discussion	205
10.4.1	Na <sub>3</sub>	205
10.4.2	Na <sub>2</sub> K	206
10.4.3	CpMn(CO) <sub>3</sub>	212
10.5	Summary	214
<b>11</b>	<b>Two-Dimensional Optical Nonlinear Spectroscopy in Liquids</b>	<b>217</b>
	<i>Keisuke Tominaga and Hiroaki Maekawa</i>	
11.1	Introduction	217
11.2	Calculation of the Two-Dimensional Spectrum	219
11.3	Two-Dimensional Spectrum	221
<b>12</b>	<b>Femtosecond Diffuse Reflectance Spectroscopy and Photochemistry of Organic Microcrystals</b>	<b>225</b>
	<i>Hiroshi Masuhara, Tsuyoshi Asahi, and Akihiro Furube</i>	
12.1	Introduction	225
12.2	System and Analysis	226
12.2.1	Femtosecond Diffuse Reflectance Spectroscopic System	226
12.2.2	Time-Dependent Kubelka–Munk Model	227
12.2.3	Temporal Characteristics and Time Resolution	229
12.3	Ultrafast Processes in Some Organic Powders	231
12.3.1	Excited Electronic Structure and Dynamics of Weak CT Microcrystals	231
12.3.2	Charge Recombination Process of Molecules Adsorbed in Zeolites	233
12.3.3	Intersystem Crossing in an Acridine Microcrystal	234
12.4	Future Perspectives	236
12.4.1	Femtosecond Absorption Spectroscopy of a Single Microcrystal	236
12.4.2	Femtosecond Light-Scattering Spectroscopy	236
12.4.3	Femtosecond Cooperative Photochromic Reaction in Organic Crystals	237
<b>13</b>	<b>Impurity Rydberg States as Probes of Local Dynamics in the Condensed Phase</b>	<b>239</b>
	<i>Franco Vigliotti and Majed Chergui</i>	
13.1	Introduction	239
13.2	Steady-State Spectroscopy	240
13.3	Time-Resolved Spectroscopy	244
13.3.1	NO in Solid Ar	244
13.3.2	NO in Solid Ne	245
13.3.3	NO in Solid Hydrogen	246
13.4	Discussion	248
13.4.1	Inertial Response ( $t < 200$ fs)	248
13.4.2	Relaxation Process ( $200$ fs $< t < 3$ ps)	250
13.5	Concluding Remarks	250

<b>14</b>	<b>Photoelectron Spectroscopy as a Probe for Investigating Chemical Dynamics</b>	<b>253</b>
	<i>Ingo Fischer</i>	
14.1	Introduction	253
14.2	The Concept	253
14.3	Molecular Photophysics	256
14.4	Monitoring Wavepacket Dynamics by ZEKE and PE Spectroscopy	259
14.5	Intensity Effects in ZEKE and Photoelectron Spectra	261
14.6	Probing Chemical Dynamics by Photoelectron and ZEKE Spectroscopy in the Frequency Domain	262
14.7	New Directions	263
<b>15</b>	<b>Femtochemistry in Nanocavities</b>	<b>267</b>
	<i>Abderrazzak Douhal</i>	
15.1	Introduction	267
15.2	Concept of Femtochemistry in Nanocavities	268
15.3	I–I Bond Breaking and Remaking in a Molecular Nanocavity	269
15.4	Intramolecular H-Bond Breaking and Making and Related Reactions in Nanocavities	273
15.5	Concluding Remarks	277
<b>16</b>	<b>Energy- and Angle-Resolved Femtosecond Photoelectron Spectra from Rotating Molecules</b>	<b>281</b>
	<i>Yasuki Arasaki, Kazuo Takatsuka, Kwanghsi Wang, and Vincent McKoy</i>	
	Abstract	281
16.1	Introduction	281
16.2	Pump-Probe Photoelectron Spectroscopy and Molecular Rotation	282
16.2.1	Formulation	282
16.2.2	Molecular Rotation	286
16.3	Photoelectron Distribution from Rotating Molecules	288
16.3.1	Vibrational Wave Packets	288
16.3.2	Photoelectrons from a Rigid Rotor	288
16.3.3	Convolution of Molecular Vibration and Rotation	289
16.4	Concluding Remarks	292
<b>17</b>	<b>Femtosecond Time-Resolved Fluorescence and Anisotropy Decay Spectroscopy of a Dendrimer with Eight Chromophores at the Rim</b>	<b>295</b>
	<i>Gerd Schweitzer, Gino De Belder, Sven Jordens, Marc Lor, Klaus Müllen, Andreas Herrmann, and Frans C. De Schryver</i>	
17.1	Introduction	295
17.2	Experimental Section	297
17.3	Results and Discussion	298

17.3.1	Steady-State Spectroscopy	298
17.3.2	Fluorescence Decays	299
17.3.3	Anisotropy Decays	303
17.4	Conclusions	305
<b>18</b>	<b>Excited-State Dynamics of Conjugated Polymers and Oligomers</b>	<b>307</b>
	<i>Jean-Yves Bigot, Thierry Barisien</i>	
18.1	Introduction	307
18.2	Femtosecond Dynamics of a Polydiacetylene Backbone	309
18.2.1	Photon Echoes and Wavepacket Dynamics of pDCH	309
18.2.2	Structural Relaxation of a Model Polydiacetylene Chain: Ab initio Calculations of the Potential Surfaces	312
18.3	Femtosecond Gain Dynamics in Phenylene-Vinylene Pentamers	314
18.3.1	Amplified Spontaneous Emission of Phenylene-Vinylene Pentamers	314
18.3.2	The Influence of Structural Disorder on the Femtosecond Gain Dynamics	317
18.4	Conclusions	318
<b>19</b>	<b>Excited-State Intramolecular Proton Transfer (ESIPT) and Energy Relaxation Processes in Hydroxyphenylbenzotriazole Derivatives: A Femtosecond Laser Study</b>	<b>323</b>
	<i>Thierry Fournier, Stanislas Pommeret, Jean-Claude Mialocq, and Anré Deflandre</i>	
19.1	Introduction	323
19.2	Experimental Section	324
19.2.1	Chemicals	324
19.2.2	Steady-State Spectroscopy	325
19.2.3	Femtosecond Time-Resolved Spectroscopy	325
19.3	Results	326
19.3.1	Steady-State Spectroscopy	327
19.3.2	Femtosecond UV/vis Absorption and Gain Spectra	328
19.4	Discussion	331
19.5	Conclusion	332
<b>20</b>	<b>Direct Detection of the Charge-Shift Reaction in Aromatic Vinyl Polymers by means of Transient Absorption and Dichroism Measurements</b>	<b>335</b>
	<i>Hiroshi Miyasaka, Takao Moriyama, Sazzadur R. Khan, and Akira Itaya</i>	
20.1	Introduction	335
20.2	Dynamic Behavior in Solid Amorphous Systems	335
20.3	Direct Detection of Charge-Shift Reactions in Aromatic Vinyl Polymers in the Solution Phase	339
20.4	Summary	343

<b>21</b>	<b>Femtosecond Chemical Events of Intramolecular Charge Transfer and Intermolecular Hydrogen Bond Breaking after Electronic Excitation: Structural Dynamics in the Condensed Phase</b>	<b>345</b>
	<i>Erik T. J. Nibbering and Jens Dreyer</i>	
21.1	Introduction	345
21.2	Structural Information on Transient States: Comparison of Vibrational Spectra with Ab initio CASSCF Calculations	347
21.3	Structural Information on Hydrogen Bonds after Electronic Excitation: Local Femtosecond Dynamics and Comparison of Vibrational Spectra with Line-Shape Theory	350
21.3.1	Ultrafast Response of Hydrogen-Bonded Complexes after Electronic Excitation of One of the Constituents	350
21.3.2	Transient IR Spectroscopy of the Phenol Dimer after Release from Optically Excited Coumarin-102: Structural Dynamics	352
21.3.3	Theory of Absorption Line Shapes of Vibrational Modes Subject to Hydrogen Bonding	353
21.3.3.1	Semi-Classical Brownian Oscillator Model Based on the Robertson–Yarwood (RY) Approach	354
21.3.3.2	Indirectly Damped Quantum Oscillator Model by Henri-Rousseau (HR)	356
21.3.3.3	Directly Damped Quantum Oscillator Model by Rösch and Ratner (RR)	357
21.3.4	Inspection of the O–H Stretch Line Shape of the Phenol Dimer with Line-Shape Theories	357
21.3.4.1	The O–H Stretch Line Shape of the Phenol Dimer at Equilibrium: Comparison of Gas-Phase and Condensed-Phase Data	357
21.3.4.2	The O–H Stretching Line Shape of the Rearranging Phenol Dimer	361
21.4	Conclusions and Prospects	361
<b>22</b>	<b>Vibrational Coherence in Electron Donor–Acceptor Complexes: Assignment of the Oscillatory Mode</b>	<b>367</b>
	<i>Igor V. Rubtsov and Keitaro Yoshihara</i>	
22.1	Introduction	367
22.2	Experimental	369
22.3	Results and Discussion	370
22.3.1	Oscillations in the TCNE–HMB Complex	370
22.3.2	Peak-Shift of the Fluorescence Spectrum	372
22.3.3	Modulation of the Mean Transition Moment by the Vibration	374
22.3.4	Assignment of the Oscillatory Modes	375
22.3.4.1	Complexes of TCNE with Different Donors in Various Solvent	375
22.3.4.2	Vibrations of TCNE and TCNE–	376
22.3.4.3	Oscillations in the Complexes with Fluoranyl and Chloranyl as Acceptors	378



<b>23</b>	<b>Femtosecond Studies of the Initial Events in the Photocycle of Photoactive Yellow Protein (PYP)</b>	<b>381</b>
	<i>Matthew A. Horn, Julie A. Gruetzmacher, Jeongho Kim, Seung-Eng Choi, Spencer M. Anderson, Keith Moffat, and Norbert F. Scherer</i>	
23.1	Introduction	381
23.2	Methods	382
23.2.1	Molecular Dynamics Simulations	382
23.2.2	Femtosecond Spectroscopy	382
23.2.3	Sample	383
23.3	Results	383
23.3.1	Pump-Probe Measurements	383
23.3.2	Anisotropy	384
23.3.3	Molecular Dynamics Simulations	385
23.4	Discussion	385
23.4.1	Energetics	385
23.4.2	Isomerization	385
23.4.3	Anisotropy	387
23.5	Conclusions	388
 <b>24</b>	 <b>Elementary Reactions in the Condensed Phase: Bond Breaking, Isomerization, and Electron Transfer</b>	 <b>391</b>
	<i>Eva Åkesson, Alexander N. Tarnovsky, Gabor Benkő, Arkady Yartsev, and Villy Sundström</i>	
24.1	Introduction	391
24.2	Bond Breaking and Isomerization in Solution	391
24.2.1	Photodissociation of Dihalomethanes	391
24.2.2	Barrierless Isomerization in Solution	393
24.3	Electron-Transfer in Dye-Sensitized Titanium Dioxide	395
 <b>25</b>	 <b>Primary Processes in Photosynthesis Studied by Femtosecond Nonlinear Spectroscopy</b>	 <b>399</b>
	<i>Jante M. Salverda and Rienk van Grondelle</i>	
25.1	Introduction	399
25.2	The Three-Pulse Echo Peak Shift and Transient Grating Methods	400
25.3	The 3PEPS/TG Experiment	403
25.4	Simulations	404
25.5	The B800 Ring of the Purple Bacterial Antenna LH2	406
25.6	The Bacterial Antenna LH1 and its Dimeric Subunit B820	409
25.7	The Accessory Bacteriochlorophylls of the Bacterial Reaction Center	411
25.8	Concluding Remarks	414

**26 Femtosecond Studies of Intramolecular Bond Twisting in Solution 417**

*Max Glasbeek, Hong Zhang, Pascale Changuenet, Pascal Plaza,  
Monique M. Martin,  
Wolfgang Rettig*

- 26.1 Introduction 417
- 26.2 Experimental 419
- 26.3 Results and Discussion 419
  - 26.3.1 Auramine 419
  - 26.3.1 (a) Transient Absorption 420
  - 26.3.1 (b) Fluorescence Up-Conversion 421
  - 26.3.2 Ionic Styryl Dyes 424
- 26.4 Conclusion 429

**Index 431**

## Preface

Femtochemistry has become a well-established field of science and its importance has been recognized by awarding Ahmed Zewail, who pioneered this area of research, with the 1999 Nobel Prize in Chemistry.

This book is a reflection of the contributions presented at the Femtochemistry IV conference, held in Leuven, Belgium, from July 18 to 22, 1999. Over 200 participants gathered from all over the world to discuss a wide range of areas in the field of Femtochemistry and to explore physical, biological and chemical phenomena on the femtosecond time scale.

In chapter one, Ahmed Zewail gives a chronological overview of his journey to the ultrafast “femtoland” from a personal point of view and gives a survey of Femtochemistry and the scope of its applications. The diversity of this field is further exemplified by 26 chapters covering topics ranging from theory, gas phase and molecular beam, mesoscopic phase and condensed phase dynamics. Furthermore, ultrafast laser chemistry was shown to be able not only to catch the ultrafast dynamics but also to control ultrafast events.

The editors wish to dedicate this book to the memory of the late Kent R. Wilson who although already undermined by the illness which took him away from the community a few months later, presented an outstanding contribution during the symposium which all participants will remember as a scientific legacy.

We are grateful to all authors which provided excellent contributions. We are grateful to F.W.O. Vlaanderen, Acros Organics and Spectra-Physics who co-sponsored the conference. Finally, we owe thanks to Peter Biel from Wiley-VCH Verlag GmbH for his patience and constructive help.

Leuven, June 2001

Frans C. De Schryver  
Steven De Feyter  
Gerd Schweitzer

## List of Contributors

***Eva Åkesson***

Department of Chemical Physics  
Chemical Center  
Lund University  
Box 124  
S-221 00 Lund  
Sweden

***Spencer M. Anderson***

Department of Biochemistry and Molecular  
Biology  
University of Chicago  
920 East 58<sup>th</sup> Street  
Chicago, IL 60637  
U.S.A.

***Yasuki Arasaki***

Department of Basic Science  
Graduate School of Arts and Sciences  
University of Tokyo  
Komaba  
Tokyo 153-8902  
Japan

***Tsuyoshi Asahi***

Department of Applied Physics  
Osaka University  
2-1 Yamada oka  
Suita 565-0871  
Japan

***Thierry Barisien***

Institut de Physique et Chimie des Matériaux  
de Strasbourg  
Groupe d'Optique Nonlinéaire et d'Opto-  
électronique  
Unité Mixte 7504 CNRS-ULP  
23, rue du Loess, B. P. 20CR  
F-67037 Strasbourg  
France

***Gabor Benkö***

Department of Chemical Physics  
Chemical Center  
Lund University  
Box 124  
S-221 00 Lund  
Sweden

***Jean-Yves Bigot***

Institut de Physique et Chimie des Matériaux  
de Strasbourg  
Groupe d'Optique Nonlinéaire et d'Opto-  
électronique  
Unité Mixte 7504 CNRS-ULP  
23, rue du Loess, B. P. 20CR  
F-67037 Strasbourg  
France

***A. Welford Castleman, Jr.***

Department of Chemistry and Physics  
Pennsylvania State University  
University Park  
Philadelphia, PA 16803  
U.S.A.

***Pascale Changenet***

Laboratoire de Photophysique Moléculaire du  
CNRS (UPR3361)  
Bâtiment 210  
Université Paris-Sud  
F-91405 Orsay Cedex  
France

***Majed Chergui***

Institut de Physique de la Matière Condensée  
Université de Lausanne  
CH-1015 Lausanne-Dorigny  
Switzerland

**Seung Eng Choi**

Department of Chemistry and the James Franck Institute  
University of Chicago  
5735 South Ellis Avenue  
Chicago, IL 60637  
U.S.A.

**Marcos Dantus**

Department of Chemistry and Center for Fundamental Materials Research  
Michigan State University  
58 Chemistry Building  
East Lansing, MI 48824–1322  
U.S.A.

**Gino De Belder**

Department of Chemistry  
Katholieke Universiteit Leuven  
Celestijnenlaan 200 F  
B-3001 Heverlee  
Belgium

**Steven De Feyter**

Department of Chemistry  
Katholieke Universiteit Leuven  
Celestijnenlaan 200 F  
B-3001 Heverlee  
Belgium

**André Deflandre**

L'ORÉAL  
1 Avenue Eugène-Schueller  
F-93601 Aulnay-sous-Bois Cedex  
France

**Frans C. De Schryver**

Department of Chemistry  
Katholieke Universiteit Leuven  
Celestijnenlaan 200 F  
B-3001 Heverlee  
Belgium

**Eric W.-G. Diau**

Arthur Amos Noyes Laboratory of Chemical Physics  
California Institute of Technology  
Pasadena, CA 91125  
U.S.A.

**Wolfgang Domcke**

Institut für Theoretische Chemie  
Heinrich Heine Universität  
Geb. 26.32 Ebene 0.3  
Universitätsstrasse 1  
D-40225 Düsseldorf  
Germany

**Nadja Došlić**

Ruder Bošković Institute  
Bijenčka cesta 54  
P.O.B. 108  
10002 Zagreb  
Croatia

**Abderrazzak Douhal**

Departamento de Química Física  
Facultad de Ciencias del Medio Ambiente  
Campus Tecnológica de Toledo  
Universidad de Castilla-La-Mancha  
Avenida Carlos III, SN  
E-45071 Toledo  
Spain

**Jens Dreyer**

Max-Born-Institut für Nichtlineare Optik und Kurzzeitspektroskopie  
Max-Born-Strasse 2A  
D-12489 Berlin  
Germany

**Volker Engel**

Institut für Physikalische Chemie  
Universität Würzburg  
Am Hubland  
D-97074 Würzburg  
Germany

**Vladimir A. Ermoshin**

Institut für Physikalische Chemie  
Universität Würzburg  
Am Hubland  
D-97074 Würzburg  
Germany

**Ingo Fischer**

Institut für Physikalische Chemie  
Universität Würzburg  
Am Hubland  
D-97074 Würzburg  
Germany

**Daniel E. Folmer**

Department of Chemistry  
 Pennsylvania State University  
 University Park  
 Philadelphia, PA 16803  
 U.S.A.

**Thierry Fournier**

CEA/Saclay  
 DSM/DRECAM/SCM-URA 331 CNRS  
 Bâtiment 546  
 F-91191 Gif-sur-Yvette  
 France

**Yuichi Fujimura**

Graduate School of Science  
 Tohoku University  
 Sendai 980-8578  
 Japan

**Akihiro Furube**

Department of Applied Physics  
 Osaka University  
 2-1 Yamada oka  
 Suita 565-0871  
 Japan

**Max Glasbeek**

Laboratory for Physical Chemistry  
 University of Amsterdam  
 Nieuwe Achtergracht 129  
 NL-1018 WS Amsterdam  
 The Netherlands

**Leticia González**

Institut für Chemie, Physikalische und  
 Theoretische Chemie  
 Freie Universität Berlin  
 Takustrasse 3  
 D-14195 Berlin  
 Germany

**Julie A. Gruetzmacher**

Department of Chemistry and the James Franck  
 Institute  
 University of Chicago  
 5735 South Ellis Avenue  
 Chicago  
 IL 60637  
 U.S.A.

**Andreas Herrmann**

Max-Planck-Institut für Polymerforschung  
 Ackermannweg 10  
 D-55128 Mainz  
 Germany

**Kunihito Hoki**

Graduate School of Science  
 Tohoku University  
 Sendai 980-8578  
 Japan

**Matthew A. Horn**

Department of Chemistry and the James Franck  
 Institute  
 University of Chicago  
 5735 South Ellis Avenue  
 Chicago, IL 60637  
 U.S.A.

**James T. Hynes**

Department of Chemistry and Biochemistry  
 University of Colorado  
 Campus Bos 215  
 Boulder, CO 803909-0215  
 U.S.A.

**Akira Itaya**

Department of Polymer Science and Engineering  
 Kyoto Institute of Technology  
 Matsugasaki  
 Kyoto 606  
 Japan

**Sven Jordens**

Department of Chemistry  
 Katholieke Universiteit Leuven  
 Celestijnenlaan 200 F  
 B-3001 Heverlee  
 Belgium

**Sazzadur R. Khan**

Department of Polymer Science and Engineering  
 Kyoto Institute of Technology  
 Matsugasaki  
 Kyoto 606  
 Japan

**Philip M. Kiefer**

Department of Chemistry and Biochemistry  
 University of Colorado  
 Campus Bos 215  
 Boulder, CO 803909-0215  
 U.S.A.

**Jeongho Kim**

Department of Chemistry and the James Franck  
 Institute  
 University of Chicago  
 5735 South Ellis Avenue  
 Chicago, IL 60637  
 U.S.A.

**Takayoshi Kobayashi**

Department of Physics  
University of Tokyo  
7-3-1 Hongo  
Bunkyo-ku  
Tokyo 113-0033  
Japan

**Dominik Kröner**

Institut für Chemie, Physikalische und  
Theoretische Chemie  
Freie Universität Berlin  
Takustrasse 3  
D-14195 Berlin  
Germany

**Oliver Kühn**

Institut für Chemie, Physikalische und  
Theoretische Chemie  
Freie Universität Berlin  
Takustrasse 3  
D-14195 Berlin  
Germany

**Marc Lor**

Department of Chemistry  
Katholieke Universiteit Leuven  
Celestijnenlaan 200 F  
B-3001 Heverlee  
Belgium

**Jörn Manz**

Institut für Chemie, Physikalische und  
Theoretische Chemie  
Freie Universität Berlin  
Takustrasse 3  
D-14195 Berlin  
Germany

**Hiroaki Maekawa**

Department of Chemistry  
Faculty of Science  
Kobe University  
Nada  
Kobe 657-8501  
Japan

**Monique M. Martin**

Laboratoire de Photophysique Moléculaire du  
CNRS (UPR3361)  
Bâtiment 210  
Université Paris-Sud  
F-91405 Orsay Cedex  
France

**Hiroshi Masuhara**

Department of Applied Physics  
Osaka University  
2-1 Yamada oka  
Suita 565-0871  
Japan

**Vincent McKoy**

Laboratory for Molecular Sciences  
California Institute of Technology  
Pasadena, CA 91125  
U.S.A.

**Christoph Meier**

Laboratoire de Collisions, Agrégats et Réactivité  
IRSAMC  
Université Paul Sabatier  
F-31062 Toulouse  
France

**Jean-Claude Mialocq**

CEA/Saclay  
DSM/DRECAM/SCM-URA 331 CNRS  
Bâtiment 546  
F-91191 Gif-sur-Yvette  
France

**Hiroshi Miyasaka**

Department of Chemistry  
Graduate School of Engineering Science  
Osaka University  
Osaka 560-8535  
Japan

**Keith Moffat**

Department of Biochemistry and Molecular  
Biology  
University of Chicago  
920 East 58<sup>th</sup> Street  
Chicago, IL 60637  
U.S.A.

**Takao Moriyama**

Department of Polymer Science and Engineering  
Kyoto Institute of Technology  
Matsugasaki  
Kyoto 606  
Japan

**Klaus Müllen**

Max-Planck-Institut für Polymerforschung  
Ackermannweg 10  
D-55128 Mainz  
Germany

**Erik T.J. Nibbering**

Max-Born-Institut für Nichtlineare Optik und  
Kurzzeitspektroskopie  
Max-Born-Strasse 2A  
D-12489 Berlin  
Germany

**Yukiyoshi Ohtsuki**

Graduate School of Science  
Tohoku University  
Sendai 980-8578  
Japan

**Pascal Plaza**

Laboratoire de Photophysique Moléculaire du  
CNRS (UPR3361)  
Bâtiment 210  
Université Paris-Sud  
F-91405 Orsay Cedex  
France

**Stanislas Pommeret**

CEA/Saclay  
DSM/DRECAM/SCM-URA 331 CNRS  
Bâtiment 546  
F-91191 Gif-sur-Yvette  
France

**Wolfgang Rettig**

Institut für Physikalische und Theoretische  
Chemie  
Humboldt Universität zu Berlin  
Bunsenstrasse 1  
D-10117 Berlin  
Germany

**Igor V. Rubtsov**

SAS  
University of Pennsylvania  
231 S 34 St.  
Philadelphia, PA 19104-6323  
U.S.A.

**Jante M. Salverda**

Department of Biophysics and Physics of Complex  
Systems  
Faculty of Science  
Vrije Universiteit Amsterdam  
De Boelelaan 1081  
NL-1081 HV Amsterdam  
The Netherlands

**Norbert F. Scherer**

University of Chicago  
Department of Chemistry and the James Franck  
Institute  
5735 South Ellis Avenue  
Chicago, IL 60637  
U.S.A.

**Gerd Schweitzer**

Department Chemistry  
Katholieke Universiteit Leuven  
Celestijnenlaan 200 F  
B-3001 Heverlee  
Belgium

**Jason R. Stairs**

Department of Chemistry  
Pennsylvania State University  
University Park  
Philadelphia, PA 16803  
U.S.A.

**Villy Sundström**

Department of Chemical Physics  
Chemical Center  
Lund University  
Box 124  
S-221 00 Lund  
Sweden

**Kazuo Takatsuka**

Department of Basic Science  
Graduate School of Arts and Sciences  
University of Tokyo  
Komaba  
153-8902 Tokyo  
Japan

**Alexander N. Tarnovsky**

Department of Chemical Physics  
Chemical Center  
Lund University  
Box 124  
S-221 00 Lund  
Sweden

**Ward H. Thompson**

Department of Chemistry  
University of Kansas  
Lawrence, KS 66045  
U.S.A.



***Keisuke Tominaga***

Department of Chemistry  
Faculty of Science  
Kobe University  
Nada  
Kobe 657-8501  
Japan

***Stefan Vajda***

Institut für Experimentalphysik  
Freie Universität Berlin  
Arnimallee 14  
D-14195 Berlin  
Germany

***Rienk van Grondelle***

Department of Biophysics and Physics of Complex  
Systems  
Faculty of Science  
Vrije Universiteit Amsterdam  
De Boelelaan 1081  
NL-1081 HV Amsterdam  
The Netherlands

***Franco Vigliotti***

Institut de Physique de la Matière Condensée  
Université de Lausanne  
CH-1015 Lausanne-Dorigny  
Switzerland

***Kwanghsi Wang***

Laboratory for Molecular Sciences  
California Institute of Technology  
Pasadena, CA 91125  
U.S.A.

***Eric S. Wisniewski***

Department of Chemistry  
Pennsylvania State University  
University Park  
Philadelphia, PA 16803  
U.S.A.

***Ludger Wöste***

Institut für Experimentalphysik  
Freie Universität Berlin  
Arnimallee 14  
D-14195 Berlin  
Germany

***Arkady Yartsev***

Department of Chemical Physics  
Chemical Center  
Lund University  
Box 124  
S-221 00 Lund  
Sweden

***Keitaro Yoshihara***

Japan Advanced Institute of Science and  
Technology  
Asahidai 1-1  
Tasunokuchi  
Ishikawa 923-1292  
Japan

***Ahmed H. Zewail***

Arthur Amos Noyes Laboratory of Chemical  
Physics  
California Institute of Technology  
Pasadena, CA 91125  
U.S.A.

***Hong Zhang***

Laboratory for Physical Chemistry  
University of Amsterdam  
Nieuwe Achtergracht 129  
NL-1018 WS Amsterdam  
The Netherlands

## Index

### **a**

ab initio  
  calculation 159, 200, 203 ff  
  quantum chemical  
    calculations 347  
absorption 226 ff  
  coefficient 227 ff  
  decay 232  
AC Stark shift 261  
acetylene 183  
acid base 89, 92  
acid ionization 89  
acridine 234  
activated complex 10, 11, 38  
alkali halide 35  
all-trans retinal 347  
allyl 256 ff  
analysis  
  of molecular dynamics 214  
  of the nuclear dynamics 199  
Anderson localization of light 230  
angular distribution 227 ff  
anharmonicity 156, 220  
anion 231  
anisotropy 295 ff  
  decay 303 ff  
  pump-probe 400, 407  
  TG 408  
antenna, light harvesting 399  
antenna, core see LH1  
antenna, peripheral see LH2  
Arrhenius 10  
ASE see amplified  
  spontaneous emission  
atomic  
  motion 73  
  scale 2

auramine 417, 419  
7-azaindole 113, 115  
azobenzene 347

### **b**

B800 406 ff  
  3peps 407 ff  
  TG 407 ff  
B820 409 ff  
  3peps 409 ff  
  peak shift 409 ff  
B850 406 ff  
bacteriochlorophyll (BChl)  
  406 ff  
  accessory 411 ff  
barrier 10  
  frequency 88  
  – less isomerization 393  
  reaction 38  
benzotriazole, hydroxyphenyl-  
  benzotriazole 324, 331 f  
Bloch equation 44  
blue-phase PDA 156, 157  
bond 267 ff  
  breakage 34  
  breaking 12, 267, 391  
  breaking dynamics 46  
  chemical 1, 4, 66, 267  
  length 162  
  making 12, 43, 267  
  remaking 267  
  – selective chemistry 50  
bridged diphenyl derivatives  
  1-(4'-dimethylaminostyryl)-  
    pyridinium dye 419  
  4-(4'-dimethylaminostyryl)-  
    pyridinium dye 419  
bromiodomethane 392  
bubble 239 ff

### **c**

caging 147 ff, 268, 273, 277  
carrier transport 337  
cascaded signal 177  
CASPT2 312  
CASSCF 312  
cation 231  
caustics 152  
CdI<sub>2</sub> 40  
CEIM 113, 115, 117  
C<sub>3</sub>H<sub>5</sub> see allyl  
charge  
  recombination 232 ff, 336  
  separation 335  
  – shift reaction 335  
  solvent-induced pseudo  
    Jahn-Teller  
      intramolecular 348, 349  
  transport 335  
  twisted intramolecular  
    transfer 88, 348  
charge separation see electron  
  transfer, alternative pathway  
charge separation 399, 413 f  
charge transfer 270  
  absorption band 232  
  complex 234 ff, 335  
  fluorescence band 232  
  intramolecular  
    photoinduced 347  
  microcrystal 230 ff  
  state 348  
  type exciton 159, 164, 312  
CH<sub>3</sub>I see methyl iodide  
chirp 206, 211, 317  
p-chloranil 337  
chloriodomethane 392  
chromophore 295 ff  
cis-trans isomerization 393  
clock 23

- cluster 113, 199 ff
- coherence 1, 5, 8, 17, 19 ff, 25, 44, 58 ff, 66 ff, 72 ff, 170, 196, 313, 401
  - optical 18
  - orientational 62
  - spin 18
  - time 45
  - vibrational 28, 272 f, 275 f
- coherent
  - control 155
  - dynamics 25
  - nuclear motion 38
  - rotational motion 27
  - superposition of states 21
  - superposition of vibrations and rotations 171
- collision 17, 147 ff
- complete active space SCF method 347
- concerted 25, 65, 69 f
- conductivity 307
- configuration interaction 232
- confinement 267
- conical intersection 70, 133
- constrained diradical 97 f, 99, 104 ff
- continuum generation 16
- control 1
  - active 199, 215
  - branching 199, 215
  - coherent 81 ff, 170, 202
  - of matter 70
  - of molecular dynamics 214
  - of the nuclear dynamics 199 ff
  - of the population 200
  - of the population and ionization 204
  - optimal 189
  - phase 21
  - quantum 45, 59, 66, 189
  - wave packet 155
- cooling, vibrational 272 f, 275 f
- correlation
  - auto- 48
  - cross- 48
  - real and complex functions 355
- Coulomb explosion 49, 113 ff
- Imaging Method (CEIM) 113 ff
- coumarin-102 347
  - phenol complexes 347
- coupling
  - anharmonic 353
  - derivative 135
  - dynamic mode 165
  - mode 136
  - vibronic 307 ff
- CpMn(CO) 212 ff
- CpMn(CO)<sub>3</sub> 199 ff
- cross-peak 222
- cyclization 99, 101, 104 ff
- cyclodextrin 268 ff
- d**
  - damping mechanism, indirect 354, 356
  - decay
    - component, fluorescence 300
    - curve, fluorescence 299
    - fluorescence 295 ff
    - free induction 177, 405
    - mono-exponential, fluorescence 302
    - nonradiative 256 ff
    - time, energy – 44
    - time, fluorescence 295, 300
    - triple-exponential fluorescence 296
  - dendrimer 295 ff
    - first-generation 301
    - monochromophoric 301
    - multichromophoric 301
    - second-generation 301
  - Density Functional Theory 99
  - density matrix 20, 35, 46, 170
    - formalism 194
    - reduced 139
  - density of states 44
  - dephasing 20, 22, 35, 44, 69, 156, 174, 194, 245, 310 ff
    - electronic 309
    - intramolecular 22
    - time 44
    - time, rotational 44
    - vibrational 312
  - DFT see Density Functional Theory
  - diabatic, PES 135
  - dichroism signal 336
  - 1,1-diethyl-2,2-cyanine 393
  - 1,1-diethyl-4,4-cyanine 393
  - dihalomethanes 391
  - diiodomethane 392
  - dimer 212 ff
    - phenol 351
    - phenol – transient IR spectroscopy 352
    - phenol, O–H stretch line shape of 358
  - p-dimethylaminobenzonitrile (DMABN) 87 ff, 347
  - dipole–dipole interaction 235
  - diradical 97, 99, 101, 105 ff, 109 ff
  - dissipation 140
  - dissociation 31, 148, 199, 268, 271 f
  - DNA base pair 113, 115, 126
  - donor-acceptor pair 234
  - Doppler broadening 180
  - double-sided Feynman diagram 352
  - dye-sensitized 395
  - dynamics 1, 4 f, 8, 11, 13, 17, 21 f, 24 f, 37, 41, 43, 46, 62, 65 f, 71, 97, 104 ff, 191, 267 ff
    - bond breakage 50
    - bond formation 50
    - chemical 15
    - C=O ligand 346
    - excited-state 307 ff
    - nonadiabatic 134
    - nuclear 34
    - quantum 152
    - remaking 46
    - solvation 350
    - transition state 50
    - vibrational 152
    - wave packet 312
  - e**
    - echo, frequency selective 407 ff
    - electron
      - delocalization 307
      - diffraction 345
      - donor–acceptor complex 367
        - electron interaction 166
        - injection 395
        - phonon interaction 166, 312

transfer 395  
 transfer alternative  
   pathway 412 ff  
 electronic state  
   bound 199 ff  
   coupled state 204  
   excited state 203, 214  
   ground state 199 ff  
   predissociated 199  
 electron transfer,  
   photoinduced 335  
   see also charge transfer  
 emission  
   amplified spontaneous  
     314 ff  
   excimer-like 295, 301  
   local 295  
   spontaneous 20  
 enantiomer 189 ff  
 energy  
   of activation 10  
   redistribution process 197  
   redistribution rate 22  
   transfer 403, 405 ff  
   transfer accessory to P  
     411  
   transfer B800 → B850  
     406 ff  
   transfer between B800s  
     406 ff  
   transfer, dipole–dipole  
     296  
   transfer LH1 409 ff  
 enol 323, 330 f  
 entropy 14, 97, 104 f, 110 f  
 enzymatic reaction 64  
 N-ethylcarbazole 340  
 evolutionary algorithm 199,  
   215  
 excimer 235 ff  
 excited state  
   absorption B850 407 ff  
   absorption P\* 412 ff  
   absorption PYP 383  
   charge transfer 88, 95  
   dynamics 367  
   intramolecular proton  
     transfer (ESIPT) 323  
   reaction 67  
 exciton 312, 318  
   (de)localization 409 ff  
   free 155 f, 158  
   free –,  $2^1 A_g$  state 155  
   self-trapped (STE) 156, 158

**f**  
 feedback  
   loop 200  
   optimization 199, 205  
 femtosecond 323, 331 f  
   diffuse reflectance  
     spectroscopic system  
       226  
   diffuse reflectance  
     spectroscopy 225 ff  
   femtosecond absorption  
     323  
   group velocity dispersion  
     325, 328  
   laser 155, 199 ff  
   light scattering  
     spectroscopy 236  
   mid-infrared spectroscopy  
     346 ff  
   pump-probe 325, 328  
   transition-state  
     spectroscopy 31  
   white-light continuum 325  
 femtosecond, spectroscopy  
   72  
 Fermi-resonance 165  
 flash photolysis 15, 225  
 fluorescence  
   anisotropy 295 ff  
   decay 295 ff  
   decay component 300  
   decay curve 299  
   decay, mono-exponential  
     296, 302  
   decay time 295, 300  
   decay, triple-exponential  
     296  
   depletion 244 ff  
   laser-induced 8  
   quantum yield 298, 327,  
     331  
   quenching 314, 318  
   Rydberg 241 ff  
   time-resolved 399 ff  
   up-conversion 295 ff, 367,  
     417, 421  
 Förster Radius 296  
 Förster type process 305  
 force constant 162  
 forward box geometry 177  
 Fourier power spectra 160  
 Fourier transform 165, 260  
 four-wave mixing  
   degenerate 50

on-resonance 172  
 ultrafast 169 ff  
 fragment 199 ff  
 fragmentation 99, 101, 104 ff,  
   200 ff  
   time 203  
 Franck-Condon window  
   150 ff  
 free energy relationship 92  
 frequency  
   correlation 401  
   correlation function 403  
   – domain techniques 262 ff  
   grating 401 ff  
 FROG 206, 211 ff  
 FWM see four-wave mixing

**g**  
 gain, dynamics 314  
 gate  
   function 161  
   width 162, 164  
 Gaussian-98 129  
 geometrical relaxation 155,  
   158 f, 307 ff  
 g-factor 303  
 global analysis 303 f  
 grating scattering 351  
 Grote-Hynes (GH) theory  
   88 f, 91  
 ground-state reaction 67  
 group delay 157  
 group velocity dispersion  
   317  
 guest 268, 270, 273, 276 f

**h**  
 H<sub>2</sub>POSH 190  
 half-width 161  
 Hammond's postulate 13  
 Hanning-type window  
   function 165  
 harmonic approximation  
   240 ff  
 HgI<sub>2</sub> 178  
 hole migration 335  
 hole transfer 338  
 hole-shift 338  
 hopping 338  
 host 268, 270, 276  
 human serum albumin 63  
 hydration 125 ff  
 hydrochloric acid (HCl) 89,  
   92

hydrogen bond 92 ff, 273, 323  
 cleavage 350  
 dynamics 352  
 intramolecular 273  
 linear spectral line shapes  
 of 353 ff  
 molecular dynamics  
 simulation 383  
 weakening of O–H bond  
 and accompanying red-  
 shift 358  
 hydrogen bonding 346 ff  
 hydrogen-bonded complexes  
 350  
 hydronium ion 92  
 2-(2'-hydroxyphenyl)benzo-  
 thiazole 346

**i**

ICl 40  
 ICN 31, 346  
 IHgI 38  
 infrared  
 excitation 67  
 photon echo 362  
 spectroscopy, nonlinear  
 techniques 362  
 spectroscopy, two-  
 dimensional pump-  
 probe 362  
 transition 196  
 inhomogeneous broadening  
 174  
 inhomogeneous transition  
 21  
 instantaneous frequency  
 161 f, 164  
 instrument response  
 function 298  
 intensity effects 261  
 interchain thermalization  
 158 f  
 intermediate 12 f, 41, 43, 66  
 internal conversion 133, 158  
 internal vibrational relaxation  
 308  
 intersystem crossing 234 ff  
 inertial response 248 ff  
 intramolecular  
 electronic-states coupling  
 44  
 hydrogen bond 273  
 intramolecular vibrational  
 relaxation 229 ff

intramolecular vibrational-  
 energy redistribution  
 (IVR) 23, 25, 32, 44, 59, 97,  
 105 f, 259, 275, 295 ff, 367,  
 392  
 nonchaotic 44  
 iodine 259 ff, 267 ff  
 ion fragmentation 109  
 ion yield 210 ff  
 ion-electron coincidence  
 ionization 49  
 ionic styryl dye 417, 424  
 ionization 206, 209 ff, 253  
 cross section 254 ff  
 multi-photon 200  
 isomerization 27, 137, 189,  
 267  
 PYP 381 ff  
 isotope effect 70  
 kinetic 92  
 isotropic polarizability,  
 instantaneous 178  
 isotropic susceptibility 178  
 IVR see intramolecular  
 vibrational-energy redistri-  
 bution

**k**

keto 323 f, 330 ff  
 keto-enol tautomerism 323  
 Kramers theory 88 f  
 Kubelka-Munk theory 225 ff  
 Kubo relaxation 44

**l**

ladder diagram 182  
 ladder-polymer 156  
 laser-selective chemistry 23  
 LH1 409 ff  
 3peps 409 ff  
 peak shift 409 ff  
 structure 409  
 LH2 406 ff  
 3peps 407 ff  
 structure 406  
 TG 407 ff  
 ligand, CO 202 ff  
 light emitting device, organic  
 314  
 light energy conversion 395  
 light harvesting 395  
 light scattering medium  
 228 ff  
 Liouville pathways 185

locally excited state 232  
 luminescent solar  
 concentrator 20

**m**

macromolecular system  
 295  
 main chain 166  
 mass spectrum 208  
 McLafferty rearrangement  
 110  
 metallocarbonyl compounds  
 346  
 methyl iodide 262 ff  
 microcrystal 234 ff  
 mode  
 accepting 141  
 C–C stretching 158 f, 161 f,  
 165 f  
 C=C stretching 158, 161 f,  
 165 f  
 C≡C stretching 158, 161 f  
 coupling – 136  
 in-plane bending 166  
 out-of-plane bending 156  
 selective chemistry 51  
 spectator 346  
 stretching 156 f  
 torsional 27, 141  
 tuning 136  
 vibrational 11, 105, 272  
 model  
 Brownian oscillator 404 ff  
 configuration coordinate  
 240 ff  
 cooperative photochemical  
 237  
 directly damped  
 oscillator – 354, 357 ff  
 Henri-Rousseau 354,  
 356 ff  
 indirectly damped quantum  
 oscillator 354, 356 ff  
 indirectly damped semi-  
 classical Brownian  
 oscillat 354 ff  
 Landau-Zener 133  
 Robertson-Yarwood 354 ff  
 Rösch-Ratner 354, 357 ff  
 simulations with Brownian  
 oscillator – 408  
 time-dependent Kubelka-  
 Munk 227 ff  
 molecular

beam 8, 99, 204  
 dynamics simulation 244 ff  
 dynamics simulation, PYP  
 381, 386, 388  
 reaction dynamics 11  
 vibration 156  
 molecule, partial roation 295  
 motion 267  
 in-plane 268  
 molecular 309, 312 f  
 nuclear 4 f, 24, 35, 65 f,  
 345  
 out-of-plane 268  
 proton 273 f, 276  
 rotational 4  
 twisting 268  
 vibrational 4, 24, 40, 65  
 M(t) 403 ff  
 exponential contribution  
 404 ff  
 gaussian combination  
 404 ff  
 oscillatory contribution  
 404 ff  
 multiplex advantage 256

## **n**

Na<sub>3</sub> 199 ff  
 NaI 31  
 NaK 206 ff  
 Na<sub>2</sub>K 199 ff  
 nanocavity 267 ff  
 nanoparticle 295, 396  
 naphthalene 233  
 NMR 21  
 NO 240 ff  
 nonconcerted 25  
 non-Condon transition 373  
 non-polar media 239 ff  
 non-radiative relaxation 232  
 Norrish type-I reaction 97,  
 99, 106, 109, 111  
 Norrish type-II reaction 97,  
 106

## **o**

off-resonance, four-wave  
 mixing 171 f, 183  
 oligomer  
 conjugated 307 ff  
 conjugated para-phenylene-  
 vinylene 314 ff  
 one-dimensional system 156,  
 158

optical parametric  
 amplification 16  
 amplifier 156  
 amplifier, non-collinear  
 156  
 generator 297  
 optical trapping 236  
 optimization 205, 210, 212  
 oscillation 373  
 spontaneous fluorescence  
 375  
 underdamped 375

## **p**

peak shift 400 ff, 401 ff  
 B820 409 ff  
 colored 408  
 correlation function 371  
 decay 401 ff  
 LH1 409 ff  
 parallel polarization 408  
 perpendicular polarization  
 408  
 3peps see three-pulse echo  
 peak shift  
 perturbation theory 148  
 peryleneimide 295 ff  
 PES see spectroscopy,  
 photoelectron  
 phase 21  
 phase matching 171  
 phenol 351  
 9-phenylanthracene 229 ff  
 Photoactive Yellow Protein  
 381  
 anisotropy 381, 384, 387  
 p-coumaric acid 382 ff  
 dynamics, hydrogen bond  
 381  
 intermediate 382  
 isomerization 381 ff  
 kinetics 381, 383, 386 f  
 molecular dynamics  
 simulation 381 f, 386,  
 388  
 photoisomerization 381,  
 385 ff  
 pump-probe 381 ff  
 rhodopsin 382, 385 ff  
 photochemical  
 dynamics 137  
 funnel 137  
 photochromic reaction 237  
 photocoloration 237  
 photoconductivity 335  
 photodetachment 67  
 photodissociation 189, 202,  
 262 ff, 391  
 photofragmentation 215  
 photoionization 210 ff  
 photoisomerization, PYP  
 381, 385 ff  
 photon echo 20, 174, 309, 351  
 pulse stimulated 177  
 three-pulse 399 ff  
 photophysics 256  
 photoprotection 323  
 photosynthesis 399  
 primary processes in – 399  
 phototaumer 273  
 polarization  
 magic angle 295, 299  
 parallel 303  
 perpendicular 303  
 polarized excitation 336  
 polaron 156, 312  
 polydiacetylene 155, 162, 166  
 polymer  
 aromatic vinyl 335  
 conjugated 156, 307 ff  
 conjugated para-phenylene-  
 vinylene 314 ff  
 conjugated polyacetylene  
 307  
 conjugated polydiacetylene  
 307 ff  
 poly(methyl methacrylate)  
 229 ff  
 poly(N-vinylcarbazole) 335  
 ponderomotive potential 261  
 population  
 dynamics 299  
 probability 139  
 time 401  
 transfer 170  
 trapping 196  
 potential energy surface 11,  
 97, 104 ff, 108, 133, 307, 312  
 potential wells, linearly  
 displaced harmonic 353  
 prompt response 298 f  
 proton  
 motion 273 f, 276  
 transfer 113, 189 ff, 275  
 transfer adiabatic 89 ff, 93  
 transfer ESIPT 324, 330 ff  
 transfer infrared-induced  
 95

- pulse
    - amplitude 199
    - chirped 205, 214
    - downchirped 205 ff
    - linearly chirped 214
    - phase 21, 199, 211 f
    - $\pi$  67
    - probe 214
    - pump 200, 212
    - sequence 209, 212
    - shape 200, 215
    - shaper 199
    - shaping 59, 189, 205
    - tailored 200
    - train 211
    - unchirped 199, 205 ff
  - pump-dump mechanism 191 ff
  - pump-probe 16, 72 f, 113, 116, 169, 200 ff, 236, 309
    - anisotropy 400, 407
    - photoelectron spectra 281
    - photoelectron spectra
      - double-minimum state in  $\text{Na}_2$  282
    - photoelectron spectra
      - energy- and angle-resolved 282
    - photoelectron spectra
      - molecular rotation 282
    - photoelectron spectra
      - photoionization matrix elements 285
    - photoelectron spectra
      - vibrational wave packets 288
    - PYP 381 ff
      - spectroscopy 351
  - purple bacteria 406 ff
    - Rb. sphaeroides* 410 ff
    - Rps. acidophila* 406 ff
    - Rs. molischianum* 406 ff
  - PYP see Photoactive Yellow Protein
  - pyrazine 183
  - pyromellitic dianhydride 230 ff
- q**
- quantum
    - beat 310
    - coherence 23
    - control 45, 59, 66, 189
    - dynamics 152
    - flux function 301
- r**
- racemate 197
  - radiationless transition 44, 134
  - Raman 162
    - Antistokes 159
    - coherent anti-Stokes – scattering 50, 185
    - coherent – scattering 182
    - coherent – spectroscopy 346
    - effect 199
    - resonance – spectroscopy 346
    - simulated – spectroscopy 67
    - Stokes Signal 159
  - rare gas solid 239 ff
  - RC see reaction center
  - reaction
    - all-Carstesian – surface Hamiltonian 193
    - bimolecular 41
    - coordinate 11, 87 ff
    - dynamics 189
    - path 89, 93, 200
    - pathway 99
    - pathways, excited state 346
  - reaction center 399, 411 ff
    - 3peps 412 ff
    - structure 411
    - TG 412 ff
  - recombination 151 ff, 268, 271 f, 393, 396
  - recrossing, transition state 87 f, 91
  - recurrence 37
  - Redfield
    - tensor 139
    - theory 140
  - reduced space 70
  - relaxation 194
  - reorganization energy,
    - internal 372
  - repeat unit 164
  - resonance 38
  - reverse transient grating 177
  - Rice-Ramsperger-Kassel-Marcus 10, 104
  - rotational
    - coherence 37, 183
    - coherence spectroscopy (RSC) 28
    - rotational orientation 67
    - rotational relaxation 340
    - RRKM see Rice-Ramsperger-Kassel-Marcus
    - Rydberg 239 ff
      - absorption 241 ff
      - fluorescence 241 ff
- s**
- scattering coefficient 227 ff
  - scraper 323
  - semiconductor 396
  - sequential 69
  - single microcrystal 236
  - single molecule 69
  - single-photon timing (SPT) 296, 300, 304
  - singlet-singlet annihilation 295 ff
  - site-specific information,
    - techniques for 345 ff
  - six-wave mixing 185
  - $\text{SN}_2$  reaction 87 f
  - snake photon 230
  - $\text{S}^n\text{-S}^1$  absorption 231 ff
  - solid
    - argon 244 ff
    - hydrogen 239 ff
    - neon 245 ff
  - soliton 156, 307
  - solvation 63, 125 ff
    - dynamics 350
  - solvent
    - coordinate 90 ff
    - fluctuations 345
    - polarization 90 f
    - relaxation 345
  - sound wave 249 ff
  - spatial coherence 172
  - spatial resolution 74
  - spectral density 194
  - spectrogram 161 f, 165
  - spectroscopy
    - adiabatic photoelectron 135
    - coherent Raman 346
    - femtosecond diffuse reflectance 225 ff

- femtosecond light scattering 236
- femtosecond mid-infrared 346 ff
- femtosecond transition-state 31
- femtosecond 72
- infrared 346
- infrared, nonlinear techniques 362
- multi photon ionization 200
- nonlinear 399, 414
- nuclear Overhauser effect 174
- optical 2D 217
- photodetachment 49
- photoelectron 253 ff
- photoelectron –, energy-resolved 49
- photoelectron –, time of flight 255 f
- photoelectron –, time-resolved 253 ff
- photoelectron –, two-photon 262 ff
- photoelectron –, ZEKE 49, 255
- pump-probe 202, 351, 399 ff
- real-time 156
- resonance Raman 262, 346
- rotational coherence (RSC) 28
- simulated Raman 67
- two-dimensional (2D) 217
- two-dimensional infrared pump-probe 262
- zero kinetic energy (ZEKE) 253 ff, 255 ff, 259 ff
- spin coating 156
- spin-echo 174
- spironaphthooxazine 237
- state
  - $2^1 A_u$  158 f
  - $1^1 B_u - Fe$  158
  - $1^1 B_u$  158
  - locally-excited 301
  - nonstationary 25
  - saddle-point transition 38
  - selective chemistry 50
  - squeezed 155
  - stationary 25
  - triplet 234
  - vibrational 24
- steady-state absorption 297 f
- stereochemistry 70, 97, 101, 104, 111
- Stokes shift 232, 240 ff
- steady-state 355
- structural
  - change 158
  - dynamics condensed phase 345 ff
- structure
  - acetylene-type 158
  - butatriene-type 158 f
- supersonic beam 22
- surface crossing 133
- suspended latex particle 230
- symmetry,  $1A_g$  159
- synchronization 16
- t**
  - T1 see decay time, energy
  - T2 310
  - Tautomer 118
  - temporal resolution 74
  - p-terphenyl 235
  - 1,2,4,5-tetracyanobenzene 232 ff
  - tetracyanobenzene (TCNB) 335
  - tetramethylene 97, 99, 101, 104 ff
  - TG see transient grating (TG)
  - thermalization 158 f
  - thioacetylacetone 194
  - third-order polarization 171, 219
  - three-pulse echo peak shift (3peps) 400 ff
    - accessory Bchl 412 ff
    - B800 407 ff
    - B820 409 ff
    - experiment 403 ff
    - frequency-selective 412 ff
    - LH1 409 ff
    - LH2 407 ff
    - method 400 ff
    - RC 412 ff
  - TICT 348 f
  - time resolved 210
  - time scale 46
- time-dependent Schrödinger equation 138, 149
- time-dependent self-consistent field 197
- time-of-flight mass spectrometer see TOF-MS
- Ti:sapphire laser 226
- Titanium dioxide 395
- TOF-MS 113, 117, 122
- torsional motion of phenyl groups 417
- trajectory 5, 11, 13, 37, 68, 150 ff
- transfer, hydrogen 109, 189 ff
- transient absorption 417, 420 spectrum 196
- transient grating (TG) 172, 400 ff
  - accessory Bchl 412 ff
  - anisotropy 408
  - B800 407 ff
  - experiment 403 ff
  - frequency-selective 412 ff
  - LH2 411 ff
  - method 400 ff
  - RC 412 ff
- transition dipole moment correlation function 355
- transition state 4 f, 11 ff, 31, 34, 37 f, 45, 61, 65 f, 69 f, 87 ff, 97
  - dynamics 50
  - lifetime 45
  - theory 46
  - theory (TST) 87 ff
- trimer 199 ff
- trimethylene 97, 99, 104 ff
- tunneling , 196
- twisting, motion 268
- twisting dynamics of ionic styryl dye 425
- twisting of phenyl group 417
- two-dimensional, vibrational spectrum 221
- two-dimensional (2D), spectroscopy 217
- u**
  - ultrafast electron diffraction 43, 57, 65 f
  - unbridged diphenyl derivatives 1-(4'-dimethylaminostyryl)-pyridinium dye 419



4-(4'-dimethylaminostyryl)-  
pyridinium dye 419  
uncertainty principle 35, 66,  
74  
UV-photostabilizer 323

**v**

valence bond 92  
van't Hoff 10  
vibrational, band 300  
  coherence 28, 367  
  cooling 272 f, 275 f, 392  
  coordinate 46  
  dynamics 152  
  Hamiltonian 220  
  level 271

mode 11, 105, 272  
redistribution 67  
relaxation 271, 295 ff  
spectroscopy 346 ff  
state 24  
vibronic coupling 133, 159  
virtual-echo 176  
viscosity 249 ff, 395  
Vycol glass 234

**w**

wave function 74  
wave packet 1, 5, 14, 24, 34 f,  
37, 40, 45, 58 f, 61 f, 67, 87,  
92 f, 94 f, 133, 147 ff, 199 ff,  
244, 267

control 155  
dynamics 14, 259 ff, 262 ff  
motion 156, 158 f  
nuclear 155  
  nuclear motion 67  
wave vector 171  
white light continuum 226  
window function 164

**x**

X-ray diffraction 65, 345  
X-ray spectroscopy 345

**z**

zeolite 233 ff  
zero-point energy (ZPE) 90 ff

## 1

# Femtochemistry: Atomic-Scale Dynamics of the Chemical Bond Using Ultrafast Lasers (Nobel Lecture)\*

Ahmed H. Zewail

Over many millennia, humankind has thought to explore phenomena on an ever shorter time scale. In this race against time, femtosecond resolution ( $1\text{ fs}=10^{-15}\text{ s}$ ) is the ultimate achievement for studies of the fundamental dynamics of the chemical bond. Observation of the very act that brings about chemistry—the making and breaking of bonds on their actual time and length scales—is the wellspring of the field of femtochemistry, which is the study of molecular motions in the hitherto unobserved ephemeral transition states of physical, chemical, and biological changes. For molecular dynamics, achieving this atomic-scale resolution using ultrafast lasers as strobes is a triumph, just as X-ray and electron diffraction, and, more recently, STM and NMR spectroscopy, provided that resolution for static molecular structures. On the femtosecond time scale, matter wave packets (particle-type) can be created and their coherent evolution as a single-molecule trajectory can be observed. The field began with simple systems of a few atoms and has reached the realm of the very complex in isolated, mesoscopic, and condensed phases, as well as in biological systems such as proteins and DNA structures. It also offers new possibilities for the control of reactivity and for structural femtochemistry and femtobiology. This anthology gives an overview of the development of the field from a personal perspective, encompassing our research at Caltech and focusing on the evolution of techniques, concepts, and new discoveries.

## 1.1

### Prologue

In the history of human civilization, the measurement of time and recording the order and duration of events in the natural world are among the earliest endeavors that might be classified as science. The development of calendars, which permitted the tracking of yearly flooding of the Nile valley in ancient Egypt and of the seasons for planting and harvesting in Mesopotamia, can be traced to the dawn of written language. Ever since, time has been an important concept<sup>[1]</sup> and is now recognized as one of the two fundamental dimensions in science. The concept of time encapsulates an awareness of its duration and of the passage from past to present to future and surely must have existed from the very beginning with humans search-

\*) Copyright© The Nobel Foundation 2000. We thank the Nobel Foundation, Stockholm, for permission to print this lecture.

ing for the meaning of birth, life, and death and—in some cultures—rebirth or recurrence.

My ancestors contributed to the beginning of the science of time, developing what Neugebauer<sup>[1d]</sup> has described as “the only intelligent calendar which ever existed in human history”. The “Nile Calendar” was an essential part of life as it defined the state of yearly flooding with three seasons, the *Inundation* or *Flooding*, *Planting*, and *Harvesting*, each four months long. A civil year lasting 365 days was ascertained by about 3000 BC or before, based on the average time between arrivals of the flood at Heliopolis, just north of Cairo; nilometers were used in more recent times, and some are still in existence today. By the time of the First Dynasty of United Egypt under Menes in about 3100 BC, the scientists of the land introduced the concept of the “Astronomical Calendar” by observing the event of the heliacal rising of the brilliant star Sothis (or Sirius). Inscribed on the Ivory Tablet, dating from the First Dynasty and now at the University Museum in Philadelphia, were the words, “Sothis Bringer of the Year and of the Inundation”.<sup>[1c]</sup> On the Palermo Stone, the annals of the kings and their time-line of each year’s chief events were documented from pre-dynastic times to the middle of the Fifth Dynasty.<sup>[1a]</sup> Thus, as early as 3100 BC, they recognized a definite natural phenomenon for the accurate timing of the coming flood and recounted the observed reappearance of the star as the New Year Day—real-time observation of daily and yearly events with the zero-of-time being well defined.<sup>1)</sup>

In about 1500 BC, another major contribution to this science was made, the development of sun-clocks, or sundials, using moving shadows (Figure 1.1). Now in Berlin, the sun-clock bearing the name of Thutmose III (or Thothmes after the Egyptian God Thoth of wisdom and enlightenment), who ruled at Thebes from 1447–1501 BC, shows the graduation of hours for daytime measurements. This clock with uneven periods for hours was man-made and transportable. For night time, the water-clock was invented, and the device provided even periods for timing. With these developments, the resolution of time into periods of year, month, day, and hour became known and has now been used for more than three

1) Recognizing the incommensurability of the lunar month and the solar year, they abandoned the lunar month altogether and used a 30-day month. Thus the year is made of 12 months, 30 days each, with 5 feast days at the end of the year. The “Civil Calendar” was therefore 365 days per year and differs from the astronomical calendar of Sothis by approximately a  $1/4$  day every year. The two calendars must coincide at intervals of  $365 \times 4 = 1460$  years, and historians, based on recorded dates of the reappearance of Sothis in dynastic periods, give the four dates for the coincidence of both calendars: 139 AD, 1317 BC, 2773 BC, and 4233 BC ( $+139 - 3 \times 1460 = 4241$  BC). Even though the Egyptians discovered the astronomical calendar,  $365 - 1/4$  days, they decided, pre-

sumably for “bookkeeping”, to use the civil calendar of 365 days per year without leap years. They also divided the day into two periods of 12 hours each for day and night time. The remarkable calendar of years, months, days, and hours was adapted throughout history and formed the basis for the 365.25-day Julian (46 BC, Alexandria school) and 365.2422-day Gregorian (from 1582 AD, Pope Gregory XIII) calendars. In the words of the notable Egyptologist J. H. Breasted,<sup>[1]</sup> “It has thus been in use uninterruptedly over six thousand years.” Many historians regard the date around 4241 BC as the beginning of history itself as it defines the period of written records; anything earlier is prehistory.

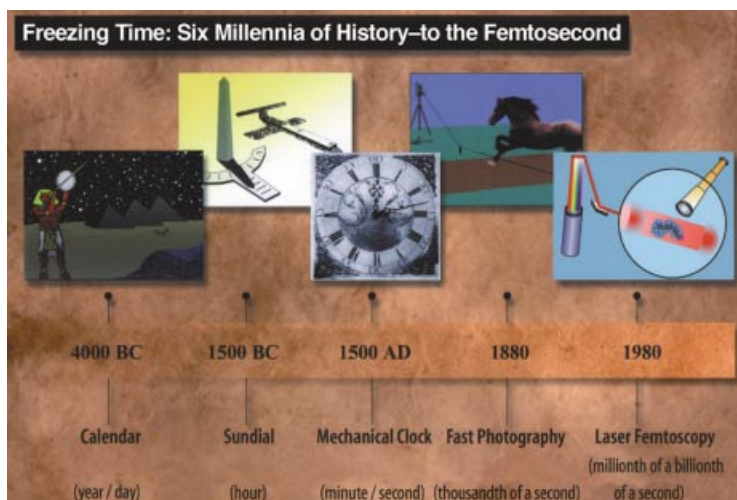


**Fig. 1.1** Timeline of some of the events in the history of the measurement of time, from yearly calendars to the femtosecond regime (see text).

millennia. The durations of minutes and seconds followed, using the Hellenistic sexagesimal system, and this division, according to Neugebauer, “is the result of a Hellenistic modification of an Egyptian practice combined with Babylonian numerical procedures.” About 1300 AD, the mechanical clock<sup>[1g]</sup> was advanced in Europe, ushering in a revolution in precision and miniaturization; Galileo began studies of pendulum motions and their clocking, using his heart beat in seconds, in 1582 AD. Our present time standard is the cesium atomic clock,<sup>2)</sup> which provides precision of about  $1:10^{13}$ , that is, the clock loses or gains one second every 1.6 million years. For this work, Norman Ramsey shared the 1989 Nobel Prize in Physics.

Until 1800 AD, the ability to record the timing of individual steps in any process was essentially limited to time scales amenable to direct sensory perception—for example, the eye’s ability to see the movement of a clock or the ear’s ability to recognize a tone. Anything more fleeting than the blink of an eye (about 0.1 s) or the response of the ear (about 0.1 ms) was simply beyond the realm of inquiry. In the nineteenth century, the technology was to change drastically, resolving time intervals into the sub-second domain. The famous motion pictures by Eadweard Muybridge (1878) of a galloping horse, by Etienne-Jules Marey (1894) of a righting cat, and by Harold Edgerton (mid-1900s) of a bullet passing through an apple and other objects are examples of these developments, with millisecond to microsecond time resolution, using snapshot photography, chronophotography, and stroboscopy, respectively.<sup>[2]</sup> By the 1980s, this resolution became ten orders of magnitude better

2) Since 1967 one second has been defined as the time during which the cesium atom makes exactly 9 192 631 770 oscillations.

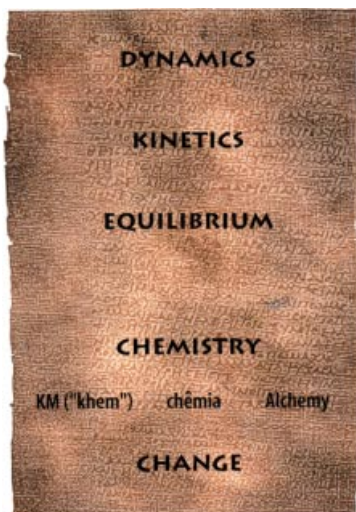


**Fig. 1.2** A picture of a page of the Stockholm papyrus (300 AD) describing the recipe for “making” (actually imitating) emerald, with key concepts overlaid. Note that “change” has been at the heart of chemistry from its millennia-old definition KM, to Chêmia and Alchemy, and to Chemistry (see ref. [B26], and references therein). Equilibrium, kinetics, and dynamics are the foundation for the description of chemical changes.

(see Section 2.2), reaching the femtosecond scale,<sup>3)</sup> the scale for atoms and molecules in motion.

The actual atomic motions involved in chemical reactions had never been observed in real time despite the rich history of chemistry over two millennia,<sup>[3]</sup> as khem became khemia, then alchemy, and eventually chemistry<sup>[3, 4]</sup> (see the Stockholm Papyrus in Figure 1.2). Chemical bonds break, form, or geometrically change with awesome rapidity. Whether in isolation or in any other phase, this ultrafast transformation is a dynamic process involving the mechanical motion of electrons and atomic nuclei. The speed of atomic motion is about  $1 \text{ km s}^{-1}$  and, hence, to record atomic-scale dynamics over a distance of an angström, the average time required is approximately 100 fs. The very act of such atomic motions as reactions unfold and pass through their transition states is the focus of the field of femtochemistry. With femtosecond time resolution we can “freeze” structures far from equilibrium and prior to their vibrational and rotational motions, or reactivity. The pertinent questions about the dynamics of the chemical bond are the following: How does the energy put into a reactant molecule redistribute among the different degrees of freedom, and how fast does this happen? What are the speeds of the chemical changes connecting individual quantum states in the reactants and products? What are the detailed nuclear motions that chart the reaction through its transition states, and how rapid are these motions? As pointed out by Jim Baggott,<sup>[4b]</sup> “the entire history of chemical reaction dynamics and kinetics has been about providing some approximate answers to these three questions.”

3) The prefix milli comes from Latin (and French), micro and nano from Greek, and pico from Spanish. Femto is Scandinavian, the root

of the word for “fifteen”; nuclear physicists call femtometer, the unit for the dimensions of atomic nuclei, fermi. Atto is also Scandinavian.

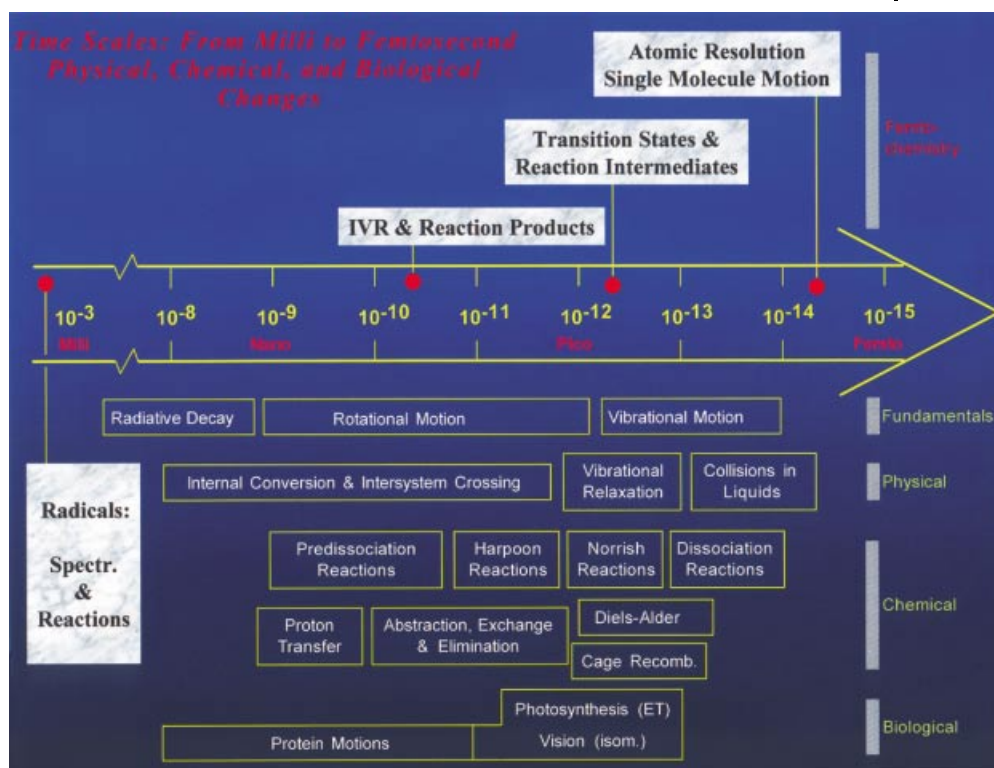


**Fig. 1.3** Time scales and their relevance to physical, chemical, and biological changes. The fundamental limit of the vibrational motion

defines the regime for femtochemistry. Examples are given for each type of change and for each scale.<sup>[B4, B10]</sup>

In femtochemistry, studies of physical, chemical, or biological changes are at the fundamental time scale of molecular vibrations: the actual nuclear motions (Figure 1.3). In this sense, femtosience represents the end of the race against time, or, as the report of ref. [5a] puts it, "... reaching the end of the road". For this same reason, Martens stated,<sup>[5b]</sup> "all chemistry is femtochemistry". The ephemeral transition states, denoted in the past by square brackets ( $[\text{TS}]^\ddagger$ ) for their elusiveness, can now be clocked as a molecular species  $\text{TS}^\ddagger$ . Moreover, on this time scale, the time-dependent description of a coherent, single-molecule trajectory represents the classical nuclear "motion picture" of the reaction as its wave packet proceeds from the initial state, through transition states, and on to final products—the language of the actual dynamics! The femtosecond time scale is unique for the creation of such coherent matter waves on the atomic scale of length, a basic problem rooted in the development of quantum mechanics and the duality of matter. Figure 1.4A highlights some steps made in the description of the duality of light-matter and time scales, and Figure 1.4B shows the importance of coherence for localization (see also Section 1.6).

### A) Matter Waves Particle-type Control & Dynamics

#### de Broglie (1924)

Einstein's light wave/particle

$$E = h\nu \quad E = cp$$

$$\therefore \lambda = h/p$$

Similarly, matter particle/wave

#### Schrödinger (1926)

The Wave Equation – Stationary waves

$$\mathcal{H}\Psi = E\Psi$$

#### Schrödinger (1926)

Micro- to Macromechanics

Quantum to Newton Mechanics

$\Psi$  to wave group

#### Femtochemistry & Quantum Limit ( $h$ ): Particle-type

$$\lambda_{\text{de Broglie}} (\text{initial localization}) = h/p$$

uncertainty in time measurement

$$\Delta x \Delta p \geq h/(2\pi) \quad \Delta t \Delta E \geq h/(2\pi)$$

for force free

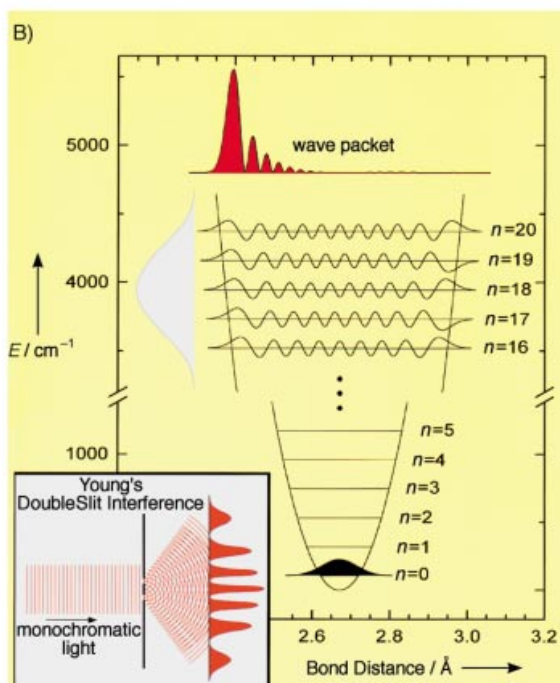
$$\Delta x = p/m \Delta t = v \Delta t$$

$$\Delta t \sim 10 \text{ fs} \quad \Delta x \sim 0.1 \text{ \AA}$$

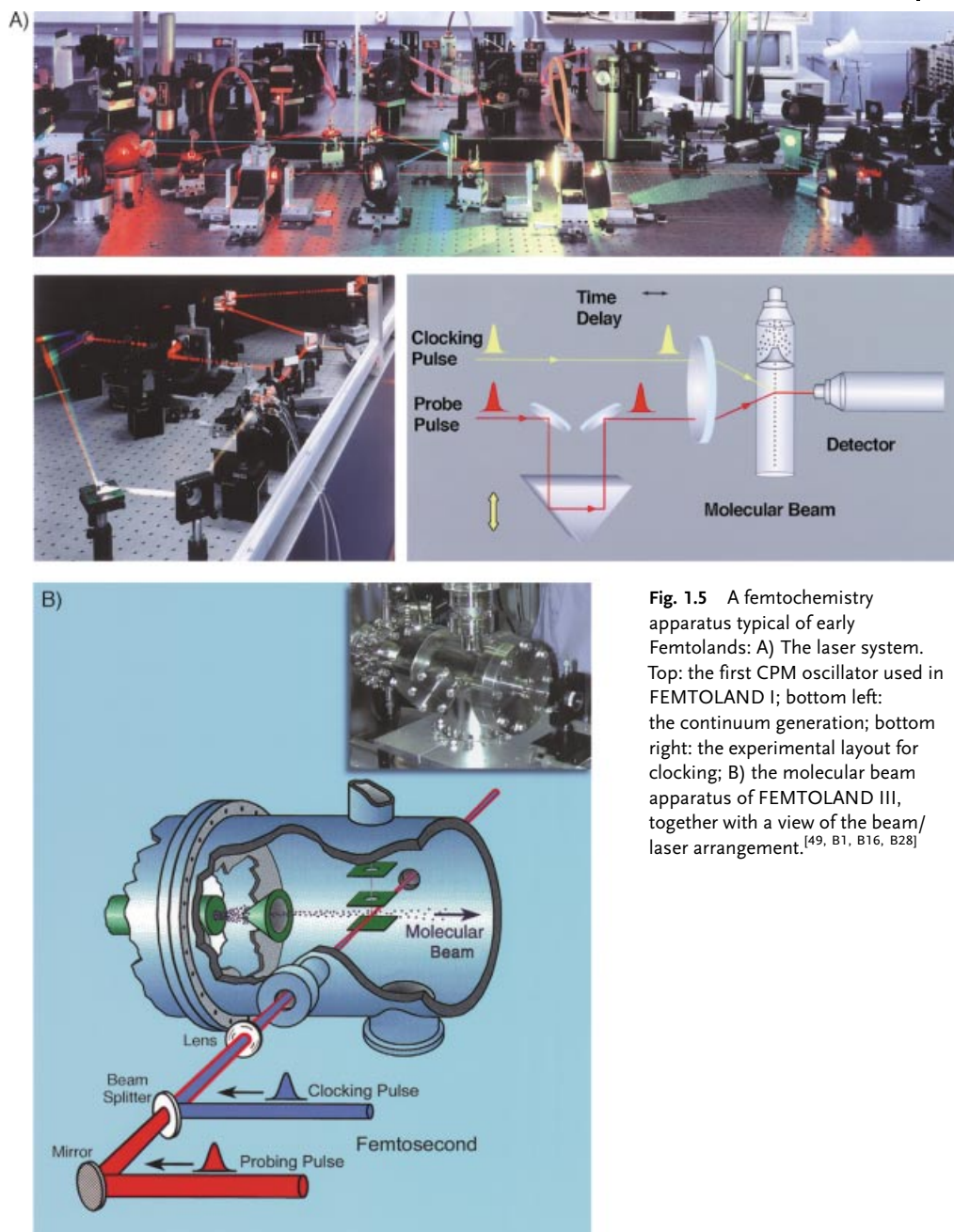
$$\Delta t \sim 10 \text{ ps} \quad \Delta x \sim 100 \text{ \AA}$$

**Fig. 1.4** Matter waves and particle-type limit of dynamics.

A) The atomic-scale de Broglie wavelength in the coherent preparation of a quantum system and the uncertainty of probe measurements are both reached on the femtosecond time scale. B) The limits of the wave packet and wave function for molecular systems, in this case a diatomic molecule (see Section 1.6). The analogy with light interference is depicted—Thomas Young's experiment of 1801.<sup>[B25]</sup>









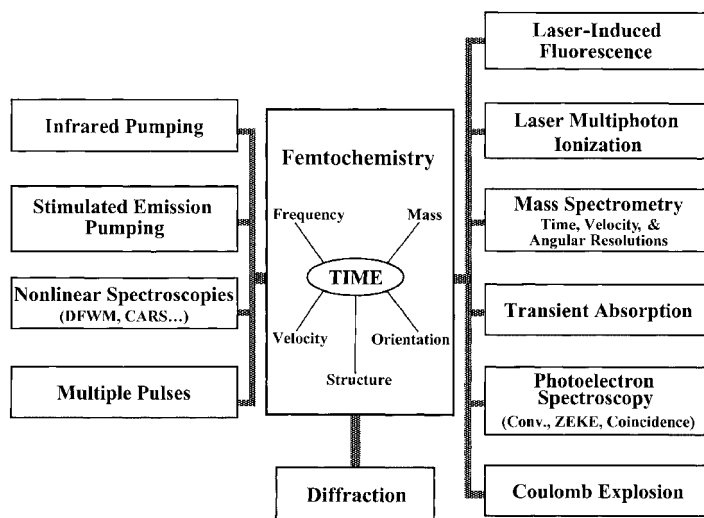


**Fig. 1.6** Techniques for probing in femtochemistry. Both excited and ground states have been probed by these methods. The correlations of time with frequency, mass,

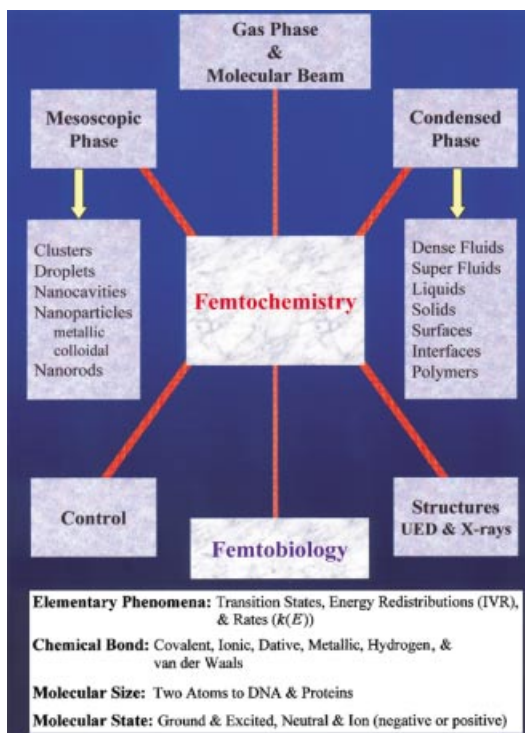
velocity, and orientation were essential in the studies of complex systems. Diffraction represents the new effort for probing structures (see text and Figure 1.29).

This powerful concept of coherence lies at the core of femtochemistry and was a key advance in observing the dynamics at atomic resolution. The realization of its importance and its detection by selectivity in both preparation and probing were essential in all studies, initially of states and orientations, and culminating in atomic motions in reactions. With these concepts in mind, the marriage of ultrafast lasers with molecular beams (Figure 1.5) proved to be essential for the initial development. Laser-induced fluorescence was the first probe used, but later we invoked mass spectrometry and nonlinear optical techniques. Now numerous methods of probing are known (Figure 1.6) and used in laboratories around the world; Coulomb explosion is the most recent powerful probe developed by Will Castleman<sup>[5c]</sup> for arresting reactive intermediates, as mentioned in Section 1.3.

Applications of femtochemistry have spanned the different types of chemical bonds—covalent, ionic, dative, and metallic, as well as the weaker ones such as hydrogen and van der Waals bonds. The studies have continued to address the varying complexity of molecular systems, from diatomics to proteins and DNA. Studies have also been made in all phases of matter: gases and molecular beams; mesoscopic phases of clusters, nanostructures, particles and droplets; condensed phases of dense fluids, liquids, solids, surfaces, and interfaces; and in sibling fields of femtoscience such as femtobiology (Figure 1.7).

Twenty-four centuries ago, the Greek philosopher Democritus and his teacher Leucippus gave birth to a new way of thinking about matter's invisible and elementary entity, the atom. Richard Feynman once asked, if you had only one sentence to describe the most important scientific knowledge we possess, what would that sentence be? He said, "everything is made of atoms". Democritus' atomism, which was

**Fig. 1.7** Femtochemistry and the scope of its applications.



rejected by Aristotle, was born on a purely philosophical basis, surely without anticipating some of the twentieth century's most triumphant scientific discoveries. Atoms can now be seen, observed in motion, and manipulated.<sup>[6]</sup> These discoveries have brought the microscopic world and its language into a new age, and they cover domains of length, time, and number. The length (spatial) resolution, down to the scale of atomic distance (ångström), and the time resolution, down to the scale of atomic motion (femtosecond), have been achieved. The trapping and spectroscopy of a single ion (electron) and the trapping and cooling of neutral atoms have also been achieved. All of these achievements have been recognized by the awarding of the Nobel Prize to scanning tunneling microscopy (1986), to single-electron and -ion trapping and spectroscopy (1989), to laser trapping and cooling (1997), and to laser femtochemistry (1999).

## 1.2

## Dynamics and Arrow of Time

## 1.2.1

## Origins—From Kinetics To Dynamics

## 1.2.1.1 The Arrhenius Seminal Contribution

At the turn of the 20th century, the study of reactivity was dominated by the question:<sup>4)</sup> How do reactions proceed and what are their kinetic rates? Svante Arrhenius gave the seminal description of the change in rates of chemical reactions with temperature and formulated in 1889 the familiar expression (1) for the rate constant,<sup>[7a]</sup>

$$k = Ae^{-E_a/RT} \quad (1)$$

which, as Arrhenius acknowledged, had its roots in van't Hoff's (1884) equations.<sup>[7b]</sup> For any two reactants, the rate constant  $k$  depends on the temperature  $T$  according to an energy of activation  $E_a$ , which is different from the thermodynamic net energy change between reactants and products, and the dependence is exponential in form.  $R$  in Equation (1) is the universal gas constant. If we think of the reaction as a finite probability of reactant A colliding with B, then the rate is simply the collision frequency times the fraction of successful collisions with an energy equal to or more than  $E_a$ . The energy of activation  $E_a$  is found from the value of equation (1) through the well-known plots of " $\ln k$  versus  $1/T$ ". Arrhenius also introduced a "hypothetical body", now known as the "activated complex", a central concept in the theory of reaction rates: the reaction, because of collisions or other means, proceeds only if the energy is sufficient to exceed a barrier whose energy is defined by the nature of the complex. Since then, various experimental data for different temperatures  $T$  were treated with Equation (1), yielding  $E_a$  and the pre-exponential factor  $A$ .

A few years after Arrhenius' contribution, Bodenstein (1894) published a landmark paper on the hydrogen/iodine system, which has played an important role in the development of gas-phase chemical kinetics, with the aim of understanding elementary reaction mechanisms.<sup>[7c]</sup> In the twenties, Lindemann (1922),<sup>[7d]</sup> Hinshelwood (1926),<sup>[7e]</sup> Tolman (1920),<sup>[7f, g]</sup> and others<sup>[8]</sup> developed, for unimolecular gas-phase reactions, elementary mechanisms with different steps describing activation, energy redistribution, and chemical rates. By 1928, the Rice-Ramsperger-Kassel (RRK) theory was formulated, and Marcus, starting in 1952, blended RRK and transition state theory in a direction which brought into focus the nature of the initial and transition-state vibrations in what is now known as the RRKM theory.<sup>[8]</sup>

The rate constant,  $k(T)$ , does not provide a detailed molecular picture of the reaction. This is because  $k(T)$ , which was obtained by analogy with van't Hoff's description of the change of the equilibrium constant  $K$  (thermodynamics) with  $T$ , is an

4) The main focus of prior studies was on the thermodynamics and equilibrium characteristics. Interestingly, chemical equilibrium was already established a century before (1798) by Claude Berthollet, during a visit to the

Natron Lakes in Napoleonic times, through his studies of the reaction  $\text{Na}_2\text{CO}_3 + \text{CaCl}_2 \leftrightarrow 2\text{NaCl} + \text{CaCO}_3$  [S. W. Weller, *Bull. Hist. Chem.* **1999**, 24, 61].

average of the microscopic, reagent-state to product-state rate coefficients over all possible encounters. These might include different relative velocities, mutual orientations, vibrational and rotational phases, and impact parameters. A new way was needed to describe, by some quantitative measure, the process of the chemical reaction itself: How reagent molecules approach, collide, exchange energy, sometimes break bonds and make new ones, and finally separate into products. Such a description is the goal of molecular reaction dynamics.<sup>[9]</sup>

### 1.2.1.2 The London, Eyring, and Polanyi Contributions

For some time, theory was ahead of experiment in studies of microscopic molecular reaction dynamics. The effort started shortly after the publication of the Heitler–London quantum-mechanical treatment (1927) of the hydrogen molecule,<sup>[10a]</sup> a breakthrough in thinking not only about the stable structure of the chemical bond, but also about how two atoms can interact at different separations. One year later (1928), for Sommerfeld’s *Festschrift* (60th birthday), London<sup>[10b]</sup> presented an approximate expression for the potential energy of triatomic systems, for example,  $H_3$ , in terms of the coulombic and exchange energies of the “diatomic” pairs. In 1931 Henry Eyring and Michael Polanyi, using the London equation, provided a semiempirical calculation of a potential energy surface (PES) of the  $H+H_2$  reaction describing the journey of nuclei from the reactant state of the system to the product state, passing through the crucial transition state of activated complexes.<sup>[10c]</sup> The birth of “reaction dynamics” resulted from this pioneering effort and, for the first time, one could think of the PES and the trajectories of dynamics on it—in those days, often, expressed in atomic units of time! No one could have dreamed in the 1930s of observing the transient molecular structures of a chemical reaction, since the time scale for those activated complexes that were far from equilibrium in the transition state was estimated to be less than a picosecond (ps).

The time scale was rooted in the theory developed for the description of reaction rates. Building on Arrhenius’ work and the work of Polanyi and Wigner (1928),<sup>[11a]</sup> in 1935, Eyring,<sup>[11b]</sup> and independently Evans and Polanyi,<sup>[11c]</sup> formulated transition-state theory, which gave an explicit expression for Arrhenius’ pre-exponential factor [Eq. (2)].

$$k = \frac{k_B T}{h} K^\ddagger = \frac{k_B T}{h} \frac{Q}{Q_A Q_B} e^{-E_0/kT} \quad (2)$$

Here  $k_B$  is Boltzmann’s constant,  $h$  is Planck’s constant, and  $Q$  is the partition function. The key idea here is to assume the equilibration of the population between reactants and the transition state:  $A+B \rightleftharpoons [TS]^\ddagger \rightarrow \text{products}$ . Thus, the rate constant can be related to the equilibrium constant for formation of the transition state  $K^\ddagger$ , and hence  $\Delta G^\ddagger$ ,  $\Delta H^\ddagger$ , and  $\Delta S^\ddagger$ ; physically,  $\Delta G^\ddagger (\Delta H^\ddagger - T\Delta S^\ddagger)$  in the exponent gives the barrier energy (through  $\Delta H^\ddagger$ ) along the reaction coordinate and the pre-exponential entropic term, which reflects the change in vibrational modes perpendicular to the reaction coordinate. By comparing Equation (2) with Arrhenius’ Equation (1), the pre-exponential  $A$  can be identified;  $E_a$ , the activation energy, and  $E_0$ , the barrier energy with zero-point energy corrections, are related.<sup>[8a]</sup> Kramers’ (1940) classic work<sup>[11d]</sup> modified the pre-exponential factor to include friction from the sur-

rounding medium, with transition-state theory giving an upper limit, and Casey Hynes, in the 1980s, provided a dynamical theory of friction with emphasis on time scales in the transition-state region and for solvent interaction.<sup>[11f]</sup> In the 1950s, Marcus<sup>[11e]</sup> obtained a transition-state-type expression for reactions of electron transfer in solutions with the Gibbs free energy of activation expressing the dependence on solvent reorganization energies. This work was awarded the 1992 Nobel Prize.

According to transition state theory, the fastest reaction is given by  $k_B T/h$ , which is basically the “frequency” for the passage through the transition state [see Eq. (2)]. At room temperature this value is  $6 \times 10^{12} \text{ s}^{-1}$ , corresponding to about 170 fs; the time scale of molecular vibrations is typically 10–100 fs. This estimate is consistent with knowledge of the speeds of nuclei and the distance change involved in the reaction. In 1936 the first classical trajectory from Hirschfelder-Eyring-Topley molecular dynamics simulations of the  $\text{H} + \text{H}_2$  reaction showed the femtosecond steps needed to follow the reaction profile, albeit on the wrong PES. Later, Karplus, Bunker, and others showed a range for the time scales, picoseconds to femtoseconds, depending on the reaction and using more realistic PESs.<sup>[9, 26]</sup>

### 1.2.1.3 The Transition State and its Definition

In general, for an elementary reaction of type (3) the whole journey from reagents to products involves changes in internuclear separation totaling about 10 Å. If the atoms moved at  $10^4$ – $10^5 \text{ cm s}^{-1}$  then the entire 10-Å trip would take  $10^{-12}$ – $10^{-11} \text{ s}^{-1}$ .



If the “transition state”  $[\text{ABC}]^\ddagger$  is defined to encompass all configurations of ABC significantly perturbed from the potential energy of the reagents  $\text{A} + \text{BC}$  or the products  $\text{AB} + \text{C}$ , then this period of 1–10 ps is the time available for its observation. To achieve a resolution of approximately 0.1 Å, the probe time window must be 10–100 fs.

The above definition of the transition state follows the general description given by John Polanyi and the author,<sup>[12]</sup> namely the full family of configurations through which the reacting particles evolve en route from reagents to products. This description may seem broad to those accustomed to seeing the TS symbol  $\ddagger$  displayed at the crest of the energy barrier to a reaction. As stated in ref. [12], even if one restricts one’s interest to the overall rates of chemical reactions, one requires a knowledge of the family of intermediates sampled by reagent collisions of different collision energy, angle, and impact parameters. The variational theory of reaction rates further extends the range of TS of interest, quantum considerations extend the range yet further, and the concern with rates to yield products in specified quantum states and angles extends the requirements most of all. A definition of the TS that embraces the entire process of bond breaking and bond making is therefore likely to prove the most enduring. This is specially important as we address the energy landscape of the reaction, as discussed in Section 1.4.

The cardinal choice of the transition state at the saddle point, of course, has its origin in chemical kinetics—calculation of rates—but it should be remembered that this is a mathematical “single point” with the division made to define the speed of a

reaction.<sup>[8]</sup> Even in thermal reactions, there is enough of an energy distribution to ensure many types of trajectories occur. Furthermore, transition state theory is not a quantum theory, but a classical one, because of the assertion of a deterministic point. Quantum uncertainty demands some delocalization<sup>[8b]</sup> and, as mentioned above, the theory invokes the equilibration of reactants and transition-state populations, using statistical thermodynamics. In fact, the term transition state is used ambiguously to refer both to the quasi-equilibrium state of the reaction and to the molecular structure of the saddle point. As discussed in ref. [13a], perhaps the molecular species at the saddle point could be referred to as the transition structure; the activated complex is more descriptive.

The location at the saddle point provides the highest energy point that must be reached, thus defining the exponential probability factor; the dynamics (forces and time states) are governed by the nature of the transition-state region. Provided that the energy landscape of the reaction is controlled by a narrow region, the structure of the transition state becomes important in structure–reactivity correlations; rates versus Gibbs energy between the TS and the ground state. (It is also useful in designing TS analogues as enzyme inhibitors and TS complements as catalysts<sup>[13b]</sup>). The position of the TS and its energy relative to that of reactants and products along the reaction path becomes relevant. In the mid 1930s, the Bell-Evans-Polanyi principle gave a predictive correlation between the changes in barrier heights and the enthalpies of reactions, especially for a series of related reactions; the TS for exoergic or endoergic reaction is very different. In 1955, this led to Hammond’s postulate which characterizes a reactantlike TS (so called “early” TS) for exoergic reactions, productlike TS (so called “late” TS) for endoergic reactions, and “central” TS for energy neutral reactions.<sup>[8d]</sup> John Polanyi, the son of Michael, formulated some concepts regarding energy disposal in relation to the position of the TS on the PES, by using molecular dynamics simulations and experimental studies of chemiluminescence.<sup>[14]</sup>

It should be recognized that selectivities, efficiencies, and stereochemistries are quantified only when the dynamics on the global energy landscape are understood. For example, the picture for simple reactions of a few (strong) bonds being made and broken is changed when the energy surface is nearly flat or there is a significant entropic contribution. Many transition states will exist in the region as in the case of protein folding.<sup>[13c]</sup> Finally, in the transition state, chemical bonds are in the process of being made and broken. In contrast, for intermediates, whose bonds are fully formed, they are in potential wells, typically “troughs” in the TS region. However, the time scale is crucial. In many cases, the residence time in intermediates approaches the femtosecond regime which is characteristic of TS structures, and the distinction becomes fuzzy. Moreover, for a real multidimensional PES, the nonreactive nuclear motions can entropically lock the system even though there is no well in the energy landscape. In addition, the presence of shallow wells in the energy landscape does not guarantee that trajectories will visit such wells.

#### 1.2.1.4 The Transition State and its Spectroscopy

Various techniques have been advanced to probe transition states more directly, especially for elementary reactions. Polanyi's analogy of transition-state spectroscopy,<sup>[14]</sup> from "spectral wing emission", to (Lorentz) collisional line broadening studies, made earlier by A. Gallagher and others, set the stage for the use of continuous wave (CW) spectroscopic methods as a probe. (In this way, only about one part in a million of the population can be detected.) Emission, absorption, scattering, and electron photodetachment are some of the novel methods presented for such time-integrated spectroscopies, and the groups of Jim Kinsey, Philip Brooks and Bob Curl, Benoit Soep and Curt Wittig, Dan Neumark, and others, have made important contributions to this area of research. The key idea was to obtain, as Kinsey<sup>[15]</sup> puts it, short-time dynamics from long-time experiments. (The renaissance of wave packet dynamics in spectroscopy, pioneered by Rick Heller, will be highlighted in Section 1.3.4. and 1.3.6.) With these spectroscopies operating in a CW mode, a distribution of spectral frequencies provides the clue to the desired information regarding the distribution of the TS over successive configurations and potential energies. Recently, this subject was reviewed by Polanyi and the author and details of these contributions are given therein,<sup>[12]</sup> and also in ref. [26].

#### 1.2.2

#### The Arrow of Time

In over a century of development, time resolution in chemistry and biology has witnessed major strides, which are highlighted in Figure 1.8.<sup>[16]</sup> As mentioned before, the Arrhenius equation (1889) for the speed of a chemical reaction gave information about the time scale of rates, and Eyring and Michael Polanyi's (1931) microscopic theoretical description made chemists think of the atomic motions through the transition state and on the vibrational time scale. But the focus naturally had to be on what could be measured in those days, namely the slow rates of reactions. Systematic studies of reaction velocities were hardly undertaken before the middle of the 19th century; in 1850 Ludwig Wilhelmy reported the first quantitative rate measurement, the hydrolysis of a solution of sucrose to glucose and fructose.<sup>[8a]</sup> In 1901, the first Nobel Prize for chemistry was awarded to van't Hoff for, among other contributions, the theoretical expressions (chemical dynamics), which were precursors to the important work of Arrhenius on rates. Arrhenius too received the Prize in 1903 for his work on electrolytic theory of dissociation.

A major advance in experiments involving sub-second time resolution was made with flow tubes in 1923 by H. Hartridge and F. J. W. Roughton for solution reactions. Two reactants were mixed in a flow tube, and the reaction products were observed at different distances. Knowing the speed of the flow, one could translate this into times of tens of milliseconds. Such measurements of nonradiative processes were a real advance in view of the fact that they were probing the "invisible", in contrast with radiative glows which were seen by the naked eye and measured using phosphoroscopes. Then came the stopped-flow method (B. Chance, 1940) that

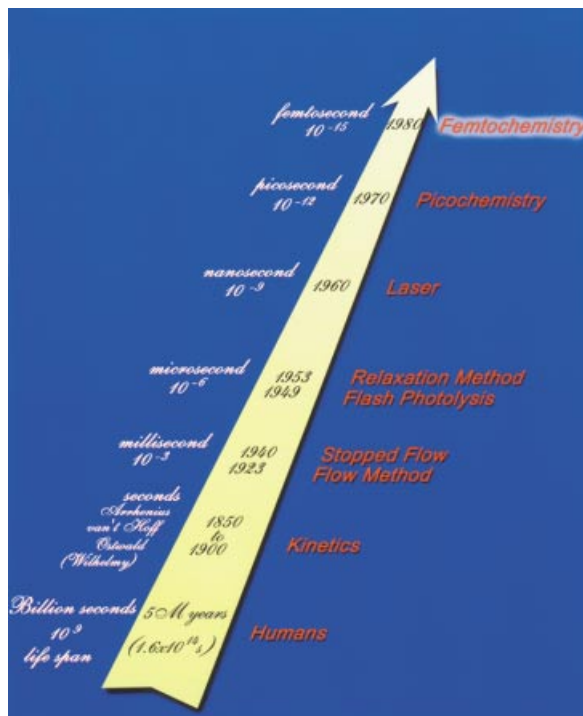


Fig. 1.8 Arrow of time in chemistry and biology showing some of the steps over a century of development (see text).<sup>[B1]</sup>

reached the millisecond scale. The stopped-flow method is still used today in biological kinetics.

Around 1950 a stride forward for time resolution in chemistry came about when Manfred Eigen in Germany and R. G. W. Norrish and George Porter in England developed techniques reaching the microsecond time scale.<sup>[17]</sup> For this contribution, Eigen and Norrish & Porter shared the 1967 Nobel Prize. The method of flash photolysis was developed by Norrish and Porter a few years after World War II, using electronics developed at the time. They produced an intense burst of light and created radicals in the sample, and, by using other light, they recorded the spectra of these radicals. They achieved kinetics on this time scale and observed some relatively stable intermediates.

Before the turn of the 20th century it was known that electrical sparks and Kerr cell shutters could have response times as short as ten nanoseconds. In an ingenious experiment, Abraham and Lemoine (1899)<sup>[18a]</sup> in France demonstrated that the Kerr response of carbon disulfide was faster than ten nanoseconds; it has now been measured to be about two picoseconds (with femtosecond response).<sup>[18b]</sup> Abraham and Lemoine used an electrical pulse which produced a spark and simultaneously activated a Kerr shutter. Light from the spark was collimated through a variable-delay path and through the Kerr cell (polarizer, CS<sub>2</sub> cell, and analyzer). The



rotation of the analyzer indicated the presence of birefringence in the cell for short optical delays; this birefringence disappeared for pathlengths greater than several meters, reflecting the total optical/electrical response time of 2.5 ns. In this landmark “pump-probe” experiment, they demonstrated in 1899 the importance of synchronization. The setting of time delays was achieved by varying the light path. Bloembergen has recently given a historical perspective of short-pulse generation<sup>[18b]</sup> and Shapiro has reviewed the early developments, including mechanical, streak, spark, stroboscope, and other high-speed photography methods.<sup>[18d]</sup> As pointed out in ref. [18b, d], flash photolysis utilized the above approach but one of the flashes was made very strong to generate high concentrations of free radicals and hence enable their utility in chemical and spectroscopic applications.

Eigen developed “the relaxation method”, which reached the microsecond time scale and close to the nanosecond scale. By disturbing the equilibrium of a solution by either a heat jump, a pressure jump, or an electric field the system shifts from equilibrium. This is the point of time zero. Then the system equilibrates, and its kinetics can be followed. (At about the same time, shock-tube methods were used to provide kinetics on similar time scales.) Eigen called these reactions “immeasurably fast” in his Nobel lecture. There was a feeling that this time resolution was the fastest that could be measured or that needed to be measured for relevance to chemistry (Section 1.4). The invention of the laser has changed the picture.

Shortly after the realization of the first (ruby) laser by Maiman (1960), the generation of giant and short pulses became possible: nanoseconds by Q-switching (Hellwarth, 1961) and picoseconds (De Maria, et al. 1966) by mode-locking (1964). Sub-picosecond pulses from dye lasers (Schäfer and Sorokin, 1966) were obtained in 1974 by Chuck Shank and Eric Ippen at the Bell Laboratories,<sup>[19a]</sup> and in 1987 a six-femtosecond pulse was achieved.<sup>[19d]</sup> In 1991, with the discovery of femtosecond pulse generation from solid-state Ti:sapphire lasers by Sibbett and colleagues,<sup>[19e]</sup> dye lasers were rapidly replaced and femtosecond pulse generation became a standard laboratory tool; the state-of-the-art, once 8 fs,<sup>[19f]</sup> is currently about 4 fs and made it into the Guinness Book of World Records (Douwe Wiersma’s group<sup>[19g]</sup>). The tunability is mastered using continuum generation<sup>[19h]</sup> and optical parametric amplification.

In the late sixties and in the seventies, ps resolution made it possible to study nonradiative processes, a major detour from the studies of conventional radiative processes to infer the nonradiative ones. As a student, I recall the exciting reports of the photophysical rates of internal conversion and biological studies by Peter Rentzepis;<sup>[20]</sup> the first ps study of chemical reactions (and orientational relaxations) in solutions by Ken Eisensthal;<sup>[21]</sup> the direct measurement of the rates of intersystem crossing by Robin Hochstrasser;<sup>[22]</sup> and the novel approach for measurement of ps vibrational relaxations (in the ground state of molecules) in liquids by Wolfgang Kaiser and colleagues.<sup>[23]</sup> The groups of Shank and Ippen<sup>[19abd]</sup> have made important contributions to the development of dye lasers and their applications in the ps and into the femtosecond regime. Other studies of chemical and biological nonradiative processes followed on the ps time scale, the scale coined by G. N. Lewis as the “jiffy”—1 jiffy is the time needed for a photon to travel 1 cm (33 picoseconds).<sup>[24]</sup>

At about the same time in the 1960s, molecular-beam studies of reactions were being developed, and, although I was not initially a member of this community, beams later became part of our effort in femtochemistry. Molecular collisions occur on a shorter time scale than a ps, and real-time studies were not possible at the time. Crossed molecular beams and chemiluminescence techniques provided new approaches for examining the dynamics of single collisions using the post-attributes of the event, the reaction products. The contributions by Dudley Herschbach, Yuan Lee, and John Polanyi<sup>[14, 25a]</sup> were acknowledged by the 1986 Nobel Prize. From the state and angular distributions of products, information about the dynamics of the collision was deduced and compared with theoretical calculations of the PES and with molecular dynamics simulations. The goal was to find self-consistency and to deduce an estimate of the lifetime of the collision complex. Laser studies using molecular beams have probed dynamics by the careful analysis of product internal energy (vibrational and rotational) distributions as well as the steady-state alignment and orientation of the products. The contributions to this important area are highlighted in the article by Dick Zare and Dick Bernstein<sup>[25b]</sup> and in the book by Raphy Levine and Bernstein.<sup>[9]</sup> An overview of femtochemistry (as of 1988) in connection with these other areas is given in a feature article<sup>[26]</sup> by myself and Bernstein.

### 1.3

#### Femtochemistry: Development of the Field

The development of the field is highlighted in this section, from the early years of studying coherence to the birth of femtochemistry and the explosion of research, or, as the report of ref. [5a] puts it, "... the revolution in chemistry and adjacent sciences." On the way, there were conceptual and experimental problems to overcome and many members of our Caltech group have made the successful evolution possible. The review article published in the *Journal of Physical Chemistry*<sup>[B14]</sup> names their contributions in the early stages of development. Here, references are given explicitly to the work discussed in the figures.

#### 1.3.1

##### The Early Years of Coherence

When I arrived in the US as a graduate student in 1969, nine years after the invention of the first laser, I had no idea of what lasers were about. When appointed to the Caltech faculty as an assistant professor in 1976, I was not thinking or dreaming of femtosecond time resolution. But I had the idea of exploring coherence as a new concept in intra- and inter-molecular dynamics. This proved to be vital and fruitful.

##### 1.3.1.1 New Techniques for Molecules

The Caltech offer included start-up funds of \$ 50 000 for capital equipment (\$ 15 000 for shop services), an empty laboratory of two rooms and an office next to it. A few months before moving to Caltech in May of 1976, I made the decision not to begin

with the type of picosecond research I was doing at Berkeley as a postdoctoral fellow. Instead, the initial effort was focused on two directions: studies of coherence in disordered solids, and the development of a new laser program for the study of the phenomena of (optical) coherence. Prior to the final move, I came down from Berkeley for several visits in order to purchase the equipment and to outline the laboratories' needs for electricity, water, gases, and so on; my feeling was that of a man left out in a desert with the challenge to make it fertile. We spent a significant fraction of the \$ 50 000 on setting up the apparatus for the optical detection of magnetic resonance (ODMR) to study disordered solids. My experience at Penn with Professor Robin Hochstrasser and at Berkeley with Professor Charles Harris was to culminate in these experiments. The key questions I had in mind were: What is the nature of energy migration when a crystal is systematically disordered? Is it coherent, incoherent, or partially coherent? Is there a relationship between optical and spin coherence?

While the ODMR apparatus was being built, I was thinking intensely about new laser techniques to probe the coherence of optical transitions (so-called optical coherence). I had the intuitive feeling that this area was rich and at the time had in mind several issues which were outlined in my research proposal to Caltech. Laser experiments were designed with objectives focused on the same issues outlined in the proposal. First, in the work I published with Charles Harris, and alone at Berkeley, the coherence probed had been that of spin (triplet excitons) and I felt that we should directly probe the optical coherence, that is, the coherence between the excited electronic state and the ground state, not that between two spin states of the same excited state (Figure 1.9). Second, I did not believe that the time scale of spin coherence was the same as that of optical coherence. Later, I wrote a paper on the subject which was published in the *Journal of Chemical Physics* (1979) with the title: "Are the homogeneous linewidths of spin resonance and optical transitions related?"

I was convinced that essentially all molecular optical transitions in solids are inhomogeneous, that is, they do not reflect the true dynamics of a homogeneous ensemble, but rather the overlapping effects of sub-ensembles. This was the key point outlined in my research proposal to Caltech. If the new set of laser experiments at Caltech proved successful, we should be able to find the answer to these important (to me) questions. However, the funds remaining were insufficient to realize our dream for the new experiments. Fortunately, Spectra Physics, started in 1961 and now a huge laser company, was proud of a new product and was interested in helping us demonstrate the usefulness of one of the first single-mode dye lasers they produced. At Caltech, we had the argon-ion pump laser, from Wilse Robinson's Laboratory, and added the dye laser we obtained from Spectra Physics with the idea that we would purchase it if the experiments were successful. David Evans of Spectra Physics was instrumental in helping us achieve this goal. What was left were the low-temperature cryostat and electronics. We could not afford a real metal cryostat, so we custom-made a glass Dewar that could cool to 1.8 K. Most of the electronics were obtained on loan for several months. To generate laser pulses we used switching methods developed at the Joint Institute for Laboratory Astrophysics (JILA) and

## Coherent Transients – phase control

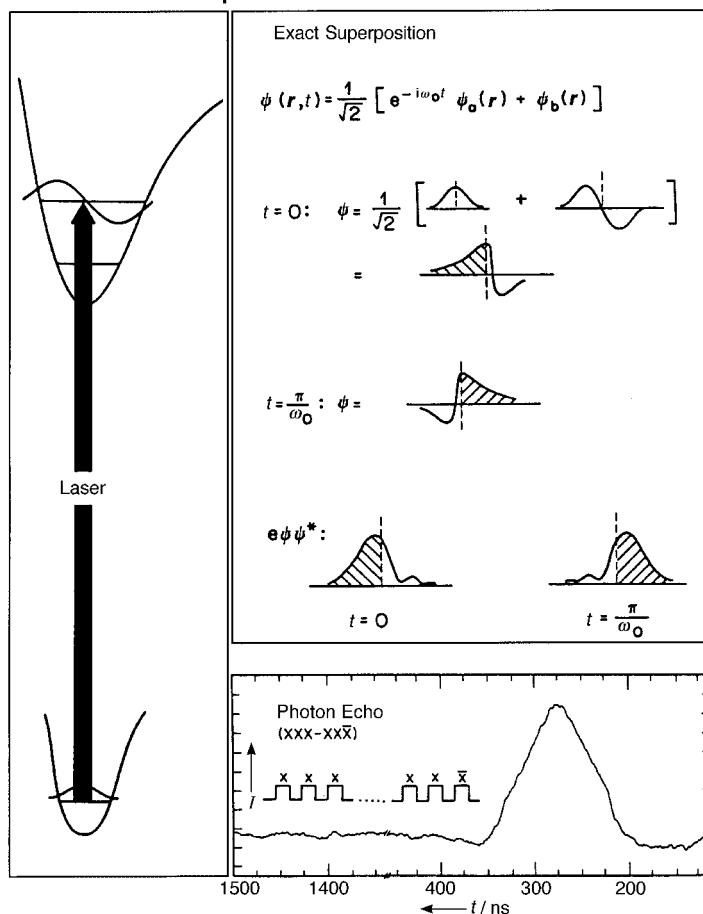


**Fig. 1.9** Molecular coherence and dephasing. Coherent transients from the superposition of states, and control of pulse phase ( $x$  or  $\bar{x}$ ) in multiple pulse experiments, the optical

analogue of NMR spectroscopy. The photon echo of iodine gas (bottom right) was observed on the spontaneous emission using the described pulse sequence.<sup>[50, B9, B13, B22, B23]</sup>

IBM. The work at IBM by Dick Brewer's group triggered our interest in using electro-optic switching methods.

We succeeded in making the laser perform according to specifications and began the first experiments with phenazine crystals. Phenazine has unique properties which I learned about in Robin Hochstrasser's laboratory. At Berkeley I published a paper outlining the nature of coherence in multidimensional systems and used phenazine as a prototype experimental system. Our first laser transient at Caltech was beautiful. Unfortunately, the transient was from the electronics, not from the crystal, but we soon realized this! We decided to abandon this particular system for a while and to try an impurity crystal of pentacene in a host of terphenyl. We also decided to study gases, and some success came our way.

With the theoretical knowledge acquired in handling coherence effects, which requires expertise with density matrix formalism and its manipulation in geometrical frames, I had a novel idea: we should be able to detect coherence on the incoherent emission at optical frequencies. From many discussions with Alex Pines and Charles Harris at Berkeley, I knew the power of “adding” pulses in NMR and ESR spectroscopy. This idea was successful and indeed we were able to observe the photon echo on the spontaneous emission (Figure 1.9) using three optical pulses. Only months after my arrival in May of 1976 we published our first scientific paper from Caltech. This success gave us confidence in the approach and in our understanding of the principles of coherence and its probing in molecular systems. We applied it to larger molecules with success but also encountered some disappointments. This work was followed by a variety of extensions to studies in gases and solids and also in a home-made (from glass) effusive molecular beam. The small group in our laboratory working on optical coherence became productive and we had an exciting time. Our group and that of Douwe Wiersma in Holland were then the two most active in these areas of chemical research.

In the meantime, the work on disorder in solids began to yield interesting results and, surprisingly, we observed an unusual change in the degree of energy transfer with concentration, which we published as evidence of Anderson localization, a hot topic in the 1970s. This was followed by detailed studies of several systems and I wrote my first research proposal to the National Science Foundation (NSF). The research was funded! The then program director at NSF, Fred Stafford, was supportive of the effort and we have maintained our support from the Division of Materials Research to this day; the NSF’s Chemistry Division continues to support our research. Knowledge of energy transfer was also helpful in another area. Terry Cole, a visiting scholar at Caltech, and I initiated work on the studies of luminescent solar concentrators (LSCs) using energy transfer between dyes as a key principle. This idea, too, was successful and funding for this research came in from SERI and from ARCO. The work on LSCs resulted, ultimately, in a patent (with Sam Batchelder; issued in 1980) and in several publications. My research group was rapidly expanding.

After 18 months at Caltech, I was pleased to learn that my colleagues were considering my case for tenure. Tenure was granted a few months later, two years after my arrival at the Institute. I was both appreciative and pleased. We continued research in four areas: optical coherence phenomena and dephasing; disorder in solids; picosecond spectroscopy; and LSCs. In my own department, some colleagues were not too excited about “this stuff of coherence and dephasing”—thinking that it was not relevant to chemistry. Many chemists on the outside were also unsure what this was all about. In fact, a notable chemist once said publicly at a conference I attended that coherence and dephasing had nothing to do with chemistry. On the physics side, I was invited to numerous conferences, including one in which the Nobel Laureate Willis Lamb asked me to have dinner to discuss our research. This was a special experience.

I was not convinced by these doubts and my faith helped us to continue along with the development. The concept of coherence turned out to be fundamental in femtochemistry, and it is now well accepted that coherence is a key process in the

probing and controlling of molecular dynamics. With the success we had with observations and studies of coherence in different systems, I wrote an article for *Accounts of Chemical Research*, published in 1980, with the title “Optical Molecular Dephasing—Principles of and Probing by Coherent Laser Spectroscopy”. I felt that the nanosecond time scale we had mastered should be extended to the picosecond time scale, but did not wish to repeat the Berkeley experience with glass lasers. Fortunately, the design for the first sub-picosecond dye laser was reported in 1974 and we decided to build one to study the phenomena of coherence—but now on a shorter time scale.

### 1.3.1.2 The Optical Analogue of NMR Spectroscopy: Controlling the Phase

From the studies of optical transients, we learned that coherence can be probed directly in real time in gases (and solids) and that incoherent decay (for example, fluorescence) can be used to monitor such coherences provided that the laser pulse(s) is capable of forming a coherent superposition of states. For two states of a transition  $\psi_a$  and  $\psi_b$ , the coherent state can be written as Equation (4). The coefficients  $a(t)$  and  $b(t)$  contain in them the familiar quantum-mechanical phase factors,  $\exp(-iE_a t/\hbar)$  and  $\exp(-iE_b t/\hbar)$ , respectively (see Figure 1.9).

$$\Psi_{\text{coherent}}(t) = a(t) \psi_a + b(t) \psi_b \quad (4)$$

By using pulse sequences we could directly monitor the behavior of the ensemble-averaged coefficients of  $\Psi\Psi^*$ ,  $\langle a(t)b^*(t) \rangle$ , which contain information on the coherence decay time (optical time  $T_2$ ); they are the off-diagonal elements of a density matrix,  $\rho_{ab}$ . The term  $\langle a(t)a^*(t) \rangle$  is the population of state  $\psi_a$  and represents the diagonal density-matrix element  $\rho_{aa}$ ;  $\langle a(t)a^*(t) \rangle$  decays with optical time  $T_1$ . We were thus able to demonstrate the power of the optical analogue of NMR pulse techniques in learning about coherence and the origin of optical dephasing in molecular systems of interest to chemical dynamics. This advance changed the thinking of many with the recognition that it was impossible to deduce  $T_1$  and  $T_2$  from measurements of the line width of inhomogeneous transitions.

One feature of this work which later helped us in the study of molecular reaction dynamics was the realization of the importance of the pulse phase (shape) in studies of coherence. With the acousto-optic modulation techniques we developed earlier, it became possible to make optical pulse sequences with well-defined phases. This development took us into the domain of selective and prescribed pulse sequences which could then be used to enhance coherences or suppress them—the optical analogue of NMR multiple pulse spectroscopy. We published several papers on phase control and extended the applications to include photon locking. We were eager to extend these techniques to the picosecond time domain in order to study solids, but, for several reasons, our attention was diverted to gas-phase molecular dynamics.

By this time, our group's efforts were narrowing on two major areas. (Dick Bernstein, who was on the Visiting Committee for our Division, hinted that I was doing too much in too many areas!) The work on disorder and LSCs was gradually brought to completion. Picosecond spectroscopy of rotational diffusion and energy transfer in liquids were similarly handled. I felt that the latter area of research was crowded with too many scientists, a characteristic I do not enjoy when venturing into a new

area. I must add that I was not too thrilled by the exponential (or near exponential) decays we were measuring and by the lack of molecular information. Our effort began to emphasize two directions: 1) the studies of coherence and dynamics of isolated molecules in supersonic beams and 2) the development of the optical analogue of NMR spectroscopy. The low-temperature facility was put to use to study the dephasing and polarization of highly vibrationally excited molecules in the ground state. Coherence in chemical dynamics was occupying my thinking, and I made a detour in the applications that turned out to be significant.

### 1.3.2

#### **The Marriage with Molecular Beams**

The Bell Laboratories design for the dye laser (passively mode-locked, CW, and cavity dumped) was too restrictive for our use and, even though we published several papers on studies in the condensed phase with 0.6-ps resolution, we decided to change to a new system. The synchronously pumped mode-locked (CW) dye laser allowed for tunability and also detection techniques for photon counting. The power of single-photon counting became apparent, and a new laser system, a synchronously pumped, cavity-dumped dye laser was constructed for studies of gas-phase molecular dynamics, but now with the benefit of all the expertise we had gained from building the first system used for the studies in the condensed phase and for probing the torsional rigidity of DNA.

Stimulated by the work on coherence, and now with the availability of picosecond pulses, I thought of an interesting problem relating to the question of intramolecular versus intermolecular dephasing. In isolated, large molecules (as opposed to diatomics), there are the so-called heat bath modes which can be a sink for the energy. The question arose: Could these bath modes in isolated, large molecules dephase the optically excited initial state in the same way that phonons of a crystal (or collisions in gases) do? This problem has some roots in the question of state preparation, and I was familiar with its relationship to the description of radiationless transitions through the work of Joshua Jortner, Wilse Robinson, and others. There was much theoretical activity about dephasing, but I felt that they were standard extensions and they did not allow for surprises. We decided on a new direction for the studies of coherence in a supersonic molecular beam.

Rick Smalley came to Caltech in May 1980 and gave a talk entitled "Vibrational Relaxation in Jet-Cooled Polyatomics". He spoke about his exciting work on the naphthalene spectra. From the line width in the excitation spectra, he inferred the "relaxation time". At the time, the work by Don Levy, Lennard Wharton, and Smalley on CW (or nanosecond) laser excitation of molecules in supersonic jets was providing new ways to examine the spectroscopy of molecules and van der Waals complexes. Listening to Rick and being biased by the idea of coherence, I became convinced that the way to monitor the homogeneous dynamics was not through the apparent width but by using coherent laser techniques. This was further kindled by the need for direct measurement of energy redistribution rates; we were encouraged by Charlie Parmenter after he had reported on a chemical timing method using col-

lisions as a “clock” to infer the rate of energy redistribution. The first “real” supersonic molecular beam was huge. We did not know much about this kind of technology. However, in a relatively short time, it was designed and built from scratch, thanks to the effort of one graduate student who must have consumed kilos of coffee! The molecular beam and picosecond system were interfaced with the nontrivial addition of a spectrometer to resolve fluorescence in frequency and time. This was crucial to much of the work to come.

### 1.3.2.1 The Anthracene Discovery: A Paradigm Shift

Our goal in the beginning was to directly measure the rate of intramolecular vibrational-energy redistribution (IVR), expecting to see a decrease with time (exponential decay) in the population of the initially excited, vibrational state and to possibly see a rise in the population in the state after the redistribution, thus obtaining  $T_1$  directly. What we saw in these large systems was contrary to the popular wisdom and unexpected. The population during IVR was oscillating coherently back and forth (Figure 1.10) with well-defined period(s) and phases. We were very excited because the results revealed the significance of coherence at its best in a complex molecular system, now isolated in a molecular beam, with many degrees of freedom. I knew this would receive attention and skepticism. We had to be thorough in our experimental tests of the observation and three of us went to the laboratory to see how robust the observation was. We published a Communication in the *Journal of Chemical Physics* (1981). Earlier there had been attempts by another group to observe such a “quantum coherence effect” in large molecules, but the observation turned out to arise from an artifact. Some scientists in the field were skeptical of our new observation and the theorists argued that a molecule is too big to see such quantum coherence effects among the vibrational states. Furthermore, it was argued that rotational effects should wash out such an observation.

We followed the initial publication with several others and the effect became even more pronounced with shorter time resolution. Physicists appreciated the new results. We published an article in *Physics Review Letters* on the nature of nonchaotic motion in isolated systems, and Nico Bloembergen and I wrote a review (1984) on the relevance to laser-selective chemistry.<sup>[B21]</sup> We and other groups subsequently showed the prevalence of this phenomenon in large molecules. As is often the case in science, after the facts have been established and in retrospect, the phenomenon was clear and was soon accepted; to some it even became obvious. Looking back, this novel and unexpected observation was a *paradigm shift* of critical importance, for a number of reasons:

1. The observation was the first to clearly show the presence of a “quantum coherence effect” in isolated complex chemical systems and only among selected vibrational states. In other words, out of the expected chaotic motion in the vibrational and rotational phase space we could see ordered and coherent motion despite the presence of numerous vibrational degrees of freedom (from  $S_0$  and  $S_1$  states). This point was theoretically appreciated by only a few scientists. In fact, at one point Stuart Rice and I drafted a paper on the subject, thinking of clarifying the point. At the time, researchers working in the



## IVR - Coherent and Dissipative Regimes

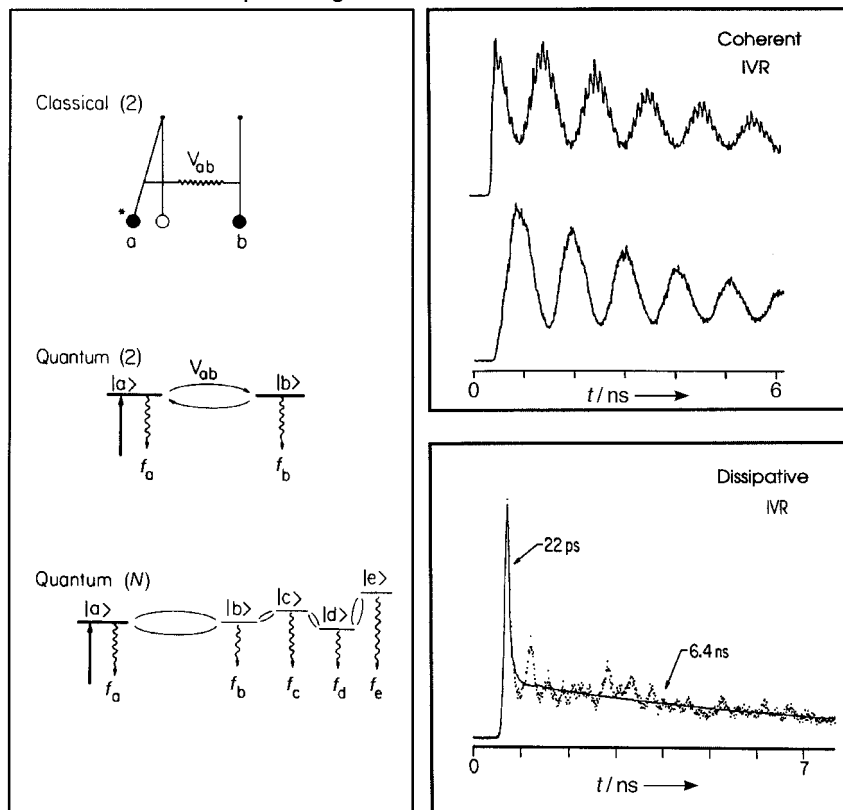


**Fig. 1.10** Dynamics of IVR showing the coherent, restricted, and the dissipative regimes. Note the exact in-phase and out-of-phase oscillatory behavior between the

vibrational states of the system (anthracene in a molecular beam). The theory for classical and quantum pictures (left) has been discussed in detail in the literature.<sup>[51, B20, B21]</sup>

area of high-resolution spectroscopy were observing complex spectra and attributing this complexity to chaotic vibrational motion in the molecule. Stuart and I argued that spectral complexity does not mean chaos, and the anthracene experiment was a clear demonstration in real time.

2. The experiment demonstrated that coherence had not previously been detected in complex systems, not because of its absence but due to the inability to devise a proper probe. Detection of total absorption or total emission (at all wavelengths) from molecules gives a nonselective window on the dynamics and in this way coherence cannot be detected. This was a key point for the success of the anthracene experiment for which both time and wavelength were resolved and correlated. For all subsequent work on wave packet dynamics, nuclear motion in chemical reactions, and femtochemistry, this concept of “window probing” was essential. The concept was further eluci-

dated by resolving the phase character. By probing at two different wavelengths, we found that the quantum oscillations exhibit identical periods, but were phase-shifted by exactly  $180^\circ$  (that is, they are out-of-phase) (Figure 1.10). The two wavelengths resolved were those corresponding to emission from the initial vibrational state and to that of the vibrational state to which the population goes by IVR. Thus, if “total detection” was invoked, the in-phase and out-of-phase oscillations will add up to cancel each other and coherence would have remained undiscovered.

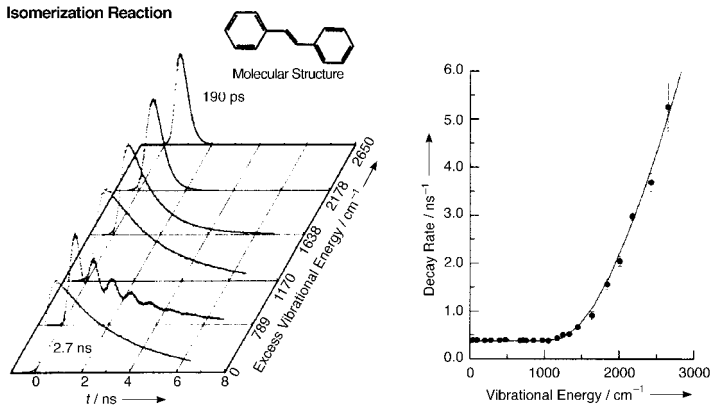
3. The observation of phase-coherent dynamics gave us a new dimension. The phase shift indicates a true transfer of population, in contrast with conventional quantum beats, and by analyzing the phases we could understand the nature of IVR: “concerted”, namely, going at the same time to all states, or “nonconcerted” that is going in a sequential redistribution of vibrational energy. We could also obtain the time scale and the effect of molecular rotations on coherence of the vibrational motion.
4. The observation of phase-coherent dynamics illustrated the importance of the “preparation of nonstationary states” in molecules. This issue was of fundamental importance in radiationless transition theories involving multiple electronic states, and experiments by Jan Kommandeur and by Doug McDonald have shown this interstate coupling. The question of interest to us was: What nuclear states do we prepare in the isolated molecule on a single surface? The anthracene experiment taught us that a coherent source spanning the stationary states can prepare a nonstationary state which evolves with time. Moreover, we can prepare molecules in-phase at time zero to observe the subsequent coherent dynamics. This concept indicates that the description, in terms of Schrödinger’s molecular stationary states, is not cardinal and that the time-dependent picture is real and directly relevant to dynamics. Most textbooks describe dynamics in terms of stationary states and it took some time for this concept of a time-dependent description to be appreciated. I recently found a theoretical article by Roy Gordon published in the 1960s touching on similar issues. In femtochemistry, the concept of time-domain dynamics is what describes elementary motions.
5. By directly probing coherence and its extent in isolated, complex molecular systems we advanced some concepts regarding the nature of IVR and its regions. We divided the regions of IVR into three basic ones: no IVR, restricted IVR, and dissipative IVR. We also established that the IVR picture of one vibrational state coupled to a continuum of vibrational levels is not adequate. Instead it is a multi-tier coupling among vibrational states.

This work and its implications were published in two series of papers and reviewed in two book chapters.

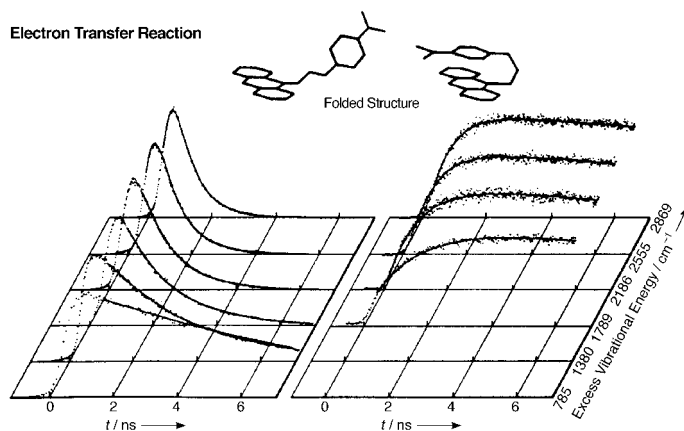
#### 1.3.2.2 The Successful 036 Laboratory

The laboratory known as 036 was in the sub-basement of Noyes. In this laboratory, the initial work on IVR was followed by fruitful applications spanning 1) studies of IVR in other systems, 2) radiationless transitions, and 3) reaction rates of a variety of

## Isomerization Reaction



## Electron Transfer Reaction



## Microscopic Solvation

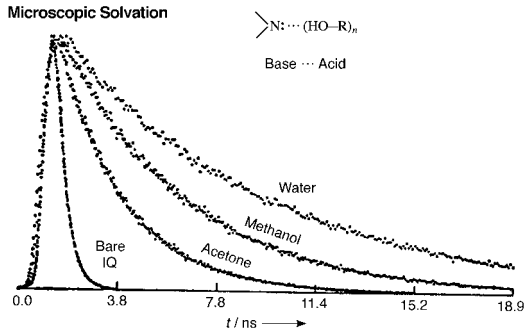


Fig. 1.11 Some examples of studies made in the early 1980s in the 036 Laboratory: The isomerization of stilbene, intramolecular electron transfer, and solvation in clusters (see text).<sup>[52, B3]</sup> IQ=isoquinoline.

systems. One of our first studies of reactions on the picosecond time scale, isomerization of stilbene, was stimulated by discussion with Robin Hochstrasser about his work on stilbene vapor at room temperature. He felt that if we could resolve the low-frequency modes in the molecular beam, we would derive a great deal of information on the torsional potential. We resolved these torsional modes. Furthermore, we decided to study the rates as a function of energy and in the process found the barrier for twisting around the double bond and observed coherent IVR in reactions, the first such observation. Even now, stilbene remains a member of our molecular family and continued studies have been pursued on the femtosecond time scale by us and others.

The following list highlights some of the work (Figure 1.11) done in this initial period from 1981 to 1983: 1) IVR in anthracene and stilbene; 2) *trans*–*cis* isomerization of stilbene; 3) quantum beats and radiationless transitions in pyrazine; 4) intramolecular hydrogen bonding in methyl salicylate; 5) intramolecular electron transfer in donor-bridge-acceptor systems; 6) IVR and dissociation of intermolecular hydrogen-bonded complexes; and 7) isomerization of diphenylbutadiene and styrene.

Over the years, in the same laboratory (036 Noyes), members of our group have made new extensions covering the following topics: isomerization in isolated molecules versus in bulk solutions; nonchaotic multilevel vibrational energy flow; mode-specific IVR in large molecules; IVR dynamics in alkylanthracenes; isotope effects on the isomerization of stilbene; charge transfer and exciton dynamics in isolated bianthracene; isotope effects on the intramolecular dephasing and molecular states of pyrazine; IVR dynamics in alkylnilines (the “ring+tail” system); mode-specific (non-RRKM) dynamics of stilbene-rare gas van der Waals complexes; solvation effects on intramolecular charge transfer; IVR dynamics in *p*-difluorobenzene and *p*-fluorotoluene (real time versus chemical timing); IVR dynamics in deuterated anthracenes; dynamics of interstate coupling in chromyl chloride; dynamics of IVR and vibrational predissociation in anthracene-Ar<sub>*n*</sub> complexes (*n* = 1–3); structural effects on the dynamics of IVR and isomerization in stilbenes; and dynamics of IVR and vibrational predissociation in *n*-hexane-solvated *trans*-stilbene. The research resulted in a series of publications.

### 1.3.2.3 Changing A Dogma: Development of RCS

The success with the anthracene experiment made us ask a similar question, but now regarding the coherent rotational motion of isolated, complex molecules. There were theories around which discarded its possibility because of the general belief that Coriolis interactions, anharmonicity, and other interactions would destroy the coherence. We worked out the theoretical implications and the results suggested possibly another surprise: if we could align the molecules with a polarized picosecond pulse and probe (polarization-selective) the rotating molecules, we should be able to observe rotational recurrences which would give the full period of rotations of the isolated (large) molecule. Classically, it is as if the molecule rotated back to its initial configuration. This rotation period gives the moment of inertia and, since the masses of the atoms are known, we can deduce distances, and hence obtain information on the molecular structures of very large molecules.

## Rotational Coherence Spectroscopy

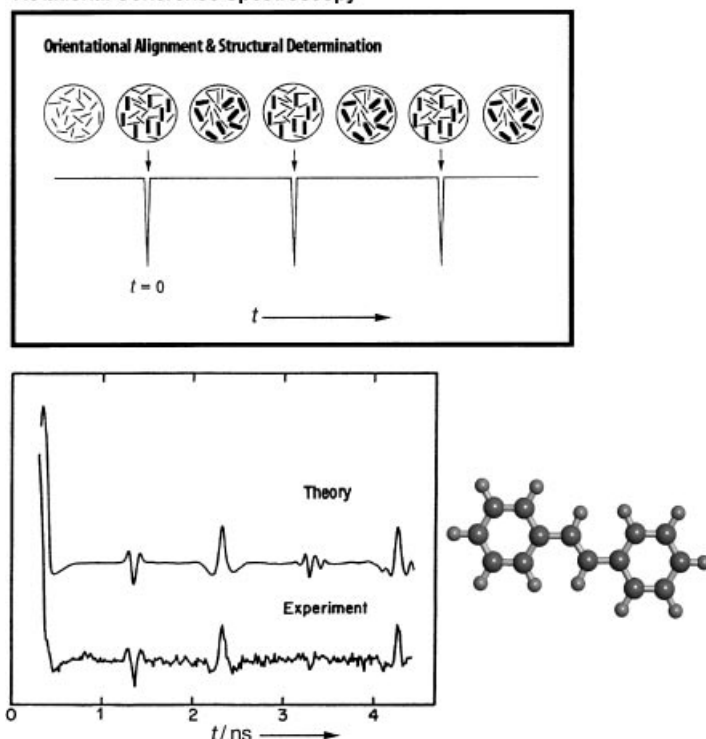


Fig. 1.12 The concept of RCS and the first experimental observation made in a beam of *trans*-stilbene.<sup>[53, B7, B13]</sup>

Indeed the recurrences in stilbene were observed with high precision, and its molecular structure deduced. Coherence in rotational motion was clearly evident and could be probed in a manner similar to what we had done with vibrational coherence. The approach was again met with some skepticism regarding its generality as a molecular structure technique. However, it is now accepted by many as a powerful Doppler-free technique; more than 120 structures have been studied this way. The method (Figure 1.12) is termed “rotational coherence spectroscopy (RCS)” and is successfully used in many laboratories. Some book chapters and review articles have been published on the subject (see the Bibliography).

Out of this first marriage between ultrafast lasers and molecular beams came the developments and concepts discussed above. We were now poised to study molecules and reactions with even shorter time resolution. We could study their vibrational and rotational dynamics and align (“orient”) them by controlling time.

## 1.3.3

**The Transition to the Sub-Picosecond Regime**

By the early 1980s, our laser time resolution for studying molecules in supersonic jets was 15 ps and detection was made using a microchannel plate (about 40 ps). With this resolution, we had already studied reactions such as the isomerization (twisting) of stilbene, charge transfer, and intra- and inter-molecular proton and hydrogen-atom transfer. How could we improve the time resolution and study, in a general way, the elementary steps of reactions? The only approach I knew of was to use two pulses, one to “pump” and the other to “probe”. Unlike liquid-state studies, where the approach was proven successful, in this case, the density of a molecular beam is very low. Furthermore, it was not clear how to establish the zero of time *in situ* in the molecular beam and how to avoid temporal broadening as a result of propagation effects.

**1.3.3.1 A New Beam Machine: Pump-Probe Mass Spectrometry**

I thought we should build a second generation beam apparatus to house a time-of-flight mass spectrometer. From the physics literature, it was clear that single atoms could be detected using ionization techniques with lasers, and such detection had already been successful with nanosecond lasers. Unlike many nanosecond studies, we should propagate the two picosecond (and later femtosecond) pulses in the same direction, otherwise we would lose the ultrashort time resolution. The same beam machine was equipped with optics for laser-induced fluorescence detection. We began a new direction of research in a separate laboratory of our group. The new beam was built and integrated with two independently tunable dye lasers. This proved to be a precursor to the femtochemistry work as this taught us to master pump-probe picosecond and sub-picosecond experiments on chemical reactions. In this same laboratory, we studied with a resolution of a few ps: 1) dissociation reactions; 2) ground-state, overtone-initiated reactions; 3) van der Waals reactions, and others (Figure 1.13). We wrote a series of papers on state-to-state microcanonical rates  $k(E)$ , and addressed theoretical consequences and deviations from the statistical regime. It was in two of these systems (reactions of NCNO and ketene) that we found that the statistical phase-space theory (PST), although successful in describing product-state distributions, failed in describing the microcanonical rates  $k(E)$  as a function of energy. Moreover, we made careful studies of the effect of rotational population on  $k(E)$ , and the effect was dramatic near the threshold value. Rudy Marcus, stimulated by these studies of  $k(E)$ , applied variational RRKM theory and we published some papers in a collaborative effort. The key point here is that the TS “moves” to different (shorter) distances along the reaction coordinate at different energies; the cardinal definition is relaxed (see Section 1.2). In another system ( $\text{H}_2\text{O}_2$ ), we studied the ground-state (“thermal”) reaction for the first time in real time by initiating the reaction with direct excitation of the overtones of the OH stretching vibration (Figure 1.13). The coupling between theory and experiment stimulated my interest in the nature of transition states which generally live for less than a picosecond. The thirst for even shorter time resolution became real.

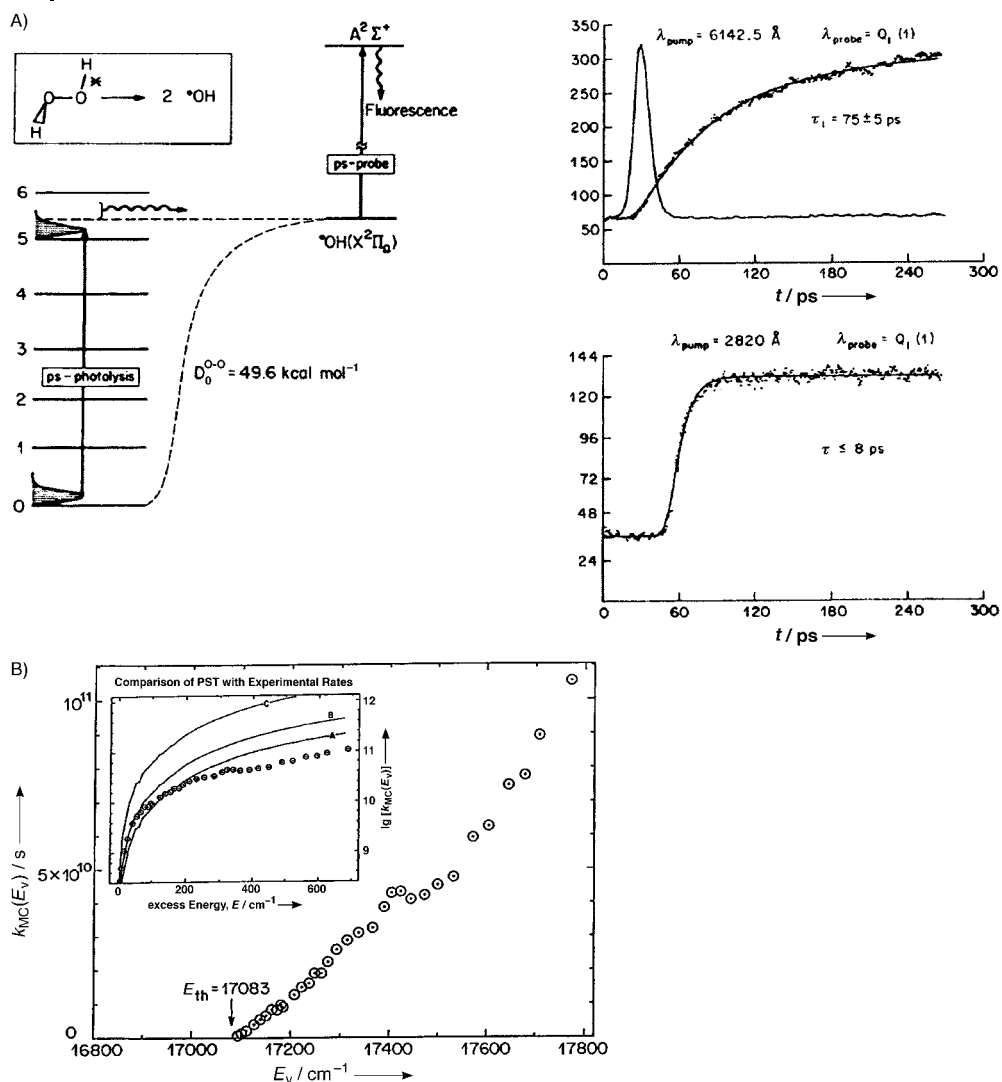


Fig. 1.13 Microcanonical rate constants.

A): Ground-state reaction of  $\text{H}_2\text{O}_2$  initiated by local-mode excitation; B): the rate constant for the dissociation of NCNO as a function

of the vibrational energy  $E_v$ , showing the breakdown of conventional PST at energies above the threshold value  $E_{\text{th}}$  (inset).<sup>[54, B1]</sup>

### 1.3.3.2 The First Experiment on ICN: Sub-picosecond Resolution

In the early 1980s, the technology of pulse compression became available and we ordered, from Spectra Physics, a pulse compressor—a fiber optic arrangement to reduce the laser pulse width to sub-picosecond. The company indicated that it would take them several months to build one, and that the only one available was at Purdue University in the laboratory of Professor Duane Smith, one of the first two graduate students I had at Caltech. I mentioned to Duane my excitement about the

experiment, which was intended to directly monitor the elementary bond breakage in a molecule, and asked if it was possible to borrow his compressor. The triatomic molecule ICN was chosen because the CN radical could be conveniently monitored by laser-induced fluorescence; we had been encouraged by the positive experience we had had with CN from NCNO and with earlier picosecond results on ICN. Also, ICN had been central to studies of dissociation reactions and to photofragment spectroscopy. Previous work, without time resolution, had provided a measurement of the so-called anisotropy parameter  $\beta$  and, hence, inference of the time scale.

All that we needed was a factor of 10–100 improvement in time resolution from what we currently had in the group. Duane shipped the compressor and joined us for two weeks. We observed the first ICN sub-picosecond transient, thus establishing the new methodology. In the same year, we wrote a paper which was accepted and published (December 1985) in the *Journal of Physical Chemistry*. We did not resolve the transition states of this reaction, but only detected the rise of the product. The last paragraph in this paper summarized what it would be possible to do if the time resolution could be improved by a further order of magnitude: “Since the recoil velocity is  $\sim 2 \times 10^5 \text{ cm s}^{-1}$ , the fragment separation is  $\sim 10 \text{ \AA}$  on the time scale of the experiment (about 500 fs). With this time resolution, we must, therefore, consider the proximity of fragments at the time of probing, namely, the evolution of the transition state to final products.” I wrote this sentence having in mind that the femtosecond resolution is the ideal one and that our next step in research should be in this direction.

Several factors influenced the fast entry into femtochemistry. The development in 1981 by Richard Fork, Ben Greene, and Chuck Shank of the colliding pulse mode-locked (CPM) ring dye laser took the pulse duration into the 90-fs regime. By 1985, when we were involved in the ICN experiment, 27-fs pulses were generated with the help of intracavity pulse compression. Soon after, in 1987, 6-femtosecond pulses were obtained by amplification and extracavity compression.<sup>[19d]</sup> With such short pulses, and with the help of the earlier development of continuum generation by Bob Alfano and Stanley Shapiro,<sup>[19h]</sup> continuously tunable femtosecond pulses became available and only (!) required expertise in ultrafast lasers and nonlinear optics.

The interaction with several colleagues was a stimulating force in the initial effort. With Rudy Marcus and Vince McKoy, my colleagues at Caltech, I discussed many experiments and theories, especially on our way to lunch at the Athenaeum, Caltech’s faculty club. John Polanyi came to Caltech in 1982 as a Fairchild Scholar. John saw the importance of (CW) transition-state spectroscopy, and his paper in a book I edited (proceedings of the conference in Alexandria) was on this subject, focussing on the reactions of  $\text{H} + \text{H}_2$  and  $\text{NaI}$  dissociation (wing emission). For some reason, we did not discuss femtosecond transition-state spectroscopy at this time, but instead we (with John providing all the notes in writing) were interested in intense-laser-field stimulated emission in the  $\text{NaI}$  system and in the field “dressing” of the potentials. I do not know why I did not think of this system as the first one for femtosecond transition-state spectroscopy. This may have been because of the earlier experience we had with the ICN picosecond experiments. Later, the potentials John sent from Toronto were helpful in my thinking of the  $\text{NaI}$  experiment.



At nearby UCLA, the arrival of Dick Bernstein to the area was a real blessing. He was extremely excited about the developments and the possibilities for real-time studies of molecular reaction dynamics. It was at his house in Santa Monica that the word *femtochemistry* was coined, helped by a discussion in the company of his wife Norma and brother Ken. Dick also came to Caltech as a Fairchild Scholar in 1986, and in 1988 we wrote a feature article together (published in *Chemical & Engineering News*<sup>[26]</sup>). We had great fun writing this article and we learned an enormous amount about molecular reaction dynamics. We also had a genuine collaboration on bimolecular reactions and published a paper in 1987. Dick came to Caltech again in 1990, but sadly died before ending his sabbatical; a number of experiments, particularly the new direction of surface femtochemistry, were designed as part of our plan. Finally, the collaboration I had with Rich Bersohn, while he was at Caltech as a Fairchild Scholar, was enlightening. We discussed the classical picture of femtosecond spectroscopy of dissociating molecules, and wrote a theoretical paper on this subject.

#### 1.3.4

#### The Femtosecond Dream

##### 1.3.4.1 A Piece of Good Fortune

To achieve the femtosecond time resolution, we needed a new laser system. A piece of good fortune came our way at a time when funding was limited and when the establishment of femtosecond lasers and molecular beam technologies required a “quantum jump” in support. Shaul Mukamel invited me to a workshop in Rochester (October 1985) on intramolecular vibrational redistribution and quantum chaos. I spoke about “IVR and chemical reactivity”, and there in the audience were two program directors from the Air Force Office of Scientific Research (AFOSR): Larry Davis and Larry Burggraf. They requested a preliminary proposal immediately, and I sent one in October, followed by a complete proposal in January of 1986.

The proposal was funded and approved in August of 1986, to start in November of the same year. Larry Davis saw to it that we could order the equipment needed as soon as possible and made the necessary arrangements to do so; AFOSR continues to support our program. We did not have laboratory space to house the new equipment, but Caltech responded. Fred Anson, our Division Chairman at the time, arranged for the space (which once housed the X-ray machines of Linus Pauling) and Murph Goldberger, our President, provided funds for the renovation without delay—Murph appreciated the physics and Fred saw the importance of the new research to chemistry. By Thanksgiving (1986), we entered the new laboratory, and the CPM laser was operational at the “femtosecond party” on December 11, 1986. We focused again on the ICN reaction, but this time on the femtosecond time scale in FEMTOLAND I.

##### 1.3.4.2 The Classic Femtosecond Discovery in ICN

The goal of the ICN experiment was to resolve in time the transition-state configurations en route to dissociation [Eq. (5)]. Not only did we wish to monitor the final CN

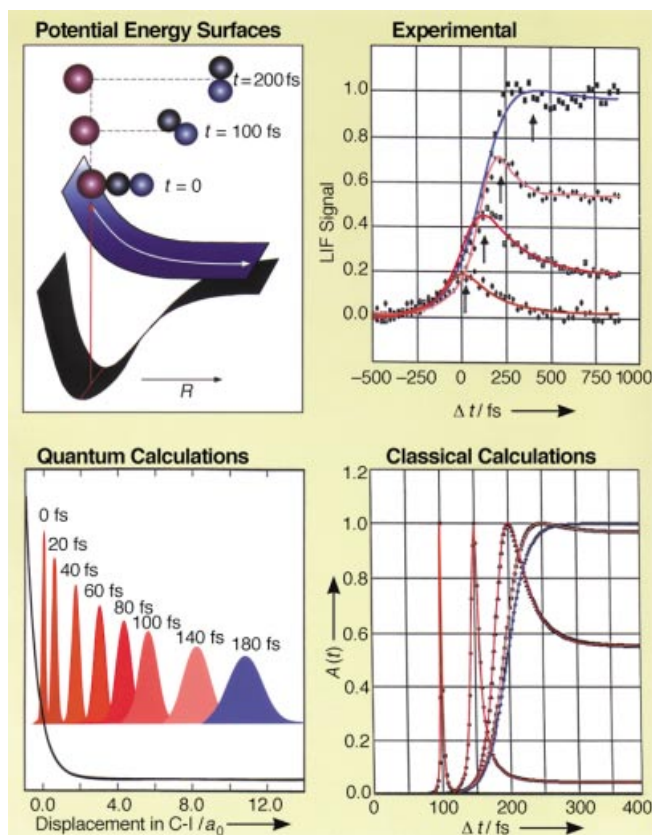


**Fig. 1.14** Femtochemistry of the ICN reaction, the first to be studied. Top right shows the experimental results for the probing of the reaction in the transition state region (rise and decay) and the final CN fragment (rise and plateau) with precise clocking of the process

( $\Delta t$ =time delay); the total time is 200 fs. The iodine fragment was also detected to elucidate the translational energy change with time. Classical and quantum calculations are also shown (see text).<sup>[55, B1, B4, B6, B14, B16, B18, B19, B28]</sup>



product, free of the force field of iodine (which we did in 1985), but also the transitory species  $\text{I} \cdots \text{CN}^{*\pm}$  (Figure 1.14). The first  $\text{I} \cdots \text{CN}^{*\pm}$  transient surprised us, but after long and late hours of discussions and control experiments it became clear that, indeed, the transition configurations and the final products could be separately monitored in real time. We submitted our first communication to the *Journal of Chemical Physics* (received June 3, 1987), and it was accepted on June 15, 1987. The referee of this paper was not only prompt, but also, in retrospect, visionary. His report was ultrashort: "It (the manuscript) has the smell that the authors are onto some very exciting new stuff... This manuscript meets all requirements for a communication. It may turn out to be a classic. Publish with all dispatch."

Our thinking about the process of bond breakage was intuitive and relied on classical concepts, as discussed in the prologue. The basic observations made (Figure 1.14) in the ICN experiment could be related to the femtosecond nuclear dynamics; the delayed appearance of the CN (on-resonance) and the build-up and decay of transition configurations (off-resonance) was understood using simple classical mechanics and even a helpful kinetic picture of the type  $A \rightarrow B \rightarrow C$ , to describe the “elementary” steps of the reaction. Two papers (I and II of a series), published in the *Journal of Chemical Physics*, outlined the methodology of “femtosecond transition-state spectroscopy (FTS)” with applications to the ICN dissociation reaction. From these first experiments, we expressed the change in internuclear separation with time, namely, the reaction trajectory and the time of bond breakage, which are measured from Equations (6a) and (6b), respectively. For a given potential of interaction  $V$ , the velocity is  $v$  and the force is  $F = -dV/dR$ .

$$\tau = \int_{R_0}^R \frac{dR'}{v(R')} \quad (6a)$$

$$\tau^\ddagger = \frac{\Delta V(R^\ddagger)}{v(R^\ddagger)|F(R^\ddagger)|} \quad (6b)$$

We obtained the time of the motion to final products ( $\tau$ ) and during the transition state ( $\tau^\ddagger$ ), as well as the distance of separation  $R(t)$ . Thus, for a given total energy  $E$ , we expressed the distance of separation between I and CN and the time of bond breakage, and compared these with experimental results, hitherto unmeasured directly. Significantly, we were able, for the first time, to observe the passage through the transition state potential energy window  $\Delta V(R^\ddagger)$ , and measure its “lifetime” or transit time  $\tau^\ddagger$  with femtosecond resolution. This experiment on the dynamics of bond breaking and another one on the dynamics of bond making ( $H + CO_2 \rightarrow OH + CO$ ) events were generally well received by colleagues in the scientific community worldwide. They even had impact on the public press with significant write-ups in popular newspapers and magazines such as New York Times, Los Angeles Times, Discover,...etc. Isaac Asimov, H. C. von Baeyer, Gary Taubes, Philip Ball, and other notable science writers gave an exposition of this published work. Many books and textbooks referred and continue to refer to this 1987 discovery.

The quantum picture was intuitive too. On the basis of the experience outlined above, we could understand that coherent preparation can lead to nonstationary states which evolve with time (motion!) (Section 1.2). Extension to chemical reaction dynamics gives the nonstationary wave packet shown in Equation (7), which evolves

$$\Psi(R,t) = \sum_i c_i \psi_i(R) e^{-iE_i t/\hbar} \quad (7)$$

in time, similar to the two-level problem [Eq. (4)], but now with spatial  $R$  localization because of the sum over many energy states. This principle of superposition holds because of the linearity of the time-dependent Schrödinger equation. The phases in [Eq. (7)] give rise to the interferences (quantum coherence) and their fluctuations, arising from intrinsic anharmonicities or interactions with the environment, lead to the delocalization. Since the packet can be synthesized easily when the sum criterion

ion is satisfied, the femtosecond pulse becomes the ideal initiator of the motion of nuclei in a reaction.

The concept of describing quantum systems using wave packets is fundamental and goes back to the 1920s (Figure 1.4) when the connection between quantum mechanics and classical phenomena was the subject of discussion and correspondence among many notable scientists such as Schrödinger, Lorentz, and others;<sup>5)</sup> Sections 1.3.4 and 1.3.6 highlight the theoretical developments since then. The ICN results demonstrated the experimental observation of wave packets in molecular systems, and since then they have been synthesized in atoms, complex molecules, and biological systems, as well as in the different phases of gases, liquids, clusters, and solids. The behavior observed for ICN was found in other studies, the most recent is an elegant series of experiments of “bubbles in solids” by Majed Chergui’s group in Lausanne.

The question then was: Would quantum calculations reproduce the experimental results obtained for ICN? Dan Imre, being skeptical in the beginning, did the first of such calculations, and the results were important in showing the influence of the wave packet motion and spreading on the observed FTS transients. Horia Metiu addressed the role of rotations. We compared the quantum results with those obtained from the classical model of Bersohn and Zewail (see Figure 1.14). The model described the experimental trends quite well, just as did the quantum picture. This was followed by reports of trajectory calculations from Kent Wilson’s group and a density-matrix description from Shaul Mukamel’s group. The latter emphasized the different limits of dephasing and the time scale for nuclear motion. All theoretical results exhibited the general trends observed experimentally. In our early papers on ICN, we suggested that the  $\delta$ -function limit of wave-packet dynamics could be obtained if proper deconvolution was made, when the temporal response of the pulses is known. Very recently, Volker Engel and Niels Henriksen reported a quantum theoretical agreement with this simple picture and discussed its generality.

#### 1.3.4.3 The NaI Discovery: A Paradigm for the Field

There were two issues that needed to be established on firmer bases: the issue of the uncertainty principle and the influence of more complex potentials on the ability of the technique (FTS) to probe reactions. The reactions of alkali halides were thought of as perfect prototypes. Since they involve two potentials (covalent and ionic) along the reaction coordinate, I thought we would have fun with these systems. Moreover, their unique historical position in crossed molecular beam experiments (“the alkali age”) made them good candidates for the “femto age”. The reaction of NaI, unlike ICN, involves two electronic coordinates and one nuclear coordinate, the separation between Na and I. The resonance motion between covalent and ionic configurations is the key to the dynamics of bond breakage. How could we probe such motion in real time? We did the FTS experiments on NaI and NaBr, and the results, published in 1988, were thrilling (Figure 1.15) and made us feel very confident about the abil-

5) Schrödinger wrote a theoretical paper (*Naturwissenschaften* 1926, 14, 664), pointing out the transition from micro- to macro-mechanics using the superposition of eigenstates. There

was a correspondence between Schrödinger and Lorentz on this problem and the difficulty of making wave groups or wave packets.

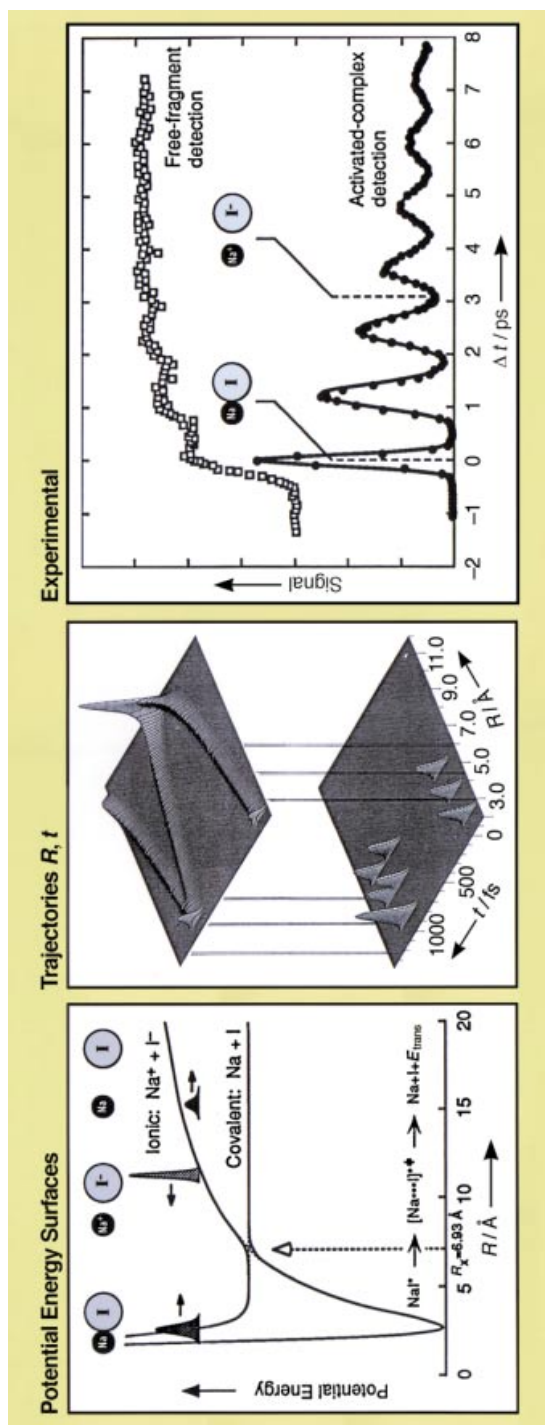


**Fig. 1.15** Femtochemistry of the NaI reaction, the paradigm case. The experimental results show the resonance motion between the covalent and ionic structures of the bond, as well as the time scales for the reaction and for the spreading of the wave packet. Two transients are shown for the activated

complexes in their transition states and for the final fragments. Note the "quantized" behavior of the signal, which is not simply an exponential rise or decay of the ensemble. The classical motion is simulated as trajectories in space and time (center). [56, B1, B4, B12, B14, B17, B19, B28]

ity of FTS to probe transition states and final fragments. The results also illustrated the importance of coherent wave packets in quasi-bound systems. The NaI experiment was a watershed event leading to an entirely new paradigm in the field of femtochemistry and establishing some new concepts for the dynamics of the chemical bond, for several reasons:

1. We could show experimentally that the wave packet was highly localized in space (about 0.1 Å), thus establishing the concept of dynamics at atomic-scale resolution.
2. The spreading of the wave packet was minimal up to a few picoseconds, thus establishing the concept of single-molecule trajectory, that is, the ensemble coherence is induced effectively, as if the molecules are glued together, even though we start with a random and noncoherent ensemble—this is the world of dynamics, *not* kinetics.
3. Vibrational (rotational) coherence was observed during the entire course of the reaction (by the detection of products or transition states), thus establishing the concept of coherent trajectories in reactions, from reactants to products.
4. On the femtosecond time scale, the description of the dynamics follows an intuitive classical picture (marbles rolling on potential surfaces) since the spreading of the packet is minimal. Thus, a time-evolving profile of the reaction becomes parallel to our thinking of the evolution from reactants, to transition states, and then to products. The emerging picture is physically and chemically appealing, and compellingly demonstrated that conversion from the energy space to the time domain is not needed.
5. NaI was the first system to demonstrate the resonance behavior, in real time, of a bond converting from being covalent into being ionic.

From the results, we obtained the key parameters of the dynamics such as the time of bond breakage, the covalent/ionic coupling strength, the branching of trajectories, etc. In the 1930s, Linus Pauling's description of this bond was that it was static at equilibrium; only now can the dynamics be described in real time by preparing structures far from equilibrium. I still reflect on the beauty of these NaI experiments and the rich number of concepts they brought to dynamics. Some of the concepts were not as clear when we first made the observations as they are now. The paradigm shift in our thinking is linked and similar in value to the work on IVR (Section 1.3.2), but the difference is major—for IVR we studied the coherence of states, but for reactions we observed the coherence of the nuclear motion with atomic resolution.

After the initial set of experiments, we continued on this system for some time, exploring other phenomena of interest. The studies included: 1) direct observation of the reaction trajectory in  $R$  and  $t$ , and the resolution of the motion into and from the transition state (this work was first published in *Nature*); 2) direct observation of recurrences (echo-type), reflecting rephasing at long times ( $t=20\text{--}40$  ps), and their relationship to quantum interference effects as a result of the resonance behavior of the motion on the covalent and ionic potentials (this work was published in *Chemical Physics Letters*); 3) studies of the effect of the velocity of the nuclei on the crossing-

to-products probability, which provided the interaction matrix element for the coupling between the covalent and ionic potentials, and the classical and quantum treatment of the dynamics (these studies were published in the *Journal of Physical Chemistry* and *Journal of Chemical Physics*).

Numerous theoretical and experimental papers have been published by colleagues and the system enjoys a central role in femtodynamics. From the beginning we understood the major features of the dynamics from the point of view of classical mechanics. The “exact” quantum calculations were first made by Volker Engel and Horia Metiu and these were important in identifying the sensitivity of the observations to details of the motion and the potential. The agreement with the experimental results was remarkable. The same agreement was found for later theoretical studies involving classical, quantum, and semiclassical approaches.

#### 1.3.4.4 The Saddle-Point Transition State

Our next goal was to examine reactions governed by multidimensional (nuclear) potentials, starting with “barrier reactions” which define a saddle-point transition state, the classic case of chemistry textbooks. If the reaction dynamics involve more than one nuclear coordinate, an interesting question arises: Can one observe in real time the reactive evolution from the TS at the saddle point to final products on the global PES? The question was addressed by performing femtochemistry on ABA systems. The IHgI system was the so-called “gift experiment” I suggested to a new postdoctoral fellow in our group, who joined us in 1988 from Ken Eisenthal’s group. Stunning observations were made—the product HgI was coherently formed from the transition state (Figure 1.16). Also, the transition state, which absorbs a probe femtosecond pulse in the red (as opposed to the HgI product which absorbs in the UV region) was found to live for only about 200 fs and this state produces different coherent product states (different periods of vibrational oscillation). It was also in this system that we studied coherence of rotational motion (real-time alignment) and learned about the geometry of the (initially prepared) transition-state, activated complex  $\text{IHgI}^{*\ddagger}$ .

With simple theoretical PES and molecular dynamics simulations we examined details of the motion, but the major features were evident in the experimental observations. Originally, we studied the TS and the evolution of HgI products by using laser-induced fluorescence. Later, we used mass spectrometry to also detect the I atoms and the translational energy; this effort triggered a great deal of theoretical work (Figure 1.16) in our group addressing, in depth, the actual meaning of classical TS structure (see Section 1.4). Features of this reaction were similarly found in other classes of reactions, including those in condensed phases and biological systems.

The studies of this ABA system were published with an emphasis on the following points: 1) coherent nuclear motion can be observed on multi-dimensional surfaces involving multiple-bond breakage (or formation); 2) coherence survives the entire reaction journey, even in multi-dimensional systems, and yields selective coherence in the products; 3) for the first time, a saddle-point TS can be seen evolving in real time; 4) the TS can be aligned (oriented) at zero time and seen evolving into rotations of the diatom (AB) and the translation of the A and AB fragments—

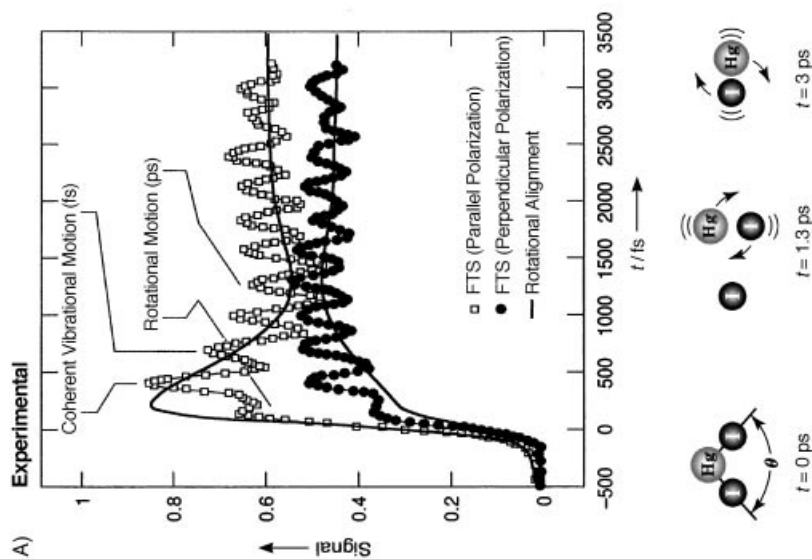
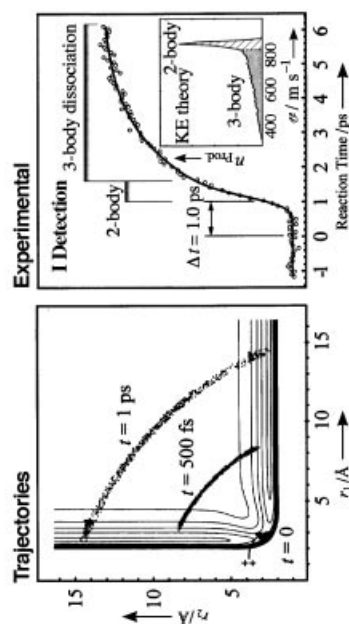
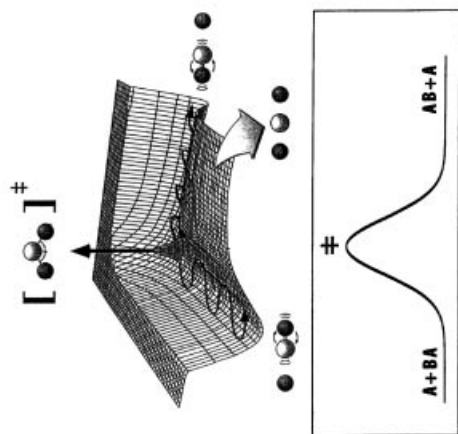


**Fig. 1.16** Femtochemistry of the I-HgI reaction with a saddle-point transition state (barrier reactions). The experimental results show both the coherent vibrational and rotational motions of the reaction (A). The transition state  $\text{IHgI}^{\ddagger}$  and final fragment HgI were probed. We also probed the I fragment and the change of translational energy with time. The classical trajectory calculations are shown in (B), together with

**B) Potential Energy Surface**



experimental results for I detection ( $n_{\text{prod}}$  in the inset corresponds to the number of atoms in the product). Both theory and experiment illustrate the family of reaction trajectories on the global PES, in time and in kinetic-energy distribution. Quantum calculations were also done (not shown). This ABA system is a prototype for saddle-point transition states.<sup>[57, 81, 84, 86, 810]</sup>



the vibrational (scalar) and rotational (vectorial) motions were easily separated using polarized femtosecond pulses.

#### 1.3.4.5 The Uncertainty Principle Paradox

At the time when I was giving lectures on the above examples of elementary reactions, some of the audience were raising a question about the “energy resolution” of the femtosecond experiments: How can a broad-energy pulse probe a sharp resonance? In the conventional teaching on spectroscopy of “eigenstates”, one thinks of stationary states and their populations (diagonal elements of the density matrix [Eq. (4)], but now we must think of coherent states. All information pertinent to eigenstates is in the wave-packet structure. This point was elucidated by our experiments on a bound nonreactive system—the iodine system (Figure 1.17). Serendipity was at work. We were initiating studies of the FTS of  $\text{CdI}_2$  (from the family of  $\text{HgI}_2$ ) and instead observed the wave-packet motion of  $\text{I}_2$ , made from the samples of  $\text{CdI}_2$  without our knowledge. It turned out that when we heated  $\text{CdI}_2$  we made  $\text{I}_2$ , which gave us striking oscillatory transients. The oscillations directly gave the periods of the nuclear (vibration) motion, and the data could be related to the change with time of the I–I separation and the rotation of  $\text{I}_2$ ; the time scales were separated (fs versus ps) and the vibrational (scalar) and rotational (vectorial) motion were clearly seen.

We used classical mechanical inversion methods, the RKR, and quantum inversion methods to characterize the potential. This was followed by a study of the  $\text{ICl}$

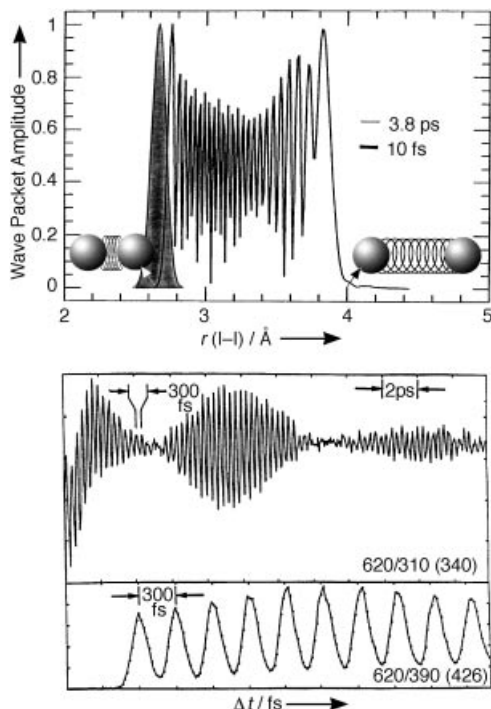


**Fig. 1.17** Femtosecond, real-time observation of the vibrational (and rotational) motion of iodine. The experiments show the anharmonic nature of the bound motion (bottom). Quantum theory (top) indicates the limit for creating a localized wave packet on the femtosecond time scale. The localized wave packet describes the classical spring motion.<sup>[58, B1, B6, B17, B18, B25]</sup>

system. It became evident that: 1) the uncertainty in energy for short pulses works in our favor, and the shorter the pulses, the better the localization of the wave packet; and 2) we could now observe the vibrations and rotations of molecules in real time, not from energy spectra. This work was first published in *Nature* and detailed later in the *Journal of Chemical Physics*. Since the initial experiments were made on a diatomic molecule, the significance of this piece of work was originally missed, until later when many complex systems showed similar behavior. The real message of this  $I_2$  experiment was in its conceptual elucidation of the role of the uncertainty principle and the robustness of time, space, and energy resolutions because of coherence: Since  $\Delta x \Delta p \sim \hbar$  and  $\Delta t \Delta E \sim \hbar$ , we can achieve localization with a very small de Broglie wavelength.

#### 1.3.4.6 Bimolecular Bond Making and Bond Breaking: Bernstein's Passion

Bimolecular reactions were ready for a femtosecond treatment, to observe the “simultaneous” processes of bonds being broken and formed. With Dick Bernstein (1987), we had studied the  $IH/CO_2$  system. The problem was that, for bimolecular reactions, the transient time for reactants to undergo a collision is generally nanoseconds to microseconds. By using van der Waals complexes, an idea introduced for the studies of product-state distributions by Benoit Soep and Curt Wittig, we could expand  $IH$  and  $CO_2$  in a single molecular beam. With the two reagents now within angstroms of each other, we could examine the dynamics of the single collision. We used the first pulse to liberate the  $H$  atom with a given translational energy and a second pulse to probe the nascent  $OH$  product—the zero of time became well-defined and the collision was that of a limited impact parameter. The results were exciting and, in our joint paper, Dick termed this the “birth of  $OH$  from  $H+CO_2$ ”. Wittig's group improved the time resolution and studied the energy dependence of the rates. Figure 1.18 gives a summary of this system.

The  $H+CO_2$  ground-state reaction proved to be important for a number of reasons: 1) it showed how reactive scattering resonances can be probed in real time during the collision and for a system with a complex number of degrees of freedom. 2) The experiments established that the intermediate  $HOCO^+$  has a lifetime  $\tau$  of about 1 ps and that for this reaction the  $OH$  bond making and the  $CO$  bond breaking are made in a nonconcerted pathway. The nuclear motions of  $HOCO$  thus determine the reaction mechanism. If  $\tau$  had been found to be 10–100 fs, the picture would have been entirely different; bond-making and breaking would occur as a result of the electron redistribution with the nuclei essentially “frozen” in configuration. Obtaining  $\tau$  directly is critical for the nature of the transition state/intermediate. This is particularly true when  $\tau$  is much longer than the vibrational and rotational periods, and all other methods will fail in deducing  $\tau$ . 3) The study provided a direct test of theory at the *ab initio* level. High quality *ab initio* calculations of the PES and dynamics have been made available by David Clary, George Schatz, John Zhang, and many others. Theory compares favorably with experiments, which shows that resonances must be considered—the vibrations of  $HOCO$  bottleneck the trajectories. The reaction  $OH+CO \rightarrow CO_2+H$  is one of the key reactions in both com-

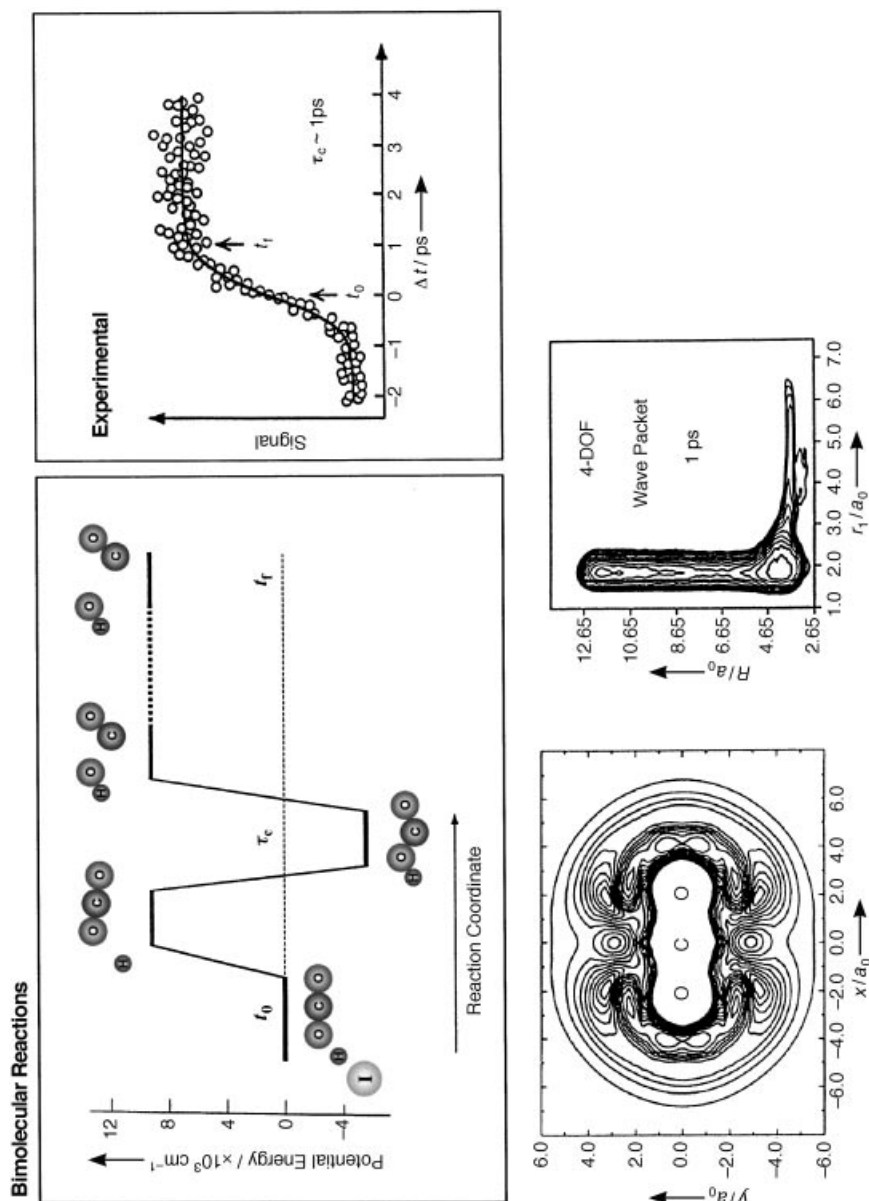


**Fig. 1.18** Femtochemistry of the bimolecular  $\text{H} + \text{CO}_2$  reaction. The precursor in this molecular beam experiment is  $\text{H}/\text{CO}_2$  in a van der Waals complex. The initial experiments utilized picosecond pulses, but later sub-picosecond pulses were used (see text). Theoretical ab initio calculations of the PES and the dynamics (classical, semiclassical, and quantum wave

packet) have all been reported. The PES and wave packet calculations are from the work of D. Clary, G. Schatz, and J. Zhang (see ref. [27]). The transit species  $\text{HOCO}^+$  lives for about 1 ps. Similar studies were made on the reactive pair  $\text{Br} + \text{I}_2$  and of the inelastic collision between  $\text{I}$  and  $\text{CH}_3\text{I}$ . [59, 81, 85, 810, 816, 819]

bustion and atmospheric chemistry, and represents the most studied four-atom reaction, both theoretically and experimentally.

We constructed FEMTOLAND II, and I thought it would be interesting to examine “halogen bimolecular reactions”. Precursors, of which the H–Br/I–I system is a prototype, were chosen to study bimolecular halogen atom+halogen molecule reactions. Upon breaking the HBr bond, the hydrogen goes many angströms away from the field of the reaction (in femtoseconds) and we are left with the Br+I<sub>2</sub> collision. This halogen reaction had a history in crossed molecular beam experiments and comparison with real-time experimental results would be interesting. The Br+I<sub>2</sub> reaction was examined and found to occur through a sticky (approximately 50 picoseconds) collision complex. It is a stable intermediate of BrII, and there is no other way we know of determining its lifetime and dynamics. We examined classical trajectories of motion and compared them with the experimental results. In more recent work, the McDonald group obtained similar times and discussed the possibility of the involvement of ground and excited halogen surfaces. In this study of a collision between an atom and a diatom, we learned the effect of impact parameters, the influence of translational energy, and the interplay between bonding and dynamics. The analogy between full-collision (Br+I<sub>2</sub>) and half-collision ( $h\nu$ +I<sub>2</sub>) dynamics was based on the change in bonding, and we used frontier orbitals to describe such an analogy. Studies of bimolecular collisions in complex systems have continued in our and other laboratories; the most recent came from NIST (John Stephenson and colleagues) on the studies of CH<sub>4</sub>+O→CH<sub>3</sub>+OH, using CH<sub>4</sub>·O<sub>3</sub> as a precursor.

#### 1.3.4.7 Ultrafast Electron Diffraction

FEMTOLAND III was the home of our next effort, Ultrafast electron diffraction (UED). Our goal was to complement the detection schemes of spectroscopy and mass spectrometry and to use diffraction to follow structural changes, especially for large systems. I proposed the idea in 1991 in an article for *Faraday Discussion*,<sup>[B17]</sup> and we had our first success in 1992. We were able to record structures with an electron pulse duration of a few picoseconds, but with no time scan. This was followed by other studies, both on the theoretical and experimental fronts. In our group, rumor had it that UED was a “No to the power 10 experiment!” We now have the third generation of UED machines, with a group of graduate students and post-doctoral fellows participating. In a paper published in *Nature* in 1997, we reported our state-of-the-art experimental development of the methodology. We also developed a “difference-method”, which allows us to record the structure of radicals, carbenes, and intermediates, and with higher sensitivity (see Section 1.3.6).

#### 1.3.4.8 Clusters, Dense Fluids and Liquids, and New Generations of FEMTOLANDS

With the above-mentioned spectroscopy, mass spectrometry, and diffraction techniques, it was becoming possible to study many new systems. In addition to FEMTOLANDS I to III, PICOLANDS I and II were still operational in order to cover the different time scales of reaction dynamics. We are now up to FEMTOLAND VI. Two additional beam machines, equipped with mass spectrometry and

spectroscopic detectors, were added. These new FEMTOLANDS were built to accommodate the expanding scope of research, from gas phase to clusters, to liquids and dense fluids, to the world of complex organic and inorganic chemistry, and to the very complex biological systems. I find complex reactions fascinating and we have devoted significant effort to this area, studying both uni- and bimolecular reactions. We also maintain strong theoretical efforts on molecular structures and molecular dynamics to compare theory with experiment on the relevant time scale.

#### 1.3.4.9 Theoretical Femtochemistry

Our involvement had roots in the study of coherence and dephasing. This line of research was initiated by using pulsed lasers to form a coherent state, [Eq. (4)]. The evolution was followed in time to obtain the pure dephasing time ( $T_2'$ ), which reflects the extent of phase interruptions, and the population or energy decay time ( $T_1$ ). We invoked theoretical techniques such as density matrix formalism, Kubo relaxation theory, and the Bloch equations to describe the optical analogue of NMR experiments. The 1957 Feynman, Vernon, and Hellwarth paper<sup>[29]</sup> was an important contribution, as it pointed out the linkage between “spin” and “optical” coherence experiments: even in the absence of a magnetic field, used in the former, one can use a rotating frame picture to describe such optical experiments. All of this was known at the time. Our interest in theory was to relate  $T_1$  and  $T_2'$  to molecular processes and to learn about their formal limits of applicability. We wrote a book chapter<sup>[B9]</sup> on the subject and published a number of papers relating these relaxation times to the anharmonicity of molecular vibrations, the phonon structure of solids, and collision dynamics in gases.

For collisionless, large molecules, the issue of intramolecular electronic-states coupling was, by the 1970s, well developed theoretically and heavily imbedded in theories of radiationless transitions that were formulated to explain the origin of nonradiative decays. Wilse Robinson, Joshua Jortner, Stuart Rice, and many others were involved in the early stages of this development. The Bixon–Jortner model gave the description for such coupling of inter-electronic states and the important role of preparing a doorway state which “dephases” and “relaxes” depending on the electronic coupling matrix element, Franck–Condon factors, and the density of states.<sup>[30]</sup>

For IVR processes (Section 1.3.2), we developed a theoretical description for the coherent preparation of a set of vibrational eigenstates on a single potential surface, defining the preparation of a nonstationary vibrational packet, with the role of rotations and vibrational couplings explicitly expressed. The probability of being in the initial state  $\psi_0$  is given by Equation (8), where the sum is over a product of

$$P(t) = |\langle \psi_0 | \Psi(t) \rangle|^2 = \sum_{i,j} \alpha(i,j) e^{-(i\omega_{ij} + \Gamma)t} \quad (8)$$

coefficients  $\alpha$  ( $\alpha(i,j)$ ), and displays the interference of states  $i$  and  $j$ , together with their damping rate  $\Gamma$ . This treatment was useful because: 1) it gives a direct view of IVR, from the initial nonstationary state and as a function of time; 2) it indicates the

critical role of selective probing—if all states were monitored, coherence would be obscured. On the other hand, selectivity provides rich information on the nature and extent of IVR, the level structure, and the phase changes; and 3) it shows that  $P(t)$  is a measure of vibrational chaos, which defines what we called restricted or nonchaotic IVR—coherence among vibrational states of a single electronic potential. Similarly, we considered the theory for rotational coherence using polarization-analyzed probes. This topic was treated in a series of papers with focus on the phenomenon of pure rotational coherence and its utility for molecular structural determination, and the rotational dephasing time.

At the time of the first femtochemistry experiment, I was thinking of the coherent state—wave packet—as an extension of the above picture. However, the span of states is now sufficient to create a localized, in  $R$  space, atomic-scale wave packet [Eq. (7)], (see Section 1.3.6). We needed a classical picture to connect with Newtonian mechanics, a simplified picture of the motion. The first of such models was published after we considered the theoretical treatment of absorption of fragments during reactions. We obtained the following Equation (9a), where  $C$  is a constant and

$$A(t; R) = C[\delta^2 + W^2(t, t^\pm)]^{-1} \quad (9a)$$

$W = V(t) - V(t^\pm)$  is the potential (or more generally, the difference of the two potentials probed);  $\delta$  is a half-width of the pulse (and damping). For exponential repulsion,  $V = E \operatorname{sech}^2(vt/2L)$ , with  $L$  defining the length scale and  $v$  being the speed at the total energy  $E$ .

Accordingly, the time for bond breakage  $\tau_{BB}$  can be related to FTS observables [Eq. (9b)] (see Section 1.3.4.2). This expression defines bond breakage time when the

$$\tau_{BB} = \frac{L}{v} \ln \frac{4E}{\delta} \quad (9b)$$

potential drops to a value of  $\delta$ . The model is basic and describes the reaction trajectory  $R(t)$  or  $\tau(R)$ . It provides a simple connection between observations and the dissociation time, transition-state lifetime, and the forces of the potential [see Eq. (6) and Figure 1.14]. While Dick Bernstein was at Caltech, we extended the model to obtain the potential using an inversion approach. We published two papers on the subject. Peter Sorokin and colleagues at IBM have addressed different limits of the classical regime in connection with their original studies of femtosecond transient absorption of dissociation.<sup>[B50]</sup>

Next, we considered the treatment of the effect of alignment and orientation on femtochemical reaction dynamics. I considered the time evolution of alignment and coherence for a single rotational angular momentum and then averaged the different trajectories to define the coherence time  $\tau_c$ ;  $\tau_c$  (in ps) becomes simple and equal to  $2.2[B\langle E_R \rangle]^{-1/2}$ , where  $B$  is the rotational constant and  $\langle E_R \rangle$  is the average thermal rotational energy (in  $\text{cm}^{-1}$ ) produced in the reaction fragment(s). We applied this to reactions and I wrote a paper on the subject, published in 1989.<sup>[B18]</sup> This was followed, in collaboration with Spencer Baskin, by a paper describing the details of the approach and its applications.

In quantum treatments, we have benefited greatly from the advances made in theoretical formalism and computation. A major step forward was made when Rick

Heller<sup>[31a]</sup> reformulated the time-dependent picture for applications in spectroscopy, and Jim Kinsey and Dan Imre<sup>[31b]</sup> described their novel dynamical Raman experiments in terms of wave packet theory. Progress was significantly helped by advances made in the theoretical execution and speed of computation by Ronnie Kosloff<sup>[31c]</sup> and, subsequently, by many others. In Section 1.3.6.2, the contributions made in the 1980s in connection with quantum control are discussed.

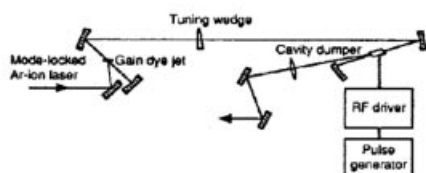
As mentioned in Section 1.3.4.2, the groups of Imre and Metiu did the first “exact” quantum calculations of femtochemical dynamics (ICN and NaI). The literature is now rich with numerous theoretical studies. There is a parallelism between the experimental diversity of applications in different areas and the impressive theoretical applications to many experiments and systems. This is summarized in the (1996 Nobel Symposium) book edited by Villy Sundström on Femtochemistry and Femtobiology.<sup>[28]</sup> Jörn Manz, who has played a significant role in this field, gave an overview of developments since Schrödinger’s 1926 paper, with 1500 references. Jörn classifies the field into periods of *origins*, *sleeping beauty*, *renaissance*, and *revolution*. In this Nobel Symposium book (and another one<sup>[30]</sup>) Jortner provides a unifying overview of molecular dynamics in femtochemistry and femtobiology, and Mukamel gives an exposition of a general approach using the density matrix formalism. In the same volume, Clary presents the state-of-the-art in quantum theory of chemical reaction dynamics while Marcus and Casey Hynes review transition state theories for rates and dynamics.

Theory and experiment are now hand-in-hand, and many laboratories are doing both. For elementary chemical reactions, the above classical/quantum picture captured the essence of the observation and in many cases the comparison between theory and experiment was tested critically. For complex systems, our theoretical effort has taken on a different approach. With the help of molecular dynamics (MD) simulations, we compare theory with experiments. Then we use the MD simulations as a tool and vary parameters until we reduce the problem to identify the important key forces of dynamics. At this point, we can provide a microscopic dynamic picture with focus on the relevant vibrational coordinates, time scales, or system parameters. Two examples illustrate the point. The first was our study of the dynamics of a guest molecule in dense fluids, with focus on the density dependence of microscopic friction,  $T_1$  and  $T_2$ , and of bond breaking/remaking dynamics. The second, the study of numerous organic reaction mechanisms. For the latter, we also use advanced computational methods, such as density functional theory (DFT), *ab initio* and CASSCF computations. For ground-state reactions, the theory can be compared in a critical way with experiment, while for excited states the situation is more challenging.<sup>[32]</sup>

#### 1.3.4.10 Experimental Femtochemistry

The generation, amplification, and characterization of ultrashort pulses is a major part of femtochemistry experiments. Another is the reaction chamber: molecular-beam machine, gas cell, ultrahigh-vacuum (UHV) surface apparatus, or the high-pressure/liquid cell. Here, only the different systems designed for the studies presented in this anthology are mentioned; further details can be found in the book

A) Synchronously Pumped Cavity-Dumped Dye Laser



Passively Mode-Locked Cavity-Dumped Dye Laser

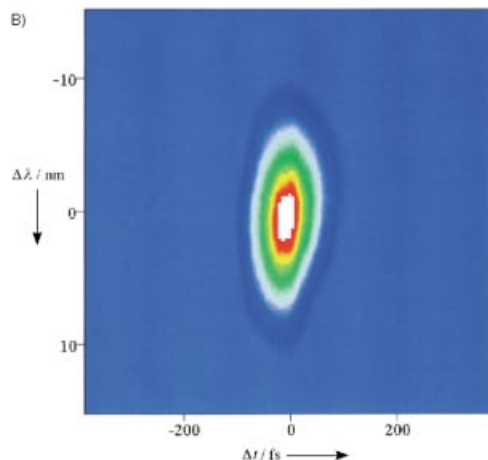
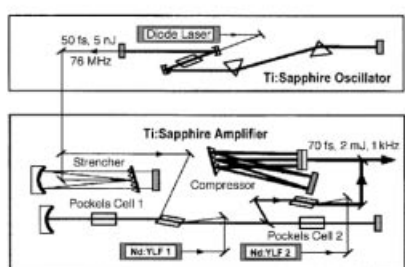
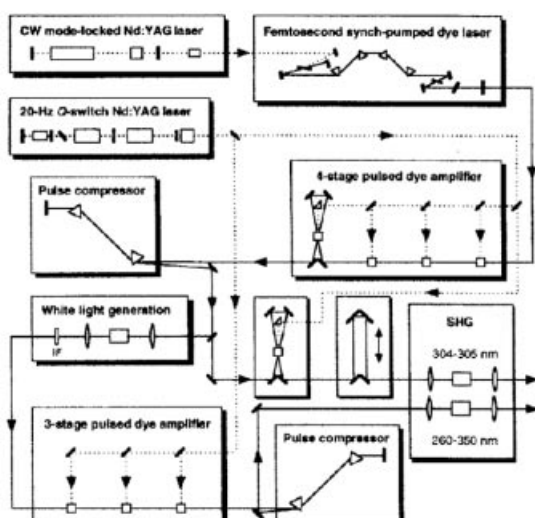
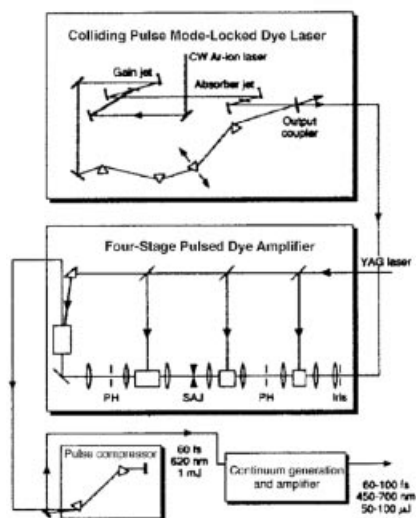
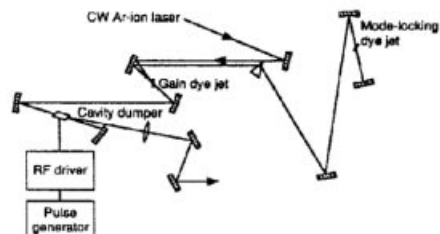


**Fig. 1.19** A) Examples of the laser systems utilized in different laboratories (for more details see text and ref. [B6]). B) The two-

dimensional (time and wavelength) correlated pattern of a femtosecond pulse (M. Chachisvilis, work from this laboratory).



chapter I wrote for the volumes edited by Manz and Wöste<sup>[B6]</sup> and in the two volumes of our collected works.<sup>[16]</sup>

At Caltech, over the years, we have constructed different types of lasers depending on the particular development and the resolution needed, picosecond to femtosecond (Figure 1.19A); one apparatus is shown in Figure 1.5. Since 1976, and in evolutionary order, these are:

- 1) Passive mode-locked, and cavity-dumped, dye laser (pumped by a CW argon ion laser); Ippen and Shank cavity design. Pulse characteristics: 615–625 nm, 2.4 ps (and 0.7 ps), 2 nJ, 100 kHz repetition rate.
- 2) Synchronously pumped, mode-locked dye laser system (pumped by an actively mode-locked argon ion laser). Pulse characteristics: 550–600 nm, 3.1 ps, 1.8 nJ, 82 MHz repetition rate.
- 3) Mode-locked argon-ion laser. Pulse characteristics: 514.5 nm, 150 ps, 12 nJ, 82 MHz repetition rate.
- 4) Synchronously pumped, cavity-dumped dye laser (pumped by a mode-locked argon-ion laser). Pulse characteristics: 550–750 nm, 15 ps, 20 nJ, 4 MHz repetition rate.
- 5) Mode-locked (CW) Nd:YAG laser which synchronously pumps two dye lasers, with two amplifiers pumped by a 20 Hz Q-switched Nd:YAG laser. Pulse characteristics: 550–750 nm, 3–5 ps, approximately 1 mJ, 20 Hz repetition rate.
- 6) Dye lasers (as described in point 5) with an extra-cavity pulse compressor (using a fiber-grating optics arrangement) to obtain ~0.4 ps pulses.
- 7) Colliding-pulse mode-locked (CPM) ring dye laser (pumped by a CW argon ion laser), and amplified in a four-stage dye amplifier pumped by a YAG laser. A compression at the output of the amplifier was also used. Pulse characteristics: 615–625 nm, 70 fs, approximately 0.5 mJ, 20 Hz repetition rate.
- 8) Synchronously pumped, cavity-dumped dye lasers (two), pumped by a Q-switched, mode-locked Nd:YAG laser. Pulse characteristics: 550–750 nm, 50 ps, 10  $\mu$ J, approximately 1000 Hz repetition rate.
- 9) Passively mode-locked, dispersion-compensated tunable dye laser (synchronously pumped by a frequency-doubled, CW, mode-locked Nd:YAG laser), amplified in a four-stage dye amplifier. The compression is after the amplifier. Pulse characteristics: 500–700 nm, 150 fs, 1 mJ, 20 Hz repetition rate.
- 10) CPM laser-amplifier system similar to that in point 7, used for ultrashort electron pulse generation. Pulse characteristics: 615–625 nm, 60 fs, 1 mJ, 30 Hz repetition rate.
- 11) Ti:sapphire laser system, Sibbett-type, argon-ion pumped; Ti:sapphire amplifier pumped by Nd:YAG laser. Pulse characteristics: 750–850 nm, 50 fs, 0.7 mJ, 1 kHz repetition rate; one optical parametric amplifier (OPA) system.
- 12) Ti:sapphire laser system; oscillator, diode pumped and amplifier (Ti:sapphire) Nd:YLF (2) pumped—all solid state (no gas lasers). Pulse characteristics: 750–850 nm, 50–100 fs, 2 mJ, 1 kHz repetition rate. With two OPAs, 1.1–2.6  $\mu$ m tunability, with 200 nm–2.6  $\mu$ m nonlinear conversions,.
- 13) Ti:sapphire laser system, same as in point 12, but pulse width 120 fs and 3 mJ energy, 1 kHz repetition rate.

For recording and clocking in any study, the resolution must be determined accurately, as must the zero-of-time ( $t = 0$ ). The pulses were characterized using auto-correlation and cross-correlation techniques, typically by scanning the time delay between the two pulses (of the same or different colors) in an interferometer arrangement and observing the sum- or difference-frequency generation in a nonlinear crystal. In this way, we can obtain the duration of the pulse. The central frequency of the pulse can be determined by passing the pulse through a calibrated spectrometer, while the shape of the pulse can be obtained from frequency-resolved-optical-gating (FROG) measurements, where the time and frequency components of the pulse are correlated and displayed as a 2D image (Figure 1.19B). In clocking experiments, the zero-of-time was precisely determined by an *in situ* measurement, typically using ionization techniques in beam experiments, lensing techniques in diffraction experiments, or the solvent response in condensed phase experiments.

The detection probes are numerous. Initially, we used laser-induced fluorescence for selectivity and sensitivity, and there we had a frequency-time correlation. Later, we invoked mass spectrometry (multiphoton ionization) for mass–time 2D correlations. This was followed by speed–time and angle–time correlations. All these correlations proved important in the studies of complex systems; a prime example was the application of the latter two correlations to the study of electron transfer in isolated bimolecular reactions and in clusters. For absorption-type measurements, we introduced nonlinear techniques such as degenerate-four-wave mixing. In a recent collaboration with the groups of Wolfgang Kiefer and Arnulf Materny, we also used

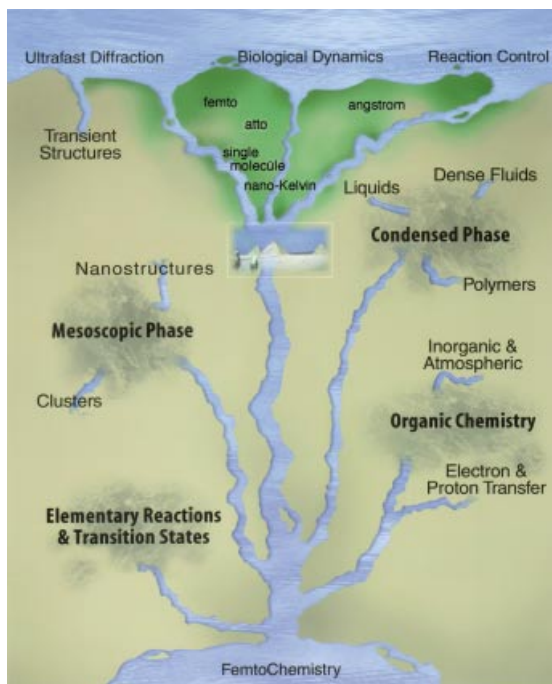


**Fig. 1.20** Femtochemistry branches, from the early days of studying elementary reactions and transition states (“southern part”) to the current activities (“northern part”). The flow of work has produced the different branches studied at Caltech.

coherent anti-Stokes Raman scattering (CARS), with frequency-time correlations to study the dynamics of ground-state systems, in this case polymers. Other detection methods are energy-resolved and ZEKE photoelectron spectroscopy, Coulomb explosion, ion–electron coincidence ionization techniques, absorption and photodetachment spectroscopy. The range of wavelengths is from the IR to the far UV. Absorption, emission, reflection, ionization, and diffraction have all been involved (see Figure 1.6).

### 1.3.5

#### **Femtocopia—Examples from Caltech**

The range of applications to different systems and phases in many laboratories around the world is extensive and beyond the purpose of this report. In this section I will limit the examples to those studied by the Caltech group. The details are given in the original publications and are summarized in the reviews and books mentioned here. Figure 1.20 gives a summary of the different areas studied at Caltech with chronological flow from the south to the north!

##### **1.3.5.1 Elementary Reactions and Transition States**

The focus here is on the studies of elementary reactions. Some of these have already been discussed above. The dynamics are generally of three classes:

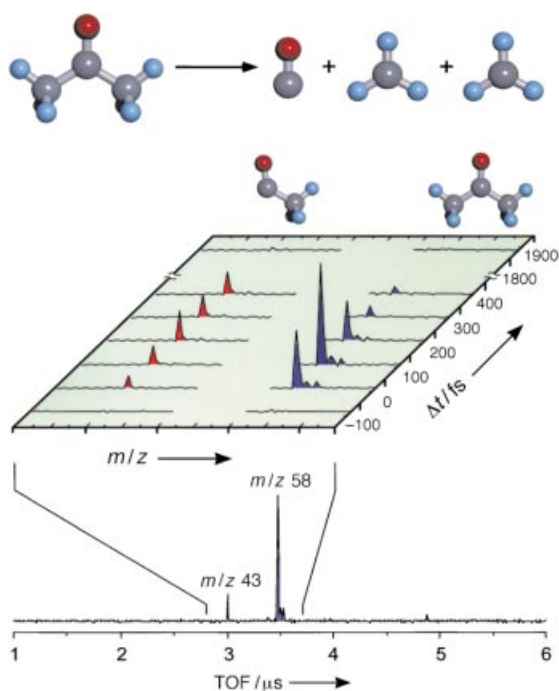
- 1) Dynamics of bond breakage
- 2) Dynamics of the (saddle) transition state
- 3) Dynamics of (bimolecular) bond breakage and bond formation

##### **1.3.5.2 Organic Chemistry**

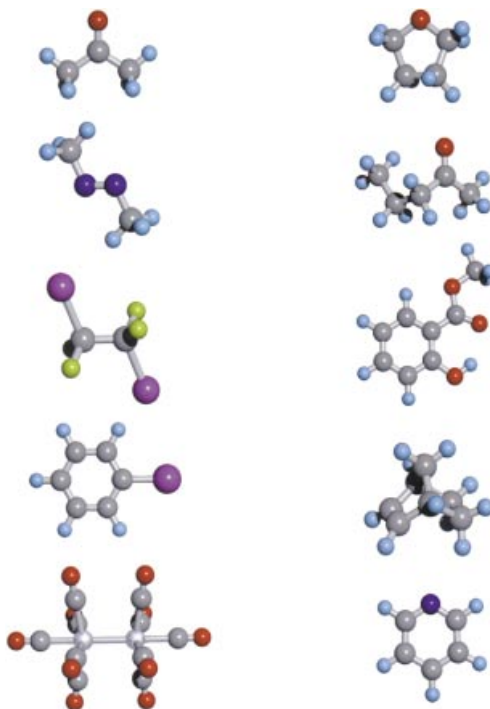
With the integration of mass spectrometry into femtochemistry experiments, the field of organic reaction mechanisms became open to investigations of multiple transition states and reaction intermediates (Figure 1.21). The technique of femtosecond-resolved kinetic-energy-time-of-flight (KETOF) provided a new dimension to the experiment—correlations of time, speed, and orientation which give scalar and vectorial dynamics. The examples of reactions include (Figures 1.21–1.26):

- 1) Isomerization reactions
- 2) Pericyclic addition and cleavage reactions
- 3) Diels–Alder/sigmatropic reactions
- 4) Norrish-type I and II reactions
- 5) Nucleophilic substitution ( $S_N$ ) reactions
- 6) Extrusion reactions
- 7)  $\beta$ -Cleavage reactions
- 8) Elimination reactions
- 9) Valence-structure isomerization
- 10) Reactive intermediates

**Fig. 1.21** Femtosecond mass spectrometry, a 2D correlation important in the studies of reactive intermediates. The example given here is for the reaction of acetone (Norrish type I) and its nonconcerted behavior.<sup>[60, 810]</sup> TOF=time of flight.



**Fig. 1.22** Molecular structures of different bond-breaking and bond-forming reactions studied, which are typical of the systems discussed in text for organic and organometallic femtochemistry: left (bond breaking): acetone,<sup>[60]</sup> azomethane,<sup>[61]</sup> diiodoethane,<sup>[62]</sup> iodobenzene,<sup>[63]</sup>  $[\text{Mn}_2(\text{CO})_{10}]$ ,<sup>[64]</sup> right (bond breaking/bond formation): cyclic ethers,<sup>[65]</sup> aliphatic ketones for Norrish II reactions,<sup>[66]</sup> methyl salicylate,<sup>[67]</sup> one of the structures studied for addition and elimination reactions,<sup>[68]</sup> pyridine (valence isomerization).<sup>[69]</sup>



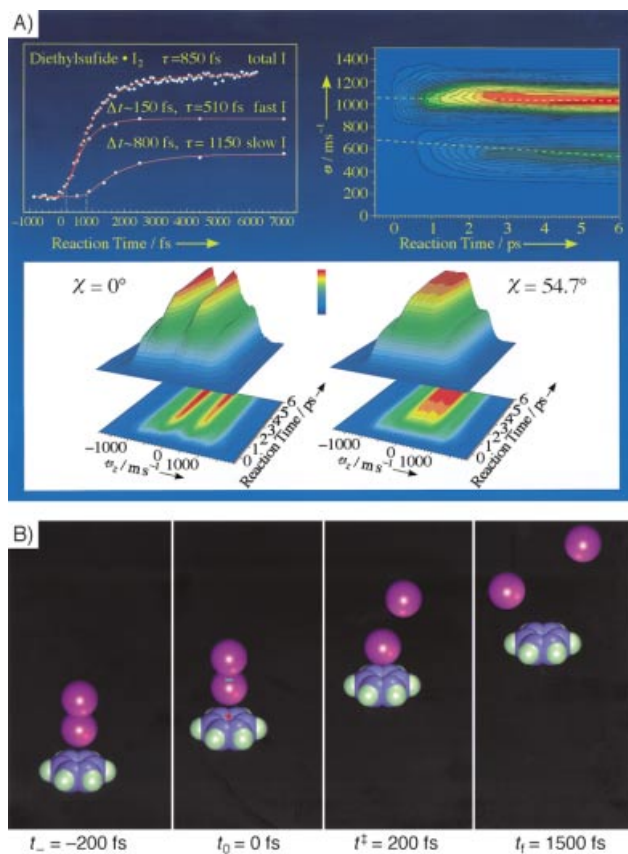


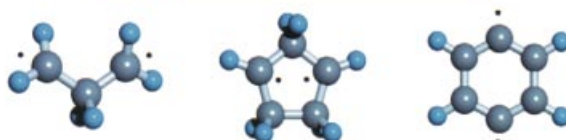
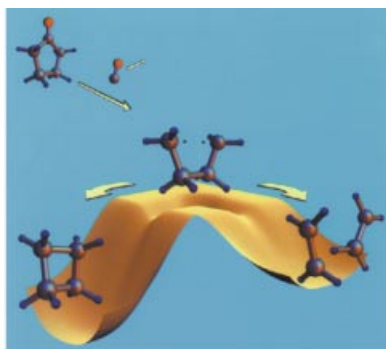
**Fig. 1.23** Femtochemistry of bimolecular electron-transfer reactions, the classic case of donors (for example, benzene or diethylsulfide) and acceptors (for example, iodine or iodomono-chloride). A) The experimental results clearly show the distinct velocity and time correlations, and thus the two-speed distributions and time scales of the reaction on the global PES. B) Snapshots of the atomic motions according to experimental findings.<sup>[70]</sup>

### 1.3.5.3 Electron and Proton Transfer

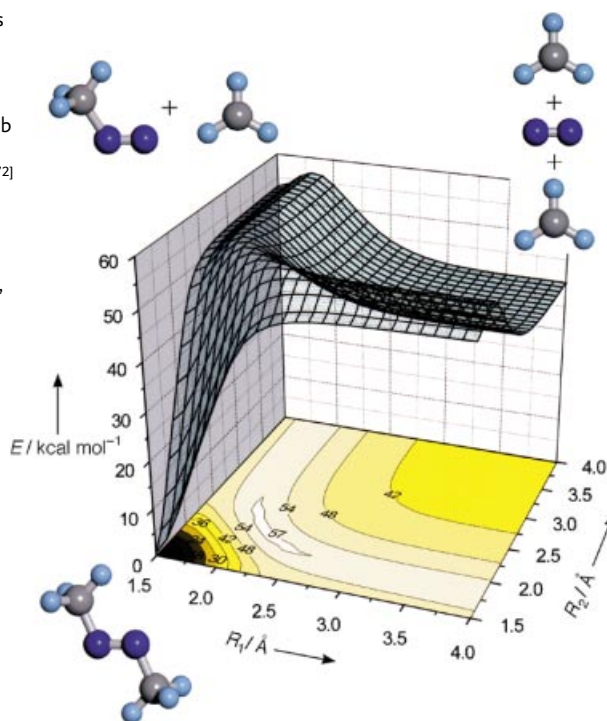
We examined both bimolecular and intramolecular electron transfer reactions, and these studies were the first to be made under solvent-free conditions. We also studied the transfer in clusters and in solutions (see Figures 1.11, 22, and 23). For proton transfer, three classes of reactions were of interest, those of bimolecular and intramolecular reactions, and those involving double proton transfer (base pair models):

- 1) Bimolecular electron transfer reactions
- 2) Intramolecular electron transfer and folding reactions
- 3) Acid–base bimolecular reactions
- 4) Intramolecular hydrogen-atom transfer
- 5) Tautomerization reactions: DNA mimics

**Fig. 1.24** Reactive intermediates on the femtosecond time scale. Here, tetramethylene, trimethylene, bridged tetramethylene, and benzyne are examples of species isolated on this timescale (see Figure 1.22 for others).<sup>[71]</sup>



**Fig. 1.25** Reaction dynamics of azomethane, based on the experimental femtosecond studies (see Figure 1.22 and associated references). The ab initio PES was obtained from state-of-the-art calculations,<sup>[72]</sup> which show the two reaction coordinates (C–N distances  $R_1$  and  $R_2$ ) relevant to the dynamics. A third coordinate, which involves a twisting motion, was also studied. Note the concerted and non-concerted pathways.



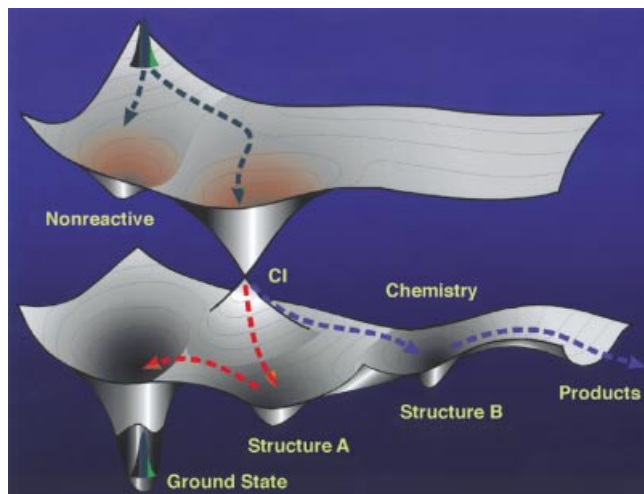


**Fig. 1.26** Generalized schematic diagram showing reactive and nonreactive pathways (bifurcation) of wave packets. Both the photophysical and photochemical processes are shown with the conical intersection (CI) playing a crucial role. Examples are given in ref. [73].

#### 1.3.5.4 Inorganic and Atmospheric Chemistry

We extended the applications of femtochemistry to complex inorganic reactions of organometallic compounds (see Figure 1.22). Organometallic compounds have unique functions and properties which are determined by the dynamics of metal–metal (M–M) and metal–ligand (M–L) bonding. The time scales for cleavage of such bonds determine the product yield and the selectivity in product channels. They also establish the nature of the reactive surface: ground-state versus excited-state chemistry. Similarly, we studied the dynamics of chlorine atom production from OCIO, a reaction of relevance to ozone depletion.

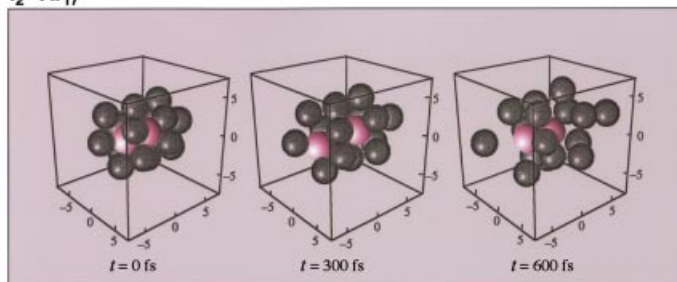
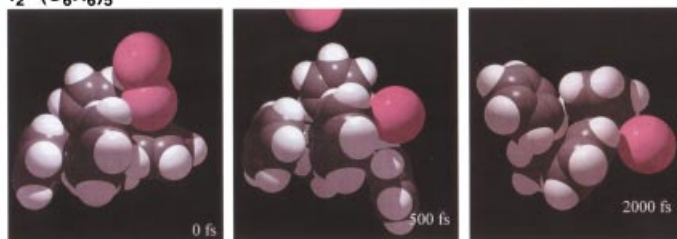
#### 1.3.5.5 The Mesoscopic Phase: Clusters and Nanostructures

We have studied different types of reactions under microscopic solvation conditions in clusters. These include (Figure 1.27):

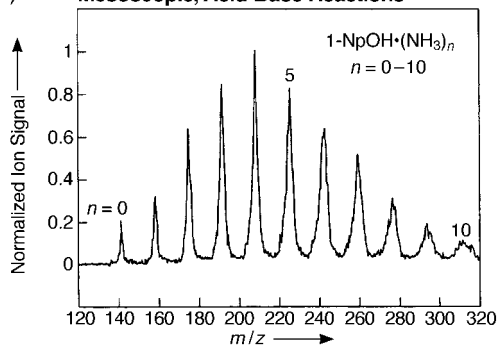
- 1) Reactions of van der Waals complexes
- 2) Unimolecular reactions
- 3) Bimolecular reactions
- 4) Recombination, caging reactions
- 5) Electron and proton transfer reactions
- 6) Isomerization reactions

#### 1.3.5.6 The Condensed Phase: Dense Fluids, Liquids, and Polymers

In this area of research, we have focused our efforts on the study of reactions in dense fluids and their comparison with dynamics in liquids. By varying the solvent density, we could study the femtosecond dynamics from gas-phase conditions to the

A)  $\text{I}_2 \cdot \text{Ar}_{17}$  $\text{I}_2 \cdot (\text{C}_6\text{H}_6)_5$ 

## B) Mesoscopic, Acid-Base Reactions



## Mesoscopic, Isomerization Reactions

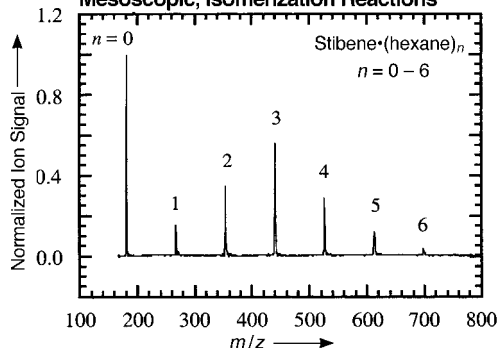


**Fig. 1.27** Femtosecond dynamics in the mesoscopic phase, reactions in solvent clusters. Several examples are given: A) The coherent nuclear dynamics of bond breakage and recombination of iodine in argon (the cage effect, top), and the dynamics of the same solute but in polyatomic solvents (benzene, bottom). It was for the  $\text{I}_2/\text{Ar}$  system that the first coherent bond breakage in the cage was observed and separated from the effect of vibrational relaxation. For the latter case, the two atoms experience different force fields and the time scales are determined by the degree of solvation. (We also studied van der Waals complexes.) B) A mass spectrum from a study of the acid-base reactions of naphthol with ammonia is shown (top), in which the number of solvent molecules is varied from 0–10. The isomerization of stilbene was similarly studied (bottom); the number of hexane solvent molecules was varied from 0–6.<sup>[74]</sup>



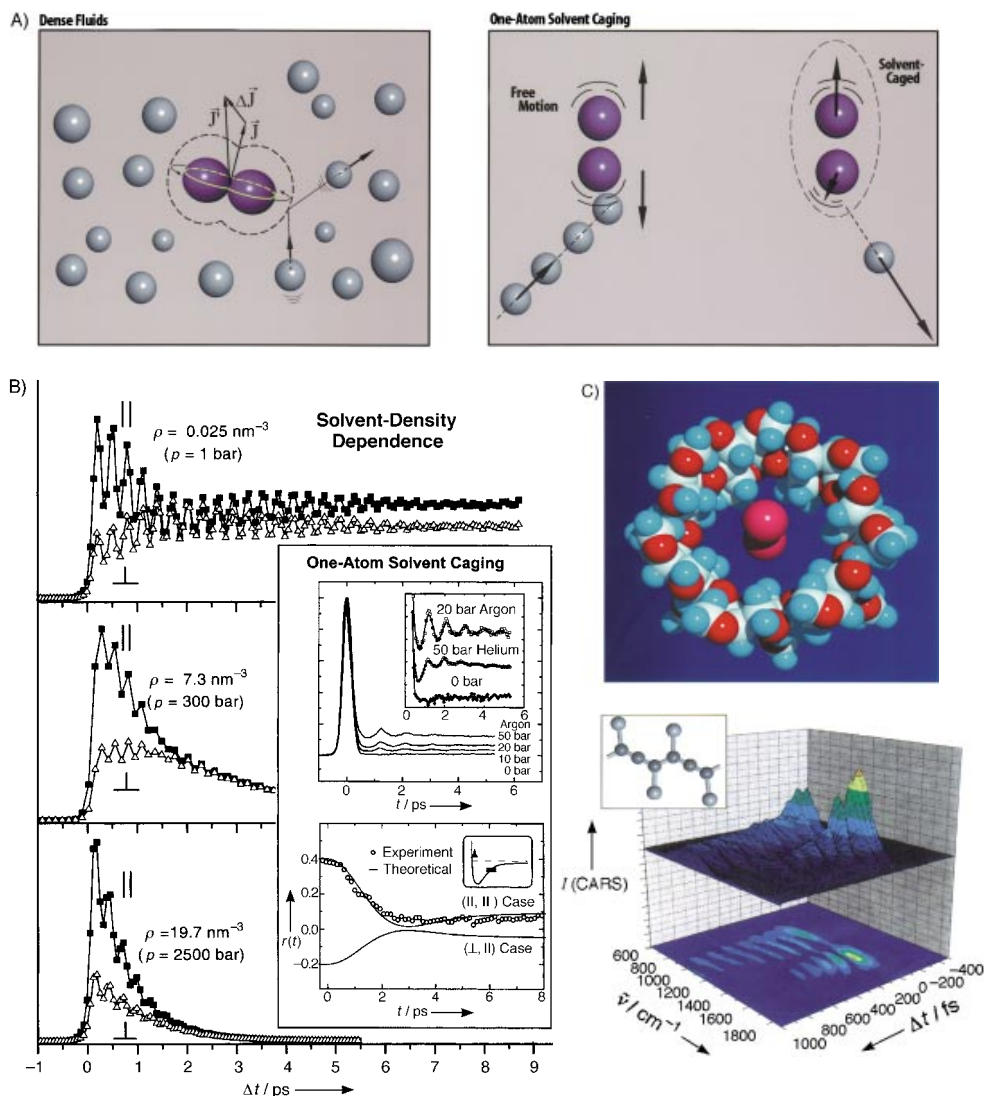


**Fig. 1.28** Femtosecond dynamics in the condensed phase: A) dense fluids; B) the coherent vibrational and rotational motions observed in dense fluids as a function of density and down to the one-atom collision with iodine; C) nanocavities in cyclodextrins (top) and polymers of polydiacetylenes

(bottom) (examples of liquids are not shown, but they can be found in the literature.<sup>[75]</sup>) Studies in these media include the one-atom coherent caging, J-coherence friction model, coherent IVR in polymer chains, and anomalous  $T_2$  behavior in dense fluids.<sup>[75]</sup>

condensed phase of liquid-state density. Accordingly, we could observe the influence of solute–solvent collisions on reaction dynamics in real time. We also did studies in liquid solutions for some of the systems examined in the gas phase: bond breakage and caging; valence structure isomerization; and double proton transfer. Similarly, we studied systems of nanocavities and polymers. Some highlights include (Figure 1.28):

- 1) Dynamics of the gas-to-liquid transition region ( $T_1$  and  $T_2$ )
- 2) Dynamics of bimolecular (one-atom) caging
- 3) Dynamics of microscopic friction
- 4) Dynamics in the liquid state
- 5) Dynamics of energy flow in polymers
- 6) Dynamics of small and large molecules in cyclodextrins

### 1.3.6

#### Opportunities for the Future

Three areas of study are discussed.

##### 1.3.6.1 Transient Structures from Ultrafast Electron Diffraction

Electron diffraction of molecules in their ground state has been a powerful tool over the past 50 years, and both electron and X-ray methods are now being advanced in several laboratories for the studies of structural changes. We have reported in *Nature* the latest advance in UED (Figure 1.29), by which major challenges were surmounted: the very low number densities of gas samples; the absence of the long-range order that is present in crystals, which enhances coherent interference; and the daunting task of determining in situ the zero-of-time when diffraction changes are on the pico- and sub-picosecond time scale.

With UED, we have been able to study molecular structures and branching ratios of final products on the picosecond time scale. The change in diffraction from before to after a chemical reaction was observed. However, the direct observation of transient structural changes in the course of a reaction was published only recently (in the *Proceedings of the National Academy of Sciences*). Specifically, we observed the transient intermediate in the elimination reaction of 1,2-diiodotetrafluoroethane ( $C_2F_4I_2$ ) to produce the corresponding ethylene derivative by the breakage of two carbon–iodine bonds (see Figure 1.29 B and C). The evolution of the ground-state intermediate ( $C_2F_4I$  radical) was directly revealed in the population change of a single chemical bond, namely the second C–I bond. The elimination of two iodine atoms is nonconcerted, with the reaction time of the second C–I bond breakage being about 17 ps. The UED results for the short-lived  $C_2F_4I$  radical favor the classical structure over the bridged radical structure. Ab initio calculations were made to compare theory with experiments.

This leap in our ability to record structural changes on the pico- and sub-picosecond time scales bodes well for many future applications to complex molecular systems, including biological systems. We have completed a new apparatus equipped

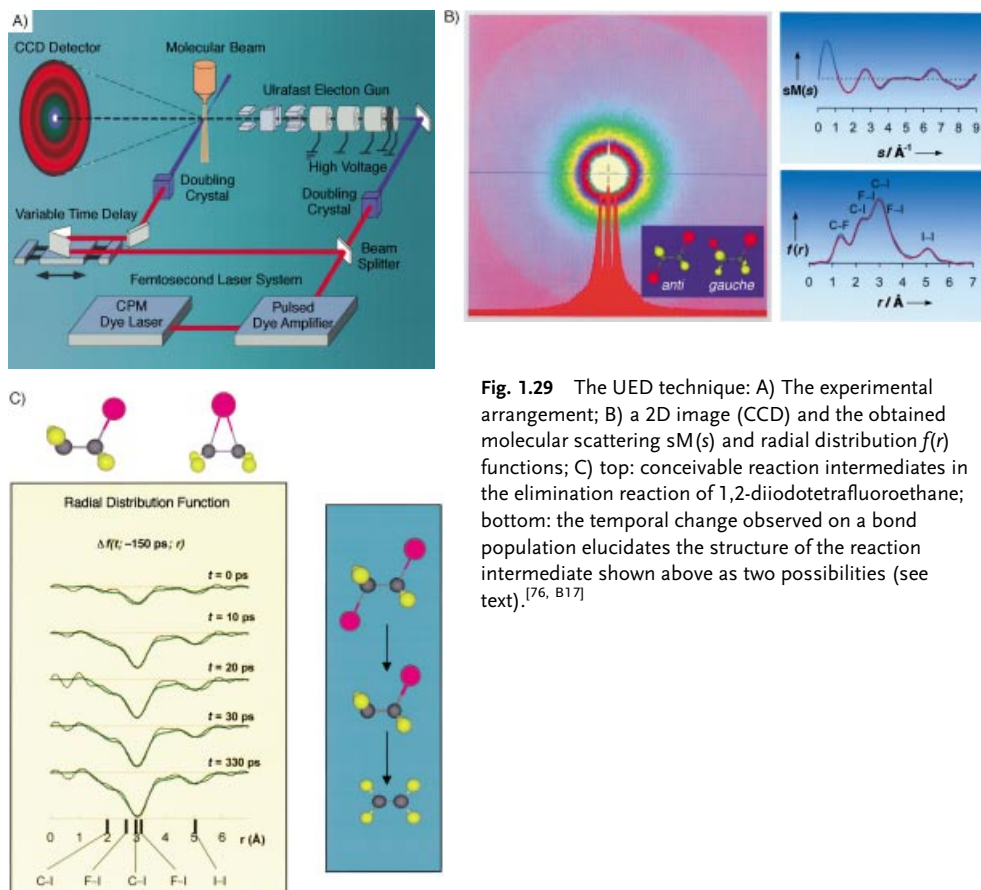


**Fig. 1.29** The UED technique: A) The experimental arrangement; B) a 2D image (CCD) and the obtained molecular scattering  $sM(s)$  and radial distribution  $f(r)$  functions; C) top: conceivable reaction intermediates in the elimination reaction of 1,2-diiodotetrafluoroethane; bottom: the temporal change observed on a bond population elucidates the structure of the reaction intermediate shown above as two possibilities (see text).<sup>[76, B17]</sup>

with diffraction detection and also with mass spectrometry. This universal system is capable of studying complex systems in the gas and other phases. It holds great opportunities for the future.

### 1.3.6.2 Reaction Control

Our interest in this area goes back to the late 1970s when a number of research groups were reporting on the possibility of (vibrational) mode-selective chemistry with lasers. At the time, the thinking was directed along two avenues. One of these suggested that, by tuning a CW laser to a given state, it might be possible to induce selective chemistry. This approach was popularized enthusiastically, but it turned out that its generalization could not be made without knowing and controlling the time scales of IVR in molecules. Moreover, state-selective chemistry is quite different from bond-selective chemistry. The second avenue was that of IR multiphoton chemistry. In this case, it was shown that selectivity was lost in the quasi-continuum vibrational manifold of molecules, but that the initial coherent IR pumping process

could be used for selective isotope separation. Such an approach has proven successful, even on the practical scale, and Letokhov has called the process “incoherent control”.<sup>[33]</sup>

The discovery (see Section 1.3.2) of coherent and selective vibrational oscillations (in-phase and out-of-phase) in a large molecule such as anthracene made me think of the possibility of temporally controlling the state of the system. The key idea was coherence among the vibrational degrees of freedom and its observation (published in 1981), which triggered significant interest in the issue of chaotic versus coherent “motion” of packets in isolated molecules. Some of us believed that, despite the complexity of the vibrational mode structure, coherence would be robust, provided it could be disentangled through proper preparation and probing. In fact, in a discussion with Richard Feynman (at Caltech) about the anthracene results, he informed me of a related problem noticed by Fermi, when both were at Los Alamos: A linear chain of springs (vibrations) showed recurrences when the energy was initially localized (on the computer) in one spring. They expected dissipation and not recurrences. Nico Bloembergen and I wrote a feature article (1984) emphasizing this point of coherent motion and its significance to mode-selective chemistry.<sup>[B21]</sup> Stuart Rice believed strongly in the concept of coherence and, as I mentioned before, we even drafted a paper that was not finalized for publication.

Earlier in 1980, I wrote a *Physics Today* article in a special issue on laser chemistry suggesting the use of ultrashort pulses (not CW or long-time lasers) to control the outcome of a chemical reaction.<sup>[B24]</sup> The title of the paper was: Laser Selective Chemistry—Is it Possible? The subtitle stated the message, “With sufficiently brief and intense radiation, properly tuned to specific resonances, we may be able to fulfill a chemist’s dream, to break particular selected bonds in large molecules.” In this article, I was concerned with the problem of IVR and so-called chaotic behavior. Stimulated by our work on IVR and coherence (Section 1.3), I thought that ultrashort pulses should be used to control the system in the desired configuration by proper choice of the time duration and delay and by the preparation of the packet which is controlled by the coherence width. Experimentally, we had already developed methods for the control of the phase of the field of optical pulses with the idea of using the phase (pulse shaping) to control molecular processes—collisions, inhomogeneous broadenings, and even photon locking which could inhibit relaxation (see Section 1.3.1.2); the time scale was nanoseconds and for the control of IVR, femtosecond pulses were needed.

Prior to this work, the optical pulse field was simply defined by the envelope  $A(t)$  and the frequency  $\omega$ ; the phase  $\phi(t)$  was unknown [Eq. (10)]. By controlling  $\phi(t)$  we

$$E(t) = E_0 A(t) \cos[\omega t + \phi(t)] \quad (10)$$

were able to make sequences of phase-coherent multiple pulses and to tailor a composite “single” pulse with a prescribed  $\phi(t)$ . We published a series of papers demonstrating the power of the approach, as mentioned in Section 1.3.1.2 (see Figure 1.9). In fact with composite shaped pulses, a sequence of phase segments and tilt angles (in the rotating frame) of, for example,  $60_x - 300_x - 60_x$ , we showed experimentally that the emission of a molecule can be made twice that as when a normal single

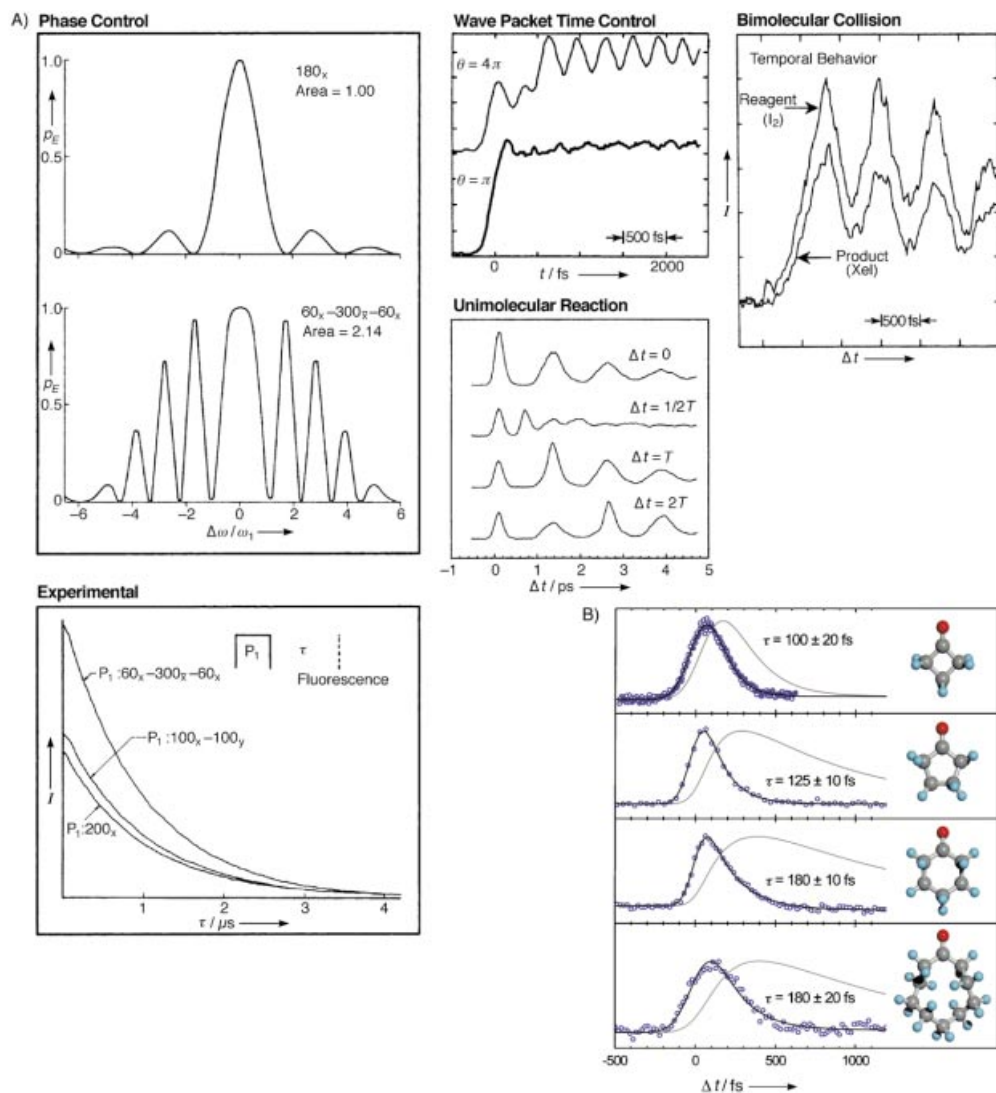


**Fig. 1.30** Control of the reaction by the phase and/or the delay, or the duration of optical pulses. A) Left: The effect of a designed composite pulse on the fluorescence of a molecule (iodine), showing the large experimental enhancement for the labeled phase-controlled sequence. Right: Control of the population ( $\text{I}_2$ ), of unimolecular reactions ( $\text{NaI}$ ), and of a bimolecular collision

( $\text{Xe} + \text{I}_2$ ) (see text). B) Localized control of the preparation of high-energy wave packets on the femtosecond time scale, which are shorter than IVR. The series has the same reaction coordinate (C–C bond) but the molecular size has increased in complexity. The behavior is far from being statistical.<sup>[77, B20, B24]</sup>

pulse was used (Figure 1.30). Similarly, by choosing pulse sequences such as  $x\text{-}\gamma\text{-}x(\bar{x})$  we experimentally locked the system and thus lengthened its relaxation time considerably. In theoretical papers, we examined the use of the approach for selectivity and control of molecular relaxations; in recent reviews,<sup>[34]</sup> Warren has discussed pulse shaping and its relevance to quantum control.

On the femtosecond time scale, the theoretical work of Heller (Section 1.3.4.9) stimulated the use of the time-dependent wave-packet picture for absorption and emission. In 1985, David Tannor and Stuart Rice, using the wave-packet picture, provided a two-photon scheme for the control of selectivity with pulse-sequence coherence being an important part of the evolution.<sup>[35a]</sup> This scheme was extended<sup>[35b]</sup> and, in their review article of 1988,<sup>[35c]</sup> they described phase-sensitive experiments such as the ones we reported earlier. An important realization was the desire to optimize the yield of a given channel. With femtosecond resolution, we began testing the idea of timing pulses on small molecular systems (see Figure 1.30). We first began with a single experiment on the control of the population in bound states (iodine). Then we reported results on the control of the yield in the reaction  $\text{Xe} + \text{I}_2 \rightarrow \text{XeI} + \text{I}$  as a function of the delay time between the pump and control. Although the mechanism is not fully resolved, the important point is that the yield of product XeI followed the temporal motion of the iodine wave packet. In a third experiment, we used pump-control-probe femtosecond pulses to control the branching of the NaI reaction; these, together with the experiment by Gustav Gerber's group on  $\text{Na}_2$  ( $\text{Na}_2^+ + \text{e}$  versus  $\text{Na} + \text{Na}^+ + \text{e}$ ), are prototypes for the Tannor-Rice-Kosloff scheme. Phase-locked pulses were extended to the femtosecond domain by Norbert Scherer and Graham Fleming in their new studies on iodine.

Recently, we turned our attention to complex molecular systems, but this time using femtosecond pulses to implement the 1980 idea. In a series of molecules of increasing complexity, but retaining the same reaction coordinate, we illustrated selectivity by beating IVR (and entering near the transition state); the rate of reaction was two to three orders of magnitude larger than the expected statistical limit. This work was published in *Science* (see Figure 1.30) and promises to be significant for achieving nonstatistical chemistry at high energies. The concept suggests that control at high energies (chemical energies) is more realistic, in contrast with the conventional wisdom which asserts the need for low energies—time is of the essence! Another example of nonstatistical femtochemistry comes from the work on surfaces.<sup>[36]</sup> Recently, the group in Berlin (Ertl and Wolf<sup>[36b]</sup>) demonstrated, in an elegant experiment, the critical role of femtosecond resolution in inducing oxidation (instead of desorption) of CO on Ru surfaces—the femtosecond nonequilibrated electron distribution of the surface gives a selective chemistry different from that of equilibrated phonon distribution, or thermal heating.

In the future, there will be extensions and new directions in light-matter control on the femtosecond time scale based on the temporal coherence of light and its interference with matter waves. One area that holds promise is the use of femtosecond pulses to induce selectivity by utilizing the three parameters of the pulse, the central frequency, the width and the “chirp”, in an iterative algorithm; the chirp is, in a way, similar to a composite pulse of the type described above. The technique of

liquid-crystal-display developed by Andy Weiner for femtosecond pulse shaping, combined with the evolutionary feedback idea of Herschel Rabitz, makes possible the generation of the desired complex  $E(t)$  field to achieve combinatorial control. This optimal control has been demonstrated nicely for a targeted second harmonic generation or a yield of chemical reaction as reported by Gerber's group in Würzburg.<sup>[37a]</sup> Kent Wilson<sup>[37b]</sup> showed the importance of chirped pulses in focusing and reflecting wave packets and, in a more recent contribution, he, with Warren Warren, used the evolutionary feedback approach to optimize the fluorescence of a molecule in solution, reminiscent of the composite pulse experiment we described above. In pulse shaping, the field is optimized and forms a complex pattern which is used through many generations to reach the fitted, desired population.

It should be noted that all of the above schemes change the coherent composition of the initial packet and hence the evolution in different channels—but we have not changed the evolution dictated by the natural forces of the atoms! Intense fields may do so. Paul Corkum, Thomas Baumert, and other colleagues have provided novel observations with intense fields.<sup>[38]</sup> Clearly these areas of control by ultrafast pulse timing ( $t$ ), phase ( $\phi$ , shape), spatial localization ( $R$ ), and intensity to alter the potential ( $V$ ) offer new opportunities for the future. Many theoretical efforts have already been advanced ahead of current experiments and Manz' group is providing new possibilities, including deracemization by controlled pulses—timed and shaped (see his review of 1500 references in ref. [28]). I did not discuss here the CW control scheme advanced by Paul Brumer and Moshe Shapiro, nor can I give references to all work done in this area.

### 1.3.6.3 Biological Dynamics

There have been important contributions to femtobiology (see ref. [28, 39], and their references) and these include: studies of the elementary steps of vision, photosynthesis, protein dynamics, and electron and proton transport in DNA. In proteins such as those of photosynthetic reaction centers and antennas, hemoglobins, cytochromes, and rhodopsin, a femtosecond event such as bond breaking, twisting, or electron transfer occurs. There exist global and coherent nuclear motions, which can be observed in these complex systems, and it is possible that the complexity is not as complicated as we think; for the chemistry and the efficiency to be unique, the system utilizes the organized structure around the “active center” with the necessary restraint on transition states and energy flow. Thus, in my view, the early femtosecond events are critical to understanding the function of complex systems, as they reflect the important locality in biological dynamics.

Our efforts in this direction have so far focused on DNA-twisting dynamics, electron transfer in DNA assemblies, DNA base-pair mimics, and on protein–ligand dynamics. The work on the torsional rigidity of DNA was published in 1980–1982, while that relating to proton transfer in model base pairs was reported in the last few years. With donors (D) and acceptors (A) covalently bonded to DNA, studies of electron transfer on more well-defined assemblies were made possible, and the effect of distance could be addressed. With femtosecond resolution, we obtained the actual time scale of electron transfer and related the rates to the distance between D

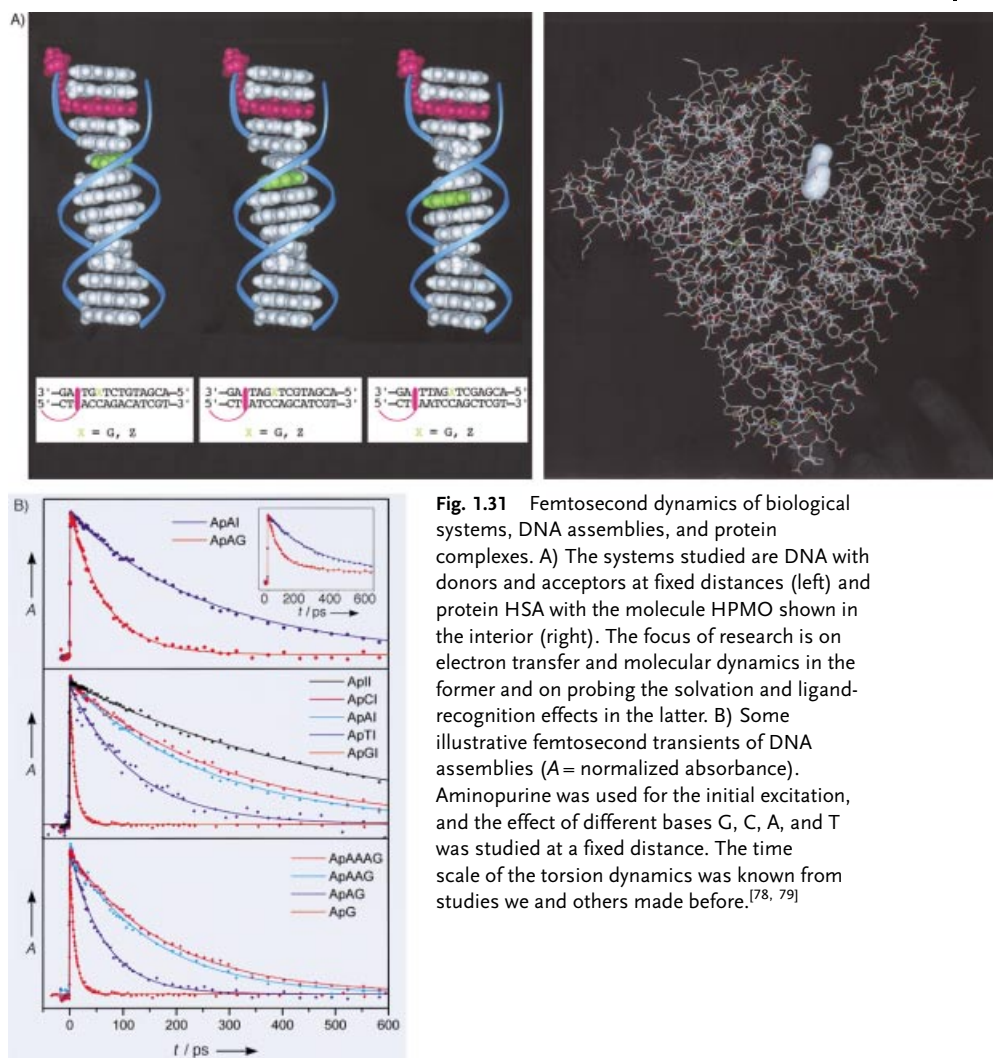


**Fig. 1.31** Femtosecond dynamics of biological systems, DNA assemblies, and protein complexes. A) The systems studied are DNA with donors and acceptors at fixed distances (left) and protein HSA with the molecule HPMO shown in the interior (right). The focus of research is on electron transfer and molecular dynamics in the former and on probing the solvation and ligand-recognition effects in the latter. B) Some illustrative femtosecond transients of DNA assemblies ( $A$  = normalized absorbance). Aminopurine was used for the initial excitation, and the effect of different bases G, C, A, and T was studied at a fixed distance. The time scale of the torsion dynamics was known from studies we and others made before.<sup>[78, 79]</sup>

and A. In collaboration with Jackie Barton's group, we published this work in the *Proceedings of the National Academy of Sciences*. The time scale of orientational coherence and solvation was also examined, allowing us to elucidate the role of molecular motions, including the effect of DNA rigidity. The results reveal the nature of ultra-fast electron transfer and its mechanism: in DNA, electron transfer cannot be described as in proteins simply by a phenomenological parameter  $\beta$ . Instead, the local involvement of the base pairs controls the time scale and the degree of coherent transport. Molecular dynamics are critical to the description of the transport. The measured rates (Figure 1.31) and the distance range of the transfer suggest that DNA is not an efficient molecular wire.



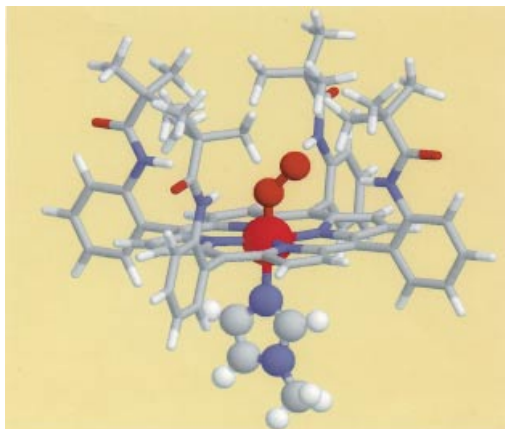
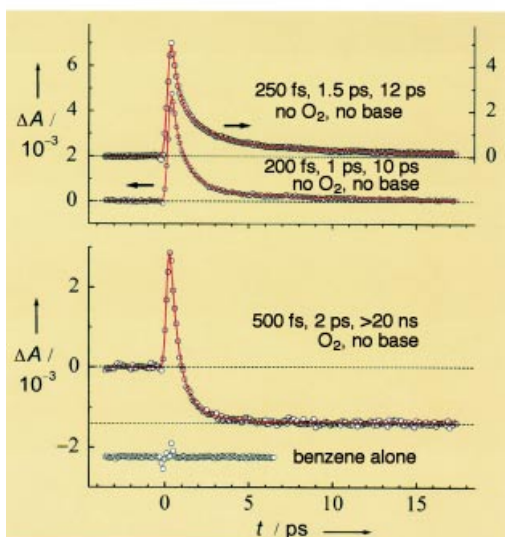


**Fig. 1.32** Femtosecond studies of model biological systems such as hemoglobin and myoglobin, DNA base pairs, and photosynthetic assemblies. Shown here are the structure of dioxygen picket fence cobalt porphyrins and the femtosecond transients which clearly show the time-scales involved and the release of  $O_2$  in 1.9 ps at room temperature. These studies on this and the other model systems (not shown) are part of the continued effort in this area.<sup>[80]</sup>



For proteins, our current interest is in the studies of the hydrophobic forces and electron transfer (Figure 1.31), and oxygen reduction in models of metalloenzymes (Figure 1.32). For the former, we have studied, with femtosecond resolution, the protein human serum albumin (HSA), probed with the small (ligand) molecule hydroxyphenylmethyloxazole (HPMO; see Figure 1.31 A); this work continues to be in collaboration with Abderrazzak Douhal. We also studied hyperthermophilic proteins. For model enzymes, we examined novel picket-fence structures which bind oxygen to the central metal with approximately 85 % efficiency at room temperature. In this system (Figure 1.32), we observed the release of  $O_2$  in 1.9 ps and the recombination was found to occur on a much slower time scale. These are fruitful areas for future research, especially in that they provide prototype systems for  $O_2$  reduction with complex metalloporphyrins in the transition state, similar to the smaller systems of

benzene/halogens (see Figure 1.23) but at room temperature. We published our first report recently in *Angewandte Chemie* in collaboration with Fred Anson's group at Caltech.

In the future, new extensions are anticipated. The nature and control of enzymatic reactions, the catalytic function of the transition state, and the design of artificial biological functions seem to be areas of great promise for dynamical studies. Also, it is envisaged that the recording of the change of a large biological structure with time and with atomic resolution may be realized. Already some success in studies of small chemical systems utilizing ultrafast electron diffraction have been reported. X-ray diffraction is another direction. The ultimate goal is the recording of all coordinates in space and time. The impact on problems such as protein folding and molecular recognition is clear.

## 1.4

### Impact and Concepts—A Retrospective

In retrospect, the key to the explosion of research (see ref. [5a]) can perhaps be traced to three pillars of femtochemistry: time resolution, atomic-scale resolution, and generality of the approach.

#### 1.4.1

##### Time Resolution—Reaching the Transition-State Limit

Three points are relevant: 1) The improvement of nearly ten orders of magnitude in time resolution, from the (milli)microsecond time scale (Eigen and Norrish & Porter) to present femtosecond resolution, opened the door to studies of new phenomena and to new discoveries; 2) the transition state, the cornerstone of reactivity, could be clocked as a molecular species  $TS^+$ , providing a real foundation to the hypothesis of Arrhenius, Eyring, and Polanyi for ephemeral species  $[TS]^+$ , and leading the way to numerous new studies. Extensions will be made to study transition-state dynamics in complex systems, but the previous virtual status of the transition state has now given way to experimental reality;<sup>[5a]</sup> 3) inferences deduced from “rotational periods” as clocks in uni- and bimolecular reactions can now be replaced by the actual clocking of the nuclear (vibrational) motion. This is particularly important when a chemical phenomenon such as concertedness is involved or the time scale of complexes or intermediates is many vibrational periods.

In the 1960s, there was some thought that the relevant time scale for chemistry was the microsecond regime.<sup>[40a]</sup> Moreover, the uncertainty principle was thought to represent a severe limit to the utility of shorter time resolution; coherence was not part of the thinking in deciphering femtosecond nuclear motion, as discussed in Section 1.3 (development of femtochemistry) and in what follows. The new vision is summarized in the following statement<sup>[40b]</sup>: “The study of chemical events that occur in the femtosecond time scale is the ultimate achievement in half a century of development and, although many future events will be run over the same course,

chemists are near the end of the race against time.” Manfred Eigen, who gave the 1967 Nobel Lecture with the title “Immeasurably Fast Reactions” (“Die ‘Unmessbar’ Schnellen Reaktionen”) told me, when I teased him about the title, that nobody in the 1950s anticipated the laser and the short pulses they can provide.

#### 1.4.2

##### Atomic-Scale Resolution

Two points are relevant: 1) The transition from kinetics to dynamics. On the femto-second time scale, one can see the coherent nuclear motion of atoms—oscillatory or quantized steps instead of exponential decays or rises. This was proved to be the case for bound, quasi-bound, or unbound systems and in simple (diatomics) and in complex systems (proteins). Because of coherence, we can speak of the motion classically and visualize it as the change actually occurs; 2) the issue of *the* uncertainty principle. Many thought that the pulse was too short in time, thus broad in energy as described by the uncertainty principle  $\Delta t \Delta E \sim \hbar$ , but as discussed before, localization is consistent with the two uncertainty relationships (see Figure 1.4) and coherence is the key. The energy uncertainty  $\Delta E$  should be compared with bond energies:  $\Delta E$  is  $0.7 \text{ kcal mol}^{-1}$  for a 60 fs pulse (details are given in ref. [B17]). In the condensed phase, localization may become shorter lived, but the basic picture is still valid.<sup>[41]</sup>

This concept of coherence was not fully appreciated, not only among some chemists, but also among notable physicists. In 1972, at a Welch Conference, picosecond time resolution was of concern because of the perceived fundamental limitation imposed on time and energy by Heisenberg’s uncertainty principle. After his lecture on lasers in chemistry, the physicist Edward Teller had a lively exchange with another physicist and friend, Eugene Wigner. Even for picosecond resolution the question was asked, is there a natural, real limit to the time...? In the Welch Prize Address (1997), I highlighted these exchanges.<sup>[42]</sup> Jacob Bigeleisen, although concerned about the uncertainty principle, asked why not venture into the “millijiffy” (femtosecond) range?<sup>[24]</sup>

#### 1.4.3

##### Generality of the Approach

Three points are relevant: 1) In retrospect, the femtosecond time scale was just right for observing the “earliest” dynamics at the actual time scale of the chemical bond, defining the earliest time possible; 2) the methodology is versatile and general, as evidenced by the scope of applications in different phases and of different systems. Moreover, it has stimulated new directions of research in both experiment and theory in areas such as quantum control and ultrafast diffraction; 3) the time resolution offers unique opportunities when compared with other methods.

First, processes often appear complex because we look at them on an extended time scale, during which many steps in the process are integrated. On the femtosecond time scale, these steps are resolved, and the process breaks down into a series of simpler events. Second, only this time resolution can give the dynamics of transi-

tion states/intermediates in real time since for reactions neither the spectra of reactants nor those of products are directly relevant. This point was amply demonstrated in complex reactions, such as those of transient, reactive intermediates of organic compounds. Even for simple, reactive systems this is still true. For example, the spectral bandwidth of the reactant, dissociative ICN gives no information about the actual dynamics of the nuclear separation between I and CN fragments or about the transient configurations, as it only reflects the steepness of the potential at the initial nuclear configuration. For unreactive molecules, there is a different complexity; the spectra are usually inhomogeneously broadened, especially in complex systems. Finally, with time resolution, we can observe the motion without resorting to a mathematical construct from eigenstates or other indirect methods.

It is worth noting that both excited and ground-state reactions can be studied. It has been known for some time that the use of multiple pulses can populate the ground state of the system and, therefore, the population and coherence of the system can be monitored.<sup>[23]</sup> The use of CARS (coherent anti-Stokes Raman spectroscopy), DFWM (degenerate four-wave mixing), SRS (simulated Raman spectroscopy),  $\pi$  pulses, or direct IR excitation are some of the approaches possible. Two recent examples demonstrate this point: one invokes the use of IR femtosecond pulses to study reactions involving hydrogen (bond) motions in liquid water (this work was done in France and Germany);<sup>[43]</sup> and the other utilizes CARS for the study of polymers in their ground state, which we published in collaboration with the groups of Kiefer and Materny (see Figure 1.28). Ground-state dynamics have also been studied by novel femtosecond photodetachment of negative ions, and the subfield of femtosecond dynamics of ions is now active in a number of laboratories.<sup>[44]</sup>

#### 1.4.4

##### Some Concepts

New concepts and phenomena have emerged and include: Localization of wave packets; reaction path coherence; single-molecule trajectory; reaction landscapes versus path; bifurcation; chemical versus spectroscopic dynamics (time scales); concertedness; dynamical active space; nonstatistical (nonergodic) behavior; dynamical caging (by energy loss as opposed to barrier confinement); microscopic friction (energy versus mechanical); and inhomogeneous dynamics of “soft matter” (for example, biological) systems, with a whole range of time scales. These concepts have been discussed in the original publications, and below, only a few will be highlighted:

##### 1.4.4.1 Resonance (Nonequilibrium Dynamics)

The concept of resonance in the structure of the chemical bond goes back to the era of Linus Pauling and the idea of interconversion between different electronic structures. The interconversion was a hypothesis, not an observable fact. Quantum mechanically, chemists usually speak of eigenstates of the system, which are stationary with no time evolution. Resonance in dynamics is a concept which is not a stationary-state picture. With coherent preparation of molecules it is possible to pre-

pare a nonstationary (nonequilibrium) state of a given nuclear structure and for the system to evolve in time. In our studies this was shown for vibrational redistribution, for rotational orientation, and for wave-packet nuclear motions. Such nonstationary evolution does not violate the uncertainty principle and is fundamental to chemical dynamics.

#### 1.4.4.2 Coherence (Single-Molecule-Type Dynamics)

Perhaps one of the most powerful concepts in femtochemistry is coherence of the molecule, of the ensemble, and of the trajectory. First, the coherence created by a femtosecond pulse is reflected in the motion of the wave packet; for a force-free motion the group velocity is that of a free particle ( $p/m$ ), a classical motion.<sup>[45]</sup> Second is the ability to “transform” the ensemble’s incoherent behavior to a coherent molecular trajectory. This is achieved because on the femtosecond time scale the system can be promoted and localized in space with a localization length ( $\Delta R$ )

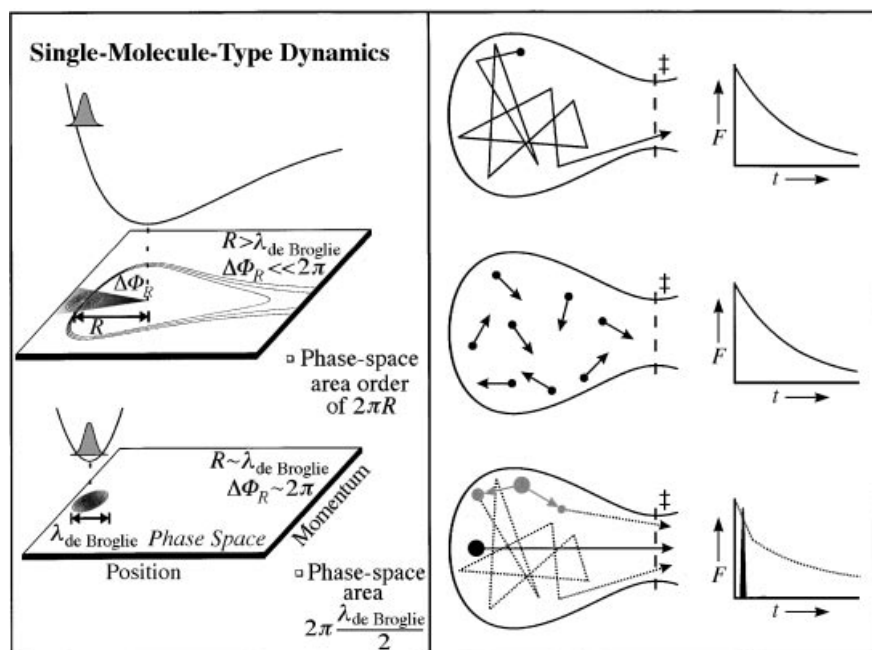


**Fig. 1.33** Concept of coherence, both in the dynamics at the atomic scale and in the control of nonstatistical behavior. Shown is the phase-space picture, describing the robustness of coherence (left); note the phase-space area of the initial state relative to that of the reaction. Right: A schematic representation of a configuration space made of the reactive coordinate and all nonreactive coordinates perpendicular to it (an equivalent phase-space picture can be made). Three cases of interest

are shown: the ergodic dynamics (top); the incoherent preparation (middle); and the coherent wave packet preparation (bottom), which show the initial localization, spatially and temporally, and the bifurcation into direct and indirect reaction trajectories. Recent theoretical work (K. Møller, this laboratory) of the corresponding temporal behavior has elucidated different regimes for the influence of the initial preparation, from a wave packet to a microcanonical limit.

which is only limited by the uncertainty of the initial system, typically about 0.05 Å; all molecules which do not interact span this range. The chemical length scale ( $R$ ) of interest is several angströms and this is why the system behaves as a single-molecule trajectory (Figure 1.33). Since the initial state is promoted nearly intact on the femtosecond time scale, the only dispersion is that which causes the different trajectories to spread under the influence of the new forces of the energy landscape or by external perturbations, such as solvation. If longer time pulses are used for the preparation, then  $\Delta R$  is on the scale of  $R$ , and kinetics of the states are recovered. Put in time-domain language, the inhomogeneous dephasing time of the ensemble is relatively long for femtosecond preparation and the homogeneous dynamics and the actual coherence of the packet become dominant, as amply demonstrated here and elsewhere. Third, the concept of coherence is crucial for achieving a coherent trajectory of reactions. Such control projects out the nonstatistical behavior through the preparation of a localized wave packet (Figure 1.33), as opposed to an incoherently prepared configuration (by, for example, chemical activation) or a spatially diffuse configuration (prepared by long-time experiments). The concept is powerful and basic to many phenomena: atomic-scale motion; reaction path coherence (from the transition state to products); reaction landscape trajectories as opposed to a single reaction path; energetic versus entropic structures near transition states and conical intersections; coherent caging by a solvent; bifurcation; and others.

#### 1.4.4.3 Transition Structures (Landscape Dynamics)

This concept became clear to us after studies of the elementary dynamics in simple reactions of three atoms and in complex reactions of organic systems. Traditionally, one uses a reaction path and makes a distinction between a transition state and a reactive intermediate by the absence or presence of a potential well—if there is no well, bonds are not formed and thus we do not speak of a “real” structure. On the femtosecond time scale, we can isolate a continuous trajectory of transition structures; none are in a potential well. Such structures are defined by the change in bond order and lead to a family of trajectories of reaction products. Thus, the two classical pathways of either a “concerted” or “sequential” process represent a very crude approximation for the actual landscape dynamics, even in a three-atom system. There is a whole distribution of reaction times and kinetic energy releases. The problem becomes even more severe if the landscape is complex and has near-flat energy regions or entropic changes, as discussed in Section 1.2 for the case of complex organic reactions and protein folding. The concept of transition structures and landscape dynamics is significant to issues addressing stereochemistry, product branching, and selectivity, and to the real distinction between transition states and intermediates in many reactions. Finally, the presence of such a family of trajectories on the energy landscape makes the restricted definition of the transition state—as only the saddle point—less clear. Concerted reactions, in the strict synchronous sense, essentially do not exist (see Sections 1.2 and 1.3).

#### 1.4.4.4 Reduced Space (Directed Dynamics)

Another important concept in dynamics is the reduction of nuclear space to the subspace critical to reactivity and nonradiative behavior in complex systems. Here, the femtosecond time scale allows one to project the primary events out of all processes possible. In complex systems with many degrees of freedom, the reduced space becomes the focus and the remaining space becomes a “continuum”, thus moving the description from a multidimensional PES ( $3N-6$  coordinates) to a few coordinates plus a weakly coupled continuum. This idea was central to our description of the dynamical isotope effect in elementary reactions, bifurcation to chemical and photophysical channels by conical intersections, concertedness and stereochemistry in organic reactions, nonstatistical behavior, and reaction control in large systems at high energies. The consequences to photochemistry are significant: reactions from high-energy states ( $\pi$ ,  $\pi^*$ , Ryberg, etc) usually result in ground-state chemistry, and bifurcation into conical intersections is the key; for transitions involving  $\sigma^*$  orbitals, the time scale of rupture becomes comparable to that of the funneling through conical intersections, and results in competitive chemical channels. It is possible that this same concept of reduced space is essential to biological dynamics. By reducing the space for dynamics, events occur efficiently and without “wasting” energy to all possible degrees of freedom. In addition, such designed local activity makes the system robust and immune to transferring “damage” over long distances. The ultrafast time scale is important because on it the system separates the important from the unimportant events—DNA bases quench their energy (nonradiatively) very rapidly, electron transfer in DNA is locally ultrafast, and the first event of vision is very efficient and occurs in 200 fs.

## 1.5

### Epilogue

As the ability to explore shorter and shorter time scales has progressed from the millisecond to the present stage of widely exploited femtosecond capabilities, each step along the way has provided surprising discoveries, new understanding, and new mysteries. In their editorial on the 10th anniversary of Femtochemistry, Will Castleman and Villy Sundström put this advance in a historical perspective.<sup>[46a]</sup> The report in ref. [5a] addresses with details the field and its position in over a century of developments. Developments will continue and new directions of research will be pursued. Surely, studies of transition states and their structures in chemistry and biology will remain active for exploration in new directions, from simple systems to complex enzymes and proteins,<sup>[47]</sup> and from probing to the controlling of matter.

Since the current femtosecond lasers (4.5 fs) are now providing the limit of time resolution for phenomena involving nuclear motion, one may ask: Is there another domain in which the race against time can continue to be pushed? Sub-femtosecond or attosecond ( $10^{-18}$  s) resolution may one day allow for the direct observation of the electron's motion. I made this point in a 1991 review article in *Faraday Discussions*<sup>[B17]</sup> and, since then, not much has been reported except for some progress in

the generation of sub-femtosecond pulses.<sup>[46b]</sup> In the coming decades, this may change and we may view electron rearrangement, say, in the benzene molecule, in real time. Additionally, there will be studies involving the combination of the “three scales” mentioned in the prologue, namely time, length, and number. We should see extensions to studies of the femtosecond dynamics of single molecules and of molecules on surfaces (for example, using scanning tunneling microscopy). Combined time/length resolution will provide unique opportunities for making the important transition from molecular structures, to dynamics, and to functions (Section 1.3.6). We may also see that all of femtochemistry can be done at micro-to-nano-Kelvin temperatures, utilizing lasers and other cooling techniques.

It seems that on the femtosecond to attosecond time scale we are reaching the “inverse” of the big bang time (Figure 1.34), with the human heartbeat “enjoying” the geometric average of the two limits. The language of molecular dynamics is even similar to that of cosmos dynamics. Cosmologists are speaking of energy landscapes and transition states for the big bang and universe inflation.<sup>[48]</sup> Perhaps we are approaching a universal limit of time!

Personally, I did not originally expect the rich blossoming in all of the directions outlined in this anthology; many more could, unfortunately, not be mentioned because of the limited space. What is clear to me is that my group and I have

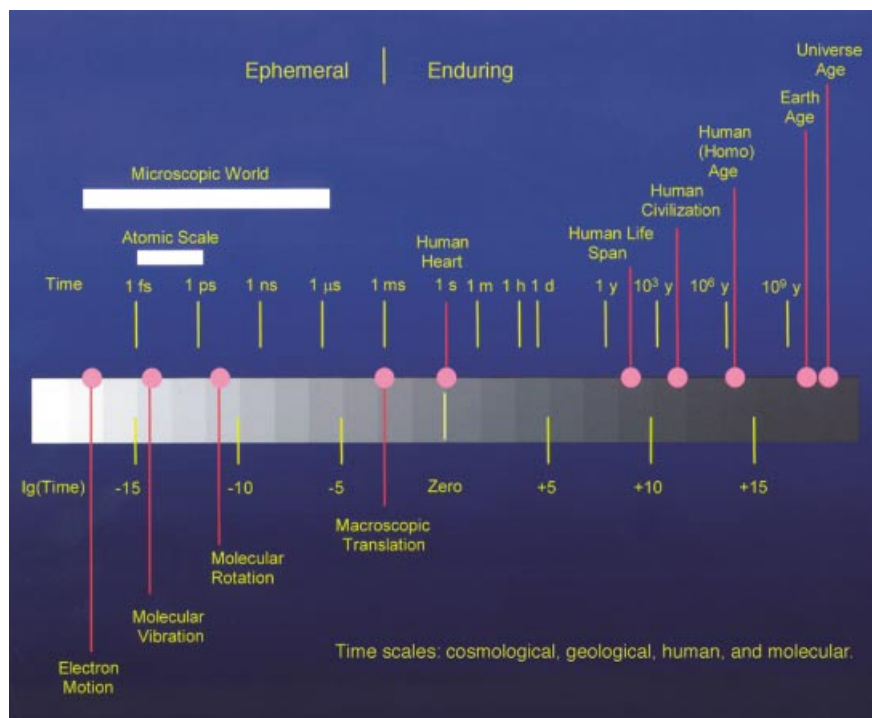


**Fig. 1.34** Timescales of cosmological, geological, human, and molecular events. Here, the time-scale spans more than thirty orders of

magnitude, from the big bang to the femtosecond age.<sup>[B25]</sup>





**Fig. 1.35** The Almond Blossom (St. Rémy, 1890) of Vincent van Gogh (1853–1890). With a good beginning, even if branching is unpredictable, the blossoms are rich and the big picture is beautiful. (Los Angeles County Museum of Art).

enjoyed the odyssey of discovery, seeing what was not previously possible, acquiring new knowledge, and developing new concepts. Perhaps the best words to describe this feeling are those of the English archaeologist, Howard Carter, on November 25, 1922 when he got his first glimpse of the priceless contents of Tutankhamen's Tomb—"At first, I could see nothing, ... then shapes gradually began to emerge". Lord Carnarvon, who financed the excavation of this discovery, asked, when looking with Carter, "What do you see?" Carter replied, "Beautiful Things", "Beautiful Things". This is the thrill of discovery in science, too. It seeks to unveil the hidden simplicity and beauty of nature's truth. On a recent visit to the Los Angeles Art Museum with my wife, I stood in front of van Gogh's masterpiece—Almond Blossom (Figure 1.35)—and wondered about the beauty of the big picture and the unpredictability of its details. That, also, is in the nature of scientific discoveries.

The future of femtosience will surely witness many imaginative and unpredictable contributions. I hope that I will be able to enjoy the future as much as I have the past. Benjamin Franklin once wrote: "The progress of human knowledge will be rapid and discoveries made of which we at present have no conception. I begin to be almost sorry I was born so soon since I cannot have the happiness of knowing what will be known in years hence."

## 1.6 Appendix

### 1.6.1

#### A Primer for Femtoscopy, Coherence and Atoms in Motion

##### 1.6.1.1 Pump–Probe Femtoscopy

In high-speed photography, a continuous motion is broken up into frames (“freezing”) using a brief exposure time. For example, in Muybridge’s experiment (Section 1.1), the shutter speed (exposure time) was about 2 ms and the speed of the motion was about  $10 \text{ m s}^{-1}$ , resulting in a well-defined resolution (speed  $\times$  exposure time) of 2 cm; the number of frames per second was about twenty since the cameras were 0.5 m apart. The huge contrast with molecular experiments is due to vast differences in speed ( $1 \text{ km s}^{-1}$ ), resolution ( $10^{-8} \text{ cm}$ ), and the number (millions) of molecules involved. Given the molecular speed and resolution, the ultrashort strobes must provide exposure time on the order of 100 fs, and in one second  $10^{13}$  frames could be recorded! Ultrafast pulsed laser techniques have made direct exploration of this temporal realm a reality (Sections 1.2 and 1.3). Spectroscopy, mass spectrometry, and diffraction play the role of ultra-high-speed photography in the investigation of molecular processes.

A femtosecond laser pulse provides the shutter speed for freezing nuclear motion with the necessary spatial resolution. The pulse probes the motion by stroboscopy, that is, by pulsed illumination of the molecule in motion and recording or photographing the particular snapshot. A full sequence of the motion is achieved by using an accurately timed series of these probe pulses, which defines the number of frames per second. This method of probing, although different from Muybridge’s, is in principle equivalent to his use of the cameras (with shutters) as probes. For molecules there exist three additional requirements in order to study the motion. First, we need to clock the motion by defining its zero of time, also accurate to tens of femtoseconds. Second, the motion must be synchronized since millions of molecules are typically used in the recording of molecular motion. Third, molecular coherence (see Section 1.6.1.2) must be induced to localize the nuclei. These requirements are satisfied by using a femtosecond pump (initiating) laser pulse, in what is referred to as a pump–probe configuration.

With this methodology, the process to be studied is clocked from the instant that the substance under investigation absorbs radiation from the pump pulse. Passage of a probe pulse through the sample at some later point in time provides a snapshot of the status of the system at that time. For femtosecond studies, where femtosecond control of relative timing is needed, the laser pump and probe pulses are produced in synchrony, then the probe pulse is diverted through an adjustable optical path length (see Figure 1.5). The finite speed of light translates the difference in path length into a difference in arrival time of the two pulses at the sample;  $1 \mu\text{m}$  corresponds to 3.3 fs. The individual snapshots combine to produce a complete record of the continuous time evolution—a motion picture, or a movie—in what may be termed femtoscopy.

### 1.6.1.2 Coherence and Atomic Motion

In a classical description, the motions of nuclei would be particlelike, that is, they would behave as “marbles on a potential”. At the scale of atomic masses and energies, however, the quantum mechanical wave/particle duality of matter comes into play, and the notions of position and velocity common to classical systems must be applied cautiously and in accord with the uncertainty principle, which places limits on the precision of simultaneous measurements. In fact, the state of any material system is defined in quantum mechanics by a spatially varying “wave function” with many similarities to light waves. Since the wave nature of light is a much more familiar concept than that of matter, we will use light to introduce the idea of wave superposition and interference, which plays an important role in atomic motion.

When light from two or more sources overlaps in space, the instantaneous field amplitudes (not intensities) from each source must be added together to produce the resultant light field. A well-known example is Young’s two-slit experiment, in which light from a single source passes through two parallel slits in a screen to produce, in the space beyond, two phase-coherent fields of equal wavelength and amplitude. At points for which the distances to the two slits differ by  $n + 1/2$  wavelengths (for integer  $n$ ) the two waves add to zero at all time, and no light is detected. Elsewhere, the amplitudes do not cancel. Thus, a stationary pattern of light and dark interference (Figure 1.4 B, inset) fringes is produced (“light + light → darkness + more light!”). A knowledge of the wavelength of light and the spacing of fringes projected on a screen provide a measurement of the separation of the slits. In X-ray diffraction such interferences make it possible to obtain molecular structures with atomic resolution—the positions of the atoms replace the slits.

In studies of motion, we have exploited the concept of coherence among molecular wave functions to achieve atomic-scale resolution of dynamics—the change of molecular structures with time. Molecular wave functions are spatially diffuse and exhibit no motion. Superposition of a number of separate wave functions of appropriately chosen phases can produce a spatially localized and moving coherent superposition state, referred to as a wave packet (Figure 1.4 B); constructive and destructive interference (as in the interference of light waves) is the origin of such spatial localization. The packet has a well-defined (group) velocity and position which now makes it analogous to a moving classical marble, but at atomic resolution. The femtosecond light induces the coherence and makes it possible to reach atomic-scale spatial and temporal resolution, without violation of the uncertainty principle.

In Figure 1.4 B, a snapshot is shown of the position probability (in red) of a wave packet, formed from wave functions  $n = 16$ – $20$  with weighting according to the distribution curve (left of the figure). This was calculated for the harmonic wave functions representing the vibrational states of a diatomic molecule, in this case iodine ( $n$  is the quantum number). As time advances, the wave packet moves back and forth across the potential well. As long as the wave packet (width approximately  $0.04 \text{ \AA}$ ) is sufficiently localized on the scale of all accessible space (about  $0.6 \text{ \AA}$  between the walls of the potential), as shown in the figure, a description in terms of the classical concepts of particle position and momentum is entirely appropriate. In this way, localization in time and in space are simultaneously achievable for reactive

and nonreactive systems (Section 1.3.4). Note that the width of the packet prepared by a 20 fs pulse is very close to the uncertainty in bond distance for the initial  $n=0$  ground state. To prepare the packet at the inner turning point with the given phase composition, it must be launched vertically at the internuclear separation of about 2.4 Å; if launched from the shown  $n=0$  distance, the packet will have a different phase composition and will be localized initially in the center of the well.

The observation of motion in a real system requires not only the formation of localized wave packets in each molecule, but also a small spread in position among wave packets formed in the typically millions of molecules on which the measurement is performed. The key to achieving this condition is generally provided by a) the well-defined initial, equilibrium configuration of the studied molecules before excitation and b) the “instantaneous” femtosecond launching of the packet. The spatial confinement (in this case about 0.04 Å) of the initial ground state of the system ensures that all molecules, each with its own coherence among the states which form its wave packet, begin their motion on the excited potential in a bond-distance-range much smaller than that executed by the motion. The femtosecond launching ensures that this narrow range of bond distance is maintained during the entire process of preparation (see Figure 1.33). Unless the molecular and ensemble coherences are destroyed by intra- and/or intermolecular perturbations, the motion is that of a classical single-molecule trajectory.

*The story told here involves many dedicated students, post-doctoral fellows, and research associates. Their contributions are recognized in the publications cited. I hope that by mentioning their work, they recognize the crucial role they have played in the journey of femtochemistry at Caltech. To me the exciting time with my research group represents the highlight of the story. For 20 years I have always looked forward to coming to work with them each day and to enjoying the science in the truly international family (Figure 1.36). All members of the current research group have helped with the figures presented here. I particularly wish to thank Dongping Zhong for the special effort and care throughout the preparation and Ramesh Srinivasan for his devoted help with some of the figures. The artistic quality of many of the figures reflects the dedicated efforts of Wayne Waller and his staff.*

*There have been a number of friends and colleagues who have supported the research field and made the experience enjoyable and humanly worthwhile—to them I wish the very best. All are with us today, except one: Dick Bernstein. Caltech proved to be the ideal scientific institution for me, not only because of the strong science it radiates, but also because of its culture, the “science village”. I will never forget the impact of the “round table” at the Athenaeum. Vince McKoy, friend, colleague, and neighbor at Caltech, has been the source of enjoyment and stimulation for over 20 years; Vince has taken an almost daily interest in our progress! Over the years I have enjoyed discussions with Spencer Baskin whose critical and wise judgment served as a sounding board for penetrating physics concepts.*

*Major support of this research came from the National Science Foundation, the US Air Force Office of Scientific Research, and the Office of Naval Research, and it is a pleasure to acknowledge all of these organizations for making it possible. I take the opportunity to thank Carl and Shirley Larson for their support and friendship. Last, but not least, I wish to thank the staff of the Division and the Institute for their care and sincere efforts which have made our ship sail along with minimal resistance.*

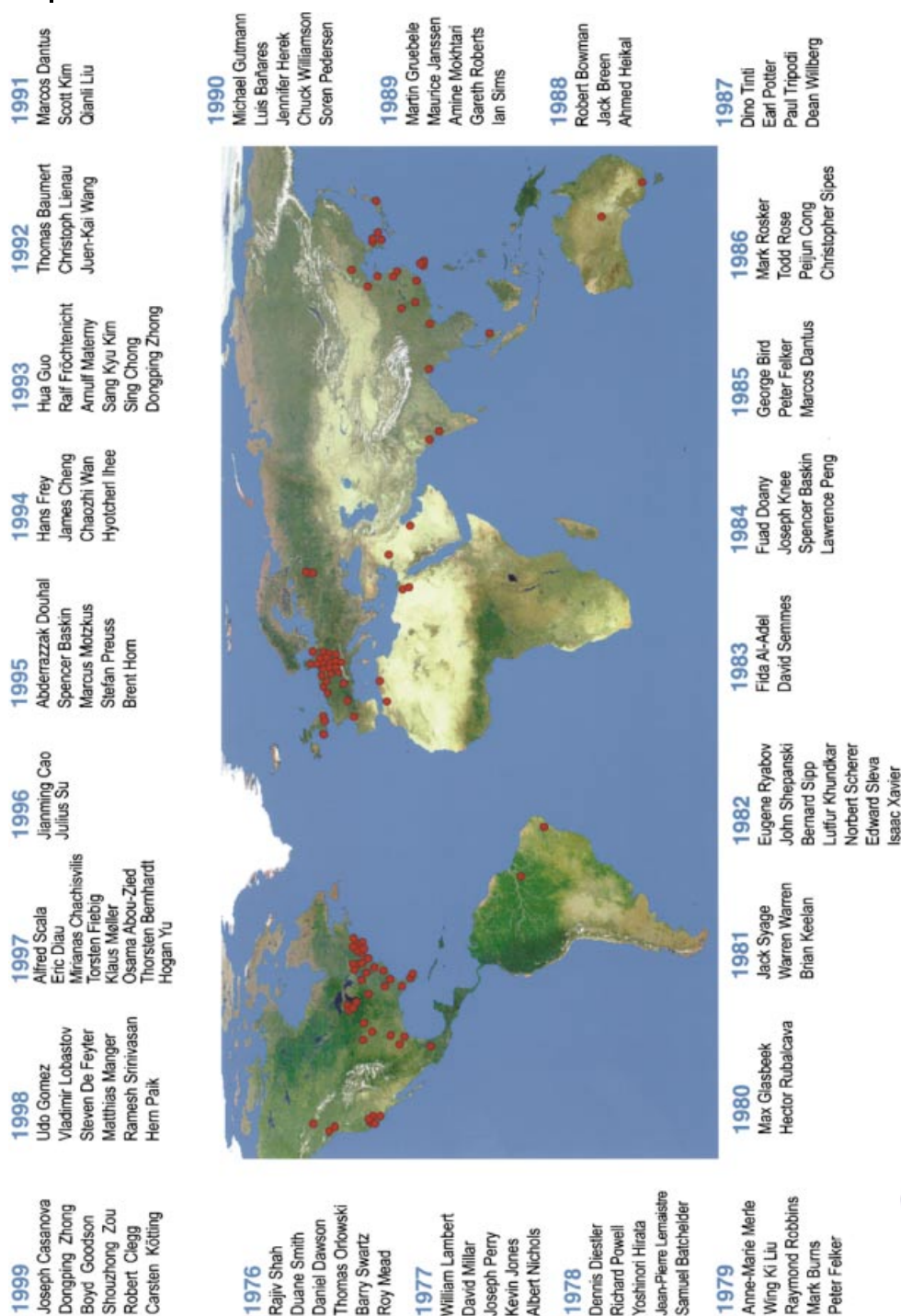


**Fig. 1.36** The International Roster of the Caltech group, 1976–1999. The red circles are usually composite of many dots, reflecting the more than one hundred graduate students, postdoctoral fellows, and visiting associates, who made up the research team over the years.

## References

- 1 a) J. H. Breasted, *A History of Egypt*, Scribner's Sons, New York, **1909** (Renewal, **1937**); b) A. Gardiner, *Egyptian Grammar*, 3rd ed., Griffith Institute Ashmolean Museum, Oxford, **1957** (first published in **1927** and lastly in **1994**); c) "The Origin of the Ancient Egyptian Calendar": H. E. Winlock, *Proc. Am. Phys. Soc.* **1940**, 83, 447; d) O. Neugebauer, *The Exact Sciences in Antiquity*, Brown University Press, Providence, RI, **1957**; e) R. K. Marshall, *Sundials*, McMillan, New York, **1963**; f) P. Tompkins, *The Magic of Obelisks*, Harper & Row, New York, **1981**; g) G. J. Whitrow, *Time in History*, Oxford University Press, Oxford, **1989**; i) *Encyclopedia of the History of Science, Technology, and Medicine in Non-Western Cultures* (Ed.: H. Selin), Kluwer Dordrecht, The Netherlands, **1997**; j) *A Walk Through Time*, 1998, <http://physics.nist.gov/GenInt/Time/time.html>; k) M. M. Soliman, *History of Science and Technology in Ancient and Middle Ages*, Alhiaa Almasria Lelkitab, Cairo, **1995** (in Arabic); l) D. Steel, *Marking time—The Epic Quest to Invent the Perfect Calendar*, Wiley, New York, **2000**.
- 2 *Sci. Am.* **1878**, 39 (Oct. 19), 241; T. K. Derry, T. I. Williams, *A Short History of Technology*, Dover, New York, **1993**; E. Jussim, G. Kayafas, *Stopping Time*, H. N. Abrams, New York, **1987**.
- 3 C. A. Ronan, *Science—Its History and Development Among the World's Cultures*, Facts on File, New York, **1982**; J. R. Partington, *A Short History of Chemistry*, Dover, New York, **1989**; J. W. Servos, *Physical Chemistry from Ostwald to Pauling*, Princeton, **1990**; C. van Doren, *A History of Knowledge*, Ballantine, New York, **1991**; W. H. Brock, *Chemistry*, Norton, New York, **1992**; C. H. Langford, R. A. Beebe, *The Development of Chemical Principles*, Dover, New York, **1995**; R. Breslow, *Chemistry Today and Tomorrow*, American Chemical Society, Washington, **1997**; J. Read, *From Alchemy to Chemistry*, Dover, New York, **1995**; *Scientists—Random House Webster's Dictionary*, New York, **1997**.
- 4 a) A. H. Zewail, *Cambridge Rev.* **1997**, 118(2330), 65; b) "Chemistry in a New Light", J. Baggott in *The New Chemistry* (Ed.: Nina Hall), Cambridge University Press, Cambridge, **2000**, p. 43.
- 5 a) B. Nordén, [www.nobel.se/announcement-99/chemistry99.html](http://www.nobel.se/announcement-99/chemistry99.html); b) A. Donoso, C. C. Martins, *J. Phys. Chem. A* **1998**, 102, 4291 (introduction to this reference); c) D. E. Folmer, W. S. Wisniewski, S. M. Hurley, A. W. Castleman, Jr., *Proc. Natl. Acad. Sci. USA* **1999**, 96, 12980, and references therein.
- 6 H. C. von Baeyer, *Taming the Atom*, Random House, New York, **1992**; P. Ball, *Designing the Molecular World*, Princeton University Press, Princeton, **1994**; P. W. Atkins, *Atoms, Electrons, and Change*, Freeman, New York, **1991**.
- 7 a) S. Arrhenius, *Z. Phys. Chem. (Leipzig)* **1889**, 4, 226; b) J. H. van't Hoff in *Etudes de Dynamiques Chimiques*, F. Muller, Amsterdam, **1884**, p. 114 (translation by T. Ewan, London, **1896**); c) M. Bodenstein, *Z. Phys. Chem. (Munich)* **1894**, 13, 56; M. Bodenstein, *Z. Phys. Chem. (Munich)* **1897**, 22, 1; M. Bodenstein, *Z. Phys. Chem. (Munich)* **1899**, 29, 295; d) F. A. Lindemann, *Trans. Faraday Soc.* **1922**, 17, 598; e) C. N. Hinshelwood, *The Kinetics of Chemical Change in Gaseous Systems*, Calendron, Oxford, **1926** (second printing, **1929**; third printing, **1933**); C. N. Hinshelwood, *Proc. R. Soc. London A* **1926**, 113, 230; f) R. C. Tolman, *J. Am. Chem. Soc.* **1925**, 47, 2652; R. C. Tolman, *J. Am. Chem. Soc.* **1920**, 42, 2506; g) J. G. Kirkwood, O. R. Wulf, P. S. Epstein, *Biographical memoirs*, Vol. 27, National Academy of Sciences (USA), p. 139.
- 8 See, for example, a) K. J. Laidler, *Chemical Kinetics*, 3rd ed., Harper Collins, New York, **1987**; b) J. I. Steinfeld, J. S. Francisco, W. L. Hase, *Chemical Kinetics and Dynamics*, Prentice-Hall, New Jersey, **1989**; c) T. Baer, W. L. Hase, *Unimolecular Reaction Dynamics*, Oxford University Press, New York, **1996**; d) S. Shaik, H. Schlegel, S. Wolfe, *Theoretical Aspects of Physical and Organic Chemistry*, Wiley, New York, **1992**; e) A. Pross, *Theoretical & Physical Principles of Organic Reactivity*, Wiley, New York, **1995**.
- 9 R. D. Levine, R. B. Bernstein, *Molecular Reaction Dynamics and Chemical Reactivity*, Oxford University Press, Oxford, **1987**, and references therein.

- 10 a) W. Heitler, F. London, *Z. Phys.* **1927**, 44, 455; b) F. London, *Probleme der Modernen Physik*, Sommerfeld Festschrift, **1928**, p. 104; c) H. Eyring, M. Polanyi, *Z. Phys. Chem. B* **1931**, 12, 279; M. Polanyi, *Atomic Reactions*, Williams, Norgate, London, **1932**.
- 11 a) M. Polanyi, E. Wigner, *Z. Phys. Chem. Abt. A* **1928**, 139, 439; b) H. Eyring, *J. Chem. Phys.* **1935**, 3, 107; see also H. Eyring, *J. Chem. Phys.* **1935**, 3, 492; c) M. G. Evans, M. Polanyi, *Trans. Faraday Soc.* **1935**, 31, 875; M. G. Evans, M. Polanyi, *Trans. Faraday Soc.* **1937**, 33, 448; d) H. A. Kramers, *Physica (Utrecht)* **1940**, 7, 284; e) R. A. Marcus, *J. Chem. Phys.* **1956**, 24, 966; R. A. Marcus, *J. Chem. Phys.* **1956**, 24, 974; f) R. F. Grote, J. T. Hynes, *J. Chem. Phys.* **1980**, 73, 2715; ref. [28].
- 12 J. C. Polanyi, A. H. Zewail, *Acc. Chem. Res.* **1995**, 28, 119, and references therein.
- 13 a) I. H. Williams, *Chem. Soc. Rev.* **1993**, 22, 277; A. Williams, *Chem Soc. Rev.* **1994**, 23, 93; W. v. E. Doering, W. Wang, *J. Am. Chem. Soc.* **1999**, 121, 10112; J. E. Baldwin, *J. Comp. Chem.* **1998**, 19, 222; b) P. G. Schultz, R. A. Lerner, *Science* **1995**, 269, 1835; c) A. R. Fersht, *Curr. Opin. Struct. Biol.* **1994**, 5, 79.
- 14 J. C. Polanyi, *Science* **1987**, 236, 680, and references therein; J. C. Polanyi, *Faraday Discuss. Chem. Soc.* **1979**, 67, 129.
- 15 B. R. Johnson, J. L. Kinsey in *Femtosecond Chemistry* (Eds.: J. Manz, L. Wöste), VCH, Weinheim, **1994**.
- 16 A. H. Zewail, *Femtochemistry—Ultrafast Dynamics of the Chemical Bond*, Vol. I and II, World Scientific, Singapore, **1994**. Most of the Caltech publications in this field, to be referenced here (1976–1994), are collected in these two volumes. References will be given for the specific topics and will be updated in the text and bibliography.
- 17 M. Eigen, *Discuss. Faraday Soc.* **1954**, 17, 194; M. Eigen in *Techniques of Organic Chemistry*, Vol. VIII, Part II, Interscience, London, **1963**; “Immeasurable Fast Reactions”: M. Eigen in *Nobel Lectures (Chemistry)*, Elsevier, Amsterdam, **1972**, p. 170, and references therein; R. G. W. Norrish, G. Porter, *Nature* **1949**, 164, 658; G. Porter in *The Chemical Bond: Structure and Dynamics* (Ed.: A. H. Zewail), Academic Press, Boston, **1992**, p. 113, and references therein.
- 18 a) H. Abraham, T. Lemoine, C. R. Hebd. *Seances Acad. Sci.* **1899**, 129, 206; for reviews, see b) N. Bloembergen, *Rev. Mod. Phys.* **1999**, 71, S283, and references therein; c) E. N. Glezer, *Spectroscopy and Dynamics of Collective Excitations in Solids*, Plenum, New York, **1997**, p. 375; d) *Ultrashort Light Pulses* (Ed.: S. L. Shapiro), Springer, Berlin, **1977**; e) *Ultrashort Laser Pulses & Applications* (Ed.: W. Kaiser), Springer, Berlin, **1988**; *Ultrafast Phenomena*, Vol. IX (Eds.: P. F. Barbara, W. H. Knox, G. A. Mourou, A. H. Zewail), Springer, New York, **1994**; *Ultrafast Phenomena Vol. XI* (Eds.: T. Elsaesser, J. G. Fujimoto, D. A. Wiersma, W. Zinth), Springer, New York, **1998**, and references therein; see also ref. [2].
- 19 a) C. V. Shank, E. P. Ippen, *App. Phys. Lett.* **1974**, 24, 373; b) R. L. Fork, B. I. Greene, C. V. Shank, *App. Phys. Lett.* **1981**, 38, 671; c) J. A. Valdmanis, R. L. Fork, J. P. Gordon, *Opt. Lett.* **1985**, 10, 131; d) R. L. Fork, C. H. Brito Cruz, P. C. Becker, C. V. Shank, *Opt. Lett.* **1987**, 12, 483; see also the reviews in ref. [18]; e) D. E. Spence, P. N. Kean, W. Sibbett, *Opt. Lett.* **1991**, 16, 42; f) J. P. Zhou, G. Taft, C. P. Huang, M. M. Murnane, H. C. Kaptyn, *Opt. Lett.* **1994**, 19, 1149; g) A. Baltuska, Z. Wei, M. S. Pshe-nichnikov, D. Wiersma, *Opt. Lett.* **1997**, 22, 102; h) R. R. Alfano, S. L. Shapiro, *Phys. Rev. Lett.* **1970**, 24, 584.
- 20 P. M. Rentzepis, *Chem. Phys. Lett.* **1968**, 2, 117; T. L. Netzel, P. M. Rentzepis, J. S. Leigh, *Science* **1973**, 182, 238; K. J. Kaufmann, P. M. Rentzepis, *Acc. Chem. Res.* **1975**, 8, 407.
- 21 T. J. Chuang, G. W. Hoffmann, K. B. Eisenthal, *Chem. Phys. Lett.* **1974**, 25, 201; K. B. Eisenthal, K. H. Drexhage, *J. Chem. Phys.* **1969**, 51, 5720; K. B. Eisenthal, *Acc. Chem. Res.* **1975**, 8, 118.
- 22 R. M. Hochstrasser, H. Lutz, G. W. Scott, *Chem. Phys. Lett.* **1974**, 24, 162; R. Anderson, R. M. Hochstrasser, H. Lutz, G. W. Scott, *Chem. Phys. Lett.* **1974**, 28, 153; R. M. Hochstrasser, *Springer Ser. Chem. Phys.* **1978**, 3, 98.
- 23 D. von der Linde, A. Laubereau, W. Kaiser, *Phys. Rev. Lett.* **1971**, 26, 954; A. Laubereau, D. von der Linde, W. Kaiser, *Phys. Rev. Lett.* **1972**, 28, 1162; A. Laubereau, W. Kaiser, *Rev. Mod. Phys.* **1978**, 50, 607.

- 24 "Chemistry in a Jiffy": J. Bigeleisen, *Chem. & Eng. News* **1977**, 55, 26. In a written correspondence, Jacob emphasized that he, in contrast to the view of the 1960s (ref. [40]) understood what could be learned from time scales below the nanosecond, but that he failed to appreciate how the two uncertainties would serve to localize the length scale.
- 25 a) D. R. Herschbach, *Angew. Chem.* **1987**, 99, 1251; *Angew. Chem. Int. Ed. Engl.* **1987**, 26, 1221, and references therein; Y. T. Lee, *Science* **1987**, 236, 793, and references therein; b) R. N. Zare, R. B. Bernstein, *Phys. Today* **1980**, 33, 11.
- 26 A. H. Zewail, R. B. Bernstein, *Chem. Eng. News* **1988**, Nov 7, 24; also in *The Chemical Bond: Structure and Dynamics* (Ed.: A. H. Zewail), Academic Press, Boston, **1992**, p. 223.
- 27 D. C. Clary, *Science* **1998**, 279, 1879; D. C. Clary in ref. [28], and references therein.
- 28 *Nobel Symposium Book: Femtochemistry and Femtobiology: Ultrafast Reaction Dynamics at Atomic-Scale Resolution* (Ed.: V. Sundström), World Scientific, Imperial College Press, London, **1997**, and references therein.
- 29 R. P. Feynman, F. L. Vernon, R. W. Hellwarth, *J. Appl. Phys.* **1957**, 28, 49.
- 30 For recent reviews, see J. Jortner, M. Bixon in ref. [28]; J. Jortner, *Phil. Trans. R. Soc. Lond. A* **1998**, 356, 477, and references therein.
- 31 a) E. J. Heller, *Acc. Chem. Res.* **1981**, 14, 368; b) D. Imre, J. L. Kinsey, A. Sinha, J. Krenos, *J. Phys. Chem.* **1984**, 88, 3956; B. R. Johnson, C. Kittrell, P. B. Kelly, J. L. Kinsey, *J. Phys. Chem.* **1996**, 100, 7743; c) R. Kosloff, *J. Phys. Chem.* **1988**, 92, 2087, and references therein.
- 32 B. Roos, *Acc. Chem. Res.* **1999**, 32, 137, and references therein.
- 33 V. Letokhov in ref. [28]; V. Letokhov in *Femtochemistry IV*, Leuven, Belgium, **1999**; V. Letokhov in ref. [B30]; V. Letokhov in ref. [B31].
- 34 W. S. Warren, *Science* **1988**, 242, 878; W. S. Warren, *Encyclopedia Magnetic Resonance*, Wiley, New York, **1996**.
- 35 a) D. J. Tannor, S. A. Rice, *J. Chem. Phys.* **1985**, 83, 5013; b) D. J. Tannor, R. Kosloff, S. A. Rice, *J. Chem. Phys.* **1986**, 85, 5805; c) D. J. Tannor, S. A. Rice, *Adv. Chem. Phys.* **1988**, 70, 44.
- 36 a) H.-L. Dai, W. Ho, *Laser Spectroscopy and Photochemistry on Metal Surfaces, Part I & II*, World Scientific, Singapore, **1995**; b) M. Bonn, S. Funk, C. Hess, D. N. Denzler, C. Stampfl, M. Scheffler, M. Wolf, G. Ertl, *Science* **1999**, 285, 1042; c) R. J. Finlay, T.-H. Her, C. Wu, E. Mazur, *Chem. Phys. Lett.* **1997**, 274, 499.
- 37 a) A. Assion, T. Baumert, M. Bergt, T. Brixner, B. Kiefer, V. Seyfried, M. Strehle, G. Gerber, *Science* **1998**, 282, 919; b) B. Kohler, J. L. Krause, F. Raksi, K. R. Wilson, V. V. Yakovlev, R. M. Whittell, Y. J. Yan, *Acc. Chem. Res.* **1995**, 28, 133.
- 38 P. B. Corkum, M. Y. Ivanov, J. S. Wright, *Annu. Rev. Phys. Chem.* **1997**, 48, 387; T. Frohnmeyer, M. Hofmann, M. Strehle, T. Baumert, *Chem. Phys. Lett.* **1999**, 312, 447; *Molecules in Laser Fields* (Ed.: A. D. Bandrauk), Marcel Dekker, New York, **1994**, and references therein.
- 39 R. M. Hochstrasser, *J. Chem. Educ.* **1998**, 75, 559, and references therein; V. Sundström, T. Pullerits, R. van Grondelle, *J. Phys. Chem. B* **1999**, 103, 2327, and references therein; S. Hahn, G. Stock, *J. Phys. Chem. B* **2000**, 104, 1146, and references therein; J.-L. Martin, M. H. Vos, *Annu. Rev. Biophys. Biomol. Struct.* **1992**, 21, 199, and references therein; L. Zhu, J. T. Sage, P. M. Champion, *Science* **1994**, 266, 629, and references therein; G. R. Fleming, R. van Grondelle, *Phys. Today* **1994** (February Issue), 48), and references therein; R. A. Mathies, S. W. Lin, J. B. Ames, W. T. Pollard, *Annu. Rev. Biophys. Biophys. Chem.* **1991**, 20, 491, and references therein; R. J. D. Miller, *Annu. Rev. Phys. Chem.* **1991**, 42, 581, and references therein; M. H. Vos, J.-L. Martin, *Biochim. Biophys. Acta* **1999**, 1411, 1, and references therein; U. Liebl, G. Lipowski, M. Négrerie, J.-C. Lambry, L.-L. Martin, M. H. Vos, *Nature* **1999**, 401, 181, and references therein; *Electron Transfer—From Isolated Molecules to Biomolecules* (Eds.: J. Jortner M. Bixon), Wiley, New York, **1999**, and references therein; see also ref. [28], [79], and [80].
- 40 a) *Nobel Symposium 5, Fast Reactions and Primary Processes in Chemical Kinetics* (Ed.: S. Claesson), Almqvist & Wiksell, Stockholm, **1967**, p. 474; b) G. Porter in *Femtosecond Chemistry*, Vol. 1 (Eds.: J. Manz, L. Wöste), VCH, Weinheim, **1995**, p. 3.
- 41 Z. Li, J.-Y. Fang, C. C. Martens, *J. Chem. Phys.* **1996**, 104, 6919.
- 42 "The 1997 Welch Prize Address, Femtochemistry": A. H. Zewail in *Proceedings of the Robert A. Welch Foundation*, 41st Conference on Chemical Research, Houston, Texas, **1997**, p. 323.



- 43 G. M. Gale, G. Gallot, F. Hache, N. Lascoux, S. Bratos, J. C. Leicknam, *Phys. Rev. Lett.* **1999**, 82, 1068; C. Chudoba, E. T. J. Nibbering, T. Elsaesser, *J. Phys. Chem. A* **1999**, 103, 5625; for the development of methods, see J. N. Moore, P. A. Hansen, R. M. Hochstrasser, *Chem. Phys. Lett.* **1987**, 138, 110; P. O. Stoutland, R. B. Dyer, W. H. Woodruff, *Science* **1992**, 257, 1913; W. Kaiser, A. Laubereau in ref. [23], and references therein.
- 44 A. W. Castleman, Jr., K. H. Bowen, Jr., *J. Phys. Chem.* **1996**, 100, 12911; S. Wolf, G. Sommerer, S. Rutz, E. Schreiber, T. Leisner, L. Wöste, R. S. Berry, *Phys. Rev. Lett.* **1995**, 74, 4177; P. Farmanara, W. Radloff, V. Stert, H. H. Ritze, I. V. Hertel, *J. Chem. Phys.* **1999**, 111, 633; W. C. Lineberger, in ref. [28]; M. T. Zanni, B. J. Greenblatt, A. V. Davis, D. M. Neumark, *J. Chem. Phys.* **1999**, 111, 2991, and references therein.
- 45 C. Cohen-Tannoudji, B. Diu, F. Laloë, *Quantum Mechanics, Vol. I & II*, Wiley, New York, **1977**; J. L. Eisberg, *Fundamentals of Modern Physics*, Wiley, New York, **1964**; D. D. Fitts, *Principles of Quantum Mechanics*, Cambridge University Press, **1999**; L. Mühlbacher, A. Lucke, R. Egger, *J. Chem. Phys.* **1999**, 110, 5851; J. Manz in ref. [28], p. 80; M. A. Morrison, *Quantum Physics*, Prentice Hall, New Jersey, **1990**.
- 46 a) A. W. Castleman, Jr., V. Sundström, *J. Phys. Chem. A* **1998**, 102, 4021 (special issue "Ten Years of Femtochemistry"); b) P. Corkum, *Nature* **2000**, 403, 845; S. E. Harris, A. V. Sokolov, *Phys. Rev. Lett.* **1998**, 81, 2894.
- 47 A. R. Fersht, *Structure and Mechanism in Protein Science*, W. H. Freeman, New York, **1999**; W. A. Eaton, *Proc. Natl. Acad. Sci. USA* **1999**, 96, 5897; C. L. Brooks III, M. Gruebele, J. N. Onuchic, P. G. Wolynes *Proc. Natl. Acad. Sci. USA* **1998**, 95, 11037; D. T. Leeson, F. Gai, H. M. Rodriguez, L. M. Gregoret, *Proc. Natl. Acad. Sci. USA* **2000**, 97, 2527.
- 48 "Which way to the Big Bang?": J. Glanz, *Science* **1999**, 284, 1448; S. Clark, *Towards the Edge of the Universe*, 2nd ed., Springer, New York, **1999**.
- 49 S. Pedersen, J. L. Herek, A. H. Zewail, *Science* **1994**, 266, 1359.
- 50 A. H. Zewail, T. E. Orlowski, K. E. Jones, D. E. Godar, *Chem. Phys. Lett.* **1977**, 48, 256; W. S. Warren, A. H. Zewail, *J. Chem. Phys.* **1981**, 75, 5956; W. S. Warren, A. H. Zewail, *J. Chem. Phys.* **1983**, 78, 2279; E. T. Sleva, A. H. Zewail, *Chem. Phys. Lett.* **1984**, 110, 582; E. T. Sleva, I. M. Xavier, Jr., A. H. Zewail, *J. Opt. Soc. Am.* **1986**, 3, 483.
- 51 W. R. Lambert, P. M. Felker, A. H. Zewail, *J. Chem. Phys.* **1981**, 75, 5958; W. R. Lambert, P. M. Felker, A. H. Zewail, *J. Chem. Phys.* **1984**, 81, 2209; W. R. Lambert, P. M. Felker, A. H. Zewail, *J. Chem. Phys.* **1984**, 81, 2217; P. M. Felker, A. H. Zewail, *Phys. Rev. Lett.* **1984**, 53, 501; P. M. Felker, A. H. Zewail, *J. Chem. Phys.* **1985**, 82, 2961; P. M. Felker, A. H. Zewail, *J. Chem. Phys.* **1985**, 82, 2975; P. M. Felker, A. H. Zewail, *J. Chem. Phys.* **1985**, 82, 2994; P. M. Felker, A. H. Zewail, *Adv. Chem. Phys.* **1988**, 70, 265; P. M. Felker, A. H. Zewail in *Jet Spectroscopy and Molecular Dynamics* (Eds.: M. Hollas, D. Phillips), Chapman and Hall, Blackie Academic, **1995**, p. 222.
- 52 A. H. Zewail, *Faraday Discuss. Chem. Soc.* **1983**, 75, 315; J. A. Syage, W. R. Lambert, P. M. Felker, A. H. Zewail, R. M. Hochstrasser, *Chem. Phys. Lett.* **1982**, 88, 266; J. A. Syage, P. M. Felker, A. H. Zewail, *J. Chem. Phys.* **1984**, 81, 4706; P. M. Felker, A. H. Zewail, *J. Chem. Phys.* **1985**, 82, 2961; P. M. Felker, A. H. Zewail, *J. Chem. Phys.* **1985**, 82, 2994; P. M. Felker, J. A. Syage, W. R. Lambert, A. H. Zewail, *Chem. Phys. Lett.* **1982**, 92, 1; J. A. Syage, P. M. Felker, A. H. Zewail, *J. Chem. Phys.* **1984**, 81, 2233; P. M. Felker, A. H. Zewail, *Chem. Phys. Lett.* **1983**, 94, 454; P. M. Felker, A. H. Zewail, *J. Chem. Phys.* **1983**, 78, 5266.
- 53 J. S. Baskin, P. M. Felker, A. H. Zewail, *J. Chem. Phys.* **1986**, 84, 4708; P. M. Felker, J. S. Baskin, A. H. Zewail, *J. Phys. Chem.* **1986**, 90, 724; P. M. Felker, A. H. Zewail, *J. Chem. Phys.* **1987**, 86, 2460; J. S. Baskin, P. M. Felker, A. H. Zewail, *J. Chem. Phys.* **1987**, 86, 2483; N. F. Scherer, L. R. Khundkar, T. S. Rose, A. H. Zewail, *J. Phys. Chem.* **1987**, 91, 6478; J. S. Baskin, A. H. Zewail, *J. Phys. Chem.* **1989**, 93, 5701.
- 54 L. R. Khundkar, A. H. Zewail, *Annu. Rev. Phys. Chem.* **1990**, 41, 15; N. F. Scherer, F. E. Doany, A. H. Zewail, J. W. Perry, *J. Chem. Phys.* **1986**, 84, 1932; N. F. Scherer, A. H. Zewail, *J. Chem. Phys.* **1987**, 87, 97; L. R. Khundkar, J. L. Knee, A. H. Zewail, *J. Chem. Phys.* **1987**, 87, 77; S. J. Klippenstein, L. R. Khundkar, A. H. Zewail, R. A. Marcus, *J. Chem. Phys.* **1988**, 89, 4761.

- 55 N. F. Scherer, J. L. Knee, D. D. Smith, A. H. Zewail, *J. Phys. Chem.* **1985**, 89, 5141; M. Dantus, M. J. Rosker, A. H. Zewail, *J. Chem. Phys.* **1987**, 87, 2395; M. J. Rosker, M. Dantus, A. H. Zewail, *Science* **1988**, 241, 1200; M. J. Rosker, M. Dantus, A. H. Zewail, *J. Chem. Phys.* **1988**, 89, 6113; M. Dantus, M. J. Rosker, A. H. Zewail, *J. Chem. Phys.* **1988**, 89, 6128; D. Zhong, A. H. Zewail, *J. Phys. Chem. A* **1998**, 102, 4031; R. Bersohn, A. H. Zewail, *Ber. Bunsen-Ges. Phys. Chem.* **1988**, 92, 373; G. Roberts, A. H. Zewail, *J. Phys. Chem.* **1991**, 95, 7973; G. Roberts, A. H. Zewail, *J. Phys. Chem.* **1995**, 99, 2520; the quantum calculations in the last reference follows the original results by D. Imre (see text).
- 56 T. S. Rose, M. J. Rosker, A. H. Zewail, *J. Chem. Phys.* **1988**, 88, 6672; T. S. Rose, M. J. Rosker, A. H. Zewail, *J. Chem. Phys.* **1989**, 91, 7415; P. Cong, A. Mokhtari, A. H. Zewail, *Chem. Phys. Lett.* **1990**, 172, 109; A. Mokhtari, P. Cong, J. L. Herek, A. H. Zewail, *Nature* **1990**, 348, 225; P. Cong, G. Roberts, J. L. Herek, A. Mokhtari, A. H. Zewail, *J. Phys. Chem.* **1996**, 100, 7832.
- 57 R. M. Bowman, M. Dantus, A. H. Zewail, *Chem. Phys. Lett.* **1989**, 156, 131; M. Dantus, R. M. Bowman, M. Gruebele, A. H. Zewail, *J. Chem. Phys.* **1989**, 91, 7437; M. Gruebele, G. Roberts, A. H. Zewail, *Philos. Trans. R. Soc. London A* **1990**, 332, 35; D. Zhong, A. H. Zewail, *J. Phys. Chem. A* **1998**, 102, 4031; K. B. Møller, A. H. Zewail, *Chem. Phys. Lett.* **1998**, 295, 1.
- 58 M. Dantus, R. M. Bowman, A. H. Zewail, *Nature* **1990**, 343, 737; M. Gruebele, G. Roberts, M. Dantus, R. M. Bowman, A. H. Zewail, *Chem. Phys. Lett.* **1990**, 166, 459; R. B. Bernstein, A. H. Zewail, *Chem. Phys. Lett.* **1990**, 170, 321; M. H. M. Janssen, R. M. Bowman, A. H. Zewail, *Chem. Phys. Lett.* **1990**, 172, 99; M. Gruebele, A. H. Zewail, *J. Chem. Phys.* **1993**, 98, 883.
- 59 N. F. Scherer, L. R. Khundkar, R. B. Bernstein, A. H. Zewail, *J. Chem. Phys.* **1987**, 87, 1451; N. F. Scherer, C. Sipes, R. B. Bernstein, A. H. Zewail, *J. Chem. Phys.* **1990**, 92, 5239; M. Gruebele, I. R. Sims, E. D. Potter, A. H. Zewail, *J. Chem. Phys.* **1991**, 95, 7763; I. R. Sims, M. Gruebele, E. D. Potter, A. H. Zewail, *J. Chem. Phys.* **1992**, 97, 4127; D. Zhong, P. Y. Cheng, A. H. Zewail, *J. Chem. Phys.* **1996**, 105, 7864; an up-to-date experimental and theoretical work is reviewed in ref. [B5] (some are adapted here) and the review by D. Clary (ref. [27]).
- 60 J. L. Knee, L. R. Khundkar, A. H. Zewail, *J. Chem. Phys.* **1985**, 82, 4715; M. Dantus, M. H. M. Janssen, A. H. Zewail, *Chem. Phys. Lett.* **1991**, 181, 281; T. Baumert, S. Pedersen, A. H. Zewail, *J. Phys. Chem.* **1993**, 97, 12447; S. Pedersen, J. L. Herek, A. H. Zewail, *Science* **1994**, 266, 1359; S. K. Kim, S. Pedersen, A. H. Zewail, *J. Chem. Phys.* **1995**, 103, 477; S. K. Kim, A. H. Zewail, *Chem. Phys. Lett.* **1996**, 250, 279; S. K. Kim, J. Guo, J. S. Baskin, A. H. Zewail, *J. Phys. Chem.* **1996**, 100, 9202.
- 61 E. W.-G. Diau, O. Abou-Zied, A. A. Scala, A. H. Zewail, *J. Am. Chem. Soc.* **1998**, 120, 3245.
- 62 L. R. Khundkar, A. H. Zewail, *J. Chem. Phys.* **1990**, 92, 231; D. Zhong, S. Ahmad, A. H. Zewail, *J. Am. Chem. Soc.* **1997**, 119, 5978; D. Zhong, A. H. Zewail, *J. Phys. Chem. A* **1998**, 102, 4031.
- 63 P. Y. Cheng, D. Zhong, A. H. Zewail, *Chem. Phys. Lett.* **1995**, 237, 399.
- 64 S. K. Kim, S. Pedersen, A. H. Zewail, *Chem. Phys. Lett.* **1995**, 233, 500.
- 65 A. A. Scala, E. W.-G. Diau, Z. H. Kim, A. H. Zewail, *J. Chem. Phys.* **1998**, 108, 7933.
- 66 S. De Feyter, E. W.-G. Diau, A. H. Zewail, *Angew. Chem.* **2000**, 112, 266; *Angew. Chem. Int. Ed.* **2000**, 39, 260.
- 67 P. M. Felker, W. R. Lambert, A. H. Zewail, *J. Chem. Phys.* **1982**, 77, 1603; J. L. Herek, S. Pedersen, L. Bañares, A. H. Zewail, *J. Chem. Phys.* **1992**, 97, 9046.
- 68 B. A. Horn, J. L. Herek, A. H. Zewail, *J. Am. Chem. Soc.* **1996**, 118, 8755; E. W.-G. Diau, S. De Feyter, A. H. Zewail, *Chem. Phys. Lett.* **1999**, 304, 134; S. De Feyter, E. W.-G. Diau, A. H. Zewail, *Phys. Chem. Chem. Phys.* **2000**, 2, 877.
- 69 D. Zhong, E. W.-G. Diau, T. M. Bernhardt, S. De Feyter, J. D. Roberts, A. H. Zewail, *Chem. Phys. Lett.* **1998**, 298, 129; M. Chachisvilis, A. H. Zewail, *J. Phys. Chem. A* **1999**, 103, 7408.
- 70 P. Y. Cheng, D. Zhong, A. H. Zewail, *J. Chem. Phys.* **1996**, 105, 6216; D. Zhong, A. H. Zewail, *Proc. Natl. Acad. Sci. USA* **1999**, 96, 2602; D. Zhong, T. M. Bernhardt, A. H. Zewail, *J. Phys. Chem. A* **1999**, 103, 10093.
- 71 S. Pedersen, J. L. Herek, A. H. Zewail, *Science* **1994**, 266, 1359; S. De Feyter, E. W.-G. Diau, A. A. Scala, A. H. Zewail, *Chem. Phys. Lett.*

- 1999, 303, 249; ref. [66]; E. W.-G. Diau, J. Casanova, J. D. Roberts, A. H. Zewail, *Proc. Natl. Acad. Sci. USA* **2000**, 97, 1376.
- 72 E. W.-G. Diau, A. H. Zewail, ref. [61] and unpublished results.
- 73 Ref. [69]; E. W.-G. Diau, S. De Feyter, A. H. Zewail, *J. Chem. Phys.* **1999**, 110, 9785.
- 74 Q. Liu, J.-K. Wang, A. H. Zewail, *Nature* **1993**, 364, 427; J.-K. Wang, Q. Liu, A. H. Zewail, *J. Phys. Chem.* **1995**, 99, 11 309; Q. Liu, J.-K. Wang, A. H. Zewail, *J. Phys. Chem.* **1995**, 99, 11 321; J. J. Breen, D. M. Willberg, M. Gutmann, A. H. Zewail, *J. Chem. Phys.* **1990**, 93, 9180; M. Gutmann, D. M. Willberg, A. H. Zewail, *J. Chem. Phys.* **1992**, 97, 8037; J. T. Su, A. H. Zewail, *J. Phys. Chem. A* **1998**, 102, 4082; J. J. Breen, L. W. Peng, D. M. Willberg, A. Heikal, P. Cong, A. H. Zewail, *J. Chem. Phys.* **1990**, 92, 805; S. K. Kim, J.-K. Wang, A. H. Zewail, *Chem. Phys. Lett.* **1994**, 228, 369; S. K. Kim, J. J. Breen, D. M. Willberg, L. W. Peng, A. Heikal, J. A. Syage, A. H. Zewail, *J. Phys. Chem.* **1995**, 99, 7421; A. A. Heikal, S. H. Chong, J. S. Baskin, A. H. Zewail, *Chem. Phys. Lett.* **1995**, 242, 380.
- 75 a) A. H. Zewail, M. Dantus, R. M. Bowman, A. Mokhtari, *J. Photochem. Photobiol. A* **1992**, 62/63, 301; b) C. Lienau, J. C. Williamson, A. H. Zewail, *Chem. Phys. Lett.* **1993**, 213, 289; C. Lienau, A. H. Zewail, *Chem. Phys. Lett.* **1994**, 222, 224; C. Lienau, A. H. Zewail, *J. Phys. Chem.* **1996**, 100, 18629; A. Materny, C. Lienau, A. H. Zewail, *J. Phys. Chem.* **1996**, 100, 18650; Q. Liu, C. Wan, A. H. Zewail, *J. Phys. Chem.* **1996**, 100, 18666; C. Wan, M. Gupta, J. S. Baskin, Z. H. Kim, A. H. Zewail, *J. Chem. Phys.* **1997**, 106, 4353; J. S. Baskin, M. Gupta, M. Chachisvilis, A. H. Zewail, *Chem. Phys. Lett.* **1997**, 275, 437; J. S. Baskin, M. Chachisvilis, M. Gupta, A. H. Zewail, *J. Phys. Chem. A* **1998**, 102, 4158; A. Douhal, T. Fiebig, M. Chachisvilis, A. H. Zewail, *J. Phys. Chem. A* **1998**, 102, 1657; M. Chachisvilis, I. Garcia Ochoa, A. Douhal, A. H. Zewail, *Chem. Phys. Lett.* **1998**, 293, 153; A. Vierheilg, T. Chen, P. Waltner, W. Kiefer, A. Materny, A. H. Zewail, *Chem. Phys. Lett.* **1999**, 312, 349; C. Wan, M. Gupta, A. H. Zewail, *Chem. Phys. Lett.* **1996**, 256, 279; M. Chachisvilis, A. H. Zewail, *J. Phys. Chem. A* **1999**, 103, 7408; T. Fiebig, M. Chachisvilis, M. M. Manger, I. Garcia Ochoa, A. de La Hoz Ayuso, A. Douhal, A. H. Zewail, *J. Phys. Chem. A* **1999**, 103, 7419.
- 76 J. C. Williamson, A. H. Zewail, *Proc. Natl. Acad. Sci. USA* **1991**, 88, 5021; J. C. Williamson, M. Dantus, S. B. Kim, A. H. Zewail, *Chem. Phys. Lett.* **1992**, 196, 529; J. C. Williamson, A. H. Zewail, *Chem. Phys. Lett.* **1993**, 209, 10; J. C. Williamson, A. H. Zewail, *J. Phys. Chem.* **1994**, 98, 2766; M. Dantus, S. B. Kim, J. C. Williamson, A. H. Zewail, *J. Phys. Chem.* **1994**, 98, 2782; J. C. Williamson, J. Cao, H. Ihee, H. Frey, A. H. Zewail, *Nature* **1997**, 386, 159; H. Ihee, J. Cao, A. H. Zewail, *Chem. Phys. Lett.* **1997**, 281, 10; J. Cao, H. Ihee, A. H. Zewail, *Chem. Phys. Lett.* **1998**, 290, 1; J. Cao, H. Ihee, A. H. Zewail, *Proc. Natl. Acad. Sci. USA* **1999**, 96, 338.
- 77 W. S. Warren, A. H. Zewail, *J. Chem. Phys.* **1983**, 78, 2279; W. S. Warren, A. H. Zewail, *J. Chem. Phys.* **1983**, 78, 2298; W. S. Warren, A. H. Zewail, *J. Chem. Phys.* **1983**, 78, 2298; J. J. Gerdy, M. Dantus, R. M. Bowman, A. H. Zewail, *Chem. Phys. Lett.* **1990**, 171, 1; J. L. Herek, A. Materny, A. H. Zewail, *Chem. Phys. Lett.* **1994**, 228, 15; E. D. Potter, J. L. Herek, S. Pedersen, Q. Liu, A. H. Zewail, *Nature* **1992**, 355, 66; E. W.-G. Diau, J. L. Herek, Z. H. Kim, A. H. Zewail, *Science* **1998**, 279, 847.
- 78 D. P. Millar, R. J. Robbins, A. H. Zewail, *Proc. Natl. Acad. Sci. USA* **1980**, 77, 5593; D. P. Millar, R. J. Robbins, A. H. Zewail, *J. Chem. Phys.* **1981**, 74, 4200; D. P. Millar, R. J. Robbins, A. H. Zewail, *J. Chem. Phys.* **1982**, 76, 2080.
- 79 T. Fiebig, C. Wan, S. O. Kelley, J. K. Barton, A. H. Zewail, *Proc. Natl. Acad. Sci. USA* **1999**, 96, 1187; C. Wan, T. Fiebig, S. O. Kelley, C. R. Treadway, J. K. Barton, A. H. Zewail, *Proc. Natl. Acad. Sci. USA* **1999**, 96, 6014; the protein work involves D. Zhong of this laboratory; the work on the aminopurine system involves T. Fiebig and C. Wan of this laboratory in collaboration with Olav Schiemann and Jackie Barton.
- 80 B. Steiger, J. S. Baskin, F. C. Anson, A. H. Zewail, *Angew. Chem.* **2000**, 112, 263; *Angew. Chem. Int. Ed.* **2000**, 39, 257; A. Douhal, S. K. Kim, A. H. Zewail, *Nature* **1995**, 378, 260; T. Fiebig, M. Chachisvilis, M. M. Manger, I. Garcia Ochoa, A. de La Hoz Ayuso, A. Douhal, A. H. Zewail, *J. Phys. Chem. A* **1999**, 103, 7419; B. A. Leland, A. D. Joran, P. M. Felker, J. J. Hopfield, A. H. Zewail, P. B. Dervan, *J. Phys. Chem.* **1985**, 89, 5571; A. D. Joran, B. A.

Leland, P. M. Felker, A. H. Zewail, J. J. Hopfield, P. B. Dervan, *Nature* **1987**, 327, 508.

### Bibliography: The Caltech Research

Over the past 20 years at Caltech my group and I have published some 300 scientific papers. The following list includes some reviews, feature articles, and a few books.

#### Books

- B1** A. H. Zewail, *Femtochemistry—Ultrafast Dynamics of the Chemical Bond, Vol. I and II*, World Scientific, New Jersey, Singapore, **1994**.  
**B2** *The Chemical Bond: Structure and Dynamics* (Ed.: A. H. Zewail), Academic Press, Boston, **1992**.

#### Book Chapters

- B3** "Molecular Clusters: Real-Time Dynamics and Reactivity": J. A. Syage, A. H. Zewail in *Molecular Clusters* (Eds.: J. M. Bowman, Z. Bacic), JAI Press, London, **1998**.  
**B4** "Femtochemistry: Dynamics with Atomic Resolution": A. H. Zewail in *Femtochemistry & Femtobiology* (Ed.: V. Sundström), World Scientific, Singapore, **1997**.  
**B5** C. Wittig, A. H. Zewail in *Dynamics of Ground State Bimolecular Reactions, Chemical Reactions in Clusters* (Ed.: E. R. Bernstein), Oxford University Press, New York, **1996**, p. 64.  
**B6** "Femtochemistry: Concepts and Applications": A. H. Zewail in *Femtosecond Chemistry* (Eds.: J. Manz, L. Wöste), VCH, New York, **1995**, p. 15.  
**B7** "Molecular Structures from Ultrafast Coherence Spectroscopy": P. M. Felker, A. H. Zewail in: *Femtosecond Chemistry* (Eds.: J. Manz, L. Wöste), VCH, New York, **1995**, p. 193.  
**B8** "Ultrafast Dynamics of the Chemical Bond—Femtochemistry": A. H. Zewail in *Ultrafast Processes in Chemistry and Photobiology, Chemistry for the 21st Century*, (Eds.: M. A. El-Sayed, I. Tanaka, Y. N. Molin), IUPAC, Blackwell Scientific Publishers, Oxford, **1995**, p. 1.  
**B9** "Molecular Mechanisms for Dephasing: Toward a Unified Treatment of Gases, Solids, and Liquids": K. E. Jones, A. H. Zewail, *Springer Ser. Chem. Phys.* **1978**, 3, 258 (Advances in Laser Chemistry).

#### Reviews

- B10** "Femtochemistry: Recent Progress in Studies of Dynamics and Control of Reactions and Their Transition States": A. H. Zewail, *J. Phys. Chem.* **1996**, 100, 12701 (Centennial Issue).  
**B11** "Proton-transfer Reaction Dynamics": A. Douhal, F. Lahmani, A. H. Zewail, *Chem. Phys.* **1996**, 207, 477 (Special Issue).  
**B12** "Direct Observation of The Transition State": J. C. Polanyi, A. H. Zewail, *Acc.Chem. Res.* **1995**, 28, 119 (Holy-Grail Special Issue).  
**B13** "Coherence—A Powerful Concept in the Studies of Structures and Dynamics": A. H. Zewail, *Laser Phys.* **1995**, 5, 417.  
**B14** "Femtochemistry": A. H. Zewail, *J. Phys. Chem.* **1993**, 97, 12427 (Feature Article).  
**B15** "Femtochemistry: Recent Advances and Extension to High-Pressures": see ref. [75a].  
**B16** "Real-Time Laser Femtochemistry: Viewing the Transition States from Reagents to Products": A. H. Zewail, R. B. Bernstein, *Chem. & Eng. News* **1988**, 66(Nov 7) 24 – Feature Article/Special Report; in: *The Chemical Bond: Structure and Dynamics* (Ed.: A. H. Zewail), Academic Press, Boston, **1992**, p. 223.  
**B17** "Femtosecond Transition-State Dynamics in Structure and Dynamics of Reactive Transition States": A. H. Zewail, *Faraday Discuss. Chem. Soc.* **1991**, 91, 207.  
**B18** "Femtochemistry: The Role of Alignment and Orientation": A. H. Zewail, *J. Chem. Soc. Faraday Trans.* **1989**, 285, 1221.  
**B19** "Laser Femtochemistry": A. H. Zewail, *Science* **1988**, 242, 1645.  
**B20** "IVR: Its Coherent and Incoherent Dynamics": A. H. Zewail, *Ber. Bunsen-Ges. Phys. Chem.* **1985**, 89, 264.  
**B21** "Energy Redistribution in Isolated Molecules and the Question of Mode-Selective Laser Chemistry Revisited": N. Bloembergen, A. H. Zewail, *J. Phys. Chem.* **1984**, 88, 5459 (Feature Article).  
**B22** "Phase Coherence in Multiple Pulse Optical Spectroscopy": W. S. Warren, A. H. Zewail in *Photochemistry and Photobiology: Proceedings of the International Conference, Vol. I and II* (Ed.: A. H. Zewail), Harwood Academic, Chur, Switzerland, **1983** (Alexandria, Egypt, January 5–10, 1983); W. S. Warren, A. H. Zewail, *Laser Chem.* **1983**, 2(1, 6), 37.

- B23** "Optical Molecular Dephasing: Principles of and Probing by Coherent Laser Spectroscopy": A. H. Zewail, *Acc. Chem. Res.* **1980**, *13*, 360.
- B24** "Laser Selective Chemistry—Is it Possible?": A. H. Zewail, *Phys. Today* **1980**, *33*, 2.
- B25** "Freezing Time—In a Femtosecond": J. S. Baskin, A. H. Zewail, *Sci. Spectra* **1998**, (14), 62.
- B26** "What is Chemistry? 100 Years After J. J. Thomson's Discovery": A. H. Zewail, *Cambridge Rev.* **1997**, *118*(2330), 65.
- B27** "Discoveries at Atomic Resolution (Small is Beautiful)": A. H. Zewail, *Nature* **1993**, *361*, 215.
- B28** "The Birth of Molecules": A. H. Zewail, *Sci. Am.* **1990**, *263*, 76. Also available in other languages: Italian, Japanese, French, Spanish, German, Russian, Chinese, Arabic, Hungarian, and Indian.
- General Bibliography**
- Books*
- B29** Nobel Symposium: *Femtochemistry & Femtobiology* (Ed.: V. Sundström), World Scientific, Singapore, **1997**.
- B30** Solvay Conference: "Chemical Reactions and Their Control on the Femtosecond Time Scale": *Adv. Chem. Phys.* **1997**, *101*.
- B31** Lausanne Conference: *Femtochemistry* (Ed.: M. Chergui), World Scientific, Singapore, **1996**.
- B32** Berlin Conference: *Femtosecond Chemistry, Vol. 1 and 2* (Eds.: J. Manz, L. Wöste), VCH, Weinheim, **1995**.
- B33** Amsterdam Conference: *Femtosecond Reaction Dynamics* (Ed.: D. A. Wiersma), Royal Netherlands Academy of Arts and Sciences, North Holland, Amsterdam, **1994**.
- B34** *Ultrafast Processes in Chemistry and Biology—Chemistry for the 21st Century* (Eds.: M. A. El-Sayed, I. Tanaka, Y. N. Molin), IUPAC, Blackwell Scientific, Oxford, **1994**.
- B35** *Density Matrix Method and Femtosecond Processes*, (Eds.: S. H. Lin, R. Alden, R. Isalampour, H. Ma, A. A. Villaes), World Scientific, Singapore, **1991**.
- B36** *Principles of Nonlinear Optical Spectroscopy*, S. Mukamel, Oxford University Press, Oxford, **1995**.
- B37** *Ultrafast Dynamics of Chemical Systems* (Ed.: J. D. Simon), Kluwer, Boston, **1994**.
- B38** E. Schreiber, *Femtosecond Real-Time Spectroscopy of Small Molecules & Clusters*, Springer, New York, **1998**.
- Special Issues*
- B39** "Femtochemistry—Ten Years of": *J. Phys. Chem. A* **1998**, *102* (June Issue).
- B40** "Femtochemistry": *J. Phys. Chem.* **1993**, *97* (December Issue).
- B41** "Ultrafast Lasers in Chemistry": *Isr. J. Chem.* **1994**, *34*(1).
- Reviews*
- B42** "Chemistry in Microtime": G. Porter in *The Chemical Bond: Structures and Dynamics* (Ed.: A. H. Zewail), Academic Press, Boston, **1992**, p. 113.
- B43** "Molecular Photophysics": G. Beddard, *Rep. Prog. Phys.* **1993**, *56*, 63.
- B44** "Time-Resolved Vibrational Spectroscopy in the Impulsive Limit": L. Dhar, J. A. Rogers, K. A. Nelson, *Chem. Rev.* **1994**, *94*, 157.
- B45** "The Dynamics of Wave Packets of Highly-Excited States of Atoms and Molecules": I. Sh. Averbukh, N. F. Perel'man, *Sov. Phys. Usp. (Engl. Transl.)* **1991**, *34*, 572.
- B46** "Hot Electron Femtochemistry at Surfaces": J. W. Gadzuk in ref. [B32], Vol. 2, p. 603.
- B47** "Dynamics of Nonthermal Reactions: Surface Femtosecond Chemistry": R. R. Cavanagh, D. S. King, J. C. Stephenson, T. F. Heinz, *J. Phys. Chem.* **1993**, *97*, 786.
- B48** "Femtochemistry": J. G. Thorne, G. S. Beddard, *Chem. Ind.* **1994**, 456.
- B49** "Wave Packet Dynamics: New Physics and Chemistry in Femto-time": B. M. Garraway, K.-A. Suominen, *Rep. Prog. Phys.* **1995**, *58*, 365.
- B50** "Femtosecond Broadband Absorption Spectroscopy of Fragments Formed in the Photodissociation of Gas-phase Molecules": J. H. Glowina, R. E. Walkup, D. R. Gnass, M. Kaschke, J. A. Misewich, P. P. Sorokin in ref. [B32], Vol. 1, p. 131.
- B51** "Theory of Ultrafast Nonadiabatic Excited-State Processes and their Spectroscopic Detection in Real Time": W. Domcke, G. Stock, *Adv. Chem. Phys.* **1997**, *100*, 1.
- B52** "Femtosecond Surface Science", J. A. Misewich, T. F. Heinz, P. Weigand, A. Kalamarides in *Advanced Series in Physical Chemistry*, Vol. 5 (Eds.: H.-L. Dai, W. Ho), World Scientific, Singapore, **1995**.

- B53** "Femtosecond Time-Resolved Photochemistry of Molecules and Metal Clusters": T. Baumert, R. Thalweiser, V. Weiss, G. Gerber in ref. [B32], Vol. 2, p. 397.
- Overviews*
- B54** "Pulse, Pump and Probe": R. Hoffmann, *Am. Sci.* **1999**, 87, 308.
- B55** "Femtochemistry": Y. Tanimura, K. Yamashita, P. A. Anfinrud, *Proc. Natl. Acad. Sci. USA* **1999**, 96, 8823; P. Anfinrud, R. de Vivie-Riedle, V. Engel, *Proc. Natl. Acad. Sci. USA* **1999**, 96, 8328.
- B56** P. Ball, *Designing the Molecular World*, Princeton University Press, Princeton, **1994**; P. Ball, *Chemie der Zukunft—Magie oder Design?*, VCH, Weinheim, **1996**.
- B57** H. C. von Baeyer, *Taming the Atom*, Random House, New York, **1992**.
- B58** P. W. Atkins, *Atoms, Electrons, and Change*, Freeman, New York, **1991**.
- B59** "The World's Fastest Camera": V. K. Jain, *The World and I*, Washington Times Publishing, **1995**, p. 156.
- B60** see ref. [5a].
- B61** "The Classical Limit of an Atom": M. Nauenberg, C. Stroud, J. Yaezell, *Sci. Am.* **1994**, 44.
- B62** "Coherent Thinking": D. L. Smith, *Eng. Sci.* **1999**, 62(4), 6.

## 2

### Transition State Theory and Reaction Dynamics – An Overview

*Ward H. Thompson, Philip M. Kiefer, and James T. Hynes*

#### 2.1

##### Introduction

The charge for this plenary contribution has been interpreted here to focus on the title topic, in the space available, through the highlighting of a very few of its key aspects in a solution reaction context, without any pretense of a general or comprehensive discussion of the topic. For this purpose, we have chosen to use examples both from our older work on  $S_N2$  reactions<sup>[1]</sup> and the excited-state photoreaction of *p*-dimethylaminobenzonitrile (DMABN),<sup>[2]</sup> and from newer work on proton-transfer reactions.<sup>[3,4]</sup>

It is useful to begin with a general insight that is in fact quite old<sup>[5]</sup> but one that, while it is a fundamental part of the modern theoretical approach to reaction rate theory,<sup>[6]</sup> may not be as generally appreciated as it should be. It is that the Transition State Theory (TST) of reaction rates, whether in isolated molecules, in clusters, in solution, or elsewhere, corresponds to a specific dynamical view and statement about the transition state. Simply and somewhat approximately stated, any trajectory heading from the reactants toward the products and passing through a dividing surface defining the transition state is a successful reactive trajectory; in other words, there is no recrossing of the transition state barrier by any trajectory on a short time scale. If this condition holds, then (classically) TST is exact. The important aspects of this in the context of femtochemistry are several-fold: first, that the statement is a dynamical one about trajectories, and second that its validity or nonvalidity involves events occurring on very short time scales related to the dynamical passage through the transition state, the observation of which is surely one of the goals of femtochemistry. It should also be noted that the statement above about the dividing surface implies that we know something about the reaction coordinate in the transition state neighborhood. Finally, the TST assumption is a classical mechanical one; does this mean that TST should be discarded in any reaction where quantum nuclear wave-packet motion is central? In the following, we address, albeit necessarily briefly, these various themes.

## 2.2

**Crossing the Transition State in Solution**

As noted in the Introduction, a key issue concerning Transition State Theory is whether there is any dynamical recrossing of trajectories of the transition state. For solution reactions, the first treatment of this issue is due to Kramers,<sup>[7]</sup> who described the influence of the surrounding solvent in inducing such recrossings, and thus reducing the rate constant below its TST approximation, in terms of the effect of a friction constant. In modern language, this amounts to a description in which the long time scale, full effect of the dynamical forces exerted by the solvent is assumed to apply. However, a key time scale is missing in the Kramers theory,<sup>[8]</sup> that which characterizes the typical time that the reaction system spends in the immediate transition state region before potential forces propel it inexorably towards reactants or products, such that any further dynamical influence of the solvent is no longer relevant. This time is the inverse of the barrier frequency  $\omega_b$ , the magnitude of the unstable frequency describing a transition state region parabolic barrier top: the higher the barrier frequency, the shorter the time spent in the critical region. Thus, the solvent frictional forces relevant to the reaction rate should not be the long time scale ones, but rather those probed on the generally quite short time scale  $\omega_b^{-1}$ . These considerations led to and are incorporated in the Grote-Hynes (GH) theory for the rate constant.<sup>[8]</sup>

Two illustrations serve to indicate some key features. In the first, a molecular dynamics simulation study of the  $S_N2$  nucleophilic substitution reaction  $\text{Cl}^- + \text{CH}_3\text{Cl} \rightarrow \text{ClCH}_3 + \text{Cl}^-$  in water<sup>[1]</sup> showed that these short time scale issues are critical for the passage through the transition state and the reaction rate constant. The barrier frequency  $\omega_b$  is quite high, of the order of  $(20 \text{ fs})^{-1}$ , due to the strong intramolecular forces in the solute reaction system, and the surrounding solvent water molecules are in fact essentially stationary during this passage, due the very short key time scale of  $\sim 20 \text{ fs}$ . Longer time scale events are thus irrelevant with regard to the rate, as evidenced by the complete agreement of GH theory with the simulation results and a marked failure of Kramers theory.<sup>[1]</sup> The strong intramolecular forces also dictate that the reaction coordinate in the transition state region is the antisymmetric stretch motion of  $[\text{ClCH}_3\text{Cl}]^-$  at the transition state, despite the fairly strong coupling of the shifting charge distribution of the reaction system with the polar water molecules.

The second illustration concerns the (long controversial) excited state charge-transfer reaction of *p*-dimethylaminobenzonitrile (DMABN) in solution.<sup>[2]</sup> With a combination of gas-phase electronic structure information, a theoretical treatment of electronic structure in solution, and a modelling of the frictional forces, GH theory was applied to the DMABN reaction in three different solvents. The results<sup>[2a]</sup> in terms of the reaction rates were in quite good agreement with the ultrafast measurements by Changuenet et al.<sup>[9]</sup> (an agreement supporting the twisting intramolecular charge transfer (TICT) perspective, Figure 2.1, over other views for the reaction). The barrier frequency  $\omega_b$  here was estimated to be of the order of  $\omega_b \sim (50 \text{ fs})^{-1}$ , so that, as for the  $S_N2$  reaction outlined above, only the short time scale friction incor-



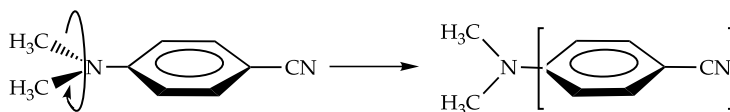


**Fig. 2.1** Schematic illustration of the excited-state photoreaction of DMABN, in the TICT mechanism (see text).

porated in GH theory is relevant; a Kramers theory prediction is very considerably in error, by one to three orders of magnitude. The calculations of the reaction paths indicate that the reaction coordinate in the transition state region, while being somewhat dependent on which solvent is considered, is largely composed of the dimethylamino group twisting angle, emphasizing again that, while intramolecular forces within the reacting molecules can certainly be modified by the solvent, they will often, if not usually, dictate the dominant coordinates for passage through a reaction transition state region. (As discussed below, quantum effects necessitate an important qualification for this remark in the context of proton-transfer reactions.)

## 2.3

### Acid–Base Proton-Transfer Reactions in Solution

An especially important and interesting reaction class for transition state/reaction dynamics issues is that of proton transfer (PT) in solution. Among the various subclasses of PT, that of the intermolecular acid ionization, e.g.  $\text{HX} + \text{H}_2\text{O} \rightarrow \text{X}^- + \text{H}_3\text{O}^+$ , holds special interest due to its wide-ranging and fundamental importance in chemistry and biochemistry. Two central aspects<sup>[10]</sup> to be highlighted in this brief discussion are that a major factor contributing to the reaction coordinate relates to the motion of the surrounding solvent molecules, and that the quantum character of the proton nuclear motion plays an essential and characteristic role in the reaction. Both features are to be contrasted with the more typical reaction situations outlined in Section 2.2 for  $\text{S}_{\text{N}}2$  and TICT reactions, and accordingly they require a different conception and description of the transition state and the associated dynamics.

These aspects have been examined in the Hynes group in a number of detailed realistic combined electronic structure/dynamics simulations of specific systems, such as hydrochloric acid in water.<sup>[10,11]</sup> For present purposes, however, it is more useful to couch the discussion in terms of an analytical study by Kiefer and Hynes<sup>[4]</sup> of the primary acid-base PT reaction event in a hydrogen-bonded complex to produce a hydrogen-bonded contact ion pair,  $\text{AH}\cdots\text{B} \rightarrow \text{A}^-\cdots\text{HB}^+$ , in a polar solvent, with the acid and base modelled to be appropriate for typical oxygen acid–nitrogen base systems; details are given in ref. [4]. Figure 2.2 displays the key features of a model overall symmetric PT reaction (for simplicity restricted here to the simplified case where the A–B separation is held fixed). Figure 2.2a shows the proton potential curve *versus* the proton coordinate for solvent configurations appropriate to that of the reactant pair, the transition state (further discussed below), and the product pair.

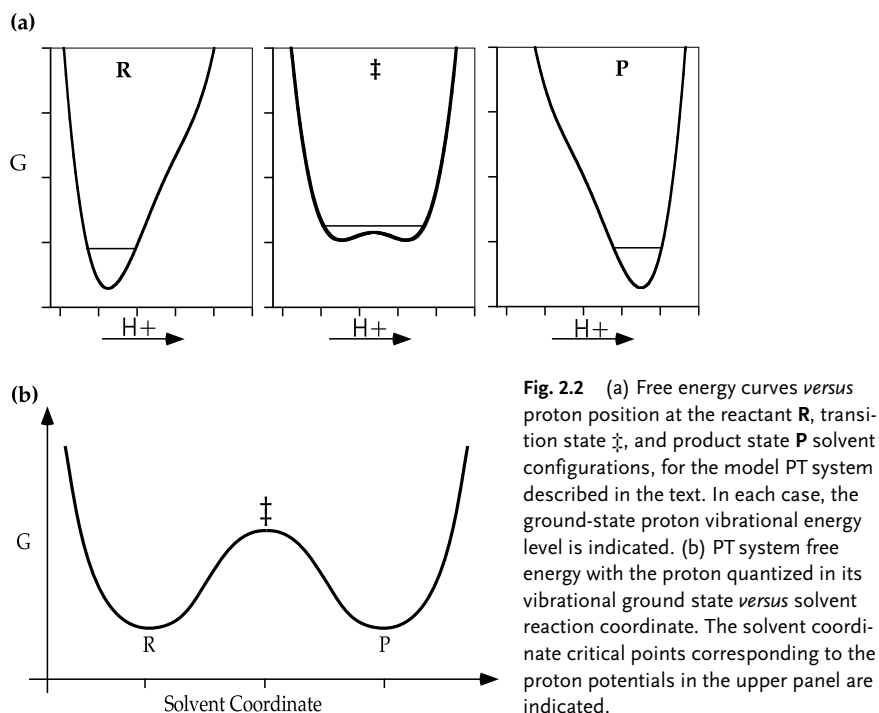


**Fig. 2.2** (a) Free energy curves *versus* proton position at the reactant **R**, transition state **‡**, and product state **P** solvent configurations, for the model PT system described in the text. In each case, the ground-state proton vibrational energy level is indicated. (b) PT system free energy with the proton quantized in its vibrational ground state *versus* solvent reaction coordinate. The solvent coordinate critical points corresponding to the proton potentials in the upper panel are indicated.

These different states of solvation, or more simply the electric polarization state of the solvent, distort the potential from being initially asymmetric favoring localization of the proton on the acid, through an intermediate situation where a proton symmetric double well is established, and on to an asymmetric potential favoring localization of the proton on the base. At this stage, it should already be clear that the solvent motion is critical, due to the strong coupling of the charge transfer in the reacting pair to the polar solvent.

For each of the three proton potentials, the quantized ground vibrational energy, i.e. the zero-point energy, is indicated. For the transition state solvent configuration, the zero-point level is above the proton barrier, the hallmark of what we term the quantum “adiabatic” PT limit. This is to be contrasted with a situation in which the level is below the barrier top, in which case the reaction would involve quantum tunneling.<sup>[10]</sup> It is important to stress that here the proton motion is a bound quantum vibration and that there is no classical barrier crossing of the proton, as in the standard description of conventional TST.<sup>[6]</sup> The physical picture of this adiabatic limit is that as the solvent reorganizes, the high frequency quantum proton vibration adiabatically adjusts. Thus, the reaction coordinate is a solvent coordinate, rather than the proton coordinate, and there is a free energy change up to the transition state activation free energy as the solvent rearranges, as shown in Figure 2.2b. A plot of total free energy *versus* the solvent reaction coordinate can be usefully dissected into two basic contributions, as shown in Figure 2.3. These are a “bare” free

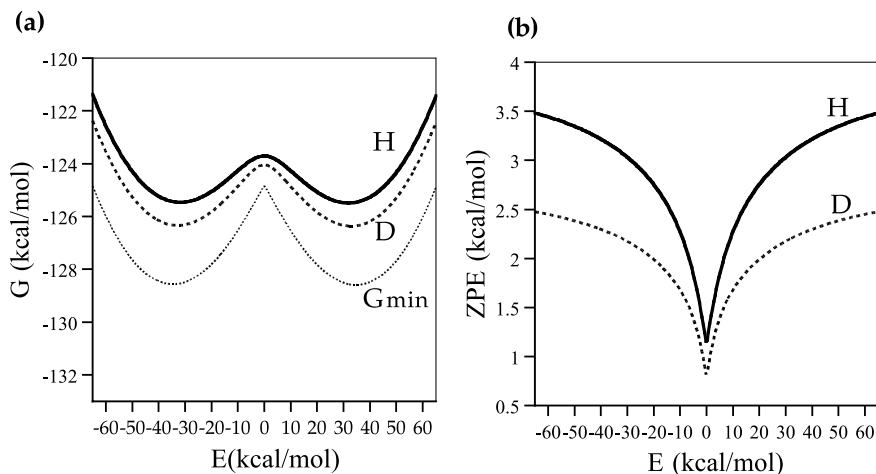


**Fig. 2.3** (a) Free energy curve for the proton (solid line) and deuteron (dashed line) for a symmetric reaction,  $\Delta G_{\text{rxn}} = 0$ . The dotted line shows the free energy curve  $G_{\min}$  excluding

the proton zero-point energy (ZPE). (b) ZPE for the proton and deuteron *versus*  $\Delta E$ . The dotted curve  $G_{\min}$  in (a) plus the ZPEs in (b) give the curves for H and D in (a).

energy,  $G_{\min}$ , which is that corresponding to the situation where the proton is located at its classical minimum position for any given solvent coordinate, and the vibrational zero-point energy (ZPE) of the proton, measured from the latter potential minimum energy. The ZPE decreases as the transition state in the solvent is approached, since the proton potential becomes more symmetrical and the proton is delocalized over a larger potential region. While both contributions to the overall free energy are cusped, due to the shift in the proton's minimum position as the symmetric proton potential situation is traversed, the overall free energy profile is of course continuous. Finally, as a technical point, the solvent coordinate in this figure is taken to be an “alter ego” of the solvent polarization, related to a certain energy gap defined such that, for a thermodynamically symmetrical PT reaction, it has a value of zero at the solvent transition state at which the proton potential is symmetrical.<sup>[4]</sup>

Transition state theory can be applied in relation to the solvent coordinate, and the rate constant for the adiabatic PT reaction is then given by<sup>[4,10,12]</sup>  $k_{\text{TST}} = (\omega_s/2\pi)\exp[-\Delta G^\ddagger/RT]$ , where the pre-exponential factor involves a solvent frequency related to the curvature of the solvent reactant well shown in Figure 2.2b and  $\Delta G^\ddagger$  is the activation free energy evident in the same figure. Several important points can be made here. First, while the quantum proton motion is accounted for, this is a classical TST result in the sense that the TST assumption has been applied to the classical solvent reaction coordinate.<sup>[13]</sup> Second, just as discussed in Section 2.2, barrier recrossing effects may be operative, thereby reducing the value of the TST rate constant. Since transition state passage means changing the solvent polarization, there can be a time-dependent friction related to such polarization changes. A correction for this has already been calculated for a model adiabatic PT in solution and was found<sup>[12]</sup> to be in good agreement with Grote–Hynes theory, although in most

cases such corrections should be minor. Third, while a symmetric reaction has been discussed here, Kiefer and Hynes<sup>[4]</sup> have analytically derived a quadratic free energy relationship between the activation free energy  $\Delta G^\ddagger$  and the thermodynamic reaction free energy  $\Delta G_{\text{rxn}}$  for general PT reaction symmetries, closely related to, but more fundamentally based than the Marcus relationship,<sup>[14]</sup> which, while widely employed, is empirical<sup>[15]</sup> for PT reactions. Finally, we have emphasized above that the free energy contains a proton zero-point energy contribution. As regards the activation free energy  $\Delta G^\ddagger$ , this will contribute the difference of the H and D ZPEs at the solvent transition state and for the reactant, as seen in panels (a) and (b) in Figure 2.3. One should note that this is quite a different picture for kinetic isotope effects than the standard one.<sup>[16]</sup> In the latter view, the proton vibration at a transition state is unstable, i.e. not bound, and contributes no ZPE at all for a symmetric reaction.

## 2.4

### Wave-Packet Evolution for Proton-Transfer Reactions

It is of course now quite common in discussions of reactions of interest to the femtochemistry community to describe nuclear dynamics in terms of wave-packets, as inspection of this volume and its predecessors will quickly confirm. While these descriptions have been largely confined to isolated gas-phase systems, or in some cases to small cluster systems, it is clearly of interest to construct a wave-packet description for chemical reaction dynamics in solution, in which the nuclear degrees of freedom of the reaction system are strongly coupled to the surrounding solvent. The most important examples for such a description would obviously be those where the quantum character of key nuclear motions is critical, and proton-transfer reactions are a natural arena here.

Thompson and Hynes<sup>[3]</sup> have explored this wave-packet aspect in some detail for a model of the acid-base PT reaction between HCl and H<sub>2</sub>O within a hydrogen-bonded complex to produce the contact ion pair involving the chloride and hydronium ions  $\text{Cl}-\text{H} \cdots \text{OH}_2 \rightarrow \text{Cl}^- \cdots \text{HOH}_2^+$  in a low polarity solvent. In contrast to the situation for this reaction in a polar solvent such as H<sub>2</sub>O,<sup>[11]</sup> where the reaction is fairly strongly downhill in terms of reaction free energy, the low polarity solvent reaction can be nearly thermoneutral in free energy terms, so that both reactants and products might, in principle, be conveniently observed.

Details of the system modelling are given in ref. [3] Briefly, the reacting pair solute subsystem is defined by a two-electron coupled valence bond electronic state description, consistent with the non-conventional Mulliken charge-transfer picture of PT,<sup>[10,17,18]</sup> and the solvent is characterized as a non-equilibrium dielectric continuum. Together, these provide a non-equilibrium free energy surface  $G(r_{\text{HCl}}, R_{\text{ClO}}, z)$  as a function of the proton coordinate, the hydrogen (H-) bond coordinate, and a collective solvent coordinate, respectively. As in Section 2.3, the latter coordinate ( $z$ ) characterizes the state of the orientational polarization of the solvent (in a fashion different from, but ultimately related to the  $\Delta E$  variable mentioned there). This free

energy surface thus provides the effective potential energy for the two-dimensional nuclear Schrödinger equation for the proton and H-bond coordinates, which is then solved by constructing the Hamiltonian matrix in a sinc-function discrete variable representation basis<sup>[19]</sup> and standard “black-box” diagonalization routines to produce the quantum (free) energy eigenvalues and eigenvectors, under the adiabatic assumption that these two quantum degrees of freedom are fast compared to the most important solvent motion.

Among the results of these calculations are the following. First, Figure 2.4 depicts the evolving double-well potential in the proton coordinate along key points of the solvent reaction coordinate, much as was discussed in Section 2.3, and, further, shows the evolving proton wavefunction. At the transition state in the solvent coordinate, it is seen that, with the zero-point vibrational level of the proton just above the local maximum in the proton potential (so that the reaction is an adiabatic PT), the proton wavefunction is fairly delocalized, in contrast to its prior and post localization at solvent coordinate values along the reaction path, corresponding to the reactants and the products, respectively.

Figure 2.5 displays the calculated free energy curves *versus* the solvent reaction coordinate, both for the zero-point vibrational level for both the proton and H-bond coordinates, as well as for the first vibrationally excited state, which corresponds to the ground state of the proton vibration and the singly-excited H-bond vibration. It can be seen that the barrier at the transition state for the PT is in fact slightly higher when the H-bond vibration is excited, a perhaps initially surprising feature previously seen and explained by Staib et al. for a different PT system.<sup>[12]</sup> Also shown is the bare free energy curve, which, as in Section 2.3, corresponds to a classical treatment of both coordinates in the reacting subsystem, so that the differences between this and the other two displayed curves give an indication of the evolving quantized vibrational energy along the solvent reaction coordinate.

Next, Figure 2.6 shows, at the three key points in the solvent coordinate along the reaction path, a two-dimensional contour plot of the evolving free energy surface in

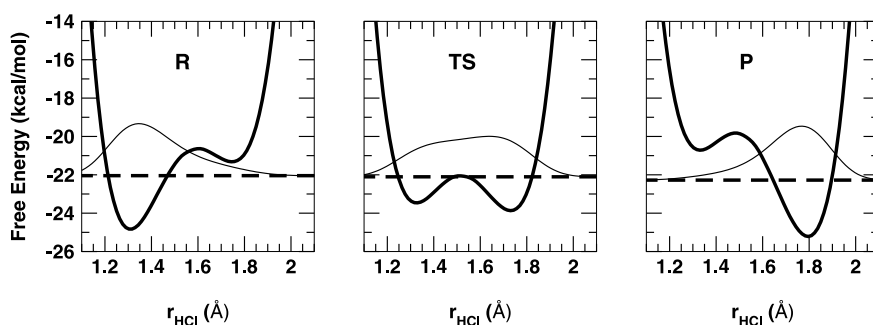


**Fig. 2.4** One-dimensional proton potentials (thick solid lines) for the  $\text{CLH}\cdots\text{OH}_2$  complex are shown as a function of  $r_{\text{HCl}}$  with the ground-state vibrational energy levels (dashed lines) and vibrational wavefunctions (thin solid lines)

at three solvent coordinate values corresponding to the reactants, transition state, and products, from left to right. The solvent is characterized by  $\epsilon = 2$  and  $\epsilon = 13$ .

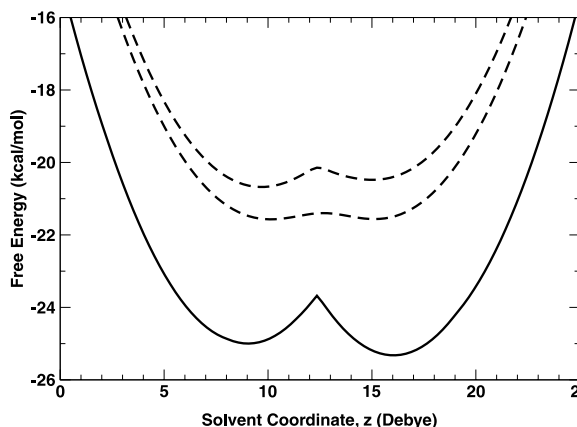


**Fig. 2.5** Vibrationally adiabatic free energy surfaces as a function of the solvent coordinate,  $z$ , for  $\text{ClH}\cdots\text{OH}_2$  in a low polarity solvent. The bare free energy surface (solid line) and ground (dashed line) and first-excited (dot-dashed line) vibrationally adiabatic surfaces are shown.

the selected coordinates (which diagonalize the kinetic energy). Also shown are “snapshots” of the two-dimensional wavefunctions in the proton and H-bond coordinates, first in the middle panel for the ground vibrational state in both coordinates and second, in the top panel, with a vibrational quantum in the H-bond vibration. Of the several interesting features of these wave-packet plots, we highlight just a few. For the ground-state reaction, the middle panel of Figure 2.6 indicates a compression of the wave-packet in the H-bond coordinate direction on going to the transition state, while at the same time the packet is elongated in the proton coordinate direction, reflecting the delocalization noted above. Overall, the progressive “tilting”

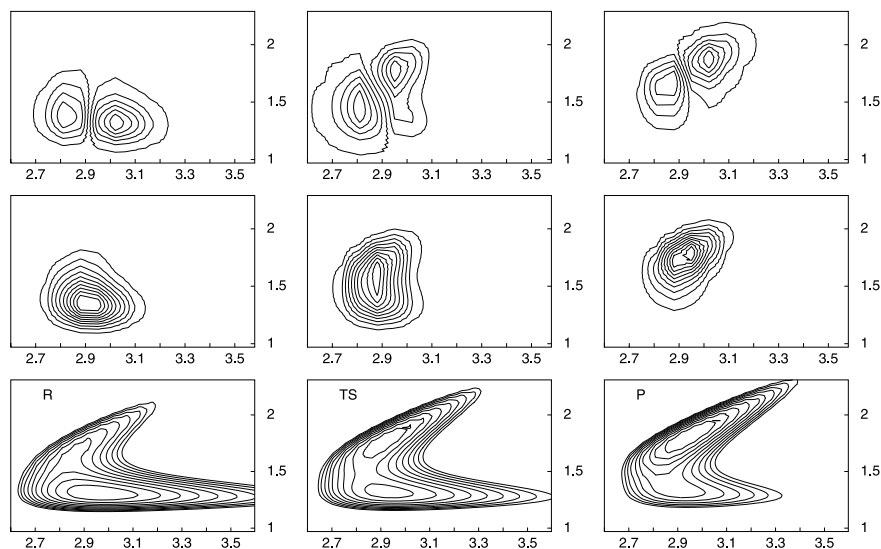


**Fig. 2.6** Contour plots of the two degrees of freedom free energy surface (lowest panels; contour increments 1 kcal/mol) and ground (middle panels) and first excited state (top panels) vibrational wavefunctions for the

reactants (left), transition state (center), products (right) for  $\text{ClH}\cdots\text{OH}_2$  in a low polarity solvent. The abscissa is  $R_{\text{ClO}}$  in Å and the ordinate is  $r_{\text{HCl}}$  in Å.

of the wave-packet reflects the underlying topology of the displayed free energy contours. For the excited-state reaction, the excitation in the H-bond vibration is retained adiabatically as the reaction proceeds, as reflected in the maintenance of the single nodal pattern along the solvent reaction coordinate.

Finally, we make two comments of direct relevance to femtochemistry studies. First, while not discussed here, corresponding results for further vibrationally excited states, including those involving a single excitation in the proton vibration,<sup>[3]</sup> lend general support to an earlier picture of the dynamics of infrared-induced proton transfer in such acid-base systems<sup>[20]</sup> and this is being vigorously pursued.<sup>[21]</sup> This is of particular interest in the transition state context, since it has been suggested<sup>[20]</sup> that the ground proton vibrational state transition state might be experimentally probed in this way. Second, PT reactions related to those described in Sections 2.3 and 2.4, but occurring in the excited electronic state, can be studied by means of femtochemistry techniques. In our opinion, such excited-state PT reactions will involve the *same* aspects as discussed herein, but with additional features related to the differing electronic structures involved, an issue now under investigation.<sup>[22]</sup>

## Acknowledgement

This work was supported in part by the National Science Foundation through grants CHE-9700419 and CHE-9709195.

## References

- 1 (a) J. P. Bergsma, B. J. Gertner, K. R. Wilson, J. T. Hynes, *J. Chem. Phys.* **1987**, 86, 1356; B. J. Gertner, J. P. Bergsma, K. R. Wilson, J. T. Hynes, *J. Chem. Phys.* **1987**, 86, 1377; B. J. Gertner, K. R. Wilson, J. T. Hynes, *J. Chem. Phys.* **1989**, 90, 3537; (b) B. J. Gertner, R. M. Whitnell, K. R. Wilson, J. T. Hynes, *J. Am. Chem. Soc.* **1991**, 113, 74.
- 2 (a) H. J. Kim, J. T. Hynes, *J. Photochem. Photobiol. A: Chem.* **1997**, 105, 337; (b) T. Fonseca, H. J. Kim, J. T. Hynes, *J. Mol. Liq.* **1994**, 60, 161.
- 3 W. H. Thompson, J. T. Hynes, *J. Phys. Chem. A*, **2001**, 105, 2582.
- 4 P. M. Kiefer, J. T. Hynes, submitted.
- 5 E. Wigner, *Trans. Faraday Soc.* **1938**, 34, 29; see also H. S. Johnston, *Gas Phase Reaction Rate Theory*, Ronald Press Co., New York, 1966.
- 6 See, e.g., (a) P. Pechukas, in *Dynamics of Molecular Collisions, Part B* (Ed.: W. H. Miller), Plenum Press, New York, 1976; (b) D. G. Truhlar, B. C. Garrett, J. T. Hynes, *J. Phys. Chem.* **1983**, 87, 2664; (c) J. T. Hynes, in *Solvent Effects and Chemical Reactivity* (Eds.: O. Tapia, J. Bertran), Kluwer, Amsterdam, 1996, pp. 231–258; (d) D. G. Truhlar, B. C. Garrett, S. J. Klippenstein, *J. Phys. Chem.* **1996**, 100, 12771.
- 7 H. A. Kramers, *Physica* **1940**, 7, 284.
- 8 R. F. Grote, J. T. Hynes, *J. Chem. Phys.* **1980**, 73, 2715.
- 9 P. Changenet, P. Plaza, M. M. Martin, Y. H. Meyer, *J. Phys. Chem. A* **1997**, 101, 8186.
- 10 K. Ando, J. T. Hynes, *Adv. Chem. Phys.* **1999**, 110, 381–430.
- 11 K. Ando, J. T. Hynes, *J. Phys. Chem. A* **1999**, 103, 10398; *J. Phys. Chem. B* **1997**, 101, 10464; *J. Mol. Liq.* **1995**, 64, 25; B. J. Gertner, J. T. Hynes, *Faraday Disc.* **1998**, 110, 301; *Science* **1996**, 271, 1563.
- 12 A. Staib, D. Borgis, J. T. Hynes, *J. Chem. Phys.* **1995**, 102, 2487–2505.

- 13 Other approaches<sup>[6d]</sup> may also be considered.
- 14 R. A. Marcus, *Faraday Symp. Chem. Soc.* **1975**, 10, 60; *J. Phys. Chem.* **1968**, 72, 891; *J. Am. Chem. Soc.* **1969**, 91, 7224; A. O. Cohen, R. A. Marcus, *J. Phys. Chem.* **1968**, 72, 4249.
- 15 N. Agmon, *Int. J. Chem. Kin.* **1981**, 13, 333.
- 16 F. H. Westheimer, *Chem. Rev.* **1961**, 61, 265; L. Melander, W. H. Saunders, *Reaction Rates of Isotopic Molecules*, Wiley, New York, 1980.
- 17 R. S. Mulliken, *J. Phys. Chem.* **1952**, 56, 801; *J. Chim. Phys.* **1964**, 61, 20; R. S. Mulliken, W. B. Person, *Molecular Complexes*, Wiley-Interscience, New York, 1969.
- 18 J. Timoneda, J. T. Hynes, *J. Phys. Chem.* **1991**, 95, 10431.
- 19 D. T. Colbert, W. H. Miller, *J. Chem. Phys.* **1992**, 96, 1982.
- 20 H. J. Kim, A. Staib, J. T. Hynes, in *Ultrafast Reaction Dynamics at Atomic-Scale Resolution – Femtochemistry and Femtobiology*, Nobel Symposium 101 (Ed. V. Sundstrom), Imperial College Press, London, **1998**, pp. 510–527.
- 21 D. Laage, W. H. Thompson, J. T. Hynes, work in progress.
- 22 G. Granucci, J. T. Hynes, Ph. Millié, T.-H. Tran-Thi, *J. Am. Chem. Soc.*, **2000**, 122, 12235.



### 3

## Organic Femtochemistry: Diradicals, Theory and Experiments

*Steven De Feyter, Eric W.-G. Diau, and Ahmed H. Zewail*

### 3.1

#### Introduction

Diradicals play a major role as intermediates in numerous thermally-activated and photochemical reactions. Their study has been at the forefront of research in physical organic chemistry as they are central to the understanding of bonding, reaction mechanisms, and stereochemistry.<sup>[1]</sup> Typically, the involvement or otherwise of diradicals in a mechanism is inferred from the stereochemistry of the reaction, its kinetics, and the effect of different precursors. The time scale or “clock” for rates is internal, namely the rotation of a single bond, and from the retention or inversion of stereochemistry the mechanism can be deduced.<sup>[2,3]</sup> Theoretical approaches involve the analysis of the energetics and semiempirical or *ab initio* calculations of the potential energy surfaces (PESs) and of the molecular dynamics.

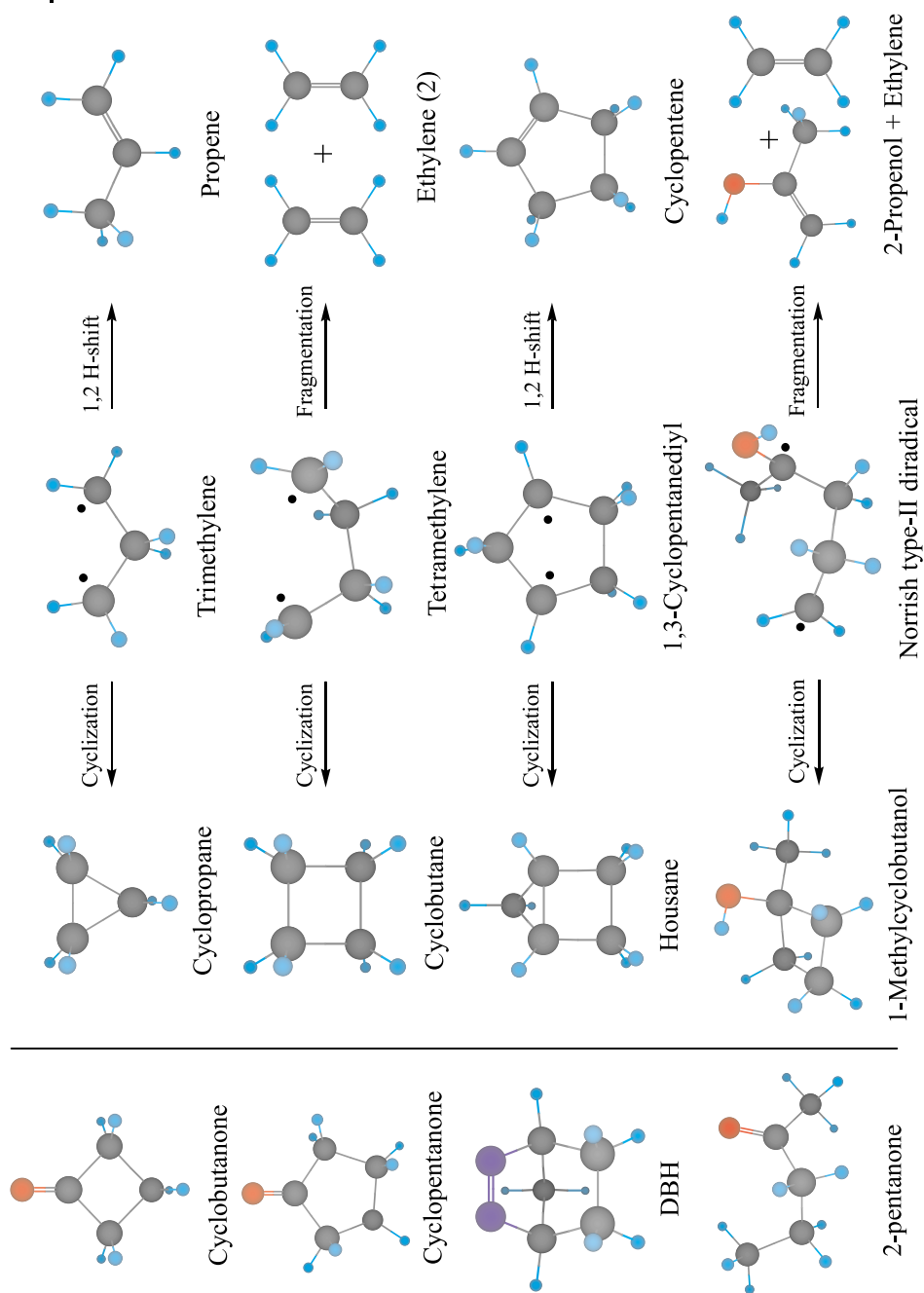
With femtosecond (fs) time resolution it is now possible to study the dynamics of these intermediates. Using fs-resolved mass spectrometry in a molecular beam, the dynamics of these diradical intermediates, produced by various precursor routes, have been studied (Scheme 3.1). The focus is on diradicals produced by Norrish-type reactions.

In the first part of this contribution, the dynamics of trimethylene and tetramethylene, as well as of the structurally-constrained (by a bridge) tetramethylene, are discussed in detail; the latter is formed by N<sub>2</sub> extrusion. In the second part, the Norrish type-II reaction and the dynamics of the diradical intermediates are discussed in detail. These comparative studies elucidate the role of transition states, entropic configurations, and intramolecular vibrational-energy redistribution (IVR) on the global potential energy surface.

### 3.2

#### Experimental

The fs laser and molecular beam apparatus have been described in detail elsewhere. [4] Briefly, the output of a colliding-pulse, mode-locked oscillator (CPM) was amplified in a four-stage dye amplifier, pumped by an Nd:YAG laser. The output,



Scheme 3.1 Molecular structures of precursors, diradical intermediates, and products.

after recompression by a four-prism pair, was typically an 80 fs wide (Gaussian) pulse with an intensity of  $\sim 150 \mu\text{J}/\text{pulse}$  at 615 nm. The pulse was split to provide the pump and probe beams. For the pump, the 615 nm output was frequency doubled. The probe beam was passed to a computer-controlled translation stage for the time delay. The zero time was measured *in situ*.<sup>[4,5]</sup>

The two beams were spatially combined and were focussed onto the supersonic molecular beam associated with the time-of-flight mass spectrometer. Both the pump and probe beams were appropriately attenuated to minimize background signals. By gating the signal due to a particular ion, the temporal evolution of each species could be measured. For the systems discussed, the dependence of the ion current on the pump intensity confirmed that the pump process involved the absorption of two photons (186 kcal/mol).

### 3.3

#### Tetramethylene, Trimethylene, and the Constrained Diradical<sup>[6]</sup>

The reaction of cyclic carbonyls is well-known to proceed through a Norrish-type  $\alpha$ -cleavage, which in this case leads to C–C bond breakage and decarbonylation. The PES involves a reaction coordinate along the C–C bonds adjacent to the CO. The reaction path is a clear decarbonylation with the formation of a diradical species (Scheme 3.1). The tetramethylene diradical can form cyclobutane (by closure) or two ethylene molecules by fragmentation. The closure of trimethylene leads to cyclopropane, whereas a 1, 2-shift forms propene.

The constrained tetramethylene diradical, on the other hand, was formed by photochemical activation of a bridged diazene, e.g., 2,3-diazobicyclo[2.2.1]hept-2-ene (DBH). After nitrogen extrusion, the 1,3-cyclopentanedyl diradical (constrained diradical) was formed. These diradicals are unique in that the additional  $\text{CH}_2$  bridge across the tetramethylene unit restricts the many degrees of freedom involved in the reaction dynamics. Cyclization of the constrained diradical leads to housane, while a 1,2-hydrogen shift leads to cyclopentene.

#### 3.3.1

##### Theoretical: PES and Reaction Pathways

Figure 3.1 depicts the reaction pathways of tetramethylene obtained by using the spin-unrestricted DFT method at the B3LYP/6–31G(d) level (see ref.<sup>[7]</sup> and references therein). The PES is rather “flat”, as was also shown by recent high-level *ab initio* calculations.<sup>[8,9]</sup> The energy difference between the stationary points was found to vary slightly depending on the level of theory, but did not exceed a few kcal/mol (*vide infra*).

Calculations of the PES (Figure 3.2) of the ground-state reaction pathways of the constrained diradical of DBH were also performed at the B3LYP/6–31G(d) level. The energetics for the constrained diradical are shown for three product channels. The barrier for ring closure (housane formation) is very small ( $\sim 3$  kcal/mol), while that

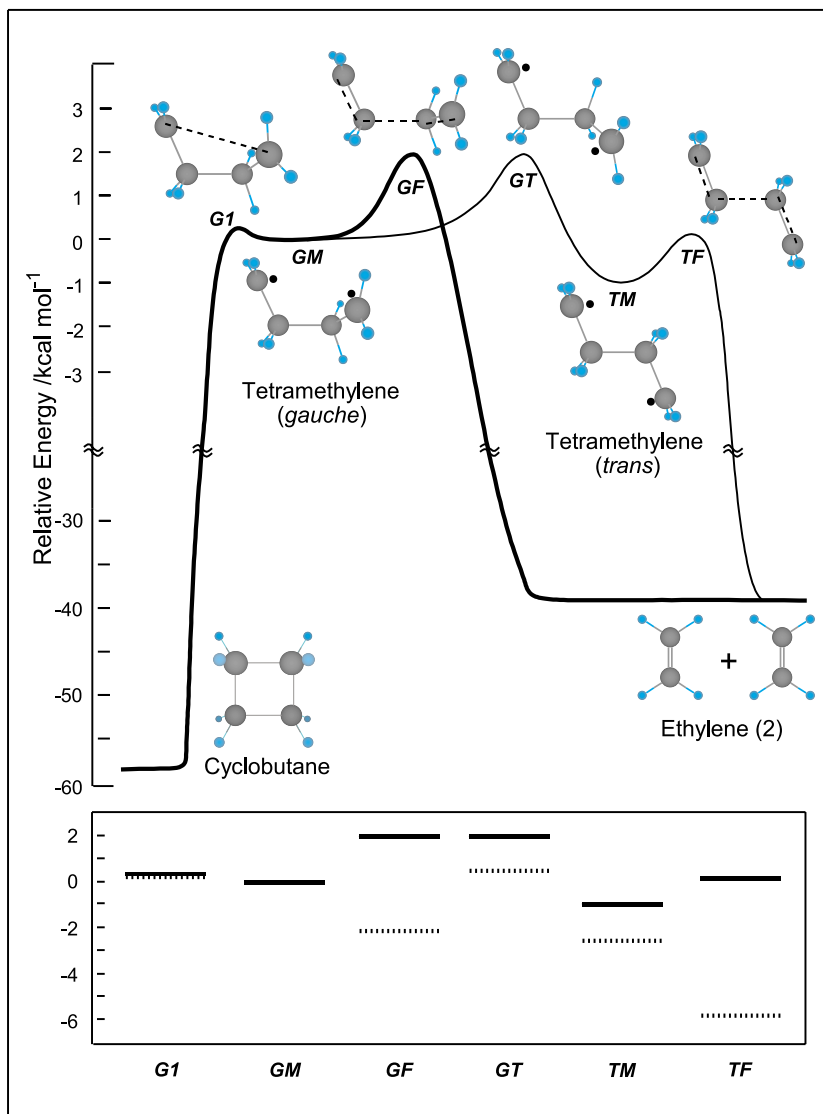


**Fig. 3.1** Ground-state reaction pathways of tetramethylene. The theoretical calculations were performed using DFT at the B3LYP/6-31G(d) level. The following stationary points were calculated: (GM) the *gauche* minimum; (TM) the *trans* minimum; (G1) the transition state from GM to cyclobutane; (GF) the transition state from GM to fragmentation; (TF) the transition state from TM to fragmentation; and (GT) the transition state for *gauche* to *trans* interconversion.

The reaction pathway involving the *gauche* minimum is shown as a heavy bold curve. In the lower panel, the energies of the stationary points relative to the *gauche* minimum are compared: the solid bars represent our DFT values, while the dotted bars correspond to the high-level *ab initio* calculations of Moriarty et al.;<sup>[9]</sup> the geometry was optimized at the CASSCF(4,4)/6-31G(d) level and the energy was calculated at the CASPT2(8,8)/ANO-2 level.

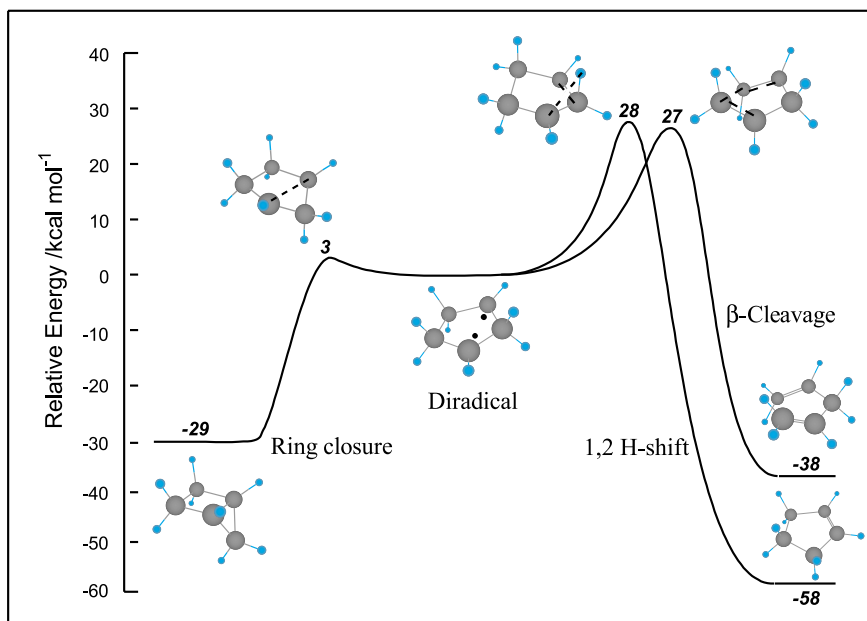


**Fig. 3.2** Ground-state PES of the constrained 1,3-cyclopentenediyl diradical obtained at the B3LYP/6-31G(d) level of theory. Three reaction paths are characterized: ring closure (housane

formation), 1,2 H-shift (cyclopentene formation), and  $\beta$ -cleavage (1,4-pentadiene formation).

for cyclopentene formation through a 1,2-hydrogen shift is  $\sim 28$  kcal/mol. The barrier for 1,4-pentadiene formation through  $\beta$ -cleavage of the  $\sigma$ -bond and formation of two  $\pi$ -bonds is  $\sim 27$  kcal/mol.

### 3.3.2

#### Tetramethylene: Dynamical Time Scales and Stereochemistry

The mass spectrum and the transients are presented in Figures 3.3A and 3.4A, respectively. The 84 amu species decays in  $120 \pm 20$  fs, while the 56 amu species, the tetramethylene diradical, builds up in  $150 \pm 30$  fs and decays with a lifetime of  $700 \pm 60$  fs. The total decay rate of the diradical is the sum of the rates for cyclization and fragmentation (Figure 3.1); the *gauche*-to-*trans* isomerization channel is not included because the decay is that of the total population. Dervan and his group have provided evidence for the existence of common 1, 4-diradicals from careful studies of the stereochemistry.<sup>[2,3]</sup> They gave the relative rates of rotation (terminal), cleavage, and closure at 712 K for tetramethylene- $d_2$  (generated from a diazene precursor) as  $k_{\text{rot}}:k_{\text{frag}}:k_{\text{cyc}} = 12 \pm 3:2.2 \pm 0.2:1.0$ .

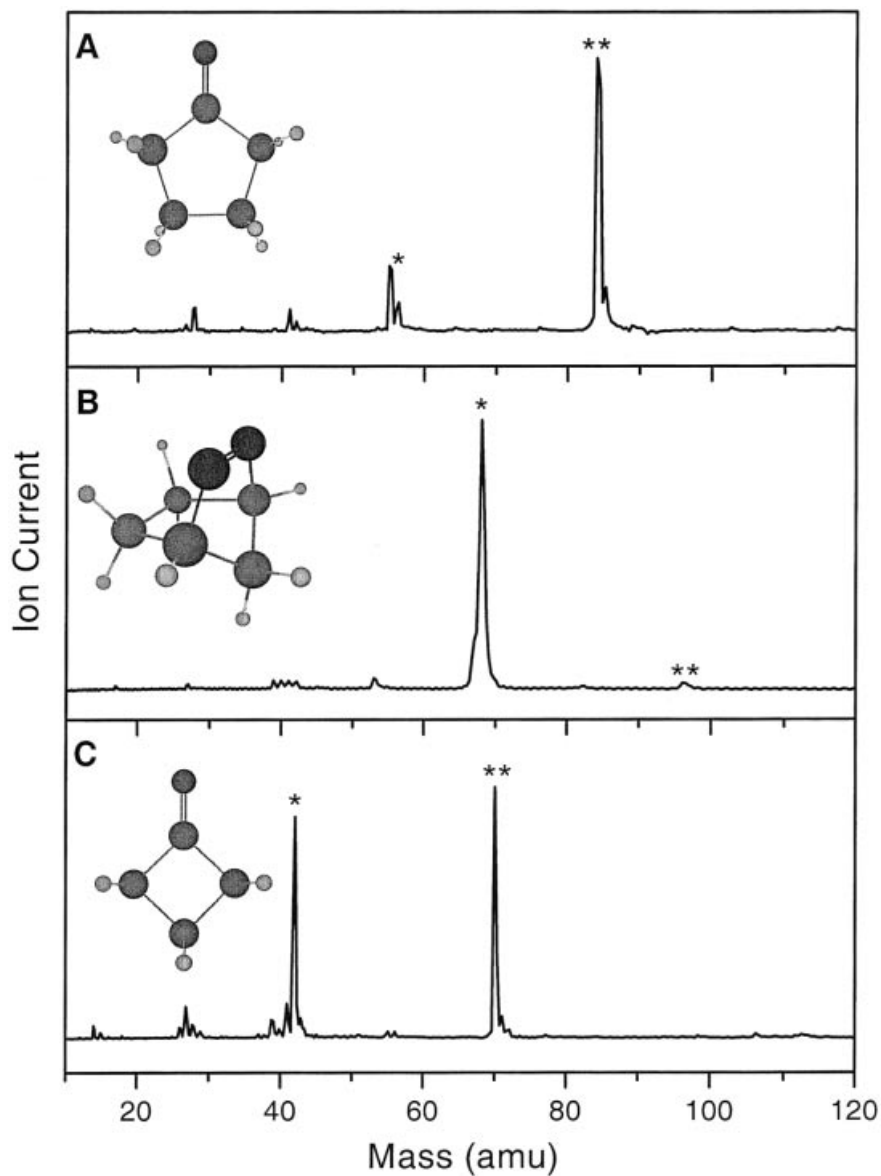


**Fig. 3.3** Mass spectra obtained with fs pulses: the parent peak (\*\*) and the diradical peak (\*) are marked: (A) cyclopentanone (tetramethylene); (B) 2,3-diazobicyclo[2.2.1] hept-2-ene

(DBH) (constrained diradical); (C) cyclobutanone (trimethylene). The molecular structures of the precursors are displayed on the left.

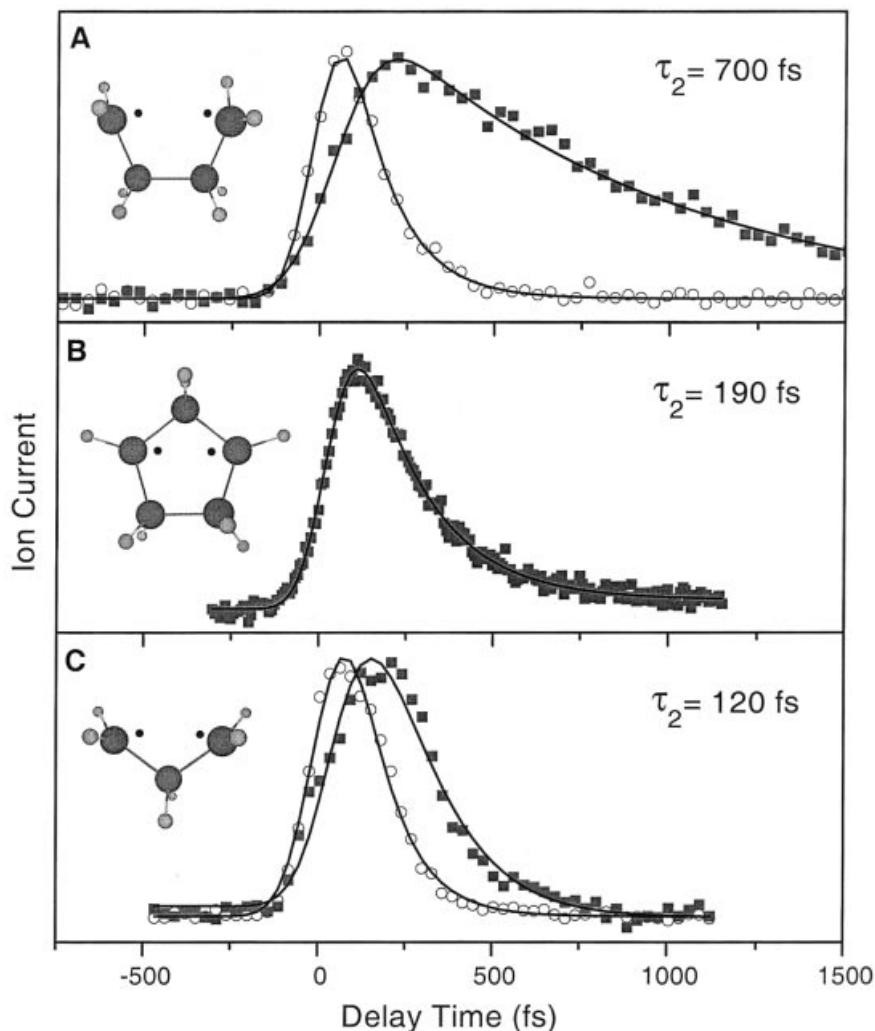


**Fig. 3.4** Femtosecond transients of the parent (○) and the diradicals (■): (A) tetramethylene; (B) constrained diradical; (C) trimethylene.  $\tau_2$  is the decay time of the diradical. The molecular structures of the radicals are shown on the left.

At our total energy, if these ratios are similar, then we can obtain the individual rates:  $k_{\text{cyc}} = 0.45 \text{ ps}^{-1}$  (2.2 ps),  $k_{\text{frag}} = 0.99 \text{ ps}^{-1}$  (1 ps), and  $k_{\text{rot}} = 5.4 \text{ ps}^{-1}$  (185 fs).

The rotational time  $\tau_{\text{rot}}$  of ~200 fs is significant for two reasons. First, its fs duration makes it a cleverly-used clock for obtaining the ratios of rate constants, as discussed below. Second, it allows a comparison with the Arrhenius-type estimate, widely used in stereochemical studies. Using our DFT calculation of the average vibrational frequencies of the two internal rotations of the terminal C–C bonds ( $150 \text{ cm}^{-1}$ ) for the pre-exponential factor, and a barrier of 0.4 kcal/mol, estimated on the

basis of experimental and *ab initio* calculations,<sup>[10,11,12]</sup> we obtain a  $k_{\text{rot}}$  of  $4.6 \text{ ps}^{-1}$  or  $\tau_{\text{rot}} = 220 \text{ fs}$ . The values of the lifetime for ring closure, fragmentation, and rotation indicate that, on average, the terminal  $\text{CH}_2$  groups rotate during the fragmentation and closure processes. Such time scales are crucial in determining the stereochemistry of the two processes.

The issue of concertedness is fundamental in mechanistic organic chemistry. It is usually defined with an operational criterion. For example, the reaction is said to be concerted if it takes place in a single kinetic step. Only the direct detection of the intermediate can answer the question as to whether a reaction follows a concerted or stepwise path. As pointed out elsewhere,<sup>[13,14]</sup> the correct criterion must address the nuclear motions in relation to the time scale of the reaction coordinate.

In numerous studies, the rotational motion of the entire molecule is invoked as a clock, and this rotation, which has a duration of a few ps, makes the reaction appear “concerted”. In stereochemical studies, physical organic chemists use internal rotations of a single bond. As discussed above, this is reasonable given the fs time scale, and so the retention or inversion of stereochemistry can be calibrated. If rotation requires a longer time, there will be a problem in deducing the mechanism of the nuclear motions.

### 3.3.3

#### The Constrained Diradical and Trimethylene

Figure 3.3B shows the mass spectrum obtained for DBH, which is dominated by the 68 amu, 1,3-cyclopentadienyl (constrained) diradical. Housane (its cyclization product), cyclopentene, and 1,4-pentadiene all have this mass, but they represent the final products. The very small peak at 96 amu fits the signal of the parent and/or the diazenyl diradical. Figure 3.4B displays the 68 amu transient, which can be fitted to a rise ( $30 \pm 10 \text{ fs}$ ) and a decay ( $190 \pm 10 \text{ fs}$ ). The signal at 96 amu was too weak to measure. The mass spectrum of trimethylene is presented in Figure 3.3C and the transients are shown in Figure 3.4C. The 70 amu signal of cyclobutanone gives a decay time of  $105 \pm 10 \text{ fs}$ . Trimethylene (42 amu) shows a transient behavior with a similar rise and decay time of  $120 \pm 20 \text{ fs}$ .

### 3.3.4

#### PES, IVR, and Entropy Effects

Direct comparison of the cyclization dynamics, the common reaction path, is only justified when the lifetimes are determined by the process, i.e., cyclization is the only or major reaction channel of the diradicals. However, for all the radicals under investigation, other reaction pathways leading to other products compete with cyclization (see Scheme 3.1). From our decay rates and the reported experimental and calculated branching ratios,<sup>[3,15,16,17]</sup> we were able to obtain the specific rate constants for cyclization:  $(240 \text{ fs})^{-1}$  for trimethylene,  $(2.2 \text{ ps})^{-1}$  for tetramethylene, and  $(330 \text{ fs})^{-1}$  for the constrained diradical; longer times are obtained for tetramethylene if the Rice–Ramsperger–Kassel–Marcus (RRKM) branching ratios are used



instead.<sup>[16]</sup> The cyclizations of trimethylene and of the constrained diradical are clearly faster than that of tetramethylene.

The PES of tetramethylene (Figure 3.1) can be seen to be flat within a few kcal/mol: the ring closure as well as the fragmentation products can be reached along paths of monotonically decreasing energy. The PES of the constrained diradical (Figure 3.2) and trimethylene<sup>[15]</sup> are similarly flat, as far as the cyclization reaction is concerned. Accordingly, the internal energy should not a priori be the dominant force in the reaction (barrierless) dynamics and IVR and entropy effects become very significant (*vide infra*). Even for barrier reactions, statistical RRKM calculations show that the rates reach a plateau and the effect of internal energy at high energies becomes less significant.<sup>[18]</sup>

Entropy and IVR effects are governed by the nature of the reaction trajectories on the (nuclear) multi-dimensional PES. Consider first the case of tetramethylene adopting a whole range of conformations without an energy minimum on the PES, the so-called “twistyl” state.<sup>[19]</sup> This situation is expected to force the molecule to spend a “long” time exploring the surface. Although this reaction-path picture is helpful, it was shown that the lengthening of time is still on the fs time scale.<sup>[20]</sup> It is mandatory to consider the landscape of the PES. The transient configurations represent an entropic trapping of the system since in these configurations the energy in, e.g.,  $A\bullet\bullet B\bullet\bullet A^\ddagger$  could be trapped in the “ $A\bullet\bullet B$  part” (very long time) but exceeds dissociation in the “ $B\bullet\bullet A$  part”; three atoms are used to illustrate two contiguous bonds. At such coordinates there are no stable vibrational modes as the system only increases the number of possible new configurations (increased entropy) for trajectories to visit. In other words, such dynamical motion is distinct from IVR between well-defined vibrational states. Experimentally, such behavior was evident in the temporal and kinetic-energy distributions.<sup>[21,22]</sup>

Moriarty et al.<sup>[9]</sup> have shown by high-level *ab initio* calculations that the PES is indeed flat to within  $0.5 \text{ kcal mol}^{-1}$ , contrary to previous theoretical calculations that yielded values of  $3\text{--}5 \text{ kcal mol}^{-1}$  (see citations in ref.<sup>[20]</sup>). They proposed the entropy effect on a microcanonical level; in ref.<sup>[20]</sup> “entropic locking” was considered on a canonical level and using the MCSCF/CI PES. From studies of lifetime change with energy<sup>[20]</sup> and using statistical theories, the depth of the well was estimated to be a few kcal/mol. However, in view of the non-statistical behavior reported recently<sup>[18]</sup> and the recent MD study of elementary systems,<sup>[21,22]</sup> the important role of entropic trapping, or what we will call the existence of “transient configurations”, must be an integral part of the description. For a barrierless PES, the dependence of rates on energy is not significant unless one considers such effects.

The phase space associated with cyclization is more limited than that for fragmentation; fragmentation may occur at any dihedral angle, while ring closure is only successful at certain angles. The *probability* of the intermediate having a favorable conformation for ring closure is likely to be smaller than that for fragmentation, resulting in a longer lifetime for ring closure. Although the nuclear rearrangement (bent) upon cyclization of the constrained diradical is substantial – the constrained diradical is almost planar whereas housane exists in a highly bent conformation – the geometry for cyclization is much more favorable in the constrained diradical.

This accounts for the shorter lifetime ( $\sim 330$  fs) than that for tetramethylene ( $\sim 2.2$  ps), which can rotate almost freely.

Both trimethylene and tetramethylene show almost free rotation of their termini and on this basis a similar time scale for cyclization might be predicted. However, trimethylene terminal motion is the only critical rotation for cyclization, while in tetramethylene there are many more motions, including rotation of the central C–C. This accounts for the order-of-magnitude difference in the cyclization times for trimethylene (240 fs) and tetramethylene (2.2 ps) and the closeness of the values for trimethylene and the constrained diradical (330 fs). Of course, upon cyclization of the constrained diradical, the p-orbitals containing the unpaired electrons need to rotate through a considerable angle in order to form the  $\sigma$  bond and bend motions are involved. For fragmentation, IVR is important. To form tetramethylene, energy has to flow into the reaction coordinate for fragmentation, which in this system occurs on the 1 ps time scale. Thus, IVR to the central bond must occur within 1 ps, which is consistent with the results in ref.<sup>[18]</sup>

Substitution of the terminal hydrogen atoms with methyl groups substantially increases the total lifetime, i.e. 1.8 ps for 1,1,4,4-tetramethyl-tetramethylene vs. 700 fs for tetramethylene. The presence of methyl groups normally increases the lifetime, or decreases the rate, a commonly-encountered observation in the literature. Three effects play a role, but all act in the same direction: (i) the rotation rate is slowed due to the mass effect (the *probability* of finding the intermediate in a favorable conformation for reaction becomes smaller); (ii) the energy barrier for ring closure may increase due to steric hindrance, and (iii) IVR for fragmentation may slow down due to the increased number of “bath modes”. These effects are more pronounced for methyl-substituted tetramethylene than for the deuterated species (total lifetime 1.15 ps), in agreement with the observed trend in the decay times.

### 3.4

#### Diradicals as Intermediates in Norrish Type-II Reactions<sup>[24]</sup>

In the previous section, the fs dynamics of Norrish type-I reactions<sup>[25]</sup> generating diradicals were discussed.<sup>[6,20]</sup> The fs dynamics of acyclic ketones have been discussed elsewhere.<sup>[13,26,27]</sup> In these reactions,  $\alpha$ -cleavage is the pathway leading to product formation. In contrast, in Norrish type-II reactions,<sup>[28]</sup> carbonyl compounds containing  $\gamma$  C–H bonds undergo a 1,5-hydrogen shift upon electronic excitation and yield new products through cleavage and cyclization processes. Figure 3.5 lists the molecular structures of the systems studied here; three have  $\gamma$  C–H bonds and one does not, the latter being used for calibration purposes.

The literature is rich with detailed studies in the solution and gas phases, with primary focus on the photochemistry of the first excited  $S_1$  state.<sup>[28,29]</sup> As noted in these studies, the Norrish type-II reaction is deduced, from yield and quenching experiments, to proceed on the nanosecond time scale and competes with vibrational relaxation and intersystem crossing; there is a barrier for excited singlet reactions of  $\sim 4$  kcal mol<sup>–1</sup>. The studies reported here were performed at higher energy

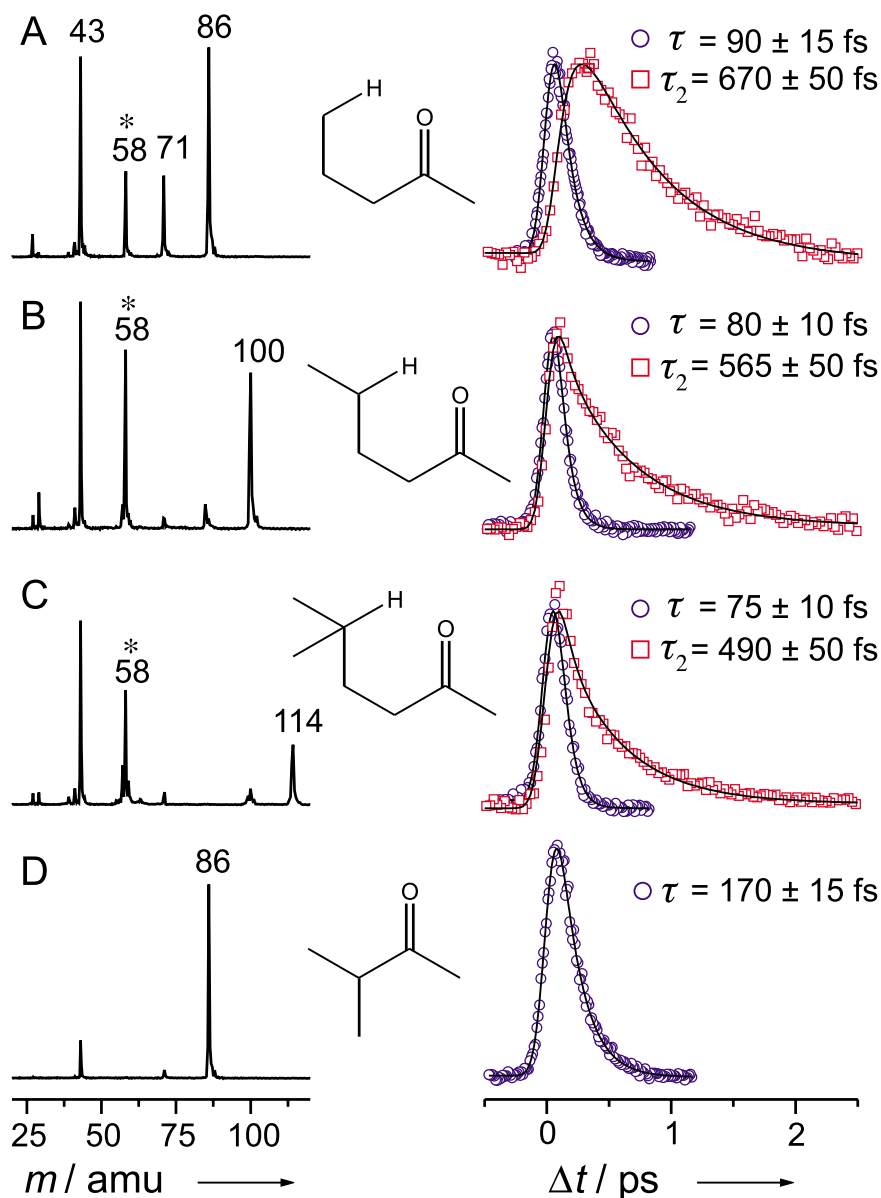


**Fig. 3.5** Femtosecond mass spectra (on the left) and transients (on the right): parent (○) and 58 amu intermediate (□) of (A) 2-pentanone, (B) 2-hexanone, and (C) 5-methyl-2-hexanone; (D) is 3-methyl-2-butanone.

The theoretical fits are represented as solid curves with the fitted time constant  $\tau$  representing the decay time of the parent and  $\tau_2$  being the decay time of the 58 amu species. The other mass peaks stem from the  $\alpha$ -cleavage of C–C bonds.

(see Figure 3.6) and were designed to address the primary ultrafast dynamics without complications from much slower relaxation processes.

Figure 3.5 displays the fs mass spectra and transients of (A) 2-pentanone, (B) 2-hexanone, (C) 5-methyl-2-hexanone, and (D) 3-methyl-2-butanone. The mass spectra of these molecules are characterized by their parent ion mass peaks at  $m/z = 86$ ,

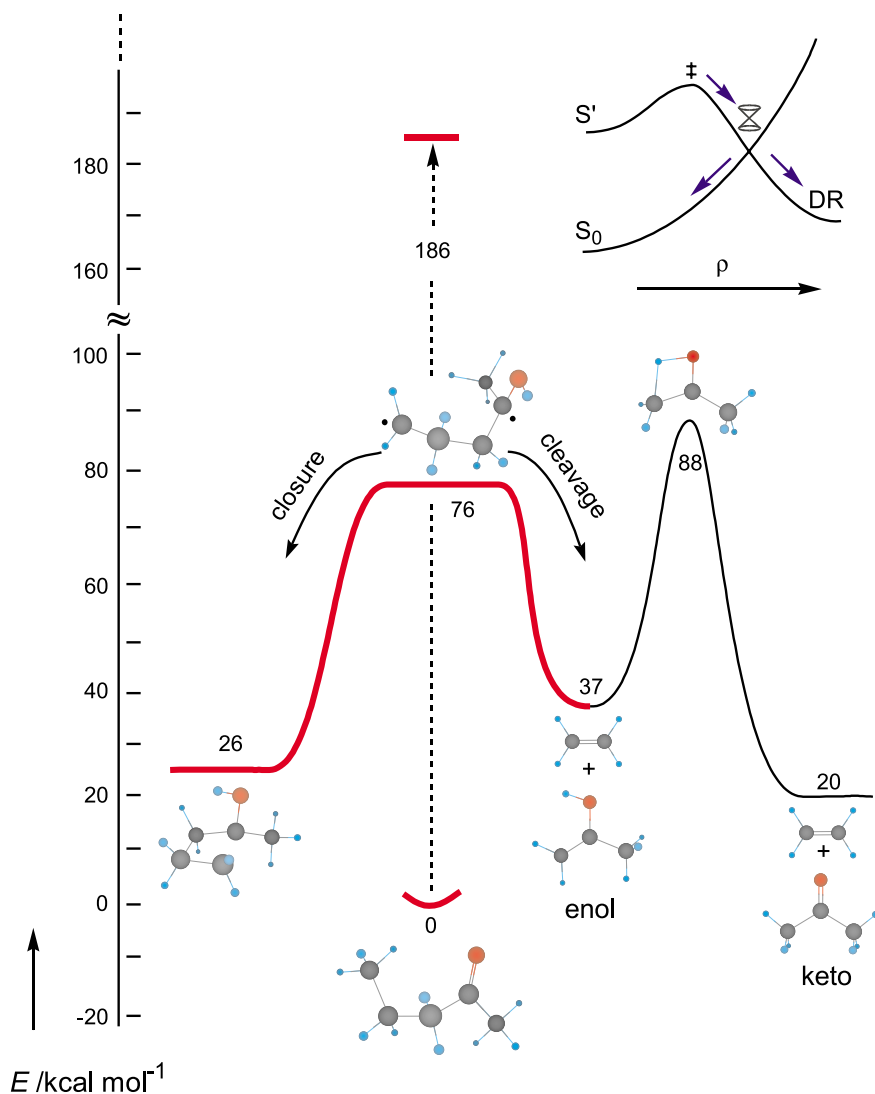


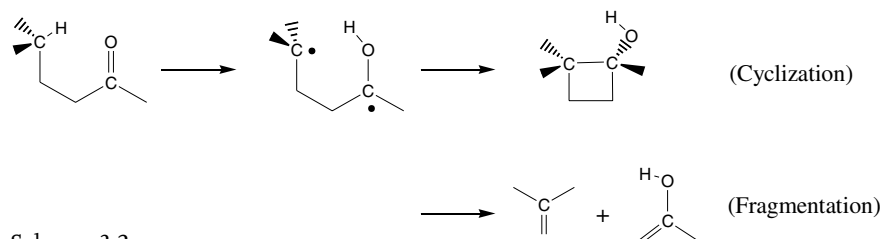
**Fig. 3.6** Ground-state potential energy surface of 2-pentanone showing the possible reaction pathways of the diradical intermediate formed after hydrogen-atom transfer. The total experimental energy is also indicated. The structures and energies shown derive from

Density Functional Theory calculations. The insert illustrates the topology of the ground- and excited-state surfaces along the hydrogen-transfer reaction coordinate ( $\pi$ ,  $\gamma$  C–H distance), see text.

100, 114, and 86 amu, respectively, and by additional peaks attributable to the radicals produced by  $\alpha$ -cleavage of the C–C bonds. The observation of these additional peaks is entirely consistent with previous studies of  $\alpha$ -cleavage in methyl alkyl ketones,<sup>[26]</sup> for which the fs mass spectra feature a peak at 43 amu, corresponding to the acetyl radical, and a peak at the mass of the parent ion minus 15 amu, corresponding to the alkyl carbonyl radical (Norrish type-I). However, all the molecules studied here (A, B, and C) show a unique additional peak in the mass spectrum at 58 amu. This peak is only present when the molecular structure (A, B, C) is predisposed for Norrish type-II reactions, as is evident from the absence of the 58 amu peak in 3-methyl-2-butanone (D), which lacks a hydrogen atom in the  $\gamma$ -position.

By gating the signal at the parent mass and at mass 58 amu, we were able to obtain the transient signals for the relevant species. The results are shown on the right-hand-side of Figure 3.5. A least-squares-fit with appropriate convolution gave the parent decay times  $\tau = 90 \pm 15$  fs,  $80 \pm 10$  fs, and  $75 \pm 10$  fs for 2-pentanone, 2-hexanone, and 5-methyl-2-hexanone, respectively. The rise times of the intermediates are comparable with the decay times of their respective parents. The 58 amu species decays in  $670 \pm 50$  fs for (A) 2-pentanone,  $565 \pm 50$  fs for (B) 2-hexanone, and  $490 \pm 50$  fs for (C) 5-methyl-2-hexanone.<sup>[30]</sup> The decay of the  $\alpha$ -cleavage intermediate is different. For example, for A,  $\tau_2$  (71 amu) =  $850 \pm 50$  fs and  $\tau_2$  (43 amu) =  $930 \pm 50$  fs.

The decay of the 58 amu species is an order of magnitude slower than that of the parent, indicating that it does not arise from ion fragmentation of the latter. Accordingly, the 70–90 fs and 400–700 fs decay times, depending on the molecule, describe Scheme 3.2.



Scheme 3.2

Since the decay of the parent and the rise of the intermediate have similar rates the hydrogen transfer must occur in 70–90 fs. This is consistent with the time scale observed for intramolecular H-atom transfer (~60 fs) in the similar structure of methyl salicylate.<sup>[31]</sup>

Figure 3.6 depicts the reaction pathways of the 2-pentanone diradical intermediate formed after intramolecular hydrogen transfer. The stationary points were calculated using the spin-unrestricted DFT method at the B3LYP/6–31G\* level. The calculations show that the  $\beta$  C–C bond of the diradical intermediate is long (1.626 Å), i.e., relatively weak. It is therefore anticipated that upon ionization the diradical species should easily undergo fragmentation to give the 58 amu signal in the TOF mass spectrum and, as such, the transients gated at this mass reflect the fs dynamics of the diradical. Second, once the diradical intermediate is formed, two

reaction pathways are possible: the diradical can undergo ring-closure forming a cyclobutanol derivative, or it can undergo C–C bond cleavage in the  $\beta$ -position to yield an ethylene derivative and 2-propenol, the enol precursor of acetone (see the above scheme depicting fragmentation and cyclization). Third, the interconversion to the keto structure (acetone) is associated with a high energy barrier (Figure 3.6) and will not take place on these ultrafast time scales.

Although both cyclization and fragmentation are essentially barrierless (Figure 3.6), the cleavage of the diradical will be the dominant reaction channel due to entropy effects, i.e. the conformational requirements for ring closure are more demanding than those for fragmentation (see also Section 3.3). The 1,4-diradical described above is similar to other diradicals studied in this laboratory, such as tetramethylene.<sup>[6,20]</sup> It is remarkable that the time scales for their decay are comparable ( $\sim 700$  fs vs.  $400\text{--}700$  fs), even though the precursors are entirely different. The entropic effects were shown to be very important; for tetramethylene, which forms ethylene and cyclobutane, fragmentation was found to be predominant over cyclization by a factor of two.<sup>[6]</sup>

The decay times (Figure 3.5) of the diradical intermediates show a systematic trend: their lifetime decreases as the number of alkyl substituents on the  $\gamma$ -carbon increases. Based on the decrease in  $\gamma$  C–H bond strength on going from 2-pentanone ( $98\text{ kcal mol}^{-1}$ ) to 2-hexanone ( $94.5\text{ kcal mol}^{-1}$ ) and 5-methyl-2-hexanone ( $92\text{ kcal mol}^{-1}$ ),<sup>[29a]</sup> it is anticipated that the internal energy content of the diradical intermediates of 2-hexanone and 5-methyl-2-hexanone will be higher than in 2-pentanone,<sup>[32]</sup> thus resulting in somewhat faster dynamics. However, the change in bond energies is small and the potential of the diradical is rather flat for such small energy changes to make a difference.<sup>[6]</sup> Thus, the increase in the number of degrees of freedom to 18 when two methyl substituents are present and the increase in rates suggest a highly non-statistical behavior. Because the H-atom transfer occurs on the fs time scale, the reaction directionality limits the phase space.

These intramolecular hydrogen-transfer reactions, which are followed by cyclization or fragmentation, are quite common. In ion chemistry, the McLafferty rearrangement,<sup>[33]</sup> studied by mass spectrometry, is a prime analogue of Norrish type-II reactions. In fact, the electron-impact mass spectra are very similar to our fs photo-induced mass spectra. Both the neutral channel (Norrish type-II reaction) and the ionic channel (McLafferty rearrangement; fragmentation of the parent ion) contribute to the overall 58 amu signal. However, as discussed above, the fs resolution allows us to distinguish unambiguously between the two processes: the contribution of the McLafferty rearrangement is reflected in a relatively short-lifetime decay component which, as expected, shows dynamics identical to the neutral parent. On the other hand, the Norrish type-II reaction dynamics occur on the longer time scales indicated in Figure 3.5. This observation is confirmed by the increase in the short-lifetime decay component with increasing probe intensity. Moreover, the mass spectrum of 3-methyl-2-butanone, a structural isomer of 2-pentanone, lacks the 58 amu peak, which is consistent with the fact that only ketones containing a  $\gamma$  C–H undergo the Norrish type-II reaction and McLafferty rearrangement, separated by the fs time scale.

## 3.5

## Conclusion

In this contribution, we have summarized experimental and theoretical studies of the fs dynamics of diradicals, which represent prototype intermediates in numerous organic reactions. We have focussed our studies on the diradical intermediates generated by the classical Norrish type-I and Norrish type-II reactions.

In order to examine the ultrafast elementary steps, we have studied the reactions at higher energy than the conventional lowest state of ns time scale. The energetics have been obtained by Density Functional Theory. Only with fs resolution can one dissect the non-concerted steps and examine differences between the reactions of neutral radicals and radical ions. Here, we address the energy landscape and the dynamics of processes involving stereochemistry, concertedness, and entropic configurations.

## Acknowledgements

This work was supported by the National Science Foundation and the Office of Naval Research. We thank Prof. Alfred A. Scala, Worcester Polytechnic Institute, for many helpful discussions and for preparing 2,3-diazobicyclo[2.2.1]hept-2-ene. SDF, a postdoctoral fellow of the Fund for Scientific Research, Flanders, acknowledges a Fulbright scholarship and financial support by the Katholieke Universiteit Leuven and by Caltech.

## References

- 1 J. Berson, *Science* **1994**, 266, 1338 and references therein.
- 2 P. B. Dervan, T. Uyehara, D. S. Santilli, *J. Am. Chem. Soc.* **1979**, 101, 2069.
- 3 P. B. Dervan, D. S. Santilli, *J. Am. Chem. Soc.* **1980**, 102, 3863.
- 4 A. H. Zewail, *Femtochemistry: Ultrafast Dynamics of the Chemical Bond*, World Scientific, Singapore, 1994, and references therein.
- 5 D. Zhong, E. W.-G. Diau, T. M. Bernhardt, S. De Feyter, J. D. Roberts, A. H. Zewail, *Chem. Phys. Lett.* **1998**, 298, 129.
- 6 S. De Feyter, E. W.-G. Diau, A. A. Scala, A. H. Zewail, *Chem. Phys. Lett.* **1999**, 303, 249.
- 7 A. A. Scala, E. W.-G. Diau, Z. H. Kim, A. H. Zewail, *J. Chem. Phys.* **1998**, 108, 7933.
- 8 C. Doubleday, *J. Phys. Chem.* **1996**, 100, 15083.
- 9 N. W. Moriarty, R. Lindh, G. Karlström, *Chem. Phys. Lett.* **1998**, 289, 442.
- 10 P. J. Krusic, P. Meakin, J. P. Jesson, *J. Phys. Chem.* **1971**, 75, 3438.
- 11 F. A. Neugebauer, in *Magnetic Properties of Free Radicals* (Ed.: H. Fischer), Landolt-Börnstein New Series, Vol. II/17b, Springer Verlag, Berlin, Heidelberg, 1987.
- 12 M. Guerra, *J. Am. Chem. Soc.* **1992**, 114, 2077.
- 13 S. K. Kim, S. Pedersen, A. H. Zewail, *J. Chem. Phys.* **1995**, 103, 477.
- 14 E. W.-G. Diau, O. K. Abou-Zied, A. A. Scala, A. H. Zewail, *J. Am. Chem. Soc.* **1998**, 120, 3245.
- 15 C. Doubleday, K. Bolton, G. H. Peslherbe, W. L. Hase, *J. Am. Chem. Soc.* **1996**, 118, 9922.
- 16 C. Doubleday, *Chem. Phys. Lett.* **1995**, 233, 509.
- 17 W. Adam, U. Denninger, R. Finzel, F. Kita, H. Platsch, H. Walter, G. Zang, *J. Am. Chem. Soc.* **1992**, 114, 5027.

- 18 E. W.-G. Diau, J. L. Herek, Z. H. Kim, A. Zewail, *Science* **1998**, 279, 848.
- 19 R. Hoffman, S. Swaminathan, B. G. Odell, R. Gleiter, *J. Am. Chem. Soc.* **1970**, 92, 7091.
- 20 S. Pedersen, J. L. Herek, A. H. Zewail, *Science* **1994**, 266, 1359.
- 21 K. B. Møller, A. H. Zewail, *Chem. Phys. Lett.* **1998**, 295, 1.
- 22 D. Zhong, A. H. Zewail, *J. Phys. Chem. A* **1998**, 102, 4031.
- 23 C. Doubleday, *J. Am. Chem. Soc.* **1993**, 115, 11968.
- 24 S. De Feyter, E. W.-G. Diau, A. Zewail, *Angew. Chem.* **2000**, 112, 266.
- 25 R. G. W. Norrish, *Trans. Faraday Soc.* **1934**, 30, 103.
- 26 (a) S. K. Kim, A. H. Zewail, *Chem. Phys. Lett.* **1996**, 250, 279; (b) S. K. Kim, J. Guo, J. S. Baskin, A. H. Zewail, *J. Phys. Chem.* **1996**, 100, 9202.
- 27 (a) S. A. Buzza, E. M. Snyder, D. A. Card, D. E. Folmer, A. W. Castleman, *J. Chem. Phys.* **1996**, 105, 7425; (b) T. Shibata, H. Li, H. Katayanagi, T. Suzuki, *J. Phys. Chem. A* **1998**, 102, 3643; (c) J. C. Owrutsky, A. P. Baronavski, *J. Chem. Phys.* **1998**, 108, 6652; (d) Q. Zhong, L. Poth, A. W. Castleman, *J. Chem. Phys.* **1999**, 110, 192; (e) J. C. Owrutsky, A. P. Baronavski, *J. Chem. Phys.* **1999**, 110, 11206; (f) P. Farmanara, V. Stert, W. Radloff, *Chem. Phys. Lett.* **2000**, 320, 697.
- 28 R. G. W. Norrish, *Trans. Faraday Soc.* **1937**, 33, 1521.
- 29 (a) P. J. Wagner, *Acc. Chem. Res.* **1971**, 4, 168, and references therein; (b) J. C. Scaiano, *Acc. Chem. Res.* **1982**, 15, 252; (c) M. V. Encina, E. A. Lissi, *J. Photochem.* **1975**, 4, 321; (d) F. S. Wettack, W. A. Noyes, Jr., *J. Am. Chem. Soc.* **1968**, 90, 3901; (e) F. S. Wettack, *J. Phys. Chem.* **1969**, 73, 1167; (f) W. N. Nau, J. C. Scaiano, *J. Phys. Chem.* **1996**, 100, 11360, and references therein; (g) M. Klessinger, J. Michl, *Excited States and Photochemistry of Organic Molecules*, VCH, New York, NY, 1995, and references therein.
- 30 Note that parent ion fragmentation contributes to the transient signal of the intermediate of 2-hexanone and 5-methyl-2-hexanone and this contribution has been accounted for in the fitting procedure.
- 31 J. L. Herek, S. Pedersen, L. Bañares, A. H. Zewail, *J. Chem. Phys.* **1992**, 97, 9046.
- 32 This trend in internal energy content has been confirmed by DFT calculations. The available internal energies of the diradical intermediates are 110, 113, and 116 kcal · mol<sup>-1</sup> for 2-pentanone, 2-hexanone, and 5-methyl-2-hexanone, respectively.
- 33 (a) F. W. McLafferty, *Anal. Chem.* **1956**, 28, 306; (b) F. W. McLafferty, F. Turecek, *Interpretation of Mass Spectra*, University Science Books, Sausalito, CA, 1993.



## 4

# The Coulomb Explosion Imaging Method and Excited-State Proton-Transfer Reactions

*Eric S. Wisniewski, Jason R. Stairs, Daniel E. Folmer, and A. Welford Castleman, Jr.*

## 4.1

### Introduction

A novel use for the Coulomb explosion phenomenon has been developed to arrest intermediate reaction states and interrogate the excited-state dynamics of a model DNA base pair in real time. This technique was employed to study the 7-azaindole dimer system and provided direct mass spectral evidence for the operation of a step-wise mechanism for double proton transfer upon excitation to the  $S_1$  state. Further femtosecond pump-probe studies were conducted to elucidate the nature of the solvated nonreactive and reactive isomers of the 7-azaindole dimer that may form under different clustering conditions.

As a result of the pioneering work by Zewail and co-workers, chemists are able to study the real-time dynamics of elementary chemical reactions in a laboratory setting.<sup>[1]</sup> Reactions are initiated with a pump photon along a chosen potential energy surface, and thereafter the reaction is explored with a probe photon that is used to generate fluorescence or ionization of the species of interest at a specific time delay. Our group has utilized the phenomenon of Coulomb explosion to “visualize” intermediate states in a reaction.<sup>[2]</sup> Here, the reactive intermediates are fragmented at specified times and the masses are resolved in a time-of-flight mass spectrometer (TOF-MS) enabling the intermediate reaction products to be identified at selected times during the course of a reaction. This method can be used to study the dynamics of reactions where arguments persist as to whether a step-wise or concerted process is operative. The Coulomb Explosion Imaging Method (CEIM) approach to studying reaction dynamics is complementary to traditional mass spectrometric pump-probe spectroscopy that utilizes the differences in the ionization cross-sections of the reacting species to determine the dynamics of a system. CEIM is the first known application of Coulomb explosion to resolve the dynamical events in a chemical reaction.

The Coulomb explosion phenomenon has been studied in our laboratories for several years and the presence of multiply-charged atomic ions has often been observed.<sup>[3,4]</sup> Femtosecond lasers have enabled the investigation of how atoms, molecules, and clusters behave in strong optical fields. Coulomb explosion occurs when the individual molecules or atoms of a cluster have multiple electrons removed due

to irradiation from high-fluence ultrashort laser pulses. The comparatively weak hydrogen bonding or van der Waals forces holding the cluster together are overcome by the Coulomb repulsion of multiple cationic centers. Fragmentation of the cluster results in the formation of many species ranging from singly-charged atoms or molecules up to atomic species that have had all of their valence electrons stripped

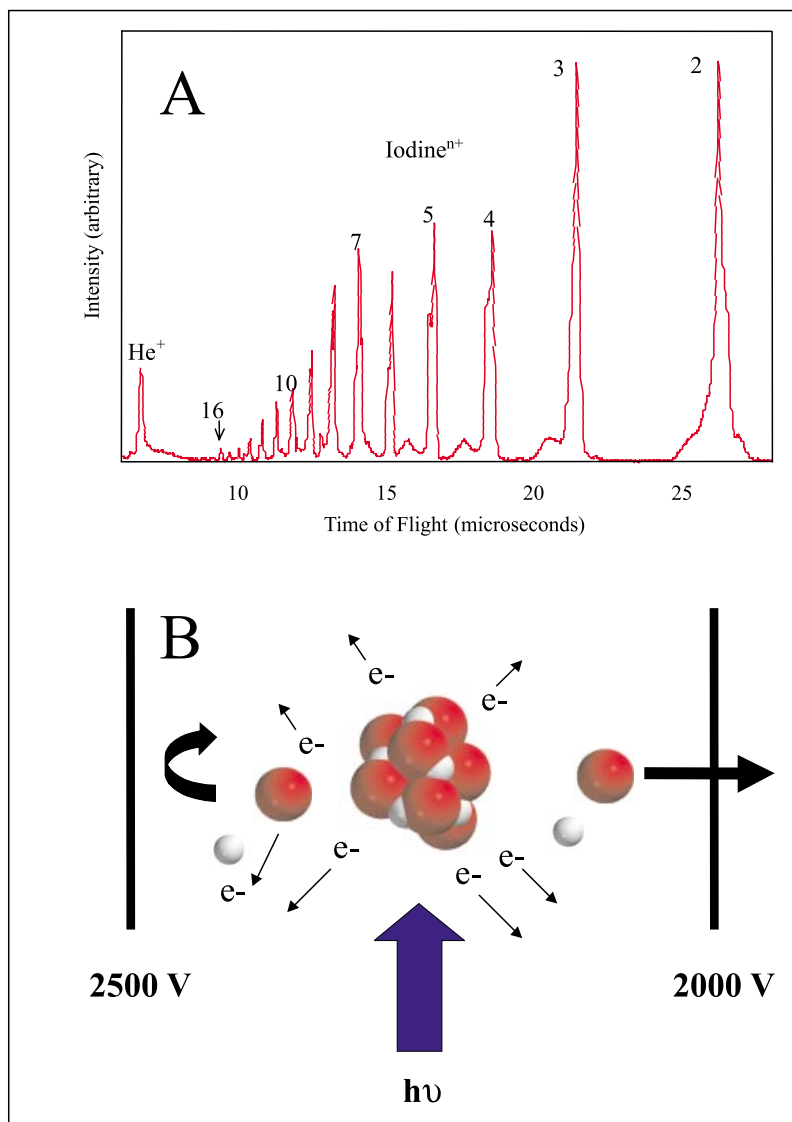


**Fig. 4.1** (A) Coulomb explosion can result in atomic fragments from which all valence electrons have been removed. (B) Schematic depiction of how Coulomb explosion occurs.

Multiple electrons are stripped away from a cluster leaving multiple cationic centers. The cluster fragments in the electric field of the time-of-flight mass spectrometer.

away;<sup>[3]</sup> a mass spectrum of this can be seen in Figure 4.1A, while Figure 4.1B depicts how the cluster fragments behave between the time-of-flight grids. Coulomb explosion experiments performed by our group have elucidated the effects of wavelength on various molecular systems.<sup>[5,6]</sup> Findings indicate that as the wavelength of the ionizing radiation is lengthened to more red frequencies, Coulomb explosion is more intense. The use of radiation of  $\lambda = 620$  nm to ionize and Coulomb explode cluster species would seem to be a suitable choice given the data reported by Ford et al.<sup>[5,6]</sup>

One of the critical characteristics of Coulomb explosion that enables its use in pump-probe femtosecond spectroscopy is that it occurs on a very short time scale. Poth has calculated that the Coulomb explosion event is completed in roughly 25 fs;<sup>[7]</sup> related findings have been published by Jortner.<sup>[8]</sup> Because of the ultrashort time scale of the event, CEIM can yield information on intermediate states such as that involved in the excited-state double proton transfer in the 7-azaindole (7aza) dimer, a system for which there has been debate as to whether or not the tautomerization occurs in one or two steps.

There is continuing interest surrounding the mechanism that can lead to mismatches in DNA base pairs. Watson and Crick initially theorized that proton transfer induced tautomers of DNA base pairs might result in point mutations due to inappropriate matching of these pairs.<sup>[9]</sup> The potential significance of these mismatches has generated a great amount of interest in the scientific community,<sup>[10–14]</sup> with the Zewail group providing the first definitive evidence of a two-step process by observing a bi-exponential decay in the pump-probe optical transients of the excited 7-azaindole dimer.<sup>[15]</sup> The Coulomb explosion method initiated by our group to determine intermediate states of a reaction proved complementary to Zewail's method of the analysis of the ionization cross-sections.

The mechanism by which tautomerization is completed in the 7-azaindole dimer is not the only debated topic in the literature concerning 7-azaindole. During some of their investigations of the 7-azaindole dimer, Kaya and co-workers observed the existence of two distinct isomers in the gas phase depending upon the backing pressure used in the supersonic expansion.<sup>[11]</sup> The two isomers were named the “reactive” and the “nonreactive” dimers. The reactive dimer was able to complete the excited-state double proton transfer and was able to emit the signature fluorescence of the tautomer. In contrast, the nonreactive dimer was unable to complete tautomerization and did not exhibit the fluorescence spectrum indicative of a completed proton transfer. Kaya and co-workers initially explained this difference by suggesting that a conformational isomer change resulting from a cooler supersonic expansion was responsible for the nonreactive species and that the geometry of the dimer inhibited the proton transfer.<sup>[10]</sup> This proposal was later supported by Lopez-Martens et al., who suggested that spectral evidence supported the formation of a hydrogen-bonded dimer with out-of-plane hydrogens.<sup>[14]</sup>

More recently, Kaya et al. revised their explanation of the nonreactive dimer with the support of evidence obtained using IR depletion spectroscopy.<sup>[13]</sup> They suggested that the nonreactive dimer is associated with a water molecule, which, upon photo-excitation, dissociates to leave a lower-energy dimer species that is unable to

undergo excited-state double proton transfer. Hydration studies performed by our group provide evidence that the presence of water in the 7-azaindole dimer does not inhibit excited-state double proton transfer, but rather facilitates the process. At higher orders of solvation, peculiar behavior is observed suggesting that the proton transfer occurs in a concerted step.<sup>[16]</sup>

## 4.2

### Experimental Techniques

#### 4.2.1

##### Femtosecond Laser System and Amplification

Femtosecond laser pulses are generated using a colliding pulse mode-locked (CPM) ring dye laser. A continuous wave argon ion laser (all lines, 4.5 W) impinges upon a dye jet comprised of Rhodamine 590 tetrafluoroborate in ethylene glycol (4.5 g in ~ 2 L). Broadband fluorescence results and is collected by two concave mirrors located opposite the dye jet. Clockwise and counterclockwise fluorescence then propagates around the laser cavity and meets at a DODCI dye jet, a saturable absorber (1 g in approximately 2 L ethylene glycol). When the two counter propagating pulses arrive at the saturable absorber, the increased intensity begins to bleach the dye. The two pulses also interfere with each other, which leads to a standing wave in the absorber region. As a result, the intensity of the laser increases further, which enhances the bleaching of the dye.<sup>[17]</sup> A 90 MHz pulse train results, with each pulse having a wavelength centered at 620 nm and being initially of ~120 fs duration with peak energies in the range of 100–150 pJ prior to amplification.

A four-stage amplification process is employed to increase the laser pulse energy to ~1.5 mJ or greater; this is accomplished by a six-pass bowtie amplifier followed by three Bethune cells. The six-pass bowtie amplifier utilizes a dye cell with sulforhodamine 640, which is transversely excited by the second harmonic (532 nm) from a pulsed (10 Hz) Nd:YAG laser. The pulse width of the Nd:YAG laser is in the nanosecond regime, and due to its repetition rate, this arrangement selectively amplifies only ten pulses per second. The femtosecond laser pulse passes through the excited dye and causes stimulated emission to occur during each pass. After the sixth pass, the slightly amplified femtosecond laser pulse enters the first Bethune cell, which has a 2 mm bore. Each Bethune cell is transversely pumped by the Nd:YAG laser. This process is repeated for a 6 mm and 12 mm bore Bethune cell until maximum amplification is achieved.

#### 4.2.2

##### Pump-Probe and Coulomb Explosion Imaging

Two-color pump-probe experiments are made possible by splitting the fundamental beam into two separate paths. One length of the split beam is passed through a beta barium borate crystal (BBO) to generate the second harmonic (310 nm). This ultra-

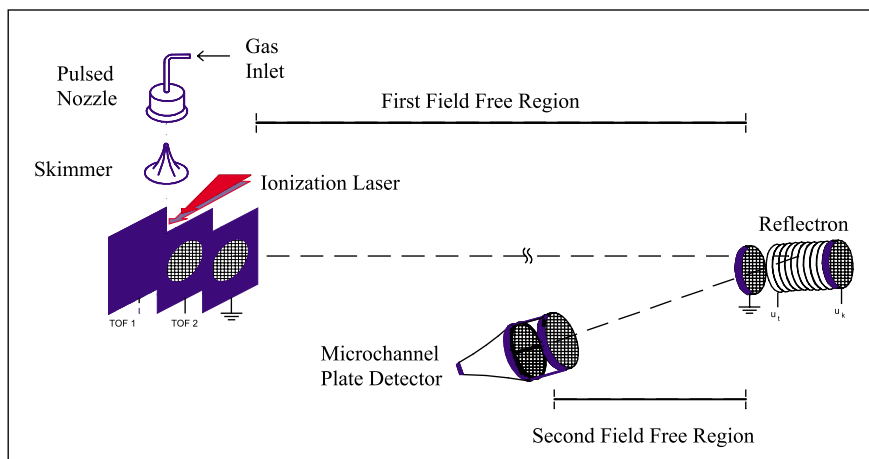


**Fig. 4.2** Time-of-flight mass spectrometer. Gas molecules and clusters are introduced into the vacuum of the mass spectrometer by supersonic expansion. Cations are formed by the ionizing presence of the femtosecond laser.

violet pulse is directed onto a precision delay stage. The two separate laser pulses (310 nm pump and 620 nm probe) are collinearly recombined and sent into a reflectron time-of-flight mass spectrometer; see Figure 4.2. Ion signals generated within the reflectron TOF-MS are digitized by an oscilloscope and analyzed on a personal computer.

For the Coulomb explosion studies, 7-azaindole dimers were formed by first heating the sample to around 120 °C and then subjecting it to supersonic expansion with a helium backing gas (< 1.2 bar) through a pulsed nozzle into the mass spectrometer. The tautomerization reaction was initiated using a weak pump pulse centered at 310 nm. After varying time delays, a high-power 620 nm probe pulse was utilized to bring about the intense field ionization and ensuing Coulomb explosion process. For the solvation studies of the 7-azaindole dimer, the helium backing gas was first bubbled into an external water cell prior to its introduction into the heated 7-azaindole sample. This arrangement produced 7-azaindole dimers solvated with up to nine water molecules.

## 4.3 Results and Discussion

### 4.3.1 Coulomb Explosion Imaging Method

The Coulomb Explosion Imaging Method was first utilized to arrest the intermediate species of an excited-state double proton transfer tautomerization in the 7-azaindole dimer. This use of Coulomb explosion is the first known application of the phenomenon to investigate a problem in the area of reaction dynamics. The 7-azaindole

dimer constituted an ideal system for employing Coulomb explosion to separate the species so as to directly reveal the intermediate reaction state in the recorded mass spectra.

The mass spectrum of the 7-azaindole system can be modified by varying a number of different parameters such as the laser fluence, the clustering conditions, and the time delay between the pump and probe lasers. The experiments were conducted with the ratio of the monomer (118 amu) to the dimer (236 amu) of 7-azaindole lying between 2:1 and 1:1; see Figure 4.3. Under conditions where no proton transfer occurs, Coulomb explosion of the dimer results in two moieties of equal

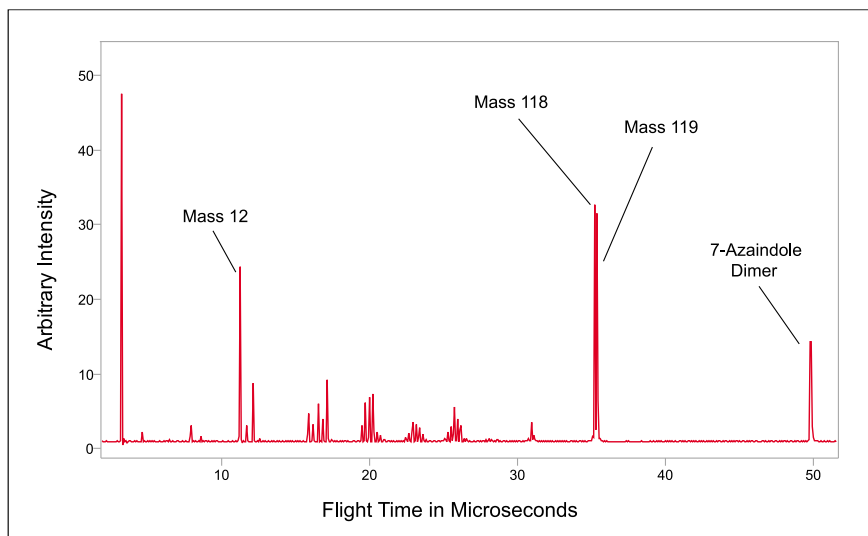


**Fig. 4.3** A typical mass spectrum of 7-azaindole. Note the low intensity mass fragments to either side of the 12 amu peak.

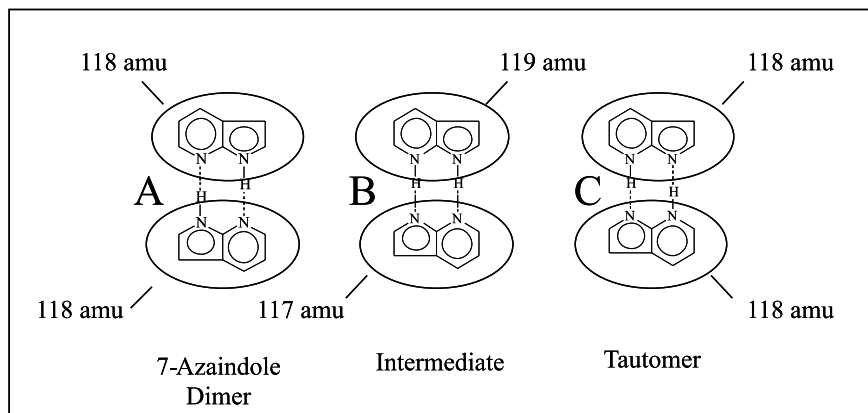


**Fig. 4.4** The 7-azaindole dimer tautomerizes in a mass of 119 amu and the other would have a species was separated, one portion would have

mass (118 amu). However, when proton transfer occurs following a pump photon, Coulomb explosion results in a species with a mass of 119 amu. This species is indicative of a partial proton transfer when both protons are associated with one half of the dimer, which could only occur if the process occurs in two steps (see Figure 4.4). The other half of the dimer that donates the proton would result in a mass fragment of 117 amu, but electron-impact studies led to the conclusion that this is an unstable species and fragments to smaller masses;<sup>[18]</sup> this can be seen in the mass spectrum (Figure 4.3). The method for performing the Coulomb explosion experiments is shown schematically in Figure 4.5.

As the delay time between the pump and probe lasers is increased, the intensity of the 119 amu species varies with respect to that of the 118 amu species. Both of

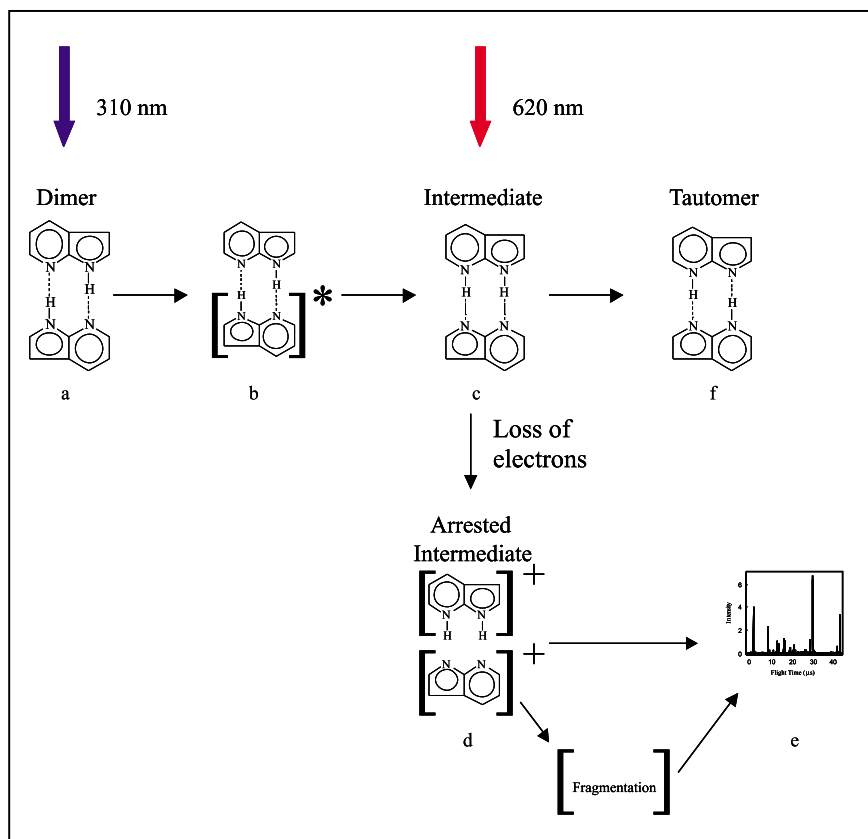


**Fig. 4.5** Mechanism for CEIM: (a) The 7-azaindole dimer is excited by a 310 nm femtosecond pulse. (b) The excited half of the 7-azaindole initiates the tautomerization process. (c) A Coulomb explosion-inducing 620 nm pulse separates the dimer in ~25 fs to freeze the reaction intermediate. (d) The intermediate fragment (119 amu) is ionized in the Coulomb

explosion process while the 117 amu portion is unstable and fragments into several charged species of low mass. (e) Cations are detected in a time-of-flight mass spectrometer. (f) Full tautomerization proceeds if the 7-azaindole dimer is not disrupted by Coulomb exploding femtosecond radiation.

these species derive from the dimer of 7-azaindole, although there is always some background intensity arising from the ionization of the 118 amu monomer species. Furthermore, a base signal of 119 amu is present due to a nominal amount of proton transfer occurring within the pulse length of the probe laser. To determine the contributions of the base amounts of the 118 amu and 119 amu species present in the mass spectra, a single-color (620 nm) ionization experiment was conducted; the information garnered was used in the numerical treatment of the optical transients during the fitting procedure. The time-dependent variation of the intermediate state (119 amu) was determined from the ratio of the 119 amu and 118 amu species. Figure 4.6 illustrates the optical transient of the ratio (119 amu/118 amu). The solid line represents the best fit of the data by applying the standard rate equations for a unimolecular consecutive reaction,  $A \xrightarrow{k_1} B \xrightarrow{k_2} C$ , where B represents the intermediate state (119 amu/117 amu dimer) and C represents the tautomer (see Figure 4.4). The fitting procedure yields a first-step rate constant of  $0.0015 \text{ fs}^{-1}$  ( $\tau = 660 \text{ fs}$ ) for the generation of the intermediate species and a second-step rate constant of  $0.0002 \text{ fs}^{-1}$  ( $\tau = 5 \text{ ps}$ ) for formation of the completed tautomer. The times determined from the fitting are in close agreement with those of the Zewail group, who obtained a first time of 650 fs and a second time of 3.3 ps. The slight differences in the times found by our group and those of the Zewail group can be attributed to experimental error.<sup>[15,19]</sup> Based on the fitting of the femtosecond optical transients to

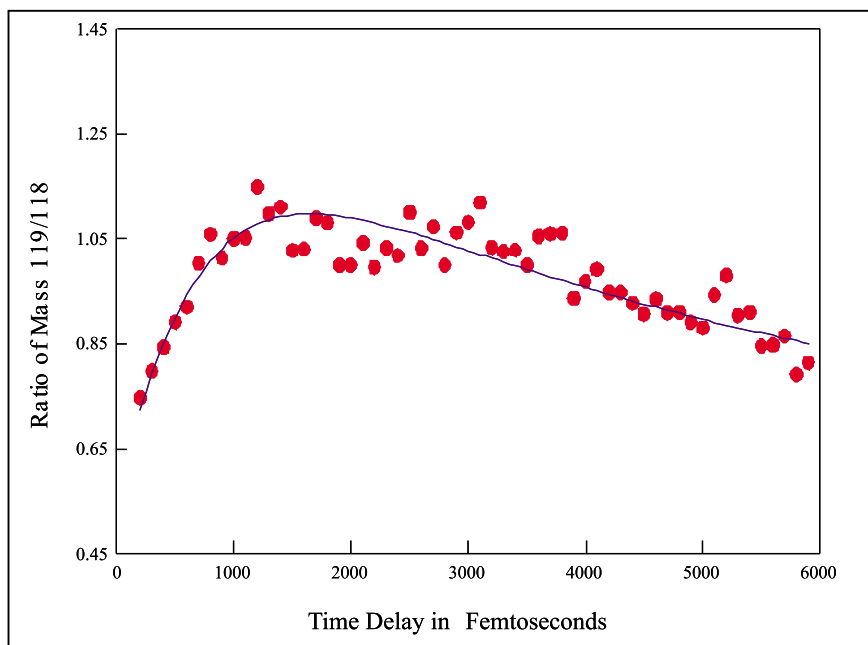


**Fig. 4.6** The optical transient for the ratio of the 119 amu fragment to the 118 amu species. The circles represent experimental data, while the solid line represents the best fit of the data. Time constants of around 660 fs and 5 ps were calculated for the first and second proton transfers.



a bi-exponential decay function, Zewail and co-workers surmised that the 7-azaindole dimer species tautomerizes in two distinct steps through an intermediate state. The Coulomb explosion of the excited-state double proton transfer reaction at various times provided direct mass spectral evidence of the intermediate experimentally predicted by Zewail and co-workers based on the observation that their data followed bi-exponential behavior.

The 7-azaindole dimer was fragmented by means of Coulomb explosion so as to isolate the intermediate state after the tautomerization reaction had been initiated. When a cluster is Coulomb exploded, particles are scattered in all directions in the mass spectrometer. However, due to the nature of the time-of-flight mass spectrometer (see Figures 4.1B and 4.2), only those fragments accelerated directly parallel to the axis of the mass spectrometer are collected by the detector; all other fragments that are accelerated off-axis are lost and remain undetected. The ion fragments that are detected are of two varieties, those that are accelerated toward and those that are accelerated away from the detector. These two types of fragments yield a signature Coulomb explosion peak when a reflectron TOF-MS is operated in hard reflection mode. Coulomb explosion mass peaks are typically comprised of a broad area along with a sharp feature; see Figure 4.7. The broad feature of the peak is due to the fragments that are accelerated toward the detector. They arrive at the detector over a broad range of times. The sharp feature of the Coulomb explosion peak is a result of the backward ejected fragments. These fragments are turned around by the first time-of-flight grid and are focused before arriving at the detector in a well-defined time. In hard reflection, the reflectron (see Figure 4.2) simply acts as an ion mirror and does not compensate for the kinetic energy differences of the forward and backward ejected ions. When the reflectron is operated in soft-reflection mode, the higher energy fragments penetrate the field of the reflectron more than the lower energy

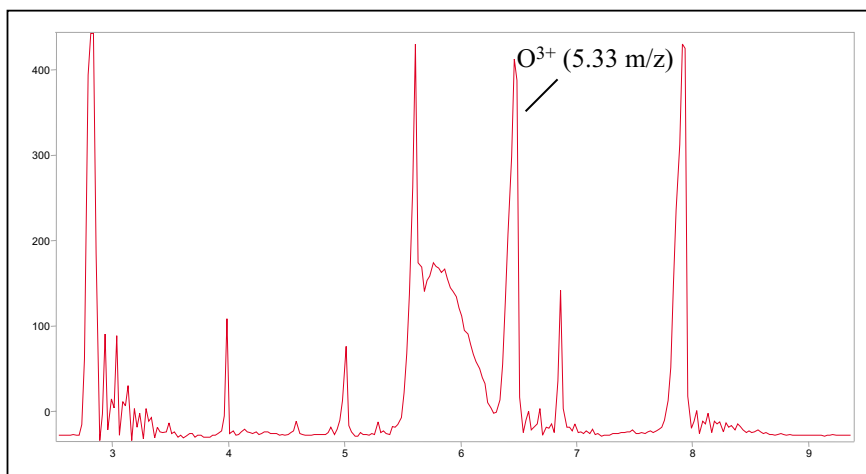


**Fig. 4.7** A mass spectrum illustrating a classic Coulomb explosion peak. The peak at  $m/z = 4$  corresponds to  $O_4^+$ , which arises from the Coulomb explosion of water clusters.

fragments. Through careful calibration of the voltages on the front and back of the reflectron, the backward and forward fragments can be made to arrive at the detector simultaneously, thereby eliminating the classic Coulomb explosion broadening of the peak of interest.

This important feature of the reflectron TOF-MS was used to confirm that Coulomb explosion was the operative mechanism involved in separating the moieties of the 7-azaindole dimer. Figure 4.8 displays two mass spectra recorded in hard reflection mode, where the kinetic energy differences of the forward and backward ejected ions was *not* compensated for. Each spectrum was recorded with an identical electric field gradient. Figure 4.8A displays a mass spectrum where clustering conditions produced the dimer species; Figure 4.8B displays a mass spectrum where clustering conditions were altered to eliminate the dimer by changing the time that the femto-second laser interacted with the molecular beam. When a gaseous packet of molecules leaves the pulsed nozzle and expands into the vacuum, the front and rear edges of the packet have a lower density. This results in a warmer portion of the molecular beam, which leads to less efficient clustering. In the center portions of the molecular beam, more collisions occur, leading to greater cooling of the mol-

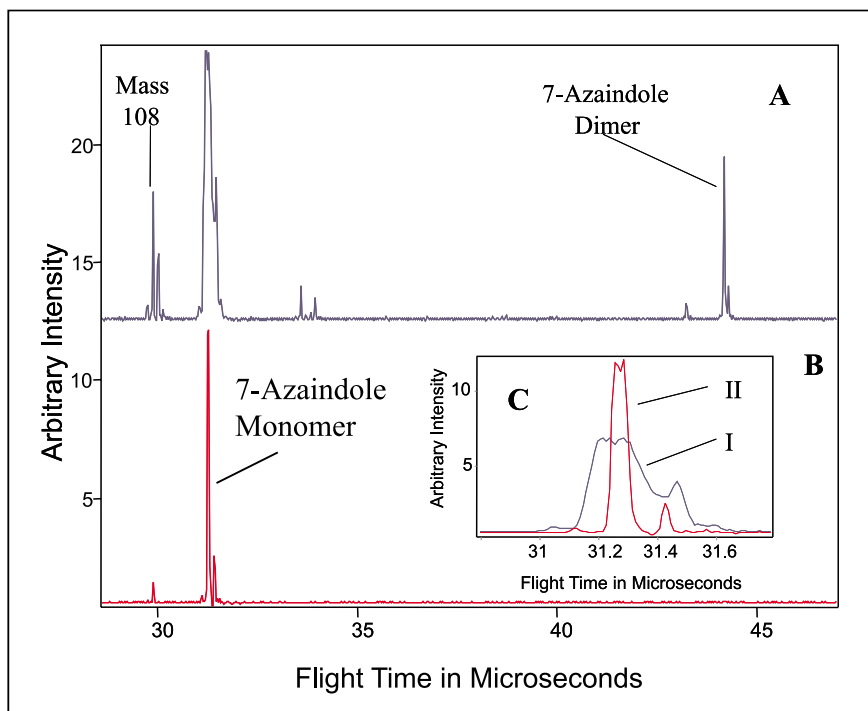


**Fig. 4.8** These mass spectra were recorded in hard reflection mode. (A) The broadening of the peak corresponding to mass 118 amu and 119 amu indicates that Coulomb explosion is operative. (B) In the absence of the dimer species, broadening of the monomer peak is not observed. Some mass 119 amu is present due to isotopic contributions. (C) Overlapped spectra of A and B for the monomer. The differences between the Coulomb exploded peak (I) and the non-Coulomb exploded peak (II) are clearly evident.

ecules and to more efficient clustering. By delaying the arrival of the femtosecond laser relative to the time that the pulsed nozzle opened, a different distribution of clusters can be sampled and, in this case, the dimer could be eliminated from the mass spectrum. In Figure 4.8A, it is clear that the dimer (and the species of mass 108, an impurity in the 7-azaindole sample) does not exhibit broadening, but the 118 amu species shows broadening indicative of Coulomb explosion that is so dramatic that the resolution between 118 amu and 119 amu is blurred. However, when the dimer is not present, the 118 amu species does not exhibit broadening. This is conclusive evidence that the separation of the dimer species is driven by Coulomb explosion and occurs on an ultrashort time scale. Soft-reflection mode was utilized for pump-probe experiments so that resolution was optimized for data analysis.

The observations made in the Coulomb explosion of the 7-azaindole dimer provide complementary evidence that the excited-state double proton transfer proceeds in two distinct steps, as first illustrated by Zewail and co-workers. Furthermore, the experimental evidence that the 119 amu to 118 amu ratio returns to the initial value at long pump-probe delay times yields additional proof that the tautomerization is completed. This technique can be broadly used in photochemical reactions where an intermediate state is proposed, which offers the opportunity to directly view mass spectral evidence of intermediates. For studying specific reactions, this method is advantageous over traditional pump-probe techniques that utilize the differences in ionization cross-sections.

Another interesting phenomenon displayed by the 7-azaindole dimer is that at least two isomers, the reactive and nonreactive, are known to exist in the gas phase depending upon the clustering conditions.<sup>[11]</sup> The reactive isomer is able to complete tautomerization following excitation to the first excited state, while the nonreactive species is unable to complete tautomerization. The two species are formed at different temperatures, depending on the backing pressure of the carrier gas used in the supersonic expansion. Femtosecond pump-probe transients for the reactive and nonreactive behavior are shown in Figure 4.9. The reactive dimer isomer can be formed by expanding the 7-azaindole seeded in helium with a backing pressure of ~300 Torr. The nonreactive dimer can be formed in the same manner but with a much higher backing pressure of ~3,000 Torr. The increase in pressure allows for more cooling of the molecular beam during supersonic expansion and may lead to a lower-energy dimer species being frozen into a particular geometry not conducive to the typical double proton transfer observed in the Coulomb explosion studies discussed above. The optical transients shown in Figure 4.9 were recorded under nearly identical experimental conditions; the only difference was the timing of the laser relative to the opening of the pulsed nozzle, which allowed probing of different temperatures of the molecular beam.

The Coulomb Explosion Imaging Method was utilized to investigate the behavior of the nonreactive dimer species. The same method was used to investigate the nonreactive dimer as was used for the reactive species; a weak 310 nm pump pulse followed by a strong, Coulomb explosion-inducing 620 nm probe pulse. The 119 amu species built up as the pump and probe laser pulses overlapped, but, in contrast to the reactive dimer, which decayed away to reveal a two-step process, its intensity

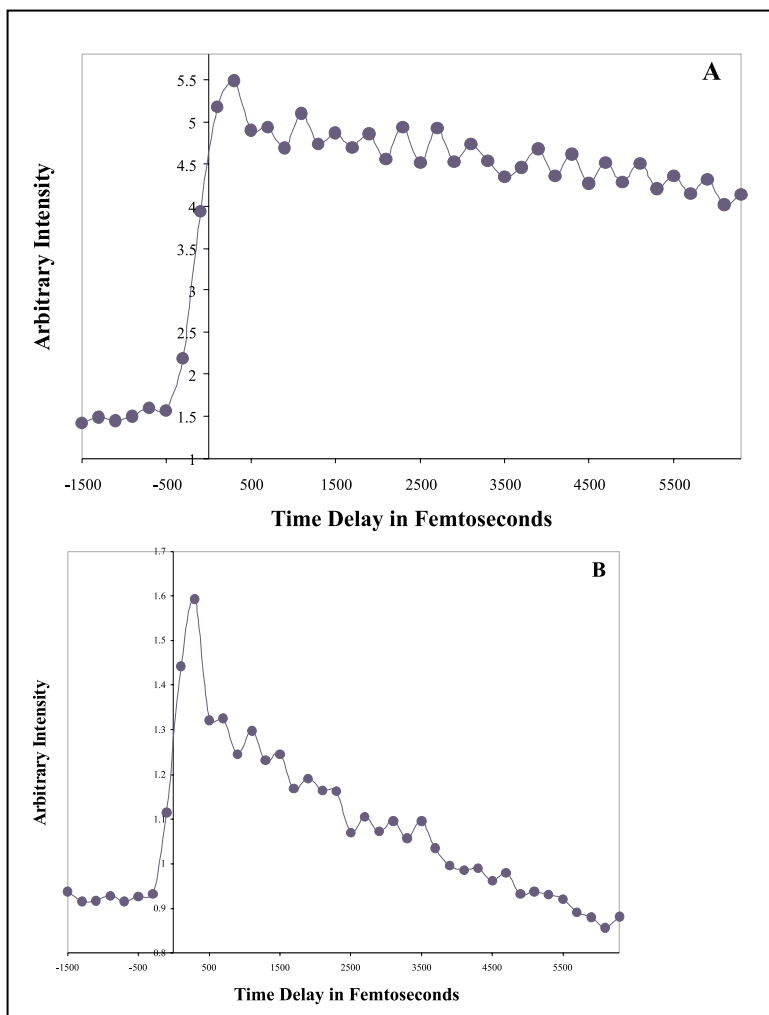


**Fig. 4.9** The nonreactive and reactive behaviors of the 7-azaindole dimer. (A) The optical transient for the nonreactive species fails to exhibit any fast time dynamics. (B) The reactive isomer exhibits fast decay caused by excited-state double proton transfer. Both sets of data were recorded at identical backing pressures.

remained constant. The optical transient of the nonreactive dimer is shown in Figure 4.10. The rise in the data suggests that the dimer is able to undergo a single proton transfer but is unable to complete the tautomerization; this may arise if the dimer is frozen into a configuration that is geometrically disadvantageous for double proton transfer. Another possible explanation is that an associated water molecule is responsible for the nonreactive dimer. Consequently, experiments were conducted to determine whether a water molecule could be responsible for the nonreactive behavior of the species generated at higher backing pressures.

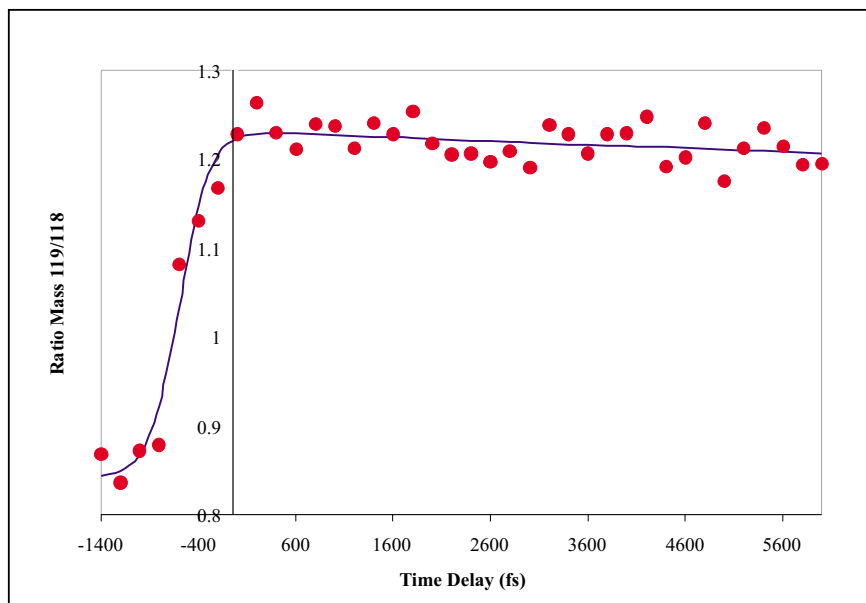


**Fig. 4.10** The Coulomb explosion depicting the ratio of the 119 amu and 118 amu fragments. The rise time in the data indicates that a first proton transfer occurs within ca. 600 fs.

#### 4.3.2

##### Hydration of 7-Azaindole

Cluster science has been used as a means of linking the gas phase to the condensed phases.<sup>[20]</sup> The solvation of clusters is also important, where the situation can range from the coordination of an individual cluster by a few solvent molecules to yield the isolated complex, up to heavily solvated species that represent bulk phases. Reports in the literature suggest that as few as six water molecules can impart liquid-like properties.<sup>[21,22]</sup> Investigation of the effect of hydration on the excited-state double proton transfer of the 7-azaindole dimer has been reported.<sup>[16]</sup> Investigations of the reactive and nonreactive species hydrated with up to nine water molecules were carried out to determine whether water had an inhibitory effect on the proton-transfer process. Pump-probe optical transients were recorded for  $(7\text{aza})_2(\text{H}_2\text{O})_n$ ,  $n = 0-9$ . The unsolvated pump-probe transient  $[(7\text{aza})_2]$ , formed at an intermediate backing pressure of 1,200 Torr, exhibited nonreactive character. The solvated 7aza optical transients all displayed a reactive behavior corresponding to completion of the tautomer. The interesting trend in the data is that as hydration of the 7-azaindole dimer is increased, the nature of the tautomerization undergoes a transition from a two-step to a single-step process, as can be seen in Table 4.1. The data were fitted to either a bi-exponential or a single-exponential decay. The optical transients for  $(7\text{aza})_2$  with one, two, and three waters fitted well to a bi-exponential decay, while the transients of  $(7\text{aza})_2$  with five through to nine waters fitted well to a single-expo-

nential function. The tetrahydrated species failed to fit well to either function and seems to represent the transition point between the two behaviors. Figure 4.11 illustrates the data for the octahydrated 7-azaindole dimer.

**Tab. 4.1** Proton transfer times for the hydrated 7-azaindole dimers.

<i>Nuber of Waters</i>	<i>First Transfer</i>	<i>Second Transfer</i>	<i>Proton Transfer</i>
1	550 fs	2800 fs	
2	565 fs	2000 fs	
3	560 fs	2000 fs	
4			
5			1800 fs
6			1600 fs
7			1300 fs
8			1100 fs
9			1000 fs

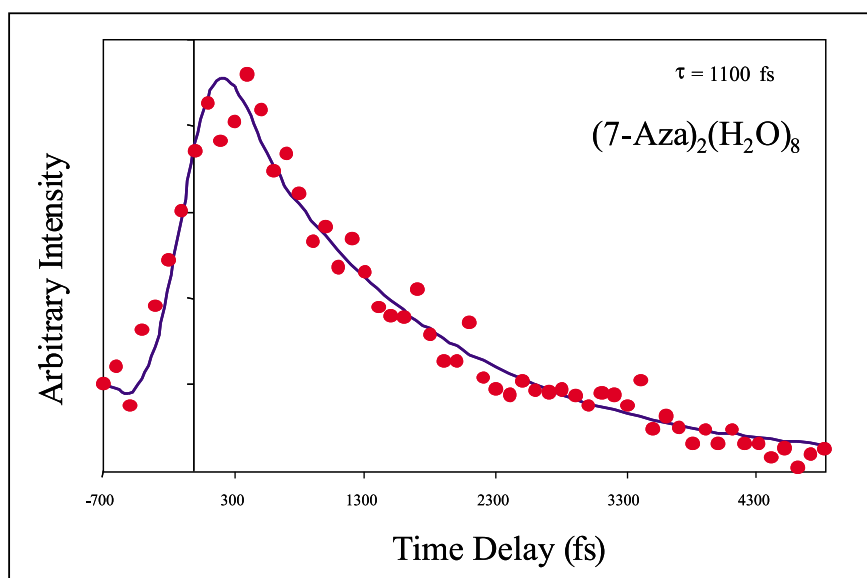


**Fig. 4.11** Optical transient for the 7-azaindole dimer clustered with eight water molecules. The circles represent experimental data while the solid line is the single-exponential decay fit corresponding to a rate of 1100 fs.

At first, the data seemed to suggest that the tautomerization occurred purely between the 7-azaindole molecules and that the water molecules present facilitated the reaction. This may not be the case in the light of preliminary calculations performed on hydrated DNA base pairs.<sup>[23]</sup> In calculations of hydrogen-bonded base pairs, Hobza found that significant hydration causes the planar base pairs to adopt a

stacked structure and that this transition is predicted to occur with hydration by four or five water molecules.<sup>[23]</sup> This suggests that the 7-azaindole dimer could slip into a card-stacked structure after solvation by around four waters and that proton transfer may occur with the water after solvation by five or more waters. Essentially, the octahydrated dimer would revert to two almost isolated monomers, each solvated by four water molecules. If this were the case, then only one half of the 7-azaindole could participate in self-tautomerization with the surrounding water molecules. This behavior could be further elucidated through experiments on the hydrated monomer of 7-azaindole.

Femtosecond pump-probe studies were performed on the hydrated 7aza monomer.<sup>[24]</sup> Despite the fact that excited-state double proton transfer in the gas phase has not hitherto been observed for these species, significant theoretical evidence suggests that the reaction should be possible. Chaban and co-workers calculated that in the ground state, the normal 7-azaindole species is more stable than the tautomer by about 14 kcal/mol; however, this trend reverses in the excited state and the tautomer is more stable by about 20 kcal/mol.<sup>[25]</sup> Chaban and co-workers also note that the addition of a water molecule to the 7-azaindole monomer results in a lowering of the reaction barrier height to an upper limit of 6 kcal/mol, and postulate that another water molecule would further lower the reaction barrier so as to allow an excited-state proton transfer. Schmedarchina and co-workers reported that water can act as an efficient proton bridge in the proton-transfer reaction of 7-azaindole.<sup>[26]</sup> They found through direct -dynamics calculations that the addition of one water molecule to 7-azaindole allowed tautomerization to occur and that the addition of a second water would allow tautomerization to occur on a similar time scale, despite the geometrical difficulties associated with triple proton transfer through the double water bridge.

Hydrated monomer clusters were generated with one to four waters, as observed in the TOF-MS. Due to wavelength restrictions, the second harmonic of the femtosecond laser was deemed unlikely to access the excited state for the monomer clustered with one water. Hence, the data for this cluster are not included in the discussion. Nakajima and co-workers have experimentally determined the photon energy necessary to excite the 7-azaindole monomer solvated with one to three water molecules.<sup>[13]</sup> They found the requisite wavelengths for attaining the excited states of the doubly- and triply-hydrated 7-azaindole monomer to be 306.45 nm and 307.18 nm, respectively. The wavelength necessary to excite the monomer with four waters is likely to be very close to those reported for two and three waters.

The optical transient pump-probe data for the 7-azaindole monomer with two through to four waters are presented in Figure 4.12. The intensity of the transient data changes in relation to the ionization cross-section of the species being detected. The results of photoelectron spectroscopy experiments performed by Lopez-Martens and co-workers indicate that the tautomer of the 7-azaindole dimer has a much lower ionization efficiency than the normal dimer.<sup>[14]</sup> On the basis of this finding, one would expect to see a decrease in ion intensity as the normal 7-azaindole monomer tautomerizes. The data from the transient signal can then be fitted by appropriate mathematical functions in order to determine the rate of proton transfer. The

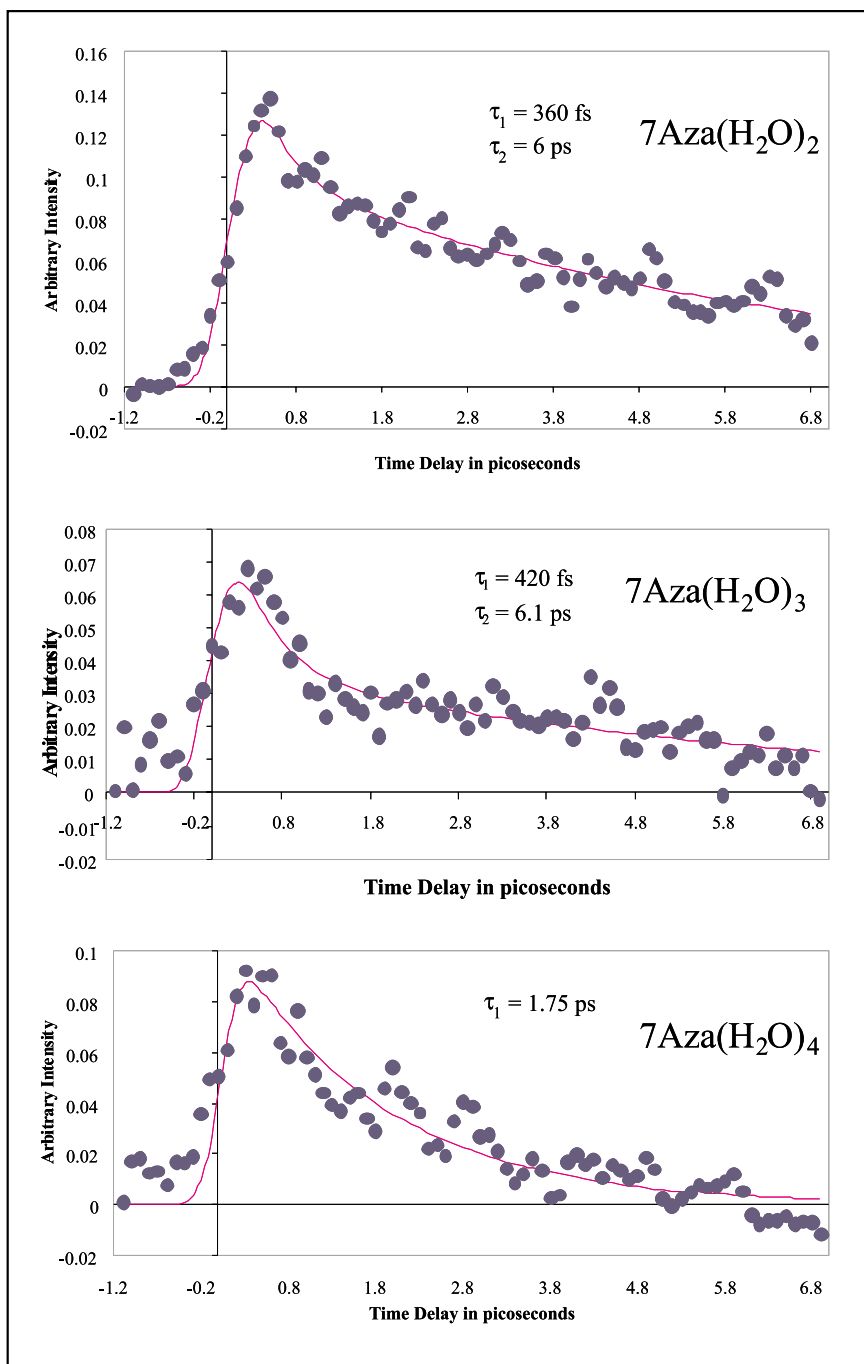


Fig. 4.12 Optical transients for the monomer clustered with two, three, and four waters, respectively.



doubly-hydrated 7-azaindole optical transient was best fitted by a bi-exponential decay function that yielded proton-transfer times of  $360 \pm 50$  fs and  $6.0 \pm 0.5$  ps. The data for the triply-hydrated 7-azaindole were best fitted by a bi-exponential decay function and yielded times of  $420 \pm 80$  fs and  $6.1 \pm 1$  ps. The data for the tetrahydrated 7-azaindole monomer produced a similar change as that seen in the case of the 7-azaindole dimer, where sufficient hydration breaks the symmetry of the planar dimer leading to a stacked structure. The data were best fitted by a single-exponential decay function to yield a time of  $1.8 \pm 0.3$  ps. Studies of the deuterated analogues of each of these three species were also conducted and the times calculated for the proton (deuteron) transfer lengthened considerably. This was to be expected due to isotope effects and further confirmed the occurrence of proton transfer.

The findings of this hydrated monomer study prompted comparisons with theoretical work in which the structures of the hydrated 7-azaindole monomers were calculated. Unfortunately, structures have only been reported in the literature for 7-azaindole clustered to one, two, and three water molecules.<sup>[13]</sup> Consequently, calculations were performed in our laboratory to determine the structures of 7-azaindole solvated with one through to four waters. Gaussian-98 was employed at the Hartree-Fock level of theory with a 6-31G basis set,<sup>[27]</sup> using the Pennsylvania State University's IBM RS/6000 SP high-performance computers. The structures obtained were compared to the lowest-energy species calculated by Nakajima and co-workers and the bond lengths were found to agree almost exactly for the 7-azaindole monomer hydrated by one to three waters. Because of the accuracy of these calculations, the bond lengths obtained for the 7-azaindole monomer with four waters were accepted as being reasonable values. Surprisingly, the bond lengths obtained for the tetrahydrated 7-azaindole were shortened by about 0.2 Å compared to the values obtained for the mono-, di-, and trihydrated cases. From these data, it seems quite feasible that the four water molecule circuit could provide a faster, more efficient route for transfer of the proton to yield the tautomer of 7-azaindole, which would also account for the transition from a bi-exponential process to a single-exponential mathematical function. Experimental studies by our group coupled with theoretical calculations like those of Cheng and co-workers<sup>[28]</sup> yield valuable information concerning the mechanism of proton transfer along "water wires" and in biological systems.

#### 4.4

#### Conclusions

The study of the 7-azaindole molecule, while not complete, has yielded much information on intermediate states, proton transfer, and solvent effects on reactions. The study of proton-transfer reactions is important since they can provide a solid foundation for the complete understanding of biological systems. The model base pair, 7-azaindole dimer, gives insight into the behavior of actual base pairs. Solvent-effect experiments are particularly important with regard to the understanding of biological systems due to the ubiquitous nature of water. Cluster science has long been

used to gain insights into condensed-phase properties while investigating gas-phase species. By clustering 7-azaindole with water, information is garnered concerning the role of solvation in proton-transfer reactions. In the case of the 7-azaindole dimer, the addition of water molecules has been found to result in an increase in the rate of proton transfer. Further solvation of the dimer provides insight as to why the 7-azaindole cannot be studied in polar media. As the solvation is discretely increased, a transition point is reached, at which a conformational change may occur that shifts the planar dimer into a stacked structure. Further solvation may completely isolate the two moieties of the dimer, so as to directly mimic the bulk solution case.

The 7-azaindole dimer also provides an ideal system for the use of the Coulomb explosion imaging method and allows direct evidence of the intermediate state to be garnered. CEIM offers an alternative technique for interrogating the dynamics of various reactions. In reactions where there is a potential for a step-wise *versus* a concerted step mechanism, CEIM offers a complementary technique to traditional pump-probe spectroscopy.

### Acknowledgements

Funding by the Air Force Office of Scientific Research, Grant No. F49620-97-1-0183, P05, and the Department of Energy, Grant No. DE-FG02-92ER14258, is gratefully acknowledged.

### References

- 1 A. H. Zewail, *Femtochemistry – Ultrafast Dynamics of the Chemical Bond*, vols. I and II, World Scientific, Singapore, 1994.
- 2 D. E. Folmer, L. Poth, E. S. Wisniewski, A. W. Castleman, Jr., *Chem. Phys. Lett.* **1998**, 287, 1–7.
- 3 J. Purnell, E. M. Snyder, S. Wei, A. W. Castleman, Jr., *Chem. Phys. Lett.* **1994**, 229, 333–339.
- 4 E. M. Snyder, S. Wei, J. Purnell, S. A. Buzza, A. W. Castleman, Jr., *Chem. Phys. Lett.* **1996**, 248, 1–7.
- 5 J. V. Ford, L. Poth, Q. Zhong, A. W. Castleman, Jr., *J. Chem. Phys.* **1999**, 110, 6257–6267.
- 6 J. V. Ford, L. Poth, Q. Zhong, A. W. Castleman, Jr., *Int. J. Mass. Spec.* **1999**, 192, 327–345.
- 7 L. Poth, A. W. Castleman, Jr., *J. Phys. Chem. A* **1998**, 102, 4075–4081.
- 8 I. Last, I. Schek, J. Jortner, *J. Chem. Phys.* **1997**, 107, 6685.
- 9 J. D. H. Watson, F. H. C. Crick, *Nature* **1953**, 171, 737.
- 10 K. Fuke, H. Yoshiuchi, K. Kaya, *J. Phys. Chem.* **1984**, 88, 5840.
- 11 K. Fuke, K. Kaya, *J. Phys. Chem.* **1989**, 93, 614–621.
- 12 Y. Huang, S. Arnold, M. Sulkes, *J. Phys. Chem.* **1996**, 100, 4734.
- 13 A. Nakajima, M. Hirano, R. Hasumi, K. Kaya, H. Watanabe, C. C. Carter, J. M. Williamson, T. Miller, *J. Phys. Chem.* **1997**, 101, 392–398.
- 14 R. Lopez-Martens, P. Long, D. Solgadi, B. Soep, J. Syage, P. Millie, *Chem. Phys. Lett.* **1997**, 273, 219–226.
- 15 A. Douhal, S. K. Kim, A. H. Zewail, *Nature* **1995**, 378, 260.

- 16 D. E. Folmer, E. S. Wisniewski, S. M. Hurley, A. W. Castleman, Jr. *PNAS* **1999**, 96, 12980–12986.
- 17 W. T. Silfvast, *Laser Fundamentals*, Cambridge University Press, New York, 1996, pp. 376.
- 18 F. W. McLafferty, D. B. Stauffer, *The Wiley/NBS Registry of Mass Spectral Data*, vol. 1, Wiley, New York, 1989, p. 115.
- 19 A. Douhal, V. Guallar, M. Moreno, J. M. Lluch, *Chem. Phys. Lett.* **1996**, 252, 370.
- 20 A. W. Castleman, Jr., K. H. Bowen, *J. Phys. Chem.* **1996**, 100, 12911–12944.
- 21 K. Liu, M. G. Brown, C. Carter, R. J. Saykally, J. K. Gregory, D. C. Clary, *Nature* **1996**, 381, 501–503.
- 22 N. Lee, R. G. Keese, A. W. Castleman, Jr., *J. Colloid Interface Sci.* **1980** 75, 555–565.
- 23 P. Hobza, Private communication.
- 24 D. E. Folmer, E. S. Wisniewski, J. R. Stairs, A. W. Castleman, Jr., *J. Phys. Chem. A* **2000**, 104, 10545–10549.
- 25 G. M. Chaban, M. S. Gordon, *J. Phys. Chem.* **1999**, 103, 185.
- 26 Z. Smedarchina, W. Siebrand, A. Fernandez-Ramos, L. Gorb, J. Leszczynski, *J. Chem. Phys.* **2000**, 112, 566.
- 27 Gaussian 98, Revision A.6 (M. J. Frisch, G. W. Trucks, H. B. Schlegel, G. E. Scuseria, M. A. Robb, J. R. Cheeseman, V. G. Zakrzewski, J. A. Montgomery, Jr., R. E. Stratmann, J. C. Burant, S. Dapprich, J. M. Millam, A. D. Daniels, K. N. Kudin, M. C. Strain, O. Farkas, J. Tomasi, V. Barone, M. Cossi, R. Cammi, B. Mennucci, C. Pomelli, C. Adamo, S. Clifford, J. Ochterski, G. A. Petersson, P. Y. Ayala, Q. Cui, K. Morokuma, D. K. Malick, A. D. Rabuck, K. Raghavachari, J. B. Foresman, J. Cioslowski, J. V. Ortiz, B. B. Stefanov, G. Liu, A. Liashenko, P. Piskorz, I. Komaromi, R. Gomperts, R. L. Martin, D. J. Fox, T. Keith, M. A. Al-Laham, C. Y. Peng, A. Nanayakkara, C. Gonzalez, M. Challacombe, P. M. W. Gill, B. Johnson, W. Chen, M. W. Wong, J. L. Andres, C. Gonzalez, M. Head-Gordon, E. S. Replogle, and J. A. Pople, Gaussian, Inc., Pittsburgh PA, 1998).
- 28 R. R. Sadeghi, H. Cheng, *J. Chem. Phys.* **1999**, 111, 2086–2094.

## 5

# Femtosecond Dynamics at Conical Intersections

Wolfgang Domcke

## 5.1

### Introduction

Although the possibility of exact degeneracies of electronic potential-energy surfaces of polyatomic molecules has been known since the early days of quantum mechanics,<sup>[1,2]</sup> it has long been assumed in the chemical literature that true surface crossings are rare phenomena, being primarily associated with high symmetries of the nuclear frame (the so-called Jahn–Teller effect<sup>[3]</sup>). Recent progress in *ab initio* quantum chemistry, in particular the development of multi-configuration self-consistent-field and configuration-interaction techniques, has allowed the systematic investigation of surface crossings in polyatomic molecules. These computational studies have revealed that so-called conical intersections<sup>[4]</sup> of adiabatic potential-energy surfaces, even between states of the same symmetry, are a very common phenomenon in polyatomic systems.<sup>[5–8]</sup> For triatomic molecules, the topology of the surfaces has been analyzed in detail.<sup>[9–13]</sup> For larger polyatomic systems, the minima of the hypersurfaces of intersection have been located with the help of geometry optimization methods.<sup>[14–16]</sup> In a few cases, the topology of polyatomic potential-energy surfaces has been characterized as a function of selected vibrational coordinates around the conical intersection by means of accurate *ab initio* calculations.<sup>[8,17]</sup> The ubiquity of conical intersections confirmed by these studies strongly supports the conjecture that conical intersections play a universal mechanistic role in photochemistry.<sup>[18–20]</sup>

Early attempts to treat the dynamics at conical intersections were based on the Landau–Zener approach.<sup>[21,22]</sup> While the Landau–Zener model<sup>[23]</sup> provides a transparent picture for one-dimensional avoided-crossing situations, its generalization to multi-dimensional nuclear motion is nontrivial, and no quantitative results were obtained in these early studies.

In an alternative approach, exact (numerical) time-dependent quantum wavepacket methods have been employed since the early 1980s to explore the dynamics of *ab initio* based models of conical intersections; see refs.<sup>[24–26]</sup> for reviews. These calculations have clearly shown that the fundamental dissipative processes of population and phase relaxation at femtosecond time scales are expressed even in few-mode systems, if a directly accessible conical intersection of the potential-energy

surfaces is involved. The results strongly support the idea that conical intersections provide the microscopic mechanism for ultrafast relaxation processes in polyatomic molecules.<sup>[24–26]</sup> More recently, these calculations have been extended to describe photodissociation<sup>[27–30]</sup> and photoisomerization<sup>[31,32]</sup> processes associated with conical intersections. The latter are particularly relevant for our understanding of the elementary mechanisms of photochemistry.<sup>[20]</sup>

While it is suggested by these studies that ultrafast internal conversion through a conical intersection typically involves only a few strongly coupled modes, it is clear that this process will create a local vibrational hot spot in a polyatomic molecule. The coupling of the active modes of the conical intersection with the many inactive modes and possibly the environment will cause vibrational energy redistribution, typically on a sub-picosecond time scale. Several attempts to account for this phenomenon have been described in the recent literature. One possibility is the solution of the time-dependent Schrödinger equation for truly multi-dimensional systems, employing efficient numerical techniques. Using the MCTDH method,<sup>[33]</sup> Meyer and collaborators have computed the absorption spectrum of the  $S_1$ – $S_2$  conical intersection in pyrazine for a vibronic-coupling model that included all 24 vibrational modes of this molecule.<sup>[34]</sup> As an alternative, the Feynman path-integral formalism has been adapted for the study of vibronic-coupling models of arbitrary dimension.<sup>[35]</sup> Computationally efficient classical or semi-classical models of electronically nonadiabatic dynamics have been developed and applied to the investigation of the effect of vibrational energy redistribution on the electronic decay dynamics at conical intersections.<sup>[36,37]</sup> Finally, the well-known system-bath formulation and reduced density-matrix theory<sup>[38]</sup> can be used to describe the effect of a dissipative environment on the dynamics at a conical intersection.<sup>[39]</sup> The latter relatively simple approach is adequate when the relaxation effects caused by the system-bath interaction are slow relative to the ultrafast dynamics driven by the active modes of the conical intersection.

Taken together, these recent works yield a view of photophysical relaxation and photochemical reaction dynamics that is substantially different from the traditional concepts in this area. In contrast to the established picture of radiationless transitions in terms of interacting tiers of zero-order molecular eigenstates,<sup>[40]</sup> the dynamics is rationalized in terms of local properties of potential-energy surfaces such as slopes, barriers, and surface intersections, a view which has now become widely accepted in photochemistry.<sup>[19,20]</sup> This picture is firmly based on *ab initio* electronic structure theory, and the molecular relaxation dynamics is described on the basis of quantum mechanics, replacing previously prevailing kinetic models<sup>[41,42]</sup> of electronic decay processes. Such a detailed and rigorous description of elementary photochemical processes appears timely in view of the rich and specific information on ultrafast chemical processes that is being provided by modern time-resolved spectroscopy.<sup>[43–45]</sup>

## 5.2

### Modeling of Conical Intersections

The construction of accurate global descriptions of the Born–Oppenheimer potential-energy surfaces of polyatomic molecules is a difficult problem. For triatomic molecules, which possess just three internal degrees of freedom, it is possible to map out the complete energy surfaces on a sufficiently dense three-dimensional grid, employing state-of-the-art electronic structure theory; see refs.<sup>[11–13]</sup> for examples. For polyatomic systems with more than four atoms, such a systematic and complete mapping of global potential-energy surfaces is not possible. One has to resort to analytical representations, characterized by relatively few parameters, which can be determined by the fitting of *ab initio* data for a representative sample of nuclear geometries.

An important technical concept for the construction of potential-energy surfaces exhibiting conical intersections is the so-called diabatic representation.<sup>[46]</sup> The conventional adiabatic or Born–Oppenheimer representation is defined by:

$$H_{el}(\mathbf{R})\psi_n^{ad}(\mathbf{r}, \mathbf{R}) = V_n(\mathbf{R})\psi_n^{ad}(\mathbf{r}, \mathbf{R}) \quad (1)$$

Here,  $\mathbf{r}$  and  $\mathbf{R}$  represent collectively the electronic and nuclear degrees of freedom and  $H_{el}$  denotes the electronic part of the molecular Hamiltonian (excluding the nuclear kinetic energy). The  $V_n(\mathbf{R})$  are the electronic eigenvalues as a function of the nuclear coordinates defining the adiabatic potential-energy surfaces. Since the electronic wavefunctions  $\psi_n^{ad}(\mathbf{r}, \mathbf{R})$  constructed in this way are  $\mathbf{R}$ -dependent, their derivatives with respect to  $\mathbf{R}$ , the so-called derivative couplings

$$f_{nm}^j(\mathbf{R}) = \int d\mathbf{r} \psi_n^{ad}(\mathbf{r}, \mathbf{R})^* \frac{\partial}{\partial R_j} \psi_m^{ad}(\mathbf{r}, \mathbf{R}) \quad (2)$$

appear in the exact (non-Born–Oppenheimer) equations for the nuclear motion. A conical intersection necessarily involves a discontinuity of  $\psi^{ad}(\mathbf{R})$  as a function of  $\mathbf{R}$ , causing a singularity of the coupling at the intersection.<sup>[47]</sup> For this reason, the adiabatic electronic representation is inconvenient at a conical intersection.

A diabatic representation is given by a set of fixed-nuclei electronic wavefunctions  $\psi_n^{di}(\mathbf{r}, \mathbf{R})$  that are weakly dependent on the nuclear coordinates  $\mathbf{R}$ . In contrast to the adiabatic electronic states defined by Eq. (1), there is no unique diabatic basis. A detailed discussion of possible definitions and explicit constructions of diabatic states is beyond the scope of this article. Comprehensive expositions of this topic can be found in recent reviews.<sup>[10,25,48,49]</sup> For an appropriately chosen diabatic basis, the derivative couplings of Eq. (2) are small and can be neglected in the treatment of the nuclear dynamics. On the other hand, the electronic Hamiltonian is no longer diagonal, and we have to consider electronic inter-state coupling elements:

$$V_{nm}(\mathbf{R}) = \int d\mathbf{r} \psi_n^{di}(\mathbf{r}, \mathbf{R})^* H_{el}(\mathbf{R}) \psi_m^{di}(\mathbf{r}, \mathbf{R}) \quad (3)$$

A generally applicable and particularly simple modeling of conically intersecting potential-energy surfaces is based on the Taylor expansion of the diabatic potential-energy functions and coupling elements around a suitable reference geometry. The reference geometry may be either the locus of intersection itself or another distin-

guished geometry in the vicinity of the intersection (e.g. the ground-state equilibrium geometry). Introducing normal coordinates  $\mathbf{Q}$  (which diagonalize nuclear kinetic energy and potential energy near the reference geometry), the diabatic potential-energy functions are approximated by Taylor expansions up to second order. The following expansions define the first-order ( $\kappa, \lambda$ ) and second-order ( $\gamma$ ) electronic-vibrational coupling constants:<sup>[24]</sup>

$$V_n(\mathbf{Q}) = V_o(\mathbf{Q})E_n + \sum_j \kappa_j^{(n)} Q_j + \sum_{ij} \gamma_{ij}^{(n)} Q_i Q_j + \dots \quad (4)$$

$$V_{nm}(\mathbf{Q}) = V_{nm}(\mathbf{0}) + \sum_j \lambda_j^{(nm)} Q_j + \dots \quad (5)$$

The terms  $\kappa_j^{(n)}$  represent the gradients of the excited-state potential-energy functions at the equilibrium geometry of the ground state and are nonzero for totally symmetric coordinates. Since these modes “tune” the energy gap of different electronic states, leading to intersections of diabatic potential-energy functions, they have been termed “tuning modes”.<sup>[24]</sup> The normal modes for which  $\lambda_j^{(nm)} \neq 0$  are responsible for electronic inter-state couplings and have therefore been termed “coupling modes”.<sup>[24]</sup>

In cases where the nuclear motion remains bounded in the vicinity of the intersection, that is, in the absence of photochemical reactions, the modeling of the potentials by Eqs. (4,5) can provide an adequate description of the photophysical dynamics. A good illustration of this situation is provided by the conical intersection of the  $S_1(n\pi^*)$  and  $S_2(\pi\pi^*)$  electronic states of pyrazine. Figure 5.1 shows a two-dimensional view of the adiabatic potential-energy surfaces, calculated at the CASSCF level, as a function of the tuning mode  $v_{6a}$  and the coupling mode  $v_{10a}$ .<sup>[17]</sup> These potential-energy surfaces can be modeled rather accurately by the low-order Taylor expansions of Eqs. (4,5) in the diabatic representation.<sup>[17]</sup>

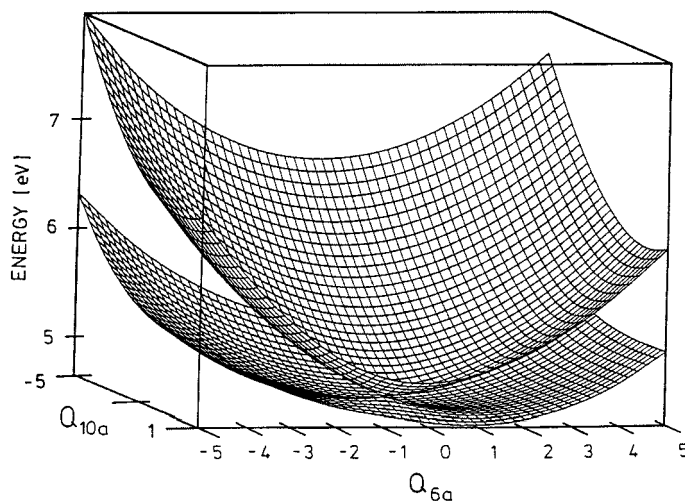


**Fig. 5.1** Perspective view of the adiabatic potential-energy surfaces of the  $S_1(n\pi^*)$ – $S_2(\pi\pi^*)$  conical intersection in pyrazine.

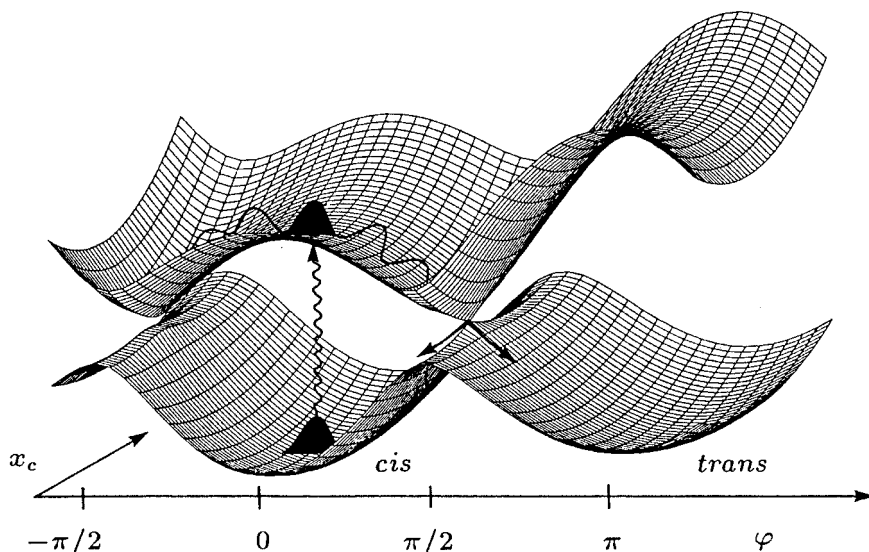


**Fig. 5.2** A model of a conical intersection associated with a *cis-trans* isomerization process.

If one wishes to describe photochemical reaction dynamics triggered by a conical intersection, a more global modeling of the potential-energy surfaces is required. Examples of considerable interest in organic photochemistry and in biophysical chemistry are photoreactions triggered by the twisting of C–C double bonds, e.g. in polyenes and in proteins involved in the process of vision. It has long since been conjectured that such ultrafast photoreactions should proceed through conical intersections, also referred to as photochemical funnels.<sup>[50]</sup> A few attempts have been undertaken to construct potential-energy models for such processes.<sup>[31,32,51]</sup> A generic model of a photochemical funnel induced by a torsional reaction coordinate  $\varphi$  and a coupling coordinate  $x_c$  is displayed in Figure 5.2. It is clear from the schematic picture of wave-packet dynamics outlined in Figure 5.2 that this type of intersection simultaneously governs internal conversion dynamics to the ground state as well as photochemical dynamics (*cis-trans* isomerization).

Although in recent years much progress has been made in *ab initio* electronic structure theory and the efficient interpolation of multi-dimensional potential-energy functions, the selection of the relevant coordinates, the construction of a diabatic representation, and the analytical modeling of potential functions of conical intersections in polyatomic molecules still represent major bottlenecks in the theoretical treatment of photochemical dynamics. In principle, one can try to avoid these bottlenecks by evaluating the adiabatic potentials and the derivative couplings at every point where they are required in a classical or quantum dynamical calculation. Several attempts combining this “on the fly” approach with classical surface-hopping trajectory calculations or similar trajectory-based methods for conical intersections have been reported in the recent literature.<sup>[52,53]</sup> Serious obstacles encountered in this type of approach are the immense cost of these calculations if reasonably accu-



rate *ab initio* methods are to be employed, the phase problem of electronic wavefunctions in the presence of intersections, and the development of quantitatively accurate surface-hopping descriptions. In any case, the development of full-dimensional on-the-fly methods for the dynamics at conical intersections will continue to be an active area of research in the future.

### 5.3

#### Time-Dependent Quantum Wave-Packet and Reduced-Density-Matrix Dynamics

The dynamics of an isolated molecular system, prepared in a nonstationary state  $|\Psi(0)\rangle$  by a short laser pulse, is governed by the time-dependent Schrödinger equation

$$i\hbar\partial/\partial t|\Psi(t)\rangle = H_M|\Psi(t)\rangle \quad (6)$$

where  $H_M = T_N + H_{el}$  is the molecular Hamiltonian,  $T_N$  being the nuclear kinetic energy operator.

The most straightforward numerical technique for the solution of Eq. (6) is based on the expansion of the state vector  $|\Psi(t)\rangle$  in a complete set of time-independent basis functions. Such a complete basis can be constructed as the direct product of diabatic electronic basis states  $\{|\psi_n\rangle\}$  and suitable orthonormal basis states  $\{|\chi_{v_j}\rangle\}$  for each nuclear degree of freedom:

$$|\Psi(t)\rangle = \sum_n \sum_{v_1 v_2 \dots} C_{n,v_1,v_2 \dots}(t) |\psi_n\rangle |\chi_{v_1}\rangle |\chi_{v_2}\rangle \dots \quad (7)$$

This expansion converts the time-dependent Schrödinger equation (6) into a set of coupled first-order differential equations

$$i\hbar \dot{\mathbf{C}}(t) = \mathbf{H}\mathbf{C}(t), \quad (8)$$

where  $\mathbf{C}(t)$  is the vector of expansion coefficients in Eq. (7) and  $\mathbf{H}$  is the corresponding matrix representation of the Hamiltonian. Eq. (8) can be solved by a variety of standard or specialized numerical algorithms.<sup>[55,56]</sup>

There are various options concerning the choice of basis functions or grid representations of the wavefunction, or combinations of both (the so-called discrete variable representation). For a discussion of these technical aspects, see refs.<sup>[25,26,56,57]</sup>

As mentioned in the introduction, only a few vibrational degrees of freedom are usually actively involved in the ultrafast dynamics at the conical intersection. To account for the effect of energy transfer from the active modes to the many inactive modes of the polyatomic molecule or a condensed-phase environment, the reduced-density-matrix formalism may be employed. The molecular Hamiltonian is written as

$$H_M = H_S + H_B + H_{SB}, \quad (9)$$

where  $H_S$  represents a few-mode model of a conical intersection,  $H_B$  stands for a harmonic vibrational bath, and  $H_{SB}$  is the (usually bilinear) system-bath coupling. The standard approximations of quantum relaxation theory<sup>[38]</sup> yield an effective equation of motion for the reduced density operator, expressed as

$$\sigma(t) = \text{tr}_B\{\rho(t)\}, \quad (10)$$

where  $\rho(t)$  is the full time-dependent density operator, and  $\text{tr}_B$  denotes the trace over the bath variables. In the eigenstate representation of the system Hamiltonian

$$H_s|\Psi_\nu\rangle = E_\nu|\Psi_\nu\rangle \quad (11)$$

the resulting equation of motion reads<sup>[38]</sup>

$$\dot{\sigma}_{\mu\nu}(t) = -i\omega_{\mu\nu}\sigma_{\mu\nu}(t) + \sum_{\kappa\lambda} R_{\mu\nu\kappa\lambda}\sigma_{\kappa\lambda}(t) \quad (12)$$

where  $\omega_{\mu\nu} = (E_\mu - E_\nu)/\hbar$ . The first term of the right-hand-side of Eq. (12) describes the time evolution of the isolated system, while the Redfield tensor  $\mathbf{R}$  accounts for the effects of the environment. The elements of  $\mathbf{R}$  are determined by matrix elements of the system-bath coupling operator and Laplace transforms of the bath correlation functions.<sup>[38]</sup> The procedure for the numerical solution of Eq. (12) is analogous to the solution of Eq. (8) (see ref.<sup>[39]</sup> for more details).

Given either the state vector  $\mathbf{C}(t)$  or the reduced density matrix  $\sigma(t)$ , the molecular observables of interest can straightforwardly be evaluated. For example, the time-dependent population probability of the  $n$ th adiabatic electronic state  $|\psi_n^{ad}\rangle$  is given by:

$$\begin{aligned} P_n^{ad}(t) &= \langle \Psi(t) | \psi_n^{ad} \rangle \langle \psi_n^{ad} | \Psi(t) \rangle \\ &= \text{tr}_s\{|\psi_n^{ad}\rangle\langle\psi_n^{ad}| \sigma(t)\}. \end{aligned} \quad (13)$$

## 5.4

### Aspects of Ultrafast Dynamics at Conical Intersections

Extensive investigations of photoinduced chemical dynamics with highest time resolution have revealed that many electronic-decay and electron-transfer processes take place much more rapidly than previously assumed.<sup>[43–45]</sup> Time scales of a few tens of femtoseconds, comparable to the period of the fastest molecular vibrations, have often been observed. Traditional rate theory, based on first-order time-dependent perturbation theory in the electronic inter-state coupling, will clearly no longer be applicable in this time regime. Time-dependent quantum wave-packet dynamics on conically intersecting surfaces, on the other hand, can account for such ultrafast non-Born–Oppenheimer processes.<sup>[24–26,31]</sup> The specific features of conical intersections responsible for the ultrafast dynamics are the singularly strong non-Born–Oppenheimer coupling and the pronounced anharmonicity of the adiabatic potential-energy surfaces in the vicinity of the intersection, leading to particularly efficient inter-mode energy-transfer processes.

A particularly well-studied example is the  $S_1$ – $S_2$  conical intersection in pyrazine, referred to above (Figure 5.1). Figure 5.3 shows the time-dependent population probability of the upper ( $S_2$ ) electronic surface, assuming preparation of the  $S_2(\pi\pi^*)$  state at  $t = 0$  by an ultrashort laser pulse. The figure compares the results of a one-dimensional model (coupling mode  $\nu_{10a}$  only, uppermost curve), a two-dimensional

model ( $\nu_{10a}$  and tuning mode  $\nu_{6a}$ ), and a three-dimensional model ( $\nu_{10a}$  and two tuning modes,  $\nu_{6a}$  and  $\nu_1$ ). Inclusion of the coupling mode alone does not lead to any significant electronic population dynamics because of the relatively large vertical energy gap of the  $S_1$  and  $S_2$  states (0.9 eV). The tuning mode  $\nu_{6a}$  induces a low-lying crossing of the  $S_1$  and  $S_2$  potentials and thus, together with  $\nu_{10a}$ , leads to the formation of a conical intersection (cf. Figure 5.1). It can be seen that the conical intersection causes an ultrafast ( $\sim 30$  fs) initial decay of the  $S_2$  population, followed by large irregular fluctuations. Inclusion of the second tuning mode  $\nu_1$  leads to even faster initial decay and to strong suppression of the population fluctuations. Very similar results have been obtained for a variety of systems with conical intersections, e.g.  $C_2H_4^+$ ,<sup>[24]</sup>  $C_6H_6^+$ ,<sup>[26]</sup> and  $NO_2$ .<sup>[24,58]</sup> In all cases that have been studied in detail, it has been found that a minimum of three strongly coupled nuclear degrees of freedom is required to obtain ultrafast irreversible decay of the electronic population.

Inspection of Figure 5.3 reveals that the upper-state population does not decay to zero, but approaches a long-time limit of  $\sim 0.1$  in the three-mode calculation, i.e., 10 % of the population remains on the upper surface. This result is a consequence of the limited phase space of the three-mode model. This limitation of few-mode models can be overcome by considering the coupling of the active modes of the conical intersection with a dissipative environment within the framework of Redfield theory (Eq. (12)). Figure 5.4 shows as a typical result the electronic population dynamics of the two-mode pyrazine model for several values of the dimensionless

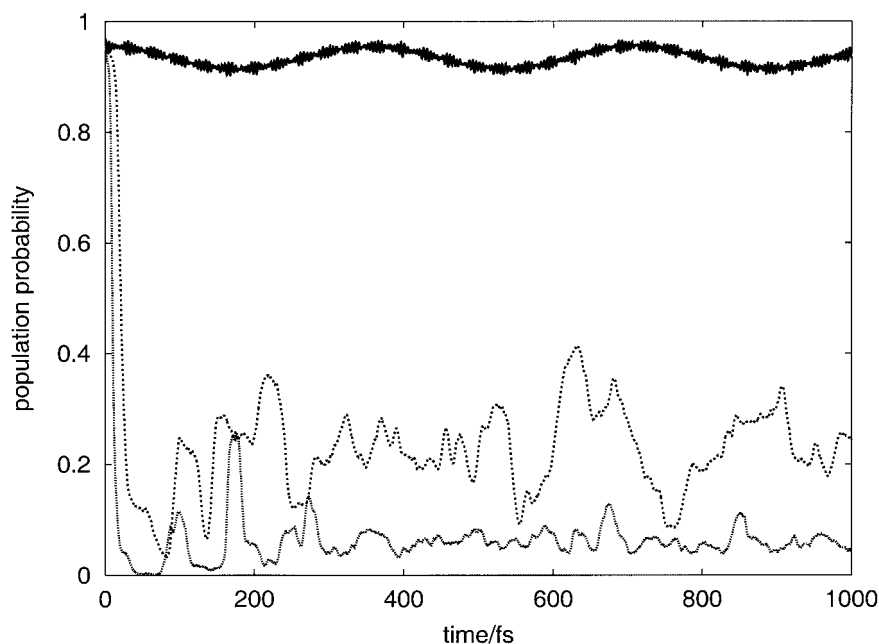


**Fig. 5.3** Time-dependent population probability of the upper adiabatic electronic state for one-dimensional ( $\nu_{10a}$ ), two-dimensional ( $\nu_{10a}, \nu_{6a}$ ), and three-dimensional ( $\nu_{10a}, \nu_{6a}, \nu_1$ ) models of the  $S_1$ – $S_2$  conical intersection in pyrazine.

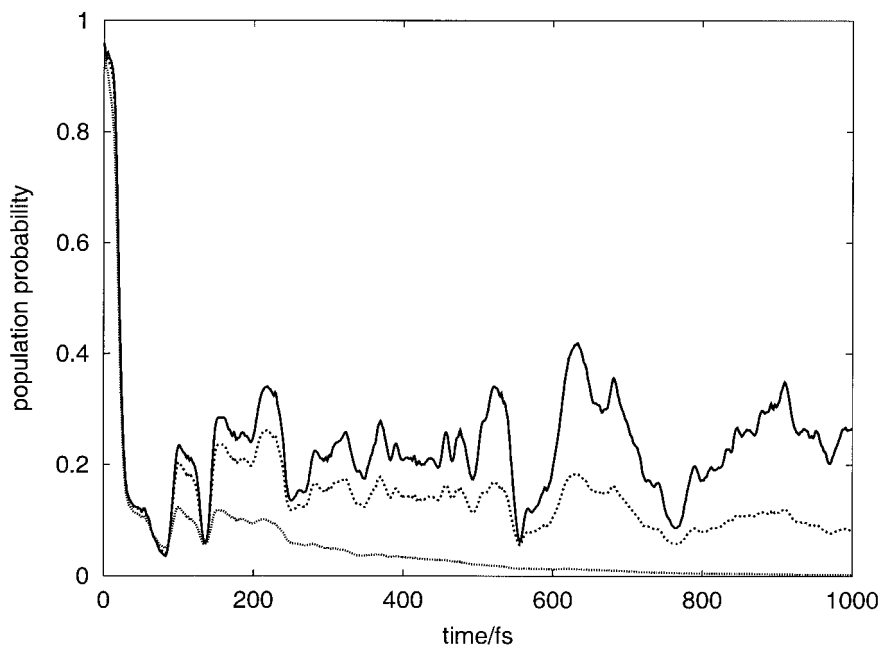


**Fig. 5.4** Time-dependent population probability of the upper adiabatic electronic state for the two-dimensional pyrazine model including dissipation, for three values of the system-bath coupling:  $\eta = 0$  (full line),  $\eta = 0.003$  (dashed line), and  $\eta = 0.015$  (dotted line).

system-bath coupling strength  $\eta$ . It can be seen that even weak dissipation efficiently reduces the amplitude of the population fluctuation of the two-mode model. For sufficiently strong dissipation (dotted curve in Figure 5.4) one observes a smooth decay of  $P_2^{\text{ad}}$  towards zero on a sub-picosecond time scale. The model of a conical intersection with vibrational damping thus predicts a characteristic bimodal radiationless decay pattern. The ultrafast initial decay, on a time scale of a few tens of femtoseconds, is driven by the active modes of the conical intersection. It is followed by slower (sub-picosecond) decay, reflecting vibrational energy relaxation on the lower adiabatic potential-energy surface.

As a second example, consider a conical intersection involving a *cis-trans* reaction coordinate as illustrated in Figure 5.2. In this case, the possibility exists to monitor both the photophysical dynamics through the population  $P_1^{\text{ad}}(t)$  of the upper ( $S_1$ ) adiabatic surface as well as the photochemical dynamics through the population probabilities  $P_{\text{cis}}(t)$  ( $P_{\text{trans}}(t)$ ) of the *cis* (*trans*) conformers. The results shown in Figure 5.5 were obtained for a three-dimensional model, including the torsional mode, a coupling mode, and an additional accepting mode.<sup>[31]</sup> While a one-dimensional model (torsion only) would lead to quasi-periodic torsional motion, the conical intersection leads to ultrafast irreversible photochemical dynamics (Figure 5.5b).

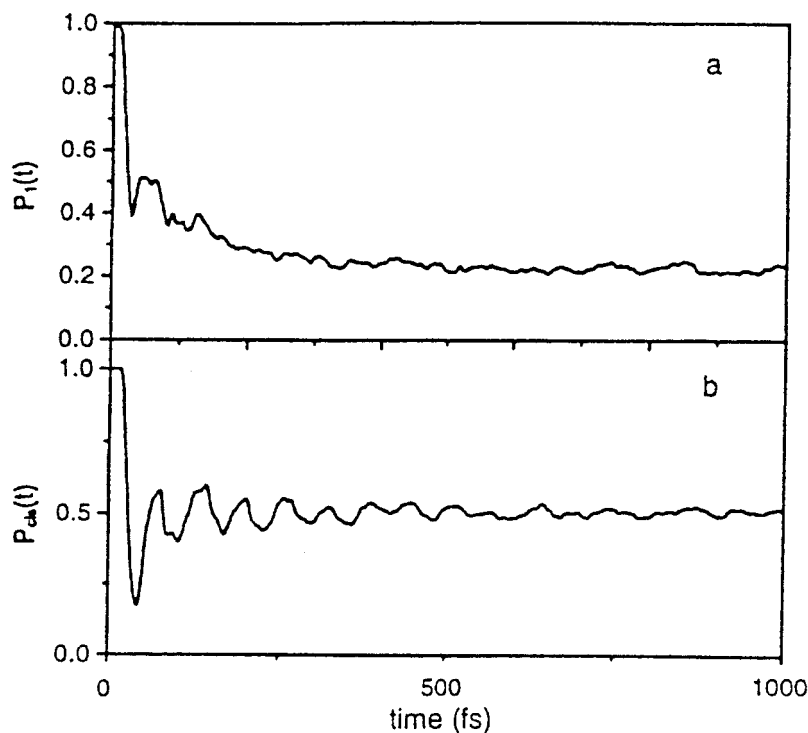


**Fig. 5.5** Time evolution of the population  $P_1(t)$  (three-dimensional conical intersection model of the  $S_1$  surface (a) and of the population  $P_{cis}(t)$  (the type illustrated in Figure 5.2. of the *cis* conformer (b) obtained for a

A detailed picture of the dynamics at a conical intersection can be obtained by analyzing the time-dependent wave-packet during its transition through the conical intersection. From such investigations,<sup>[31,59,60]</sup> the following qualitative picture of the mechanism of a conical intersection emerges. As shown schematically in Figure 5.6, the relevant dynamical phenomena are (i) focusing of the initial wave-packet towards the apex of the cone due to the convex shape of the upper ( $S_1$ ) adiabatic surface, (ii) a first transition through the intersection, which leads to the lower ( $S_0$ ) surface with high probability, (iii) deflection of the recurring wave-packet by the concave shape of lower ( $S_0$ ) adiabatic surface, which prevents return of the wave-packet to the upper surface, and (iv) vibrational energy relaxation involving one or more additional (accepting) modes or a dissipative environment, which lowers the energy content of the active modes below the energy of the point of intersection and ensures the irreversibility of the process.

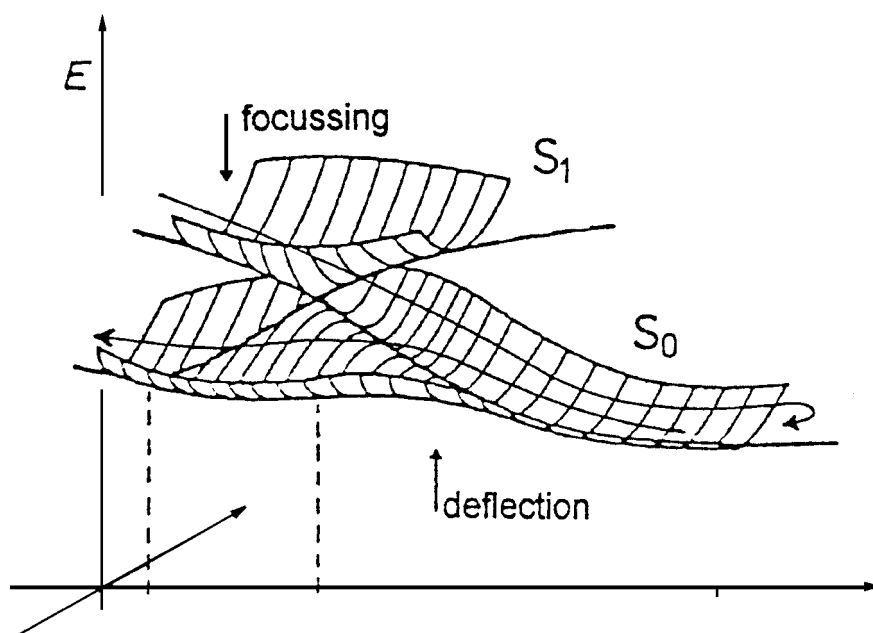


**Fig. 5.6** Qualitative picture of the mechanism of a conical intersection.

## References

- 1 J. von Neumann, E. Wigner, *Physik Z.* **1929**, 30, 467.
- 2 E. Teller, *J. Phys. Chem.* **1937**, 41, 109.
- 3 H. A. Jahn, E. Teller, *Proc. Roy. Soc. (London) A* **1937**, 161, 220.
- 4 G. Herzberg, H. C. Longuet-Higgins, *Discuss. Faraday Soc.* **1963**, 35, 77.
- 5 S. S. Xantheas, G. J. Atchity, S. T. Elbert, K. Ruedenberg, *J. Chem. Phys.* **1991**, 94, 8054.
- 6 D. R. Yarkony, *J. Chem. Phys.* **1994**, 100, 3639.
- 7 F. Bernardi, S. De, M. Olivucci, M. A. Robb, *J. Am. Chem. Soc.* **1990**, 112, 1737.
- 8 A. L. Sobolewski, C. Woywod, W. Domcke, *J. Chem. Phys.* **1993**, 98, 5627.
- 9 G. J. Atchity, K. Ruedenberg, *J. Chem. Phys.* **1993**, 99, 3790.
- 10 D. R. Yarkony, *J. Chem. Phys.* **1996**, 100, 18612.
- 11 C. Woywod, M. Stengle, W. Domcke, H. Flöthmann, R. Schinke, *J. Chem. Phys.* **1997**, 107, 7282.
- 12 E. Leonardi, C. Petrongolo, G. Hirsch, R. J. Buenker, *J. Chem. Phys.* **1996**, 105, 9051.
- 13 D. Simah, B. Hartke, H.-J. Werner, *J. Chem. Phys.* **1999**, 111, 4523.
- 14 N. Koga, K. Morokuma, *J. Chem. Phys.* **1985**, 119, 371.
- 15 D. R. Yarkony, *J. Chem. Phys.* **1993**, 97, 4407.
- 16 F. Bernardi, M. Olivucci, M. A. Robb, *Chem. Soc. Rev.* **1996**, 321.
- 17 C. Woywod, W. Domcke, A. L. Sobolewski, H.-J. Werner, *J. Chem. Phys.* **1994**, 100, 1400.
- 18 E. Teller, *Isr. J. Chem.* **1969**, 7, 227.
- 19 M. A. Robb, F. Bernardi, M. Olivucci, *Pure & Appl. Chem.* **1995**, 67, 783.
- 20 M. Klessinger, J. Michl, *Excited States and Photochemistry of Organic Molecules*, VCH, New York, **1995**.
- 21 E. E. Nikitin, in *Chemische Elementarprozesse* (Ed.: H. Hartmann), Springer, Berlin, **1968**, p. 70.
- 22 M. Desouter-Lecomte, D. Dehareng, B. Leyh-Nihant, M. T. Praet, A. J. Lorquet, J. C. Lorquet, *J. Chem. Phys.* **1985**, 89, 214.
- 23 C. Zener, *Proc. Roy. Soc. (London) A* **1932**, 137, 696.
- 24 H. Köppel, W. Domcke, L. S. Cederbaum, *Adv. Chem. Phys.* **1984**, 57, 59.
- 25 W. Domcke, G. Stock, *Adv. Chem. Phys.* **1997**, 100, 1.
- 26 H. Köppel, W. Domcke, in *Encyclopedia of Computational Chemistry* (Ed.: P. v. R. Schleyer), Wiley, New York, **1998**.
- 27 U. Manthe, H. Köppel, L. S. Cederbaum, *J. Chem. Phys.* **1991**, 95, 1708.
- 28 R. Schinke, *Photodissociation Dynamics*, Cambridge University Press, UK, **1993**.
- 29 H. Guo, G. C. Schatz, *J. Chem. Phys.* **1990**, 92, 1634.
- 30 P. Cattaneo, M. Persico, *J. Phys. Chem.* **1997**, 101, 3454.
- 31 L. Seidner, W. Domcke, *Chem. Phys.* **1994**, 186, 27.
- 32 S. Hahn, G. Stock, *J. Phys. Chem. B* **2000**, 104, 1146.
- 33 M. H. Beck, A. Jäckle, G. A. Worth, H.-D. Meyer, *Phys. Rep.* **2000**, 324, 1.
- 34 A. Raab, G. Worth, H.-D. Meyer, L. S. Cederbaum, *J. Chem. Phys.* **1999**, 110, 936.
- 35 S. Krempel, H. Winterstetter, W. Domcke, *J. Chem. Phys.* **1995**, 102, 6499.
- 36 G. Stock, *J. Chem. Phys.* **1995**, 103, 10015.
- 37 M. Thoss, W. H. Miller, G. Stock, *J. Chem. Phys.* **2000**, 112, 10282.
- 38 K. Blum, *Density Matrix Theory and Applications*, Plenum Press, New York, **1981**.
- 39 A. Kühn, W. Domcke, *Chem. Phys.*, **2000**, 259, 227.
- 40 E. S. Medvedev, V. I. Osherov, *Radiationless Transitions in Polyatomic Molecules*, Springer, Berlin, **1995**.
- 41 B. Bagchi, G. R. Fleming, D. V. Oxtoby, *J. Chem. Phys.* **1983**, 78, 735.
- 42 M. Tachiya, S. Murata, *J. Am. Chem. Soc.* **1994**, 116, 2434.
- 43 A. H. Zewail, *Femtochemistry – Ultrafast Dynamics of the Chemical Bond*, World Scientific, Singapore, **1994**.
- 44 D. A. Wiersma (Ed.), *Femtosecond Reaction Dynamics*, North Holland, Amsterdam, **1994**.
- 45 T. Elsaesser (Eds.), *Ultrafast Phenomena XI*, Springer, Berlin, **1998**.
- 46 F. T. Smith, *Phys. Rev.* **1969**, 179, 111.
- 47 H. C. Longuet-Higgins, in *Advances in Spectroscopy* (Ed.: H. W. Thompson), Interscience, New York, **1961**, Vol. 2, p. 429.
- 48 V. Sidis, *Adv. Chem. Phys.* **1992**, 82, 73.
- 49 T. Pacher, L. S. Cederbaum, H. Köppel, *Adv. Chem. Phys.* **1993**, 84, 293.

- 50 J. Michl, V. Bonacic-Koutecky, *Electronic Aspects of Organic Photochemistry*, Wiley, New York, **1990**.
- 51 A. Ferretti, A. Lami, G. Villani, *Adv. Quant. Chem.* **2000**, 36, 283.
- 52 P. Cattaneo, M. Persico, *Chem. Phys. Lett.* **1998**, 289, 160.
- 53 M. Ben-Nun, T. J. Martinez, *Chem. Phys. Lett.* **1998**, 298, 57.
- 54 W. H. Press, B. P. Flannery, S. A. Teukolsky, W. T. Vetterling, *Numerical Recipes*, Cambridge University Press, UK, **1987**.
- 55 C. Leforestier, R. H. Bisseling, C. Cersan, M. D. Feit, R. Friesner, A. Guldberg, A. Hammerich, G. Jolicard, W. Karrlein, H. D. Meyer, N. Lipkin, O. Roncero, R. Kosloff, *J. Comput. Phys.* **1991**, 94, 59.
- 56 R. Kosloff, in *Numerical Grid Methods and their Application to Schrödinger's Equation* (Ed.: C. Cerjan), NATO ASI Series C 412, Kluwer, Dordrecht, **1993**.
- 57 J. C. Light, T. Carrington, Jr., *Adv. Chem. Phys.*, **2000**, 114, 263.
- 58 F. Santoro, C. Petrongolo, *J. Chem. Phys.* **1999**, 110, 4419.
- 59 R. Schneider, W. Domcke, H. Köppel, *J. Chem. Phys.* **1990**, 92, 1045.
- 60 U. Manthe, H. Köppel, *J. Chem. Phys.* **1990**, 93, 345, 1658.



## 6

# Femtosecond Spectroscopy of Molecular Caging: Quantum and Classical Approaches

Vladimir A. Ermoshin, Volker Engel, and Christoph Meier

## 6.1

### Introduction

Femtosecond pulse-excitation of an ensemble of molecules generally leads to the attainment of a non-stationary quantum mechanical state. The subsequent quantum dynamics can then be detected by pump-probe experiments, as is demonstrated extensively in the present and the former book on *Femtosecond Chemistry*.<sup>[1]</sup> The topic of this chapter is the time-resolved spectroscopy of collision processes. In particular, we are interested in the following scenario: an optical excitation with an ultrashort pulse (pump) induces a transition from the electronic ground state  $|g\rangle$  to an excited state  $|e\rangle$  of a molecule AB. The latter state possesses a potential  $V_e$ , which, in our case, provides bound states. Nevertheless, if the carrier frequency of the pulse is chosen to be sufficiently large, the prepared wave-packet is composed of continuum states, as is indicated in Figure 6.1. Thus, the excitation results in fragmentation. Imagine now a collision of

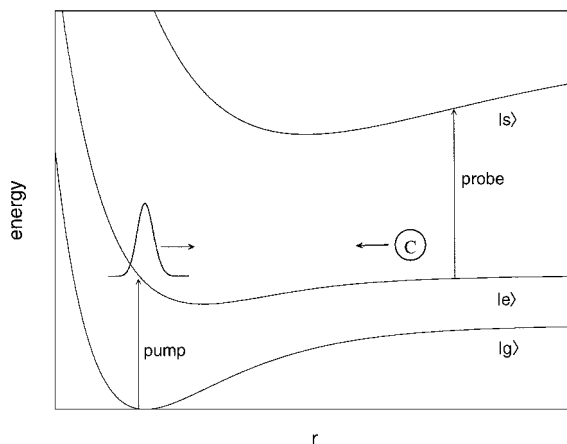


**Fig. 6.1** Schematic illustration of the pump-probe spectroscopy of a collision process. The pump pulse prepares a wave-packet within the dissociation continuum of an AB molecule in the electronically excited state  $|e\rangle$ . A collision

with an atom C may lead to recombination. Finally, the probe pulse populates the molecular electronic state  $|s\rangle$  and the total fluorescence from this state is detected as a function of the pump-probe delay.

the dissociating AB molecule with an atom C. If the collision takes place at an early stage when the wave-packet (describing the relative motion of A–B) is still located in the region above the  $|e\rangle$ -state potential well, an efficient energy transfer to the atom can lead to recombination. The dynamics of the “caged” molecules can then be investigated using a time-delayed second pulse (probe) to record pump-probe signals.

The above process has indeed been observed in a beautifully designed experiment by Zewail and co-workers.<sup>[2]</sup> They used  $I_2$  molecules in rare-gas environments and the transients, which were obtained under different pressure conditions, showed clear evidence of iodine caging. In the following, we will use the  $I_2/Ar$  system to illustrate theoretical approaches for the description of femtosecond time-resolved spectroscopy applied to such collision processes.

## 6.2

### Quantum Treatment

We consider first the single collision between a molecule AB and an atom C. Before the scattering event takes place, AB is excited with a femtosecond laser pulse from its electronic ground state  $|g\rangle$  to an electronically excited state  $|e\rangle$ . Treating this excitation within first-order perturbation theory, one arrives at the following equation for the molecular state (atomic units are used):

$$|\Psi_e^{(1)}(t)\rangle = -i \int_{-\infty}^t dt' U_e(t-t') W_1(t') U_g(t') |\Psi_g\rangle \quad (1)$$

Here,  $|\Psi_g\rangle$  is the initial state,  $U_{g,e}(t)$  is the time-evolution operator in the respective electronic state, and the field–molecule interaction in the dipole approximation is given as

$$W_1(t) = -\frac{1}{2} \mu_{eg} f(t) e^{-i\omega_1 t} \quad (2)$$

In this expression,  $f(t)$  denotes the pulse envelope,  $\omega_1$  is the frequency, and  $\mu_{eg}$  is the projection of the transition dipole moment on the polarization axis of the electric field. Only the term leading to absorption was kept in Eq. (2).

For a short pulse, several nuclear eigenstates (in the electronic  $|e\rangle$  state) of the system are excited simultaneously so that  $|\Psi_e^{(1)}(t)\rangle$  consists of a coherent superposition of these states.

Next, we consider a collision where the incoming scattering state is of the product form

$$|\Psi_{in}(t)\rangle = |\Psi_e^{(1)}(t)\rangle |\Psi_C(t)\rangle \quad (3)$$

Here,  $|\Psi_C(t)\rangle$  describes the free motion of the atom C. The simulation of the scattering event, which can be performed by solving the time-dependent Schrödinger equation numerically, requires the specification of initial conditions; in particular, the parameters for the atomic wave-packet have to be defined.<sup>[3]</sup>

When the collision is over at time  $t = t_{sc}$ , the outgoing scattering state is no longer of the simple form of Eq. (3). An expansion in terms of a discrete set of free atomic states  $|k\rangle$  yields

$$|\Psi_{out}^{(1)}(t)\rangle = U_e(t - t_{sc}) U_C(t - t_{sc}) \sum_k |\Psi_k^{(1)}(t_{sc})\rangle |k(t_{sc})\rangle \quad (4)$$

Since the collision partners have separated for times  $t > t_{sc}$ , the three-body Hamiltonian is the sum of the Hamiltonians of AB and C with no interaction term present. As a consequence, the propagator splits into a molecular ( $U_e$ ) and an atomic ( $U_C$ ) part.

Within the same formalism as used for the pump transition, the probe transition, occurring to another molecular electronic state  $|s\rangle$  yields

$$|\Psi_{out}^{(2)}(t)\rangle = -i \int_{-\infty}^t dt' U_s(t - t') U_C(t - t') W_2(t' - \tau) U_e(t') U_C(t') |\Psi_{out}^{(1)}(0)\rangle \quad (5)$$

where, for convenience, the time  $t_{sc}$  is set to zero. We can now introduce the molecule-field interaction

$$W_2(t - \tau) = -\frac{1}{2} \mu_{se} f(t - \tau) e^{-i\omega_1(t - \tau)} \quad (6)$$

which is centered around the delay time  $\tau$ , the notation used being as that used above. By virtue of the fact that the atom is not coupled to the field, inserting expansion (4) into Eq. (5) one arrives at the expression:

$$|\Psi_{out}^{(2)}(t)\rangle = -i U_s(t) U_C(t) \sum_k |k\rangle \int_{-\infty}^t dt' U_s(-t') W_2(t' - \tau) U_e(t') |\Psi_k^{(1)}(0)\rangle \quad (7)$$

Assuming that the pump-probe signal is proportional to the norm of the state  $|\Psi_{out}^{(2)}(t)\rangle$  after the pulses have passed the sample, the signal takes the form

$$S(\tau) = \lim_{t \rightarrow \infty} \sum_k \langle \Psi_k^{(2)}(t) | \Psi_k^{(2)}(t) \rangle \quad (8)$$

with the definition

$$|\Psi_k^{(2)}(t)\rangle = \int_{-\infty}^t dt' U_s(-t') W_2(t' - \tau) U_e(t') |\Psi_k^{(1)}(0)\rangle \quad (9)$$

Some comments are in order here. First, we note that the calculation of the signal needs solutions of the time-dependent Schrödinger equation for the coupled AB/C system. Using the expansion as above, the problem can be reduced to the evaluation of a set of solutions for fixed atomic states  $|k\rangle$  in the AB subspace. The description outlined above neglects collisions that take place during the optical transitions. This simplification was made purely to keep the discussion as transparent as possible. If the atomic and molecular densities are sufficiently low, such that the mean collision time between two scattering events is much longer than the pulse widths, this approximation is reasonable.

Of particular interest is the time-dependent aspect of the collision: since the AB molecule is not in a stationary state, it is of importance *when* the collision takes place. Depending on this time, the momentum transfer between the collision partners differs. This means that even if the initial translational energies and angular momenta of AB and C are well defined, a realistic prediction of the outcome of the scattering event requires an average over time. In practice, one has to vary the initial position of the incoming wave-packet for the C atom. The values for these positions are determined taking the experimental conditions (such as the pressure and temperature) into account.

### 6.3

#### Classical Treatment

Given the interaction potential of the collision complex AB–C, a classical treatment of a single scattering event is easily performed by solving the classical equations of motion. However, we first have to introduce a classical scheme for treating the femtosecond excitation and calculating the pump-probe signals. There are many procedures for achieving this<sup>[4,5,6]</sup> and we will outline one of them in the following.

In a first step, the quantum mechanical wave-packet  $|\psi_e^{(1)}(r)\rangle$  ( $r$  denotes the internal coordinates of AB) is represented by an ensemble of trajectories. The initial conditions for the coordinates  $r$  and the momenta  $p$  of AB are sampled from the distribution function:

$$\rho_B(r, p) = \exp\left(-\frac{V_g(r) + p^2/2m}{k_B T}\right) \exp\left(-\tau^2(V_e(r) - V_g(r) - \omega_1)^2\right) \quad (10)$$

Here,  $T$  is the temperature,  $m$  is the reduced mass of AB, and  $V_{e,g}(r)$  is the potential in the electronic state  $|e\rangle, |g\rangle$ , respectively. The sampling function is a product of two exponential functions. The first one gives the (Boltzmann) statistical weights, while the second exponential in Eq. (10) defines the Franck–Condon window for the pump transition. The latter is obtained as the Fourier-transform of the pump-pulse temporal shape function with respect to the difference in potentials,  $V_e - V_g$ . Mathematically, the Franck–Condon window results from an approximate evaluation of the integral in Eq. (1), where the kinetic-energy operators appearing in  $U_e$ ,  $U_g$  are neglected.<sup>[7,8,9]</sup>

Having defined the initial conditions for the AB internal motion, we also have to specify initial conditions for the AB and C translational motion. These can be taken from the Maxwell–Boltzmann distribution defined by the experimental conditions. A straightforward method to account for different pressures of the C atoms is to consider a fixed spatial box of volume  $V$  and to distribute  $N_C$  atoms within the box. The pressure is then proportional to the density,  $N_C/V$ .

The transient signal can be approximated classically as (see, e.g., refs.<sup>[4,5,6]</sup>)

$$S(\tau) = \frac{1}{N} \sum_{i=1}^N \int dt f(t - \tau) g(r_i(t)) \quad (11)$$

where the sum extends over the number  $N$  of initial configurations for the AB/C system. Here,  $g(r_i(t))$  denotes the Franck–Condon window for the probe transition. The time-integral represents the temporal window accounting for the finite width of the excitation pulse. Thus,  $S(\tau)$  counts the AB trajectories located within the window during the probe process.

### 6.4

#### I<sub>2</sub>/Ar Caging

Quantum mechanically calculated pump-probe signals for the unperturbed I<sub>2</sub> molecule and for I<sub>2</sub> molecules in an argon environment at 50 bar pressure are displayed in Figure 6.2 (lower panel); details of the numerical calculations can be found in

ref.<sup>[3]</sup> At zero argon pressure, we find a single peak in the transient signal. By inspection of Figure 6.1, it is easy to identify the origin of this peak: the pump pulse generates a wave-packet that is composed of continuum states within the electronic state  $|e\rangle$  (here: the B-state of iodine). This packet moves outward and passes the Franck–Condon window for the probe transition giving rise to a maximum in the signal. In fact, the curve closely resembles the modulus of the coordinate-space wave-packet describing molecular dissociation.<sup>[10]</sup>

The appearance of the pump-probe signal changes in an Ar environment: a background exhibiting regular structures appears with increasing pressure. Obviously, this effect is due to  $I_2$ –Ar collisions: if a dissociating iodine molecule is hit by an argon atom, it loses energy so that recombination becomes possible. This process is effective at short times after the pump process is over, i.e., as long as the I–I distances are not too large. Analysis of the quantum results shows that only collisions

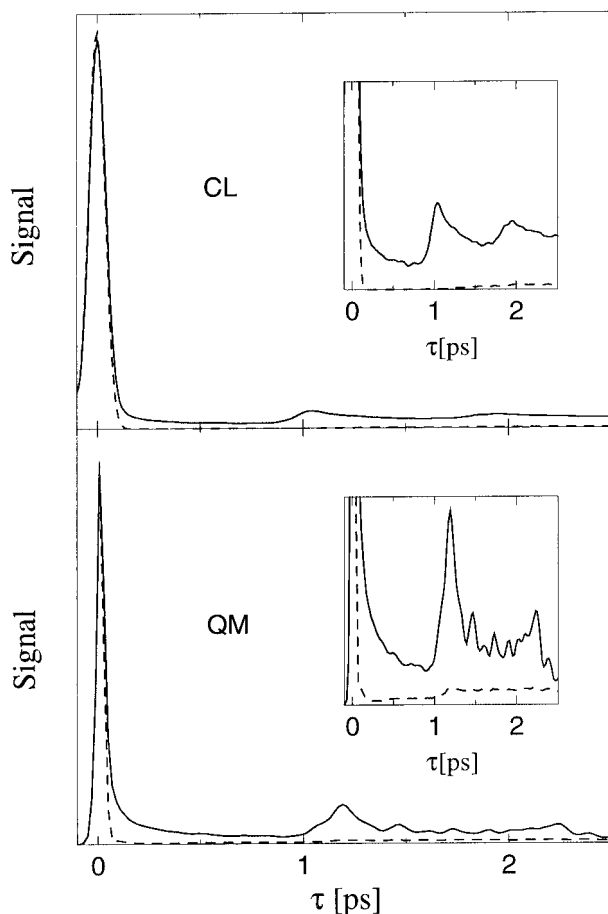


**Fig. 6.2** Pump-probe signals calculated quantum mechanically (lower panel) and classically (upper panel). Curves for 0 bar argon (dashed

line) and 50 bar argon (solid line) are displayed. The inserts show the background signals on an enlarged scale.

occurring close to the collinear I–I–Ar configuration lead to significant caging. It is remarkable that the long time scale signals do not merely show a structureless background, as might be expected from randomly occurring collisions, but instead exhibit regular and prominent features. The latter resemble peaks arising from the detection of the vibrational dynamics performed by a localized wave-packet.

The classically calculated transients are displayed in the upper panel of Figure 6.2. Comparison with the quantum results reveals minor differences, which can be attributed to the different statistical methods employed in the two calculations and the approximations introduced. Nevertheless, the classically obtained results show the same background signal with the superimposed structures. The agreement gives us confidence in a complete classical characterization of the recombination process. We note in passing that an even simpler calculation within a random perturber model yields almost identical results.<sup>[11,12]</sup> Besides the numerical efficiency of the classical calculation, the latter approach has another big advantage: from all the trajectories we may isolate those that correspond to the caging process. This provides a valuable means for interpreting the structures appearing in the signals.

Although it is clear that, upon caging, pump-probe transients will exhibit evidence for this process, it is not clear as to why they should exhibit regular temporal variations at longer delay times. To gain insight into the origin of these features, let us consider the classical distribution of I<sub>2</sub> trajectories, defined as

$$\rho(r, t) = \frac{1}{N} \sum_{i=1}^N \delta(r - r_i(t)) \quad (12)$$

The  $\delta$  function selects all trajectories that assume the value of  $r$  at time  $t$  (in practice one has to introduce a box of length  $\Delta r$  around  $r$ ). Figure 6.3 shows  $\rho(r, t)$ , calculated for an Ar pressure of 50 bar. The dark areas indicate a high density of trajectories. It can be taken from the figure that many orbits move outward at early times, so that they correspond to dissociating molecules. Clearly, there exist caged trajectories and, in particular, one finds several lines of high intensity. Since the probe window is located at around ca. 8.6 a.u., these maxima give rise to peaks in the pump-probe signal. A careful analysis of the properties of those trajectories that correspond to recombined iodine molecules shows the following:<sup>[13]</sup> the collisions generate a manifold of orbits, which, at a specific time, are well-localized in the bond length  $r$  but have a broad momentum distribution. The dynamical behavior of such an ensemble of trajectories is illustrated in Figure 6.3. The bound orbits were started at a distance of 5 a.u. with different momenta. When they reach their outer turning points for the second time, it can be seen that they intersect with each other. The crossing points of the adjacent trajectories define a curve that coincides with the intensity maxima in the radial distribution function obtained from the full-dimensional scattering calculation. The same features were encountered at later times after several vibrational periods had elapsed. Such behavior is well known in optics and the corresponding surfaces that are associated with a higher light intensity are known as caustics;<sup>[14]</sup> for a more detailed discussion concerning the caustics and their relation to the quantum dynamics, see ref.<sup>[13]</sup>

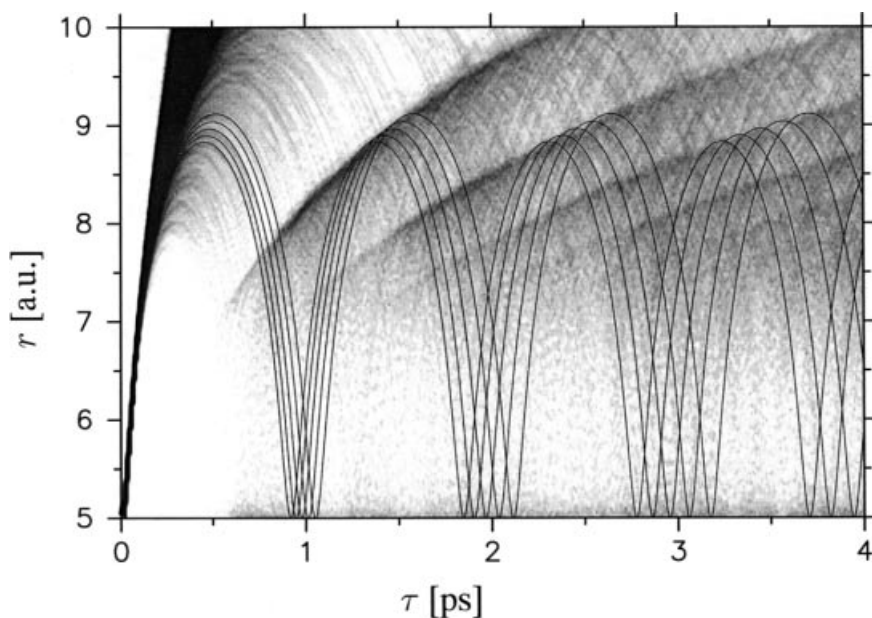


**Fig. 6.3** Time dependence of the classical radial density. Also shown are several trajectories moving in the B-state potential. They were started at the same position with

different momenta. The intersections of the orbits close to their outer turning points give rise to the intensity maxima seen in the density.

## 6.5 Summary

We have outlined theoretical approaches to describe femtosecond experiments on molecules that are perturbed by collisions with atoms. Whereas the quantum mechanical calculation is numerically demanding and does not allow for a treatment of multiple collisions, the computationally efficient classical molecular dynamics simulation is capable of describing more complicated systems such as that considered here. We have presented an application to the time-resolved spectroscopy of  $I_2$  in Ar. Here, both methods give excellent agreement with experiment. Within the classical simulation, we were able to explain the regular patterns seen in the transients at higher pressures. These structures reflect the classical dynamics of trajectories corresponding to recombined molecules. The ensemble of orbits exhibits density maxima in analogy to optical rays characterized by caustics.

## Acknowledgements

This work was supported by the Deutsche Forschungsgemeinschaft (Schwerpunktprogramm "Time-dependent phenomena and methods in quantum systems of physics and chemistry"), the PROCOPE program, and the Fonds der Chemischen Industrie.

## References

- 1 J. Manz, L. Wöste (Eds.), *Femtosecond Chemistry*, VCH, Weinheim, 1995.
- 2 C. Wan, M. Gupta, J. S. Baskin, Z. H. Kim, A. H. Zewail, *J. Chem. Phys.* **1997**, *106*, 4353.
- 3 C. Meier, V. Engel, A. J. Beswick, *Chem. Phys. Lett.* **1998**, *106*, 487.
- 4 Z. Li, J.-Y. Fang, C. C. Martens, *J. Chem. Phys.* **1996**, *104*, 6919.
- 5 H. Dietz, V. Engel, *J. Phys. Chem. A* **1998**, *102*, 7406.
- 6 Y.-C. Shen, J. A. Cina, *J. Chem. Phys.* **1999**, *110*, 9793.
- 7 M. Lax, *J. Chem. Phys.* **1952**, *20*, 1752.
- 8 M. Braun, C. Meier, V. Engel, *J. Chem. Phys.* **1995**, *103*, 7907.
- 9 E. M. Hiller, J. A. Cina, *J. Chem. Phys.* **1996**, *105*, 3419.
- 10 V. Engel, N. E. Henriksen, *J. Chem. Phys.* **2000**, *112*, 106.
- 11 H. Dietz, V. Engel, *J. Chem. Phys.* **1999**, *110*, 3335.
- 12 K. B. Møller, A. H. Zewail, *Chem. Phys. Lett.* **1999**, *309*, 1.
- 13 V. A. Ermoshin, C. Meier, V. Engel, *J. Chem. Phys.*, **2000**, *113*, 6585.
- 14 M. Born, E. Wolf, *Principles of Optics*, Cambridge University Press, Cambridge, 1997.



## 7

# Ultrafast Geometrical Relaxation in Polydiacetylene Induced by Sub-5-fs Pulses

*Takayoshi Kobayashi*

### Abstract

The relaxation time of the free-exciton→geometrically relaxed  $2^1A_g$  state in a polydiacetylene is determined as 65–80 fs depending on the probe energy. It includes the processes of internal conversion, geometrical relaxation from the acetylene-type configuration to the butatriene-type configuration, and thermalization among intra-chain vibrational modes. The vibrational non-equilibrium in the relaxed  $2^1A_g$  state is characterized by the modulations of instantaneous frequencies and amplitudes of the C–C, C=C, and C≡C stretching modes with long oscillation periods. The most prominent modulation was found between the C–C and C=C modes. This is the first real-time observation of dynamic vibrational mode coupling.

### 7.1

#### Introduction

Recent progress in the field of femtosecond lasers has enabled us to observe the real-time dynamics of nuclear motions in molecular systems. Femtosecond lasers with pulse widths shorter than 100 fs are commercially available and even sub-5-fs pulses have been reported.<sup>[1–3]</sup> These are expected to find application in various fields. Of the many possible applications of such short pulses, femtochemistry is one of the most actively studied fields.<sup>[4,5]</sup> Wavelength conversion, pulse shaping, and phase modulation are applicable to the coherent control of chemical reactions.<sup>[4,5]</sup> Recently, the study of how optical phase properties affect nuclear wavepacket motion in the excited-state and ground-state dynamics in molecular systems has emerged as an important issue. One example of an application in basic science is the generation of a vibrationally squeezed state by using an ultrashort or chirped pulse.<sup>[6]</sup> An application-oriented line of research is the selection of a chemical channel with a view to increasing the efficiency of target molecule production relative to the formation of by-products.<sup>[7]</sup> In order to achieve such wavepacket control or coherent control of a chemical reaction through modification of the phase and chirp of the short pulses, the technique needs to be applicable to molecules in condensed phases.

Recently, a sub-5-fs visible laser has been developed by the author's group based on a novel optical parametric amplifier with a non-collinear configuration, i.e. a non-collinear optical parametric amplifier (NOPA) with pulse-front matching.<sup>[3]</sup> The laser system generating such short pulses has permitted the real-time observation of the transmittance change associated with molecular vibrations. Real-time spectroscopy has been applied to a conjugated polymer and energy migration among the C–C, C=C, and C≡C stretching modes and other low-frequency out-of-plane bending modes through mode coupling have been observed using the sub-5-fs visible laser.<sup>[8]</sup>

Conjugated polymers are of interest not only from the applications viewpoint, but also in the context of basic physics since they are models of one-dimensional systems showing characteristic spectroscopic properties. These can be ascribed to the formation of localized nonlinear excitations such as soliton pair, polaron pair, and self-trapped excitons (STEs) formed through strong coupling between electronic excitations and lattice vibrations.<sup>[9–22]</sup> On the basis of previous extensive studies,<sup>[20–22]</sup> the initial spectral changes and their kinetics after photoexcitation of conjugate polymers with non-degenerate ground states can be explained in terms of the geometrical relaxation of a free exciton (FE) to a thermalized self-trapped exciton (STE) within 150 fs. The STE and FE in polydiacetylenes (PDAs) are considered to have butatrienic ( $-\text{CR}=\text{C}=\text{C}=\text{CR}'-$ )<sub>n</sub> and acetylenic ( $-\text{CR}-\text{C}\equiv\text{C}-\text{CR}'-$ )<sub>n</sub> configurations, respectively,<sup>[17–22]</sup> with R and R' side groups. Recent experimental and theoretical studies have revealed the lowest-lying singlet state in a blue-phase PDA to be an optically forbidden  $2^1\text{A}_g$  state lying  $\sim 0.1$  eV below a  $1^1\text{B}_u$ -FE state.<sup>[23]</sup> Internal conversion (IC) is then expected along with self-trapping,<sup>[21,22]</sup> but the dynamic behavior has yet to be fully understood. Recent progress in femtosecond pulsed lasers has enabled studies of molecular dynamics on a 10-fs time scale.<sup>[24,25]</sup> Rapid damping of the C=C stretching and  $\sim 700\text{ cm}^{-1}$  modes within 100 fs observed in the previous process was explained in terms of dephasing due to anharmonicity.<sup>[26,27]</sup> The present study has revealed a continuing oscillation beyond the 400-fs delay, even after the population decay to the thermal STE. The population change also decays quickly along with the oscillating component due to wave-packet motion. This fast decay is observed in the transients for probe-photon energies  $E_{\text{probe}} < \sim 2.0$  eV. In the region  $E_{\text{probe}} > \sim 2.0$  eV, on the other hand, the amplitude of the oscillations is maintained or even increases slightly in the initial positive signal range.<sup>[28]</sup> The coherence is maintained for as long as one picosecond in the delay-time range of negative transmittance change due to photo-induced absorption (PIA).<sup>[28]</sup>

## 7.2

### Experimental

The PDA used in the present study was a newly synthesized ladder-polymer, poly[5,7,17,19-tetracosatetraynylene bis(*N*-butyloxycarbonylmethyl)carbamate] (PDA-4BCMU4A (8)), consisting of two PDA backbones linked by methylene chains.<sup>[29]</sup> The sample used was a film of thickness 370 nm prepared by spin coating.

The pulse-front-matched NOPA generated 4.7-fs, 5- $\mu$ J pulses at 1 kHz, which were used as both pump and probe pulses.<sup>[3,28]</sup> The spectrum of the pulses covered a range between 500 and 800 nm, with the phase being almost constant. This enabled highly coherent excitation of the manifold vibronic states to be discussed in the following section. The phase was calculated from the measured group delay (GD) of the uncompressed pulses and the computed GD of the compressor. The excitation photon density was about  $2.1 \times 10^{15}$  photons/cm<sup>2</sup>. The polarizations of the pump and probe pulses were mutually parallel. The probe was detected by a coupled system consisting of a monochromator with a 5-nm resolution, the photodiode, and a lock-in amplifier. All measurements were performed at 295 K.

### 7.3

#### Results and Discussion

The stationary absorption spectrum shows a characteristic  $1^1B_u$ -FE peak at 1.956 eV, which classifies PDA-4BCMU4A (8) as a typical blue-phase PDA.<sup>[9]</sup> The absorption spectrum is composed of vibronic structures coupled to the C=C and C $\equiv$ C stretching modes at 2.12 and 2.21 eV, respectively. The time dependence of the transient difference transmittance was probed at various photon energies, as shown in Figure 7.1.

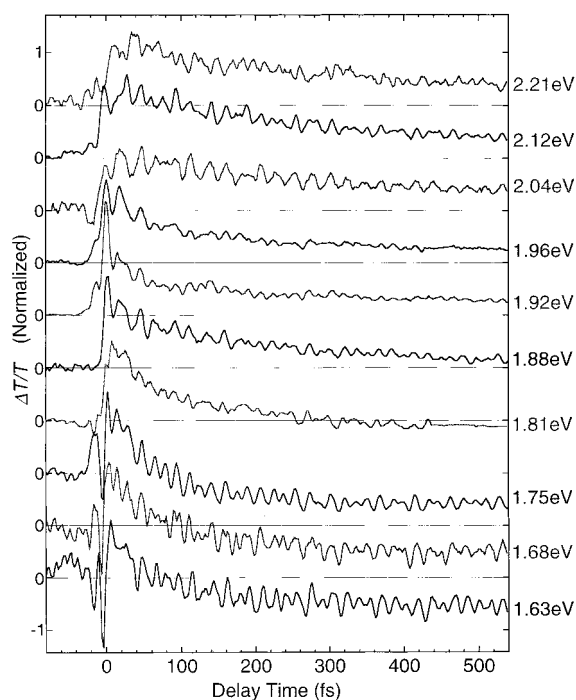


**Fig. 7.1** Time dependence of the normalized transmittance change at ten probe-photon energies from –80 fs to 540 fs. The intensities are normalized at their peaks.

The time dependence of population change was analyzed by removing the oscillatory structures. The traces  $\Delta T(t)/T$  could be fitted to the following equation:

$$\Delta T(t)/T = \int_{-\infty}^t dt' I(t') [A_d \delta(t - t') + A_1 e^{-(t-t')/\tau_1} + A_2 e^{-(t-t')/\tau_2} (1 - e^{-(t-t')/\tau_1})] \quad (1)$$

In Figure 7.1, the traces arising from the three terms in the above equation are plotted. The first term in parentheses in Eq. (1) stems from the instantaneous interaction due to coherent coupling. The time constant  $\tau_1$  ranges from 19 to 120 fs depending on the probe wavelength, as has also been seen for other PDAs.<sup>[17–19]</sup> This can be explained in terms of the different contributions of the following three mechanisms: (1) internal conversion (IC) from the  $1^1B_u$ -FE state to the  $2^1A_g$  state; (2) geometrical relaxation (GR) from an acetylene-type to a butatriene-type structure, and (3) thermalization (TH) in the main chain.

The low quantum efficiency of fluorescence from the second lowest excited state, namely the  $1^1B_u$  state, is estimated to be  $(1-2) \times 10^{-5}$ . The natural lifetime of this state is estimated to be 2–3 ns using the oscillator strength obtained from the absorption saturation of excitonic transition in a pump-probe experiment. The excited-state lifetime is estimated to be 20–60 fs based on the aforementioned natural lifetime and fluorescence yield. It is thus predominated by the radiationless process, which can be attributed to the absence of a potential barrier between the STE and FE in one-dimensional systems.<sup>[17,30]</sup> Therefore, the structural change that follows the photoexcitation is expected to take place within a single period of the coupled vibrations. However, thermalization must involve energy redistribution among the mutually coupled modes and takes a longer time than the oscillation periods of the high-frequency modes discussed above. The resultant wave-packet motion in the short-lived  $1^1B_u$ -STE then quickly decays in the ensuing IC process to the geometrically relaxed non-fluorescent  $2^1A_g$  state, and the PIA to the  $nB_u$  state becomes dominant. The small, long-duration signal in the bleaching region (1.96 and 2.12 eV) is thus assigned to a ground-state weak wave-packet motion driven by the impulsive stimulated Raman scattering.<sup>[31]</sup>

The GR process is supposed to take place within an oscillation period of the vibrational mode relevant to the configuration change in such a one-dimensional system owing to the lack of the potential barrier.<sup>[17,30]</sup> In the case of PDAs, the  $C\equiv C$ ,  $C=C$ , and  $C-C$  stretching modes are considered to be most strongly coupled to the GR process because the electronic excitation is of bonding to antibonding character.<sup>[1]</sup> Therefore, it might be considered to be terminated within 30 fs, since the oscillation periods of the stretching modes are 16 fs ( $C\equiv C$ ), 22 fs ( $C=C$ ), and 27 fs ( $C-C$ ). However, the GR processes are only fully completed after intrachain thermalization, which is the energy redistribution process among the various vibrational modes of the main chain. The time needed for this process is estimated to be several tens to a hundred femtoseconds because of the low-frequency main-chain modes involved. Therefore, the rate-determining step is the intrachain thermalization. The average vibrational energy of the geometrically relaxed  $2^1A_g$  state is reduced during the process of thermalization. Hence, the lifetime is longer for higher probe photon energies in the case of induced absorption and *vice versa* in the case of stimulated emission.<sup>[18]</sup> Since the GR process must include the rearrangement of the geometrical

structure of the system, low-frequency modes are also involved. Therefore, it becomes difficult to fully separate GR and TH processes at longer delay times.

Thermalization processes in molecular systems including polymers have been studied by monitoring the changes in the electronic spectra in the hot band region. The decay of the instantaneous temperature determined by the intensity ratio between the Stokes and anti-Stokes Raman signals offers information concerning the thermalization dynamics. The time constant for the TH process varies widely between a few hundreds of femtoseconds and several tens of picoseconds. In previous work, it was concluded that intrachain and interchain thermalization take place with time constants of about 150 fs and a few tens of picoseconds, respectively. Therefore, the process of intrachain thermalization is included in the second term of Eq. (1).

The third term in Eq. (1) corresponds to the IC process from the  $2^1A_g$  state to the  $1^1A_g$  ground state by quantum mechanical tunneling, and has a longer time constant  $\tau_2$  that is relatively insensitive to temperature. The time constant is also dependent on the probe photon energy, which can be explained in terms of thermalization in the geometrically relaxed state of  $1A_g$  symmetry.

The traces of normalized transmittance change, probed at various photon energies as shown in Figure 7.1, clearly exhibit a complex oscillatory behavior. The oscillation is ascribed to a wave-packet motion composed of several modes, as has often been observed in molecular systems. From the complex features, it is clear that more than two modes contribute to the time-dependent transmittance change. In spite of the complexity, systematic features can be seen in the phases of the oscillations. The mode frequencies and the phase relation of the wave-packet motion could be obtained from the Fourier transform of the normalized transmittance change. Integration was performed over whole delay times ranging from 20 fs to 2.5 ps after slowly removing the varying envelope as shown in Figure 7.2. The Fourier analysis of the oscillation components revealed characteristic stretching modes of the C–C ( $\sim 1220\text{ cm}^{-1}$ ), C=C ( $\sim 1455\text{ cm}^{-1}$ ), and C $\equiv$ C ( $\sim 2080\text{ cm}^{-1}$ ) bonds. In addition, low-frequency modes were seen at about 230 and  $700\text{ cm}^{-1}$ , attributable to the deformation modes of the backbone.<sup>[32]</sup> The relative intensities were seen to depend on the probe wavelength.

Theoretical calculations predicted a charge-transfer-type exciton with  $A_g$  symmetry, with the electron and hole being separated at adjacent sites.<sup>[33]</sup> Calculations of the structure of a prototypical diacetylene oligomer  $C_{14}H_8$  by ab initio and QCFF/PI methods led to the conclusion that the  $2^1A_g$  state has a butatrienic-like structure. On the other hand, the  $1^1B_u$  state shows features intermediate between those of the acetylenic and butatrienic structures.<sup>[33]</sup> Therefore, it is reasonable to assign the  $2^1A_g$  state as the geometrically relaxed state in the “butatriene-like” configuration. This theoretical work points to a strong vibronic coupling of carbon–carbon stretching modes to the electronic transition. The integrated Fourier analysis of the oscillations merely offers information on the averaged vibrational frequency of the wave-packet motion over the integrated range. In order to study of the dynamic behavior of the geometrical relaxation, the time-frequency analysis was performed by calculat-

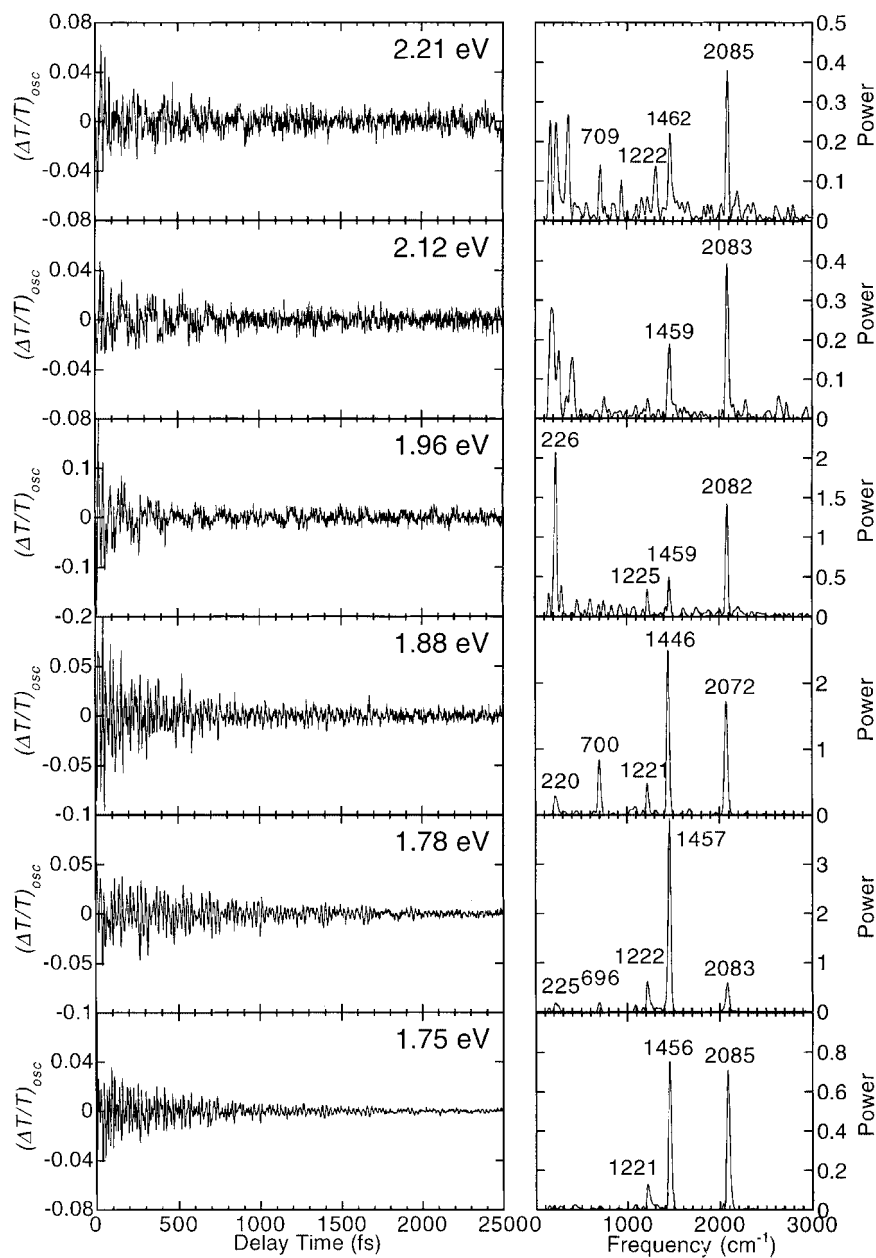


**Fig. 7.2** Transmittance changes after removal of the low-frequency components in the FT of  $\Delta T/T$ . The Fourier power spectra of oscillating components integrated between 20 fs and 2.5 ps are shown on the right.

ing spectrograms.<sup>[34]</sup> Care must be taken in discussing the modulation of frequencies and amplitudes utilizing spectrograms, as will be discussed below.

Spectrograms were calculated for a model molecular system with vibrational spectra composed of three C–C stretching modes of single, double, and triple bonds without any mode coupling. The calculated spectrograms, using Gaussian gate functions with half-widths of 150, 180, and 200 fs, are shown in Figures 7.4a, 7.4b, and 7.4c, respectively. The results show a modulation due to the finite spectral width used for the calculation of instantaneous frequency and amplitude induced by an artificial interference between the neighboring modes of C–C and C=C stretching. This interference becomes prominent when the width of the gate function is decreased so that it is close to the inverse of the frequency separation of the relevant modes. Therefore, this type of interference affects the calculated results for the amplitude and frequency modulations. This behavior can be explained as follows.

Here it is assumed that there are two neighboring modes at frequencies  $\omega_1$  and  $\omega_2$  with a separation of  $\Delta\omega_{12} = \omega_1 - \omega_2$  and with constant amplitudes  $A_1$  and  $A_2$ , respectively. The Fourier time-windowed transform of the two-mode oscillation is then given by the following equation:

$$\left| \int_{-\infty}^{\infty} (A_1 e^{i\omega_1 t} + A_2 e^{i\omega_2 t}) \exp\left\{-(t - \tau)^2 / \tau_0^2\right\} e^{-i\omega t} dt \right|^2 = \quad (2)$$

$$|A_1|^2 \exp\{-\tau_0^2/2\} + |A_2|^2 \exp\{-\tau_0^2 \Delta\omega_2^2/2\} + A_1 A_2^* \exp\{-\tau_0^2 \Delta\omega_1^2/4 - \tau_0^2 \Delta\omega_2^2/4\}$$

$$\exp(i\Delta\omega_{12}t) + c.c.$$

where  $\Delta\omega_1 = \omega - \omega_1$  and  $\Delta\omega_2 = \omega - \omega_2$  represent the detuning of the optical frequency from the vibrational frequencies. The power spectrum  $I$  can be converted to the following form with a phase  $\phi_{12}$ :

$$I = I_1 + I_2 + M \cos(\Delta\omega_{12}t + \phi_{12}) \quad (3)$$

The delay time dependences of the instantaneous amplitudes and frequencies were calculated using the spectrogram data in Figure 7.3, which were obtained with a gate width of 150 fs. The calculated results for the instantaneous amplitude and frequency of the three stretching modes are shown in Figure 7.4. Comparison with the instantaneous frequencies and amplitudes calculated using the spectrograms shows that there are non-negligible modulation effects in the C–C and C=C stretching frequencies and amplitudes in the spectrograms obtained with this 150 fs gate width. Since the time-integrated Fourier transforms of the real-time spectra clearly show the component at  $230 \text{ cm}^{-1}$ , this modulation is considered to be real. It also stems from the enhanced anharmonicity due to the Fermi resonance between the sum frequency of  $230 \text{ cm}^{-1}$  and the C–C stretching mode ( $\sim 1220 \text{ cm}^{-1}$ ) and the frequency of C=C stretching mode ( $\sim 1455 \text{ cm}^{-1}$ ).

The spectrogram of the real-time spectral data probed at 1.75 eV, calculated with three different gate widths, is shown in Figure 7.5. The power spectra of the modulation frequencies of the instantaneous frequencies were calculated for simulated and experimental data; Figure 7.6 depicts that for the experimental data probed at

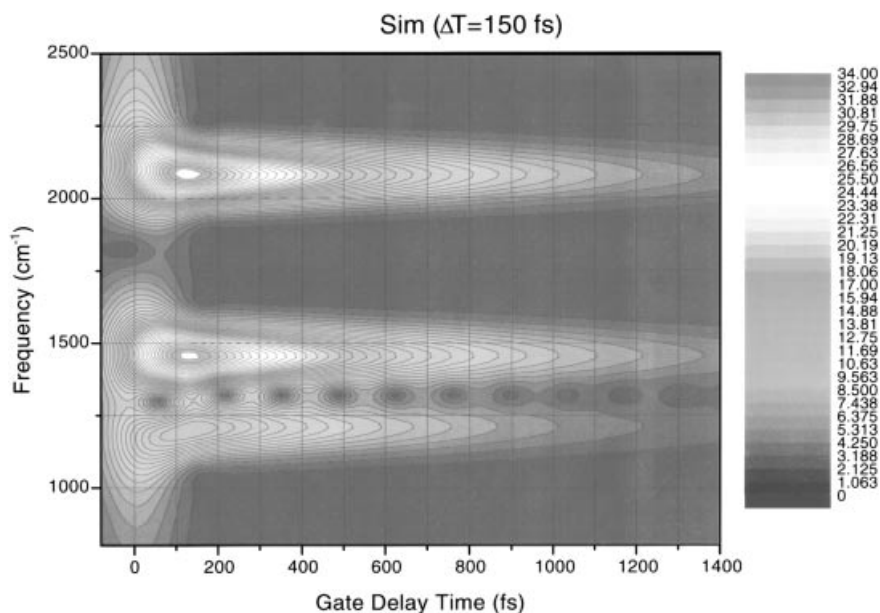


**Fig. 7.3** Spectrogram calculated for a model molecular system with vibrational spectra composed of the three stretching modes of single, double, and triple bonds without any mode coupling. The full width at half-maximum (FWHM) of the Gaussian gate functions is 150 fs.

1.75 eV with a gate width of 150 fs. On comparing these spectra, the effect on the instantaneous frequencies and amplitudes can be seen to be negligible, the modulation frequencies being lower than  $200\text{ cm}^{-1}$  in the case of gate widths of 180 and 200 fs. At both 1.75 eV and 1.78 eV, the C–C single- and triple-bond stretching mode frequencies are modulated at 50 and  $90\text{ cm}^{-1}$ , while the double-bond stretching frequency is modulated at 50 and  $115\text{ cm}^{-1}$ . Apparent modulation peaks below  $30\text{ cm}^{-1}$  are meaningless because of the limited delay-time range of 1.5 ps, corresponding to a bandwidth of  $22\text{ cm}^{-1}$ . The modulations with frequencies of 50, 90, and  $115\text{ cm}^{-1}$  corresponding to 670, 370, and 290 fs, respectively, can be seen in the spectrogram. Therefore, these are undoubtedly related to frequency modulation and probably amplitude modulation, even though there are no Raman data of polydiacetylenes in this frequency range in literature. From the above results, it is concluded that the  $50\text{ cm}^{-1}$  frequency corresponds to the mode that changes the force constants, and hence the lengths, of all three C–C bonds. The  $90\text{ cm}^{-1}$  mode modifies the force constants and relevant bond lengths of the single and triple bonds, and the  $115\text{ cm}^{-1}$  mode changes those of the double bond. These three modes are not reported, but they can be characterized from the present data. Mode a ( $50\text{ cm}^{-1}$ ) is an out-of-plane bending that modifies the bond lengths of the three C–C bonds. Mode b ( $90\text{ cm}^{-1}$ ) is considered to be an in-plane bending that affects the C–C and C≡C bonds. Mode c ( $115\text{ cm}^{-1}$ ) is considered to be a mode that does not alter the full length of the repeat unit of the polymer such that the single- and triple-bond stretch-



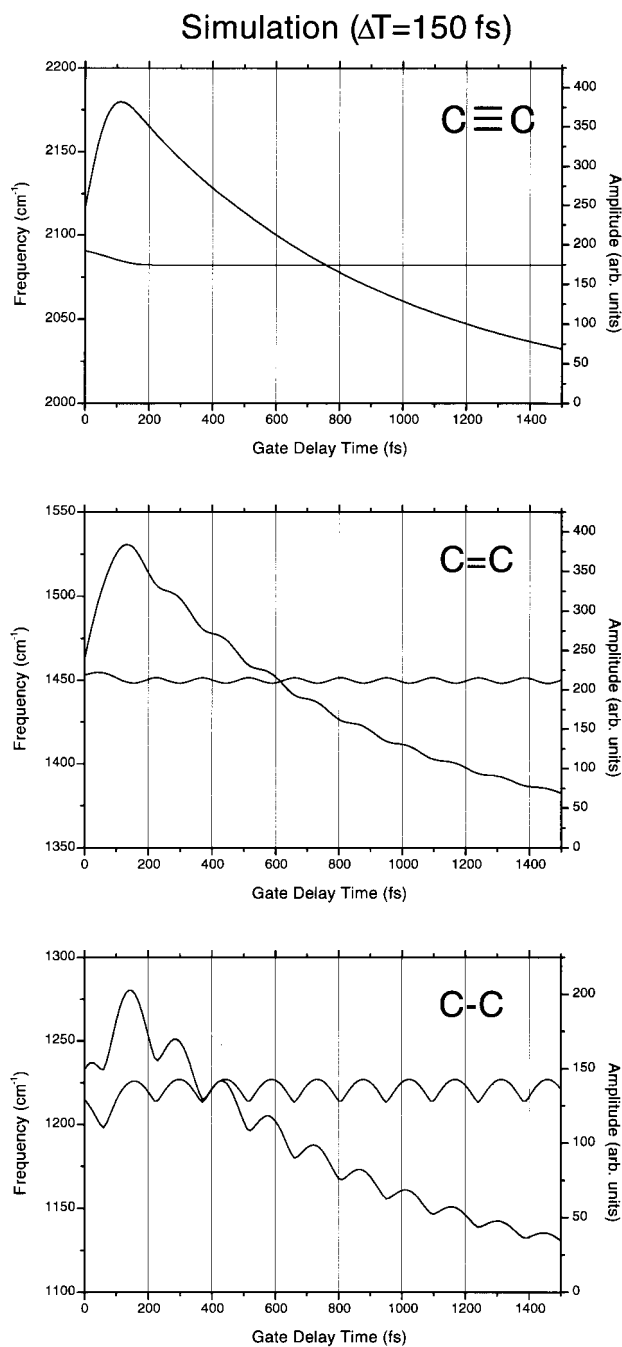


**Fig. 7.4** Instantaneous amplitudes and frequencies calculated using the spectrograms shown in Figure 7.3. The bandwidth of the integration is 200 cm<sup>-1</sup>.

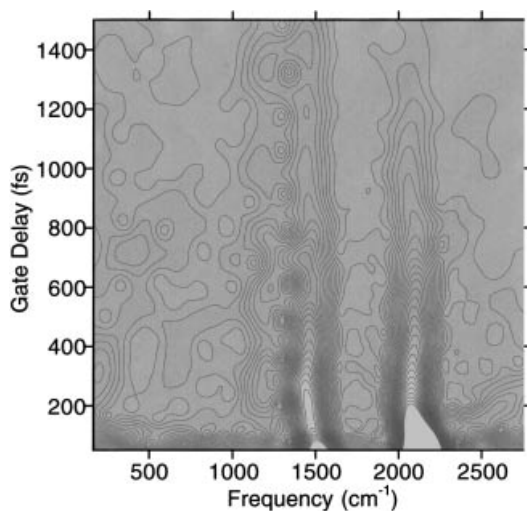


**Fig. 7.5** Spectrogram calculated for the trace probed at 1.75 eV. The window function is a Gaussian with an FWHM of 150 fs.

ing frequencies remain unchanged. These mode frequencies are very low and are presumably not localized in one repeat unit but are rather slightly delocalized over a few repeat units, along with the delocalization of the electronic excitation forming the charge-transfer exciton. Modulation at higher frequencies is discussed below.

As mentioned in the previous sections, the mixing in the spectrogram gives artificial modulations in both frequencies and amplitudes. Since the double- and single-

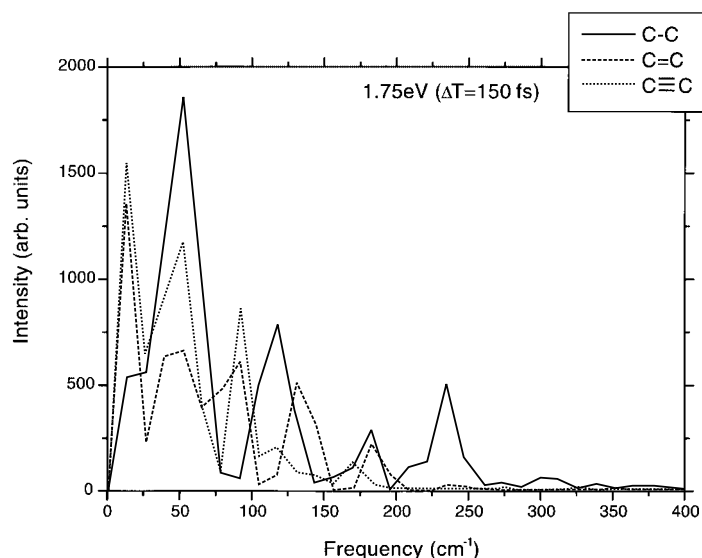


**Fig. 7.6** Power spectra of the modulation frequencies of the instantaneous frequency probed at 1.75 eV, calculated using a gate width of 150 fs.

bond stretching modes are close to each other, it is not possible to completely eliminate the modulation with a frequency of  $235\text{ cm}^{-1}$ , which corresponds to the difference in frequencies of the two modes at  $1220$  and  $1455\text{ cm}^{-1}$ . The coincidence of the frequency difference and the mode  $d$  at  $230\text{ cm}^{-1}$  experimentally observed in the Fourier transform (Fig. 7.6) of the time dependence means that there is a high possibility of Fermi-resonance-type enhancement of the mode coupling. In a recent publication by the author's group,<sup>[8]</sup> the spectrogram and dynamic mode coupling between C–C and C=C stretching modes were analyzed using a Hanning-type window function with an FWHM of  $150\text{ fs}$ . This window function corresponded to a bandwidth of  $200\text{ cm}^{-1}$ . Spectrograms were calculated at several photon energies. That at  $175\text{ eV}$  in particular clearly exhibited the characteristic features of mode-frequency modulations in the excited state, since it corresponded to the transmittance change due to excited absorption. These spectrograms, including their fine structures, are highly reproducible, with the exception of those at  $2.12$  and  $1.96\text{ eV}$ , where the fast decay of the oscillations prevents precise determination of the spectrogram at a delay time longer than  $500\text{ fs}$ . The time-dependent amplitudes and center-of-mass frequencies of the C≡C ( $\nu_{\text{C}\equiv\text{C}}$ ) and C=C ( $\nu_{\text{C}=\text{C}}$ ) stretching modes showed modulation with a mutual  $\pi$  out-of-phase relationship with a period of  $\sim 145\text{ fs}$  ( $230\text{ cm}^{-1}$ ). On the other hand, the frequency of the C=C stretching mode does not show any strong correlation with the other modes at this modulation frequency. In the spectrograms calculated at  $E_{\text{probe}} < 1.9\text{ eV}$  (not shown), the oscillations show similar features to those seen at  $1.75\text{ eV}$ . In the earlier publication, these features were explained in terms of the formation of the geometrically relaxed butatrienic structure. The coherent nuclear motion coupled to the FE takes place near the deformed configuration after self-trapping; the stretching motions of adjacent C≡C and C=C bonds are clearly correlated with each other. The observed mode frequencies are red-shifted and become lower than those of diacetylene oligomers.<sup>[35,36]</sup> This shift can be ascribed to the delocalization of  $\pi$ -electrons. The  $\pi$ -bond orders of the C=C ( $1 - \delta_0$ ) and C≡C ( $2 - \delta_0$ ) bonds in the ground state decrease to  $1 - \delta$  and  $2 - \delta$ , respectively ( $\delta_0 < \delta < 1$ ), in the equilibrium. This equilibrium geometry corresponds to the center configuration of the vibrational motion in the geometrically relaxed  $2^1A_g$  state. The same frequency of  $\sim 230\text{ cm}^{-1}$  is also observed in the Fourier transform of the transmittance change representing the coherent wavepacket motion, especially for  $E_{\text{probe}} > 1.9\text{ eV}$ . This mode was assigned to the planar bending mode of C–C=C bonds. It lies in the typical frequency range of the C–C=C bending modes of olefins. Recent ab initio calculations have shown that these bending modes have large Franck–Condon (FC) factors in molecules such as diacetylene oligomers ( $\text{C}_{14}\text{H}_8$ ,  $\sim 160\text{ cm}^{-1}$ )<sup>[35]</sup> and octatetraene ( $\text{C}_8\text{H}_{10}$ ,  $220\text{--}400\text{ cm}^{-1}$ ).<sup>[36]</sup> A clear analysis is very difficult, even when such data have extremely high signal-to-noise ratios. Efforts are now in progress to improve the data so as to detect the extra signal height induced by the real coupling effect over the artificial modulation in the frequency and amplitude modulations.

The above discussion is based on a spectrogram that has some limitations with regard to the simultaneous determination of frequency and time. Therefore, although the Fermi resonance among the relevant modes discussed above is expected to enhance the mode coupling, it hampers analysis using the spectrogram because

of the aforementioned artificial interference. Therefore, it will be necessary to obtain data with an even higher signal-to-noise ratio in order to subtract the contaminating contribution of the neighboring mode.

#### 7.4

#### Conclusion

The primary dynamics of polydiacetylenes has been studied with the highest time resolution. The vibrational non-equilibrium in the relaxed state is characterized by the modulations of instantaneous frequency and amplitude with an oscillation period of 145 fs. This phenomenon is explained in terms of a coupling of the C=C and C-C stretching modes through an in-plane bending mode in the main chain. This is the first real-time observation of dynamic coupling between two modes. The present results offer much information about the configurational change and the geometrical relaxation. Theoretical investigations of the electron-phonon and electron-electron interactions in various molecular systems are needed. In addition, the present study opens a novel technique for investigating the real-time inter-mode exchange of vibrational energy among various modes, which is closely related to photo- and thermochemical reactions.

#### Acknowledgements

The author thanks Drs. A. Shirakawa, M. Takasaka, H. Matsuzawa, and H. Nakanishi and Mr. T. Saito for their collaboration and Profs. Y. Toyozawa, H. Okamoto, M. Yoshizawa, K. Misawa, and Y. Takasu for valuable discussions. This work was partly supported by the Research for the Future of Japan Society for the Promotion of Science (JSPS-RFTF-97P-00101).

#### References

- 1 A. Baltuska, Z. Wei, M. S. Pshenichnikov, D. W. Wiersma, *Opt. Lett.* **1997**, 22, 102.
- 2 M. Nisoli, S. De Silvestru, O. Svelto, R. Stipocs, K. Ferencz, S. Sartania, Ch. Spielmann, F. Krausz, *Opt. Lett.* **1997**, 22, 1562.
- 3 A. Shirakawa, I. Sakane, M. Takasaka, T. Kobayashi, *Appl. Phys. Lett.* **1999**, 74, 2268.
- 4 M. Chergui (Ed.), *Femtochemistry*, World Scientific, Singapore, 1996.
- 5 M. Dantus, M. J. Rosker, A. H. Zewail, *J. Chem. Phys.* **1987**, 87, 2395; R. L. Fork, C. H. Brito Cruz, P. C. Becker, C. V. Shank, *Opt. Lett.* **1987**, 12, 483.
- 6 J. Janszky, P. Adam, A. V. Vinogradov, T. Kobayashi, *Chem. Phys. Lett.* **1993**, 213, 368.
- 7 C. J. Bardeen, J. Che, K. R. Wilson, V. V. Yakovlev, V. A. Apkarian, C. C. Martens, R. Zadoyan, B. Kohler, M. Messina, *J. Chem. Phys.* **1997**, 106, 8486.
- 8 T. Kobayashi, A. Shirakawa, H. Matsuzawa, H. Nakanishi, *Chem. Phys. Lett.* **2000**, 321, 385.
- 9 T. Kobayashi (Ed.), *Nonlinear Optics of Organics and Semiconductors*, Springer Proceedings Physics, Vol. 36, Springer, Berlin, **1989**.

- 10 T. Kobayashi (Ed.), *Relaxation in Polymers*, World Scientific, Singapore, 1993.
- 11 W. P. Su, J. R. Schrieffer, A. J. Heeger, *Phys. Rev. Lett.* **1979**, 42, 1698.
- 12 W. P. Su, J. R. Schrieffer, A. J. Heeger, *Phys. Rev.* **1980**, B22, 2099.
- 13 M. Yoshizawa, T. Kobayashi, H. Fujimoto, J. Tanaka, *J. Phys. Soc. Japan* **1982**, 56, 768.
- 14 Z. Vardeny, *Physica* **1984**, 127B, 338.
- 15 L. Rothberg, T. M. Jedju, S. Etemad, G. L. Baker, *Phys. Rev. Lett.* **1985**, 57, 3229.
- 16 B. I. Greene, J. F. Mueller, J. Orenstein, D. H. Rapkine, S. Schmitt-Rink, M. Thakur, *Phys. Rev. Lett.* **1988**, 61, 325.
- 17 T. Kobayashi, M. Yoshizawa, U. Stamm, M. Taiji, M. Hasegawa, *J. Opt. Soc. Am. B* **1990**, 7, 1558.
- 18 M. Yoshizawa, K. Nishiyama, M. Fujihira, T. Kobayashi, *Chem. Phys. Lett.* **1993**, 207, 461.
- 19 M. Yoshizawa, Y. Hattori, T. Kobayashi, *Phys. Rev. B* **1994**, 49, 13259.
- 20 T. Kobayashi, A. Furuta, S. Shimada, H. Matsuda, *Chem. Phys. Lett.*, to be published.
- 21 T. Kobayashi, M. Yasuda, S. Okada, H. Matsuda, H. Nakanishi, *Chem. Phys. Lett.* **1997**, 267, 472.
- 22 J. Kinugasa, S. Shimada, H. Matsuda, H. Nakanishi, T. Kobayashi, *Chem. Phys. Lett.* **1998**, 287, 639.
- 23 T. Kobayashi, A. Furuta, S. Shimada, H. Matsuda, Technical Digest of the CLEO/Pacific Rim '99, Seoul, Korea, 3 September 1999.
- 24 See, e.g., Q. Wang R. W. Shoenlein, L. A. Peteanu, R. A. Mathies, C. V. Shank, *Science* **1994**, 266, 422.
- 25 G. Cerullo, G. Lanzani, M. Muccini, C. Taliani, S. De Silvestri, *Phys. Rev. Lett.* **1999**, 83, 231.
- 26 T. A. Pham, A. Daunois, J. C. Merle, J. Le Moigne, J. Y. Bigot, *Phys. Rev. Lett.* **1995**, 74, 904.
- 27 J. Y. Bigot, T. A. Pham, T. Barisien, *Chem. Phys. Lett.* **1996**, 259, 469.
- 28 A. Shirakawa, I. Sakane, T. Kobayashi, *Opt. Lett.* **1998**, 23, 1292.
- 29 H. Matsuzawa, S. Okada, H. Matsuda, H. Nakanishi, *Chem. Lett.* **1997**, 1105.
- 30 E. I. Rashba, in *Excitons (Selected Chapters)* (Eds.: E. I. Rashba, M. D. Sturge), North Holland, Amsterdam, 1987, p. 273.
- 31 See, e.g., W. T. Pollard, S. L. Drexheimer, Q. Wang, L. A. Peteanu, C. V. Shank, *J. Phys. Chem.* **1992**, 96, 6147.
- 32 Z. Iqbal, R. R. Chance, R. H. Baughman, *J. Chem. Phys.* **1977**, 66, 5520.
- 33 H. Tanaka, M. Inoue, E. Hanamura, *Solid State Commun.* **1987**, 63, 103.
- 34 M. J. J. Vrakking, D. M. Villeneuve, A. Stolow, *Phys. Rev. A* **1996**, 54, 37.
- 35 F. Zerbetto, *J. Phys. Chem.* **1994**, 98, 13157.
- 36 F. Zerbetto, M. Z. Zgierski, *J. Chem. Phys.* **1994**, 101, 1842.

## 8

# Ultrafast Probing and Control of Molecular Dynamics: Beyond the Pump-Probe Method

*Marcos Dantus*

## 8.1

### Introduction

The development of ultrafast laser pulses has for decades outpaced the ability to create detectors with comparable time resolution. This mismatch has necessitated the development of techniques based on two or more laser pulses with a time resolution that is limited only by the duration of the laser pulses themselves. The most common of these methods, capable of initiating a dynamic process and interrogating its time evolution, is known as pump-probe (PP). Probing can be achieved by monitoring absorption, laser-induced fluorescence (LIF), ionization, multi-photon ionization, photoelectron detection, chemiluminescence, and so forth. The pump-probe method has proved to be extremely powerful for the observation of ultrafast dynamics.<sup>[1–4]</sup> Each laser interaction involves the transfer of population, usually from the ground state to a state of interest by the pump, and then to a second state by the probe. Because two populations are involved, the optical phase of the lasers is not important in these measurements.<sup>[5,6]</sup>

Observation of the coherent interaction between the two laser pulses and the sample during a PP measurement requires phase locking and a detection system that filters out all the incoherent contributions. In order to harness the coherent properties in the observation and control of molecular dynamics, laser set-ups that coherently combine multiple laser beams are preferred. In this contribution, four-wave mixing (FWM) methods for the observation and control of molecular dynamics in the gas phase are highlighted. Four-wave mixing involves the use of three nonlinear electric field interactions to create a resulting fourth wave. Four-wave mixing methods can be considered as being analogous to pump-probe processes in that they operate through the same order of nonlinearity. In the context of this chapter, the first two interactions may induce a transfer of population while the third one probes the dynamics of that state.

Herein, on- and off-resonance experimental data are presented to illustrate the power of FWM techniques. A semi-classical model is used to simulate the experimental results and to illustrate the mechanism for signal formation. Although FWM has been known for three decades and has been used to study solids, liquids, and gases, the author's group has focused on the study of relatively simple

and well-understood molecules in the gas phase in order to gain a deeper understanding of the FWM process itself. The observation of rotational and vibrational motion of ground-state  $\text{HgI}_2$  using off-resonance impulsive excitation, as well as of purely rotational motion for acetylene,  $\text{CO}_2$ ,  $\text{N}_2$ , and pyrazine is described. For on-resonance FWM, two types of nonlinear optical phenomena, namely photon-echo and reverse transient grating are compared and contrasted. The former leads to the cancelling out of inhomogeneous broadening in the sample, while the latter does not. A brief theoretical formulation is given to explain the mechanism that results in the cancellation of inhomogeneous broadening. When carrying out FWM measurements with three time-ordered laser pulses, the pulse sequence can be used to control the nonlinear pathways that lead to signal observation. Herein, this point is illustrated by a demonstration of coherent control over the observation of ground- or excited-state dynamics by changing the time between the first two pulses. Current and future applications of ultrafast four-wave mixing are also discussed.

## 8.2

### Four-Wave Mixing Techniques

#### 8.2.1

#### Differences Between the Pump-Probe Method and Four-Wave Mixing

In this section, FWM techniques are analysed from the point of view of the PP method. For a thorough treatment of FWM methods, the reader is referred to the texts of Mukamel and Boyd.<sup>[7,8]</sup> FWM experiments are best understood using a density-matrix approach. PP experiments, on the other hand, are usually represented by wave-packet formalism in Hilbert space. The aim of this section is to illustrate the different dynamics that can be addressed by the PP and FWM methods.

In a PP experiment, the first step involves a population transfer from the ground  $|g\rangle$  to the excited state  $|e\rangle$ . The probability  $P_{eg}$  of this process occurring can be written quantum mechanically as follows:

$$P_{eg} = |\langle e|\mu E(t)|g\rangle|^2 = \langle e|\mu E(t)|g\rangle\langle g|\mu E(t)^*|e\rangle \quad (1)$$

where  $\mu$  is the induced dipole moment and  $E$  is the electric field. The probing step in a PP experiment involves the transfer of population from state  $|e\rangle$  to state  $|f\rangle$ . However, one must take into account the fact that the population in state  $|e\rangle$  evolves with time. In a typical PP experiment, one might monitor fluorescence resulting from the population in state  $|f\rangle$ . Coherent interactions between the laser pulses and off-resonance contributions occurring when pump and probe pulses overlap in time usually play a minimal role and are often neglected.

In contrast to PP, FWM methods are coherent spectroscopic techniques. That is to say, coherent interactions between the laser pulses account for most of the signal. The interaction between the lasers and the molecules takes place on a time scale that is much shorter than the fluorescence lifetime. For this reason, nonlinear opti-

cal methods are concerned with the transient polarization of the sample induced by the electromagnetic field. The FWM processes can be described in terms of the third-order polarization resulting from the interaction with electromagnetic radiation:

$$P = P^{(0)} + P^{(1)} + P^{(2)} + P^{(3)} + \dots \quad (2)$$

where the total polarization is expanded to higher-order terms.<sup>[8]</sup> High-order polarization can be achieved by a single intense laser pulse or by a series of less intense laser pulses that interact coherently. The discussion here is restricted to the latter as it applies to isotropic media where even powers of the polarization vanish.

In order to distinguish between different FWM processes that contribute to the third-order polarization, one can take advantage of the wave vector properties of the laser pulses. Each laser pulse can be represented by the expression

$$E(t) = E_0(t) \exp[-i(\omega t - \mathbf{k} \cdot \mathbf{r})] + E_0^*(t) \exp[i(\omega t - \mathbf{k} \cdot \mathbf{r})] \quad (3)$$

where  $E_0(t)$  is the time-dependent envelope of the pulse,  $\omega$  is the carrier frequency,  $\mathbf{k}$  is the wave vector, and  $\mathbf{r}$  is the sample spatial coordinate. If each laser has a different wave vector, that is, they are not collinear or they have different wavelengths, signals resulting from a particular combination of laser pulses can be isolated. This selection process is typically referred to as phase matching. Phase matching ensures conservation of energy and momentum for each nonlinear optical process. In the following, the treatment will be restricted to the case of three degenerate pulses, where the detection geometry and pulse sequence is used to identify the different signals.

The phase-matching condition restricts the sign of each electric field interaction, that is  $e^{i\omega t}$  or  $e^{-i\omega t}$ . The system, after a single resonant electric field interaction, is left in a coherence state between the ground and excited states. Two electric field interactions are required to create a population in the ground or the excited state. This is consistent with Equation 1 as well as with the linear dependence on laser intensity  $I \propto |E_0(t)|^2$ . These facts, together with the requirement that electric field interactions occur coherently, are responsible for most of the differences between PP and FWM measurements.

### 8.2.2

#### Off-Resonance FWM

For off-resonance laser interactions, the polarization created by one electric field in the sample decays on a timescale shorter than that of most ultrafast laser pulses. When two laser pulses are overlapped in time, however, a population can be obtained in the ground state through an impulsive Raman process. If the bandwidths of the lasers overlap several rotational and/or vibrational states, the coherent superposition of states evolves as a function of time. The coherent superposition of vibrations and rotations in the ground state is probed by the third laser pulse, which creates the third-order polarization in the sample. The signal corresponds to the electric field that is generated by the third-order polarization in the sample.<sup>[7]</sup> Off-



resonance FWM is also known as transient grating spectroscopy.<sup>[9]</sup> The grating is formed in the sample by the crossing of the two plane-wave beams. Interference creates regions of high or low polarization in the sample. The third laser is Bragg diffracted by the grating thereby generating the observed signal. The diffraction process is very similar to the diffraction of X-rays by crystalline systems in that the spatial arrangement of the lasers leads to *spatial coherence* in the sample.

The homodyne-detected FWM signal intensity, resulting from the interaction between three incident laser pulses can be evaluated using

$$I_{\text{FWM}}(\tau) = \int_{-\infty}^{+\infty} |P^{(3)}(t)|^2 dt \quad (4)$$

where  $P^{(3)}(t)$  represents the time-dependent third-order polarization for a given phase-matching condition. At the impulsive limit, where the laser pulse duration is negligible in comparison to the rotational and vibrational periods, FWM signal intensity can be simply expressed as:

$$I_{\text{FWM}}(\tau) = |\chi^{(3)}(\tau)|^2 \quad (5)$$

where  $\chi^{(3)}(\tau)$  is the third-order susceptibility associated with the molecular system. We can expand the susceptibility in terms of isotropic and anisotropic components  $\chi^{(3)}(t) = \chi_{\text{iso}}(\tau) + \chi_{\text{aniso}}(\tau)$  <sup>[10]</sup>

$$\chi_{\text{iso}}(t) = \langle \frac{i}{\hbar} [\alpha(t), \alpha(0)] \rangle \quad (6)$$

$$\chi_{\text{aniso}}(t) = \langle \frac{i}{\hbar} [\beta(t), \beta(0)] \rangle \langle C''(\theta(t)) \rangle \quad (7)$$

where  $[\cdot]$  indicates commutator,  $\langle \cdot \rangle$  indicates quantum mechanical averaging, and  $\alpha$  and  $\beta = (\alpha_{\parallel} + \alpha_{\perp})$  are the scalar and anisotropic part of polarizability, respectively.  $C''(\theta(t))$  is the imaginary part of the correlation function of molecular orientation referenced to the angle  $\theta$  between the molecular axis and the laser's plane of polarization and is given by:

$$C''(\theta(t)) = \frac{\hbar}{2} \frac{1}{k_B T} \frac{d}{dt} C(t), \quad (8)$$

where  $C(t)$  is the correlation function for molecular rotation.<sup>[7]</sup>

### 8.2.3

#### On-Resonance FWM

On-resonance excitation by a single electric field leads to a coherence that is much longer lived than that resulting from off-resonance excitation. According to Eq. 1, the probability of population transfer from the ground to the excited state depends on two electric field interactions with the sample. In FWM, the lasers can be arranged such that each is responsible for a single field interaction. In such an arrangement, the interaction with  $E(t)$  and  $E(t)^*$  can be manipulated independently. It is therefore possible to control the observed population transfer by varying the optical phase or the time delay between the first two pulses.

### 8.2.3.1 Controlling Ground or Excited-State Observation

The time delay between the first two pulses can be used to control the source of the FWM signal. This can be illustrated with a simple model that includes two vibrational levels in the ground state and two in the electronically excited state. For this simplified system (see Figure 8.1), it is possible to formulate the dynamics as a function of the time delay between the first two pulses. The vibrational levels are separated by  $\hbar\omega_g$  and  $\hbar\omega_e$  in the ground and excited states, respectively. The laser pulses are considered as being very short, such that their bandwidth is larger than  $\omega_g$  or  $\omega_e$ . The three pulses are degenerate and are resonant with the electronic transitions. The system is assumed to be at such a temperature that the two ground-state levels are equally populated. After the first laser interaction, the first-order density-matrix components depend on the sign of the electric field. Interaction with  $e^{-i\omega t}$  yields

$$\rho_{eg}^{(1)} \propto \exp(-i\omega_{eg}t), \quad (9)$$

whereas, interaction with  $e^{i\omega t}$  yields

$$\rho_{ge}^{(1)} \propto \exp(i\omega_{eg}t), \quad (10)$$

The vibronic coherence induced by the first laser interaction involves four vibrational levels from the two electronic states, as shown in Figure 8.1. After one electric field interaction, no population has been transferred, as is confirmed by the zeros in the diagonal elements of the first-order density matrix in Figure 8.1.

Population transfer occurs upon interaction with the second laser pulse. The resulting expression contains the populations of the four levels. Notice that the populations (diagonal elements) are time-independent. No relaxation has been included in the present model. The simplified second-order elements of the density matrix are given by populations

$$\rho_{gg}^{(2)} = -A \cos(\omega_e \tau_{12}/2), \quad \rho_{ee}^{(2)} = A \cos(\omega_g \tau_{12}/2), \quad (11)$$

and vibrational coherences

$$\rho_{g'g}^{(2)} = -A \cos(\omega_e \tau_{12}/2) \exp(-i\omega_g t), \quad \rho_{ee'}^{(2)} = A \cos(\omega_g \tau_{12}/2) \exp(-i\omega_e t), \quad (12)$$

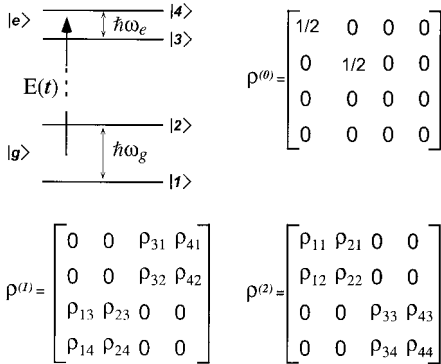


**Fig. 8.1** Energy diagram showing two electronic states each with two vibrational levels. The density matrix is given before the electric field interaction  $\rho^{(0)}$ , and after one  $\rho^{(1)}$  and two electric field interactions  $\rho^{(2)}$ . The diagonal

terms correspond to the populations. The initial state has levels 1 and 2 equally populated. The off-diagonal elements in  $\rho^{(1)}$  correspond to vibronic coherences, while those in  $\rho^{(2)}$  correspond to vibrational coherences.

where the time delay between the two laser pulses is given by  $\tau_{12}$ , and  $A$  is a constant that depends on the laser intensity and transition dipole moment. The primes indicate different vibrational levels. The spatial dependence of the lasers has been neglected for the sake of clarity. Notice that the population and the vibrational coherence matrix elements include a term that depends on the time delay between the first two pulses. For certain values of this time delay, one can cancel contributions from ground- or excited-state dynamics. The third electric field interaction generates the third-order polarization indicated by the corresponding density-matrix elements, as shown in Figure 8.1.

### 8.2.3.2 Inhomogeneous Broadening and Photon-Echo Measurements

Photon-echo and spin-echo are quite different phenomena. Nevertheless, they show numerous similarities. The Hahn spin-echo<sup>[11]</sup> is illustrated in Figure 8.2 (top). Notice that a coherent superposition of spins, originally aligned in the  $Z$  axis, is rotated by  $90^\circ$  into the  $XY$  plane. Inhomogeneous broadening in the sample causes dephasing of the coherent superposition as a function of time. The application of a  $180^\circ$  pulse causes an inversion in space and hence the spreading motion becomes a focusing motion that leads to a rephasing of the original superposition. This generates the spin-echo. The process can also be carried out by separating the  $180^\circ$  pulse into two  $90^\circ$  pulses. This set-up is also known as nuclear Overhauser effect spectroscopy (NOESY).<sup>[12]</sup>

The photon-echo process involves different physics. The first interaction creates a coherent superposition of states (see Eq. 9). Here, the key feature is that the first pulse interacts with the *bra*, that is, the interaction is with  $e^{i\omega t}$ . All quantum mechanical states involved, as well as the relaxation phenomena, evolve with a positive sign. Subsequent  $e^{-i\omega t}$  interaction with two electric fields changes the sign of the evolution and the initial dephasing is reversed.

Here, a brief description of the photon-echo phenomenon is given in terms of the model introduced in the previous section. The second-order density-matrix elements have an additional term that results from the spatial coherence in the sample. This term is described by

$$\rho_{\text{grating}}^{(2)} \propto \cos(\omega_{\text{eg}}\tau_{12}) = \{\exp(i\omega_{\text{eg}}\tau_{12}) + \exp(-i\omega_{\text{eg}}\tau_{12})\}/2 \quad (13)$$

The third-order density-matrix elements belonging to the phase-matching geometry having the first electric field interaction with  $e^{i\omega t}$ , also known as action on the *bra*, only have the positive component of Eq. 3. The third-order density matrix associated with photon-echo phenomena is

$$\rho_{\text{PE}}^{(3)} \propto \exp(i\omega_{\text{eg}}\tau_{12}) \exp\{-i\omega_{\text{eg}}(t-\tau_{12})\} \quad (14)$$

A maximum value is achieved when  $t = 2\tau_{12}$ . An experimental demonstration of this phenomenon is presented in Section 8.4.

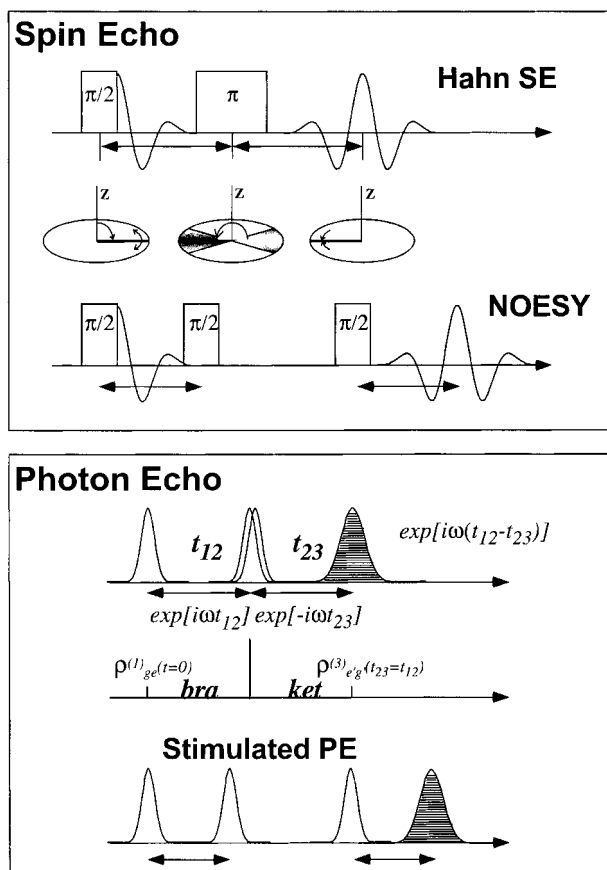


**Fig. 8.2** (Top) Schematic representation of the Hahn spin-echo used in nuclear magnetic resonance. The diagrams indicate the pulse sequence as well as a representation of the spin in spatial coordinates. The second pulse sequence corresponds to nuclear Overhauser effect spectroscopy (NOESY). (Bottom) Schematic representation of the photon-echo phenomenon. Notice the similarity with the Hahn spin-echo pulse sequence. The first electric field interaction creates a coherence

represented here by the first-order density-matrix elements  $\rho_{ge}^{(1)}$  with evolution on the *bra*; after two more electric field interactions the third-order density matrix elements  $\rho_{eg}^{(3)}$  evolve on the *ket*. The photon-echo is strongest after a time equal to the time delay between the first two pulses. The second optical pulse sequence corresponds to the stimulated photon-echo phenomena, which is analogous to the NOESY sequence used in nuclear magnetic resonance.

### 8.3 Experimental Methods

Collinear laser geometry, as used for most PP measurements, is usually avoided in FWM. The most common FWM laser configurations are shown schematically in Figure 8.3. The first set-up shows two laser beams crossing at the sample; one beam interacts twice with the sample while the other one interacts only once. Two types of

signals can be obtained. That with phase-matching geometry  $\mathbf{k}_{PE} = -\mathbf{k}_1 + (\mathbf{k}_2 + \mathbf{k}_2)$  can be used to make photon-echo measurements. The second coincides with the beam with wave vector  $\mathbf{k}_2$  and is given by  $\mathbf{k}_S = \pm (\mathbf{k}_1 - \mathbf{k}_1) + \mathbf{k}_2$ . This signal contains photon-echo and virtual-echo components.<sup>[13]</sup> It is possible to use this arrangement with pairs of phase-locked pulses in order to exert better control over the pulse sequence and to heterodyne the signal.

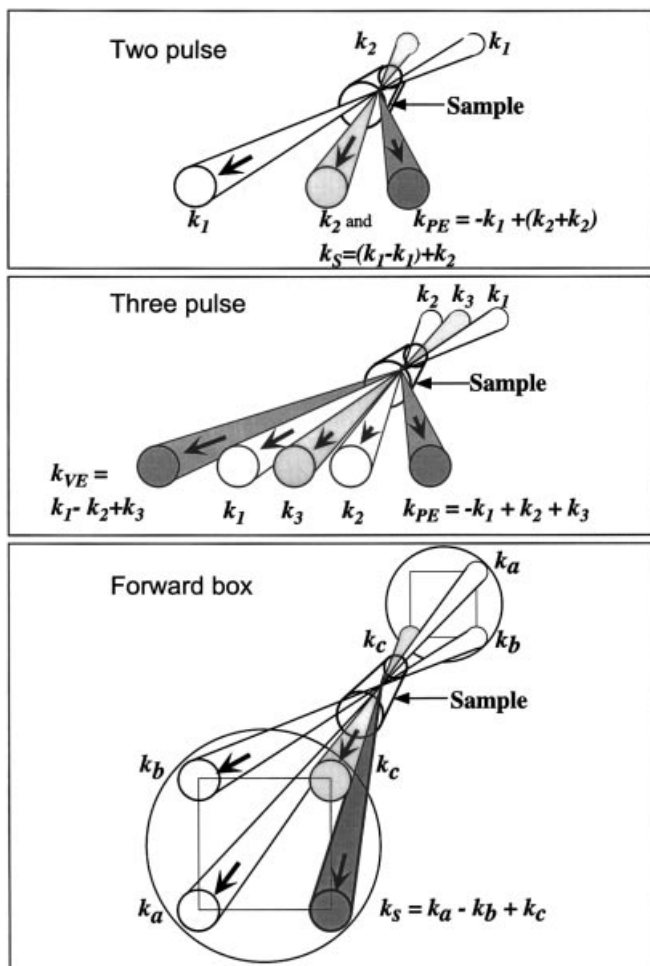


**Fig. 8.3** Experimental set-ups for FWM. (Top) Two-pulse set-up. There are two possible phase-matching directions where a signal can be detected. The signal that coincides with  $\mathbf{k}_2$  contains photon-echo and virtual-echo components. The  $\mathbf{k}_{PE}$  direction can be detected background-free. Notice that this set-up is symmetrical and a similar signal can be expected on the opposite side of  $\mathbf{k}_1$ . (Middle)

Three-pulse set-up. This setup allows the simultaneous collection of a background-free virtual-echo signal at  $\mathbf{k}_{VE}$  and a photon-echo signal at  $\mathbf{k}_{PE}$ . (Bottom) Forward box geometry. This set-up allows background-free detection of a virtual-echo and a photon echo signal at  $\mathbf{k}_S$ ; the nature of the signal depends on the pulse sequence (see text).

The second laser arrangement shown in Figure 8.3 (center) involves three distinct laser pulses in a plane crossing at the sample.<sup>[14]</sup> In this case, the background-free signal can be collected in two phase-matching conditions. The virtual-echo signal is collected at  $\mathbf{k}_{VE} = \mathbf{k}_1 - \mathbf{k}_2 + \mathbf{k}_3$ , while the photon-echo signal is collected at  $\mathbf{k}_{PE} = -\mathbf{k}_1 + \mathbf{k}_2 + \mathbf{k}_3$ . These two three-pulse signals can be used to determine the homogeneous and inhomogeneous relaxation rates of the sample using the same laser arrangement with two detectors.

The third laser arrangement shown in Figure 8.3 (bottom) is known as forward box geometry<sup>[15]</sup> and has a number of advantages. First, virtual-echo and photon-echo measurements can be made with a single detector at the phase-matching geometry. The beams can take any ordering and for this reason they have been labeled  $\mathbf{k}_a$ ,  $\mathbf{k}_b$ , and  $\mathbf{k}_c$ . Second, the coherence is spatially achieved by the laser and it is not necessary to phase-lock the laser pulses. Third, for this arrangement there is no possibility of interference between the beams. Background-free detection requires only one detector.

In the forward box configuration, the different nonlinear phenomena are determined by the pulse ordering. Here, reverse transient grating (RTG) using  $\mathbf{k}_{RTG} = \mathbf{k}_c - (-\mathbf{k}_a + \mathbf{k}_b)$ , photon-echo  $\mathbf{k}_{PE} = -\mathbf{k}_b + (\mathbf{k}_a + \mathbf{k}_c)$ , virtual-echo  $\mathbf{k}_{VE} = \mathbf{k}_a - \mathbf{k}_b + \mathbf{k}_c$ , and stimulated pulse photon-echo  $\mathbf{k}_{SPE} = -\mathbf{k}_b + \mathbf{k}_a + \mathbf{k}_c$  are demonstrated. The pulse ordering is written from left to right and time-overlapped pulses are indicated with parentheses. The observation of a cascaded signal involving the free-induction decay emission from one or more of the laser pulses is possible for the pulse sequence  $\mathbf{k}_{C-FID-FWM} = \mathbf{k}_a + \mathbf{k}_c - \mathbf{k}_b$ , as has been discussed elsewhere.<sup>[16,17]</sup>

The experiments discussed here were performed with an amplified colliding-pulse mode-locked laser producing ~60 fs transform-limited pulses with an energy of 0.3  $\mu$ J per pulse.<sup>[18]</sup> The central wavelength of the pulses was 620 nm. This wavelength is important for resonant excitation of the B–X transition in molecular iodine.<sup>[19]</sup>

Experimental results are shown for two different samples. Off-resonance experiments are shown for  $\text{HgI}_2$ . The sample was sealed in a quartz cell evacuated to  $10^{-6}$  Torr. For the measurements, the cell was heated to 280 °C to obtain a vapor pressure of approximately 100 Torr. The resonance measurements were made on molecular iodine. Iodine was also sealed in an evacuated quartz cell. Data was obtained as a function of temperature to demonstrate the temperature dependence of inhomogeneous and homogeneous broadening. Other samples were examined at room temperature.

## 8.4 Results

In the PP method, the signal gives a measure of the population-transfer induced by the pump and probe lasers, while in the FWM method the signal arises from the laser-induced polarizations in the sample. This fact accounts for most of the differences between the two methods. In most PP experiments, the signal arises from the

population of molecules excited by the pump laser that absorbs the radiation of the probe laser. The FWM signal depends on the coherent mixing of the incident electric fields and their enhancement by the sample.

#### 8.4.1

##### Off-Resonance Measurements

The following gives an illustration of the advantage of off-resonance FWM for the observation of ultrafast rotational and vibrational motion in ground states. The experimental data on gas-phase  $\text{HgI}_2$  together with the theoretical simulation are shown in Figure 8.4. The transient consists of three contributions. At time zero, there is a sharp feature corresponding to the instantaneous isotropic polarizability. This feature is independent of the number of intramolecular degrees of freedom and is observed in all media, as well as for the isolated atoms.<sup>[20,21]</sup> The data reveal a fast vibration that is modulated by a very low frequency envelope. The vibrations with a 211 fs period correspond to the symmetric stretch, this being the only Raman-active mode in this linear molecule.<sup>[22]</sup> The slow modulation stems from the anisotropic contribution to the signal that depends on the molecular orientation.

Modeling of the data in Figure 8.4 requires definition of the isotropic and anisotropic contributions to the susceptibility. Only vibrational motion contributes to the isotropic susceptibility (Eq. 6). Based on the bandwidth of the laser pulse used, only a few vibrational overtones are excited coherently. The isotropic susceptibility may be approximated as:

$$\chi_{iso}(t) = A_v \cos(1/2\omega_v t + \phi_v) \quad (15)$$

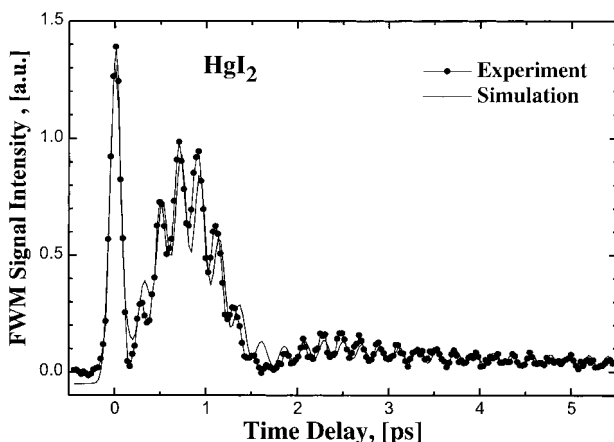


**Fig. 8.4** Off-resonance FWM signal obtained for gas-phase  $\text{HgI}_2$  as a function of the time delay between the first two pulses and the third. The data shows a sharp response at time zero due to the instantaneous polarizability. The fast, 211 fs modulation corresponds to the coherent

symmetrical stretch vibration. The slow picosecond modulation corresponds to the rotational dynamics of the sample. The experimental data are shown as points, while the relevant theoretical simulation is shown as a continuous line.

where  $A_v$  is the relative amplitude of the vibrational contribution,  $\omega_v$  is the frequency of the vibrational mode involved, and  $\phi_v$  is the phase.

The anisotropic part of the susceptibility depends on the changes in orientation of the anisotropic molecules caused by rotational motion with some contribution from vibrational motion. For rotations, a semi-classical approximation for the correlation function may be used

$$C_J(t) = \cos(\omega_J t) \quad (16)$$

where the rotational frequency  $\omega_J$  depends on the Raman selection rules  $\Delta J = 0, \pm 2$  and is given by  $2\pi c[(4B)(J + 3/2)]$ , where  $B$  is a rotational constant. Taking the derivative denoted as Eq. 8 and performing the averaging over all the rotational states indicated in Eq. 7, one obtains:

$$\langle C''(\theta(t)) \rangle \propto \sum_J n_J \omega_J \sin(\omega_J t) \quad (17)$$

where  $n_J$  is the thermal population of rotational states with different momenta  $J$ . For samples in thermal equilibrium, a rotational Boltzmann distribution is used for  $n_J$ . Combining the vibrational and rotational contributions, one obtains the following expression for the anisotropic susceptibility:

$$\chi_{\text{aniso}}(t) = A_r \cos(1/2 \omega_v t + \phi_r) \sum_J n_J \omega_J \sin(\omega_J t) \quad (18)$$

where  $A_r$  is proportional to the anisotropic polarizability,  $\beta$ , and is inversely proportional to the temperature of the sample. There is an additional zero-time feature with amplitude  $A_z$  that arises from the equilibrium isotropic polarizability  $\alpha_0$ . The complete formula for this model is:

$$\chi^{(3)}(t) = A_z(t) + A_v \cos(1/2 \omega_v t + \phi_v) + A_r \cos(1/2 \omega_v t + \phi_r) \sum_J n_J \omega_J \sin(\omega_J t) \quad (19)$$

Convolution of the simulation by the finite temporal width of our laser pulses yields the final results.

The simulation of the  $\text{HgI}_2$  data is shown in Figure 8.4 (line) together with the experimental data (dots). It is clear that the model reproduces the most salient characteristics of the data. The small differences between the model and data could be reduced using a nonlinear least-squares fitting routine. In the model presented here, only the three amplitude parameters were adjusted; all other values were obtained from spectroscopic parameters.<sup>[22,23]</sup>

#### 8.4.2

##### Resonance Measurements

As discussed above for on-resonance FWM, the first laser pulse induces a polarization in the sample. Here, this process is illustrated by contrasting reverse transient grating (RTG)<sup>[21]</sup> and photon-echo (PE) experiments. In these experiments, the first laser pulse induces a polarization and after a variable time  $\tau$  the remaining two lasers, overlapped in time, probe this polarization. The experiments are carried out in gas-phase molecular iodine and the polarization involves a coherent superposition of electronic, vibrational, and rotational states.



The data for the RTG and PE measurements are shown in Figure 8.5. The pulse sequence for RTG is  $E_c$  followed by  $E_a$  and  $E_b$  ( $\mathbf{k}_S = \mathbf{k}_1 + \mathbf{k}_2 - \mathbf{k}'_2$ ), while for PE it is beam  $E_b$  followed by beams  $E_a$  and  $E_c$  ( $\mathbf{k}_S = -\mathbf{k}_1 + \mathbf{k}_2 + \mathbf{k}'_2$ ). The differences observed in the background, undulation, and apparent signal-to-noise of these data stem from the difference in the first pulse interaction. As discussed in Section 8.2.3.2, when the first beam acts on the *bra*, the subsequent laser interactions lead to a cancelling out of the inhomogeneous broadening in the sample and to observation of the photon-echo. When the first interaction occurs on the *ket*, there is no mechanism allowing cancelling of the inhomogeneous contributions to the signal. For gas-phase molecules, inhomogeneous contributions arise from differences in molecular speed, the so-called “Doppler broadening”, as well as from differences stemming from the thermal distribution of initial rotational and vibrational states in the sample prior to laser excitation. The RTG data shows a strong background, that is, a slow undulation that results from the inhomogeneous rotational population of the sample. After the first 3 ps, the RTG data show a mixture of ground- and excited-state dynamics. The observation of ground-state dynamics results from the initial thermal population of different vibrational modes. This inhomogeneity is manifested in vibrational “hot bands” in this time-domain spectrum. In the PE data, only excited-state vibrational dynamics are observed.

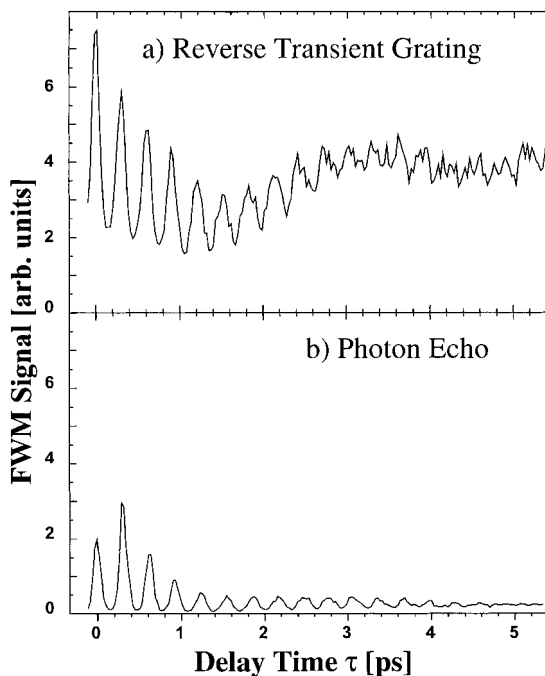


**Fig. 8.5** Comparison between (a) reverse transient grating (RTG) and (b) photon-echo (PE) signals for molecular iodine. The two scans were obtained under identical conditions, except for the pulse sequence (see text). The RTG

transient shows a large background, i.e. a slow modulation due to rotational dynamics, and a mixture of ground- and excited-state vibrations. The PE transient shows only excited-state vibrational motion.

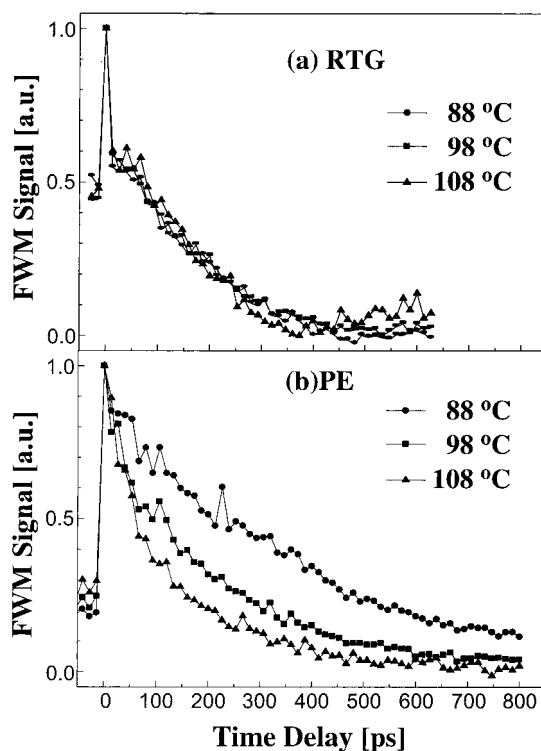


**Fig. 8.6** (a) Reverse transient grating signal for molecular iodine obtained with long time delays. The data were obtained as a function of sample temperature. The average decay time measured was  $150 \pm 20$  ps. Notice that the RTG data show very little temperature dependence because dephasing is overwhelmed by inhomogeneous broadening in this temperature

range. (b) Photon-echo signal obtained under the same conditions as the RTG data. Notice that the PE transients do show a marked temperature dependence; this reflects the homogeneous relaxation, which depends on sample density. The measured coherence relaxation times are  $390 \pm 17$ ,  $204 \pm 9$ , and  $168 \pm 10$  ps for 88, 98, and 108 °C, respectively.

The cancellation of inhomogeneous broadening in PE measurements has been recognized since the first photon-echo measurement in 1964.<sup>[24,25]</sup> This advantageous feature has often been exploited, for example, to measure the homogeneous lifetime of complex systems such as large organic molecules in solution.<sup>[26–28]</sup> Here, the application of this method to molecular iodine is illustrated. Figure 8.6 depicts the results of RTG and PE measurements on molecular iodine taken with long time delays. The measurements were made as a function of temperature to illustrate the different mechanisms for coherence relaxation. Notice that the RTG measurements are apparently independent of the temperature in this temperature range (see Figure 8.6a). This is due to the fact that the inhomogeneous contributions overwhelm the homogeneous relaxation. In the PE measurements, the homogeneous relaxation times are seen to be much longer and to decrease with temperature. The origin of the decreased coherence lifetime is an increase in the number density with a concomitant increase in the collision frequency.

## 8.4.3

## Coherent Control with FWM

The coherent nature of FWM experiments provides an opportunity to harness the coherent properties of lasers for controlling intra- and intermolecular degrees of freedom. The author's group has been exploring FWM methods with a view to achieving coherent control of molecular dynamics.<sup>[18,29,30]</sup> This work is illustrated here with one such example. The data in Figure 8.7 were obtained with molecular iodine. The time delay between the first two pulses was set at 614 fs (upper transient) or 460 fs (lower transient). The upper transient shows mostly ground-state vibrations with a 160 fs period. The lower transient shows exclusively excited-state vibrations with a period of 307 fs.

The mechanisms of signal formation are illustrated in the inserts using ladder diagrams. For the upper transient, the process can be rationalized in terms of a

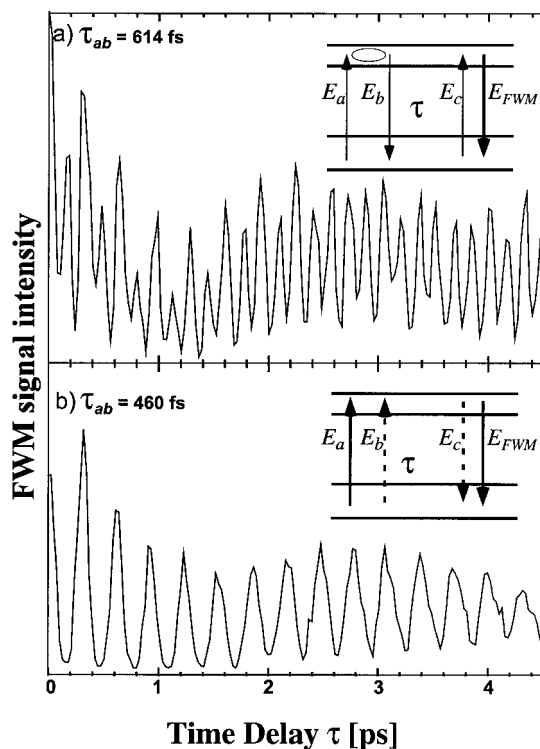


**Fig. 8.7** Virtual-echo measurements on molecular iodine obtained for two different time delays between the first two pulses. (a) When the time delay between the first two pulses is 614 fs, ground-state vibrational motion is observed. (b) When the time delay between the first two pulses is 460 fs, excited-state vibrational motion is observed. The two

transients were obtained as a function of time delay between the second and third pulses under otherwise identical conditions. The ladder diagrams indicate the nonlinear pathway responsible for signal formation; solid arrows indicate action on the *ket*, dashed arrows indicate action on the *bra*.

coherent Raman scattering process. The second pulse creates a coherent superposition of vibrational states in the ground state. This process is enhanced when the time between the first and second pulses matches the vibrational period of the excited state.<sup>[18,29]</sup> The third laser pulse probes the resulting ground-state vibrational coherence. For the lower transient, the time delay between the first two pulses does not permit the transfer of the excited-state superposition of states to the ground state. In this case, signal formation occurs by excitation of a new excited-state superposition by pulse  $E_b$ , as shown with gray arrows. Probing with pulse  $E_c$  results in the observation of excited-state dynamics. The model described in Section 8.2.3.1 can be used to explain these results more rigorously. These results illustrate just one of the several coherent manipulations that are possible using FWM.

## 8.5

### Discussion

#### 8.5.1

#### Off-Resonance FWM and Time-Resolved Measurements of Ground-State Dynamics

Off-resonance FWM is analogous to coherent Raman scattering, and, like its spectrally-resolved cousins, provides ground-state spectroscopic information. Herein, the observation of vibrational and rotational motion of ground-state  $\text{HgI}_2$  has been demonstrated. Elsewhere, other groups as well as the author's group, have shown that this method readily permits the observation of rotational coherence in gas-phase ensembles of molecules.<sup>[21,31–33]</sup> The observation of rotational revivals for time delays of 100 ps with a time resolution of 10 fs allows the determination of rotational constants with a  $10^{-5} \text{ cm}^{-1}$  resolution.<sup>[21,34]</sup> With additional care,  $10^{-6} \text{ cm}^{-1}$  accuracy is possible. This level of accuracy is already in the range of some high-resolution frequency-resolved methods. Time-resolved rotational coherence has been pursued for the determination of complex molecular systems in the gas phase.<sup>[34]</sup> Femtosecond time resolution allows work on lighter molecules such as  $\text{D}_2$ <sup>[35]</sup> and work at high temperatures.

Off-resonance experiments can be used to measure molecular dynamics in gas mixtures. Figure 8.8 depicts the types of experiments that are possible. The experimental data show only the early-time rotational dynamics for three different samples, namely acetylene, car exhaust, and pyrazine. The time at which the first feature reaches its maximum can be used to derive the rotational constant, albeit with less accuracy than for a full recurrence. For acetylene and pyrazine, values of 1.8 and  $0.21 \text{ cm}^{-1}$ , respectively, were obtained. These values are in good agreement with the published rotational constants.<sup>[36]</sup> The data for the car exhaust sample obtained at room temperature demonstrate the utility of off-resonance FWM in the analysis of mixtures of compounds and products of chemical reactions. In this example, the initial dephasing feature was deconvoluted as a sum of three components. The first feature is due to the instantaneous polarizability at time zero, the second is due to nitrogen, and the third to carbon dioxide. Direct measurement of the rotational

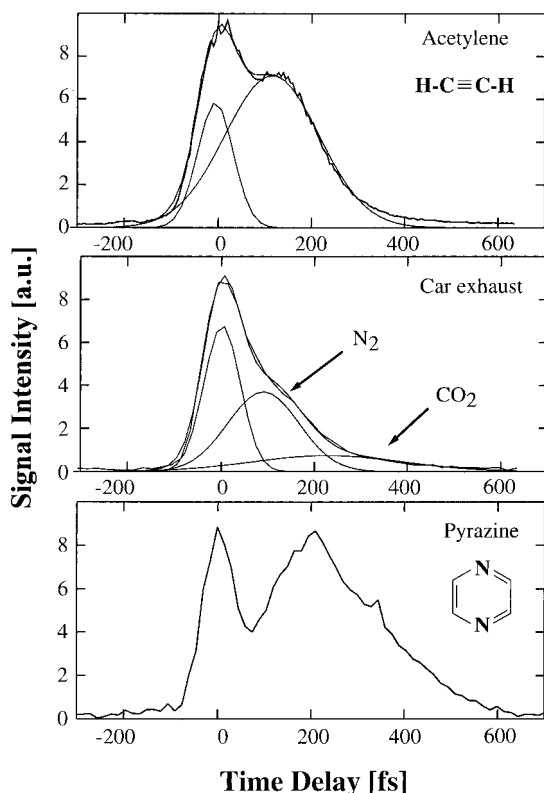


**Fig. 8.8** Off-resonance FWM signals for various compounds. (Top) Initial rotational dynamics observed for gas-phase acetylene molecules. (Middle) Initial rotational dynamics observed from a sample collected from car exhaust. The two main components are nitrogen and carbon dioxide. (Bottom) Initial rotational dynamics observed for gas-phase pyrazine.

recurrences results in much higher accuracy, as discussed earlier.<sup>[21]</sup> At present, the author's group is pursuing different applications of off-resonance FWM in the study of chemical reactivity.

### 8.5.2

#### Resonance FWM, Ground and Excited-State Dynamics

Resonance FWM allows the coherent excitation of ground- as well as excited-state dynamics. In the above, results have been presented for molecular iodine in the gas phase. The goal of these experiments has been to illustrate the possibilities offered by coherent spectroscopic methods such as FWM. It has been shown how, using a specific laser configuration, the sign of the electric field interactions may be regulated. This control leads to photon-echo-type measurements where inhomogeneous contributions to the signal are cancelled out. Although the photon-echo phenomenon has been known for over two decades, it seems valuable to demonstrate the pro-

cess experimentally in a well-understood sample. A simple formulation that is independent of molecular complexity has been included. The reverse transient grating measurements have been contrasted to show the effect of inhomogeneities in the sample.

Resonant FWM experiments have other advantages over PP methods. In FWM, the dynamics depend on the ground or excited states. In the PP method, the dynamics depend on a population-transfer from the ground to the excited state and on the time-dependent transition probability between that state and a second excited state. This second transition is not always well-known because potential energy surfaces are not easily determined. Interpretation of the PP data depends on assumptions concerning the spectroscopic probe transition. In FWM measurements, the ground state can be obtained from off-resonant measurements, leaving only the first excited state to be determined. This should make these methods more powerful than PP methods for inverting the time domain data and constructing the potential energy surfaces.

The experiments described here demonstrate the use of a time delay to enhance the FWM signal from the ground state. These experiments can be understood in terms of coherent anti-Stokes Raman scattering (CARS). With tunable femtosecond lasers, it is possible to deposit any amount of excess energy in the ground state and to follow the ensuing dynamics. Zewail and co-workers have used degenerate FWM for probing real-time reaction dynamics.<sup>[37]</sup> Femtosecond CARS experiments have been carried out by Hyden and Chandler,<sup>[38]</sup> Materny,<sup>[39,40]</sup> and Prior.<sup>[41]</sup>

It is well known that multi-photon transitions are easily achieved with ultrafast pulses. In fact, it is sometimes extremely difficult to observe single-photon transitions in certain molecular systems. Using FWM, one can determine the phase-matching geometry based on the type of process that one wants to observe. Detection at that geometry provides a means of filtering out all other processes and counting the number of photons involved in the laser-molecule interactions.

When the FWM signal is time-gated, a second dimension is uncovered that identifies the nature of the coherent superposition of states that leads to signal formation. This information can also be obtained by spectrally dispersing the FWM signal.<sup>[30,42]</sup> The additional information allows the elucidation of dynamic processes that are masked in one-dimensional techniques. The two-dimensional information obtained in this measurement promises to unravel the mechanisms of energy transfer in complex liquid systems.<sup>[7]</sup> The author's group has used this method to determine the role of chirp in laser excitation. Efforts on six-wave mixing are currently underway in various laboratories.<sup>[43-47]</sup>

In the author's group, efforts are ongoing to use FWM methods as a convenient way to coherently combine three laser pulses. The use of different pulse sequences for controlling the various Liouville pathways that lead to signal formation have been explored.<sup>[17]</sup> The long coherence lifetimes of gas-phase molecules provide an opportunity for designing arrangements whereby multiple coherent interactions are possible. Such set-ups should be of interest for the coherent manipulation of large numbers of quantum mechanical states. Currently, work is in progress aimed at

extending these methods to ultraviolet wavelengths in order to interrogate chemical reactions.

### Acknowledgements

The research presented here is the result of the hard work and dedication of Igor Pastirk, Emily J. Brown, Dr. Vadim V. Lozovoy, and Dr. Bruna I. Grimberg of the Dantus Laboratory. Support of this work by the National Science Foundation (Grant no. CHE-9812584) is gratefully acknowledged. Additional funding has been provided by a Packard Science and Engineering Fellowship, an Alfred P. Sloan Research Fellowship, and a Camille Dreyfus Teacher-Scholar award.

### References

- 1 A. H. Zewail (Ed.), *Femtochemistry*, World Scientific, Singapore, 1994, Vols. I and II.
- 2 J. Manz, L. Wöste (Eds.), *Femtosecond Chemistry*, VCH, Weinheim, 1995, Vols. I and II.
- 3 M. Chergui (Ed.), *Femtochemistry: Ultrafast Chemical and Physical Processes in Molecular Systems*, World Scientific, Singapore, 1996.
- 4 V. Sundström (Ed.), *Femtochemistry and Femtobiology*, World Scientific, Singapore, 1998.
- 5 L. E. Fried, S. Mukamel, *J. Chem. Phys.* **1990**, 93, 3063–3071.
- 6 Y. Tanimura, S. Mukamel, *J. Chem. Phys.* **1995**, 103, 1981–1984.
- 7 S. Mukamel, *Principles of Nonlinear Optical Spectroscopy*, Oxford University Press, New York, 1995.
- 8 R. W. Boyd, *Nonlinear Optics*, Academic Press, San Diego, 1992.
- 9 M. D. Fayer, *Annu. Rev. Phys. Chem.* **1982**, 33, 63.
- 10 M. Cho, M. Du, N. F. Scherer, G. R. Fleming, *J. Chem. Phys.* **1993**, 99, 2410.
- 11 E. L. Hahn, *Phys. Rev.* **1950**, 80, 580.
- 12 R. R. Ernst, G. Bodenhausen, A. Wokaum, *Principles of Nuclear Magnetic Resonance in One and Two Dimensions*, Oxford University Press, New York, 1987, Vol. 14.
- 13 M. S. Pshenichnikov, W. P. de Boei, D. A. Wiersma, *Phys. Rev. Lett.* **1996**, 76, 4701.
- 14 A. M. Weiner, S. D. Silvestri, E. P. Ippen, *J. Opt. Soc. Am. B* **1985**, 2, 654.
- 15 Y. Prior, *Appl. Opt.* **1980**, 19, 1741.
- 16 V. V. Lozovoy, I. Pastirk, M. G. Comstock, *Chem. Phys. Rev.* **2001**, 266, 205.
- 17 V. V. Lozovoy, I. Pastirk, E. J. Brown, B. I. Grimberg, M. Dantus, *Int. Rev. Phys. Chem.* **2000**, 19, 531.
- 18 I. Pastirk, E. J. Brown, B. I. Grimberg, V. V. Lozovoy, M. Dantus, *Faraday Discuss.* **1999**, 113, 401–424.
- 19 J. Tellinghuisen, *J. Quant. Spectrosc. Radiat. Transfer* **1978**, 19, 149.
- 20 Y. R. Shen, *The Principle of Nonlinear Optics*, Wiley, New York, 1984.
- 21 E. J. Brown, Q. Zhang, M. Dantus, *J. Chem. Phys.* **1999**, 110, 5772.
- 22 R. J. H. Clark, D. M. Rippon, *J. Chem. Soc., Faraday Trans. 2* **1973**, 69, 1496.
- 23 V. P. Spiridonov, A. G. Gershikov, B. S. Butayev, *J. Mol. Struct.* **1979**, 52, 53.
- 24 N. A. Kurnit, I. D. Abella, S. R. Hartmann, *Phys. Rev. Lett.* **1964**, 13, 567–570.
- 25 C. K. N. Patel, R. E. Slusher, *Phys. Rev. Lett.* **1968**, 20, 1087–1089.
- 26 G. R. Fleming, M. H. Cho, *Ann. Rev. Phys. Chem.* **1996**, 47, 109.
- 27 P. Vohringer, D. C. Arnett, T. S. Yang, N. F. Scherer, *Chem. Phys. Lett.* **1995**, 237, 387.
- 28 W. P. de Boei, M. S. Pshenichnikov, D. A. Wiersma, *Annu. Rev. Phys. Chem.* **1998**, 49, 99–123.
- 29 E. J. Brown, I. Pastirk, B. I. Grimberg, V. V. Lozovoy, M. Dantus, *J. Chem. Phys.* **1999**, 111, 3779–3782.
- 30 V. V. Lozovoy, B. I. Grimberg, E. J. Brown, I. Pastirk, M. Dantus, *J. Raman Spectrosc.* **2000**, 31, 41–49.
- 31 J. P. Heritage, T. K. Gustafson, C. H. Lin, *Phys. Rev. Lett.* **1975**, 34, 1299.
- 32 H. M. Frey, P. Beaud, T. Gerber, B. Mischler, P. P. Radi, A. P. Tzannis, *Appl. Phys. B* **1999**, 68, 735–739.
- 33 B. Lavorel, O. Faucher, M. Morgen, R. Chaux, *J. Raman Spectrosc.* **2000**, 31, 77–83.

- 34 C. Hattig, B. A. Hess, *J. Phys. Chem* **1996**, *100*, 6243.
- 35 O. M. Sarkisov, D. G. Tovbin, V. V. Lozovoy, F. E. Gostev, A. A. Autipin, S. Y. Umanskii, *Chem. Phys. Lett.* **1999**, *303*, 458–466.
- 36 G. Herzberg, *Molecular Spectra and Molecular Structure*, Vol. III, Kriger Publishing Company, Florida, 1991.
- 37 M. Motzkus, S. Pedersen, A. H. Zewail, *J. Phys. Chem.* **1996**, *100*, 5620–5633.
- 38 C. C. Hayden, D. W. Chandler, *J. Chem. Phys.* **1995**, *103*, 10465–10472.
- 39 M. Schmitt, G. Knopp, A. Materny, W. Kiefer, *Chem. Phys. Lett.* **1997**, *280*, 339–347.
- 40 M. Schmitt, G. Knopp, A. Materny, W. Kiefer, *Chem. Phys. Lett.* **1997**, *270*, 9–15.
- 41 G. Knopp, I. Pinkas, Y. Prior, *J. Raman Spectrosc.* **2000**, *31*, 51–58.
- 42 I. Pastirk, V. V. Lozovoy, B. I. Grimberg, E. J. Brown, M. Dantus, *J. Phys. Chem. A* **1999**, *103*, 10226–10236.
- 43 K. Tominaga, G. P. Keogh, Y. Naitoh, K. Yoshihara, *J. Raman Spectrosc.* **1995**, *26*, 495–501.
- 44 A. Tokmakoff, M. J. Lang, D. S. Larsen, V. Chernyak, S. Mukamel, *Chem. Phys. Lett.* **1997**, *272*, 48–54.
- 45 J. C. Kirkwood, A. C. Albrecht, *J. Raman Spectrosc.* **2000**, *31*, 107–124.
- 46 D. A. Blank, L. J. Kaufman, G. R. Fleming, *J. Chem. Phys.* **1999**, *111*, 3105–3114.
- 47 W. Zhao, J. C. Wright, *Phys. Rev. Lett.* **2000**, *84*, 1411–1414.



## 9

# Quantum Control of Ultrafast Laser-Driven Isomerization Reactions: Proton Transfer and Selective Preparation Of Enantiomers

### 9.1

#### Introduction

The real-time analysis of chemical reaction dynamics using ultrafast laser sources has become common practice in Femtochemistry. In addition, recently developed pulse-shaping techniques provide almost arbitrary laser pulses over a wide range of frequencies, time scales, and intensities. This flexibility has supported the step forward from the analysis to the control of reaction dynamics.<sup>[1]</sup> The purpose of this survey is to summarize some of our theoretical results concerning the design of laser pulses for the quantum control of isomerization reactions, in particular for intramolecular hydrogen or proton transfer, with applications in the laser preparation of pure enantiomers (Section 9.2), and proton transfer in the condensed phase (Section 9.3). Among the various methods for finding laser pulses capable of driving a reaction from an initial (reactant) to a target (product) state, optimal control theory is certainly one of the most powerful approaches. While the success of the optimal control strategy is almost guaranteed, at least for the dynamics in one-dimensional bound potentials, it often confronts us with rather complicated pulse shapes. However, subsequent analysis of numerically generated pulses may point to simpler ones that should be capable of driving the system along the most favorable reaction paths. In the following, we present some results demonstrating how optimal control theory can guide us to the design of simpler analytical pulse forms. Related discussions of this aspect of laser-driven reactions have already been given in refs.<sup>[2–8]</sup> In retrospect, one may also consider the model studies of Tannor and co-workers<sup>[9–11]</sup> as a pioneering example: in their 1989 paper<sup>[11]</sup> they derived an optimal laser pulse for bond-selective photodissociation, which pointed to two simple pump-dump laser pulses, as they had anticipated already in their earlier papers.<sup>[9,10]</sup>

A realistic modeling of laser-driven dynamics relies on the choice of the molecular Hamiltonian. In several studies of isomerization reactions, a double-minimum potential energy curve along a one-dimensional reaction coordinate has been considered. These simple model investigations may serve as a reference for more realistic, multi-dimensional treatments that include the coupling between the reaction coordinate and the molecule's remaining degrees of freedom. We will consider laser-

driven reactions in the electronic ground state, which can be modeled by the Hamiltonian:

$$\mathcal{H} = \mathcal{H}_{\text{sys}} + \mathcal{H}_{\text{env}} + \mathcal{H}_{\text{sys-env}} + \mathcal{H}_{\text{field}}(t) \quad (1)$$

The four terms on the right-hand-side describe the relevant system (reaction coordinate(s)), additional degrees of freedom of the environment (intramolecular vibrations and/or rotations as well as possible solvent coordinates), the coupling between the system and environment, and the interaction with the external field.

Concerning the light-matter interaction, we assume a semi-classical dipole approximation, that is,  $\mathcal{H}_{\text{field}} = -\mu \mathbf{E}(t)$ . The external field is specified either using optimal control theory<sup>[2-11]</sup> or analytically. In the latter case, we use the parameterized form:<sup>[12]</sup>

$$\mathbf{E}(t) = \sum_i \mathbf{e}_i E_i(t - t_i) \cos(\Omega_i t) \quad (2)$$

with  $\mathbf{e}_i$ ,  $E_i$ , and  $\Omega_i$  denoting polarization, envelope, and center frequency, respectively. For medium-sized molecules, the potential energy and dipole moment surfaces in Eq. (1) can be obtained using ab initio quantum chemistry methods. For large molecules or molecules in solution, this approach has to be combined with the concepts of condensed-phase dynamics.<sup>[13]</sup>

In the following, we present two exemplary studies of laser-driven hydrogen- or proton-transfer (PT) reactions, which demonstrate the path from optimal control to control by analytical laser pulses, and from simple one-dimensional to multi-dimensional models. In the first part, we discuss the preparation of pure enantiomers with optimized polarized light fields. In the second part, different strategies for PT in the condensed phase are given.

## 9.2

### Laser Preparation of Pure Enantiomers

Our first example is the preparation of pure enantiomers by laser pulses, an active field of research in femtosecond chemistry.<sup>[14-17]</sup> Our chosen model system is H<sub>2</sub>POSH, which is assumed to be pre-oriented, with the P-S bond pointing along the z-axis, see Fig. 9.1. H<sub>2</sub>POSH has two atropisomers depending on the sign (+, “left, L”, or –, “right, R”) of the torsional angle  $\varphi = \varphi_1 - \varphi_2$ , where  $\varphi_1$  and  $\varphi_2$  describe the rotations of the S-H and H<sub>2</sub>PO fragments around the P-S bond. Our 1D model describes laser-driven motions along  $\varphi$ , corresponding to transfer of the hydrogen atom of the S-H bond relative to the fixed heavy H<sub>2</sub>PO group. The related torsional eigenstates  $|\Phi_{v\pm}\rangle$  are labeled by torsional and symmetry quantum numbers,  $v$  and  $\pm$ , respectively (see Figure 9.1, adapted from ref.<sup>[15]</sup>). The 2D model also includes, in addition, the rotation of the entire molecule around the pre-aligned P-S bond, and the corresponding states are labeled  $|\Phi_{v\pm M}\rangle$ , where  $M = 0, \pm 1, \pm 2, \dots$  are the rotational quantum numbers. All eigenstates have equal probabilities (0.5:0.5) for both enantiomers, whereas superpositions (see Eq. (3)), are localized preferably as right, R, and left, L, enantiomers.<sup>[18]</sup>

$$|\Phi_{vL(M)}\rangle = [|\Phi_{v+(M)}\rangle + |\Phi_{v-(M)}\rangle]/\sqrt{2} \quad (3)$$

$$|\Phi_{vR(M)}\rangle = [|\Phi_{v+(M)}\rangle - |\Phi_{v-(M)}\rangle]/\sqrt{2}$$

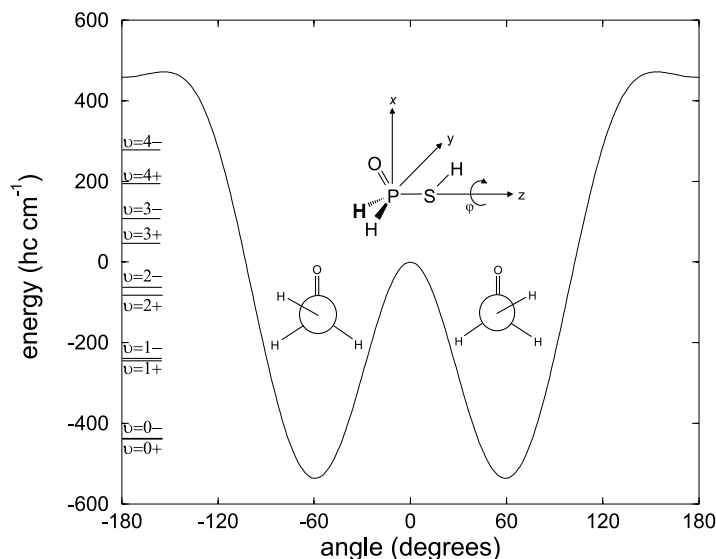


**Fig. 9.1** Ab initio potential-energy curve *versus* torsional angle  $\varphi = \varphi_1 - \varphi_2$  for the model system  $\text{H}_2\text{POSH}$  showing the torsional levels.

In the following, we assume that the system is initially ( $t = 0$ ) in its ground state  $|\Phi_{0+(0)}\rangle$ , corresponding to equal probabilities of both enantiomers. The task is then to design a laser pulse that is able to drive the system so as to favor a single, R or L, enantiomer, represented by dominant superpositions of states, either  $|\Phi_{vR(M)}\rangle$  or  $|\Phi_{vL(M)}\rangle$ , respectively.

The resulting optimal laser pulse for the 1D model is shown in Figure 9.2A, together with the populations of states  $|\Phi_{v\pm}\rangle$  and the localizations of the enantiomers. Perfect (near 100 %) preparation of the left enantiomer is obtained by means of the local optimal control method, [4]. The population dynamics points to a sequential pump-dump mechanism, where 50 % of  $|\Phi_{0+}\rangle$  is transferred to  $|\Phi_{0-}\rangle$  via the excited doublet  $|\Phi_{1+}\rangle$ ,  $|\Phi_{1-}\rangle$ , thus preparing  $|\Phi_{0L}\rangle$ . Based on this mechanism derived from optimal control, we designed a laser pulse with analytical ( $\sin^2$ ) shape capable of inducing an equivalent pump-dump mechanism. The result is shown in Figure 9.2B (compare with Figure 9.2A). Next, we show equivalent results for the local optimal control applied to the 2D model; see Figure 9.3A. The resulting mechanism is apparently similar to that operative in the 1D system, but in this case the sequential pump and dump transitions occur almost simultaneously yielding only rather small intermediate populations of the excited states. Accordingly, the pump and dump

laser pulses appear to be merged into a single pulse. The yield of the target enantiomer, however, is somewhat reduced, due to the coupling of the overall rotation with the torsion. This result suggests the use of the corresponding analytical laser pulse that induces a similar mechanism and yield; see Figure 9.3B, where ca. 50 % of the original population in  $|\Phi_{0+0}\rangle$  is transferred via the excited states  $|\Phi_{1+1}\rangle$ ,  $|\Phi_{1-1}\rangle$  to  $|\Phi_{0-0}\rangle$ , thereby yielding  $|\Phi_{0L0}\rangle$ . The duration of the analytical pulses has been shortened, as compared to that of the optimal pulses, exploiting tunneling in the lowest doublet of states, which ultimately yields the same overall localization.

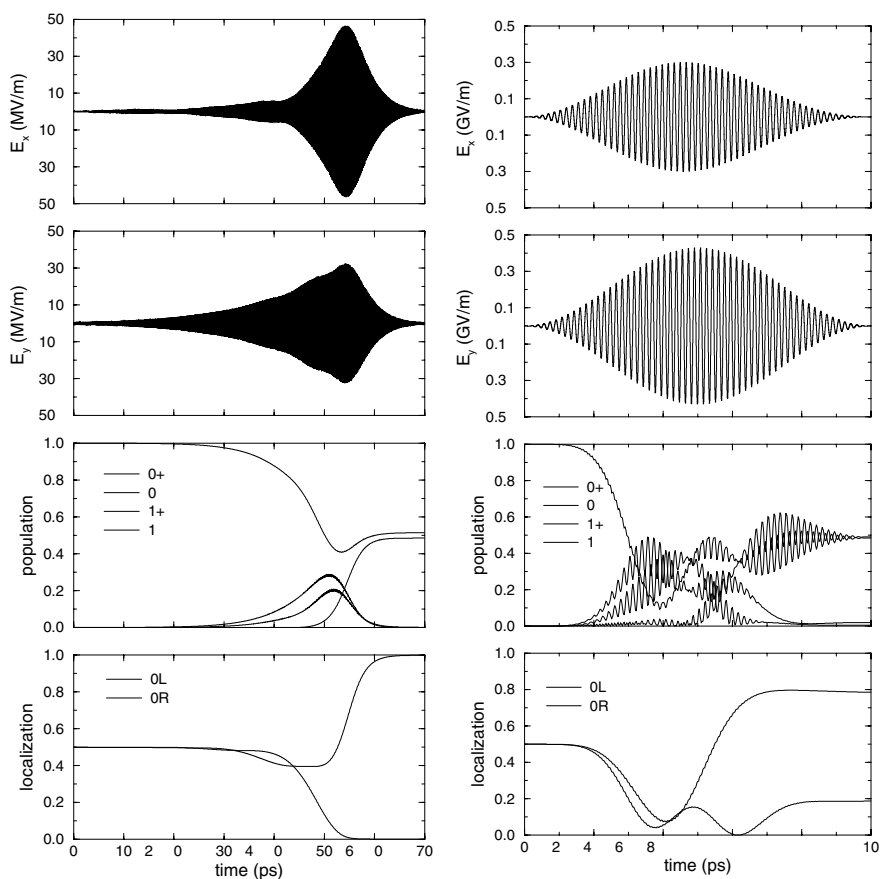


**Fig. 9.2** Left Panel: Optimal laser pulses  $E_x, E_y$  and the resulting populations and localization for the selective preparation of the left-hand enantiomer of H<sub>2</sub>POSH. The results are for the

1D model, including the laser-driven torsion. Right Panel: The optimal laser pulse is replaced by a pulse with  $\sin^2$  shapes.

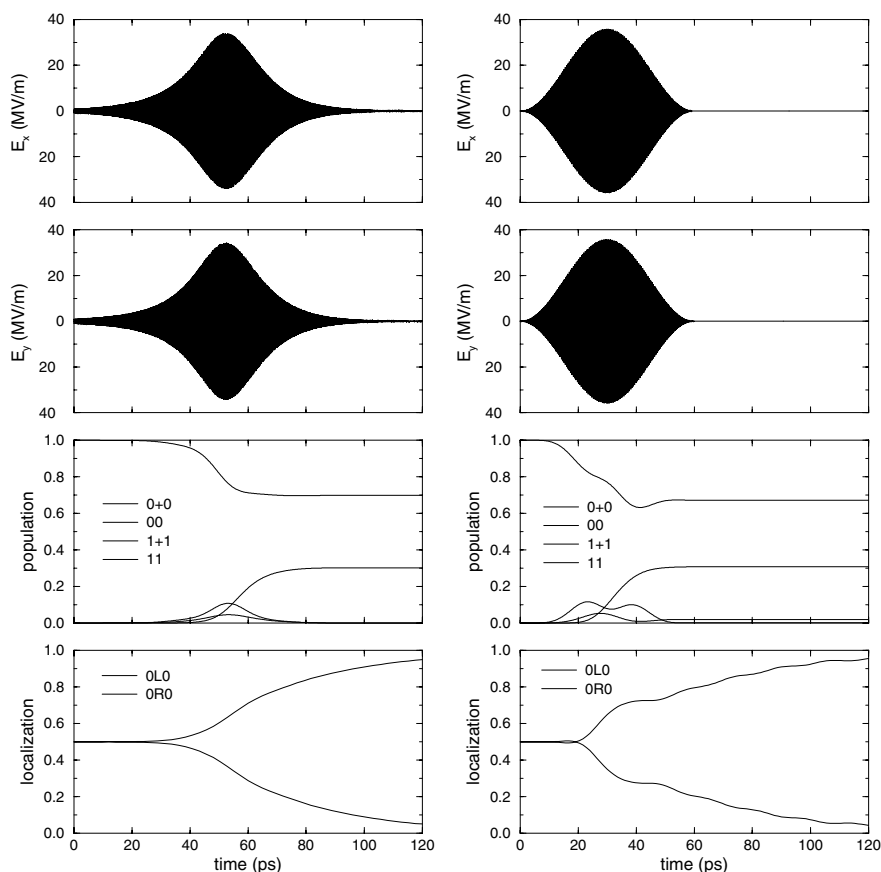


**Fig. 9.3** Left Panel: As Figure 9.2, but the 1D model is replaced by a 2D one, including coupled laser-driven torsion and rotations of

$\text{H}_2\text{POSH}$  around the pre-aligned P–S bond. Right Panel: The optimal laser pulse is replaced by a pulse with  $\sin^2$ -shapes.

### 9.3

#### Proton Transfer

Intramolecular proton or hydrogen atom transfer is usually coupled to motions of the molecular scaffold. A convenient concept to account for this multi-dimensionality is the reaction surface Hamiltonian.<sup>[19–21]</sup> Here, the environmental or substrate coordinates are treated within the harmonic approximation with normal mode frequencies that depend on the actual value of the reaction coordinate. The latter can be defined as following the minimum energy path<sup>[19]</sup> or in terms of internal coordinates.<sup>[20]</sup> While this leads to a non-diagonal kinetic energy operator, one can formulate an all-Cartesian reaction surface Hamiltonian, thus shifting the couplings into the potential energy operator.<sup>[21,22]</sup>

An approximate Cartesian proton-transfer Hamiltonian can also be constructed from a few *ab initio* data for the stationary and saddle points of the potential-energy surface.<sup>[23]</sup> Using this idea, the laser-driven PT dynamics has been investigated along a one-dimensional reaction coordinate for the enol–enethiol tautomerism in thioacetylacetone with perturbative<sup>[24]</sup> and non-perturbative<sup>[25]</sup> inclusion of the harmonic environment. Here, we will discuss a 2D model for this reaction, as shown in Figure 9.4.<sup>[23]</sup> The reaction coordinate  $x$  describes the proton's position (in linear approximation), while the heavy atom normal mode coordinate  $Q$  accounts for the O–S vibration, which strongly modifies the reaction barrier. Thus, in contrast to the previous 1D model,<sup>[24,25]</sup> one substrate mode is included into  $H_{\text{sys}}$ . The remaining degrees of freedom can be incorporated into the environment, that is, into  $H_{\text{env}}$ . The coupled dynamics of these two subsystems can then be treated using the density-matrix formalism, which accounts for  $H_{\text{sys-env}}$  in terms of second-order perturbation theory.<sup>[13]</sup> The resulting relaxation and dephasing processes, which compete against the laser-driven dynamics, are expressed in terms of the so-called spectral

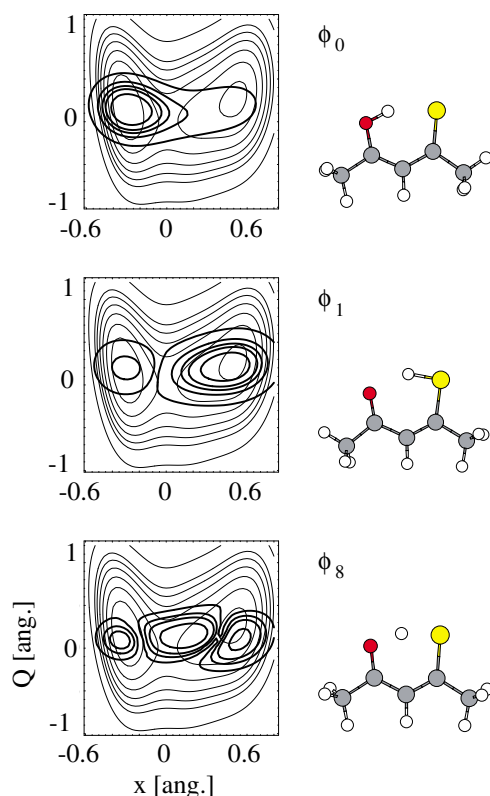


**Fig. 9.4** Two-dimensional potential-energy surface for proton transfer in thioacetylacetone (see text and ref.<sup>[23]</sup>). The two lowest vibrational eigenstates are localized on the enol ( $\Phi_0$ ) and

enethiol ( $\Phi_1$ ) side of the barrier. Also shown is the delocalized above-barrier state ( $\Phi_8$ ), which can be used in the pump-dump control scheme.

density  $J(\omega)$ . In ref.<sup>[23]</sup> the simple analytical form  $J(\omega) = g\omega/\omega_c \exp(1 - \omega/\omega_c)$  was employed, which is typical for condensed-phase environments.<sup>[13]</sup> The cut-off frequency  $\omega_c$  characterizes the upper limit of the relevant frequency range of the environment, which was estimated to be  $370 \text{ cm}^{-1}$  for thioacetylacetone ( $g$  is the coupling strength parameter). The reduced density operator is conveniently represented in terms of the system eigenstates obtained from  $H_{\text{sys}}\Phi_v = E_v\Phi_v$ ; the equations of motion for  $\rho_{vv'}$  have to be solved numerically.<sup>[23]</sup>

Switching the proton's position from the reactant to the product side of the barrier can to some extent be accomplished by a population inversion between the states  $\Phi_0$  and  $\Phi_1$  (compare Figure 9.4). In principle, a pump-dump scheme could be employed using the state  $\Phi_8$  as an intermediate.<sup>[26]</sup> In ref.<sup>[6]</sup> it was shown that this pump-dump scheme may be derived from optimal control theory if one allows for high pulse intensities. However, on increasing the penalty for high pulse intensities in the control functional, population switching may also occur through tunneling.<sup>[6,23]</sup> In the extreme case, tunneling can be driven by a rectangular-type, "switch

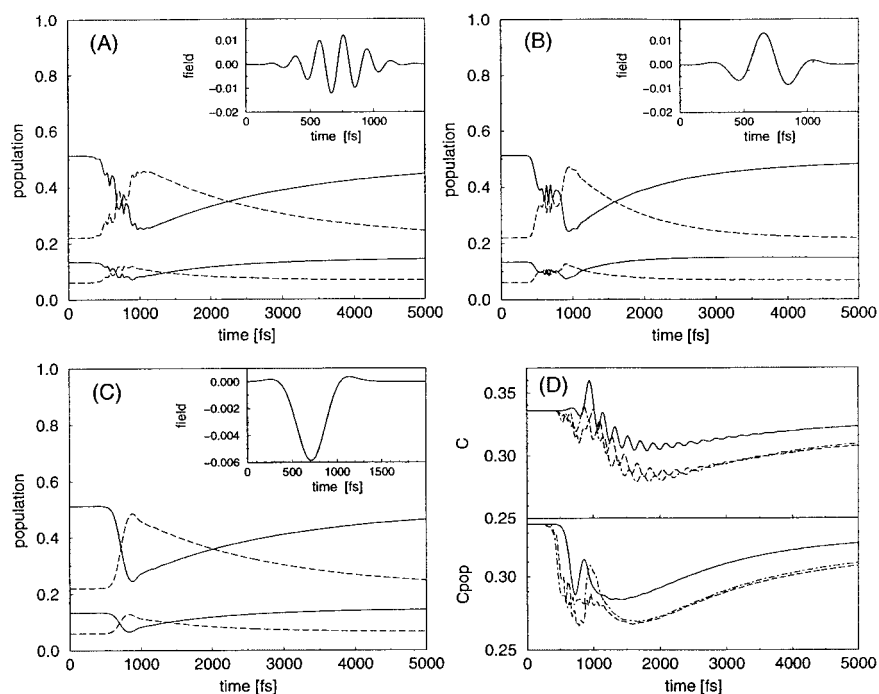


**Fig. 9.5** Population dynamics of the four lowest vibrational eigenstates in the 2D model of the laser-driven proton transfer in thioacetylacetone, see Figure 9.4 for  $g=3 \cdot 10^{-4}$ . Starting from a thermal distribution ( $T = 300 \text{ K}$ ), the populations of states  $\Phi_0/\Phi_1$  (solid/dashed) and  $\Phi_2/\Phi_3$  (solid/dashed), and therefore the proton's position, are switched by the pulses

shown in the insert [(A)  $t_p = 712 \text{ fs}$ ,  $\Delta_p = 407 \text{ fs}$ ,  $E_p = 0.0125 E_h/ea_0$ ; (B)  $t_p = 675 \text{ fs}$ ,  $\Delta_p = 386 \text{ fs}$ ,  $E_p = -0.0133 E_h/ea_0$ ; (C)  $t_p = 725 \text{ fs}$ ,  $\Delta_p = 415 \text{ fs}$ ,  $E_p = +0.0059 E_h/ea_0$ ]. In panel (D), the coherence degree  $C(t)$  as well as its population part  $C_{\text{pop}}(t)$  are shown for the situation of panels (A): dashed, (B): dash-dot, (C): solid line.

on – tunnel – switch off”, pulse.<sup>[6]</sup> However, the optimal control pulse used in ref. [23] suggested that pulses having a finite carrier frequency  $\Omega_p$  lower than  $(E_1 - E_0)/\hbar$  can also trigger population switching. The mechanism is dictated by the effects of tunneling and direct excitation in the potential distorted by the field. Following the suggestion of optimal control theory, we designed analytical Gaussian-type pulses, that is, in Eq. (2)  $E_{i-p}(t - t_p) = E_p(2/(\pi\Delta_p^2))^{1/2} \exp[-2(t - t_p)^2/\Delta_p^2]$ , for population inversion. Keeping the intensity low and the pulse duration below 1.5 ps, we found three possible driving frequencies,  $\Omega_p = 176 \text{ cm}^{-1}$  [ $= (E_1 - E_0)/\hbar$ ],  $77 \text{ cm}^{-1}$ , and  $24 \text{ cm}^{-1}$ , that met our goal; see Figure 9.5. The pulses, being optimized for the coherent case, perform equally well in the presence of dissipation. However, the smaller the value of  $\Omega_p$ , the lower is the required pulse intensity. The different dynamics triggered by the three pulses can be discussed in terms of the coherence degree  $C(t) = \text{tr}(\rho(t)^2)$ ,<sup>[13]</sup> shown in Figure 9.5 (D). The largest values for  $C(t)$  are observed for the lowest-frequency pulse, since it does not cause an appreciable non-thermal population redistribution over many states as compared to the other two pulses; see the plot of  $C_{\text{pop}}(t) = \sum_v \rho_{vv}(t)^2$ . The behavior of  $C(t)$  points to a gradual change from a pure IR transition (Figure 9.5 (A)) to mostly quantum tunneling (Figure 9.5 (C)).

The different dynamics in the presence of the analytically designed pulses is also reflected in the transient absorption spectrum.<sup>[27]</sup> As can be seen in Figure 9.6, the success of laser driving can be scrutinized by monitoring the transient absorption of a probe pulse tuned in resonance either with the  $\Phi_0 \rightarrow \Phi_8$  or with the  $\Phi_1 \rightarrow \Phi_8$  transition during and after the action of the driving pulse. Relaxation processes cause a decay of the signal at large time delays, that is to say, control is achieved only on an intermediate time scale. Note that the negative signal (ground-state bleaching) does not decay to zero in the given interval. This effect, first seen in our 2D reaction model, is due to temporary population trapping in the heavy atom mode. It is not so pronounced for the lowest-frequency pulse due to the reduced overall population redistribution.

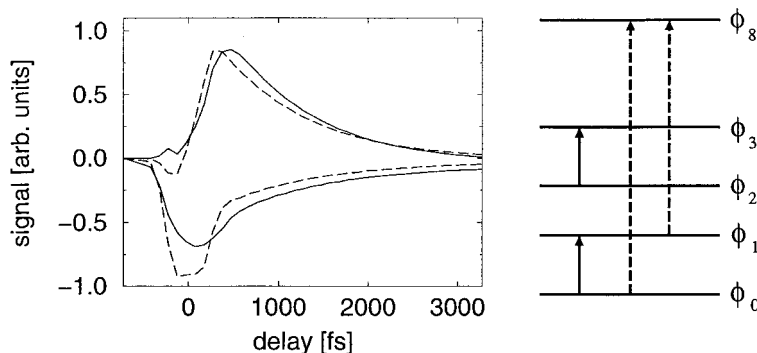


**Fig. 9.6** Transient absorption signal observed for the driving pulses of Figures. 9.5 (A) (solid) and (C) (dashed). Positive and negative signals correspond to probing the  $\Phi_0 \rightarrow \Phi_8$  (ground-

state bleaching/stimulated emission) and  $\Phi_1 \rightarrow \Phi_8$  (excited-state absorption) transitions, respectively. The width of the Gaussian test pulse is 200 fs.



## 9.4

## Conclusions

It has been demonstrated through studies of two types of isomerization reactions that optimal control theory can be used to derive simple analytical pulse schemes for reaction control. Increasing the number of degrees of freedom participating in the reaction does not necessarily require a change of the control scheme, but laser driving has to compete with energy redistribution processes. Thus, pulse schemes having a shorter overall duration or causing a smaller degree of vibrational excitation might perform better in this case.

The present study allows for various extensions. In the case of the preparation of pure enantiomers, the present scenario, which starts from the reactant in the torsional/rotational ground state, can be replaced by an initial racemate of “left” and “right” enantiomers at low temperature, calling for simulations of the laser-driven representative density matrix.<sup>[17]</sup> Finally, more intramolecular degrees of freedom can be taken into account, combining, for instance, time-dependent self-consistent field methods with a full-dimensional reaction surface Hamiltonian.<sup>[28]</sup>

## References

- 1 A. H. Zewail, in *Femtochemistry and Femtobiology: Ultrafast Reaction Dynamics at Atomic-Scale Resolution*, Nobel Symposium Vol. 101 (Ed.: V. Sundström), World Scientific, Singapore, **1997**, p. 1–53.
- 2 S. Shi, H. Rabitz, *J. Chem. Phys.* **1990**, *92*, 2927–2937.
- 3 M. Kaluza, J. T. Muckerman, P. Gross, H. Rabitz, *J. Chem. Phys.* **1994**, *100*, 4211–4228.
- 4 M. Sugawara, Y. Fujimura, *J. Chem. Phys.* **1994**, *100*, 5646–5655.
- 5 J. L. Krause, R. M. Whitnell, K. R. Wilson, Y. J. Yan, in *Femtosecond Chemistry* (Eds.: J. Manz, L. Wöste), Verlag Chemie, Weinheim, **1995**, p. 743–779.
- 6 N. Došlić, O. Kühn, J. Manz, K. Sundermann, *J. Phys. Chem. A* **1998**, *102*, 9645–9650.
- 7 I. R. Solá, J. Santamaría, D. J. Tannor, *J. Phys. Chem. A* **1998**, *102*, 4301–4309.
- 8 J. Manz, K. Sundermann, R. de Vivie-Riedle, *Chem. Phys. Lett.* **1998**, *290*, 415–422.
- 9 D. J. Tannor, S. A. Rice, *J. Chem. Phys.* **1985**, *83*, 5013–5018.
- 10 D. J. Tannor, R. Kosloff, S. A. Rice, *J. Chem. Phys.* **1986**, *85*, 5805–5820.
- 11 R. Kosloff, S. A. Rice, P. Gaspard, S. Tersigini, D. J. Tannor, *Chem. Phys.* **1989**, *139*, 201–220.
- 12 G. K. Paramonov, V. A. Savva, *Phys. Lett. A* **1983**, *97*, 340–342.
- 13 V. May, O. Kühn, *Charge and Energy Transfer Dynamics in Molecular Systems*, Wiley-VCH, Berlin, **2000**.
- 14 M. Shapiro, P. Brumer, *J. Chem. Phys.* **1991**, *95*, 8658–8661.
- 15 Y. Fujimura, L. González, K. Hoki, J. Manz, Y. Ohtsuki, *Chem. Phys. Lett.* **1999**, *306*, 1–8; *Corrigendum* **1999**, *310*, 578–579.
- 16 M. Shapiro, E. Frishman, P. Brumer, *Phys. Rev. Lett.* **2000**, *84*, 1669–1672.
- 17 Y. Fujimura, L. González, K. Hoki, D. Kröner, J. Manz, Y. Ohtsuki, *Angew. Chem.* **2000**, *112*, 4785–4788; *Internatl. Ed.* **2000**, *39*, 4586–4588.
- 18 F. Hund, *Z. Phys.* **1927**, *43*, 805–826.
- 19 W. H. Miller, N. C. Handy, J. E. Adams, *J. Chem. Phys.* **1980**, *72*, 99–112.
- 20 N. Shida, P. F. Barbara, J. E. Almlöf, *J. Chem. Phys.* **1989**, *91*, 4061–4072.
- 21 B. A. Ruf, W. H. Miller, *J. Chem. Soc., Faraday Trans. 2*, **1988**, *84*, 1523–1534.
- 22 H. Naundorf, J. A. Organero, A. Douhal, O. Kühn, *J. Chem. Phys.* **1999**, *110*, 11286–11293.

- 23 N. Došlić, K. Sundermann, L. González, O. Mó, J. Giraud-Girard, O. Kühn, *Phys. Chem., Chem. Phys.* **1999**, 1, 1249–1258.
- 24 O. Kühn, Y. Zhao, F. Sheng, Y.-J. Yan, J. *Chem. Phys.* **2000**, 112, 6104–6122.
- 25 O. Kühn, *Eur. J. Phys. D*, **1999**, 6, 49–55.
- 26 N. Došlić, O. Kühn, J. Manz, *Ber. Bunsenges. Phys. Chem.* **1998**, 102, 292–297.
- 27 N. Došlić, O. Kühn, *Chem. Phys.* **2000**, 255, 247–257.
- 28 G. K. Paramonov, H. Naundorf, O. Kühn, *Eur. J. Phys. D* (in press).

## 10

**Controlling the Vibration and Dissociation Dynamics in Small Molecules and Clusters***Štefan Vajda and Ludger Wöste***Abstract**

This contribution is devoted to the real-time analysis and control of the nuclear dynamics of small molecules and clusters by using tailored femtosecond laser pulses. First, the vibrational dynamics of the bound electronic states of the homonuclear trimer  $\text{Na}_3$  are discussed, then the branching control of different predissociated electronic states of the heteronuclear trimer  $\text{Na}_2\text{K}$  is dealt with, and finally results relating to the fragmentation control of photo-excited  $\text{CpMn}(\text{CO})_3$  are presented. With unchirped fs-laser pulses and a moderate laser intensity, a pronounced wave-packet motion was observed exhibiting the eigenfrequencies of the electronically excited B-state of  $\text{Na}_3$ . When, however, 400 fs downchirped pulses were employed, oscillations corresponding to the vibrational frequencies of the electronic ground state appeared. This observation can be explained in terms of the stimulated Raman effect. The leading blue spectral edge of the downchirped pulse creates a non-stationary wave-packet in the B-state of the homonuclear trimer, which is then dumped down by the following red spectral tail of the same pulse into the vibrationally excited part of the ground state. An active control of the experiment by means of feedback optimization was achieved by exciting differently branching ionization and fragmentation pathways of photo-excited  $\text{Na}_2\text{K}$  and  $\text{CpMn}(\text{CO})_3$ . By employing an evolutionary algorithm for optimizing the phase and amplitude of the applied laser field, the yield of the resulting parent and fragment ions could be significantly controlled, and intrinsic properties of the photoinduced process emerged in the resulting pulse sequences. In the  $\text{Na}_2\text{K}$  system, for example, the obtained light intensity sequences of the optimized pulses correspond very well to the sequential cross-sections of the irradiated transitions; their temporal structures reflect the vibrational eigenfrequencies of the corresponding mother molecule or fragment.

## 10.1

**Introduction**

The development of pulse-shapers, which allow the modulation of laser pulses in the amplitude and phase domains, has opened fascinating new perspectives for driving molecular reaction dynamics in real time. This topic becomes most exciting

when self-learning feedback loop algorithms are employed.<sup>[1]</sup> In this way, tailored laser pulses are generated, which can drive the photoinduced reaction along a desired reaction path on a complex potential energy surface to give maximum yield. An important first experiment in this field was performed by Gerber and co-workers,<sup>[2]</sup> who used a genetic algorithm to optimize a femtosecond laser pulse profile. This was then used to drive the dissociative multi-photon ionization process of metal carbonyl compounds to maximize the yield of either the parent ion or a chosen fragment ion. An important issue in this regard remains the question of the information coded in the optimized laser pulse shape. The extraction and interpretation of the information from the acquired optimal laser field is a very important aspect, since it may lead to a conceptionally new approach to the investigation of molecular dynamics. Employing evolutionary strategies, Nature's concept itself, not only allows for an effective control the dynamics of a molecular system by optimizing a problem of high dimensionality, but also supplies valuable information about the molecular potential energy surface(s) involved in the reaction path. To gain this information from the optimized laser field, a detailed understanding is required of fundamental questions concerning, for example, energy dissipative effects that may lead to a loss of coherence in a system of increasing complexity, where IVR and conical intersections influence the dynamical processes. In this regard, it is most important to begin the investigations on simple model systems for which the underlying molecular dynamics can still be understood on the basis of available experimental and theoretical data. Based on these findings, more complex systems with more degrees of freedom may then become experimentally controllable and understandable as well.

## 10.2

### The Choice of the Molecular Systems

Small metal clusters and organometallic complexes are suitable model systems for the investigation of optimum control scenarios. These substances differ in binding energy and exhibit a large number of bound-bound and bound-free electronic transitions, allowing the study of their vibrational dynamics and fragmentation by means of transient multi-photon ionization spectroscopy. In recent years, we have performed systematic femtosecond pump-probe experiments on various homo- and heteronuclear alkali metal clusters and organometallic compounds with the goal of characterizing the dynamical processes of these, albeit still rather simple systems, which exhibit different elementary intramolecular processes.

The previously reported<sup>[3,4]</sup> spectra of the sodium trimer reflect extended oscillatory wave-packet motions in its bound B-state when excited by a one-photon transition through a femtosecond pump pulse with a central wavelength of 620 nm (Figure 10.1). In this one-color experiment, the evolution of the wave-packet was monitored by one-photon ionization of the excited trimer. By employing amplified laser pulses, Gerber and coworkers<sup>[5]</sup> observed an enrichment of the oscillatory structure in the pump-probe spectra arising from a motion of a wave-packet propa-

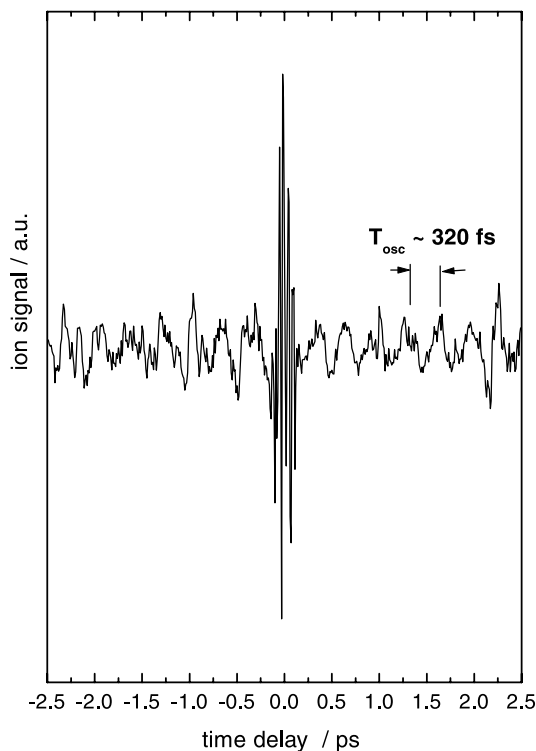


**Fig. 10.1** Temporal evolution of a transient two-photon ionization signal of  $\text{Na}_3$  obtained by employing 120 fs unchirped pump and probe laser pulses with a central wavelength of 620 nm. The 320 fs oscillation period reflects the symmetric stretch mode of the B-state of the sodium trimer.

gating in the ground state of the trimer. The sodium trimer was chosen as a prototype system for controlling the population of bound electronic states by means of modulated weak femtosecond laser pulses.

In the case of the heteronuclear  $\text{K}_2\text{Na}$  and  $\text{Na}_2\text{K}$  trimers, a rapid fragmentation process was observed in the excitation wavelength region of 730–840 nm<sup>[6]</sup> and only in the case of excitation of the latter triatomic at 770 nm could the surviving residue of the oscillatory behavior be followed during the fast dissociation process.<sup>[7]</sup> The related eigenfrequencies could then be extracted from a Fourier analysis. The corresponding one-color pump-probe spectrum is shown in Figure 10.2a. It clearly exhibits an exponential decay with a time constant of 3.28 ps and superimposed oscillations with a period of about 500 fs. In this pump-probe experiment, the first femtosecond pump-pulse excites  $\text{Na}_2\text{K}$  in a one-photon transition from its ground state to an electronically excited state, creating a coherent vibrational wave-packet. According to preliminary *ab initio* calculations by Bonačić-Koutecký et al.,<sup>[8]</sup> the applied excitation wavelength corresponds to a transition into the bound excited electronic state  $3^2\text{A}_1$ . This state is crossed by a second electronic state  $1^2\text{A}_2$  above its vibrational dissociation limit. The temporal evolution of the oscillating parent molecule

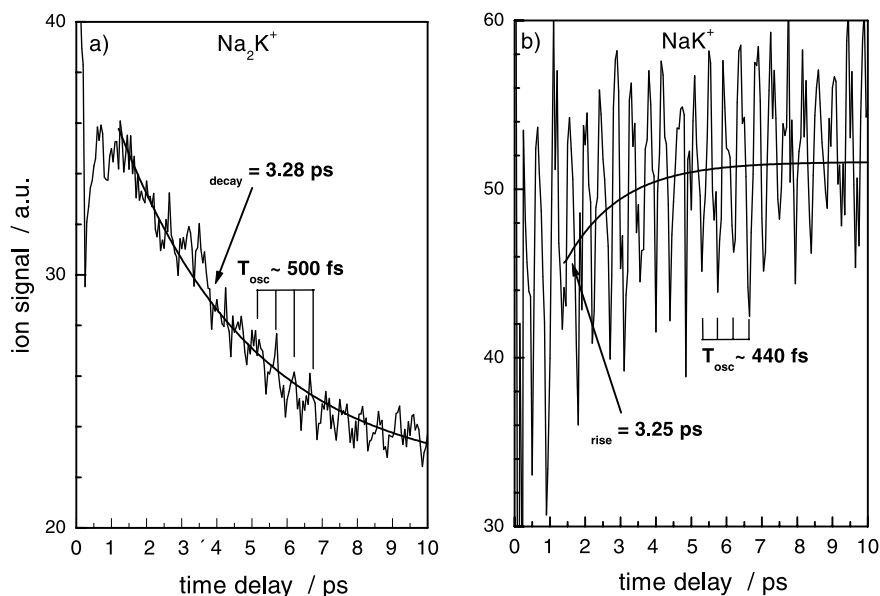


**Fig. 10.2** Temporal evolution of the transient three-photon ionization signal of decaying  $\text{Na}_2\text{K}$  (a) and its emerging fragment  $\text{NaK}$  (b). The decay time of the excited trimer corresponds

well to the rise time of its diatomic fragment. The superimposed oscillations indicate wave-packet oscillations in the coherently excited system.

is then monitored by the probe pulse, which ionizes the electronically excited species in a two-photon process, leading to  $\text{Na}_2\text{K}^+$ . Figure 10.2b shows the one-color pump-probe spectrum of the  $\text{NaK}$  dimer fragment recorded at 770 nm. The transient exhibits an exponential rise with a time constant of 3.25 ps and superimposed oscillations with a period of about 440 fs, a known vibrational period for the excited  $\text{NaK}$  dimer.<sup>[9]</sup> Since coherence survives in this photodissociating system, the fragmentation dynamics of the excited heteronuclear  $\text{Na}_2\text{K}/\text{NaK}$  cluster system is well suited for a *coherent control* experiment.

Organometallic compounds containing CO ligands can serve as good model systems for investigating and controlling unimolecular photofragmentation channels. The chromophoric character of the metallic core allows the excitation of these molecules into different electronic states. After the electronic excitation, fast energy redistribution and loss of ligands can be observed.<sup>[10]</sup> The time evolution of the photofragmenting system can be followed by means of pump-probe spectroscopy. In the past decade, several such systematic investigations have been performed, for example, by Zewail et al.,<sup>[11]</sup> Banares et al.,<sup>[12]</sup> and Trushin et al.<sup>[13]</sup> The observed transient ionic fragmentation patterns indicate an ultrafast loss of the CO ligands with different intermediate states being involved in the process of photodissociation. Figure 10.3 shows a set of pump-probe spectra recorded for the parent ion  $\text{CpMn}(\text{CO})_3^+$  and its fragment ions  $\text{CpMn}(\text{CO})_2^+$ ,  $\text{CpMn}(\text{CO})^+$ , and  $\text{CpMn}^+$ . In the

data analysis, a deconvolution algorithm taking into account the real pulse length was used. The resulting decay times and the time shift of the transient signal maximum are listed in Table 10.1. The progressive shift of the transient ion signal maximum is indicative of a fast dissociation process accompanied by the consecutive population of several neutral precursor states upon optical excitation. *Ab initio* calculations revealed two electronic states in the excitation energy region probed in the experiment.<sup>[14]</sup> Generally, each precursor may possess its own individual ionic fragmentation pattern with progressive loss of ligands (see, for example, ref.<sup>[13]</sup>). The *ab initio* calculations of Manz et al.<sup>[14]</sup> predict a fragmentation time of 63 fs for the departure of the first CO ligand. This is in good agreement with the experimental observation of the decay time of the parent ion signal having a sub-100 fs time constant ( $\tau_{\text{decay}} = 66$  fs, see Table 10.1). We have to note here that despite the approximations made in these calculations, such as the neglect of internal vibrational energy distribution and the loss of dissociative kinetic energy (which can lead to smaller values of  $\tau_{\text{diss}}$ ) and the neglect of diabatic couplings and crossings of potential energy surfaces (which can result in larger values of  $\tau_{\text{diss}}$ ), the loss of the first CO ligand clearly takes place on the sub-100 fs time scale. The two intersecting excited states that are populated during electronic excitation can undergo rapid relaxation along different pathways, and the experimentally observed 66 fs decay time may represent the effective lifetime of the parent molecule, being made up of the displacement on the potential energy surface(s) and the loss of a ligand. Moreover, the decay times of the intermediate products shown in Table 10.1 can be

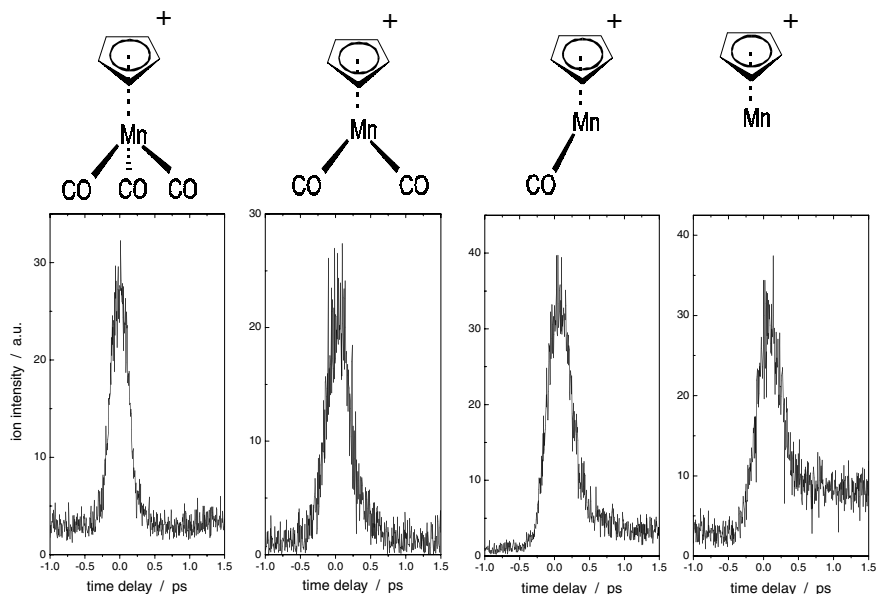


**Fig. 10.3** Set of transients reflecting the time evolution of the ion signal of the parent molecule  $\text{CpMn(CO)}_3$  and all its fragments.

viewed as effective lifetimes reflecting the complex intrinsic molecular dynamics that take place in this multi-photon excitation and ionization process. Theoretical calculations show that the loss of the first CO ligand results in the first excited  $S_1$  state of  $\text{CpMn}(\text{CO})_2$ .<sup>[14]</sup> In its ground state, the  $\text{CpMn}(\text{CO})_2$  molecule probably has sufficient excess vibrational energy to eliminate a second CO ligand. At this point, it is worthy of note that, on the basis of simple energetic considerations such as the excitation energy of 3.1 eV, the almost simultaneous cleavage of two metal–CO ligand bonds upon excitation of the parent molecule cannot be completely ruled out. However, it is evident that there are several intermediate states, some of which belong to different species that are consecutively populated.  $\text{CpMn}(\text{CO})_3$  and its fragments may thus serve as a model system for *feedback control of the population and ionization of coupled electronic states* in a highly dissociative system.

**Tab. 10.1**  $\text{CpMn}(\text{CO})_3$  system: Peak shifts and decay times obtained from the transients.

<i>Transient ion signal</i>	<i>Peak shift <math>\Delta t/\text{fs}</math></i>	<i>Decay time <math>\tau_{\text{decay}}/\text{fs}</math></i>
$\text{CpMn}(\text{CO})_3^+$	0	66
$\text{CpMn}(\text{CO})_2^+$	55	90
$\text{CpMnCO}^+$	75	180
$\text{CpMn}^+$	90	220

### 10.3

#### Experimental Set-Up

##### 10.3.1

##### Molecular Beam and Laser Systems

Our experimental set-up has been described in detail elsewhere.<sup>[7]</sup> Briefly, the molecular beam is co-expanded in an adiabatic expansion of alkali metal vapor or sublimated  $\text{CpMn}(\text{CO})_3$  from a heated oven together with argon carrier gas across a nozzle of diameter 70–80  $\mu\text{m}$  into the vacuum. After collimation with a skimmer, the molecular beam passes between the electrical lenses of a quadrupole mass spectrometer (Balzers QMG 420), which are oriented perpendicularly to both the propagation of the cluster beam and the laser beam in order to extract the resulting photoions. The laser light used in such collinear pump-probe arrangements was provided by three different laser set-ups as outlined below.

In the  $\text{Na}_3$  experiment, a commercial TiSa-OPO femtosecond laser system (Spectra Physics Tsunami and OPO) pumped by a 15 W argon-ion laser was used, which produced 120 fs laser pulses with a central wavelength of 620 nm after frequency doubling.

In the  $\text{Na}_2\text{K}$  experiment, a commercial femtosecond laser was used (Spectra Physics 3960 Tsunami), which was pumped by an Nd:YLF laser (Spectra Physics Millennia X) and produced pulses of 80 fs duration with a central wavelength of 770 nm.



The Ti:Sa amplifier system used in the experiments on  $\text{CpMn}(\text{CO})_3$  consisted of a commercial femtosecond Ti:Sa Tsunami seed laser, which was pumped by a 5 W Nd:YLF Millennia laser. The seed laser delivered seed pulses of 70 fs duration with a central wavelength of 800 nm for the regenerative multi-pass amplifier (Quantronix RegA/MPA). The amplifier produced 87 fs pulses of energy 1.5 mJ at a repetition rate of 1 kHz. In the pump-probe experiment, the light pulses were split and the pump pulse was frequency doubled.

### 10.3.2

#### Pulse Shaping

##### 10.3.2.1 Simple Pulse Shaping: Generation of Linearly Chirped Pulses

A set-up consisting of a grating pair with adjustable separation between the two gratings was used to create downchirped laser pulses of 200 fs–2 ps duration from unchirped 120 fs laser pulses centered at 620 nm.

##### 10.3.2.2 Active Feedback Optimization: Search for System-Specific Tailor-Made Pulses

In the multi-photon optimization experiment, a single laser beam passes through a pulse-shaper set-up, which allows for a simultaneous phase- and amplitude modulation of the laser pulses by applying voltages to a liquid-crystal spatial light modulator (SLM) consisting of 2 (128 pixels).<sup>[15]</sup> The shaper is placed in the center of a linear 4f arrangement. By computer control, pulses of arbitrary form can be generated. These modulated pulses are then focussed on the molecular beam and the desired mass-selected product ion current is taken as a reference feedback signal for the optimization algorithm. The optimization algorithm alters the pulse-shaper settings iteratively in order to maximize the ion signal. This iterative procedure is shown schematically in Figure 10.4. An algorithm based on evolutionary strategies<sup>[16]</sup> is applied in order to find the pulse shape that yields the highest feedback signal. The optimization procedure proceeds until a convergence of the ion yield is achieved.

## 10.4

### Experimental Results and Discussion

#### 10.4.1

##### $\text{Na}_3$

A set of one-color pump-probe spectra of  $\text{Na}_3^+$  was measured using downchirped excitation pulses with a central wavelength of 620 nm and an unchirped ionization pulse of the same wavelength. Two typical spectra, obtained using 250 fs and 400 fs downchirped pulses, are shown in Figures 10.5a and 10.5b, respectively.<sup>[4]</sup> On comparison with the  $\text{Na}_3^+$  transient obtained with unchirped 120 fs and 250 fs downchirped pump pulses (see Figures 10.1 and 10.5a), one can still clearly distinguish the 320 fs oscillatory component arising from the wave-packet propagation in the excited B-state of the trimer. The signal features change dramatically when a chirped pulse of 400 fs duration is employed: the oscillation period suddenly changes to 230

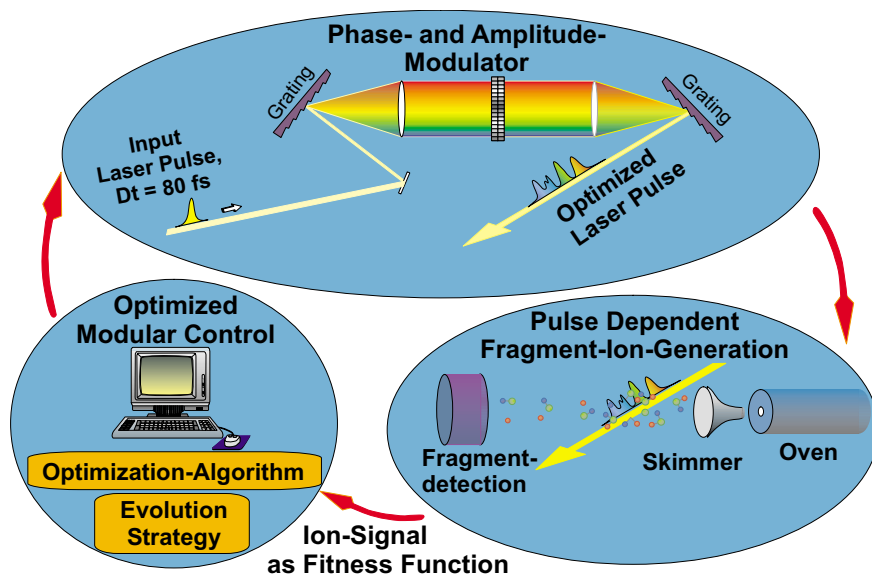


**Fig. 10.4** Schematic view of the feedback loop for optimizing the ion yields of particular reactive channels by employing a self-learning algorithm.

fs, i.e. to a period characteristic for the wave-packet propagation in the ground state of this trimer.<sup>[5]</sup> This observation can be explained as outlined in Figure 10.6. The frontal frequency components (shorter wavelengths) create a propagating wave-packet in the B-state of the trimer, which is then dumped down into the ground state (X-state) by the delayed longer-wavelength components of the same pulse. The vibrational motion of the ground state is then monitored by the unchirped probe pulse through two-photon ionization. The length of the employed pulses was determined by intensity cross-correlation. The orientation and order of the chirp were determined from wavelength-resolved cross-correlation measurements. Due to the lack of a pulse-analyser system (FROG, Frequency-Resolved Optical Gating) in this early stage of our very first control experiments, there was no possibility of obtaining detailed information on the exact phase of the applied chirped pulses.

#### 10.4.2

##### **Na<sub>2</sub>K**

We have performed a series of optimization experiments on the Na<sub>2</sub>K/NaK system by modulating the phase of the laser pulses. Figure 10.7 shows a typical evolution of the ion yield during the optimization procedure for the triatomic mother ion Na<sub>2</sub>K<sup>+</sup> and the diatomic fragment ion NaK<sup>+</sup> (Figures 10.7a and 10.7b, respectively). At the beginning, the pulses possess a random phase and the resulting ion yield is very small. During the iteration procedure, the ion yield increases and converges after about 150 and 70 generations for the Na<sub>2</sub>K<sup>+</sup> and NaK<sup>+</sup> ions, respectively. The ion

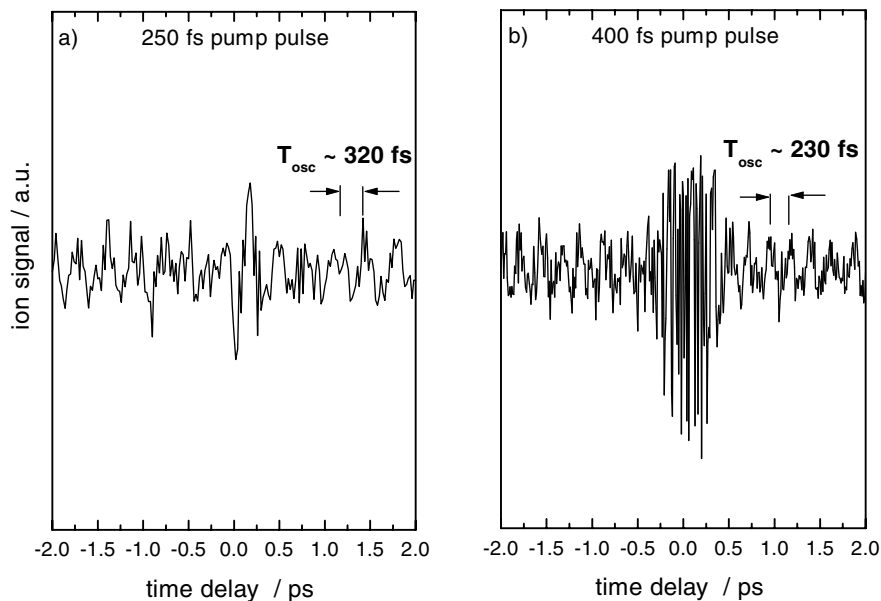


**Fig. 10.5** Time-dependent spectrum of the signal of  $\text{Na}_3^+$  obtained by employing 250 fs (a) and 400 fs (b) downchirped pump pulses. The oscillation periods 320 fs and 230 fs correspond

to the well-known symmetric stretch modes of the B- and X-states of the sodium trimer, respectively.

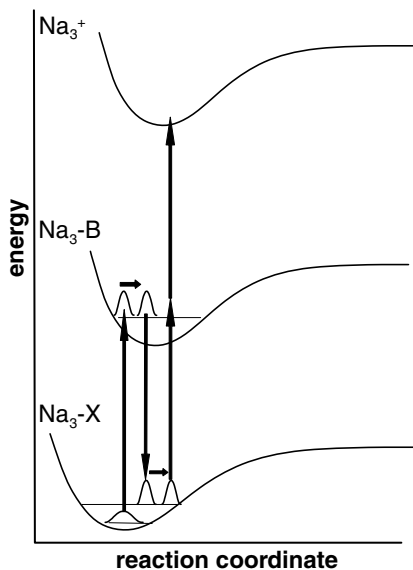


**Fig. 10.6** Schematic view of the method of monitoring the ground-state dynamics in  $\text{Na}_3$  by means of downchirped excitation pulses.

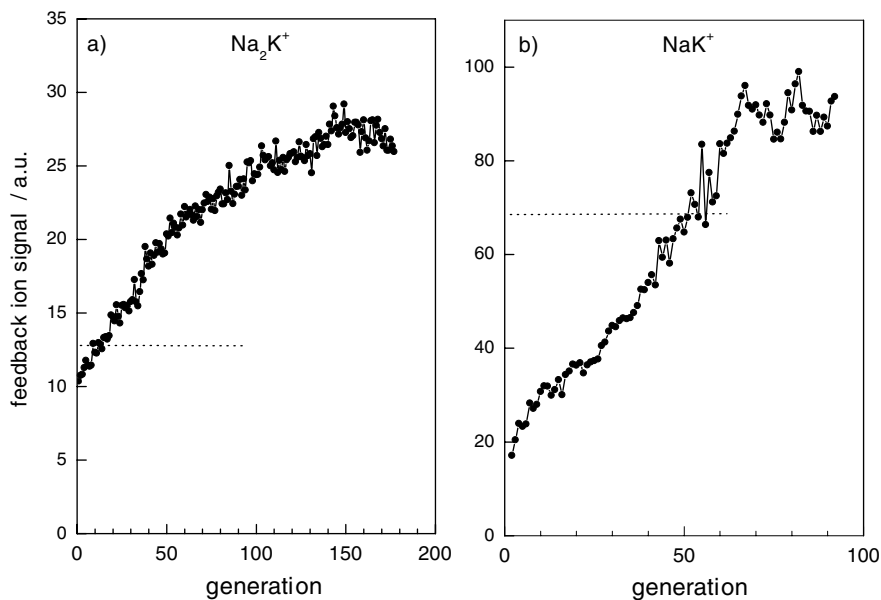


**Fig. 10.7** Evolution of the ion yield during the optimization experiment plotted for the  $\text{Na}_2\text{K}^+$  signal (a) and the  $\text{NaK}^+$  signal (b). The dotted

lines indicate the ion yield obtained by employing an unchirped laser pulse of same intensity as the modulated pulse.

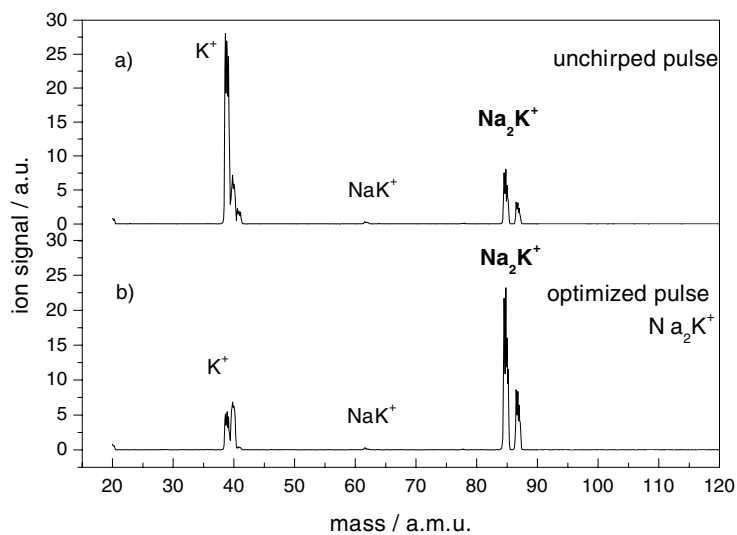


**Fig. 10.8** Comparison of mass spectra obtained with unchirped femtosecond pulses (a) and with optimized pulse shape for obtaining maximum intensity of the  $\text{Na}_2\text{K}^+$  signal (b).

intensity obtained with an unchirped pulse of the same intensity as the chirped one is also indicated in the figure. It shows an increase in the parent ion signal by roughly 150 % and is accompanied by a sharp decrease of the potassium mass peak intensity. The optimization of  $\text{Na}_2\text{K}^+$  yields an ion signal increase of about 45 % when compared to short-pulse ionization. In Figure 10.8, a typical mass spectrum obtained with the pulse form producing the highest yield of unfragmented parent  $\text{Na}_2\text{K}^+$  ions is compared with a reference spectrum produced by an unchirped laser pulse of the same intensity. We have to mention here that, under the given experimental conditions, the overall  $\text{NaK}^+$  ion signal consists not only of diatomic photo-fragments of  $\text{Na}_2\text{K}$ , but that there is also a contribution from directly photoionized  $\text{NaK}$  dimers that are also present in the molecular beam. The contribution of these ionic fragments to the overall signal is about 20 %, as estimated from the pump-probe spectrum of  $\text{NaK}$ . We also note that, depending on the laser pulse structure, an  $\text{Ar}^+$  peak emerges between the  $^{39}\text{K}^+$  and  $^{41}\text{K}^+$  isotope peaks.

From analysis of the SHG autocorrelation trace, as shown in Figure 10.9, a double-pulse sequence was retrieved for  $\text{Na}_2\text{K}$ , and the ordering of the pulses was determined from cross-correlation measurements. The time shift between the first and second pulses was approximately 1240 fs. This time corresponds exactly to 2.5 oscillation periods of the electronically excited parent trimer. Moreover, the peak intensity of the second pulse is ca. 80 % higher than that of the first, which can be explained by the fact that the first pulse excites the system through one-photon

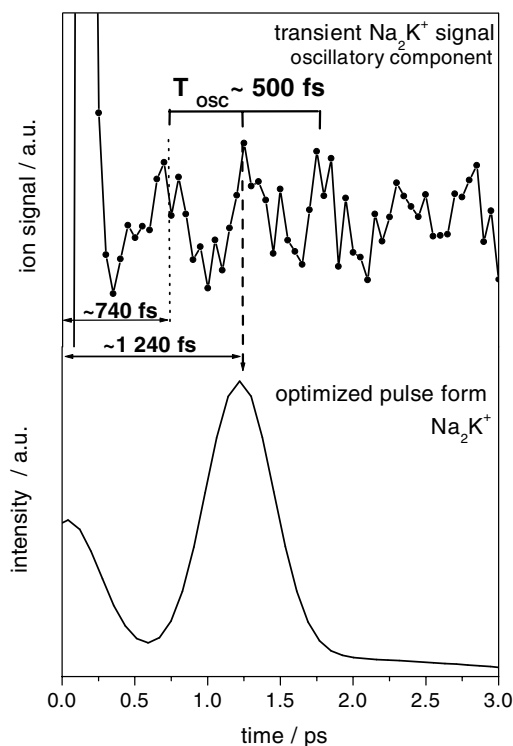


**Fig. 10.9** Oscillatory component of the transient pump-probe  $\text{Na}_2\text{K}^+$  signal compared with the acquired pulse shape for producing a maximum yield of this ion.

absorption, whereas two photons are needed for the following ionization. As known from time-resolved measurements,<sup>[10]</sup> the photoionization of the electronically excited  $\text{Na}_2\text{K}$  trimer is most efficient at the outer turning point of the propagating wave-packet. The time separation of the double pulse corresponds to 2.5 oscillations of the trimer and the first two passages through the ionization Franck–Condon window are not found. We see no obvious explanation for this. It may stem from the fact that the optimization is started with random phases, corresponding to long, structureless pulses, so that earlier passages at the open FC-window are missed. It may also be due to complicated non-adiabatic dynamics involving several electronically-excited states, which will have to be investigated further.

In Figure 10.10, the pulse form obtained from the optimization process for the maximum  $\text{NaK}$  ion yield is shown together with the related  $\text{NaK}^+$  transient. In this case, the pulse form was recorded by SHG-FROG and then analyzed. The resulting pulse train consists of three pulses and the timing of the pulse elements was determined by intensity cross-correlation. The second pulse arrives approximately 730 fs after the first pulse and is followed by a third pulse after a further 440 fs. The time shift between the first and second pulses corresponds very well to 1.5 oscillation periods of the excited  $\text{NaK}$  dimer, while the time between the second and third pulses exactly matches the established oscillation period of this excited dimer. The peak intensity of the second pulse exceeds that of the first pulse by 70 %, in accordance with the one-photon excitation and two-photon ionization step deduced from

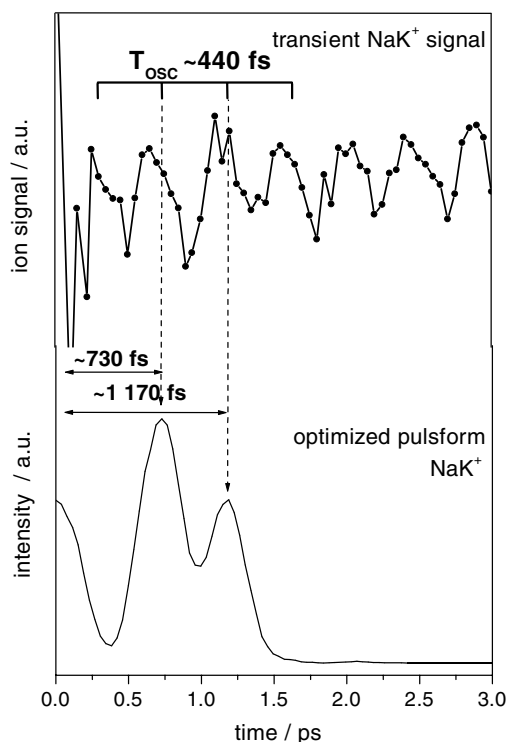


**Fig. 10.10** Time-resolved pump-probe signal for  $\text{NaK}^+$  compared with the acquired pulse shape for producing a maximum yield of this ion.

previous measurements. The leading pulse is considerably longer than the other two. Analysis of the temporal phase profile of the three individual pulse train elements revealed fourth-order components for the leading pulse and third-order components for the second and third pulses. All pulses possess a negative chirp (down chirp) in the time domain: a cubic and a quadratic down chirp for the leading pulse and the remaining two pulses, respectively. Strongly downchirped excitation pulses can cause a very effective focussing of the propagating wave-packet in other locations on the relevant anharmonic potential energy surface(s) at later times after electronic excitation and thus lead to the highest achievable ion yield at the moment of arrival of the probe pulse.

Other optimization experiments performed on the  $\text{Na}_2\text{K}/\text{NaK}$  molecular system led to similar pulse forms, i.e. mainly double pulses for the trimer  $\text{Na}_2\text{K}$  and three-pulse sequences for the dimer  $\text{NaK}$ . These pulse forms were characterized by intensity cross-correlation only. The cross-correlation signals confirmed the time sequence and relative intensities of the pulse elements contained in the pulse train, i.e. a leading weaker pulse followed by a stronger one. We have to point out here that two optimization runs led to pulse trains with non-intuitive timing between the individual pulse-train elements. An example of this is shown in Figure 10.11. The separation between the pulses ( $\sim 330$  fs) was seemingly independent of the oscillation period of the excited electronic state addressed in the experiment. A similar interesting feature of the pulse train has recently been observed in  $\text{K}_2$ .<sup>[17]</sup> It is still an open question as to which electronic states located in the excitation energy region are involved in this multi-step photoionization process. The answer may be hidden in the phase profile of the pulse sequences.

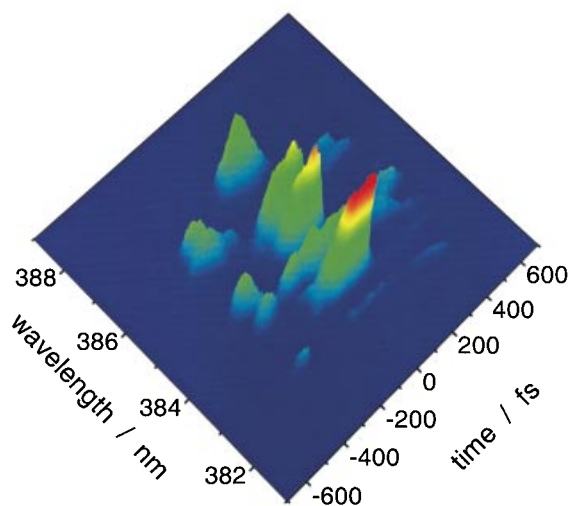


**Fig. 10.11** FROG trace of a pulse obtained for producing a maximum yield of  $\text{Na}_2\text{K}^+$ . The timing between the pulse

elements seems to be independent of the vibrational period observed in the excited trimer.

In order to observe the ‘fingerprints’ of the excited parent trimer vibrations in the fragment signal, fragment NaK dimers and the dimers emerging from a cluster source have to be separated. To this end, a new experiment is under preparation that will employ an additional, chopped cw-laser that selectively removes the Na<sub>2</sub>K particles in the cluster beam. In this way, it will be possible to quantitatively determine the fraction of fragmenting Na<sub>2</sub>K\* contributing to the NaK<sup>+</sup> signal. Naturally, we cannot fully exclude a partial channeling of the Na<sub>2</sub>K\* dissociation into the second possible fragmentation pathway leading to a loss of the potassium atom.

#### 10.4.3

##### CpMn(CO)<sub>3</sub>

In order to avoid laser pulse energy effects in the optimization procedure, only the phase of the laser pulse was modulated in the experiment. The change of the ion yields of CpMn(CO)<sub>3</sub><sup>+</sup> and CpMn(CO)<sup>+</sup> during the phase-optimization procedure and comparison of the resulting mass peak intensities (Table 10.2) indicates that the control experiment leads to a substantial increase in the yields of the desired ions. The ratio of the CpMn(CO)<sup>+</sup>/CpMn(CO)<sub>3</sub><sup>+</sup> ion yields changed by a factor of ~2.5 in the two optimization runs for CpMn(CO)<sup>+</sup> and CpMn(CO)<sub>3</sub><sup>+</sup>, respectively.

**Tab. 10.2** CpMnCO<sup>+</sup>: CpMn(CO)<sub>3</sub><sup>+</sup> mass peak ratio obtained from the optimization experiments.

<i>Pulse form</i>	<i>CpMnCO<sup>+</sup>: CpMn(CO)<sub>3</sub><sup>+</sup> mass peak ratio</i>
optimized for CpMn(CO) <sub>3</sub> <sup>+</sup>	1:16
reference pulse (no chirp)	1:13
optimized for CpMnCO <sup>+</sup>	1:6

The FROG traces of the optimal pulses for CpMn(CO)<sub>3</sub><sup>+</sup> and CpMn(CO)<sup>+</sup> yield optimization are shown in Figure 10.12, while the resulting pulse forms are shown in Figure 10.13. The pulse sequence for maximum CpMn(CO)<sub>3</sub><sup>+</sup> ion yield, as retrieved from FROG analysis, consists of three pulses of about 40 fs duration (Figure 10.13a). The effective duration of the leading double pulse is approximately 100 fs, which is similar to the duration of the initial unchirped laser pulse (87 fs) centered at 800 nm. The pulse form can be readily understood by considering the two-photon excitation process and the subsequent three- or four-photon ionization step, together with the very short 66 fs lifetime of the electronically excited state of CpMn(CO)<sub>3</sub> from which the parent ions originate. The first pulse acts as a pump pulse, whereas the second pulse ionizes the excited CpMn(CO)<sub>3</sub> molecules. The third pulse of low intensity most probably represents a second ionization pulse that ionizes an additional fraction of the remaining parent molecules excited by the second pulse.

In the case of the fragment ion CpMn(CO)<sup>+</sup>, the pulse train consists of two pulses (Figure 10.13b). The first pulse starts the molecular process by exciting the CpMn(CO)<sub>3</sub> molecule (pump pulse). The second pulse arrives approximately 80 fs



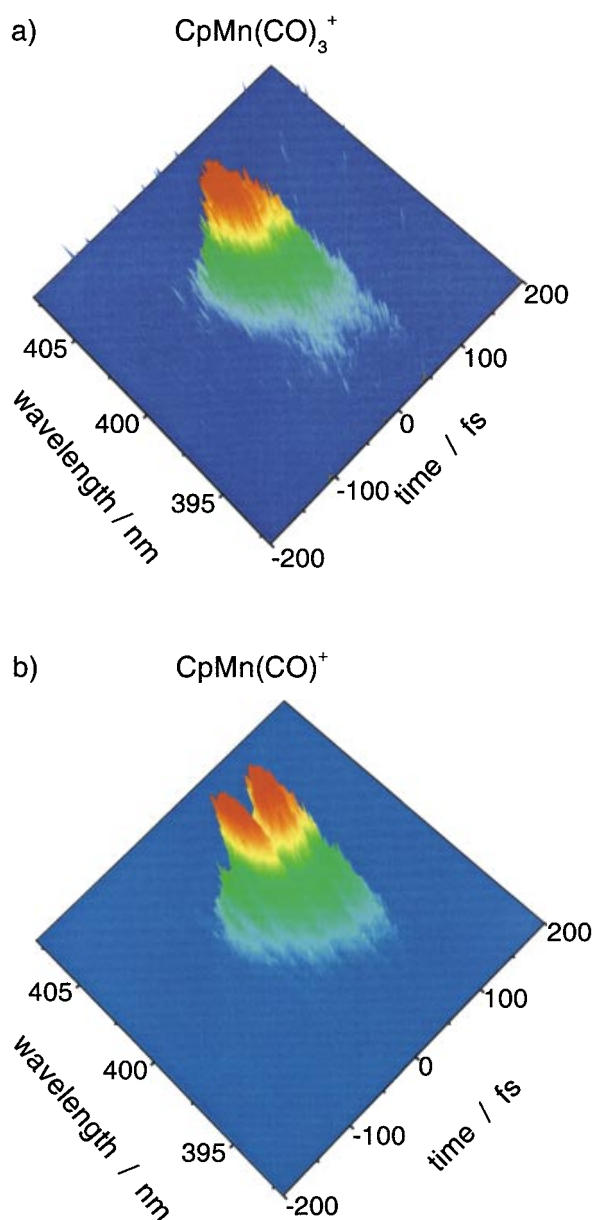


**Fig. 10.12** SHG FROG traces of the optimized pulses acquired from the feedback optimization experiment for  $\text{CpMn(CO)}_3^+$  (a) and the  $\text{CpMn(CO)}^+$  (b).

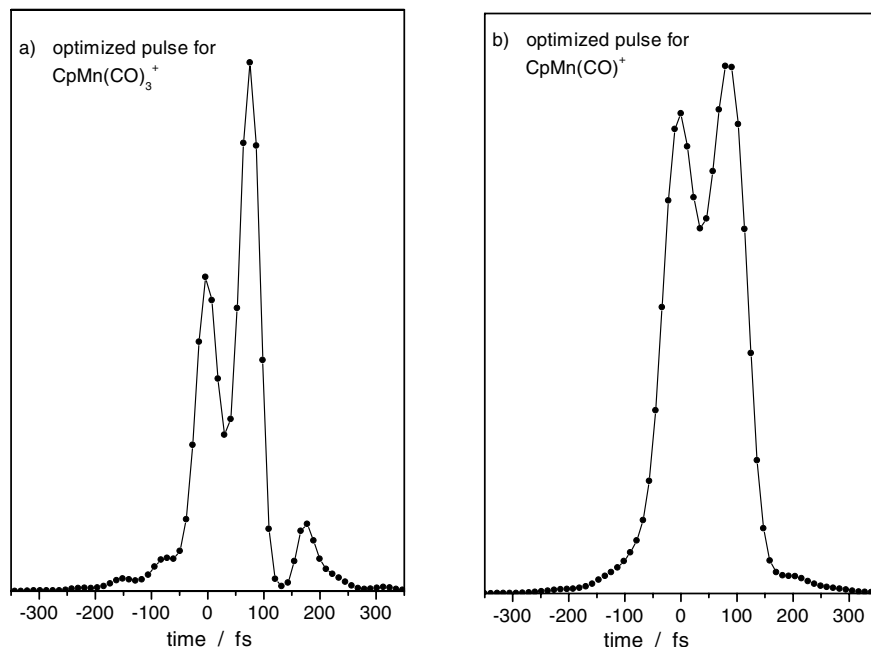


**Fig. 10.13** Optimized pulse shapes resulting from the analysis of the FROG traces shown in Figure 10.12 for the maximum yields of  $\text{CpMn(CO)}_3^+$  (a) and the  $\text{CpMn(CO)}^+$  (b).

after the first pulse and the effective duration of this double pulse is about 145 fs. The second pulse ionizes the relevant state(s) of the neutral molecule giving rise to the  $\text{CpMn(CO)}^+$  fragment ion (probe pulse). The timing of the second pulse corresponds very well to the peak shift of the  $\text{CpMn(CO)}^+$  transients.

## 10.5

### Summary

In this contribution, we have addressed the femtosecond laser analysis and control of molecular dynamics in bound electronic states of the homonuclear alkali metal trimer  $\text{Na}_3$  and in more complex systems exhibiting highly fragmentative behavior. Our palette has included the heteronuclear triatomic  $\text{Na}_2\text{K}$  and the pseudo five-body  $\text{CpMn(CO)}_3$ . In the case of  $\text{Na}_3$ , the propagation of the wave-packet in the B-state (i.e. the second excited state) and X-state (ground state) of the trimer was followed and subsequently selectively controlled through the use of low-intensity linearly chirped laser pulses. In the case of unchirped (120 fs) or slightly chirped excitation pulses (up to  $\sim 300$  fs), the wave-packet motion in the B-state was clearly resolved. On employing a 400 fs downchirped pulse, oscillations corresponding to ground-state vibrations suddenly occurred, which are well known from previous measure-

ments with amplified laser pulses. This observation can be explained in terms of the stimulated Raman effect (SIRS). Thus, the leading blue spectral wavelength component of the downchirped pulse creates a non-stationary wavepacket in the B-state of the  $\text{Na}_3$  trimer, which is dumped down into the X-state by the red spectral wavelength components of the pulse tail.

The time evolution of the  $\text{Na}_2\text{K}$  and  $\text{CpMn}(\text{CO})_3$  molecular systems has been studied by pump-probe techniques. In the case of the mixed alkali metal trimer  $\text{Na}_2\text{K}$ , a fragmentation process taking place on the picosecond scale was observed in one-color experiments. At a wavelength of 770 nm, a rise in the  $\text{NaK}$  fragment ion signal and a surviving oscillating wave-packet motion was resolved in the pump-probe data. The transients of  $\text{CpMn}(\text{CO})_3^+$  and its photoproducts revealed complex ultrashort dynamics, indicating a loss of the first CO ligand with a time constant of less than 100 fs.

An active control of branching between different ionization and fragmentation pathways of the electronically excited  $\text{Na}_2\text{K}$  and  $\text{CpMn}(\text{CO})_3$  could be achieved by means of feedback optimization of shaped femtosecond laser pulses. By employing an evolutionary algorithm for optimizing the applied laser field, the gained signal intensities of the resulting parent and fragment ions could be significantly controlled. The obtained pulse shapes correspond very well to the cross-sections of the irradiated transitions in the  $\text{Na}_2\text{K}$  system; their temporal structure reflects the wavepacket propagation in the  $\text{Na}_2\text{K}$  system or the transient consecutive population of states during the multi-step photofragmentation and photoionization process in larger molecules such as  $\text{CpMn}(\text{CO})_3$  and its photoproducts. Several optimization runs lead to high ionic yields with rather non-intuitive pulse sequences, underlining the important role of the phase.

## Acknowledgements

The authors are grateful to Prof. Vlasta Bonačić-Koutecký, Prof. Jörn Manz, Prof. Herschel Rabitz, Dr. Werner Fuß, and Dr. Sergei Trushin for many stimulating discussions, Ms. Cristina Kaposta, Mr. Andreas Bartelt, Mr. Marcel Krenz, Mr. Cosmin Lupulescu, and Dr. Porfirio Rosendo Francisco for their participation in the experiments. This work was supported by the Deutsche Forschungsgemeinschaft in the framework of the Sonderforschungsbereich 450 research project.

## References

- 1 R. S. Judson, H. Rabitz, *Phys. Rev. Lett.* **1992**, *68*, 1500.
- 2 A. Assion, T. Baumert, M. Bergt, T. Brixner, B. Kiefer, V. Seyfried, M. Strehle, G. Gerber, *Science* **1998**, *282*, 919.
- 3 S. Rutz, S. Greschik, E. Schreiber, L. Wöste, *Chem. Phys. Lett.* **1996**, *257*, 365.
- 4 P. Rosendo-Francisco, Ph. D. thesis, Berlin, 2000.
- 5 T. Baumert, R. Thalweiser, G. Gerber, *Chem. Phys. Lett.* **1993**, *209*, 29.
- 6 P. Rosendo-Francisco, C. Lupulescu, B. Baptist, Š. Vajda, *J. Chinese Chem. Soc.* **2000**, *47*, 705.
- 7 Š. Vajda, S. Rutz, J. Heufelder, P. Rosendo, H. Ruppe, P. Wetzl, L. Wöste, *J. Phys. Chem. A* **1998**, *102*, 4066.
- 8 V. Bonačić-Koutecký, private communication
- 9 L.-E. Berg, M. Beutler, T. Hansson, *Chem. Phys. Lett.* **1996**, *253*, 327.
- 10 C. Brechignac, Ph. Brechignac, P. Fayet, W. A. Saunders, L. Wöste, *J. Chem. Phys.* **1988**, *89*, 2419.
- 11 S. K. Kim, S. Pedersen, A. Zewail, *Chem. Phys. Lett.* **1995**, *233*, 500.
- 12 A. Banarez, T. Baumert, M. Bergt, B. Kiefer, G. Gerber, *Chem. Phys. Lett.* **1997**, *267*, 141
- 13 S. A. Trushin, W. Fuss, W. E. Schmid, L. Kompa, *J. Phys. Chem.* **1998**, *102*, 4129.
- 14 C. Daniel, J. Full, L. González, C. Kaposta, M. Krenz, C. Lupulescu, J. Manz, S. Minemoto, M. Oppel, P. Rosendo-Francisco, Š. Vajda, L. Wöste, *Chem. Phys.* 2000, special issue, submitted.
- 15 A. Weiner et al., *IEEE J. Quantum Electron.* **1992**, *28*, 908.
- 16 H.-P. Schwefel, *Evolution and Optimum Seeking*, Wiley, New York, 1995.
- 17 T. Hornung, R. Meier, M. Motzkus, *Chem. Phys. Lett.* **2000**, *326*, 445.

## 11

# Two-Dimensional Optical Nonlinear Spectroscopy in Liquids

*Keisuke Tominaga and Hiroaki Maekawa*

### Abstract

We have theoretically investigated two-dimensional vibrational spectra for a two-mode system in terms of a diagrammatic approach. The two vibrational modes are anharmonically coupled. The perturbed stationary states are obtained by treating the cubic anharmonicity as a perturbation, and expressions for the third-order response functions are derived. The physical origin of the cross-peaks in the spectrum is discussed.

### 11.1

#### Introduction

The development of optical two-dimensional (2D) spectroscopy is one of the major topics in the field of contemporary ultrafast laser spectroscopy.<sup>[1–18]</sup> Optical 2D spectroscopy is an optical analogue of the 2D magnetic resonance technique, which permits the resolution of congested spectra by spreading them out into the frequency domain. In principle, the basic idea of 2D NMR can be applied to any quantum mechanical two-level system such as vibrational and electronic states. Over the past decade, 2D vibrational and electronic spectroscopies have been developed theoretically and experimentally. These techniques are expected to be capable of providing novel information concerning condensed phases, such as correlation among the states, dynamics in the states, and so on.

In this contribution we theoretically investigate a spectral pattern obtained by 2D vibrational spectroscopy in terms of a diagrammatic approach. By analogy with 2D NMR techniques, one may expect to observe a cross-peak between two vibrational modes if these modes are correlated in some way. If there is no correlation between the modes, peaks will only be observed along the diagonal line in the 2D spectrum. The fundamental questions concerning vibrational 2D spectroscopy are what kind of conditions are necessary for the observation of cross-peaks and how do the intensities of the cross-peaks compare to those of the peaks along the diagonal line. In this work, we investigate the 2D vibrational spectra by constructing perturbed stationary states and treating fluctuation of the transition frequencies in terms of stochastic theory.<sup>[18]</sup>

Here, we consider three-pulse heterodyne-detected photon-echo experiments with short IR pulses. A pulse scheme and a schematic picture of the experiment are shown in Figure 11.1. During the first time interval  $t_1$ , the system is in the coherent state, which is followed by the evolution period of the diagonal state during  $T$ . The system is again changed to a coherent state by the third excitation at  $t_1 + T$ . The photon-echo signal results from an induced third-order nonlinear polarization and appears at the phase-matching direction,  $\mathbf{k}_s = -\mathbf{k}_1 + \mathbf{k}_2 + \mathbf{k}_3$ , where  $\mathbf{k}_i$  is the wavevector of the  $i$ -th pulse and  $\mathbf{k}_s$  is the wavevector of the photon-echo signal. A time profile of the echo signal is detected by a gating pulse  $\mathbf{k}_g$  at  $t_1 + T + t_2$  in a heterodyne way. The signal intensity is measured as a function of  $t_1$  and  $t_2$  with a fixed value of  $T$ . By performing a double Fourier transform with respect to  $t_1$  and  $t_2$ , a 2D spectrum is constructed.

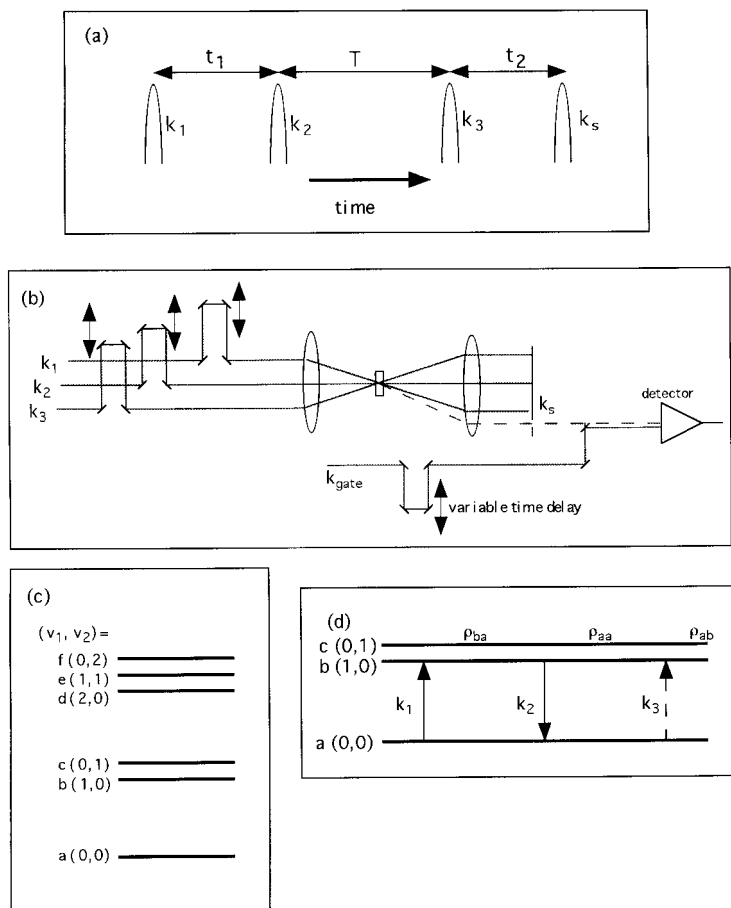


**Fig. 11.1** (a) A pulse scheme for two-dimensional optical spectroscopy.  
(b) A schematic picture of the heterodyne-detected three-pulse photon-echo experiment.

(c) An energy level diagram for the two vibrational mode case.  
(d) One of the 20 diagrams for two-dimensional vibrational spectroscopy.

We consider a model system with two vibrational modes having close but different transition frequencies to see how the vibrational correlation appears in the 2D spectrum. Accordingly, it is assumed that the input optical pulse is spectrally so broad that several vibrational levels are coherently excited. Figure 11.1(c) shows a schematic picture of the six quantum states that need to be taken into account in the case of 2D vibrational spectroscopy for a two-mode system.

## 11.2

### Calculation of the Two-Dimensional Spectrum

Our approach for evaluating the time-evolution of the system is similar to the standard method,<sup>[15,18,19]</sup> in which we construct all the possible quantum pathways contributing to the third-order polarization and calculate a response function for each of them. There are 20 diagrams for this nonlinear optical process, one of which is shown in Figure 11.1(d). The time-evolution of the density matrix is illustrated by means of a Lee–Albrecht ladder diagram<sup>[20]</sup> in each case, where the solid and broken lines correspond to action of the electromagnetic field on the *bra* and *ket* states, respectively. For simplicity, we restrict ourselves here to the pulse sequence with all positive time delays ( $t_1 > 0$ ,  $T > 0$ ,  $t_2 > 0$ ).

We further assume  $T = 0$  to simplify the model. The extension to the general three-pulse photon-echo experiment with  $T > 0$  is feasible. Each quantum pathway has a corresponding response function expressed as:<sup>[1,18,21]</sup>

$$R_i^{(3)}(t_1, t_2) \propto \varepsilon \mu_1 \mu_2 \mu_3 \exp(-i\omega_{kl}t_1 - i\omega_{mn}t_2) \times \left\langle \exp \left\{ -i \int_0^{t_1} \Delta\omega_{kl}(\tau) d\tau - i \int_{t_1}^{t_1+t_2} \Delta\omega_{mn}(\tau) d\tau \right\} \right\rangle \quad (1)$$

where the density matrix of the system is  $\rho_{kl}$  during the first time interval ( $t_1$ ) and  $\rho_{mn}$  the during the third time interval ( $t_2$ );  $\hbar\omega_{kl}$  is the energy difference ( $E_k - E_l$ ),  $\mu_i$  is the transition dipole moment associated with the  $i$ -th pulse, and  $s$  denotes the signal.  $\varepsilon = 1$  ( $-1$ ) when the number of action of the electromagnetic field on the *ket* state is even (odd). The parenthesis in Eq. (1),  $\langle \dots \rangle$  denotes the ensemble average in the equilibrium state and can be expanded in terms of the line-shape function  $g_{kl,mn}(t)$ ,

$$\left\langle \exp \left\{ -i \int_0^{t_1} \Delta\omega_{kl}(\tau) d\tau - i \int_{t_1}^{t_1+t_2} \Delta\omega_{mn}(\tau) d\tau \right\} \right\rangle = \exp(-g_{kl,kl}(t_1) - g_{mn,mn}(t_2) + g_{kl,mn}(t_1) + g_{kl,mn}(t_2) - g_{kl,mn}(t_1 + t_2)) \quad (2)$$

where

$$g_{kl,mn}(t) = \int_0^t d\tau_1 \int_0^{\tau_1} d\tau_2 \langle \Delta\omega_{kl}(\tau_1) \Delta\omega_{mn}(\tau_2) \rangle. \quad (3)$$

The third-order polarization is evaluated by convoluting the response function  $\sum_i R_i(t_1, t_2, t_3)$  with the electromagnetic fields of the three excitation pulses. The intensity of the heterodyne-detected signal is proportional to the polarization.

First, the energy levels and wavefunctions are obtained for the two-mode case. Most models for vibrational dephasing begin with a common perturbation approach to solvent–solute interaction. The vibrational Hamiltonian for a molecule interacting with a bath is written as:

$$\mathcal{H}_{\text{tot}} = \mathcal{H}_h + \mathcal{H}_{\text{anh}} + \mathcal{H}_c(t). \quad (4)$$

Here,  $\mathcal{H}_h + \mathcal{H}_{\text{anh}}$  is the Hamiltonian for an isolated molecule,  $\mathcal{H}_h$  being the harmonic term and  $\mathcal{H}_{\text{anh}}$  being the anharmonic term,

$$\mathcal{H}_h = \frac{1}{2m_1} p_1^2 + \frac{1}{2} m_1 \omega_1^2 x_1^2 + \frac{1}{2m_2} p_2^2 + \frac{1}{2} m_2 \omega_2^2 x_2^2 \quad (5)$$

$$\mathcal{H}_{\text{anh}} = \frac{1}{6} f_{111} x_1^3 + \frac{1}{6} f_{112} x_1^2 x_2 + \frac{1}{6} f_{122} x_1 x_2^2 + \frac{1}{6} f_{222} x_2^3 \quad (6)$$

where the symbols have their usual meanings.<sup>[18]</sup> The solvent–oscillator interaction  $\mathcal{H}_c(t)$  is expanded in the oscillator coordinates up to the second order:

$$\mathcal{H}_c(t) = F_1(t)x_1 + F_2(t)x_2 + G_{12}(t)x_1x_2 + G_{11}(t)x_1^2 + G_{22}(t)x_2^2. \quad (7)$$

The wavefunctions for the anharmonic oscillators are expressed by a linear combination of a basis set for a harmonic oscillator:

$$\Phi_{mn} = \sum c_{mn,\xi\eta} \psi_\xi^1 \psi_\eta^2. \quad (8)$$

where  $\psi_\xi^1$  and  $\psi_\eta^2$  are the wavefunctions for the harmonic Hamiltonian of modes 1 and 2, respectively. The usual procedure is to first solve for the eigenstates of  $\mathcal{H}_h + \mathcal{H}_{\text{anh}}$  in terms of the eigenstates for a harmonics oscillator  $\{|\xi\eta\rangle\}$  by treating the anharmonicity as a perturbation. Solving the equation according to first-order perturbation theory, it is found that the non-zero coefficients of  $c_{mn,\xi\eta}$  are of the order of  $(\gamma_i^2 f_{ijkl} / \varepsilon_m)$ , where  $\gamma_i = \sqrt{\frac{\hbar}{2m_i\omega_i}}$  and  $\varepsilon_i = \hbar\omega_i$ .

For anharmonic oscillators, the energy levels of the vibrational states are empirically expressed as:

$$\frac{E_{mn}}{\hbar} = \kappa_1(m + \frac{1}{2}) + \kappa_2(n + \frac{1}{2}) + \kappa_{11}(m + \frac{1}{2})^2 + \kappa_{22}(n + \frac{1}{2})^2 + \kappa_{12}(m + \frac{1}{2})(n + \frac{1}{2}) + \dots \quad (9)$$

The empirical spectroscopic parameters such as  $\kappa_1$  or  $\kappa_{22}$  are expressed in terms of the parameters in the Hamiltonian such as the cubic anharmonicities.<sup>[22]</sup>

The time-dependent transition frequency between the vibrational states ( $v_1 = m$ ,  $v_2 = n$ , abbreviated as  $(mn)$  and  $(ij)$ ) is expressed as:

$$\begin{aligned} \Delta\omega_{mn,ij}(t) &= \frac{1}{\hbar} \left[ \int dr \Phi_{mn}^* H_c(t) \Phi_{mn} - \int dr \Phi_{ij}^* H_c(t) \Phi_{ij} \right] \\ &= \frac{1}{\hbar} [\langle mn | H_c(t) | mn \rangle - \langle ij | H_c(t) | ij \rangle] \end{aligned} \quad (10)$$

Finally, the time correlation functions of the frequency fluctuations are evaluated, for example:



$$\begin{aligned} \langle \Delta\omega_{ba}(t)\Delta\omega_{ba}(0) \rangle &= \frac{4\gamma^8 f_1^2}{\hbar^2 \epsilon_1^2} \langle F_1(t)F_1(0) \rangle + \frac{4\gamma^4 \gamma^4 f_2^2}{9\hbar^2 \epsilon_2^2} \langle F_2(t)F_2(0) \rangle \\ &\quad + 4\frac{\gamma^4}{\hbar^2} \langle G_{11}(t)G_{11}(0) \rangle \end{aligned} \quad (11)$$

Here, we assume the following relationships:

$$\langle F_i(t)F_j(0) \rangle \ll \langle F_i(t)F_i(0) \rangle \text{ and } \langle G_{ii}(t)G_{jj}(0) \rangle \ll \langle G_{ii}(t)G_{ii}(0) \rangle \text{ if } i \neq j \quad (12)$$

and that the time correlation functions between  $F_i(t)$  and  $G_{ii}(t)$  or  $G_{jj}(t)$  are negligible.

### 11.3 Two-Dimensional Spectrum

In this section, we investigate the spectral pattern of the 2D vibrational spectrum. Figure 11.2 shows a schematic representation of the 2D spectrum obtained from the 20 diagrams. The parameters used to calculate the 2D spectrum in Figure 11.2(a) were  $\omega_1 = 2850 \text{ cm}^{-1}$ ,  $\omega_2 = 3050 \text{ cm}^{-1}$ ,  $\kappa_{11} = -60 \text{ cm}^{-1}$ ,  $\kappa_{22} = -50 \text{ cm}^{-1}$ , and  $\kappa_{12} = -40 \text{ cm}^{-1}$ . For Figure 11.2(b), all parameters were the same as those for Figure 11.2(a), except for  $\kappa_{12} = -1 \text{ cm}^{-1}$ . Cross-peaks such as  $(\omega_{ba}, -\omega_{ca})$  and  $(\omega_{ca}, -\omega_{ba})$  appear in the spectrum, as we expected for an anharmonically-coupled two-mode case. It should be noted that there are, in principle, ten different peaks in the 2D spectrum even for the two-mode case. Each peak is labeled with an upper case letter and has a sign (+ or -) depending on the phase of the polarization.

To calculate the 2D spectrum shown in Figure 11.2, we adopt the Kubo form for all the time correlation functions of the frequency fluctuations:

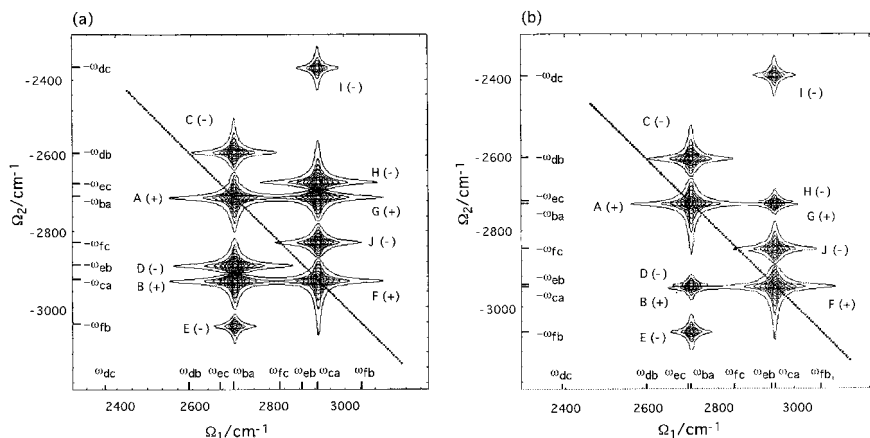


**Fig. 11.2** A schematic representation of the two-dimensional vibrational spectrum for the two vibrational mode case. Each peak is labeled with an upper case letter. The sign for the peaks A, B, F, and G is plus, while that for the peaks C,

D, E, H, I, and J is minus. A diagonal line is shown for eye guidance. A large anharmonic splitting case (a) and a small anharmonic splitting case (b) are shown; see text for details.

$$\langle \Delta\omega_{ij}(t)\Delta\omega_{kl}(0) \rangle = D_{ij,kl}^2 \exp(-t/\tau_{ij,kl}) \quad (13)$$

where  $D_{ij,kl}$  and  $\tau_{ij,kl}$  are the pre-exponential factor and time constant of the time-correlation function, respectively. If the frequency fluctuation is in the so-called rapid modulation limit ( $D_{ij,kl}\tau_{ij,kl} \ll 1$ ), then the line-shape function,  $g_{ij,kl}(t)$  (Eq. (3)), is equal to  $D_{ij,kl}^2 \tau_{ij,kl} t$ . Here,  $(1/D_{ij,kl}^2 \tau_{ij,kl})$  is the vibrational dephasing time, which determines the linewidth of the spectrum. As shown in ref.,<sup>[18]</sup> if the fluctuations of the frequencies  $\omega_{ba}$  and  $\omega_{ca}$  are in the rapid modulation limit, the line shape of the cross-peak is similar to that of the diagonal peak.

To calculate the 2D spectra in Figure 11.2, we assume that all the frequency fluctuations are in the rapid modulation limit and that the time dependencies of all eight time-correlation functions for the diagonal terms such as  $\langle \Delta\omega_{ba}(t)\Delta\omega_{ba}(t) \rangle$  are similar. Then, the intensities of the peaks in the 2D spectrum are determined solely by the magnitudes of the transition dipole moment term ( $\mu_1\mu_2\mu_3\mu_s$ ) as seen in Eq. (1). In this case, all the peaks with the exception of *I* and *E* have almost equal intensities if cancellation of the peaks does not occur, which will be explained in detail in the following.

The peaks *I* and *E* stem from the fact that the forbidden transitions for the harmonic oscillator case (*bf* and *cd*) are allowed due to the presence of the anharmonic coupling. Considering the expressions for the transition dipole moment and coefficient of  $c_{mn,pq}$ , the relative intensities of the peaks *I* and *E* with respect to those of the other eight peaks are of the order of  $(\gamma_i^3 f_{jkl}/\epsilon_m)^2$ . For ordinary organic molecules, this quantity is at most of the order of  $10^{-2, [23]}$  suggesting that the peaks *E* and *I* should be negligibly small compared to the diagonal peaks. In Figure 11.2, the intensities of the peaks *I* and *E* are exaggerated in order to show their presence.

The other eight peaks can be categorized into four groups: (*A* and *C*), (*F* and *J*), (*G* and *H*), and (*B* and *D*). Two groups, (*B* and *D*) and (*G* and *H*), disappear if the off-diagonal anharmonicities are zero, because the corresponding transition frequencies become equal,  $\omega_{ca} = \omega_{eb}$  and  $\omega_{ba} = \omega_{ec}$ , and the peaks have almost equal intensities with opposite signs. In other words, the quantum pathways for the *B* and *D* peaks destructively interfere with each other if the off-diagonal anharmonicities are zero. If the anharmonic splitting  $\delta (= |\omega_{ca} - \omega_{eb}|)$  is sufficiently large compared to the linewidth of the peak  $\Delta\nu$  (full-width at half-height), the peaks *B* and *D* are well-separated. In Figure 11.2(a),  $\Delta\nu = 10 \text{ cm}^{-1}$  and  $\delta = 40 \text{ cm}^{-1}$ . However, if  $\delta \ll \Delta\nu$ , then the two peaks cancel each other out, and the intensity of the resulting peak becomes small. In Figure 11.2(b), such a small splitting case is illustrated ( $\Delta\nu = 10 \text{ cm}^{-1}$  and  $\delta = 1 \text{ cm}^{-1}$ ) to explain the cancellation of the cross-peaks. Thus, the linewidth of the peak as well as the anharmonicity is important with regard to the appearance of the cross-peaks (*B* and *D*) and (*G* and *H*). It can be concluded that the cross-peaks (*B* and *D*) and (*G* and *H*) carry information on correlation between the two modes. The other two groups of diagonal peaks, (*A* and *C*) and (*F* and *J*), disappear due to destructive interference if the corresponding diagonal anharmonicity is zero. In the case of the two modes being harmonic, no peaks are observed in the spectrum.

## Acknowledgements

This work was partially supported by a grant in the Priority Area of “Chemical Reaction Dynamics in Condensed Phases” (No. 10206207), a grant (No. 10440181) from the Ministry of Education, Science, Sports, and Culture of Japan, and a JSPS research grant with the framework of the Future Program.

## References

- 1 R. F. Loring, S. Mukamel, *J. Chem. Phys.* **1985**, 83, 2116; D. Vanden Bout, L. J. Muller, M. Berg, *Phys. Rev. Lett.* **1991**, 67, 3700; R. Inaba, K. Tominaga, M. Tasumi, K. A. Nelson, K. Yoshihara, *Chem. Phys. Lett.* **1993**, 211, 183.
- 2 X. D. Zhu, Y. R. Shen, *Appl. Phys. B* **1990**, 50, 535; P. Guyot-Sionnest, *Phys. Rev. Lett.* **1991**, 66, 1489.
- 3 Y. Tanimura, S. Mukamel, *J. Chem. Phys.* **1993**, 99, 9496.
- 4 S. Mukamel, A. Piryatinski, V. Chernyak, *Acc. Chem. Res.* **1999**, 32, 145.
- 5 K. Tominaga, K. Yoshihara, *Phys. Rev. Lett.* **1996**, 74, 3061; *J. Chinese Chem. Soc.* **2000**, 47, 631.
- 6 T. Steffen, K. Duppen, *Phys. Rev. Lett.* **1996**, 76, 1224.
- 7 A. Tokmakoff, G. R. Fleming, *J. Chem. Phys.* **1997**, 106, 2569.
- 8 K. Okumura, Y. Tanimura, *J. Chem. Phys.* **1997**, 106, 1687.
- 9 R. L. Murry, J. T. Fourkas, T. Keyes, *J. Chem. Phys.* **1998**, 109, 2814.
- 10 S. Saito, I. Ohmine, *J. Chem. Phys.* **1998**, 108, 240.
- 11 M. Cho, *J. Chem. Phys.* **2000**, 112, 9978.
- 12 J. C. Kirkwood, D. J. Ulness, A. C. Albrecht, M. J. Stimson, *Chem. Phys. Lett.* **1998**, 293, 417.
- 13 J. D. Hybl, A. W. Albrecht, S. M. Gallagher Faeder, D. M. Jonas, *Chem. Phys. Lett.* **1998**, 297, 307.
- 14 D. Blank, L. Kaufman, G. R. Fleming, *J. Chem. Phys.* **1999**, 111, 3105.
- 15 P. Hamm, M. Lim, W. F. DeGrado, R. M. Hochstrasser, *J. Chem. Phys.* **2000**, 112, 1907.
- 16 W. Zhao, J. C. Wright, *Phys. Rev. Lett.* **1999**, 83, 1950.
- 17 M. C. Asplund, M. T. Zanni, R. M. Hochstrasser, *Proc. Natl. Acad. Sci. USA* **2000**, 97, 8219.
- 18 K. Tominaga, H. Meakawa, *Bull. Chem. Soc. Jpn.* **2001**, 74, 279.
- 19 P. A. Madden, R. M. Lyden-Bell, *Chem. Phys. Lett.* **1976**, 38, 163; D. W. Oxtoby, S. A. Rice, *Chem. Phys. Lett.* **1976**, 42, 1.
- 20 D. Lee, A. C. Albrecht, in *Advances in Infrared and Raman Spectroscopy*, vol. 12 (Ed.: R. J. Clark, R. E. Hester), Wiley-Heydon, New York, 1985.
- 21 S. Mukamel, *Principles of Nonlinear Optical Spectroscopy*, Oxford University Press, New York, 1995.
- 22 B. T. Darling, D. M. Dennison, *Phys. Rev.* **1940**, 57, 128.
- 23 See, for example: G. Herzberg, *Molecular Spectra and Molecular Structure*, Van Nostrand Reinhold, New York, 1966.

## 12

# Femtosecond Diffuse Reflectance Spectroscopy and Photochemistry of Organic Microcrystals

*Hiroshi Masuhara, Tsuyoshi Asahi, and Akihiro Furube*

### 12.1

#### Introduction

Since the flash photolysis method was first proposed by Norrish and Porter in 1949,<sup>[1]</sup> time-resolved UV/visible absorption spectroscopy has contributed greatly to studies of chemical, physical, and biological processes. Thus, excited states and transient chemical species have been identified, their relaxation/reaction rates have been determined directly, and, in turn, this has allowed molecular mechanisms to be elucidated in detail. The temporal resolution has been improved from ms to  $\mu$ s, from ns to ps, and now from sub-ps to real fs by introducing various kinds of pulsed lasers as excitation and monitoring light sources.<sup>[2,3]</sup> Absorption spectroscopic measurements have typically been performed on optically clear samples such as transparent films, gaseous, or solution systems; in other words, transmittance-mode optical alignment has usually been applied. However, in Nature, most materials and living systems are opaque or translucent rather than optically transparent, preventing the application of conventional transmittance-mode spectroscopy. Consequently, the interesting photoprimary processes of such materials remain largely unknown.

In 1981, Wilkinson et al. proposed the ns diffuse reflectance spectroscopic method and analyzed its optical requirements,<sup>[4,5]</sup> which, in principle, are based on Kubelka–Munk theory.<sup>[6]</sup> A few years later, we were able to improve the time-resolution to ps,<sup>[7,8]</sup> and, as a result, the photoprimary processes of organic microcrystals, semiconductor photocatalysts, insoluble polymer powders, molecules adsorbed on metal oxides and zeolites, etc., became as accessible to study as transparent solutions. Recently, fs diffuse reflectance spectroscopy has been developed through the introduction of fs laser pulses and their white continuum as pump and probe pulses, respectively.<sup>[9]</sup> Systematic data on ultrafast processes in optically scattering solids and colloidal solutions can be acquired, but their temporal analysis is not so simple as fs pulses become broad during propagation in scattering materials. Thus, it is necessary and indispensable to analyze the propagation of fs pulses and to evaluate their temporal resolution, as well as to compare the simulated curves with experimental data. In the present chapter, we describe the development of a fs diffuse reflectance spectroscopic system and its application to organic powder systems; some examples and future perspectives are also discussed.

harmonic generator; RF: retroreflector; L: lens; F: filter; MCPD: multi-channel photodiode array; P: polarizer.

where  $R$  and  $R_0$  represent the intensity of the diffuse reflected light of the probe pulse with and without excitation, respectively.<sup>[5,7–9]</sup> The origin of the time axis is the delay time between the excitation and probe pulses being incident on the sample surface, and it is equal to that in transmission-mode experiments.

### 12.2.2

#### Time-Dependent Kubelka–Munk Model

In the Kubelka–Munk theory,<sup>[6]</sup> a thick and isotropic opaque medium is considered to be composed of a number of thin layers. The distribution of light intensity in the light-scattering medium is given, as a function of depth  $x$ , by the following set of differential equations:

$$dI(x)/dx = -(K + S)I(x) + SJ(x), \quad (2a)$$

$$dJ(x)/dx = (K + S)J(x) - SI(x), \quad (2b)$$

where  $I(x)$  and  $J(x)$  represent the intensities of the light travelling in the positive and negative  $x$ -directions, respectively.  $K$  and  $S$  denote the absorption and scattering probabilities, respectively, of a thin layer of thickness  $dx$ .

For a sample of infinite thickness, it was shown that the ratio of  $K$  to  $S$  is given by its diffuse reflectance,  $r = J(0)/I(0)$ ,

$$\frac{K}{S} = \frac{(1-r)^2}{2r}. \quad (3)$$

This is known as the Kubelka–Munk re-emission function and gives an absorption spectrum of the sample.

Since  $I$  and  $J$  consist of the light propagating three-dimensionally, the average path length of the light within the layer  $dx$  is not equal to  $dx$ . By introducing the mean value of the optical path length  $\omega dx$ , Eqs. (2a, 2b) can be rewritten as:

$$dI(x)/dx = -\omega(k + s)I(x) + \omega sJ(x), \quad (4a)$$

$$dJ(x)/dx = \omega(k + s)J(x) - \omega sI(x). \quad (4b)$$

Here,  $K$  and  $S$  are replaced by  $\omega k$  and  $\omega s$ , where  $k$  and  $s$  are absorption and scattering coefficients, respectively. The value of  $\omega dx$  is given by

$$\omega dx = dx \int_0^{\pi/2} \frac{1}{I_0 \cos \theta} \cdot \frac{\partial I(\theta)}{\partial \theta} d\theta, \quad (5)$$

where  $\partial I(\theta)/\partial \theta$  represents the angular distribution of light intensity,  $\theta$  is the angle from the  $x$ -axis, and  $I_0$  is the total intensity in the hemisphere.<sup>[11]</sup> When the intensity in all directions is the same for  $I$  (and  $J$ ), then  $\omega = 2$ .

While a stationary incident light is considered in the Kubelka–Munk theory, we must extend it to a time-dependent form to analyze the experimental results, particularly those obtained by fs time-resolved measurements. We propose here a simple model based on the Kubelka–Munk theory to deal with propagation of a short light pulse in a dense scattering medium. The average velocity of light in the sample is given by  $v = c_0/n_{av}$ , where  $c_0$  is the velocity of light in vacuum and  $n_{av}$  is a mean

refractive index. We set  $\Delta t = \omega \Delta x / v$  as the mean time of passage of light through the layer of thickness  $\Delta x$  and introduce it into the difference forms of Eqs. (4a, 4b). The following set of time-dependent equations is obtained, which is shown schematically in Figure 12.2.

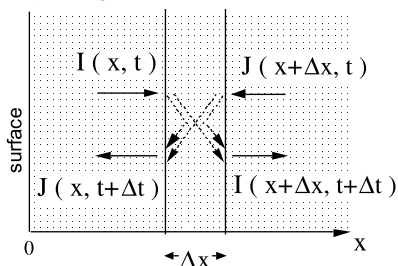


**Fig. 12.2** An illustration of a thin layer in a homogeneous light-scattering medium for a numerical simulation of the propagation of a light pulse according to the time-dependent Kubelka–Munk model.

$$I(x + \Delta x, t + \Delta t) = \{1 - \omega(k + s) \Delta x\} I(x, t) + \omega s \Delta x J(x + \Delta x, t), \quad (6a)$$

$$J(x, t + \Delta t) = \{1 - \omega(k + s) \Delta x\} J(x + \Delta x, t) + \omega s \Delta x I(x, t). \quad (6b)$$

For an incident light pulse  $I(0, t)$ , the diffuse light intensity  $J(0, t)$  can be calculated numerically using Eqs. (6a, 6b). The value of  $\Delta x$  was set at  $1 \mu\text{m}$ , the adequacy of which was tested for values of  $s$  less than a few  $100 \text{ cm}^{-1}$ . The thickness of the sample was set at  $2 \text{ mm}$ , and the light arriving at its rearside was assumed to go out of the sample.

For transient absorption measurements, in which light propagation of both the pump and probe pulses is calculated simultaneously, absorption of the pump pulse at depth  $x$  is given by

$$k_{\text{pump}} [I_{\text{pump}}(x, t) + J_{\text{pump}}(x, t)] \Delta t. \quad (7)$$

The transient absorption of a probe pulse is proportional to the value of Eq. (7). Hence, the absorption coefficient for a probe pulse,  $k_{\text{probe}}(x, t)$ , is given by

$$k_{\text{probe}}(x, t) = k_{\text{probe}}(x, t - \Delta t) + 2.303 \times 10^3 \epsilon_{\text{probe}} \times k_{\text{pump}} [I_{\text{pump}}(x, t) + J_{\text{pump}}(x, t)] \Delta t, \quad (8)$$

where  $\epsilon_{\text{probe}}$  is the molar extinction coefficient of the transient species at the probe wavelength, and the units of  $I$  and  $J$  are  $[\text{mol cm}^{-2} \text{ s}^{-1}]$ , counting the number of photons in terms of moles. Here, it is assumed that the ground state shows no absorption at the probe wavelength. By integration of the diffuse reflected light of the probe pulse that is incident on a sample at  $t = T$  (the delay time), the % absorption change is given by

$$\% \text{absorption}(T) = \left(1 - \frac{\int J_{\text{probe}}(0, t) dt}{\int J_{\text{probe}}^0(0, t) dt}\right) \times 100, \quad (9)$$

where  $J_{\text{probe}}^0$  denotes the diffuse reflected light intensity without excitation.

## 12.2.3

## Temporal Characteristics and Time Resolution

We have examined the transient absorption spectra of poly(methyl methacrylate) (PMMA) powders doped with 9-phenylanthracene in order to demonstrate our analysis method. The absorption band of the lowest excited singlet ( $S_1$ ) state and the rise curve of 9-phenylanthracene are shown in Figure 12.3. The formation of the  $S_1$  state is instantaneous because excitation photon energy is just identical to the  $S_1$  energy leading to no intramolecular vibrational relaxation, and the  $S_1$  lifetime is sufficiently long in the present time range. Therefore, the rise curve of  $S_1$  absorption is expected to give a stepped response, but the observed temporal profiles show a very slow rise from negative values of several 10's of ps, which is very long compared with the duration of the incident pulses.

The solid curves in Figure 12.3 are the simulation results according to the aforementioned time-dependent Kubelka–Munk model, where the parameters are  $s = 90 \text{ cm}^{-1}$ ,  $k_{\text{pump}} = 30 \text{ cm}^{-1}$  and  $s = 26 \text{ cm}^{-1}$ ,  $k_{\text{pump}} = 13 \text{ cm}^{-1}$  for doped PMMA powders of mean diameters 5 and 20  $\mu\text{m}$ , respectively. The value of  $s$  used here was that determined independently by examining the temporal profiles of diffuse reflected light from undoped PMMA particles without excitation, while  $k_{\text{pump}}$  was estimated by analyzing the ground-state absorption with the Kubelka–Munk function. It is worth noting that simulated curves using  $\omega = 6$  reproduce the experimental results very well for each sample, whereas those with  $\omega = 2$  do not.

Beyond delay times of several ps, % absorption is constant because the preceding pump pulse is already absorbed by the molecules and can no longer propagate when the probe pulse enters the sample. However, at negative or near-zero delay times, both the pump and probe pulses are propagating in the sample. Therefore,

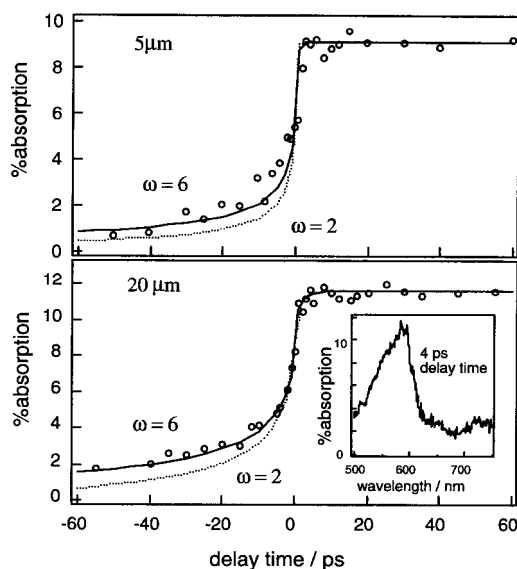


**Fig. 12.3** Temporal response of a transient absorption of samples of a poly(methyl methacrylate) powder (mean diameter 5 and 20  $\mu\text{m}$ ) doped with 9-phenylanthracene observed at 591 nm. Solid curves show simulated results based on the time-dependent Kubelka–Munk model. The insert shows the transient absorption spectrum at a delay time of 4 ps after the excitation.



% absorption in the negative delay depends on the delay time and, more importantly, its large value indicates that the probe light is retained until the pump pulse enters into the sample. For  $\omega = 6$ , light can effectively stay in the powder for a long time, because, for  $\omega = 2$  and 6, diffuse light starts to disperse from the rearside of the cell (2 mm thickness) about 20 and 60 ps, respectively, after its incidence.

The meaning of the large  $\omega$  is considered as follows. Applying Eq. (5), it is assumed that, in a sufficiently thin layer, most of the light proceeds in a straight line without changing its direction. In a powder, however, light will be propagated in a very complicated manner by reflection or refraction at the interfaces between the particles, and between the particles and air. Therefore, the light can be expected to change its direction many times in a layer containing many particles. In other words, in a dense scattering medium such as a powder, light proceeding in a haphazard zigzag fashion should be propagated. Alfano et al. proposed a concept of snake photons that propagate essentially in one direction, but deviate from straight-line paths in suspensions, i.e. these snake photons are delayed temporally.<sup>[12,13]</sup> Furthermore, Shimizu and Ishimaru have reported experimental results indicating that the effective velocity of light in suspended latex particles is reduced by a factor of  $\sqrt{3}$ .<sup>[14]</sup> This effect will be more pronounced in powders than it is in suspensions. Moreover, Wiersma et al. recently reported experimental evidence for Anderson localization of light in strongly scattering semiconductor powders.<sup>[15]</sup> Here, scattered light tends to localize in a small area through interference rather than propagating away. Such a coherent effect may serve to confine the scattered light in a thin layer, although we do not take into account the wave properties of light.

On the other hand, ultrafast decay relaxation processes can be followed directly by means of diffuse reflectance spectroscopy. The pump pulse creates transient states during propagation in the scattering medium, but the excited states quickly decay and their homogeneous distribution is never achieved when their lifetimes are very short. The probe pulse can only be absorbed when it overlaps spatially and temporally with the transient species, irrespective of how long it has propagated before absorption. For an illustrative demonstration, transient absorption spectra of charge-transfer (CT) microcrystals of hydroquinone–pyromellitic dianhydride (PMDA) were measured. The absorption rise shows a tail towards negative delay times as in Figure 12.3, while the absorption decay shows a time constant of 1.5 ps. According to the simulation, the sub-ps decay component can be measured under conditions of a sufficiently large absorption coefficient at the excitation wavelength. Hence, it is concluded that the time resolution of the fs diffuse reflectance spectroscopy is sub-ps.

## 12.3

## Ultrafast Processes in Some Organic Powders

## 12.3.1

## Excited Electronic Structure and Dynamics of Weak CT Microcrystals

The transient absorption spectra of microcrystals of PMDA adducts of durene, hexamethylbenzene (HMB), and *p*-dimethoxybenzene (*p*DMB) are shown in Figure 12.4. An absorption maximum at around 700 nm resembles the absorption band of the PMDA anion radical, although compared to the anion radical in solution, the bandwidth seen for the crystals is broader and the peak position shifts to longer wavelengths. All the transient absorption spectra were seen to increase within the temporal response of the spectroscopic system and to decay monotonously without any appreciable spectral change. Moreover, when the excitation intensity was low, the decay behavior was seen to be approximately the same as that of a CT fluorescence measured by a streak camera. Therefore, it was concluded that the absorption spectra are due to the relaxed excited singlet state (the fluorescence state) and not to other ionic species.<sup>[16]</sup> The  $S_n - S_1$  absorption spectral shape depends on the donor molecule (D), while the spectra in ethyl acetate solution are almost the same.

First, we have to ascertain whether the excited state is delocalized over multiple donor (D) and acceptor (A) moieties in the crystals or whether it is localized on one D-A pair. To this end, we compared the transient absorption spectrum of a 1:1 CT crystal of durene–PMDA with that of a  $10^{-4}$  M PMDA-doped durene crystal and

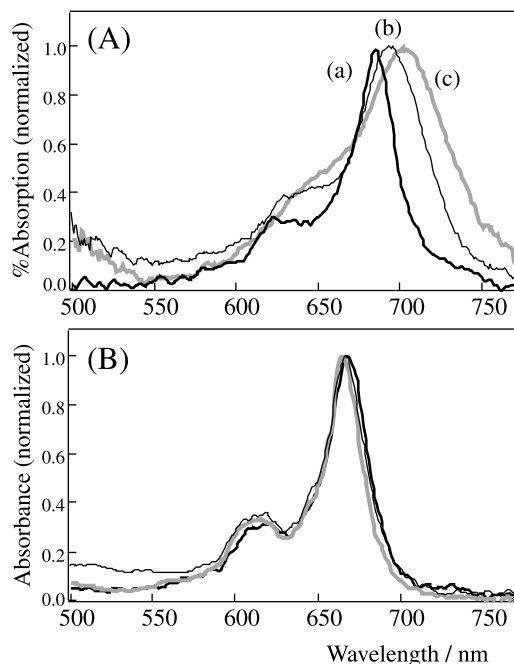


**Fig. 12.4** (A) Transient absorption spectra of promellitic dianhydride (PMDA) CT microcrystals of (a) *p*-dimethoxybenzene–PMDA, (b) hexamethylbenzene–PMDA, and (c) durene–PMDA at 10 ps after a 390 nm excitation, and (B) spectra recorded in ethyl acetate solution.

found a good agreement between these spectra. Thus, the absorption band, which is broad and red-shifted compared to that of the PMDA anion radical, was observed irrespective of the concentration ratio of D and A. A similar result was also obtained for the *p*DMB–PMDA complex. Consequently, we can conclude that the electronic excitation is localized on one D-A pair, and that the electronic interactions between this pair and neighboring neutral molecules are quite small. Therefore, we can treat the surrounding ground-state D and A molecules as a solvent (an oriented-gas model) and consider the excited electronic structure of the CT crystals in terms of a single D-A pair. Actually, Hochstrasser et al.<sup>[17]</sup> and Haarer et al.<sup>[18]</sup> considered the CT excited states of molecular crystals of weak D-A complexes to be rather localized (self-trapped) due to their alternating molecular stacks, strong electron-phonon coupling, as well as an appreciable Coulombic interaction between the highly ionic component molecules generated.

Next, we discuss the differences between the  $S_n - S_1$  absorption spectra of these PMDA complexes in terms of the extent of CT in the excited state. The relative contributions of the locally excited (LE) and the non-bonded ground-state configurations in the excited state depend on the geometrical conformations of D and A and the oxidation potential of D. In general, configurational interactions among the non-bonded ground state, the full CT state, and the LE states of D and A are associated with a change in the extent of CT that depends on their energy levels as well as on the mutual geometries of D and A. The present D-dependent spectrum indicates that the extent of CT increases on lowering the CT energy level, i.e. with decreased oxidation potential of D.

The transient absorption decay of each of the crystals examined here is approximately represented by a single exponential function under low excitation conditions. The lifetime of the excited state changes drastically on varying D; it decreases on lowering the CT energy level. When the excitation intensity is not so high and the unimolecular decay rate is fast, the decay can be ascribed to non-radiative relaxation to the ground state, which can be qualitatively regarded as charge recombination (CR). In Figure 12.5, the values of  $k_{CR}$  ( $= \tau_0^{-1}$ ) are plotted against  $-\Delta G$  between the excited and the ground states, as estimated from the peak energies of the CT absorption band ( $h\nu_{max}^a$ ) and the CT fluorescence band ( $h\nu_{max}^f$ ) according to Eq. (10).

$$-\Delta G = h\nu_{max}^a - \Delta h\nu / 2, \quad (10)$$

where  $\Delta h\nu$  represents the Stokes shift ( $= h\nu_{max}^a - h\nu_{max}^f$ ). The result obtained can be adequately described by Eq. (11).

$$\ln k_{CR} = \alpha - \beta | -\Delta G | \quad (11)$$

A similar relationship has previously been reported for the charge recombination of contact ion-pair states in homogeneous solution<sup>[19,20]</sup> and in heterogeneous environments.<sup>[21]</sup> Recently, a study on the energy gap minima for the CT excited state of arene–1,2,4,5-tetracyanobenzene (TCNB) and arene–methylviologen CT crystals based on ps diffuse reflectance spectroscopy was reported by Hubig and Kochi, in which a similar linear dependence was also observed.<sup>[22]</sup> These results suggest that the linear relationship between  $k_{CR}$  and  $| -\Delta G |$  is general for the contact ion-pair state or the CT excited state in molecular crystals.

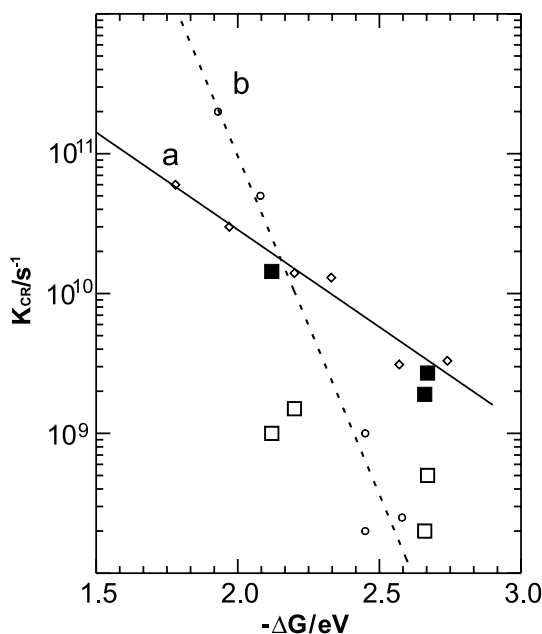


**Fig. 12.5** Charge recombination decay rate constant as a function of the energy gap. (a) In porous Vycor glass and acetonitrile solution<sup>[21]</sup> and in  $1.0 \times 10^{-2}$  mol  $\text{g}^{-1}$  hydrated NaY [●]. (b) In CT microcrystals and in dehydrated NaY [○].

### 12.3.2

#### Charge Recombination Process of Molecules Adsorbed in Zeolites

Zeolites have attracted much attention in photochemistry since they host various organic transformations in their cavities and channels, often leading to product distributions considerably different from those achieved in solution. It has long been realized that zeolites have the potential to control the photophysical and photochemical behavior of organic molecules adsorbed in their cavities. Thus, in recent years, much effort has been devoted to elucidating the photophysical and photochemical processes occurring in zeolites and the remarkable specificity and selectivity that they can impart to photochemical reactions. Transient absorption spectroscopic studies using diffuse reflectance spectroscopy have proved especially useful and we describe herein some interesting results for CT complexes within zeolites.<sup>[23]</sup> We have found that TCNB molecules interact strongly with framework oxygens adjacent to Al and are reduced to the corresponding anion radical upon excitation as faujasite zeolites, NaY and CsNaY, have considerable electron-donating abilities.

In Figure 12.6, the transient absorption spectra obtained in the absence and presence of  $10 \text{ mol} \cdot \text{g}^{-1}$  water following photoexcitation of the TCNB–naphthalene CT complex assembled within an NaY zeolite are compared. The transient absorption signals evolved within the temporal response of the spectroscopic system (a few ps) and decayed without any appreciable accompanying spectral change. These transient spectra resemble a superposition of the spectra of the naphthalene cation and TCNB anion. It is thus reasonable to assume that the transient absorption decay is

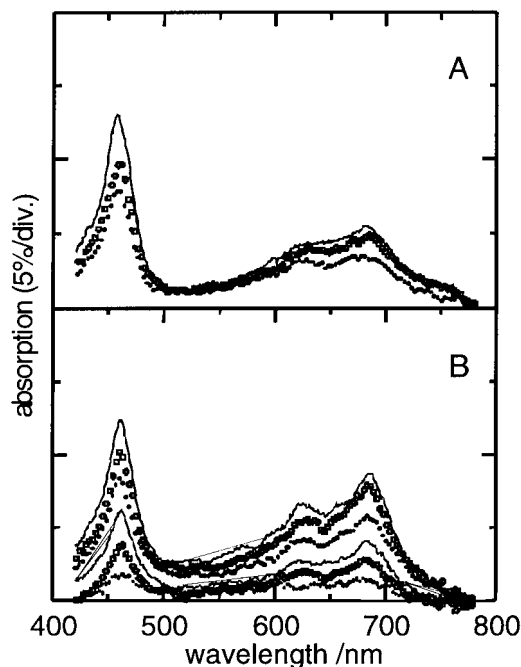


**Fig. 12.6** Transient absorption spectra of 1,2,4,5-tetracyanobenzene-naphthalene CT complex. (A) Dehydrated NaY. Delay times were 10 ps, 2 ns, and 5 ns from the top. (B)  $1.0 \times 10^{-2} \text{ mol g}^{-1}$  hydrated NaY. Delay times were 10 ps, 100 ps, 200 ps, 300 ps, 500 ps, and 1 ns from the top.

due to the charge recombination process of the excited CT state to the ground state, since the time course of the decay is similar at the peak wavelengths of both the cation of D and the anion of A. The experimental decay curves were analyzed; for the decay of excited CT complexes, the validity of Eq. (11) was confirmed.

The energy gap dependent rate constants, the values of  $k_{\text{CR}}$  versus  $-\Delta G$ , are plotted in Figure 12.5 along with the results obtained in solution and in Vycor glass by Miyasaka et al.<sup>[21]</sup> and those obtained for microcrystals by Asahi et al.<sup>[16]</sup> In CT crystals of PMDA adducts with electron-donating benzene derivatives, the same linear relationship is observable with a  $\beta$  value ca. three times larger than that in solution or in porous Vycor glass. A similarly large  $\beta$  value is expected in dehydrated NaY since the rigidity of the donor-acceptor pairs will lead to only limited structural changes in the excited state. Thus, we consider the higher-frequency quantum modes in the excited CT state to be responsible for the decay process in rigid, solid states.

### 12.3.3

#### Intersystem Crossing in an Acridine Microcrystal

Intersystem crossing is one of the fundamental relaxation channels of excited singlet-state molecules, and the generated triplet state often plays a key role as an important intermediate in various photochemical reactions in solution and probably in the solid phase as well. Although the dynamics and mechanism have been studied for a number of molecules in various solvents, few cases have been reported concerning the crystalline phase. To characterize the intersystem crossing process in molecular

crystals, electronic interactions, mainly a dipole-dipole interaction between an excited molecule and a neighboring molecule in the ground state, would be an important factor. Such interactions not only modify the energy level of the excited state from that of the individual molecules, but also strongly affect the relaxation dynamics. A typical example involving such interactions is excimer formation. Intersystem crossing also takes place from the excimer, which should be very different from that in the monomer. Furthermore, the dielectric properties of the surrounding molecules in the crystal, being different from those of the solvent, may also influence the intersystem crossing. For example, the energy levels of the  $n\pi^*$  and  $\pi\pi^*$  singlet and triplet states are determined by the solvent polarity and/or hydrogen-bond formation, which may be rather rare in a crystal. Furthermore, strong restrictions of conformational relaxations do not allow molecular conformational change and consequently affect the intersystem crossing process. This has been clearly demonstrated for a *p*-Terphenyl crystal.<sup>[7]</sup>

We now describe the intersystem crossing process of acridine microcrystals, for which the molecular structure should be identical in both the solution and crystalline phases.<sup>[24]</sup> This molecule is well-known as a compound showing ultrafast intersystem crossing in aprotic solvents and the mechanism and dynamics in the solution and gas phases have been studied in detail. It was confirmed by fs diffuse reflectance spectroscopy that an excimer was formed in the microcrystal within a few ps after excitation. The time constant for the triplet formation from the  $S_1$  state was estimated to be about 900 ps at room temperature, which is about ten times slower than that in an aprotic solvent. Slow intersystem crossing in the crystal was explained in terms of a selective stabilization of the  $^1\pi\pi^*$  electronic configuration due to excimer formation. The acridine crystal has a structure comprising stacked dimer units, which are arranged in anti-parallel pairs with respect to the nitrogen atom. In this dimer unit, the  $^1\pi\pi^*$  electronic structure can be stabilized by excimer formation, whereas the  $^1n\pi^*$  structure cannot as the lone-pair electron orbital on the nitrogen atom is orthogonal to the  $\pi$ -orbital of the neighboring ground-state molecule. The  $\pi\pi^*$  electronic character of the excimer state was confirmed by the experimental observation of a broad fluorescence in spite of the rather short lifetime (900 ps). Although it is difficult to determine the stabilization energy of excimer formation, we roughly estimate it to be  $1500\text{ cm}^{-1}$ , which corresponds to half the energy difference between the excimer fluorescence peak and the 0-0 transition of the monomer in benzene solution.

Fast intersystem crossing of the acridine molecule is considered to occur solely through the transition from  $^1n\pi^*$  to  $^3\pi\pi^*$  ( $T_3$ ). In an aprotic solvent, the energy levels of the lowest  $^1n\pi^*$  and  $^1\pi\pi^*$  states are very close to each other, and the time constant for triplet formation is very short (60 ps in benzene). On the other hand, since in the crystalline phase the  $^1\pi\pi^*$  state is selectively stabilized by excimer formation, as described above, the internal conversion from  $^1\pi\pi^*$  to  $^1n\pi^*$  requires thermal activation, resulting in slower triplet formation from the  $S_1$  state. This interpretation is nicely supported by the temperature dependence of the fluorescence lifetime. Moreover, the obtained activation energy is consistent with the stabilization energy of  $^1\pi\pi^*$  due to excimer formation that was estimated from the fluorescence spectrum.

## 12.4

### Future Perspectives

#### 12.4.1

##### Femtosecond Absorption Spectroscopy of a Single Microcrystal

All the samples discussed in the present review have been polycrystalline powders, so that the absorption spectroscopic data obtained has been that averaged over an ensemble of microcrystals. Of course, photophysical and photochemical data should be dependent on the size and shape of the microcrystal, thus it is envisaged that the nature of specific microcrystals may be interrogated by measuring them individually. To this end, we have developed a fs UV/visible absorption microspectrophotometer combined with optical trapping.<sup>[25]</sup> A pump beam, a probe white continuum generated by focusing an intense fs laser in water, and a trapping beam are coaxially introduced into a microscope and focused onto a single microcrystal by a reflecting objective lens. The spatial and temporal resolutions that have been achieved are  $<2.5\ \mu\text{m}$  and 200 fs, respectively. The maximum sensitivity is comparable with that of a conventional transient absorption spectroscopic system. This system is proving very useful for the analysis of photophysical and photochemical dynamics of various kinds of non-fluorescent particles, polymer films, and biological samples, as well as  $\mu\text{m}$ -sized crystals. Optical trapping techniques can be applied to fix a living cell, hence its photochemical primary processes may be probed *in vivo* without its destruction or any pre-treatment.

A representative example is the perylene microcrystal, for which  $\alpha$ - and  $\beta$ -forms are well-known. The transient absorption spectrum of a single  $\alpha$ -perylen crystal shows a peak at 510 nm and a broad absorption ranging from 570 to 720 nm. On the other hand, a sharp peak is seen at 500 nm for a single crystal of the  $\beta$ -form. These bands are tentatively assigned to the partially and fully overlapped dimer cations induced by two-photon excitation.

#### 12.4.2

##### Femtosecond Light-Scattering Spectroscopy

Although photophysical and photochemical studies on a single microcrystal are geared towards small-scale systems, the fs system outlined above cannot give appreciable absorption intensities when the path length is less than  $1\ \mu\text{m}$ . There is an urgent need for the development of a new sensitive method giving time-dependent absorption spectra of single  $\mu\text{m}$ - to nm-sized particles. In this context, a system consisting of an inverted microscope and a fs laser, and utilizing pump-probe measurements has been applied.<sup>[26]</sup> Here, a small microcrystal is excited by a fs laser pulse, a white continuum light pulse illuminates the excited surface, and some of the latter pulse is scattered due to the change in refractive index of the complex, giving information on the transient absorption. Transient scattering difference spectra can be related to the transient absorption spectrum, which is now being confirmed using perylene microcrystals of different sizes.

## 12.4.3

**Femtosecond Cooperative Photochromic Reaction in Organic Crystals**

Photochromism in solution and in polymer matrices is a well-known phenomenon, whereas there have only been a few examples of crystalline-state photochromism. Spironaphthooxazines and related compounds do not undergo photocoloration in the crystal as extensive structural change to the stable photoisomer is inhibited. However, these microcrystalline powders do show coloration when excited by fs laser pulses.<sup>[27]</sup> In diffuse reflectance spectroscopy, the % absorption of the product merocyanine increases superlinearly with laser fluence, whereas no appreciable coloration is identified under a weak excitation. We are currently carrying out systematic examinations of temperature and excitation intensity effects by means of diffuse reflectance spectroscopy and double-pulse excitation experiments. On the basis of these experimental results, we propose a cooperative photochemical model. Excited states and consequently strained planar isomers are formed densely by fs intense excitation, and when the plural transient species undergoing isomerization are in contact with each other, photochromism is induced. Thermal back-reaction from the photoisomer to the starting spironaphthooxazine is prohibited by the rigid crystal structure and hence the colored state is stable. This is very interesting as the isolated strained isomer in the crystal simply reverts to the original ground state. The fs excitation is envisaged as leading to rapid formation of small hot reactive sites, which is followed by rapid cooling.

**Acknowledgements**

The authors thank the collaborators whose names are listed in the references. This work has been partly supported by a Grant-in-Aid for Scientific Research on Priority Area (B) "Laser Chemistry of Single Organic Nanoparticles" from the Ministry of Education, Science, Sports, and Culture of Japan (No. 10207204).

**References**

- 1 R. G. W. Norrish, G. Porter, *Nature (London)* **1949**, 164, 658.
- 2 G. R. Fleming, *Chemical Application of Ultrafast Spectroscopy*, Oxford University Press, New York, **1986**.
- 3 J. Manz, L. Wouste (Eds.), *Femtosecond Chemistry*, Wiley-VCH, Weinheim, **1995**.
- 4 R. W. Kessler, F. Wilkinson, *J. Chem. Soc., Faraday. Trans. I* **1981**, 77, 309.
- 5 R. W. Kessler, G. Krabichler, S. Uhl, D. Oelkrug, W. P. Hagan, J. Hyslop, F. Wilkinson, *Opt. Acta* **1983**, 30, 1099.
- 6 P. Kubelka, F. Munk, *Z. Tech. Physik (Leipzig)* **1931**, 12, 593.
- 7 N. Ikeda, K. Imagi, H. Masuhara, N. Nakashima, K. Yoshihara, *Chem. Phys. Lett.* **1987**, 140, 281; N. Ikeda, M. Koshioka, H. Masuhara, K. Yoshihara, *Chem. Phys. Lett.* **1988**, 150, 452.
- 8 N. Fukazawa, H. Fukumura, H. Masuhara, J. Prochorow, *Chem. Phys. Lett.* **1994**, 220, 461.
- 9 T. Asahi, A. Furube, H. Fukumura, M. Ichikawa, H. Masuhara, *Rev. Sci. Instrum.* **1998**, 69, 361.



- 10 A. Furube, T. Asahi, H. Masuhara, *Jpn. J. Appl. Phys.* **1999**, 38, 4236.
- 11 P. Kubelka, *J. Opt. Soc. Am.* **1948**, 38, 448.
- 12 T. M. Yoo, B. B. Das, R. R. Alfano, *Opt. Lett.* **1992**, 17, 958.
- 13 F. Lin, K. M. Yoo, B. B. Das, R. R. Alfano, *Opt. Lett.* **1994**, 19, 740.
- 14 K. Shimizu, A. Ishimaru, *Opt. Lett.* **1980**, 5, 205.
- 15 D. S. Wiersma, P. Bartolini, A. Lagendijk, R. Ringhini, *Nature* **1997**, 390, 671.
- 16 T. Asahi, Y. Matsuo, H. Masuhara, H. Koshima, *J. Phys. Chem. A* **1997**, 101, 612; T. Asahi, Y. Matsuo, H. Masuhara, *Chem. Phys. Lett.* **1996**, 256, 525.
- 17 R. M. Hochstrasser, S. K. Lomer, C. Reid, *J. Chem. Phys.* **1964**, 41, 1073.
- 18 D. Haarer, M. R. Philott, *J. Chem. Phys.* **1975**, 63, 5238.
- 19 T. Asahi, N. Mataga, *J. Phys. Chem.* **1989**, 93, 6575.
- 20 H. Segawa, C. Takehara, K. Honda, T. Shimizu, T. Asahi, N. Mataga, *J. Phys. Chem.* **1992**, 96, 503.
- 21 H. Miyasaka, S. Kotani, A. Itaya, *J. Phys. Chem.* **1995**, 99, 5757.
- 22 S. Hubig, T. K. Kochi, *J. Phys. Chem.* **1995**, 99, 17578.
- 23 S. Hashimoto, N. Hagiwara, T. Asahi, H. Masuhara, *Langmuir* **1999**, 15, 3123.
- 24 T. Asahi, A. Furube, H. Masuhara, *Bull. Chem. Soc. Jpn.* **1998**, 71, 1277.
- 25 N. Tamai, T. Asahi, H. Masuhara, *Rev. Sci. Instrum.* **1993**, 64, 2496.
- 26 T. Itoh, T. Asahi, H. Masuhara, Abstract for the 8th JST International Symposium, 2000, p. 110.
- 27 T. Asahi, H. Masuhara, *Chem. Lett.* **1997**, 1165.

## 13

### Impurity Rydberg States as Probes of Local Dynamics in the Condensed Phase

*Franco Vigliotti and Majed Chergui*

#### Abstract

We report on structural dynamics in simple van der Waals solids (Ar, Ne, and H<sub>2</sub>), as driven by the excitation of an impurity (NO) Rydberg state. The resulting charge redistribution induces a local radial deformation of the medium ("bubble" formation). This process can be characterized by steady-state spectroscopy and analyzed within the framework of the configuration coordinate model and harmonic approximation. Intermolecular potentials describing the impurity-medium interaction are obtained, allowing us to establish observables for the dynamics of the process in a femtosecond pump-probe experiment. In the very soft H<sub>2</sub> (D<sub>2</sub>) environment, "bubble" formation is a one-way process without recurrence of the cage motion and is complete in ~1.5 ps (3 ps). The data are rationalized in terms of a continuum model, where the overdamped nature of the medium response is attributed to energy dissipation by emission of sound waves and through friction. In the case of solid Ne and solid Ar, the expansion mechanism is characterized by a short inertial response at early times (100–200 fs), followed by an oscillatory motion of the cage over 2–3 ps. These results are complemented by molecular dynamics simulations, which allow us to identify the inertial response. Our experimental procedure establishes an approach for the study of electronic solvation dynamics in non-polar media, which is now being extended to liquids.

#### 13.1

##### Introduction

The response of the medium to a charge redistribution plays a crucial role in a wide range of phenomena in material science, chemistry, and biology. For example, in liquids, the medium responds to charge redistribution by undergoing a conformational rearrangement in order to adapt to the new field of forces in the excited state. This process, also common to biological systems, is referred to as electronic solvation dynamics. It is classified as polar when the solvent molecule reorientation is predominant, and as non-polar when the center-of-mass motion predominates. In most systems, it is difficult to clearly separate the non-polar from the polar contributions.<sup>[1–7]</sup> Furthermore, the nature of non-polar solvation dynamics is poorly under-

stood owing to the lack of reliable model systems. This fundamental mechanism is addressed in this work using NO-doped rare-gas solids and solid hydrogen as model systems. Selective photoexcitation of the dopand drives the dynamics of the medium rearrangement, which is akin to solvation dynamics in more complex media.

There are three main aspects to this work. The first is the direct observation of the coherent structural response of the medium to the charge redistribution of the impurity. The second is the use of the same impurity in all systems; this provides valuable information on the respective environments, which have different microscopic and macroscopic properties. Finally, the results shed light on the general issue of non-polar solvation and its characteristic time scales in the simplest structured media that approach liquids, i.e. rare-gas solids and solid hydrogen. In this sense, we feel that our approach, which is based on the use of impurity Rydberg states that are extremely sensitive to the local structural conformation, offers a technique for probing solvation dynamics in more complex media, particularly liquids.

In the following, we first consider the results of the steady-state spectroscopic characterization of low- $n$  Rydberg states and how they can be used to address local solvation mechanisms. Based on these spectroscopic observations, intermolecular potential-energy curves are derived, which describe the interaction between the impurity and its environment. Along with the discussion of the potentials, a tentative attempt is made to link structural and energetic parameters with macroscopic properties such as the bulk modulus. The intermolecular potentials are then used to establish observables relating to the dynamics of the medium response, and the femtosecond pump-probe results are presented in the case of solid Ar, Ne, and H<sub>2</sub>. In our concluding remarks, we summarize some key relevant issues and outline future prospects.

## 13.2

### Steady-State Spectroscopy

The absorption band of the lowest Rydberg state A(3s $\sigma$ ) of NO in rare-gas and hydrogen matrices is strongly blue-shifted (by up to  $\sim 1$  eV in Ne matrices) as compared to the gas phase and is severely broadened (80 to 300 meV). Fluorescence occurs at energies significantly lower than absorption (Figure 13.1). This unusually large absorption–emission Stokes shift is indicative of an extensive structural rearrangement of the medium around the excited molecule. The interpretation of these spectroscopic features is based on the mechanism of electronic “bubble” formation and is rationalized using the harmonic approximation within the configuration coordinate model (Figure 13.2).<sup>[8,9]</sup> In this model, the configuration coordinate is the radius of the cage surrounding the NO impurity. Excitation of ground-state NO promotes the 2p $\pi$  electron to the A(3s $\sigma$ ) state (step **a** in Figure 13.2). The size of the nearly spherical Rydberg orbital is comparable to the distance to the nearest neighbor, and a significant repulsive overlap of the Rydberg electron with the closed-shell matrix species ensues. Pauli repulsion pushes the first shells of solvent species away from the impurity to accommodate the Rydberg electron cloud, leading to the for-

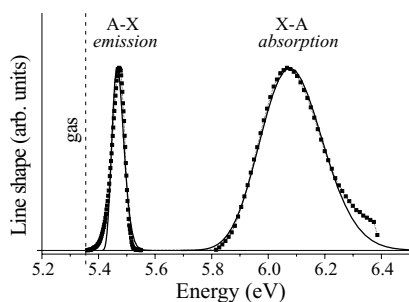


Fig. 13.1 Experimental (squares) and simulated (solid lines) absorption and emission line shapes in solid  $\text{H}_2$ .

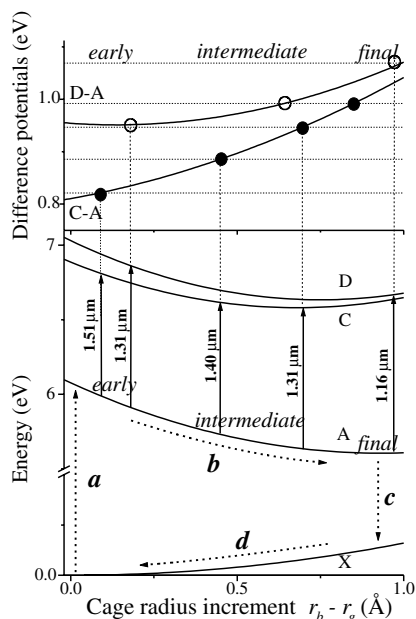


Fig. 13.2 Intermolecular potentials for the  $\text{A}(3s\sigma)$ ,  $\text{C}(3p\pi)$ , and  $\text{D}(3p\sigma)$  states of  $\text{NO}$  in solid hydrogen extracted from the analysis of the steady-state spectra. The arrows show the probe wavelengths at given configurations of the cage during expansion (circles in top frame). The absorption–expansion–emission–contraction cycle is shown from *a* to *d*.

mation of a “bubble” (step *b*). Once a new equilibrium is reached in the expanded cage, fluorescence to the ground state occurs, with a lifetime of several hundreds of nanoseconds<sup>[10]</sup> (*c*). Finally, when the system is back in the ground state, cage relaxation by contraction brings it back to its initial configuration (*d*).

In this description, the tighter the cage around the impurity in the ground state, the stronger the repulsive interaction between the Rydberg electron and its environment and, accordingly, the greater the blue-shift of the absorption on going from gas to matrix (Table 13.1). The extent of structural relaxation (i.e. the cage size increment), which determines the Stokes shift (Table 13.1), depends on both the repulsive interaction and the mechanical properties of the medium. Beyond these qualitative considerations, the absorption and emission profiles can be used in a line-shape analysis to derive intermolecular harmonic potentials that describe the molecule–cage interaction in the ground and excited states.

**Tab. 13.1** A-Rydberg absorption and emission bands of NO in rare-gas solids and in solid hydrogen. The band maxima ( $E$ ) and the Stokes shifts  $\Delta E = E_{X \rightarrow A} - E_{A \rightarrow X}$  are given in eV.

	Gas	Ne	Ar	Kr	Xe	H <sub>2</sub>	D <sub>2</sub>
$E_{X \rightarrow A}$	5.48	6.44	6.34	6.11	5.87	6.06	6.21
$E_{A \rightarrow X}$		5.65	5.77	5.71	5.56	5.48	5.48
$\Delta E$		0.79	0.57	0.40	0.31	0.58	0.73

Intermolecular harmonic potential curves were similarly obtained for the higher C and D Rydberg states<sup>[8,9]</sup> (Figure 13.2). The intermolecular potentials were optimized by adjusting the simulated line shapes to fit the experimental ones. Figure 13.2 shows the potentials for NO in solid H<sub>2</sub>, while the corresponding simulated line shapes are the solid lines in Figure 13.1. The results of the line-shape analysis shows that:<sup>[8,9]</sup>

- The cage radius increment corresponds to an increase in the nearest neighbor distance of the solid in the ground state by ~10 % (Ar) to ~30 % (D<sub>2</sub>).
- The ground-state effective curvature is best reproduced by phonon frequencies falling within the one-phonon density of states of the respective solids, i.e. the NO impurity does not significantly perturb the crystal in the ground state.
- The effective frequencies in the A state in solid Ne, H<sub>2</sub>, and D<sub>2</sub> correspond to energies beyond the Debye frequencies of the crystals. This points to a drastic change in the force constants in the lightest matrices. Solid Ar is more rigid and its cage is looser. The effective frequency lies within the phonon density of states, despite the significant structural rearrangements that occur therein.
- Most importantly, the absorption and emission line shapes, which were simulated without adjustable parameters, reproduce their experimental counterparts to better than 90 % in all the matrices, suggesting that the radial displacement of the cage species is by far the dominant contribution. This is in line with the spherical shape of the 3s $\sigma$  orbital of the A state.

Thus, steady-state spectroscopy indicates that NO-doped, van der Waals crystals present an ideal model system for the investigation of photoinduced structural modifications. Moreover, since the medium is non-polar and the impurity has a small dipole moment in the excited state, polarization effects should be minimal, thus making the system ideal for studies of non-polar electronic solvation dynamics.

In order to obtain a common physical picture of the steady-state spectroscopic data in the investigated van der Waals media, we resorted to macroscopic properties. It is clear that that relevance of bulk properties to the local dynamical response is central to the use of continuum models (viscoelastic,<sup>[3]</sup> hydrodynamic), as will be seen later in the case of solid hydrogen.<sup>[11,12]</sup> On the other hand, at the molecular level, one would expect intermolecular potentials to determine the details and outcome of the dynamics. The line-shape analysis also provides estimates of the energy released during the cage expansion in the excited state ( $E_{rel}^A$ ) and during cage contraction in the ground state ( $E_{rel}^X$ ).<sup>[8,9]</sup> Figure 13.3 shows the ratio of the excess energy

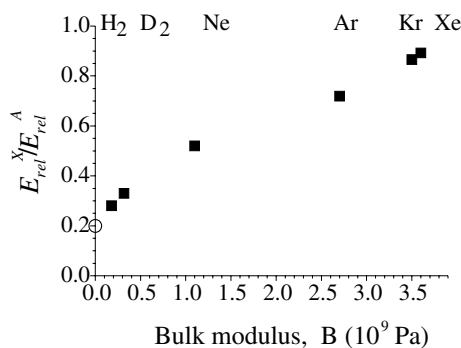


**Fig. 13.3** Ratio of the relaxation energy in the ground and A states determined by line-shape analysis as a function of the Bulk modulus. The value corresponding to  $B = 0$  is that of the NO-Ar complex, based on the Lennard–Jones parameters for the ground and A states (see text).

in the ground and excited states,  $E_{rel}^X/E_{rel}^A$ , as a function of the bulk modulus  $B$ . The whole set of van der Waals crystals that we have studied is shown in order to check the consistency of the arguments presented below. A characteristic  $B = 0$  value is that of the NO-Ar complex, based on the intermolecular Lennard–Jones potential for the ground and A states. It can be seen that  $E_{rel}^X/E_{rel}^A$  tends toward unity as the medium becomes less compressible. Moreover, this dependence is monotonous and quasi-linear with  $B$ . This implies that for more rigid solids, the energy used to compress the medium in the cage expansion process is returned in the contraction process, i.e. the elastic contribution of the medium is more important than that in softer media characterized by smaller values of  $B$ . As the first shell of neighbors expands, it tends to impinge into the medium. If the latter is soft and nearly continuous (like solid hydrogen) notable deformations can occur, accompanied by significant dissipation of energy. This can be viewed as an inelastic collision of the first shell with the rest of the medium, which is described as a continuum (see below and ref.<sup>[12]</sup>). If the medium is more rigid and thus resists compression, deformation will be less extensive and may stress the medium in a regime where the response remains largely elastic. This qualitative picture also points to the nature of the dynamical response in the time-resolved experiments. In the soft  $H_2$  and  $D_2$  crystals, the medium undergoes extensive deformation and the pressure exerted outwards by the expanding cage greatly exceeds the resistance of the medium to compression. As a result, no oscillation is observed, as will be seen later. On going to Ne and Ar, the increased stiffness of the medium offers more resistance to the expansion of the cage. The cage increment is somewhat less pronounced<sup>[8]</sup> and a damped oscillatory motion of the cage appears.

This macroscopic approach is only a qualitative and intuitive one. Nevertheless, while the details of the dynamics can, in principle, only be addressed by taking into account the intermolecular interactions in molecular dynamics simulations, we feel that some understanding of the local processes can probably also be gained by considering macroscopic entities.

## 13.3

**Time-Resolved Spectroscopy**

The dynamics of cage expansion (step **b** in Figure 13.2) was observed in a two-color pump-probe (UV/IR) experiment. The same principle was applied in all the matrices, as described in more detail elsewhere.<sup>[13]</sup> Briefly, a pump pulse (200 nm, 50 nJ  $\mu$ J,  $\sim$ 280 fs) excites the NO molecule to its lowest A-Rydberg state. A tunable IR probe pulse (1.1–1.5  $\mu$ m, 10  $\mu$ J, 120 fs) then probes the dynamics of cage expansion at adjustable time delays. The experimental time resolution was approximately 320 fs. Given the gradients of the A-C and A-D difference potentials, one or several energies (see Figure 13.2, top) corresponds to a given configuration of the cage, which allows a transition from A to the higher Rydberg states at that precise configuration. If the probe-pulse energy matches one of these vertical transition energies, depopulation of the A state occurs, resulting in a loss of A-state fluorescence. Thus, by tuning the probe wavelength along the deformation coordinate, we can probe different configurations during the cage expansion. Given the above discussion on the line-shape analysis, the time-dependent configuration coordinate can be safely associated with the cage radius and the procedure outlined here simply yields the time-dependent cage radius increment.

Experimentally, no difference was found in the transients between parallel and perpendicular pump-probe polarizations at any probe wavelength. In the following, characteristic experimental pump-probe transients are shown, which correspond to early, intermediate, and final stages of the dynamics (see also Figure 13.2). They are presented for NO in Ar, Ne, and H<sub>2</sub> matrices, and are discussed individually. All transients were obtained in linear intensity regimes and their relative amplitudes normalized to the probe laser power are given in each case on a scale of 1 to 100 within  $\pm$ 30 %, given the experimental uncertainties.

## 13.3.1

**NO in Solid Ar**

Pump-probe transients in solid Ar (Figure 13.4) show a peak at early and intermediate stages of the dynamics. Its width reflects the pump-probe cross-correlation and its intensity varies by a factor of three. At intermediate stages, recurrences appear  $\sim$ 1 ps after the occurrence of the peak and the signal levels off to a constant level after 3 ps. The transient probing the final stage of the dynamics looks like a step-function with some unresolved but nevertheless unambiguous modulations after ca. 1.5 ps. Experimentally, the signal level at times beyond 3 ps remains constant over the hundreds of ns of the A-state lifetime. A discussion of these results has been presented previously.<sup>[14]</sup> The peak at early times represents a signature for the departure of the wavepacket from the ground-state configuration upon Rydberg excitation. The recurrences seen at intermediate stages have been recognized as signatures of coherent oscillations of the cage during its relaxation. This interpretation is supported by molecular dynamics simulations<sup>[15,16]</sup> of NO-doped solid Ar, which unambiguously indicate two distinct steps in the dynamics of “bubble” formation.

A sudden, highly spatially coherent expansion of the cage boundaries on the 100–200 fs time scale overshoots the equilibrium configuration of the excited state, which is followed by a multi-mode relaxation on a time scale of several ps. This multi-mode rearrangement is subject to some dephasing among the classical trajectories, but still leads to clear oscillations in the case of a delta-pulse excitation.<sup>[15]</sup> Experimentally, the rather long duration of the pump-pulse considerably blurs the oscillatory response of the cage motion. Figure 13.4 (right) presents a selection of trajectories compatible with the spectral and temporal characteristics of the pump pulse. Each trajectory represents the temporal evolution of the cage radius averaged over the first shell of neighbors. The peak at early times in the early and intermediate transients corresponds to a swarm of trajectories in the very first cage-expansion event. This step corresponds to an inertial response of the medium, as has been discussed in detail both in the case of solid Ar and in the case of Xe-doped Ar clusters.<sup>[17]</sup> At longer times, the classical trajectories still indicate cage oscillations, but these cannot be directly linked to the recurrences in the pump-probe signals. This is due to the long duration of the pump pulse used in the experiment, the poor quality at long range of the NO(A)-Ar potential used in the simulations,<sup>[18]</sup> and the classical nature of the trajectories.

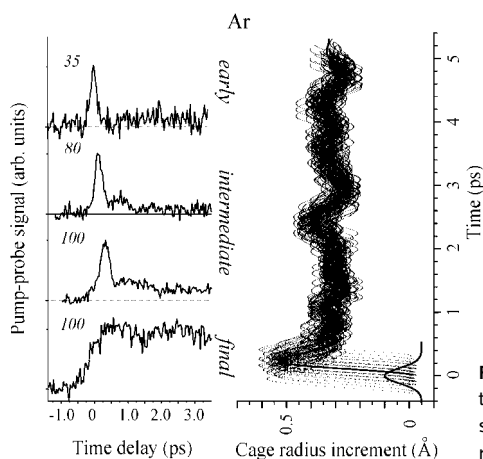


**Fig. 13.4** Experimental pump-probe transients for NO in solid Ar (left) and scenario of cage expansion obtained in a molecular dynamics simulation (right).

### 13.3.2

#### NO in Solid Ne

Figure 13.5 shows the pump-probe transients obtained for NO in solid Ne. There is a clear similarity with the Ar data. The early times are characterized by a single peak, the width of which reflects the pump-probe cross-correlation, and a beat pattern can be distinguished for intermediate probe wavelengths. The evolution of the peak can be followed from the transients characteristic of the early stages of the dynamics all the way to those corresponding to the final stages. As for the Ar matrix, the intensity of the peak in all the transients only varies by a factor of  $\sim 2$  and is seen



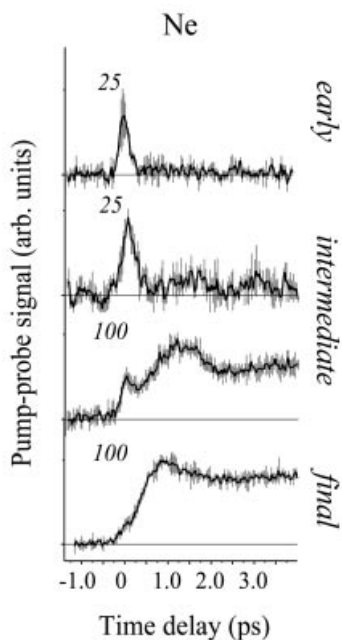


Fig. 13.5 Experimental pump-probe transients for NO in solid Ne.

to retain its shape. As regards the time scale for completion of the process, the transients indicate that cage expansion and thermalization is complete within about 3 ps. Based on an analysis of the Ar data, a similar scenario of cage relaxation can be proposed for the transients, i.e. a first inertial jump overshooting the final equilibrium configuration on a 100 fs time scale followed by a low-frequency beat pattern of the cage radius on the ps time scale.

These results for solid Ar and Ne (as well as for solid Kr, not shown here) show that the response of the first shell of atoms retains a certain degree of spatial coherence, as though the system consisting of NO and its twelve nearest neighbors behaves like a supermolecule embedded in the crystal, to which it is weakly coupled. Remarkably though, the beat frequency in both Ne and Ar is confined within the respective phonon density of states of these media.

### 13.3.3

#### NO in Solid Hydrogen

The pump-probe transients in solid hydrogen are very different from those in solid Ar or Ne. As can be seen in Figure 13.6, they are also characterized by a peak at early times with a FWHM of 320 fs, but its intensity changes by over one order of magnitude in the course of the process. Furthermore, the transients show no recurrence and thermalization is complete after 1.5 ps. Accordingly, while the pump-probe transients corresponding to the early stages show a marked peak, the final stages (the lowest transients in Figure 13.6) are characterized by a rising back-

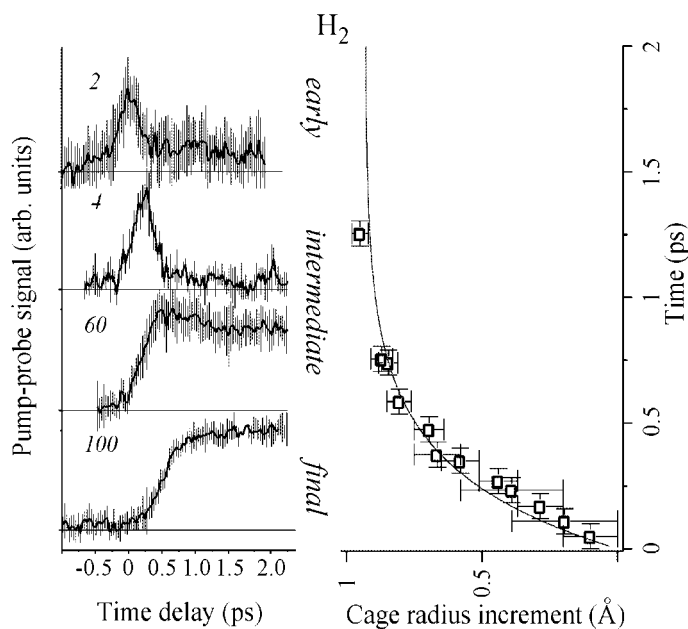


**Fig. 13.6** Experimental pump-probe transients and quantitative scenario of cage expansion based on the harmonic intermolecular potentials and on the experimental transients.

ground, reflecting the population achieving the relaxed configuration. These experimental results indicate that “bubble” formation in solid  $\text{H}_2$  is a one-way process that occurs in  $\sim 1.5$  ps without recurrence (coherent or incoherent) of the cage boundaries. In other words, the system behaves like an overdamped oscillator, implying no multi-mode relaxation (as in Ar or Ne). The intermolecular harmonic potentials in Figure 13.2 have been used to directly retrieve<sup>[12,19]</sup> a quantitative scenario of “bubble” formation from the experimental pump-probe transients. The result is shown in the right frame of Figure 13.6. The temporal error bars reflect the degree of uncertainty in determining the internal clock of the dynamics, as is explained in detail elsewhere.<sup>[12,19]</sup> The spatial error bars result from the spectral width of the probe pulse combined with the intermolecular difference potential curves (Figure 13.2, top). The fit is a rising exponential with a time constant of  $\sim 300$  fs. Qualitatively similar results have been obtained in the case of solid  $\text{D}_2$ , except that the time scale for “bubble” formation is longer, as expected from the mass isotope effect. The overdamped nature of the cage motion should be viewed in the context of the trends shown in Figure 13.3 and the relevant discussion (see above).

## 13.4

## Discussion

The foregoing section indicates very clear experimental differences between the quantum solids  $H_2$  ( $D_2$ ) and the more classical Ar and Ne solids. In the remainder of this discussion, these differences will be addressed by considering in more detail: (a) the experimental evidence for the inertial expansion at times  $< 200$  fs, as supported by MD simulations, and (b) the relaxation process on the ps time scale, during which the medium undergoes extensive rearrangement.

## 13.4.1

Inertial Response ( $t < 200$  fs)

In the very first instants of the cage relaxation process (immediately after charge redistribution of the NO impurity), the twelve atoms constituting the cage start their first radial expansion. In the case of Ar (and most probably of Ne as well), they overshoot the equilibrium configuration of the excited state. This has been very well established in the case of solid Ar through molecular dynamics simulations.<sup>[15]</sup> During this early expansion, energy remains highly localized on one coordinate for  $\sim 150$  fs (in the case of Ar). Indeed, the twelve matrix species are found to evolve freely while the rest of the crystal is essentially frozen. This behavior is therefore referred to as *inertial*. Indeed, it takes a time of the order of 100–200 fs for the expanding first shell of neighbors to meet and exchange energy with the subsequent shells. This has been very clearly established in the MD simulations,<sup>[16]</sup> where the third and fourth shells (the second remaining essentially silent) were found to be set in motion only 150–200 fs after the commencement of the expansion of the first shell. Accordingly, in the case of Ar, the expansion velocity is identical to that of a gas-phase NO-Ar<sub>12</sub> cluster dissociating with the same excess energy.<sup>[14]</sup> The computational result indicating the inertial response is corroborated by a corresponding experimental feature. Indeed, the inertial response was found to be borne out experimentally in the case of Ar and Ne in the temporal width of the early peak (Figures 13.4 and 13.5) in these media and its nearly constant intensity. The small variations in the peak intensity between solid Ar and Ne reflect the velocity of the departing wavepacket as well as the size and amplitude of the spectral observation windows determined by the intermolecular potentials. The dependence of the peak intensity on the probe wavelength has been rather well reproduced by numerical simulation for NO in solid Ar.<sup>[14]</sup>

In the case of solid  $H_2$ , the experimental data do not point to a signature of an inertial response in the sense of constant peak height and width (see above). This indicates that the process most probably lasts for a time significantly shorter than our experimental resolution, implying that energy is very quickly dissipated to the rest of the crystal. This behavior would be consistent with the largely delocalized nature of solid hydrogen, which has a radial pair distribution function<sup>[21]</sup> that closely resembles that of a typical Lennard–Jones liquid<sup>[22]</sup> near its triple point. Accordingly, “bubble” formation in solid  $H_2$  has been modeled using a hydrodynamic approach

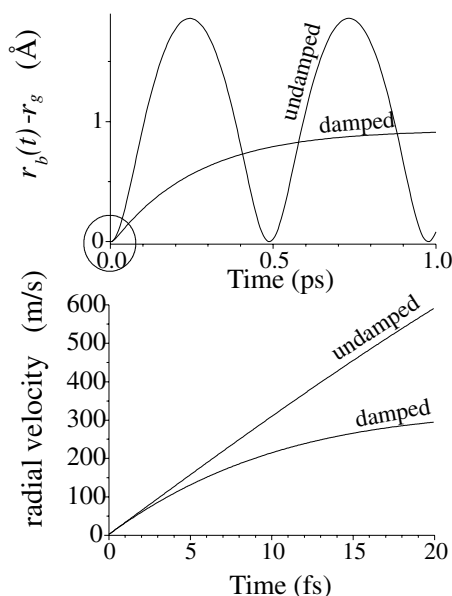


**Fig. 13.7** Hydrodynamic scenario of “bubble” formation in solid  $\text{H}_2$ . The comparison between the damped and undamped (ideal) cases provides an order of magnitude for the time scale of the inertial response.

invoking sound emission and friction<sup>[12,23]</sup> as dissipating mechanisms. Figure 13.7 shows the time-dependent cage radius increment (top) and expansion velocity (bottom) in the damped and oscillating regimes. The pulsating regime corresponds to the ideal case where there is no energy dissipation, which would result in oscillation of the “bubble”. The damped regime corresponds to the expansion scenario that best fits the experimental results and pump-probe transients. An indication of the time scale for the inertial response is given, for example, by the lower graph in Figure 13.7: it takes about 10–20 fs for the expansion velocity in the (realistic) damped regime to clearly depart from that in the (ideal) undamped regime. Thus, it is proposed that the inertial time scale in solid  $\text{H}_2$  is of the order of a few tens of fs.

Ultimately, the inertial time scales (in Ar, Ne, or  $\text{H}_2$ ) can be compared to those characterizing the pure crystals. In this respect, there are two main time scales that need to be distinguished: the time scale of collective coherent motion of the crystal species, roughly given by the inverse of the Debye phonon frequency, and the time scale associated with the decay of the bath correlation function. While the phonon characteristic time is of the order of 500–600 fs in Ar or Ne, the bath correlation function in solid Ar typically has a decay time of 150 fs.<sup>[24]</sup> It was noted above that during the inertial expansion the rest of the crystal remains frozen. This is consistent with the much longer time scale associated with the collective motion of the crystal species. On the other hand, the inertial time scale should be smaller than or equal to that for the decay of the correlation function. This is precisely the case in solid Ar. The scenario in solid Ne or solid  $\text{H}_2$  should be very similar, but with decay times depending on the nature of the medium. However, bath correlation functions have (to the best of our knowledge) not been calculated for such systems and a direct

comparison between these environments is therefore not possible at the present time.

#### 13.4.2

##### Relaxation Process ( 200 fs < $t$ < 3 ps)

In the very soft solid H<sub>2</sub> (where no oscillation occurs), a one-dimensional approach is sufficient to describe the dynamics of the medium response (overdamped oscillator). On the other hand, it was found in the molecular dynamics studies of doped solid Ar<sup>[15]</sup> and doped Ar clusters<sup>[17]</sup> that the oscillatory patterns in the average time-dependent cage radius after the inertial response are due to a summation of damped harmonic oscillators. This pointed to a multi-mode relaxation of the cage, as confirmed by the normal mode analysis performed on NO-doped solid Ar<sup>[15]</sup>, which indicated the involvement of five radial modes in the relaxation process. In solid Ne, although there is no available MD study yet, the situation should be very similar, given the similarities of the experimental transients. It can be seen from Figures 13.4 and 13.5 that the limited experimental time-resolution hinders the observation of the finer details of the oscillatory pattern. Accordingly, somewhat poorly resolved oscillations are found in the experimental transients of NO in solid Ar, although their occurrence is now clearly established. Their low frequencies in solid Ar and especially Ne indicate that these modes are resonance modes of the crystal. From an experimental point of view, increasing the time resolution should yield valuable information. This, coupled with more refined molecular dynamics simulations, will probably help provide a more precise idea about the nature of the cage oscillatory response. Nevertheless, the observation of coherent cage oscillations at frequencies corresponding to resonance modes of the crystal is a remarkable result. Vibrational coherence in many-body systems hitherto reported has been limited to *intramolecular* modes of impurities in solids,<sup>[25]</sup> solutes in liquids,<sup>[26]</sup> and chromophores in proteins.<sup>[27]</sup> To the best of our knowledge, the results presented in this article show for the first time coherence in *intermolecular* modes localized around a photoexcited center.

#### 13.5

##### Concluding Remarks

In this contribution, we have reported on impurity Rydberg states as probes of photoinduced local dynamics in non-polar media. The use of NO as an impurity has several advantages, including its small size in the ground state and the fact that it provides the same dynamical process (of near spherical symmetry) in a wide range of van der Waals media. Accordingly, steady-state and dynamical studies have been presented here in environments ranging from the very soft hydrogen to the rigid solid Xe. In solid Ar, Ne, and H<sub>2</sub>, the ongoing dynamics at the molecular level could be directly observed experimentally, providing valuable information on how these non-polar media respond to a sudden local charge redistribution. From an experi-

mental point of view, an increased time resolution would provide valuable information, unraveling more details of the experimental pump-probe transients. In combination with molecular dynamics simulations, the results presented here certainly allow considerable insight into the dynamics at the molecular level. The general picture that emerges from comparison of the individual behaviors in H<sub>2</sub> (D<sub>2</sub>), Ne, Ar, and more rigid matrices with the macroscopic bulk modulus seems intuitively satisfying and is consistent with the experimental results.

The present study has been carried out on crystals that provide ordered media with rather slowly decaying bath correlation functions. The fact that these media are slowly modulated allows observation of inertial responses despite the relatively low temporal resolution used here. The dynamics in solid hydrogen already approaches the liquid-state dynamical regime and points to the need for improved time resolution for future extensions into the liquid state. We believe that the use of impurity Rydberg states represents a valuable tool for the investigation of non-polar solvation dynamics. Such an approach complements the other available experimental techniques for studying liquid-state dynamics, such as light-scattering studies, neutron diffraction, and dielectric studies.

### Acknowledgements

We wish to thank C. Jeannin, M. T. Portella-Oberli, and S. Jimenez for their significant contributions in the early stages of these studies. This work was supported by the Swiss NSF through contracts 20-50427.97, 2100-47100.96, and 2000-53811.98.

### References

- 1 M. Maroncelli, *J. Mol. Liq.* **1993**, 57, 1.
- 2 R. Jimenez, G. R. Fleming, P. V. Kumar, M. Maroncelli, *Nature* **1994**, 369, 471.
- 3 M. Berg, *J. Phys. Chem.* **1998**, 102, 17, and references therein.
- 4 M. F. Emde, A. Baltuska, A. Kummrow, M. S. Pshenichnikov, D. A. Wiersma, *Phys. Rev. Lett.* **1998**, 80, 4645.
- 5 J. S. Baskin, M. Chachisvilis, M. Gupta, A. H. Zewail, *J. Phys. Chem.* **1998**, 102, 4158.
- 6 M. D. Stephens, J. G. Saven, J. L. Skinner, *J. Chem. Phys.* **1997**, 106, 2129.
- 7 R. M. Stratt, *Acc. Chem. Res.* **1995**, 28, 202.
- 8 M. Chergui, N. Schwentner, V. Chandrasekharan, *J. Chem. Phys.* **1988**, 89, 1277.
- 9 F. Vigliotti, M. Chergui, *Chem. Phys. Lett.* **1998**, 296, 316 and **1999**, 305, 187.
- 10 F. Vigliotti, G. Zerza, M. Chergui, J. Rubayo-Soneira, *J. Chem. Phys.* **1998**, 109, 3508.
- 11 F. Vigliotti, E. Sarraf, M. Chergui, R. Scholz, *Phys. Rev. Lett.* **1999**, 83, 2355.
- 12 F. Vigliotti, L. Bonacina, B. Lang, M. Chergui, *J. Chem. Phys.* (submitted)
- 13 C. Jeannin, M.-T. Portella-Oberli, F. Vigliotti, M. Chergui, *Chem. Phys. Lett.* **1997**, 279, 65.
- 14 C. Jeannin, M.-T. Portella-Oberli, S. Jimenez, F. Vigliotti, B. Lang, M. Chergui, *Chem. Phys. Lett.* **2000**, 316, 51.
- 15 S. Jimenez, A. Pasquarello, R. Car, M. Chergui, *Chem. Phys.* **1998**, 233, 343.
- 16 S. Jimenez, M. Chergui, G. Rojas-Lorenzo and J. Rubayo-Soneira, *J. Chem. Phys.* **2001**, 114, 5264.
- 17 A. Goldberg, J. Jortner, *J. Chem. Phys.* **1997**, 107, 8994.
- 18 K. Tsuji, K. Shibuya, K. Obi, *J. Chem. Phys.* **1994**, 100, 5441.

- 19 F. Vigliotti, C. Jeannin, M. T. Portella-Oberli, M. Chergui, R. Scholz, *J. Lumin.* **1999**, 83–84, 135.
- 20 F. Vigliotti, Thesis Dissertation, University of Lausanne, 2000.
- 21 D. F. Coker, R. O. Watts, *J. Chem. Phys.* **1987**, 86, 3, 5703.
- 22 M. P. Allen, D. J. Tildesley, *Computer Simulation of Liquids*, Oxford Clarendon Press, 1992.
- 23 I. Rips, *J. Chem. Phys.* **1996**, 106, 2707.
- 24 M. Ovchinnikov, V. A. Apkarian, *J. Chem. Phys.* **1998**, 108, 2277.
- 25 R. Zadoyan, M. Sterling, M. Ovchinnikov, V. A. Apkarian, *J. Chem. Phys.* **1997**, 107, 8446 and references therein.
- 26 G. A. Voth, R. M. Hochstrasser, *J. Phys. Chem.* **1996**, 100, 13034 and references therein.
- 27 M. H. Vos, M. R. Jones, J.-L. Martin, *Chem. Phys.* **1998**, 233, 179 and references therein.

## 14

# Photoelectron Spectroscopy as a Probe for Investigating Chemical Dynamics

Ingo Fischer

### 14.1

#### Introduction

Over the last decade, short-pulse spectroscopy has been applied to numerous different problems of molecular dynamics.<sup>[1–4]</sup> This success has been partly due to the implementation of a variety of probe schemes, permitting the selection of that best suited to a particular problem. The subject of this chapter is photoelectron spectroscopy (PES), a probe method that has become very popular in time-domain experiments over the last couple of years. Here, an overview is given on the different experimental strategies and the various applications of time-resolved photoelectron spectroscopy (TR-PES), as well as the investigation of chemical dynamics by PES in the frequency domain.

### 14.2

#### The Concept

The different probe methods used in time-resolved experiments can be distinguished with respect to the final state that the dynamics is projected onto. One can, for example, project the dynamics onto a higher electronic state of the molecule (or the reaction product) and measure either the fluorescence emitted from this state, or, less commonly in the gas phase, the absorption spectrum of the final state. Both methods have been successfully applied in short-pulse spectroscopy.<sup>[1,5]</sup> The best known final state is, of course, the ground state of the neutral molecule. However, experiments employing stimulated emission pumping back to the ground state have proved to be difficult.<sup>[6]</sup>

Alternatively, one can ionize the molecule in the probe step and use the ground state of the ion, or a higher-lying ionic state, as the final state. This choice has numerous advantages:

1. Charged-particle detection is considerably more sensitive than photon detection.
2. The ground state of the ion is often well-characterized spectroscopically and/or can be assessed by *ab initio* calculations.



3. Ionization is invariably an allowed process, with selection rules that are relaxed compared to those for optical spectroscopy. It permits the probing of molecules with excited states that fluoresce with only low quantum yields. Many reactive intermediates, such as organic radicals, fall into this category.
4. Detection of the ions provides mass information.
5. Additional information can be obtained from an analysis of the photoelectron spectrum. It is this last point that is the focus of this chapter.

Upon collection of the total ion signal, transitions into all energetically accessible final states appear at the same position in the mass spectrum. In the photoelectron spectrum, on the other hand, transitions to different final states are manifested in the appearance of signals at different energies or times of flight, respectively. In this sense, collecting the mass signal constitutes an *integral* detection technique, while collecting the electron signal constitutes a *differential, final state selective* detection technique. There is a parallel here to fluorescence detection, where monitoring the dispersed fluorescence<sup>[7]</sup> distinguishes between different final states, making it analogous to electron detection, while collecting the total fluorescence is an integral detection technique.

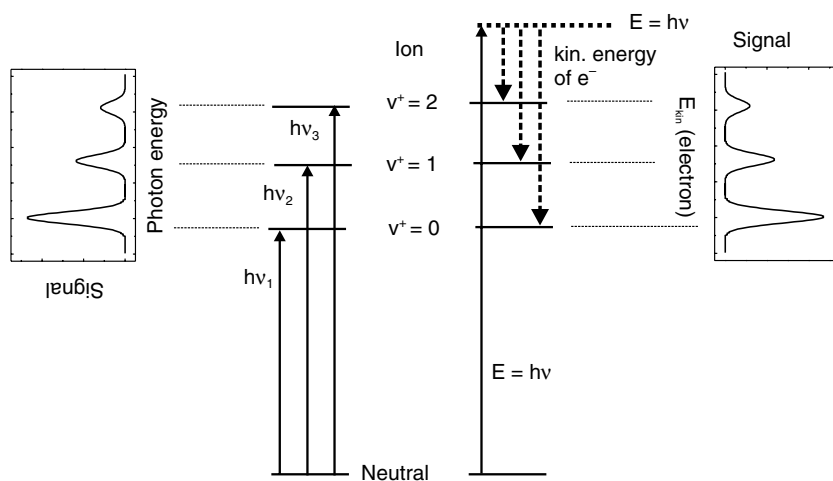
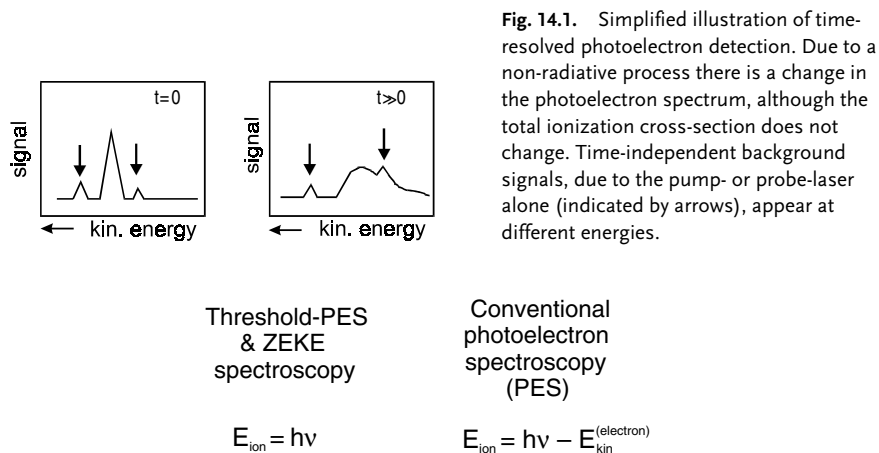
The first advantage of final state selective detection is rather technical. A major problem in short-pulse spectroscopy is the appearance of background signals, firstly due to multi-photon processes induced by the pump or probe laser alone, and secondly due to time-dependent processes of higher photon order.

Since short laser pulses are inherently of high intensity, both problems are difficult to avoid. If the total ion signal is collected, both the time-independent background and higher-order processes will contribute to the signal and can, in principle, obscure the dynamics that one wants to observe. In the photoelectron spectrum, the processes contributing to the background are separated in energy, and can thus be distinguished, leading to a superior signal-to-noise ratio.

The second advantage, on the other hand, is conceptual. Time-resolved mass spectrometry is only sensitive to a change in the total ionization cross-section, while the photoelectron spectrum is sensitive to a change in the partial ionization cross-sections to different ionic states. In the course of a chemical or physical process, it is possible that the electronic character of the intermediate state, excited by the pump laser, will change. This will lead to drastic changes in the partial ionization cross-sections to different final states, although the total ionization cross-section might hardly change at all. TR-PES is ideally suited for probing such a change, occurring, for example, in nonradiative decay processes. The groups of Colson<sup>[8]</sup> and Reilly<sup>[9]</sup> first realized this in their investigations on  $S_1$ - $T_1$  intersystem crossing in *sym*-tetrazine and benzene, respectively, by nanosecond time-resolved PES. The concept behind these experiments is outlined in Figure 14.1. At early times ( $t = 0$ ), the probe-pulse ionizes the  $S_1$  state and produces ions with low vibrational excitation, yielding fast photoelectrons. Upon ISC, population flows into the triplet state, leading to a significant amount of vibrational excitation in  $T_1$ . Ionization from this state at  $t \gg 0$  yields a broad distribution of slow photoelectrons as Franck–Condon factors favor the formation of vibrationally-excited ions. Consequently, TR-PES on the

pico- and femtosecond time scale represents a perfect tool for studying the much faster decay by internal conversion and through conical intersections.

There are numerous approaches for recording photoelectron spectra. The two protocols most often applied are: (I) time-of-flight (TOF), and (II) zero kinetic energy (ZEKE) photoelectron spectroscopy (PES). The basic principles are illustrated in Figure 14.2. In TOF-PES,<sup>[10]</sup> molecules are ionized by a fixed-frequency light source and the resulting electrons are analyzed according to their time-of-flight to the detector,



which gives an indication of the excess kinetic energy. If the energy resolution is sufficient, a discrete band appears in the spectrum for each ionic state formed upon ionization. TOF photoelectron detection is background-free, because the signals originating from processes of different photon order will be detected at different flight times. ZEKE spectroscopy,<sup>[11,12]</sup> on the other hand, relies on optical excitation of the molecule to high-lying, long-lived Rydberg states, a few  $\text{cm}^{-1}$  below the ionization limit.<sup>[13]</sup> After a delay time of the order of 1  $\mu\text{s}$ , the molecules are field-ionized by a pulsed electric field. Since all kinetic electrons are lost during the delay time, only electrons originating from Rydberg states are detected. In a ZEKE-type experiment, the light source has to be tuned. Only if it is in resonance with Rydberg states converging onto the threshold of a certain ionic state will a signal be obtained. Higher-order processes result in the formation of kinetic electrons rather than Rydberg states, and are suppressed in the ZEKE spectrum, again rendering detection background-free.

A major difference between the two protocols is the energy resolution. The typical resolution achievable in a conventional TOF-PES experiment is around  $120 \text{ cm}^{-1}$ , but even this requires considerable effort. For example, the experiment has to be carefully shielded from the Earth's magnetic field. Experiments with a better resolution are possible, but require substantial investments in terms of both work and money. On the other hand, in ZEKE experiments employing nanosecond lasers, sub- $\text{cm}^{-1}$  resolution is obtained on a routine basis,<sup>[12]</sup> i.e. in a time-resolved experiment the energy resolution is always limited by the laser bandwidth. This is a significant advantage for a laser pulse duration of 200 fs or larger.

The requirement of a tunable light source constitutes the major disadvantage of ZEKE-PES, since wavelength-tuning of short-pulse lasers is still expensive and technically demanding, despite the recent advent of devices relying on optical parametric processes. In contrast, TOF-PES benefits from the multiplex advantage. Thus, the signal from all final ionic states energetically accessible by the probe laser light is collected simultaneously, rendering a tunable probe superfluous.

A problem associated with TOF-PES is its small collection efficiency. Only the fraction of electrons emitted within the relevant solid angle reaches the detector. In one variant of a TOF spectrometer, namely the "magnetic bottle",<sup>[14,15]</sup> the electrons are steered towards the detector in an inhomogeneous magnetic field. As collection efficiencies of more than 30 % are achieved, the magnetic bottle TOF-spectrometer is ideally suited for experiments on systems that can only be produced with small number densities.

### 14.3

#### Molecular Photophysics

As an example of the investigation of nonradiative processes in molecules by TR-PES, this section deals with work performed by the author's group on the excited-state dynamics of the allyl radical,  $\text{C}_3\text{H}_5$ , an important intermediate in combustion chemistry.<sup>[16–18]</sup> Its geometry and electronic structure are illustrated in Figure 14.3. The primary photophysical processes upon UV excitation to the B-, C-, and D-states

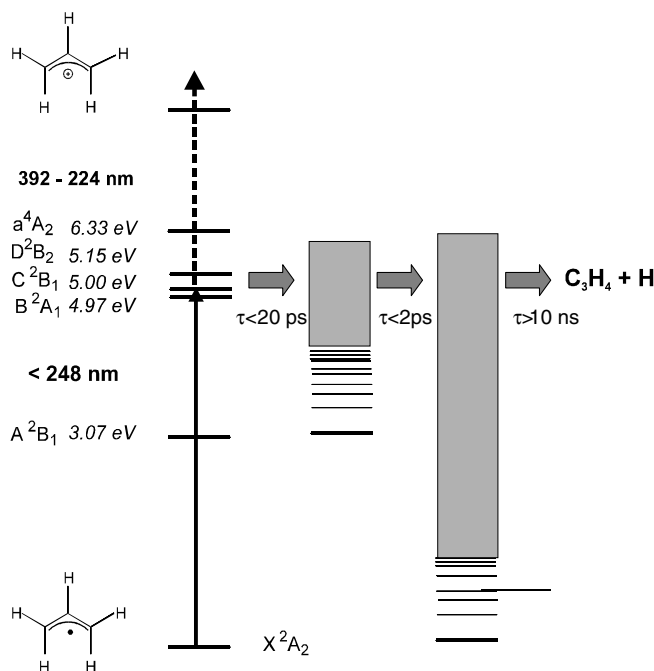


**Fig. 14.3** Photophysics of the allyl radical upon UV excitation. Three time scales were identified: (a) internal conversion to the lower lying A-state within 20 ps or less, (b) a very fast decay to the electronic ground state through a conical intersection, and (c) a statistical (ns-time scale) dissociation to  $\text{C}_3\text{H}_4 + \text{H}$  on the ground-state surface.

have been investigated by TR-PES employing 2 ps pulses. A typical photoelectron spectrum is depicted in Figure 14.4. The pump laser (248.1 nm) excited the radical to the origin of the  $C^2B_1$  state. The population flow from this state was subsequently monitored by ionization with a second laser at 274.3 nm.

The spectrum in Figure 14.4 shows two relatively sharp peaks. A time-independent one at 1.8 eV corresponds to a [1+1] process induced by the pump laser alone. In addition, an intense time-dependent band develops at around  $t = 0$  and decays mono-exponentially with a time constant,  $\tau$ , of 15 ps. From the electron kinetic energy of 1.37 eV, we can deduce that it originates from a [1+1'] process. Since the geometry of the initially excited C-state is very similar to that of the ionic ground state, the transition to the ground vibrational state of the ion is very strong. The spectrum demonstrates how signals originating from processes of different order can be distinguished in the PE spectrum.

In Figure 14.5, a second spectrum is depicted, recorded at a probe wavelength of 390 nm, which corresponds to the ionization threshold. The signal due to the population flow from the  $C^0_0$  state is again visible at very low kinetic energies. In addition, a broad and featureless band, extending for up to 3 eV, develops after  $t = 0$ . This band is due to ionization from the electronic ground state in a [1+2'] process. It would not be discernible if the total ion signal was collected.

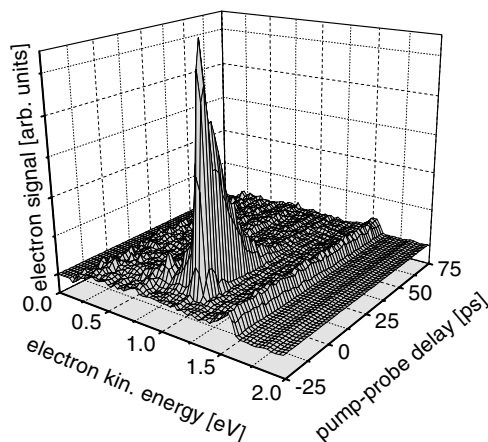


**Fig. 14.4** Typical TR-PES spectrum of the allyl radical, obtained at 248.1 nm pump/274.3 nm probe. The time-dependent [1+1'] ( $t = 16$  ps) and the time-independent [1+1] signal can easily be distinguished.

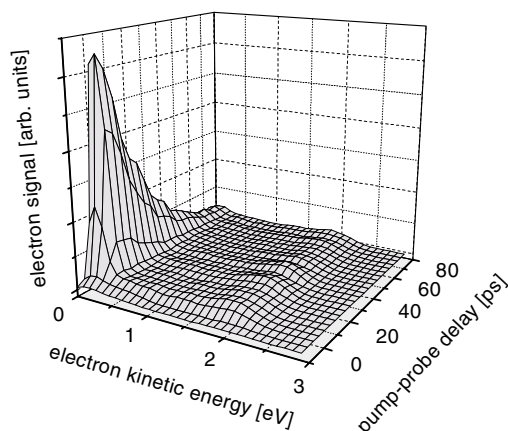


**Fig. 14.5** In the TR-PES spectrum of the  $C\ 0_0^0$  state, recorded with 390 nm probe, a broad band develops due to [1+2'] ionization of the hot electronic ground-state radicals formed upon IC.

In order to corroborate this data, experiments were carried out on the fully deuterated allyl radical,  $C_3D_5$  and ab initio calculations were performed<sup>[18]</sup>. The overall picture obtained is summarized in Figure 14.3. The UV bands of the allyl radical are seen to decay in a two-step process, the first step being internal conversion to the lower-lying A-state within  $\leq 20$  ps, and the second step being a very fast decay of this state through a conical intersection to the electronic ground state. Since electronic energy is converted into vibrational energy in this process, internally-hot ground-state radicals are formed. These radicals have negligible Franck–Condon overlap with low-lying ionic states. Transitions to very high-lying vibrational states of the cation are nevertheless possible if two probe photons are absorbed. Since the ionization probability will be distributed over many ionic states, the photoelectron spectrum from such a highly vibrationally excited state will invariably be rather diffuse, as shown in Figure 14.5. In the case of allyl, the radical possesses sufficient internal energy to dissociate into the  $C_3H_4$  isomer allene and an H-atom on a nano-second time scale, as discussed elsewhere.<sup>[17,19]</sup>

TR-PES of nonradiative processes has been reported by a number of groups. Internal conversion from the  $S_2$  state in 1,3,5-hexatriene constituted the first example of a real-time observation of non-radiative decay on the femtosecond time scale by TR-PES.<sup>[20]</sup> An important application concerns molecular clusters. Since the PE spectra of molecules embedded in solvent clusters are sensitive to the orientation of the solvent molecules, TR-PES is well-suited for studying solvent dynamics in molecular clusters. This was first shown in work on excited-state proton transfer in phenol/ammonia clusters<sup>[21]</sup> and over the last couple of years has been extended to studies of electron solvation dynamics in cluster anions.<sup>[22,23]</sup>

The Ottawa group<sup>[24]</sup> recently reported on experiments concerning the non-adiabatic coupling of excited electronic states in  $\pi$ -conjugated polyenes. They projected the intermediate-state dynamics onto different **electronic** states of the ion. The individual cross-sections of the two coupled intermediate states differ for ionization to either of the two continua. This approach permits the separation of the electronic from the nuclear dynamics.

#### 14.4

#### Monitoring Wavepacket Dynamics by ZEKE and PE Spectroscopy

The observation and analysis of molecular coherences and wavepackets is a fascinating area of short-pulse spectroscopy. Due to its final-state selectivity, photoelectron detection is particularly well-suited for monitoring wavepacket motion. This was first demonstrated in ps experiments on restricted intramolecular vibrational-energy redistribution (IVR) in fluorene, as manifested in its ZEKE spectrum.<sup>[25]</sup> By tuning the probe laser to a particular vibronic state of the ion, quantum beats with a period of 125 ps were observed due to the dynamic interaction of two zero-order vibrational levels in the  $S_1$  state coherently excited by the pump laser. By selecting different final states of the ion, both the in-phase and out-of-phase components of the quantum beats could be monitored, in a manner akin to dispersed fluorescence experiments.<sup>[7,26]</sup> This would clearly not have been possible if only the total ion signal had been collected!

The Ottawa group studied vibrational wavepacket motion in the B-state of  $I_2$  by means of femtosecond time-resolved ZEKE spectroscopy.<sup>[27,28]</sup> In these experiments, the pump laser created a vibrational wavepacket centered at around  $v' = 15$  at the inner turning point of the B-state. The motion of this wavepacket was subsequently probed by ionization. One goal of the experiment was to investigate the probe wavelength dependence. The appearance of the signal is strongly dependent on where ionization occurs in the B-state potential well, i.e. on the location of the Condon point. This is the point of best overlap between the states comprising the intermediate state wavepacket and the final state of the ion. Kinetic energy does not change in a transition occurring at this point. Detecting the signal from many final states thus corresponds to sampling a wide range of Condon points. In fact, no wavepacket motion is discernible in the ion signal if a large amount of excess energy is available, since there will be a suitable final state accessible for the wavepacket at every point

of the potential well.<sup>[29]</sup> ZEKE spectroscopy, on the other hand, dissects the signal into a small range of ionic states, and thus probes the Condon point for ionization to this range of states. About three vibrational states of the ion proved to be accessible within the bandwidth of the probe pulse.

In Figures 14.6 and 14.7, the time-resolved ZEKE spectra of  $I_2$  are depicted, obtained with probe wavelengths of 345 nm (Figure 14.6) and 323 nm (Figure 14.7), corresponding to excitation of a few ionic states around the threshold (345 nm) and  $v^+ = 19$ , respectively. The insets in the figure show the associated Fourier transforms. The two spectra are strikingly different. That obtained at 345 nm shows a modulation period of 340 fs, corresponding to frequencies of around  $100\text{ cm}^{-1}$ . In contrast, that obtained at 323 nm shows a modulation with half the period, i.e. 170 fs. This is due to a shift of the Condon point for intermediate-state ionization. If only the ionization threshold is accessible, ionization will occur at the inner turning point of the potential. If the excess energy in the ion is increased, the Condon point moves towards the middle of the B-state potential well and the wavepacket is ionized twice during one vibrational period.

Wavepacket motion can also be visualized by conventional PES, as experimentally demonstrated<sup>[30]</sup> and theoretically investigated<sup>[31,32]</sup> for  $Na_2$ . In these experiments,

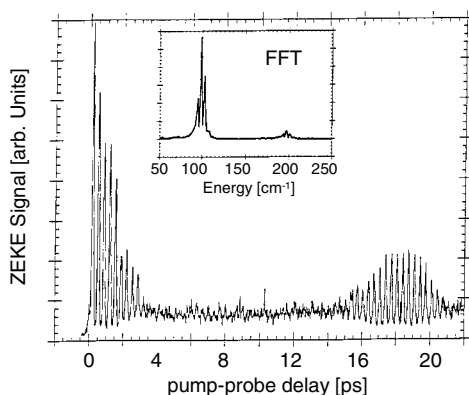


**Fig. 14.6** Time-resolved ZEKE spectrum from the B-state of  $I_2$ , obtained at 345 nm probe, i.e. very low-lying ionic states are populated in the probe step. Ionization of the wavepacket occurs at the inner turning point of the B-state with a period of 340 fs.

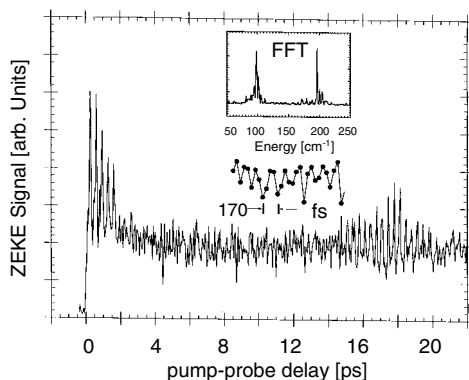


**Fig. 14.7** When the probe wavelength is increased to 323 nm, ionic states around  $v^+ = 19$  are populated in the ZEKE spectrum. Ionization then occurs from the middle of the B-state well, i.e. twice per vibrational period. This leads to a 170 fs modulation.

two different processes, namely [1+2] and [2+1] ionization, were operative. In the former process, ionization of wavepackets at the inner turning point of the A-state is observed, while in the latter a wavepacket moving in the  $2^1\Pi_g$  state is ionized at both turning points of the potential well. Ionization at the outer turning point results in excited vibrational states of the ion and slow electrons having less kinetic energy than those produced at the inner turning point. The photoelectron signal thus oscillates between high and low kinetic energies as a function of pump-probe delay.

## 14.5

### Intensity Effects in ZEKE and Photoelectron Spectra

Due to the short pulse duration used in time-resolved experiments, one is often forced to use high laser intensities in order to obtain reasonable photon fluences and significant transition probabilities. This leads to problems with unwanted multi-photon background signals, as mentioned above. One also has to be aware that there is another problem associated with electron detection in experiments using high-intensity lasers. As is well-known in atomic physics, the influence of the laser field on the ionization process is non-negligible.<sup>[33]</sup> It introduces an AC Stark shift on free electrons and Rydberg states alike, leading to a shift of the ionization potential to higher energies.<sup>[34,35]</sup> As a laser pulse contains a distribution of intensities in space and time, the shift is different for different atoms (or molecules, respectively), introducing a spectral broadening of the states that might destroy the final-state selectivity. In a classical picture, the electron oscillates in the electric field of the laser under the influence of the so-called ponderomotive potential  $U_p$

$$U_p = e^2 E_0^2 / \omega^2 4m_e \quad (1)$$

$E_0$  being the electric field of the laser,  $\omega$  its frequency, and  $m_e$  the mass of the electron. As an example, a ponderomotive shift of around 10 meV for each TW/cm<sup>2</sup> is introduced upon 330 nm irradiation. This corresponds to a pulse with an energy of 1  $\mu$ J/100 fs or 10  $\mu$ J/1 ps, focussed by  $f/40$  optics. Thus, one has to be aware that using higher intensities or optics with smaller F-number introduces a broadening, which can obscure the state-selectivity of photoelectron or ZEKE detection. As  $U_p$  increases quadratically with the wavelength, the effects of the broadening are particularly drastic if multi-photon ionization with visible or infrared pulses is chosen as a probe. In 1995, it was shown that a ZEKE spectrum can be recorded under conditions where the ponderomotive broadening is still negligible.<sup>[36]</sup>



## 14.6

## Probing Chemical Dynamics by Photoelectron and ZEKE Spectroscopy in the Frequency Domain

Despite the successful application of time-domain techniques in chemical dynamics, frequency-domain techniques continue to yield considerable information on fast molecular processes. Resonance Raman spectroscopy, for example, provides insight into fast dissociation processes.<sup>[37]</sup> After excitation to a dissociative state, a photon is emitted and a spectrum of the ground state is obtained with a structure that reflects the intermediate-state dynamics. Alternatively, the dynamics can be projected onto the ground state of the ion when the second photon is absorbed rather than emitted.<sup>[38]</sup> The advantages of this latter approach are again (as in time-domain spectroscopy) the sensitivity of charged-particle detection and the more relaxed selection rules. New information on the photodissociation of methyl iodide,  $\text{CH}_3\text{I}$ , in the A-state band into a methyl radical,  $\bullet\text{CH}_3$ , and an iodine atom was obtained from the nanosecond two-photon ZEKE spectrum recorded through this dissociative intermediate state.<sup>[39]</sup>

In principle, the process can be illustrated in either a time-dependent or a time-independent picture. In a time-independent frequency-domain picture, a continuum state is formed upon excitation, which shows considerable overlap with highly excited vibrational states of the ion. Figure 14.8 illustrates the alternative time-dependent picture.<sup>[40]</sup> The process is viewed in terms of an excited-state wavepacket,<sup>[41]</sup> created by absorption of a first photon, which evolves on the excited-state surface along the C–I coordinate. A possible outcome is dissociation

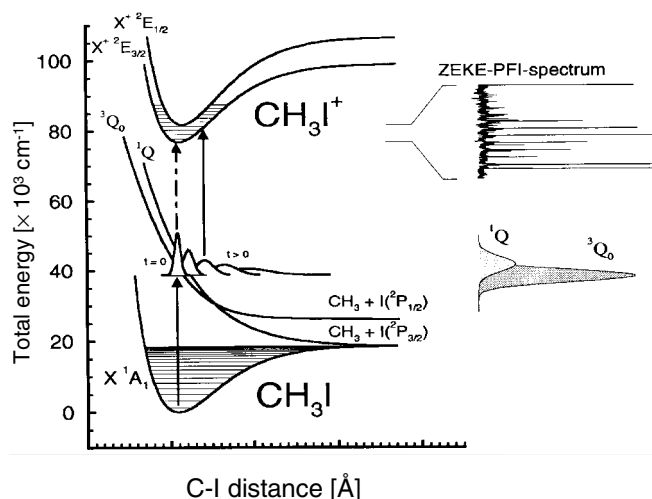


**Fig. 14.8** Time-dependent picture of two-photon photoelectron or ZEKE-spectroscopy involving a dissociative intermediate state. The wavepacket created on the A-state surface

evolves in time, developing Franck–Condon overlap with vibrationally excited states of the ion. The ZEKE spectrum is shown on the upper right-hand-side of the figure [from Ref. 40].

within a time comparable to one vibrational period. Alternatively, absorption of a second photon leads to the appearance of ZEKE bands that are absent in the one-photon spectrum.<sup>[42]</sup> Since the C–I distance increases with time and the wavepacket develops overlap with higher vibrational wavefunctions of the ion, the intensity of these bands depends on the delay time between the two absorption events. The resulting ZEKE spectrum<sup>[39]</sup> is given as an inset in the upper-right part of the figure. It shows a large progression in the C–I stretching vibration  $\nu_3^+$ , as well as several combination bands of  $\nu_3^+$  with the C–H bending vibration  $\nu_2^+$ , reflecting the fact that the  $\text{CH}_3$  radical formed in the dissociation has a planar equilibrium geometry. As is also indicated in the figure, several electronic states contribute to the A-state continuum of  $\text{CH}_3\text{I}$ , the most important ones being the  $^1\text{Q}_1$  state, corresponding to dissociation into  $\text{CH}_3$  and I in its  $j = 3/2$  ground state, and the  $^3\text{Q}_0$  state, corresponding to the  $j = 1/2$  spin-orbit excited state of the iodine atom. It is assumed that the two states are coupled through the  $\text{H}_3\text{–C–I}$  bending mode  $\nu_6$ . Interestingly, this mode is seen in the two-photon ZEKE spectrum of  $\text{CH}_3\text{I}$ , providing support for this model, although it is absent in the resonance Raman spectrum. The experimental approach was also investigated theoretically.<sup>[43]</sup>

Similar experiments have been reported for the photodissociation dynamics of a number of other molecules, e.g.  $\text{C}_2\text{H}_5\text{I}$ ,<sup>[44]</sup>  $\text{CF}_3\text{I}$ ,<sup>[45]</sup> and  $\text{IBr}$ .<sup>[46]</sup> Conventional photoelectron spectra can yield similar information,<sup>[47,48]</sup> albeit at inferior resolution.

## 14.7

### New Directions

The preceding sections have shown how time-resolved photoelectron spectroscopy advances our understanding of molecular dynamics. In addition to the techniques mentioned so far, several promising new approaches in TR-PES are currently being pursued: (a) In coincidence experiments,<sup>[49]</sup> the detection of a photoelectron provides the trigger for the detection of the mass spectrum, which allows for unambiguous identification of the origin of the electron signals. This is particularly useful in neutral cluster experiments, where the presence of a mixture of species is often unavoidable. (b) Another direction is the investigation of the time dependence of the photoelectron angular distribution,<sup>[50,51]</sup> a sensitive probe for the intermediate state alignment. It can be used to monitor the evolution of the rotation-vibrational coupling (ps-domain), as well as that of the electronic symmetry (fs-domain). (c) Imaging techniques provide energy information in time-domain experiments through an analysis of ion and electron kinetic energy.<sup>[52]</sup> With the newly developed velocity map imaging approach,<sup>[53]</sup> the energy resolution might become comparable to that of conventional photoelectron detection. Recently, coincidence detection of electrons and ions has been combined with imaging,<sup>[54]</sup> providing angular-resolved electron and ion spectra that yield all the information discussed above.

In conclusion, TR-PES looks set to find increasing application in problems of chemical dynamics in the near future, since it permits the extraction of details of chemical processes that are not readily accessible by other methods.

## Acknowledgements

I would like to thank my coworkers on the various projects described, in particular the Ottawa group (Albert Stolow, David M. Villeneuve, and Marc J. J. Vrakking; I<sub>2</sub>), Thomas Schultz (ETH Zürich; C<sub>3</sub>H<sub>5</sub>), and Andreas Strobel (TU München; CH<sub>3</sub>I). Financial support from the German (1990–95) and Swiss (since 1996) Science Foundations is gratefully acknowledged.

## References

- 1 A. H. Zewail, *Femtochemistry*, Vols. 1 and 2, World Scientific, Singapore, 1994.
- 2 J. Manz, L. Wöste (Eds.), *Femtosecond Chemistry*, VCH, Weinheim, 1995.
- 3 M. Chergui, *Femtochemistry*, World Scientific, Singapore, 1996.
- 4 T. Elsaesser, J. G. Fujimoto, D. A. Wiersma, W. Zinth (Eds.), *Ultrafast Phenomena XI*, Springer, Berlin, 1998.
- 5 J. H. Glowina, J. Misewich, P. P. Sorokin, in *The Supercontinuum Laser Source* (Ed.: R. R. Alfano), Springer, Berlin, 1990.
- 6 Y. Chen, L. Hunziker, P. Ludowise, M. Morgen, *J. Chem. Phys.* **1992**, 97, 2149.
- 7 P. Felker, A. Zewail, *Phys. Rev. Lett.* **1984**, 53, 501.
- 8 J. B. Pallix, S. D. Colson, *Chem. Phys. Lett.* **1985**, 119, 38.
- 9 E. Sekreta, J. P. Reilly, *Chem. Phys. Lett.* **1988**, 149, 482.
- 10 J. H. D. Eland, *Photoelectron Spectroscopy*, Butterworth, London, 1974.
- 11 K. Müller-Dethlefs, M. Sander, E. W. Schlag, *Z. Naturforsch.* **1984**, 39a, 1089.
- 12 K. Müller-Dethlefs, E. W. Schlag, *Angew. Chem. Int. Ed. Engl.* **1998**, 37, 1346.
- 13 G. Reiser, W. Habenicht, K. Müller-Dethlefs, E. W. Schlag, *Chem. Phys. Lett.* **1988**, 152, 119.
- 14 P. Kruit, F. H. Read, *J. Phys. E: Sci. Instrum.* **1983**, 16, 313.
- 15 C. A. de Lange, in *High Resolution Laser Photoionisation and Photoelectron Studies* (Eds.: C. Y. Ng, T. Baer, I. Powis), Wiley, New York, 1995, p. 195.
- 16 T. Schultz, I. Fischer, *J. Chem. Phys.* **1998**, 109, 5812.
- 17 I. Fischer, *Chimia* **2000**, 54, 96.
- 18 T. Schultz, J. S. Clarke, H.-J. Deyerl, T. Gilbert, I. Fischer, *Faraday Discuss.* **2000**, 115, 17.
- 19 H.-J. Deyerl, I. Fischer, P. Chen, *J. Chem. Phys.* **1999**, 110, 1450.
- 20 D. R. Cyr, C. C. Hayden, *J. Chem. Phys.* **1996**, 104, 771.
- 21 J. A. Syage, *Chem. Phys. Lett.* **1993**, 202, 227.
- 22 L. Lehr, M. T. Zanni, C. Frischkorn, R. Wein-kauf, D. M. Neumark, *Science* **1999**, 284, 635.
- 23 C. Frischkorn, M. T. Zanni, A. V. Davis, D. M. Neumark, *Faraday Discuss.* **2000**, 115, 49.
- 24 V. Blanchet, S. Lochbrunner, M. Schmitt, J. P. Shaffer, J. J. Larsen, M. Z. Zgierski, T. Seide-  
man, A. Stolow, *Faraday Discuss.* **2000**, 115, 33.
- 25 J. M. Smith, C. Lakshminarayan, J. L. Knee, *J. Chem. Phys.* **1990**, 93, 4475.
- 26 P. M. Felker, A. H. Zewail, *Adv. Chem. Phys.* **1988**, 70, 265.
- 27 I. Fischer, D. M. Villeneuve, M. J. J. Vrakking, A. Stolow, *J. Chem. Phys.* **1995**, 102, 5566.
- 28 I. Fischer, M. J. J. Vrakking, D. M. Villeneuve, A. Stolow, *Chem. Phys. Lett.* **1996**, 207, 331.
- 29 M. Seel, W. Domcke, *J. Chem. Phys.* **1991**, 95, 7806.
- 30 A. Assion, M. Geisler, J. Helbing, V. Seyfried, T. Baumert, *Phys. Rev. A* **1996**, 54, R4605.

- 31 C. Meier, V. Engel, *Phys. Rev. Lett.* **1994**, 73, 3207.
- 32 Y. Arasaki, K. Takatsuka, K. Wang, V. McKoy, *Chem. Phys. Lett.* **1999**, 302, 363.
- 33 N. B. Delone, V. P. Krainov, *Atoms in Strong Light Fields*, Springer, Berlin, 1985.
- 34 P. H. Bucksbaum, R. R. Freeman, M. Bashkanský, T. J. McIlrath, *J. Opt. Soc. Am.* **1987**, B4, 760.
- 35 R. R. Freeman, P. H. Bucksbaum, T. J. McIlrath, *IEEE J. Quantum Electron.* **1988**, 24, 1488.
- 36 A. Zavrijev, I. Fischer, D. M. Villeneuve, A. Stolow, *Chem. Phys. Lett.* **1995**, 234, 281.
- 37 D. Imre, J. L. Kinsey, A. Sinha, J. J. Krenos, *J. Phys. Chem.* **1984**, 88, 3956.
- 38 A. Strobel, A. Lochschmidt, I. Fischer, G. Niedner-Schatteburg, V. E. Bondybey, *J. Chem. Phys.* **1993**, 99, 733.
- 39 A. Strobel, I. Fischer, A. Lochschmidt, K. Müller-Dethlefs, V. E. Bondybey, *J. Phys. Chem.* **1994**, 98, 2024.
- 40 A. Strobel, *Einfarben-Zweiphotonen ZEKE-Spektroskopie an dissoziierenden Alkylhaliden und (NO)<sub>2</sub>*, Herbert Utz Verlag Wissenschaft, München, 1997.
- 41 E. J. Heller, *Acc. Chem. Res.* **1981**, 14, 368.
- 42 Y. F. Zhu, E. R. Grant, *J. Phys. Chem.* **1993**, 97, 9582.
- 43 D. G. Abrashkevich, M. Shapiro, *J. Chem. Phys.* **1996**, 105, 9493.
- 44 N. Knoblauch, A. Strobel, I. Fischer, V. E. Bondybey, *J. Chem. Phys.* **1995**, 103, 5417.
- 45 N. A. Macleod, S. Wang, J. Hennessy, T. Ridley, K. P. Lawley, R. J. Donovan, *J. Chem. Soc., Faraday Trans.* **1998**, 94, 2689.
- 46 D. A. Beattie, N. A. MacLeod, K. P. Lawley, R. J. Donovan, *J. Elec. Spectrosc. Rel. Phenom.* **1998**, 97, 191.
- 47 T. Schultz, I. Fischer, *J. Phys. Chem. A* **1997**, 101, 5031.
- 48 P. C. Samartzis, B. L. G. Bakker, D. H. Parker, T. N. Kitsopoulos, *J. Phys. Chem. A* **1999**, 103, 6106.
- 49 V. Stert, W. Radloff, C. P. Schulz, I. V. Hertel, *Eur. Phys. J. D* **1999**, 5, 97.
- 50 K. L. Reid, T. A. Field, M. Towrie, P. Matousek, *J. Chem. Phys.* **1999**, 111, 1438.
- 51 S. C. Althorpe, T. Seideman, *J. Chem. Phys.* **1999**, 110, 147.
- 52 L. Wang, H. Kohguchi, T. Suzuki, *Faraday Discuss.* **1999**, 113, 37.
- 53 A. T. J. B. Eppink, D. H. Parker, *Rev. Sci. Instrum.* **1997**, 68, 3477.
- 54 J. A. Davies, J. E. LeClaire, R. E. Continetti, C. C. Hayden, *J. Chem. Phys.* **1999**, 111, 1.

## 15

### Femtochemistry in Nanocavities\*

*Abderrazzak Douhal*

#### Abstract

This contribution addresses the simple concept of femtochemistry in nanocavities. Initial studies of the femtosecond dynamics of bond-breaking, bond-making/remaking, and the twisting motion of selected chemical bonds (iodine–iodine, hydrogen, and carbon–carbon bonds) in molecular nanocavities are described. The results show the effect of confinement on the dynamics of a nascent wavepacket,<sup>[1,2]</sup> and open a new window in the femtochemistry field that may be extended to femtobiology.

#### 15.1

##### Introduction

From its inception to the present time, the field of femtochemistry (and of femtobiology) has been explored by selectively studying the breaking and making of chemical bonds in simple and complex systems in gases (clusters), liquids, or in the solid state.<sup>[3–6]</sup> The results show how it is now possible to witness in real time the “birth” and “death” of a chemical bond and to extract important information about its structure, reactivity, and dynamics, which, in turn, allows one to build accurate potential-energy surfaces (PES’s). There have been numerous applications to different classes of reactions in different molecules and phases by many research groups around the world.<sup>[3–10]</sup>

In the gas phase, the molecular system under study is free from solvent perturbations and can therefore evolve along several internal coordinates. However, in the condensed phase, the solvent response is so fast that it can govern the spread of the nascent wavepacket by changing the physical patterns of the PES’s. For example, studies of solvent-induced relaxation of nascent fragments in chemical-bond dissociation have provided much information on solvated wavepacket dynamics.<sup>[3–10]</sup> For the solvated wavepacket motion in dissociation, formation, and barrierless isomerization reactions, the nature of the coupling (coherent vs. diffuse) to the solvent

\*) This work is based on refs.<sup>[1]</sup> and <sup>[2]</sup>

during the reaction has been directly observed.<sup>[3–10]</sup> For systems with a large number of degrees of freedom ( $N$ ), a full understanding of the situation requires knowledge of the  $(N - 1)$  possible motions perpendicular to the reaction coordinate and the spread of the wavepacket, which involves a large number of modes. A twisting motion may be one of these modes, as occurs in the famous case of *cis*-stilbene isomerization, which may involve several in-plane and out-of-plane reaction coordinates; their respective motions may work coherently to deliver the system to the final product.<sup>[7–10]</sup>

## 15.2

### Concept of Femtochemistry in Nanocavities

Classical methods for controlling the dynamics and related PES's for dissociation/recombination and twisting motion and to possibly arrest intermediate(s) are based, for example, on judicious choice of the temperature or the viscosity (caging effect) of the medium. Modern methods take advantage of the advances in laser technology and involve, for example, fs-pulse timing, pulse shaping, and pulse sequencing.<sup>[3–6,9,10]</sup> A few years ago, the author proposed a simple means of controlling the dynamics and spectroscopy of the system under study.<sup>[11]</sup> Thus, the confined geometries of molecular nanocavities offer a unique opportunity to study size-controlled environment effects such as a reduction in the number of degrees of freedom and modified coupling to the heat reservoir. By selecting the size and nature of the molecular chamber offered by the host to the guest under consideration, one should be able to explore and control the spectroscopy (space domain) and dynamics (time domain) of the system under study.<sup>[11–14]</sup> Upon ultrafast electronic excitation of the embedded solute, the created wavepacket is trapped in a small area of the PES (caged wavepacket) and its evolution along the reaction coordinates of this surface will be funnelled and controlled by the restricted confined geometry. A similar situation occurs in semiconductors, where the conduction electrons are not only particles, but waves. Thus, trapped in a confined area, electrons can only have energies dictated (and then tuned) by the wave patterns present that will fit in this small region.<sup>[15]</sup> In a similar manner, a “free-born” wavepacket of a chemical system can be trapped and tuned by a molecular chamber or channel entity such as those of cyclodextrins (CD's), micelles, vesicles, proteins, zeolites, carbon nanotubes, calixarenes, or Cram boxes. Such molecular cavities protect the guest from highly reactive species that might be present in solution, significantly alter the local dielectric field, and reduce the number of degrees of freedom (in-plane and out-of-plane motions) of the system under study. Thus, specific and non-specific interactions between the solute and solvent at both static and dynamical levels can be affected by the molecular cage. Additionally, the results might provide information on the ultrafast relaxation dynamics of the cavity. Of no less importance, the physics and chemistry of the bound solvent molecules to the molecular cavity is of considerable interest as it plays a crucial role in many chemical and biological processes.<sup>[16]</sup> This is true, for example, of the so-called biological water, or bound water, located at the immediate

vicinity of a biomolecule such as a protein.<sup>[16]</sup> Thus, femtochemistry in nanocavities studies can be expected to provide new insights into the dynamics within relevant environments to help understand many chemical, physical, and biological processes in terms of time and space.

### 15.3

#### I–I Bond Breaking and Remaking in a Molecular Nanocavity

Molecular iodine ( $I_2$ ) has been extensively studied under a variety of experimental conditions by many groups using an array of techniques.<sup>[17–26]</sup> This section deals with its dynamics in a heptakis(2,6-di-O-methyl)- $\beta$ -cyclodextrin (DM $\beta$ -CD) nanocavity surrounded by water (Figure 15.1). Cyclodextrins (CD's, Figure 15.1A), which are oligosaccharides made up of six, seven, or eight glucopyranose units forming an interior hydrophobic cavity ( $\alpha$ -,  $\beta$ -, or  $\gamma$ -CD with internal diameters of 5.7, 7.8, and 9.5 Å, respectively) are widely used as host molecular chambers to encapsulate many functional molecules.<sup>[27,28]</sup>

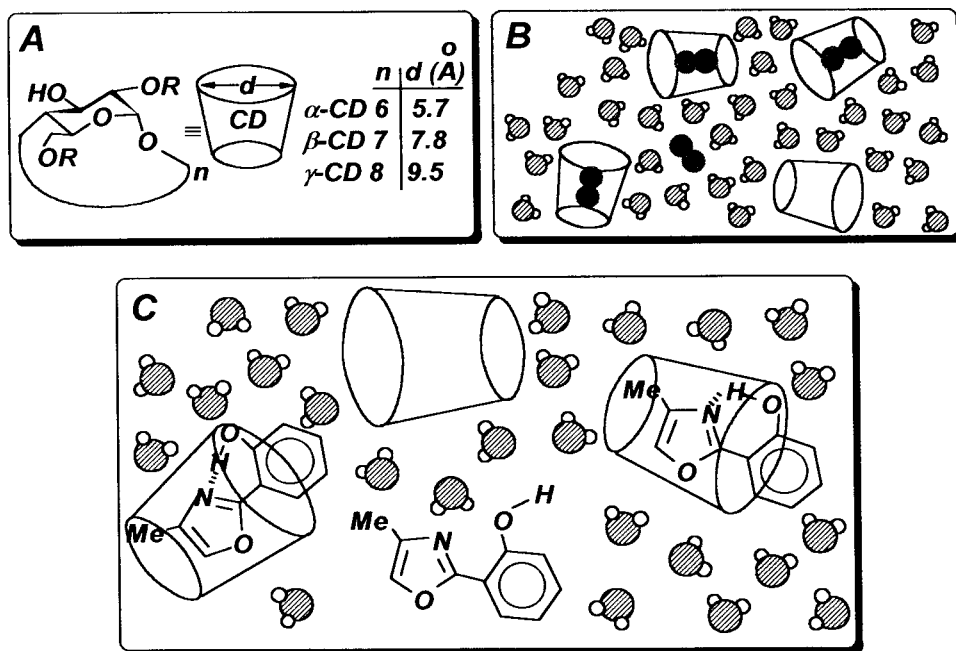


**Fig. 15.1** (A) Molecular structures of  $\alpha$ -,  $\beta$ -, and  $\gamma$ -cyclodextrin ( $R = H$ , of  $\alpha$ -,  $\beta$ -, and  $\gamma$ -CD) and heptakis-(2,6-di-O-methyl)- $\beta$ -cyclodextrin ( $R = CH_3$ , DM- $\beta$ -CD). (B) Schematic representation of iodine molecules ( $I_2$ ) in water

containing a CD nanocavity. (C) Open and closed structures of 2-(2'-hydroxyphenyl)-4-methyloxazole (HPMO) in water and in  $\beta$ -CD, respectively (see text).

Figure 15.2 shows UV/vis absorption spectra of  $I_2$  in several media, including DM $\beta$ -CD in neutral water. Inspection of the spectra reveals that upon encapsulation of  $I_2$  by DM $\beta$ -CD, two strong, broad absorption bands appear at 293 and 385 nm. The former may be assigned as a charge-transfer (CT) band, as observed in pure water solution.<sup>[29,30]</sup> The latter is the visible band ( $\lambda_{\text{max}} \approx 460$  and 520 nm in water and  $\text{CCl}_4$ , respectively) that is shifted due to the repulsive interactions between  $I_2$  and the oxygen atoms of DM $\beta$ -CD that exist in solution.<sup>[29]</sup> It may also contain a contribution from a second CT band. An X-ray study of the  $I_2$ /dimethyl- $\alpha$ -CD inclusion complex (1:1 stoichiometry) suggested that the confined geometry may lead to the formation of a CT complex between the guest and host.<sup>[31]</sup> Analysis of the concentration dependence of the intensity of these bands indicated the formation of an  $I_2$ /DM $\beta$ -CD complex with 1:1 stoichiometry and an equilibrium constant  $K = 7800 \pm 800 \text{ M}^{-1}$  at 296 K. Because the addition of 7-maltoheptaose (a linear oligosaccharide with seven glucopyranoside units, but lacking the torus-shape of CD's) to aqueous solutions of  $I_2$  does not lead to a significant change in the absorption spectrum (Figure 15.2), and based on the results of X-ray crystallographic measurements on  $I_2$ / $\alpha$ -CD complexes,<sup>[31]</sup> it can be concluded that the iodine molecule in the  $I_2$ /DM $\beta$ -CD entity is encapsulated within the molecular pocket of the cyclodextrin. In view of a possible short distance between the guest and the host (2.77 Å in the case of the  $I_2$ /DM $\alpha$ -CD complex<sup>[31]</sup>), there is a likelihood of CT from the di-O-methylglucose units of the CD pocket to the iodine molecule, as is seen in the case of  $I_2$  in dioxane (interatomic distance  $\sim 2.81 \text{ Å}$ ).<sup>[32]</sup>

Transient-absorption pump-probe spectroscopy has been used to study the ultrafast dynamics of  $I_2$ /DM $\beta$ -CD in aqueous solution. The femtosecond experimental apparatus used in the study has been described elsewhere.<sup>[2]</sup> For comparison, solutions of  $I_2$  in tetrahydrofuran (THF) were studied under similar excitation and probing conditions. The  $I_2$ /DM $\beta$ -CD complex in a neutral aqueous solution was excited by a fs-laser pump at 400 nm and subsequently interrogated by a fs laser probe at

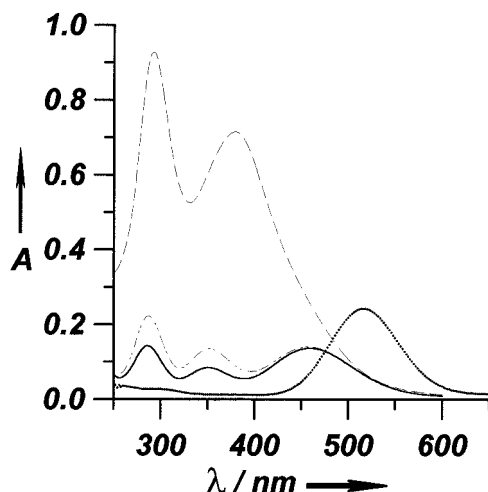


**Fig. 15.2** Solution absorption spectra of  $I_2$  in neat water (—) and after the addition of  $\sim 2 \text{ mM}$  DM $\beta$ -CD (---) and  $\sim 2 \text{ mM}$  7-maltoheptaose (.....). For comparison, the spectrum in  $\text{CCl}_4$  (— · —) is also shown. Adapted from ref.<sup>[2]</sup>



several wavelengths. Depending on the wavelength of the probe, the observed transient absorptions shown in Figures 15.3 and 15.4 can be classified into two families. At wavelengths shorter than  $\sim 470$  nm, the transient is mainly due to ground-state bleaching, while at longer wavelengths the signal is due to excited-state absorption. The wavelength of the probe is critical for locating the window in which internuclear separation occurs. In general, longer wavelengths probe longer I $\cdots$ I internuclear distances.<sup>[18,21,23,24]</sup>

For the longer-wavelength family, the initial part of the transient (appearing as a peak), which reflects the absorption of the initially prepared wavepacket, has a lifetime of  $\sim 200$  fs. The system then evolves towards longer I $\cdots$ I separations. After this ultrafast decay, a transient absorption appears with a rise time increasing with the energy of the probe. Probing at 700 nm, the rise time is fast, of the order of 1 ps. This rise is due to the absorption from upper vibrational levels of the (ground) electronic state of recombined iodine molecules. Thus, dissociation and most of the recombination processes are complete within  $\sim 1$  ps. However, probing at 630 and 480 nm, the rise time becomes slower, amounting to 1.2 and 1.8 ps, respectively. At these shorter wavelengths, the population being probed is that of lower-lying vibrational levels, and therefore the observed dynamics involves the rate of vibrational relaxation from upper levels.

After the ps rise, all transients show a non-exponential behavior with a slower decay at shorter probe wavelengths. For the transients at longer wavelengths, the decay can be fitted with a bi-exponential function, and the time constant of the

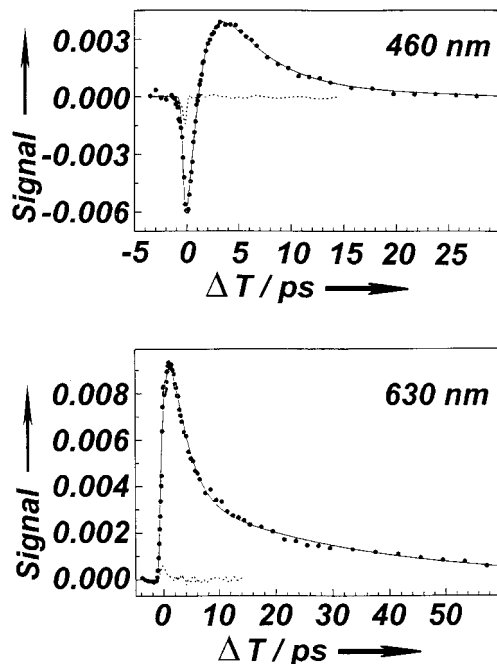


**Fig. 15.3** Femtosecond (fs) transient absorption of  $I_2$  in water containing DM $\beta$ -CD, observed after excitation at 400 nm. The probe (signal) wavelengths are indicated.  $\Delta T$  is the time delay (in picoseconds, ps) between the excitation and probe pulses. The solid lines represent the results of a multi-exponential fit. The dotted lines are transients measured for saturated  $I_2$  solution in pure water. Adapted from ref.<sup>[2]</sup>

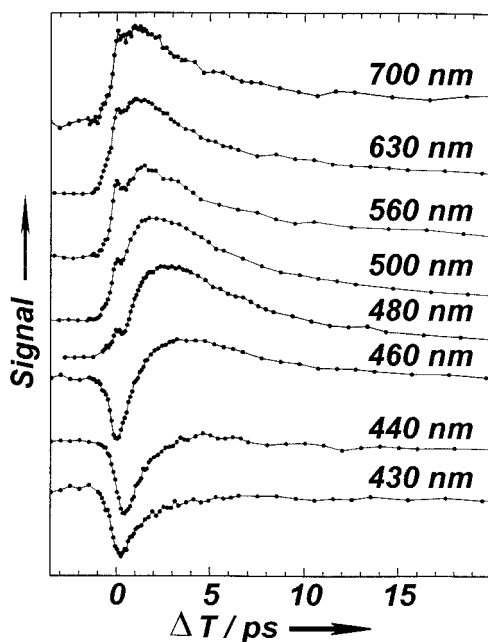


**Fig. 15.4** Fs-transient absorption of  $I_2$  in DM $\beta$ -CD in aqueous solution probed at different wavelengths. The excitation was centered at  $\sim 400$  nm. Adapted from ref.<sup>[2]</sup>

dominant fastest component (from 1.3 to 2.6 ps) increases with the energy of the probe. However, the time constant of the slower component remains essentially unchanged ( $\sim 30$  ps). Probing at shorter wavelengths (e.g. 440 and 430 nm) shows that bleaching and recovery processes occur in  $\sim 1$  ps.

Based on the results of studies of the dissociation and recombination dynamics of the iodine molecule in the gas-phase<sup>[18,22,26]</sup> and in solution and solids,<sup>[21,23–26]</sup> the following picture emerges for  $I_2$ /DM $\beta$ -CD ultrafast dynamics. The fs-excitation pulse (400 nm) puts the confined geometry in a region where the wavepacket moves to longer I–I internuclear distances in a time of  $\sim 200$  fs. Due to the molecular cage provided by CD, the two iodine atoms recombine and undergo vibrational relaxation, and cross to the ground-state potential (or A state) in a time of  $\sim 1$  ps. Note that in the solvent cage, the recombination time is ultrashort, of the order of 0.6 ps.<sup>[22]</sup> The vibrational cooling of the confined entity after crossing to the ground state occurs in  $\sim 30$  ps. For  $I_2$ /THF solutions, comparable times for the initial dissociation and recombination were found. However, the  $\sim 30$  ps subsequent relaxation observed in the molecular pocket is slower in THF, taking  $\sim 46$  ps. Vibrational relaxation times of up to  $\sim 150$  ps were found for  $I_2$ /CCl $_4$  and chlorinated methanes, which was explained in terms of vibrational-to-rotational energy transfer.<sup>[33]</sup> Because of CT coupling between the guest and host, and the large number of vibrational modes of the molecular chamber, the rates of vibrational cooling of  $I_2$  are enhanced in the CD cavity. Moreover, the nanosecond background component observed in  $I_2$ /THF transients, due to geminate recombination,<sup>[18]</sup> is absent in the confined geometry transients indicating a significant effect of the confinement on the rate of

remaking of this bond. Thus, the confinement offered by the molecular nanocavity enhances the rates of both vibrational cooling and geminate recombination processes. The spectroscopy and dynamics of iodine molecule can thus be controlled simply by caging it in a selected molecular chamber.

#### 15.4

#### Intramolecular H-Bond Breaking and Making and Related Reactions in Nanocavities

2-(2'-Hydroxyphenyl)-4-methyloxazole (HPMO, Figure 15.1C), which was selected for this purpose, is a heterocyclic molecule with two moieties forming an intramolecular H-bond. It has been studied from the point of view of quantum theory (ab initio molecular structure calculations at  $S_0$  and  $S_1$ ) and of experiment (jet-cooled molecular-beam fluorescence and steady-state absorption and emission spectroscopy in solution and in chemical and biological caging media).<sup>[14,34,35]</sup> It is capable of undergoing a photoinduced intramolecular proton-transfer reaction, which may be followed by a twisting motion.<sup>[14,34]</sup> The driving force for the proton motion is provided by simultaneous large changes in the acidity and basicity of the OH and  $-N=$  groups involved in the internal H-bond. The shift in  $pK_a$  values arises from a fast electronic redistribution induced by light and a vibrational coherence of the elementary modes that modulate the H-bond coordinates.<sup>[11]</sup> The tautomer structure, produced by an excited-state intramolecular proton-transfer (ESIPT) reaction, emits a significantly Stokes-shifted emission band. The emission lifetime and spectral characteristics of the formed tautomer depend on the nature of the solvent and on the space available to the solute.<sup>[14]</sup> This was explained in terms of the involvement of a  $C_2-C_1'$  bond twisting motion in the proton-transferred tautomer produced.<sup>[14,34]</sup> The femtosecond dynamics of HPMO was examined in a non-interacting solvent (3-methylpentane, 3MP) and caged by a  $\beta$ -cyclodextrin ( $\beta$ -CD) molecular pocket (Figure 15.1C) in order to explore the dynamics in both environments.

Figure 15.5 shows the steady-state spectra of HPMO in 3MP and in neutral water in the presence and absence of 6 mM  $\beta$ -CD. The longely Stokes-shifted emission band in 3MP is assigned to the phototautomers that result from an ESIPT reaction in the so-called closed enol (E) form.<sup>[14,34]</sup> The emission bands with maxima at 350 and 415 nm in pure water solution are attributable to water-solvated open enol and phenolate-type species, respectively.<sup>[14]</sup> In the last structure, the proton has moved from the OH group of HPMO to the solvent molecules. Addition of CD's leads to a significant decrease in the intensity of both bands and to the appearance of a blue-shifted emission due the phototaomer of E confined in the cavity of the CD (Figure 15.3B).<sup>[14]</sup> The inclusion equilibrium constant for the reaction leading to a 1:1 complex of HPMO and  $\beta$ -CD is  $1400 \pm 50 \text{ M}^{-1}$  at 300 K. The  $^1\text{H}$  NMR spectra of HPMO in  $\text{D}_2\text{O}$  in the absence and presence of  $\beta$ -CD indicate that the ground-state geometry of the confined structure is that in which the oxazole moiety of the guest resides near the small gate of the CD (Figure 15.1C). The emission of the tautomers produced by an ESIPT reaction in the guest is greatly enhanced in intensity and spec-

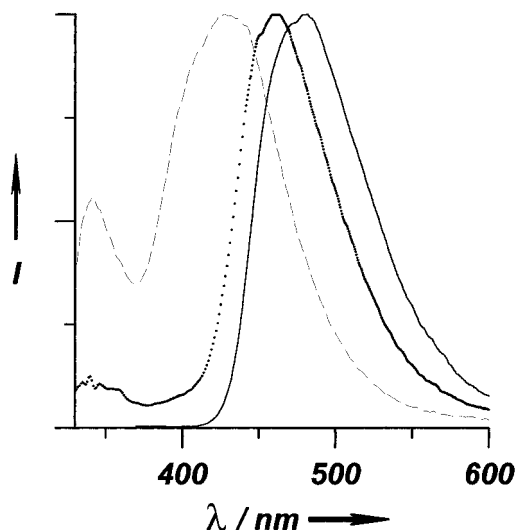


**Fig. 15.5** Normalized emission ( $\lambda_{\text{ex}} = 320$  nm) spectra of HPMO in 3-methylpentane (3MP) (—), neutral water (---), and in neutral water containing 6 mM  $\beta$ -CD (....).  $I$  = emission intensity.

trally separated from the weak, water-solvated open enol and phenolate-type emission bands. Therefore, the specific ultrafast dynamics related to the intramolecular proton-transfer reaction and subsequent processes in the cavity can be studied without interference from these structures. To this end, the emission of HPMO in 3MP (a non-interacting solvent) and in water solution containing 6 mM  $\beta$ -CD was followed in time (fs) and space (different wavelengths). A fs-laser pulse at 266 nm was used for excitation, and the emission (magic angle) was gated at the left, center, and right of the fluorescence band of the tautomer. The set up (up-conversion technique) has been described elsewhere.<sup>[1]</sup> The temporal response function of the pulses and detection was  $\sim 300$  fs.

The obtained result is shown in Figure 15.6. In 3MP, the fluorescence transient is strongly dependent on the observation wavelength. At the blue side of the emission band (420 nm), the transient shows a fast decay ( $\tau_1 \sim 0.7$  ps, 60%;  $\tau_2 \sim 9$  ps, 30%), followed by a sub-nanosecond ( $\sim 0.4$  ns, 11%) component. However, when the emission is gated at  $\sim 470$  nm, the transients display a rise with two time constants ( $\sim 0.2$  ps, 20% and  $\sim 9$  ps, 30%). The nanosecond component is reached later, as found by probing in the blue region. The fact that the 420 nm emission rises with no detectable rise time within the time resolution of the set-up used, and decays with a time constant on the sub-ps time scale (and longer), indicates that the proton motion is very fast ( $< 300$  fs). Therefore, the 470 nm (steady-state) emission band is not that of the nascent tautomer following the transfer (Figure 15.5). At 530 nm, the transient shows an initial non-resolved fast rise time ( $< 300$  fs) and a rising emission with components of  $\sim 0.4$  ps and  $\sim 8$  ps (Figure 15.6A).

The following picture of the dynamics of HPMO in 3MP has emerged. The nascent tautomer structure arising from an ultrafast ESIPT reaction in HPMO is generated in different vibrational distributions and with a high excess vibrational energy

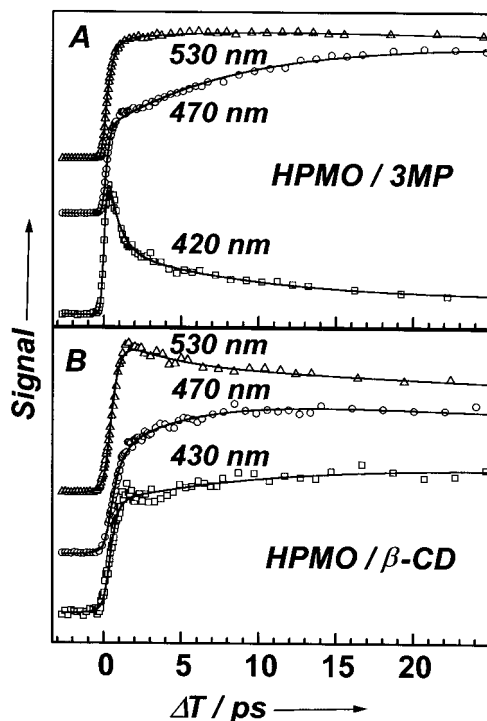


Fig. 15.6 Fs-fluorescence transients gated at different wavelengths for HPMP in 3-methylpentane (HPMO/3MP) and in aqueous solution containing  $\beta$ -CD (HPMO/ $\beta$ -CD). The observation wavelengths are indicated. Adapted from ref.<sup>[1]</sup>

(at least  $\sim 6500 \text{ cm}^{-1}$ ), since the excitation is performed at 266 nm and the  $S_0 \rightarrow S_1$  transition is located at around 320 nm.<sup>[14]</sup> The associated wavepacket bifurcates into two main competing pathways. One is driven by fast solvent polarization, intramolecular vibrational-energy redistribution (IVR), and vibrational relaxation (VR)/cooling processes. The time scales of these processes range from tens of fs to a few ps.<sup>[36]</sup> The second competing channel involves a twisting motion about the  $C_2-C_1'$  bond, leading to different, more stable rotamer configuration(s) (Figure 15.7). The rotational motion is associated with a barrier crossing and occurs within a few ps, while the proton transfer is associated with a small or null barrier, as suggested by *ab initio*

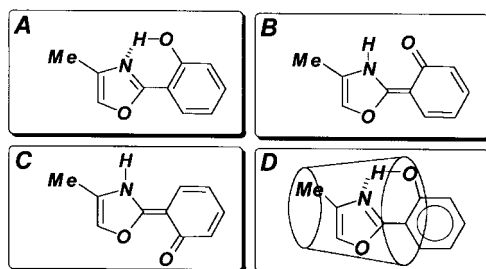


Fig. 15.7 Molecular structures of HPMP in the closed enol structure (A), the keto-type tautomer (B), the rotamer of the keto-type structure (C), and encapsulated by  $\beta$ -CD (D).

calculations.<sup>[34]</sup> The very rapid proton transfer is also consistent with results obtained for isolated molecules in gas- and solution-phase studies.<sup>[36–45]</sup> Note that the barrier crossing of the twisting motion involves the N $\cdots$ O mode, which may acquire energy from the solvent, thereby enhancing the twisting rate. The rise of the emissions at 470 and 530 nm in 3MP is not instantaneous. In fact, the rise at 470 nm takes  $\sim 0.2$  ps, and that at 530 nm takes  $\sim 0.4$  ps; for both wavelengths, the long-time rise component is  $\sim 8$  ps, as mentioned above. These results are consistent with dynamics involving a fast sub-ps solvent response due to the new electronic situation, ps IVR and VR/thermalization of the nascent tautomer (without twisting), and the generation of a rotamer structure due to a ps-twisting motion in the nascent tautomer. Thus, upon fs-proton motion in the initially excited structure of HPMO and charge redistribution, IVR together with VR/cooling processes, solvent polarization, and dielectric friction will lead to different solute/solvent configurations. The emission at longer wavelengths, e.g. 530 nm, may reflect these local structures of the tautomers.

The transient behavior of HPMO in  $\beta$ -CD at 430 nm is different from that observed in 3MP at 420 nm (Figure 15.6B). The steady-state emission in aqueous solutions of  $\beta$ -CD is not very different from that in 3MP, except for a  $\sim 10$  nm blue shift in the latter. The transient at 430 nm in  $\beta$ -CD is not instantaneous and shows a rise time of  $\sim 0.3$  ps. After this ultrafast rise, ps decay and rise are observed. At 470 and 530 nm, the initial rise times are similar (0.4–0.5 ps). However, after this sub-ps rise, the global behavior of the rest of the dynamics is wavelength-dependent. At 470 nm, the transient shows a ps rise followed by a ns decay. At 530 nm, the transient exhibits a ps decay. This difference reflects the complex dynamics of the confined geometry of HPMO/ $\beta$ -CD. The following picture of the confined geometry can be deduced. In-plane and out-of-plane motions involving the N $\cdots$ O mode are important for both proton transfer and the twisting motion.<sup>[11,40,42]</sup> The twisting process might be considerably restricted due to the confinement. Because of the size of the guest (HPMO, length  $\sim 9$  Å and diameter  $\sim 5$  Å) and that of the host cavity ( $\beta$ -CD, largest diameter  $\sim 8$  Å), a reduction in the number of degrees of freedom involved in proton-transfer and twisting events of the encapsulated dye is to be expected (Figures 15.1 and 15.7). Entrapped by  $\alpha$ -,  $\beta$ -, and  $\gamma$ -CD (Figure 15.1), the emission maxima appear at 450, 465, and 470 nm, respectively, suggesting the involvement of a twisting motion in the formed tautomer.<sup>[14]</sup> Using  $\beta$ - and  $\gamma$ -CD as hosts, the steady-state anisotropy,  $\langle r \rangle_0$ , is in the range of 0.12–0.14. In rigid films of poly(methyl methacrylate), where reorientation of the fluorophore is almost prevented,  $\langle r \rangle_0 \approx 0.33$ .<sup>[14]</sup> In contrast, in fluid media such as dioxane, 3MP, and triacetin, zero anisotropy was recorded. Thus, the cavity of  $\beta$ -CD may restrict in-plane and out-of-plane motions, thereby slowing the dynamics of HPMO. From a structural point of view, the dynamics in the cavity can be readily understood. First, the existence of several configurations of encapsulated HPMO with different angles between the oxazole ring (H-bond acceptor) and phenol moiety (H-bond donor) leads to large motions of these subunits in order to reach an adequate geometry for the intramolecular proton transfer. These motions need time to modulate the proton jump as well as the subsequent relaxation to the different rotamers.

Second, the existence of several nanostructures of HPMO/ $\beta$ -CD with different degrees of penetration and variable locations of the guest inside the host might lead to the observation of a wavelength-dependence of the dynamics. The motion of these conformations will contribute to the dynamics. Third, because of confinement, the amplitude of the motion for barrier crossing to twisted structures is reduced with the consequence of limiting structural changes. However, short-time ( $< 1$  ps) dynamics involving dissociative and/or vibrational modes acting in the bulk solvent might still be observed in the confined geometry. The observed fast decay before the ps-rise at 430 nm and the rises at 470 and 530 nm might be due to the dynamics of these modes (Figure 15.6B). It is noteworthy that some of the water molecules found at the gates of the molecular chamber, and thus in the immediate vicinity of the embedded guest, are not totally free to move due to the H-bond network that they establish with the glucopyranoside units of the capsule. To some extent, this prevents them from playing a more important role in the ultrafast dynamics of the guest. However, their instantaneous polarization response to the electronic redistribution in the guest plays a role in the dynamics. A sub-ps component can still be observed, albeit with a lesser contribution in the ultrafast part (Figure 15.6B). Moreover, due to the restrictions imposed by the cavity, the contribution of the long-time component in the full dynamics due to translational solvation time might be enhanced in the molecular capsule. Modelization<sup>[46]</sup> of the dynamics of ionic coumarin-480 dye encapsulated by  $\gamma$ -CD, as studied by Vajda et al.,<sup>[47]</sup> suggests a significant increase in the long-time decay of the solvation time correlation function of the guest. A freezing of the solvent (bound water at the gates) translational modes might be responsible for the observed retardation of the solvation dynamics in the cavity. In free bulk solution, these modes enhance the collective rotational relaxation process of the solvent molecules nearest to the solute. Their interactions with the capsule may also induce a long-time component in the full dynamics of the confined nanostructure, due to relaxation of the host.<sup>[46]</sup> Note also that because of the many vibrational modes of the reservoir cavity, the rate of thermalization might be enhanced, as was observed in the case of the iodine/DM $\beta$ -CD nanostructure discussed above. The results discussed here show the influence of caging by a nanocavity on the dynamics of a molecule that undergoes bond-breaking/making and twisting reactions. Further work, including the effects of excess energy of excitation, polarization, diameter, and the nature of the molecular cavity can be expected to give more detailed information on the femtochemistry of this molecule in nanocavities, and on the role of water molecules bound to the capsule.

## 15.5

### Concluding Remarks

Both studies indicate that it is possible to control the spread of a nascent wavepacket simply by caging the system under study in an appropriate molecular nanocavity. Application to different classes of chemical and biological reactions can easily be

extended to different hosts, with the possibility of selecting the diameter and nature of the cavity and its surrounding medium. The results should provide an accurate basis for a better understanding of the trial structure/reactivity/dynamics, with possible potential technological applications. Indeed, they might shape the future of many technological arenas, ranging from nanometer-sized molecular devices, photonic crystals, polymers, gels, ultrafast optical computing and communications, dye-sensitized solar cells, biological sensors, protein delivery, and gene therapy.

## Acknowledgement

This work is the result of a fruitful collaboration with Prof. Ahmed H. Zewail. It has been supported in part by the Ministry of Science and Technology of Spain through projects 1FD1997–1658 and PB98-0310, and the U.S.A.–Spain cooperative program.

## References

- 1 A. Douhal, T. Fiebig, M. Chachisvilis, A. H. Zewail, *J. Phys. Chem. A* **1998**, 102, 1657.
- 2 M. Chachisvilis, I. Garcia-Ochoa, A. Douhal, A. H. Zewail, *Chem. Phys. Lett.* **1999**, 293, 153.
- 3 A. H. Zewail, *Femtochemistry: Ultrafast Dynamics of the Chemical Bond*, Vols. I and II, World Scientific, Singapore, **1994**.
- 4 A. H. Zewail, *J. Phys. Chem. (Centennial Issue)* **1996**, 100, 12701.
- 5 J. Manz, L. Wöste (Eds.), *Femtochemistry: Ultrafast Dynamics of the Chemical Bond*, World Scientific, Singapore, **1994**.
- 6 V. Sundström (Ed.), *Femtochemistry and Femtobiology, Nobel Symposium 101*, Imperial College Press, London, **1997**.
- 7 A. Z. Szarka, N. Pugliano, D. Palit, R. M. Hochstrasser, *Chem. Phys. Lett.* **1995**, 240, 25.
- 8 J. S. Baskin, L. Bañares, S. Pedersen, A. H. Zewail, *J. Phys. Chem.* **1996**, 100, 11920.
- 9 *J. Phys. Chem. Special Issue* **1993**, 79, 48.
- 10 *J. Phys. Chem. A, Special Issue* **1998**, 102, 23.
- 11 A. Douhal, *Science* **1997**, 276, 221.
- 12 A. Douhal, F. Amat-Guerri, A. U. Acuña, *Angew. Chem. Int. Ed. Engl.* **1997**, 36, 1514.
- 13 C. R. Mateo, A. Douhal, *Proc. Natl. Acad. Sci. USA* **1998**, 95, 7245.
- 14 I. Garcia-Ochoa, M.-A. Díez-López, M. H. Viñas, L. Santos, E. Martínez-Atáz, F. Amat-Guerri, A. Douhal, *Chem. Eur. J.* **1999**, 5, 897.
- 15 C. Weisbuch, B. Vinter, *Quantum Semiconductor Structures*, Academic Press, San Francisco, **1991**.
- 16 R. B. Gregory (Ed.), *Protein Solvent Interactions*, Marcel Dekker Inc., New York, **1995**.
- 17 R. S. Mulliken, *J. Chem. Phys.* **1971**, 155, 288.
- 18 C. Lienau, A. H. Zewail, *J. Phys. Chem.* **1996**, 100, 18629.
- 19 T. J. Chuang, G. W. Hoffman, K. B. Eisenthal, *Chem. Phys. Lett.* **1974**, 25, 201.
- 20 D. Nesbit, J. T. Hynes, *J. Chem. Phys.* **1982**, 77, 2130.
- 21 A. L. Harris, J. K. Brown, C. B. Harris, *Ann. Rev. Phys. Chem.* **1988**, 39, 341.
- 22 Q. Liu, J.-K. Wang, A. H. Zewail, *Nature* **1993**, 364, 427.
- 23 N. F. Scherer, D. M. Jonas, G. R. Fleming, *J. Chem. Phys.* **1993**, 99, 153.
- 24 R. Zadoyan, M. Sterling, M. Ovchinnikov, V. A. Apkarian, *J. Chem. Phys.* **1997**, 107, 8446.
- 25 M. Chergui, N. Schwentner, in *Trends in Chemical Physics*, Vol. II (Ed.: J. Menon), Tri-vandum, India, **1992**, 89.
- 26 J. S. Baskin, M. Chachisvilis, M. Gupta, A. H. Zewail, *J. Phys. Chem. A* **1998**, 102, 4158.
- 27 J. Szejtli, *Cyclodextrins and their Inclusion Complexes*, Akademiai Kiado, Budapest, **1982**.
- 28 P. Bortolus, S. Monti, *Adv. Photochem.* **1996**, 21, 1.



- 29 R. S. Mulliken, W. B. Person, *Molecular Complexes*, A Lecture and Reprint Volume, Wiley-Interscience, New York, 1969.
- 30 P. Y. Cheng, D. Zhong, A. H. Zewail, *J. Chem. Phys.* **1996**, 105, 6216.
- 31 K. Harata, *Bull. Chem. Soc. Jpn.* **1990**, 63, 2481.
- 32 O. Hassal, *Acta Chem. Scand.* **1965**, 19, 2259.
- 33 A. L. Harris, M. Berg, C. B. Harris, *J. Chem. Phys.* **1986**, 84, 788.
- 34 V. Guallar, M. Moreno, J. M. Lluch, F. Amat-Guerri, A. Douhal, *J. Phys. Chem.* **1996**, 100, 19789.
- 35 A. Douhal, F. Lahmani, A. Zehnacker-Rentien, F. Amat-Guerri, in *Fast Elementary Processes in Chemical and Biological Systems* (Ed.: A. Tramer), AIP Conference Proceedings, American Institute of Physics, Woodbury, New York, **1996**, Vol. 346, p. 383.
- 36 T. Fiebig, M. Chachisvilis, M. Manger, A. H. Zewail, A. Douhal, I. Garcia-Ochoa, A. De La Hoz Ayuso, *J. Phys. Chem. A* **1999**, 103, 7419.
- 37 J. L. Herek, S. Pedersen, L. Bañares, A. H. Zewail, *J. Chem. Phys.* **1992**, 97, 9046.
- 38 Th. Arthen-Engeland, T. Bultman, N. P. Ernsting, M. A. Rodriguez, W. Thiel, *Chem. Phys.* **1992**, 163, 43.
- 39 A. Douhal, F. Lahmani, A. Zehnacker-Rentien, F. Amat-Guerri, *J. Phys. Chem.* **1994**, 98, 12198.
- 40 A. Douhal, F. Lahmani, A. H. Zewail, *Chem. Phys.* **1996**, 207, 477.
- 41 A. Douhal, S. K. Kim, A. H. Zewail, *Nature* **1995**, 378, 260.
- 42 C. Chudoba, E. Riedle, M. Pfeiffer, T. Elsaesser, *Chem. Phys. Lett.* **1996**, 263, 622.
- 43 P. Prosposito, D. Marks, H. Zhang, M. Glasbeek, *J. Phys. Chem. A* **1998**, 102, 8894.
- 44 H. Limbach, J. Manz (Eds.), *Hydrogen Transfer: Experiment and Theory*, *Ber. Bunsengens. Phys. Chem.* **1998**, 102, *Special Issue*.
- 45 N. Agmon, M. Gutman (Eds.), *Proton Solvation and Proton Mobility*, *Isr. J. Chem.* **1999**, 39 (3/4), *Special Issue*.
- 46 N. Nandi, B. Bagchi, *J. Phys. Chem.* **1996**, 100, 13914.
- 47 S. Vajda, R. Jimenez, S. J. Rosenthal, V. Fidler, G. R. Fleming, E. W. Castner, *J. Chem. Soc., Faraday Trans.* **1995**, 91, 867.

## 16

### Energy- and Angle-Resolved Femtosecond Photoelectron Spectra from Rotating Molecules

*Yasuki Arasaki, Kazuo Takatsuka, Kwanghsi Wang, and Vincent McKoy*

#### Abstract

We have extended our formulation of energy- and angle-dependent pump-probe photoelectron spectroscopy for vibrational wavepackets to account for the effects of molecular rotation. We employ a classical model for rotation, which should be applicable to many cases of interest, and present some results of applications to photoelectron spectra for wavepackets on the double-minimum state of Na<sub>2</sub>. The results provide useful insights into such time-resolved photoelectron spectra and suggest strategies for deconvolution of the vibrational and rotational content of the photoelectron signals.

#### 16.1

##### Introduction

Femtosecond time-resolved spectroscopy has now been widely exploited in numerous applications ranging from fundamental studies of real-time motion in the photodissociation of NaI to studies of electron transfer.<sup>[1–3]</sup> In this spectroscopic technique, a femtosecond pulse (pump) is used to launch a wavepacket to a state where it evolves in accordance with the time scales for vibrational ( $\sim 10^{-13}$  s) and rotational ( $\sim 10^{-10}$  s) motion. The evolution of the wavepacket is monitored following time-delayed femtosecond excitation to a higher electronic state, which serves as a template. Various techniques, including absorption, laser-induced fluorescence, multi-photon ionization, photoelectron spectroscopy, time-resolved mass spectrometry, and stimulated emission pumping, have been used to probe these wavepackets.<sup>[2–8]</sup>

Time-resolved ionization offers several advantages as a means of probing these wavepackets.<sup>[5,9–11]</sup> For example, the ground state of an ion is often more readily characterized than higher excited states of the molecule. Ionization also provides ions and photoelectrons, and while ion detection provides mass- and kinetic-energy resolution, pump-probe photoelectron spectra are well-suited for monitoring wavepacket dynamics and the evolution of electronic structure along all energetically

allowed internuclear distances simultaneously.<sup>[5–8]</sup> This advantage of time-resolved photoelectron spectroscopy has already been well-demonstrated in the picosecond domain.<sup>[12–14]</sup> Its potential for probing molecular dynamics in the femtosecond regime has also been exploited experimentally for several systems.<sup>[5–7,15]</sup> Furthermore, Davies et al.<sup>[8]</sup> have recently reported the results of the first femtosecond photoelectron–photoion coincidence imaging studies of photodissociation dynamics.

In recent papers,<sup>[16–19]</sup> we have presented the results of our studies of energy- and angle-resolved photoelectron spectra for femtosecond pump-probe ionization of wavepackets in the  $^1\Sigma_u^+$  double-minimum state in  $\text{Na}_2$  molecules aligned by a linearly polarized pump-pulse. For these studies, we employed geometry- and energy-dependent photoelectron matrix elements derived from sophisticated descriptions of the wavefunctions for this double-minimum state and for the molecular photoelectrons. We reported spectra for molecules aligned by a linearly polarized pump-pulse and ionized by a probe-pulse polarized either parallel or perpendicular to the pump-pulse. The following important points emerged: First, a robust description of the photoionization amplitudes can significantly enhance the utility of femtosecond photoelectron spectroscopy as a probe of wavepacket motion and of the evolution of electronic structure. In fact, this is particularly true when the wavepacket moves through an avoided crossing. Secondly, photoelectron angular distributions are informative fingerprints of vibrational wavepacket dynamics.

In the aforementioned studies, however, we assumed that the molecule did not rotate but remained fixed in space with its axis aligned along the polarization vector of the pump laser and that the probe-pulse was either parallel or perpendicular to the molecular axis. While this may be a reasonable assumption for rotationally cold systems, it is clearly of interest to examine how these photoelectron spectra depend on molecular rotation. Although our formulation of energy- and angle-resolved pump-probe photoelectron spectra<sup>[17]</sup> can account for quantum molecular rotation, the computational effort increases significantly. In cases where coherent interactions among vibrational and rotational modes are not large, which will be assumed here, a classical treatment of molecular rotation is a practical and valuable first step in exploring the influence of molecular rotation on these pump-probe photoelectron spectra. In this contribution, we present the first results of studies of such energy- and angle-resolved pump-probe photoelectron spectra.

## 16.2

### Pump-Probe Photoelectron Spectroscopy and Molecular Rotation

#### 16.2.1

##### Formulation

Figure 16.1 illustrates the key features of the pump-probe femtosecond photoelectron spectroscopy scheme considered here. Application of this scheme to the probing of vibrational dynamics on the  $^1\Sigma_u^+$  double-minimum state of the  $\text{Na}_2$  molecule by energy- and angle-resolved time-dependent photoelectron spectra has been de-

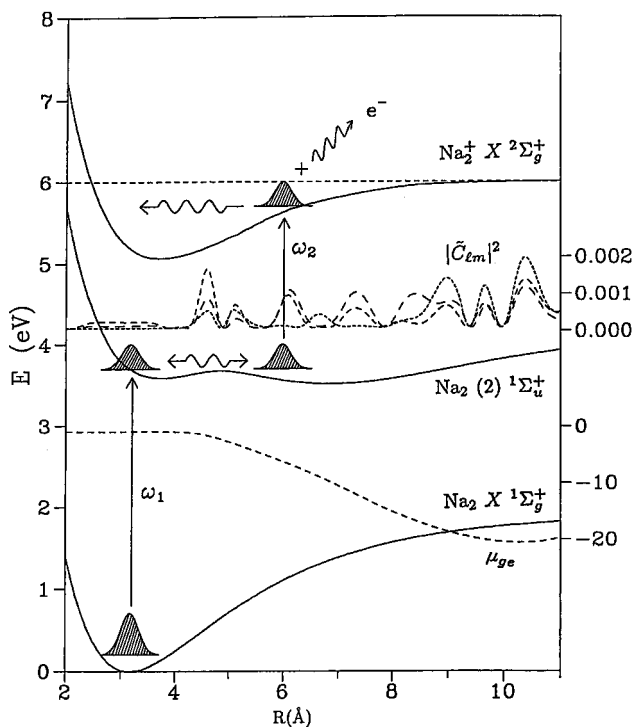


**Fig. 16.1** Potential curves for the  $X^1\Sigma_g^+$  and  $(2)^1\Sigma_u^+$  states of  $\text{Na}_2$  and the  $X^2\Sigma_g^+$  state of  $\text{Na}_2^+$ . The dipole amplitude ( $\mu_{ge}$ ) and photoionization coefficients ( $\tilde{C}_{\ell m}$ ) for the molecule parallel to the pump and probe fields are also shown for a

photoelectron energy of 0.5956 eV. The partial waves  $\ell = 0, 2$ , and  $4$  with  $m = 0$  are denoted by long, medium, and short dashed lines, respectively.

scribed in detail in a previous paper.<sup>[17]</sup> We first briefly review the general theoretical formulation employed in these studies, with an emphasis on the coordinate frames that are used to describe molecular orientation.

A linearly polarized femtosecond laser pulse of frequency  $\omega_1$  prepares a wavepacket on the double-minimum  $^1\Sigma_u^+$  state, which is then ionized by a time-delayed linearly polarized femtosecond laser pulse of frequency  $\omega_2$ . The polarized pump-pulse produces an aligned distribution of  $\text{Na}_2$  molecules since only those molecules with their transition moments parallel or nearly parallel to the polarization vector of the pump-pulse are excited. The dynamics of the system is monitored by means of the energy and angular distributions of photoelectrons produced from ionization of the wavepacket.

The orientation of the molecule and the pump and probe laser fields is shown in Figure 16.2. Three coordinate frames naturally arise in this picture. Since the pump-pulse prepares an aligned distribution of molecules, the time-dependent molecular orientation  $\hat{R} = (\theta_R, \phi_R)$  is best defined in the pump frame  $(X, Y, Z)$ , where the  $Z$ -axis lies in the direction of the pump polarization vector. The probe polarization vec-

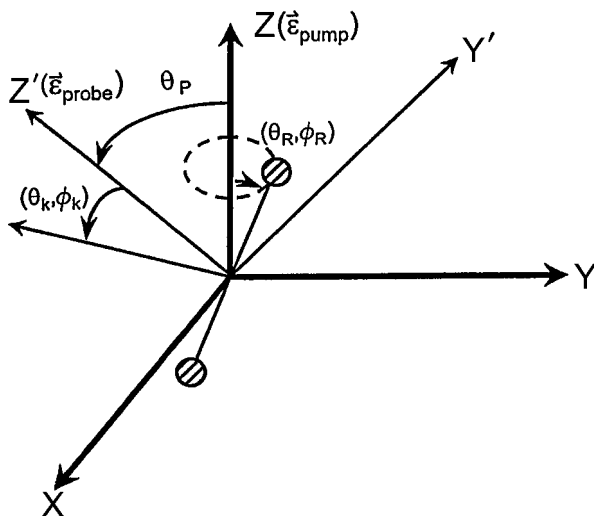


**Fig. 16.2** Orientation of the molecule and pump and probe laser fields: molecular orientation angles  $(\theta_k, \phi_k)$  in the probe frame.

tor defines the  $Z'$ -axis of the probe frame  $(X', Y', Z')$ , in which it is most convenient to define the photoelectron detection angle  $(\theta_k, \phi_k)$ . The molecule-field interaction is best described in the molecular body frame  $(x, y, z)$ . Without any loss of generality, the probe polarization vector can be taken to lie in the  $XZ$ -plane, so that a single angle  $\theta_P$  conveniently describes the relative orientation of pump and probe. Taking the probe frame  $Y'$ -axis to coincide with the pump frame  $Y$ -axis, the probe frame is unambiguously oriented in relation to the pump frame.

The time-dependent wavefunction for this system can be written as:

$$\Psi(\mathbf{r}, \mathbf{R}, t) = \chi_g(\mathbf{R}, t)\Phi_g(\mathbf{r}; R) + \chi_e(\mathbf{R}, t)\Phi_e(\mathbf{r}; R) + \int d\mathbf{k}\chi_k(\mathbf{R}, t)\Phi_k^{(-)}(\mathbf{r}; R), \quad (1)$$

where  $\Phi_g$ ,  $\Phi_e$ , and  $\Phi_k^{(-)}$  are the electronic eigenfunctions for the ground, excited, and final ionized adiabatic states, respectively;  $\chi_g$ ,  $\chi_e$ , and  $\chi_k$  are nuclear wavepackets on the respective potential curves,  $\mathbf{r}$  denotes electronic coordinates, and  $\mathbf{k}$  is the wave-vector of the emitted photoelectron. The nuclear coordinates  $\mathbf{R} = (R, \hat{R})$ , with  $R$  being the internuclear distance, describe both vibrational and rotational motion. The interaction between the molecule and the laser fields is given by:

$$V(t) = V_1(t) + V_2(t; \Delta T) \\ = E_{01}f_1(t)\sin(\omega_1 t)\epsilon_{\text{pump}} \cdot \mathbf{d} + 1/2E_{02}f_2(t - \Delta T)\exp(-i\omega_2(t - \Delta T))\epsilon_{\text{probe}} \cdot \mathbf{d}, \quad (2)$$

where  $E_{01}$  and  $E_{02}$  are the field amplitudes,  $f_1(t)$  and  $f_2(t - \Delta T)$  are the pulse envelope functions with  $\Delta T$  being the time delay between the two pulses,  $\epsilon_{\text{pump}}$  and  $\epsilon_{\text{probe}}$  are the polarization vectors, and  $\mathbf{d}$  is the electric dipole operator. The centers of the envelope functions for the pump and probe pulses are at  $t = 0$  and  $t = \Delta T$ ,

respectively, and are taken here to be Gaussian functions although the formulation is general.

The interaction matrix element between the ground and excited states is given by

$$V_{eg}(R, t, \theta_R) = \langle \Phi_e(R) | V_1(t) | \Phi_g(R) \rangle = E_0 f_1(t) \sin(\omega_1 t) d_{eg}(R) \cos(\theta_R), \quad (3)$$

where  $d_{eg}$  is the magnitude of the dipole matrix element between the ground and excited states and  $\theta_R$  is the angle between the molecular axis and the polarization of the pump-pulse. To obtain the photoionization matrix elements needed for  $V_2$ , we write  $\Phi_k^{(-)}$  as an antisymmetrized product of an ion wavefunction,  $\Phi_+$ , and a photoelectron orbital,  $\phi_k^{(-)}$ ,

$$\Phi_k^{(-)} = \mathcal{A}(\Phi_+ \cdot \phi_k^{(-)}), \quad (4)$$

where

$$\phi_k^{(-)} = \sum_{\ell, m, \lambda} i^\ell e^{-i\eta_\ell} \mathcal{D}_{\lambda m}^\ell(\hat{R}') Y_{\ell m}^*(\hat{k}) \psi_{k\ell\lambda}^{(-)}(\mathbf{r}'; R), \quad (5)$$

with  $\mathbf{r}'$  being the electronic coordinate in the molecular frame. In Eq. (5),  $\psi_{k\ell\lambda}^{(-)}$  is a partial-wave component of the photoelectron orbital in the molecular frame with momentum  $\mathbf{k}$ ,  $\lambda$  is the projection of  $\ell$  in the molecular frame,  $\mathcal{D}_{\lambda m}^\ell$  transforms the molecular-frame wavefunctions to those in the laboratory (probe) frame, and  $\eta_\ell$  is the Coulomb phase shift.<sup>[20]</sup>

Photoelectrons are, of course, detected with respect to the polarization vector of the probe laser. The dipole operator is thus given by

$$D_{\mu 0} = \sqrt{\frac{4\pi}{3}} r \sum_{\mu} \mathcal{D}_{\mu\mu_0}^1(\hat{R}') Y_{1\mu}(\hat{r}') \quad (6)$$

in the probe laser frame. The interaction  $V_2$  between the probe laser and the molecule now becomes

$$V_2 = \frac{1}{2} E_{02} \cdot f_2(t - \Delta T) \exp(-i\omega_2(t - \Delta T)) D_{\mu_0} \quad (7)$$

and the coupling matrix element between the excited state  $\Phi_e$  and the final ionized state can be written as

$$\begin{aligned} V_{ie}(R, t) &= \langle \Phi_k^{(-)}(R) | V_2(t; \Delta T) | \Phi_e(R) \rangle \\ &= \frac{1}{2} E_{02} \cdot f_2(t - \Delta T) \exp(-i\omega_2(t - \Delta T)) \sum_{\ell m} C_{\ell m} Y_{\ell m}(\hat{k}), \end{aligned} \quad (8)$$

with

$$C_{\ell m}(R; k, \theta_R, \phi_R, \theta_P) = \sqrt{\frac{4\pi}{3}} \sum_{\lambda\mu} I_{\ell\lambda\mu} \mathcal{D}_{\lambda m}^{\ell*}(\hat{R}') \mathcal{D}_{\mu\mu_0}^1(\hat{R}'). \quad (9)$$

Here,  $I_{\ell\lambda\mu}$  is a partial-wave matrix element in the molecular frame. These are formed from dipole matrix elements between  $|\Phi_+ \psi_{k\ell\lambda}^{(-)}\rangle$  and the components of the

CI wavefunction used to describe  $\Phi_e$ . In the case of ionization of an orbital  $\phi_i$  into  $\psi_{k\ell\lambda}^{(-)}$ , these assume the form

$$I_{\ell\lambda\mu}^{(0)}(R) = (-i)^\ell e^{i\eta_\ell} \sum_{\ell_0\lambda_0} \langle \psi_{k\ell\lambda}^{(-)} | r Y_{1\mu}(\hat{r}') | \phi_{i,\ell_0\lambda_0}(r) Y_{\ell_0\lambda_0}(\hat{r}') \rangle \quad (10)$$

These  $C_{\ell m}$  coefficients provide the underlying dynamical information needed to describe the photoionization of an oriented  $\text{Na}_2$  molecule by the probe laser. The angular momentum coupling inherent in molecular photoelectrons can be seen in a single-center expansion of  $\psi_{k\ell\lambda}$  for a linear molecule

$$\psi_{k\ell\lambda}^{(-)}(\mathbf{r}, R) = \sum_{\ell'} g_{\ell'\lambda}^{(-)}(k, r, R) Y_{\ell'\lambda}. \quad (11)$$

The use of photoelectron orbitals that correctly incorporate such angular momentum coupling is essential for a quantitative description of molecular photoionization. The partial-wave components of the photoelectron orbital,  $\psi_{k\ell\lambda}^{(-)}$ , are obtained numerically using a procedure described in detail elsewhere.<sup>[20]</sup>

Expanding the ion nuclear wavepacket  $\chi_k$  in partial waves about  $\hat{k}$ ,

$$\chi_k(\mathbf{R}, t) = \sum_{\ell m} \chi_{k\ell m}(\mathbf{R}, t) Y_{\ell m}(\hat{k}), \quad (12)$$

and using Eqs. (4) and (1), we obtain the following equations of motion:

$$i\hbar \frac{\partial}{\partial t} \chi_g(\mathbf{R}, t) = [T_N + V_g] \chi_g(\mathbf{R}, t) + V_{ge}(R, t, \theta_R) \chi_e(\mathbf{R}, t), \quad (13)$$

$$\begin{aligned} i\hbar \frac{\partial}{\partial t} \chi_e(\mathbf{R}, t) = & [T_N + V_e] \chi_e(\mathbf{R}, t) + V_{eg}(t, \theta_R) \chi_g(\mathbf{R}, t) \\ & + \frac{1}{2} \sum_{\ell m} \int dk k^2 E_0 f_2(t - \Delta T) \exp(i\omega_2(t - \Delta T)) C_{\ell m}^*(k, R, \theta_R, \phi_R, \theta_P) \chi_{k\ell m}(\mathbf{R}, t; \Delta T, \theta_P), \end{aligned} \quad (14)$$

and

$$\begin{aligned} i\hbar \frac{\partial}{\partial t} \chi_{k\ell m}(\mathbf{R}, t; \Delta T, \theta_P) = & \left[ T_N + V_{\text{ion}} + (k\hbar)^2 / 2m_e \right] \chi_{k\ell m}(\mathbf{R}, t; \Delta T, \theta_P) \\ & + \frac{1}{2} E_0 f_2(t - \Delta T) \exp(-i\omega_2(t - \Delta T)) C_{\ell m}(k, R, \theta_R, \phi_R, \theta_P) \chi_e(\mathbf{R}, t). \end{aligned} \quad (15)$$

Discretization of the continuum integration over  $\mathbf{k}$  in Eq. (14) through a quadrature leads to coupled equations for  $\chi_g$ ,  $\chi_e$ , and  $\chi_{k\ell m}$ . Details of the procedures employed in solving these equations are given in ref. [17].

### 16.2.2

#### Molecular Rotation

The aforementioned total wavefunction and its associated equations of motion are sufficiently general to account for both molecular vibrations and rotations in a

quantum mechanical treatment. For instance, the nuclear wavepackets, say  $\chi_{\mathbf{k}}(\mathbf{R}, t)$ , can be expanded in terms of rotational wavefunctions  $\Theta_{LM}(\hat{R})$  such that

$$\chi_{\mathbf{k}}(\mathbf{R}, t) = \sum_{L,M} \chi_{\mathbf{k},LM}(R, t) \Theta_{LM}(\hat{R}). \quad (16)$$

Accordingly, one may formulate coupled equations of motion for  $\chi_{\mathbf{k},LM}(R, t)$ . Here,  $L$  and  $M$  are, respectively, the rotational angular quantum number and its projection onto, for instance, the pump field. Coherent interactions among rotational levels and rotation-vibration levels may be important in angle-resolved photoelectron spectra for light molecules or rotationally hot systems. Nonetheless, in our previous study we assumed that the molecule did not rotate significantly on the vibrational time scale. We made this assumption for several reasons. First, we are primarily interested in these photoelectron spectra as a means of probing dynamics in regions of nonadiabatic behavior between electronic states. Secondly, it is a valid assumption for rotationally cold states where the rotational time scale is orders of magnitude longer than the vibrational time scale. Finally, the inclusion of rotational states would lead to a dramatic increase in the number of channels in our coupled equations of motion. On the other hand, for a molecule with fixed orientation, the coupled equations of motion need only describe the vibrational wavepackets. The studies of coherent rotational excitation of ref. [21] assumed a rigid rotor and neglected vibrational motion.

As a first step in exploring the effect of rotation on these pump-probe photoelectron spectra, we resort to a classical model. Here, we assume that molecular rotation is slow and explicitly account for molecular rotation simply by changing the molecular orientation  $(\theta_R, \phi_R)$  through the pump-probe delay time. This procedure requires evaluation of the  $C_{\ell m}$  coefficients for every delay time, but does not significantly increase the overall computational cost.

In the following we assume, for simplicity, that the molecule rotates in the  $XZ$ -plane, the plane containing the polarization vectors of the pump and probe lasers (see Figure 16.2), at a constant angular velocity such that  $\theta_R$  is a linear function of time and  $\phi_R = 0$ . Photoelectrons are also detected in the  $XZ$ -plane. Furthermore, this treatment ensures that molecular rotation is dynamically uncoupled from vibrational motion. Clearly, this cannot be a good approximation in cases where the bond length changes significantly during rotation as in such cases there may be considerable energy exchange between rotational and vibrational modes. When pumped to an energy above the potential barrier, motion on the double-minimum state of  $\text{Na}_2$  is just such a case as the bond stretches from about 3 to 10 Å. Nonetheless, we have studied this case simply to explore the photoelectron spectra from a rotating molecule rather than as a simulation of an actual experiment.



## 16.3

## Photoelectron Distribution from Rotating Molecules

## 16.3.1

## Vibrational Wave Packets

Figure 16.3 shows the behavior of vibrational wavepackets prepared by two different pump photons. The left panel, (a), shows the case for a pump-pulse of  $\hbar\omega_1 = 3.600$  eV, and the right panel, (b), for  $\hbar\omega_1 = 3.676$  eV. The full-width at half-maximum (FWHM) is 120 fs in both cases. In the lower-energy case, (a), the wavepacket does not have enough energy to go beyond the potential barrier and remains in the inner well, oscillating between 3.5 Å and 4.0 Å with a vibrational period of 340 fs. In the higher energy case, (b), the energy lies at the top of the barrier so that part of the wavepacket goes over the potential barrier and moves out to large internuclear distances. At the barrier, this wavepacket splits into a lower-energy component that remains in the inner well, and a higher-energy component that travels out to the outer well. At time  $t = 605$  fs after the pump-pulse, the wavepacket is peaked near 4.4 Å, at the potential barrier, and at 8.7 Å, the outer turning points of each well. The longer vibrational period is about 1 ps.

## 16.3.2

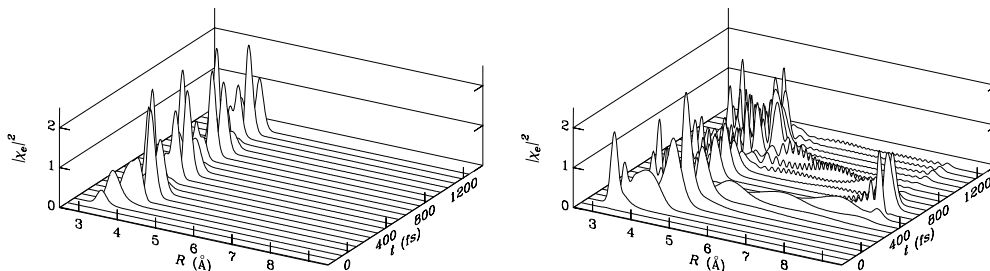


**Fig. 16.3** Time evolution of the absolute square of the excited-state wavepackets for pump energies (a)  $\hbar\omega_1 = 3.600$  eV and (b)  $\hbar\omega_1 = 3.676$  eV.

## Photoelectrons from a Rigid Rotor

Before presenting the full photoelectron spectra from a classically rotating  $\text{Na}_2$  molecule, we show in Figure 16.4 the angular dependence of the photoionization amplitude (see Eq. (8))

$$\left| \sum_{\ell m} C_{\ell m} Y_{\ell m}(\theta_k, \phi_k) \right|^2 \quad (17)$$

from a rigid  $\text{Na}_2$  rotor frozen at a specific internuclear distance. These distributions do not include any effects due to vibrational motion. Each row of Figure 16.4 dis-

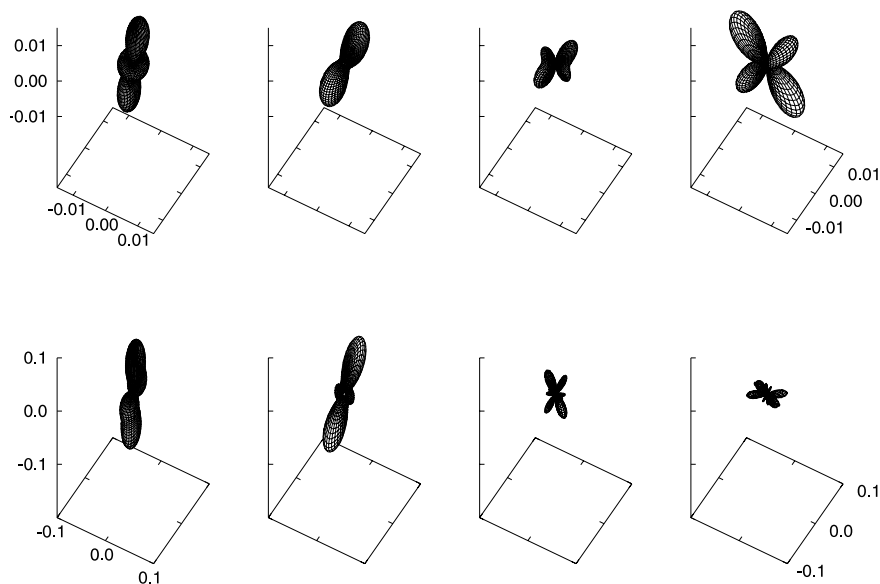


**Fig. 16.4** Angular dependence of the photoionization amplitudes  $|\sum_{lm} C_{lm} Y_{lm}(\theta_k, \phi_k)|^2$  for a photoelectron energy of 0.7689 eV and bond lengths of (a) 3 Å and (b) 9 Å.

plays the angular dependence of the photoionization amplitude for  $\text{Na}_2$  tilted to  $\theta_R = 10, 30, 60$ , and  $80^\circ$  in the XZ-plane for internuclear distances  $R$  of (a) 3.0 Å and (b) 9.0 Å, at a photoelectron energy of 0.7689 eV and for  $\theta_P = 0^\circ$ . In the inner-well region (3.0 Å), the distribution is clearly seen to be of  $d_{z^2}$  character as the molecule lies nearly parallel to the probe-pulse polarization vector, and of  $d_{xz}$  character when perpendicular to the probe-pulse polarization. The spatial distribution for the rotating molecule loses its  $d_{z^2}$  character and acquires  $d_{xz}$  character as the molecule rotates from the parallel to the perpendicular position. At the larger internuclear distance (9.0 Å), inclusion of the higher  $\ell$  components in Eq. (17) causes additional features to appear in the spatial distribution.

### 16.3.3

#### Convolution of Molecular Vibration and Rotation

We now show the pump-probe spectra for a rotating  $\text{Na}_2$  molecule. We assume a classical model for molecular rotation in the XZ-plane and 4080 fs per revolution. In the time that the molecule takes to rotate  $90^\circ$  from an initial orientation parallel to the probe polarization vector to a perpendicular orientation, the inner-well component of the wavepacket (pump photon of 3.600 eV) oscillates about three times while the outer-well component (pump photon of 3.676 eV) executes a single vibrational period. We probed the excited-state dynamics with a pulse of  $\hbar\omega_2 = 2.278$  eV

and a FWHM of 40 fs at various delay times. The rotation angle  $\theta_R$  is simply related to the delay time  $\Delta T$  by  $\theta_R = 0.08824(\Delta T)^\circ$  and the photoelectron kinetic energy distribution is given by

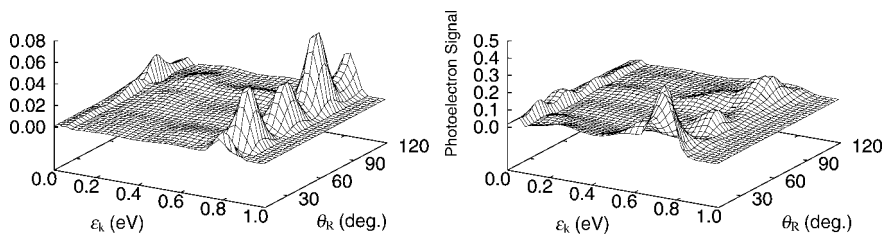
$$P(\varepsilon_k; \theta_R(\Delta T), \theta_P) = \sum_{\ell m} k \int dR |\chi_{k\ell m}(R, t_f; \theta_R(\Delta T), \theta_P)|^2. \quad (18)$$

Figure 16.5 shows these distributions for  $\theta_P = 0$  (parallel polarization). As discussed above, the photoelectron energy distribution changes only slightly with relative orientation of the probe polarization to the molecular axis, hence the effect of rotation is not immediately evident in Figure 16.5. In the case of the lower pump-photon energy (a), the effect of the depleted photoionization amplitudes in the region near 4 Å is apparent and the energy spectrum reflects the vibrational motion quite nicely. The peak at about  $\theta_R = 90^\circ$  is slightly larger than the others, as ionization is somewhat greater for the perpendicular case than for the parallel case at this pump energy.

In the case of the higher pump-photon energy, (b), the spectra are a little more complex since the wavepacket moves over larger distances and samples changes in the photoionization amplitudes across the well. The feature seen at the higher photoelectron energy arises from the inner-well and shows an oscillatory structure due to depletion of the photoionization amplitudes around the right turning point of the inner-well region. As originally noted by Engel *et al.*<sup>[22]</sup> and discussed more recently by ourselves,<sup>[16,17]</sup> the intense feature at low photoelectron energy for a pump-probe delay time of about 600 fs (see Figure 16.3(b)) arises from the wavepacket at its far turning point in the outer well. In Figure 16.5, this feature corresponds to  $\theta_R = 53^\circ$ , and is noticeably less intense than the strongest peak at  $\theta_R = 0^\circ$ . This is so because the photoelectron spectrum with the probe laser parallel to the molecular axis ( $\theta_R = 0$ ) is more intense than that with the probe laser perpendicular to the molecular axis and, at  $\theta_R = 53^\circ$ , a significant contribution to the spectrum arises from the perpendicular configuration of probe and molecular axes.

The angular distributions, integrated over photoelectron energy,

$$A(\theta_k; \theta_R(\Delta T), \theta_P) = \int dk k^2 \int dR \left| \sum_{\ell m} \chi_{k\ell m}(R, t_f; \theta_R(\Delta T), \theta_P) Y_{\ell m}(\theta_k, \phi_k) \right|^2 \quad (19)$$



**Fig. 16.5** Photoelectron kinetic energy distribution,  $P(\varepsilon_k, \theta_R)$ , for pump energies (a)  $\hbar\omega_1 = 3.600$  eV and (b)  $\hbar\omega_1 = 3.676$  eV.

reflect the role of molecular rotation more strongly than do the energy distributions in Figure 16.5. Figure 16.6 shows the angular dependence ( $\theta_k$ ) of the photoelectron spectra in the XZ-plane as the molecule rotates ( $\theta_R$ ). At low rotation angles, the angular distributions are generally of the  $d_{zz}$ -type whereas near  $\theta_R = 90^\circ$  the distribution shows  $d_{xz}$  character. The distributions vary between these two extremes as the molecule rotates. The photoelectron spectra for the lower (3.600 eV) and higher (3.676 eV) pump-photon energies, Figures 16.6(a) and (b), show a similar dependence on detection angle  $\theta_k$ , but differ greatly in their dependence on molecular orientation ( $\theta_R$ ). This is due more to vibrational dynamics than to rotational dynamics since it arises from the strong dependence of the photoionization amplitudes on internuclear distance. Figure 16.7, however, shows the corresponding angular distributions divided by the total ion signal in each case, i.e., by

$$P_{\text{ion}} = \int \sqrt{P(\varepsilon_k)} d\varepsilon_k^k. \quad (20)$$

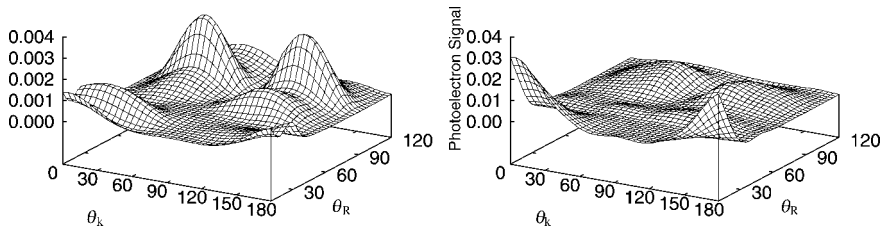


**Fig. 16.6** Photoelectron angular distribution,  $A(\theta_k, \theta_R)$ , in the XZ-plane ( $\phi_k = 0$ ) for pump energies (a)  $\hbar\omega_1 = 3.600$  eV and (b)  $\hbar\omega_1 = 3.676$  eV.

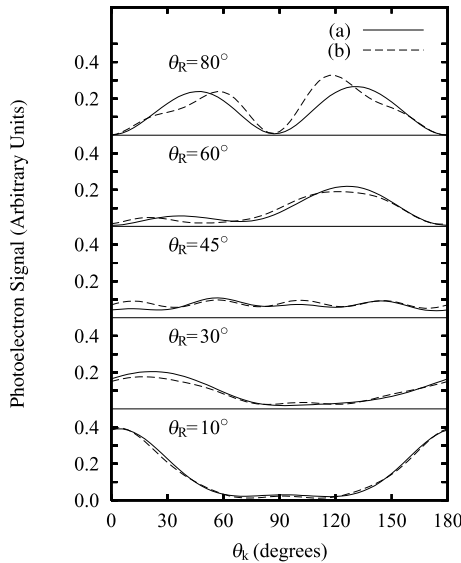


**Fig. 16.7** Normalized angular distributions,  $A(\theta_k, \theta_R)/P_{\text{ion}}$ , [see Eqs. (19) and (20)] for pump energies (a)  $\hbar\omega_1 = 3.600$  eV and (b)  $\hbar\omega_1 = 3.676$  eV.  $\phi_k = 0$  as in Figure 16.6.

The resulting angular distributions for the lower and higher photon energies are seen to be quite similar. The distribution for the larger pump-photon energy shows somewhat more structure when the molecule is almost perpendicular to the probe pulse. This stems from the effect of higher  $\ell$  components of the photoionization amplitudes at the larger internuclear distances accessed in this case. In both cases, the overall spectral shape gives a useful indication of molecular orientation with respect to the probe laser and can thus be used to monitor molecular rotation.

#### 16.4

##### Concluding Remarks

We have incorporated a classical treatment of molecular rotation into our formulation of energy- and angle-resolved pump-probe photoelectron spectroscopy,<sup>[17]</sup> which we have previously applied to molecules with fixed orientation relative to the probe laser.<sup>[16,17]</sup> This classical model of rotation is primarily suitable for describing the case of vibrational motion associated with slow rotation and where coherent couplings between rotational levels and between rotational and vibrational levels are weak. As a numerical example, we have shown how the energy- and angle-resolved photoelectron spectra for wavepackets on the  $^1\Sigma_u^+$  double-minimum state of the  $\text{Na}_2$  molecule are modified by rotation. The angle-resolved spectra are seen to sensitively reflect molecular rotation. On the other hand, although the energy-resolved spectra are less sensitive to rotation, the strong dependence of the photoionization amplitudes on internuclear distance and the large amplitude motion of the wavepacket on this double-minimum state introduce an additional complexity in the time-dependence of the photoelectron signal. Elsewhere, we propose a strategy for factoring out this rotational dependence from photoelectron signals that are dominated by vibrational motion.<sup>[23]</sup>

##### Acknowledgements

This work has been supported by a grant from the Ministry of Education, Science, and Culture (Japan) and the National Science Foundation (U.S.).

##### References

- 1 T. S. Rose, M. J. Rosker, A. H. Zewail, *J. Chem. Phys.* **1988**, 88, 6672.
- 2 A. H. Zewail, *Femtochemistry: Ultrafast Dynamics of the Chemical Bond*, World Scientific, Singapore, **1994**, Vols. 1 and 2.
- 3 J. Manz, L. Wöste (Eds.), *Femtochemistry*, VCH, Weinheim, **1995**.
- 4 P. Gaspard, I. Burghard, I. Prigogine, S. A. Rice (Eds.), *Chemical Reactions and Their Control on the Femtosecond Time Scale*, XXth Solvay Conference on Chemistry, *Adv. Chem. Phys.* **1997**, 101, Wiley, New York.

- 5 I. Fischer, D. M. Villeneuve, M. J. J. Vrakking, A. Stolow, *J. Chem. Phys.* **1995**, *102*, 5566; V. Blanchet, M. Z. Zgierski, T. Seideman, A. Stolow, *Nature* (London), **1999**, *401*, 52.
- 6 A. Assion, M. Geisler, J. Helbing, V. Seyfried, T. Baumert, *Phys. Rev. A* **1996**, *54*, R4605.
- 7 C. Juvet, S. Martrenchard, D. Solgadi, C. Dedonder-Lardeux, M. Mons, G. Grégoire, I. Dimicoli, F. Piuze, J. P. Visticot, J. M. Mestdagh, P. D'Oliveira, P. Meynadier, M. Perdrix, *J. Phys. Chem.* **1997**, *101*, 2555.
- 8 J. A. Davies, J. E. LeClaire, R. E. Continetti, C. C. Hayden, *J. Chem. Phys.* **1999**, *111*, 1.
- 9 T. Baumert, J. L. Herek, A. H. Zewail, *J. Chem. Phys.* **1993**, *99*, 4430.
- 10 T. Baumert, G. Gerber, *Adv. At. Mol. Opt. Phys.* **1995**, *35*, 163.
- 11 H. Ruppe, S. Rutz, E. Schreiber, L. Wöste, *Chem. Phys. Lett.* **1996**, *257*, 356.
- 12 X. Song, C. W. Wilkerson, J. Lucio, S. Pauls, J. P. Reilly, *Chem. Phys. Lett.* **1990**, *174*, 377.
- 13 M. R. Dobber, W. J. Buma, C. A. de Lange, *J. Chem. Phys.* **1993**, *99*, 836.
- 14 J. A. Syage, *Z. Phys. (D)* **1994**, *30*, 1.
- 15 T. Suzuki, L. Wang, K. Kohguchi, *J. Chem. Phys.* **1999**, *111*, 4859.
- 16 Y. Arasaki, K. Takatsuka, K. Wang, V. McKoy, *Chem. Phys. Lett.* **1999**, *302*, 363.
- 17 Y. Arasaki, K. Takatsuka, K. Wang, V. McKoy, *J. Chem. Phys.* **2000**, *112*, 8871.
- 18 Y. Arasaki, K. Takatsuka, K. Wang, V. McKoy, *J. Elec. Spec. Related Phen.*, **2000**, *108*, 89.
- 19 K. Takatsuka, Y. Arasaki, K. Wang, V. McKoy, *Faraday Discussions*, **2000**, *115*, 1.
- 20 R. R. Lucchese, D. K. Watson, V. McKoy, *Phys. Rev. A* **1980**, *22*, 421; R. R. Lucchese, G. Raseev, V. McKoy, *ibid.* **1982**, *25*, 2572; S. N. Dixit, V. McKoy, *J. Chem. Phys.* **1985**, *82*, 3546; R. R. Lucchese, K. Takatsuka, V. McKoy, *Phys. Rep.* **1986**, *131*, 147; K. Wang, V. McKoy, *J. Chem. Phys.* **1991**, *95*, 4977; *Annu. Rev. Phys. Chem.* **1995**, *46*, 275.
- 21 S. C. Althorpe, T. Seideman, *J. Chem. Phys.* **1999**, *110*, 147.
- 22 See, for example, V. Engel, *Chem. Phys. Lett.* **1991**, *178*, 130; Ch. Meier, V. Engel, *Chem. Phys. Lett.* **1993**, *212*, 691; M. Braun, Ch. Meier, V. Engel, *J. Chem. Phys.* **1996**, *105*, 530.
- 23 Y. Arasaki, K. Takatsuka, K. Wang, V. McKoy, *J. Chem. Phys.* **2001**, *114*, 7941.

## 17

**Femtosecond Time-Resolved Fluorescence and Anisotropy Decay Spectroscopy of a Dendrimer with Eight Chromophores at the Rim****Abstract**

The time-resolved fluorescence decay and fluorescence anisotropy depolarization of a second-generation flexible core dendrimer decorated with eight peryleneimide chromophores at the rim have been investigated using polarization-sensitive fluorescence up-conversion detection with a time resolution of ca. 250 fs. Under magic-angle polarization conditions, besides a nanosecond component related to the fluorescence decay times of the local and excimer-like emissions, two further major components are found, attributable to vibrational relaxation (5 ps) and singlet-singlet annihilation (5 ps), respectively. The vibrational-relaxation component is also found in the anisotropy measurements. In addition, an energy-transfer component of the order of 100–200 ps, a sub-ps process attributable to internal vibrational-energy redistribution (IVR), and a nanosecond process attributable to a partial rotation of the molecule have been identified.

**17.1****Introduction**

Dendrimers are highly branched, macromolecular systems, the structures of which can be defined on a molecular level and, as a result, they have been attracting a lot of attention not only from the synthetic point of view, but also from the point of view of their physical and chemical properties. Through synthetic modifications, one can control the number of peryleneimide chromophores attached to the surface of the nanoparticles. Applications of such dendrimers in several fields, such as host-guest chemistry,<sup>[1]</sup> analytical chemistry,<sup>[2]</sup> optoelectronics,<sup>[3]</sup> catalysis,<sup>[4]</sup> biology,<sup>[5]</sup> and medicine,<sup>[6]</sup> have been suggested. Dendrimers are also used to mimic the photo-physical processes of basic photosynthetic light-harvesting antenna systems.<sup>[7–11]</sup> Within our research group, dendrimers consisting of a polyphenylene core and decorated with peryleneimide chromophores at the rim have been investigated by single-molecule spectroscopy,<sup>[11]</sup> atomic-force microscopy,<sup>[12]</sup> as well as femtosecond<sup>[13–15]</sup> and picosecond<sup>[16]</sup> time-resolved spectroscopy. All the studies reported herein were performed on a second-generation flexible dendrimer **G2F8** (see

Figure 17.1a for its molecular structure) having a biphenyl core leading to a conical disc-shaped structure, and bearing eight peryleneimide chromophores at the rim. For comparison, the model compound **G0** (Figure 17.1b), consisting of one identical peryleneimide chromophore attached to a hexaphenyl structure, was also investigated.

In a previous publication, the photophysical properties of **G2F8**, as studied by means of single-photon timing (SPT) and femtosecond transient absorption, were reported.<sup>[13]</sup> The hydrodynamic volume calculated from anisotropy decay measurements led to an estimate of the rigid rotor diameter of **G2F8** of 4 nm. Based on steady-state spectroscopic data for the peryleneimide model compound **G0**, the Förster radius for dipole–dipole energy transfer was calculated to be 3.8 nm. It is therefore very probable that in **G2F8** two chromophores will be closer to each other than the Förster radius. The fluorescence decay of **G0** in chloroform measured by SPT was found to be mono-exponential with a decay time of 4.2 ns, while that of **G2F8** was found to be triple-exponential with a long decay time of 7.6 ns. It was suggested that this longest-decay component could be due to excited-state, excimer-like interactions between neighboring peryleneimide moieties.

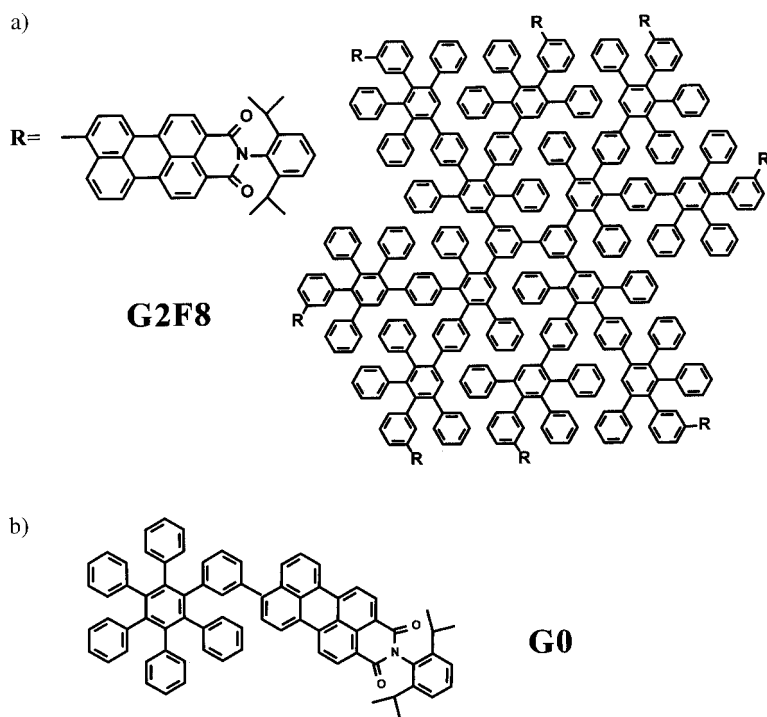


**Fig. 17.1** Molecular structures of the compounds investigated: **G2F8**: second-generation peryleneimide dendrimer; **G0**:

hexaphenylbenzene-peryleneimide model compound.



In order to gain further insight into the properties of the excited state of the chromophores in the dendrimer, time-resolved measurements aimed at investigating both the ultrafast fluorescence decay and the femtosecond depolarization kinetics have been carried out, the results of which are reported herein. By global analysis of data acquired throughout the complete emission spectrum, several decay components have been extracted and attributed to kinetic processes.

## 17.2

### Experimental Section

The syntheses of the dendrimer **G2F8** and the peryleneimide model compound **G0** (see Figure 17.1 for molecular structures) have been reported elsewhere.<sup>[17]</sup> As the solvent, chloroform (*Aldrich, spectrophotometric grade*) was used without further purification. All spectrophotometric measurements were made at room temperature on a chloroform solution of the dendrimer in a 1 mm optical path length cuvette. The sample solution showed an optical density of 0.5 per mm at the peak absorption wavelength.

The laser system has previously been described in detail.<sup>[18]</sup> In brief, an Nd:YVO<sub>4</sub> laser (*Millennia V, Spectra Physics*) is used to pump a Ti:sapphire laser (*Tsunami, Spectra Physics*), the output of which seeds a regenerative amplifier (*RGA, Spitfire, Spectra Physics*). The output of the RGA (1 mJ, 100 fs, 800 nm) is split into two equal parts, one of which is used to pump an optical parametric generator/amplifier (*OPA-800, Spectra Physics*). The output wavelength range of the OPA is extended by harmonic generation using one or two BBO crystals, thus making a range of 300–900 nm accessible.

The set-up used to detect the fluorescence up-conversion signal has also been described in detail elsewhere.<sup>[14]</sup> It utilizes the second part of the RGA output, which is sent to a variable delay and serves as the optical gate for the up-conversion of the sample fluorescence in an LBO crystal. The generated sum frequency light is then filtered out, collimated, and focused into the entrance slit of a 300 mm monochromator (*300I, Acton Research Co.*). A UV-sensitive photomultiplier tube (*R1527p, Hamamatsu*) is employed as a detector. The electrical signal from the photomultiplier tube is gated by a boxcar averager (*SR250, Stanford Research Systems*) and phase-sensitively detected by a lock-in amplifier (*SR830, Stanford Research Systems*).

For all the measurements performed here, the excitation wavelength was kept constant at 495 nm. All samples were irradiated with an excitation energy of ca. 350 nJ. By recording a steady-state absorption spectrum before and after each set of measurements, the sample integrity under these conditions was verified. Each measurement consisted of 1024 delay positions, at each of which the fluorescence signal, the excitation laser intensity, and the gate pulse intensity were recorded, with averaging over five seconds, thus resulting in a measurement time ca. 5000 s per delay scan. For each detection wavelength, a set of nine such measurements was made (three different polarization settings of 0°, 54.8°, and 90°; three different time windows of 5 ps, 50 ps, and 450 ps). Such a set of measurements was made for all

wavelengths in the range from 540 nm to 670 nm at intervals of 10 nm. In order to account for the system prompt response, scattered light from the sample was routinely used to determine the instrument response function, which was found to vary slightly with the detection wavelength; in all cases, a value of approximately 250 fs was obtained.

### 17.3

## Results and Discussion

### 17.3.1

#### Steady-State Spectroscopy

The steady-state absorption and fluorescence spectra of **G0** and **G2F8** are shown in Figure 17.2. The ground-state absorption spectra of the two compounds are very similar; minor differences are seen in the maxima of the spectra, that of **G0** being structured, and in the spectral bandwidth, which is  $140\text{ cm}^{-1}$  wider in the case of **G2F8**. The fluorescence spectra show more drastic differences; the spectrum of **G0** has a maximum at 574 nm and a shoulder at 600 nm, while that of **G2F8** is structureless and its maximum is red-shifted by  $1450\text{ cm}^{-1}$ . As reported previously, the fluorescence quantum yield decreases from 96 % in **G0** to 76 % in **G2F8**.<sup>[13]</sup>

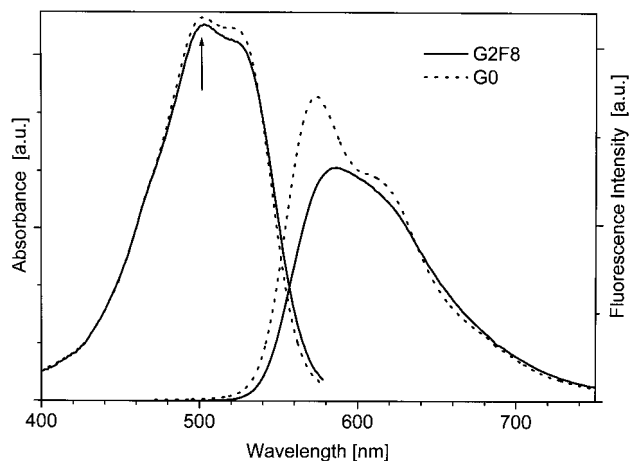


**Fig. 17.2** Steady-state absorption and normalized fluorescence emission spectra (*cf.* right ordinate) of the dendrimer **G2F8** (solid

lines) and the model compound **G0** (dotted lines). Arrow marking: excitation wavelength for all time-resolved measurements.

## 17.3.2

## Fluorescence Decays

The population dynamics in the samples could be derived from the data sets obtained in the magic-angle polarization configuration ( $54.8^\circ$ ). In Figure 17.3, typical examples of the fluorescence decay curves measured for **G0** and **G2F8**, detected at four different wavelengths, are shown together with the corresponding fitted curves. After deconvolution with the system prompt response, the data could be successfully fitted by a function comprised of a sum of exponentials, as judged by inspection of the residual plots and minimizing the  $\chi^2$  value.

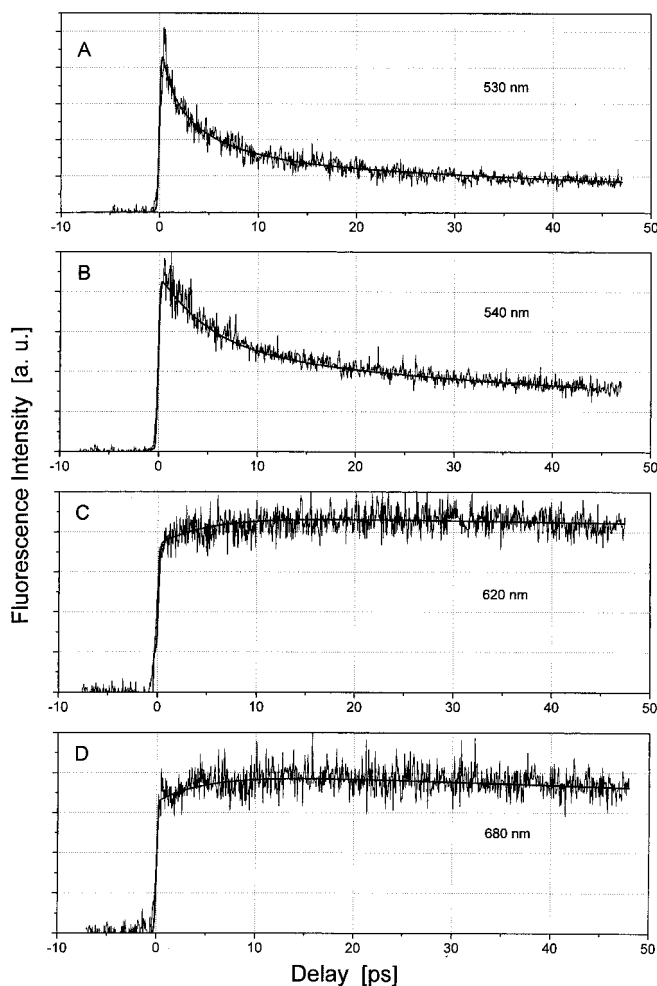


**Fig. 17.3** Fluorescence decay curves measured under magic-angle conditions and fit results for the dendrimer **G2F8** as determined for different detection wavelengths: A: 530 nm, B: 540 nm, C: 620 nm, D: 680 nm.

The data obtained for the model compound **G0** could be successfully fitted using two decay components with related times of  $\tau_2 = 5$  ps and  $\tau_4 = 4$  ns. The latter ( $\tau_4$ ) could not be determined precisely in the time windows used for the measurements here (maximum 450 ps), thus, while still varying the related amplitude  $a_4$  during the fitting procedure, this time was kept constant at  $\tau_4 = 4$  ns, a value known from previous SPT measurements.<sup>[13]</sup> Moreover, it was carefully checked that fixing the time  $\tau_4$  to any arbitrary value in the range from 2 ns to 10 ns did not alter in any way the fit results. Clearly, this component can be attributed to the fluorescence decay of the peryleneimide chromophore. It should be noted, however, that any other possible decay times in the nanosecond range (e.g., from dimeric chromophores) cannot be distinguished here and are not within the focus of this contribution.<sup>[16]</sup>

The amplitudes  $a_2$  associated with the 5 ps time constant, as determined for the model compound **G0**, are plotted as a function of wavelength in Figure 17.4 (solid line). These amplitudes are positive in the shorter wavelength domain, become almost zero at wavelengths between 560 nm and 600 nm, and are then strongly negative at wavelengths between 600 nm and 700 nm, which correspond to the maximum of the 0–1 vibrational band of the fluorescence at 625 nm. Such behavior of the amplitude spectrum and the corresponding decay time is found for many chromophores,<sup>[19–21]</sup> is typical of relaxation processes,<sup>[22–24]</sup> and can thus be attributed to a vibrational-relaxation process operative in the excited state of the peryleneimide chromophore. Moreover, this confirms previous results obtained for the same chromophore when it was attached to the rim of first-generation dendrimers with a rigid core.<sup>[25]</sup>

In contrast, the data obtained for the dendrimer **G2F8** could only be globally fitted with a wavelength-independent set of three exponential components. In this case, the corresponding decay times were found to be  $\tau_2 = 5$  ps,  $\tau_3 = 200$  ps, and  $\tau_4$  of

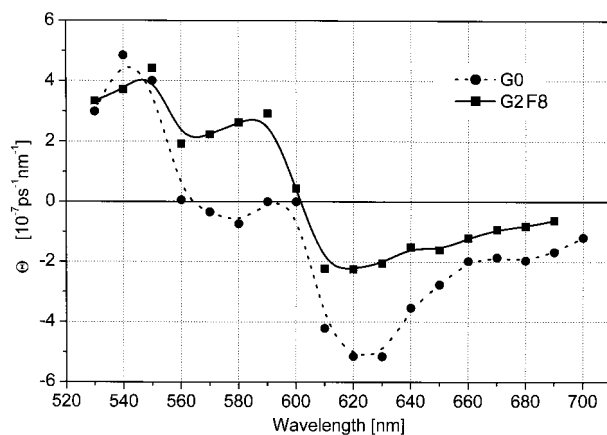


**Fig. 17.4** Quantum flux functions of the 5 ps kinetic component as found for the dendrimer **G2F8** (solid line) and the model compound

**G0** (dotted line) as a function of the fluorescence detection wavelength.

the order of a few nanoseconds. The latter is related to the fluorescence decays of the locally-excited state and the excimer-like emission, as discussed in detail in a separate publication.<sup>[26]</sup>

The time constant  $\tau_2$  determined for the dendrimer has the same value as that obtained for the model compound **G0**. However, the wavelength-dependent variation of the amplitude  $a_2$ , as displayed in Figure 17.4 (dotted line), is clearly different. On the one hand, the curve obtained is very similar in shape to that obtained for the monochromophoric model compound, while on the other hand, the whole curve appears to be shifted to higher amplitudes by an offset that is almost constant over the entire wavelength range. These observations are identical to those found for a different series of compounds consisting of identical peryleneimide chromophores attached to the rim of a first-generation dendrimer, which in this case contained a rigid core.<sup>[25]</sup>

In these previous studies, it was clearly shown that the kinetic component showing a very similar time constant of 6–10 ps was actually a combination of two kinetic contributions. The first of these proved to be wavelength-dependent and was seen both in mono- and multichromophoric compounds, including the model system **G0**, which is identical to that used here. It was attributed to a vibrational-relaxation process in the excited state and was found again here.

In the same studies, the second part of the 6–10 ps component was only found in multichromophoric compounds. It had a positive value for the amplitude, which proved to be independent of the detection wavelength. Moreover, its partial amplitude was clearly dependent on the excitation intensity. Taken together, these results gave a strong indication that this component was actually related to a singlet-singlet annihilation process operative in the multichromophoric dendrimer. By a straightforward extrapolation, the same assignment can seemingly be made for the multichromophoric **G2F8** investigated here (the fact that the actual value for this time constant is reduced to 5 ps might be due to the change from a first-generation to a second-generation dendrimer, as reported previously<sup>[13]</sup>). Thus, it is assumed that the 5 ps component shown in Figure 17.4 for **G2F8** (solid line) is *actually comprised of two different contributions*, namely a *vibrational-relaxation* process, which is identical to that found in **G0** (see Figure 17.4, dotted line), and an additional *singlet-singlet annihilation* component, which is only found in multichromophoric compounds such as **G2F8** investigated here.

The second-longest-lived component ( $\tau_3 = 200$  ps) is only found for the dendritic compound **G2F8**. An analogous component was found in the earlier investigation of the rigid-core dendrimers.<sup>[25]</sup> It proved to be dependent on the sample concentration and could be partly attributed to an intermolecular process; it is not discussed further here.

In order to further analyze the data, the fluorescence quantum flux function was calculated as described previously<sup>[14]</sup> and was plotted against the wavelength at various fixed delay times after excitation. Figure 17.5 depicts the results obtained for the model compound **G0** (left panel). In the first picoseconds, a rise of the 0–1 vibronic band at 624 nm can clearly be observed. These spectral changes can be attributed to the relaxation of vibrationally-hot, excited molecules,<sup>[27–29]</sup> from which emission

leading to the vibrationally-excited ground state is forbidden. At times longer than 20 ps, no further structural changes are observed, which is consistent with the single-exponential decay in the nanosecond time scale reported previously.<sup>[13]</sup> Thus, this analysis further supports the assignment of the 5 ps component to a vibrational-relaxation process that is operative in the excited state of the peryleneimide chromophore.

The time-dependent spectra of **G2F8** (see Figure 17.5, right panel) are more complex. Immediately after the excitation, the spectrum is similar to that of **G0** at this time, with a structure that is typical of the isolated peryleneimide chromophore. However, during the following 20 ps, the spectrum loses its vibrational structure

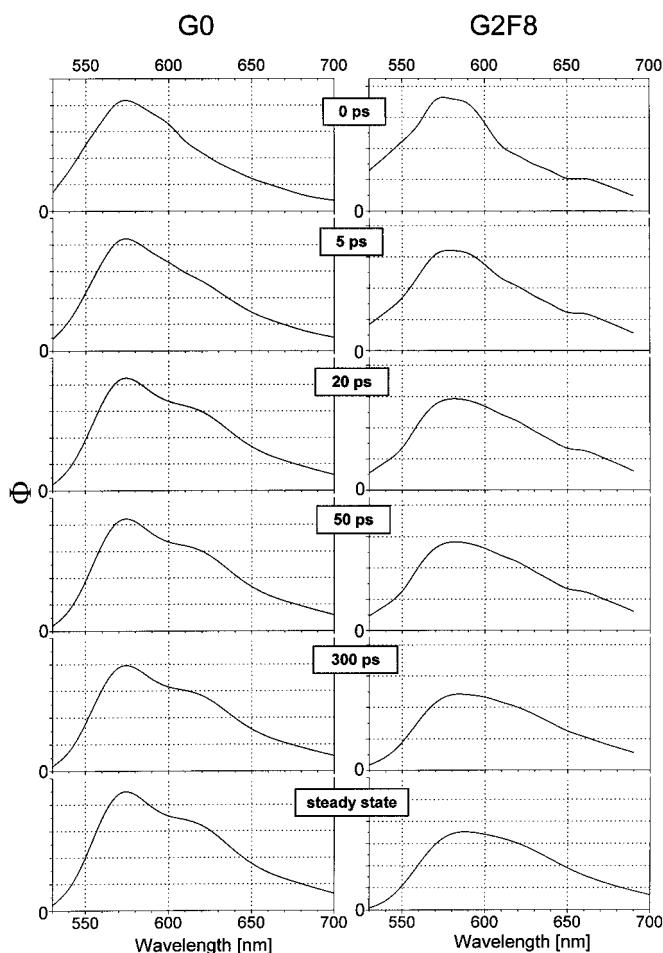


**Fig. 17.5** Fluorescence quantum flux as a function of the detection wavelength calculated for various delay times after excitation. Left panel: results for the model compound **G0**.

Right panel: results for the dendrimer **G2F8**. Bottom row: *measured* steady-state fluorescence spectra for the dendrimer (right) and the model.

and becomes similar to the steady-state spectrum of **G2F8**. At longer times, the emission spectrum of the dendrimer, in contrast to that of the model compound, becomes structureless.

### 17.3.3

#### Anisotropy Decays

The results of typical measurements performed to determine the depolarization properties are depicted in Figure 17.6 A (top), which shows the decays detected for compound **G2F8** with both parallel and perpendicular polarizations under otherwise identical conditions (i.e., detection wavelength 550 nm, time window 450 ps). Figure 17.6 B (bottom) shows a result determined under identical conditions with the sole exception that in this case the detection wavelength was set at 660 nm. After appropriate *g*-factor correction, these raw data were used to calculate the anisotropy decays as described previously.<sup>[13]</sup> Figure 17.7 shows the curves calculated for detection wavelengths of 560 nm, 610 nm, and 660 nm, respectively, along with the corresponding curves derived from the fits.

In the analysis of the data sets calculated in this manner, the data from all detection wavelengths and all three time windows were also deconvoluted and globally fitted by a function comprised of a sum of exponentials. As a result, four different exponential components were found to be necessary for an adequate fit of the data.

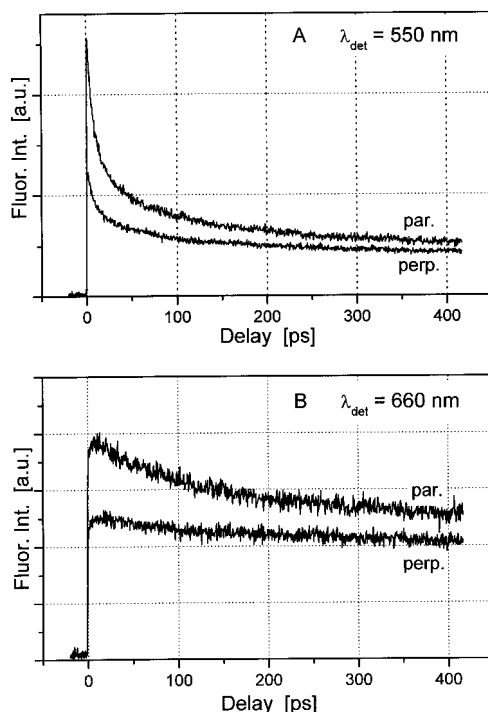


**Fig. 17.6** Fluorescence decays of the dendrimer **G2F8** measured under parallel (*par*) and perpendicular (*perp*) polarization conditions. Top (A): fluorescence detected at 550 nm; bottom (B) at 660 nm.

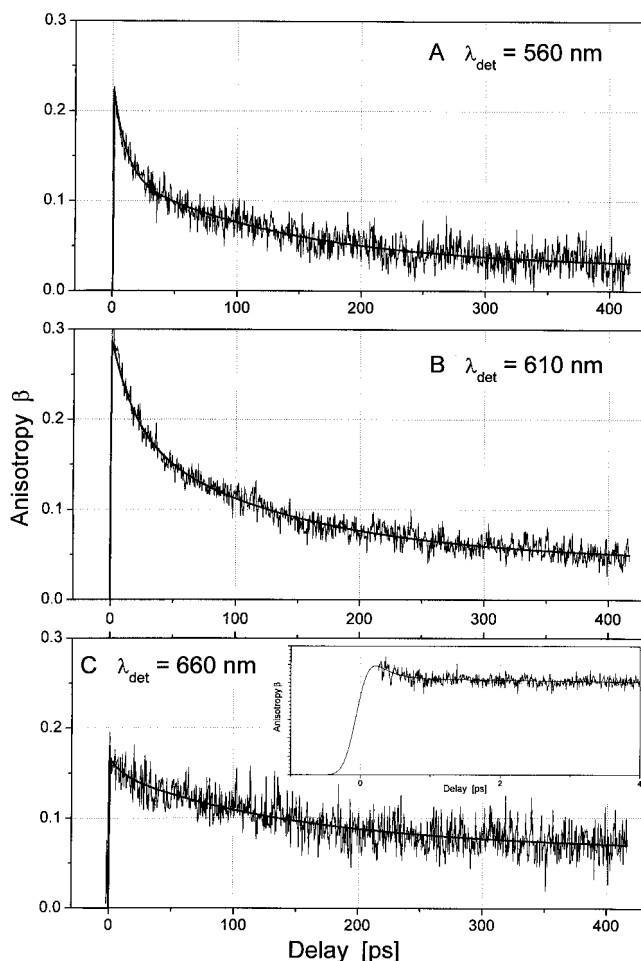


**Figure 17.7** Anisotropy decays for the dendrimer **G2F8** as calculated from measurements performed under parallel and perpendicular polarization conditions. Top (A); detected at 560 nm; middle (B); at 610 nm;

bottom (C) at 660 nm. Inset: Magnified view of 4 ps immediately after excitation. Thin lines: measured data; thick solid lines: results from fits.

Again, the longest time component could not be precisely determined here and was instead taken from SPT results.<sup>[13]</sup> All anisotropies, except for the shortest component, are almost independent of the detection wavelength:  $\tau_2$  is found to be 12 ps ( $\beta_2 = 0.09$ ),  $\tau_3 = 128$  ps ( $\beta_3 = 0.11$ ), and  $\tau_4 = 3.5$  ns (fixed,  $\beta_4 = 0.06$ ).

The fastest component of  $\tau_1 = 0.4$  ps shows a significant anisotropy of  $\beta_1 = 0.09$  when detected at 560 nm, and of 0.13 at 630 nm, whereas for all detection wavelengths longer than 630 nm the anisotropy  $\beta_1$  resulting from the global analysis is very close to zero. It is thus the only component that shows a variation of time ( $\tau_1$ ) and anisotropy ( $\beta_1$ ) upon changing the detection wavelength. Its significance is dem-



onstrated in Figure 17.7 (inset), which shows a temporal expansion of the time immediately after excitation detected at 580 nm. In agreement with other results obtained for the same chromophore in the subpicosecond time range,<sup>[25]</sup> this component can be assigned to an intramolecular vibrational-energy redistribution (IVR) process occurring within the peryleneimide immediately after the excitation. Such a process should clearly be dependent on the detection wavelength. However, it should be mentioned that the determination of this anisotropy time, associated with a rather low amplitude, is certainly at the limit of detection and analysis of our experiment.

In the light of the previous investigations,<sup>[13,25]</sup> and the results of the magic-angle measurements described above, a possible assignment can be made. Thus, the anisotropy decay time constant of 12 ps determined here may be related to the annihilation process as discussed above and/or to a reorientation of the chromophores that might occur during the relaxation process.

The third component ( $\tau_3$ ,  $\beta_3$ ) may reflect the energy transfer caused by the intramolecular Förster-type processes, which is in agreement with the values reported elsewhere<sup>[26]</sup> based on SPT. The small differences observed might stem from the fact that the previous results were obtained by polarization-selective pump-probe experiments, which monitor kinetic transitions from a different point of view.

The longest anisotropy component ( $\tau_4$ ,  $\beta_4$ ) can thus be directly attributed to a rotation or vibration of the entire dendritic molecule. As mentioned above, the time constant was not determined here, but was rather taken from SPT measurements.<sup>[13]</sup> The value obtained was in line with previous investigations on dendrimers of this type.<sup>[13–15,25]</sup>

## 17.4

### Conclusions

By applying polarization-sensitive fluorescence up-conversion detection techniques to the investigation of a second-generation flexible core dendrimer decorated with eight peryleneimide chromophores at the rim, various kinetic components have been determined and assigned. The fastest component found (0.4 ps anisotropy decay) is attributed to an IVR process. Additionally, two processes each having a time constant of 5 ps have been determined: the first is found both in the multichromophoric dendrimer and the monochromophoric model compound and is attributed to a vibrational-relaxation process that is operative in the electronic excited state. The second part is only seen in the multichromophoric dendrimer and is attributed to a singlet-singlet annihilation process.

### Acknowledgements

This work was supported by the FWO, the Flemish Ministry of Education through GOA 1/96, the Volkswagenstiftung, the EC through the TMR Sisitomas, and the DWTC (Belgium) through IUAP-IV-11.

## References

- 1 J. F. G. A. Jansen, E. M. M. De Brabander-Van den Berg, E. W. Meijer, *Science* **1994**, *266*, 1226.
- 2 O. A. Mathews, A. N. Shipway, J. F. Stoddard, *Prog. Polym. Sci.* **1998**, *23*, 1.
- 3 J. L. Atwood, J. E. C. Davies, D. D. Macnicol, F. Vögtle, J. M. Lehn, *Supramolecular Chemistry*, Pergamon Press, Oxford **1996**.
- 4 S. C. Stinson, *Chem. Eng. News* **1997**, *75*, 28.
- 5 J. C. Roberts, M. K. Bhalgat, T. R. Zera, *J. Biomed. Mater. Res.* **1996**, *30*, 53.
- 6 L. J. Twyman, A. E. Beezer, R. Esfand, M. J. Hardy, J. C. Mitchell, *Tetrahedron Lett.* **1999**, *40*, 1743.
- 7 E. K. L. Yeow, K. P. Ghiggino, J. N. H. Reek, M. J. Crossely, A. W. Bosman, A. P. H. J. Schenning, E. W. Meijer, *J. Phys. Chem. B* **2000**, *104*, 2596.
- 8 V. Balzani, F. Scandola, *Supramolecular Photochemistry*, Horwood, New York **1990**.
- 9 S. L. Gilat, A. Adronov, J. M. Frechet, *Angew. Chem. Int. Ed.* **1999**, *38*, 1422.
- 10 A. Bar-Haim, J. Klafter, R. Kopelman, *J. Am. Chem. Soc.* **1997**, *119*, 6197.
- 11 J. Hofkens, M. Maus, T. Gensch, T. Vosch, M. Cotlet, F. Köhn, A. Herrmann, K. Müllen, F. C. De Schryver, *J. Am. Chem. Soc.* **2000**, *122*, 9278.
- 12 H. Zhang, P. C. M. Grim, P. Foubert, T. Vosch, P. Vanoppen, U. M. Wiesler, A. J. Berresheim, K. Müllen, F. C. De Schryver, *Langmuir* **2000**, *16*, 9009.
- 13 J. Hofkens, L. Latterini, G. De Belder, T. Gensch, M. Maus, T. Vosch, Y. Karni, G. Schweitzer, F. C. De Schryver, A. Herrmann, K. Mullen, *Chem. Phys. Lett.* **1999**, *304*, 1.
- 14 Y. Karni, S. Jordens, G. De Belder, G. Schweitzer, J. Hofkens, T. Gensch, M. Maus, F. C. De Schryver, A. Herrmann, K. Mullen, *Chem. Phys. Lett.* **1999**, *310*, 73.
- 15 Y. Karni, S. Jordens, G. De Belder, J. Hofkens, G. Schweitzer, F. C. De Schryver, *J. Phys. Chem. B* **1999**, *103*, 9378.
- 16 M. Maus, S. Mitra, M. Lor, J. Hofkens, T. Weil, A. Herrmann, K. Müllen, F. C. De Schryver, *J. Phys. Chem.* **2001**, *105*, 3961.
- 17 F. Morgenroth, C. Kübel, K. Müllen, *J. Mat. Chem.* **1997**, *7*, 1207.
- 18 G. Schweitzer, L. Xu, B. Craig, F. C. De Schryver, *Opt. Commun.* **1997**, *142*, 283.
- 19 P. K. McCarthy, G. J. Blanchard, *J. Phys. Chem.* **1996**, *100*, 14592.
- 20 T. Gustavsson, G. Baldacchino, J. C. Mialocq, S. Reekmans, *Chem. Phys. Lett.* **1995**, *236*, 587.
- 21 W. Jarzeba, G. C. Walker, A. E. Johnson, M. A. Kahlou, P. F. Barbara, *J. Phys. Chem.* **1998**, *92*, 7039.
- 22 L. Reynolds, J. A. Gardecki, S. J. V. Frankland, M. L. Horng, M. Maroncelli, *J. Phys. Chem.* **1996**, *100*, 10337.
- 23 P. Changenet, H. Zhang, M. J. van der Meer, M. Glasbeek, P. Plaza, M. M. Martin, *J. Phys. Chem. A* **1998**, *102*, 6716.
- 24 P. Changenet, H. Zhang, M. J. van der Meer, K. J. Hellingwerf, M. Glasbeek, *Chem. Phys. Lett.* **1998**, *282*, 276.
- 25 G. De Belder, G. Schweitzer, S. Jordens, M. Lor, S. Mitra, J. Hofkens, S. De Feyter, M. Van der Auweraer, A. Herrmann, T. Weil, K. Mullen, F. C. De Schryver, *Chem. Phys. Chem.* **2001**, *1*, 49.
- 26 M. Maus et al., to be published.
- 27 R. M. Stratt, M. Maroncelli, *J. Phys. Chem.* **1996**, *100*, 12981.
- 28 S. N. Goldie G. J. Blanchard, *J. Phys. Chem. A* **1999**, *103*, 999.
- 29 Q. H. Zhong, Z. H. Wang, Y. Sun, Q. H. Zhu, F. N. Kong, *Chem. Phys. Lett.* **1996**, *248*, 277.

## 18

# Excited-State Dynamics of Conjugated Polymers and Oligomers

*Jean-Yves Bigot, Thierry Barisien*

### 18.1

#### Introduction

The delocalization of the  $\pi$  molecular orbitals in conjugated polymers, involving the electrons of the non-hybridized carbons of the polymer backbone, gives rise to some interesting physical properties. For example, the high conductivity of doped polyacetylenes<sup>[1]</sup> and the large third-order nonlinear optical susceptibility of polydiacetylenes<sup>[2]</sup> can both be attributed to this electron delocalization, which leads to a long-range coupling between the different carbons of the polymer chains. However, taking into account the delocalized character of the electronic wavefunctions is not sufficient for an understanding of the mechanisms of energy transfer that are operative in conjugated polymers. In addition, it is crucial to consider the coupling of the electronic excitations with the vibrations (vibronic coupling). This was clearly sensed in the early works of Su et al.,<sup>[3]</sup> who predicted the existence of neutral trapped states in *trans*-polyacetylene, these being associated with geometrical deformations of the polymer backbone. As a result of the degenerate dimerized ground state of this polymer, these deformations were shown to propagate like solitons.

The case of polydiacetylenes is particularly interesting to study since two different conformations of the backbone are possible. These are the polydiacetylenic (PDA) and polybutatrienic (PBT) structures, respectively, as represented in Figure 18.1 (a). In addition, the vibronic coupling between the first excited state and the stretching vibrations of the unsaturated carbon bonds is large. This can be seen in Figure 18.1 (b), which shows the optical density spectrum of a polydiacetylene pDCH thin film measured at 2 K. The side bands  $X_{C=C}$  and  $X_{C\equiv C}$  on the higher energy side of the excitonic resonance X give a signature of the strong vibronic coupling between the C=C and C $\equiv$ C backbone stretches and the excitons. In Section 18.2, we show that dynamic studies of polydiacetylenes, using femtosecond spectroscopy techniques, provide important information concerning the polymer configuration. In particular, the study of the dynamics of the excited states reveals that an ultrafast geometrical relaxation from the PDA to the PBT conformation takes place within  $\sim 150$  fs (Section 18.2.1). These experiments are modeled by the propagation of a wavepacket on the potential surfaces of a model polydiacetylene, which are determined by *ab initio* calculations of the ground and excited states using interaction

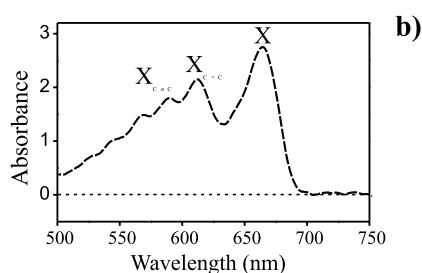
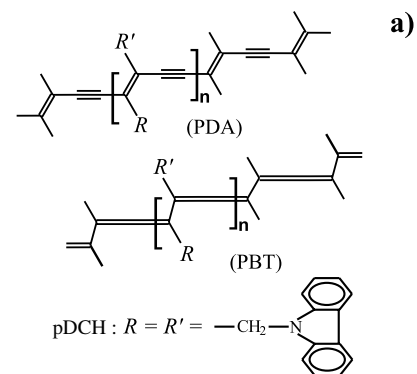


**Fig. 18.1** (a) Acetylenic and butatrienic geometrical conformations of a polydiacetylene chain (b) Optical density of a pDCH thin film.

configuration techniques (Section 18.2.2). The results indicate that the internal vibrational relaxation is a very efficient process leading to a trapping of the excitons in the lower-energy PBT potential, for which symmetry prevents the occurrence of radiative recombination.

The vibronic coupling is an intrinsic factor affecting the structure of polymers. In addition, there are extrinsic factors that induce chain distortions. An example of this arises from the structural defects that one finds in packed environments such as polymer aggregates or thin films. Both intrinsic and extrinsic geometrical factors have important consequences with regard to the optical properties of conjugated polymers. In particular, they play a determining role in the excited states, where they may open non-radiative channels for energy dissipation. In Section 18.3, we describe studies on the emission properties of a phenylene-vinylene pentamer having different degrees of structural disorder. First, it is shown that the structural disorder induces a fluorescence quenching of these conjugated oligomers (Section 18.3.1), as determined by static measurements of the amplified spontaneous emission (ASE). We then address the connection between structural disorder and fluorescence quenching by studying the femtosecond gain dynamics in thin films having varying degrees of disorder (Section 18.3.2).

## 18.2

### Femtosecond Dynamics of a Polydiacetylene Backbone

In a first approximation, conjugated polymers can be considered as one-dimensional systems where the main characteristic of the molecular motion is expected to be that propagating along the backbone through carbon–carbon stretching vibrations. Therefore, valuable information on the vibronic coupling can be obtained by studying the coherent molecular motion using femtosecond optical spectroscopy. The observation of such coherent molecular processes has been reported, for example, for the covalent and ionic predissociation stages of the molecule NaI,<sup>[4]</sup> as well as for the vibrational dynamics of large molecules in solution.<sup>[5]</sup> The wavepacket dynamics associated with such molecular motions has been investigated in several studies.<sup>[6–8]</sup> In the present case, the challenge has been the resolution of the fast movement associated with the high-frequency modes. For example, a  $1500\text{ cm}^{-1}$  C=C stretch corresponds to an oscillatory movement with a period of 23 fs. In the following section, we describe the observation of such ultrafast coherent molecular motion in the case of the polydiacetylene pDCH {poly[1,6-di(*n*-carbazolyl)-2,4 hexadiyne]}.

#### 18.2.1

##### Photon Echoes and Wavepacket Dynamics of pDCH

We performed photon-echo and pump-probe measurements using two optical pulses of 9 fs duration, which were propagated with a small angle between them. The pulses were obtained from a 60 fs colliding-pulse mode-locked laser, which was amplified with a copper-vapor laser operating at a repetition rate of 5 kHz. The 9 fs pulses, with a central wavelength of 620 nm, were obtained through a standard scheme<sup>[9]</sup> involving the generation of a spectral continuum in a 5  $\mu\text{m}$  core silica fiber and compensation for the phase dispersion using a sequence of gratings and prisms. The main beam was split into the pump and probe beams with an intensity ratio of 10:1. The maximum energy density focused on the sample was  $\sim 50\text{ }\mu\text{J cm}^{-2}$ . For the photon-echo experiment, the signal  $S_{\text{PE}}(\tau)$  generated in the direction  $2\mathbf{k}_{\text{probe}} - \mathbf{k}_{\text{pump}}$  was measured with a slow detector as a function of the pump-probe delay  $\tau$ . For the pump-probe measurements, differential transmission spectra  $\Delta T/T(\lambda, \tau)$  were measured in the probe direction using a 600 lines/mm dispersing spectrometer with a 120 mm focal length and a dual-array multichannel analyzer. The pDCH samples were oriented thin films obtained by a quasi-epitaxial growing technique on crystalline substrates of potassium acid phthalate.<sup>[10,11]</sup> Monocrystalline domains were obtained, which displayed a large dichroic ratio when the absorption spectra in the directions parallel and perpendicular to the chains were compared.

The phase dynamics of the excitonic resonance was studied by means of photon-echo techniques.<sup>[12]</sup> Figure 18.2 depicts a typical  $S_{\text{PE}}(\tau)$  signal. Its temporal variation displays rapidly damped oscillations that are characteristic of the quantum beats seen during the electronic dephasing process. In order to obtain more quantitative information, the photon-echo signal could be fitted with the modulated exponential decay associated with an inhomogeneously broadened three-level system. The tem-

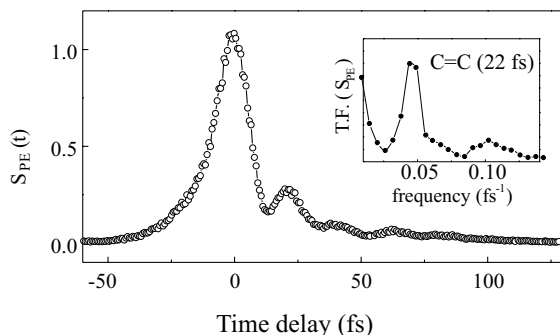


**Fig. 18.2** Photon-echo signal obtained with a pDCH thin film. The inset depicts the Fourier transform of  $S_{PE}$ .

poral period of the beats was found to be  $23 \pm 1$  fs and the dephasing time  $T_2$  was  $55 \pm 5$  fs. This is the signature of quantum beats between the exciton X and the double-bond vibronic level  $X_{C=C}$ . The short dephasing time indicates that an efficient relaxation mechanism is operative in the excited state, which contributes to the loss of coherence of the excitonic polarization.

The pump-probe experiments allow deeper insights into the dynamics associated with the molecular motion. The broad-band spectrum of the unchirped 9 fs pump pulse initially induces a coherent superposition of vibronic excited states. The associated non-stationary wavepacket can then be probed at various wavelengths as a function of the pump-probe delay  $\tau$ . Figure 18.3 (a) shows the spectro-temporal variation of the differential transmission. Three main features can be distinguished. First, well-contrasted oscillations with a period of 23 fs are observed. Their contrast reaches a maximum near the excitonic resonance ( $\lambda_x = 653$  nm). Second, the oscillations are seen to be rapidly damped. They vanish after long temporal delays, as can be seen in Figure 18.3 (b) which depicts the temporal variation of the integrated spectrum  $\Delta T/T(\tau)$ . The third interesting feature in Figure 18.3 (a) is the existence of an induced absorption for probe wavelengths  $\lambda > 670$  nm. The negative signal in this spectral region also oscillates with a period of 23 fs, but the oscillations have an opposite phase with respect to those measured in the vicinity of the excitonic resonance. This is shown in Figure 18.3 (c), where a contour plot of the differential transmission is displayed. The half-period dephasing between the oscillations is indicated by the arrows.

The oscillatory behavior of the pump-probe signal can be unambiguously attributed to the wavepacket motion associated with the stretching vibrations of the polymer backbone. The dominant contribution characterizing this coherent motion is that of the C=C double bond ( $23 \text{ fs} \leftrightarrow 1450 \text{ cm}^{-1}$ ). The induced absorption is due to excited-state transitions from the excitonic level to higher electronic levels. It is quasi-instantaneous since the 9 fs pump pulse initially populates a broad spectral density of excitonic states, allowing immediate absorption of probe photons to higher states. The  $\pi$  dephasing between the oscillations is due to the motion of the wavepacket in the configurational space, as sketched in Figure 18.4, which depicts the interaction of the pump and probe fields with three potential surfaces.

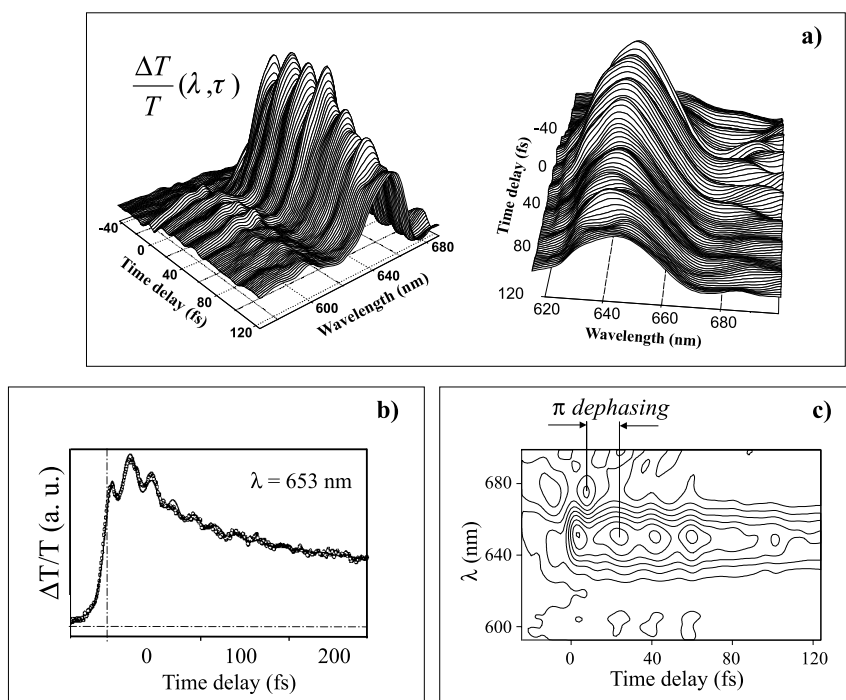


**Fig. 18.3** (a) Differential transmission  $\Delta T/T(\lambda, \tau)$  showing the excitonic (left) and induced absorption (right) wave packets.

(b) Spectrally integrated differential transmission  $\Delta T/T(\tau)$  showing the damping of the wavepacket. (c) Contour plot of  $\Delta T/T(\lambda, \tau)$ .

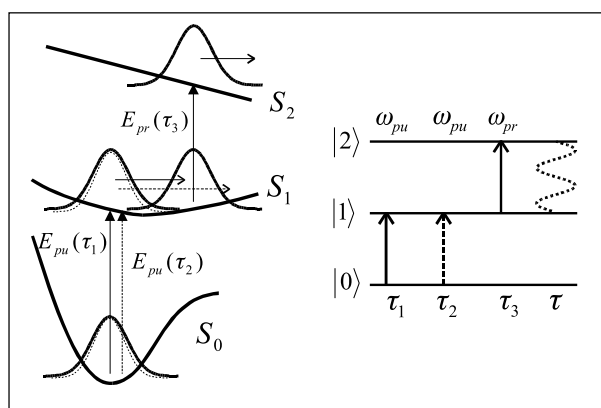


**Fig. 18.4** Sketch of wavepacket dynamics with  $\pi$  dephasing in the region of excited-state absorption.

The most interesting feature of the wavepacket dynamics shown in Figure 18.3 is its rapid damping. This requires an efficient mechanism for energy dissipation in the excited state, whereby the coherent molecular motion of the polymer backbone is damped. This mechanism is certainly different from that which leads to the vibrational dephasing  $\tau_{2\text{vib}}$  in the ground state. This can be simply inferred from the narrow spectral widths  $\Delta\nu_{\text{R}}$  of the Raman lines associated with the C=C and C $\equiv$ C bonds ( $\Delta\nu_{\text{R}} \approx 10 \text{ cm}^{-1}$ ). In earlier studies, an initial fast decay of the excitonic populations in various polydiacetylene films has been reported.<sup>[13–17]</sup> Fast trapping of the excitons has been invoked in order to account for this observation. In the next section we comment on this trapping process, which can be better understood in terms of a geometrical relaxation of the polymer chain in the excited state.

### 18.2.2

#### Structural Relaxation of a Model Polydiacetylene Chain: *Ab initio* Calculations of the Potential Surfaces

Various approaches can be used to model electronic excitations in conjugated polymers. In essence, these differ in the relative importance given to the correlation properties of the electrons with respect to the vibrations of the polymer chain. The band model description of a periodic solid, including electron–phonon interactions, is useful for describing the transport properties of the electrons in relation to the chain deformations (polarons).<sup>[3]</sup> However, such a description underestimates the electronic correlation when only single-particle interactions are considered. Correlation effects are better taken into account by including the many-body Coulomb interaction through the use of semiempirical models. At the Hartree–Fock level, this allows us to take into account correlated electron–hole pairs or excitons. Several models based on such an approach have successfully been used to describe the energy of the first excited states in polydiacetylenes.<sup>[18–20]</sup> The picture that emerges from such models is one of charge-transfer excitons, delocalized over a few monomer units, which are coupled to the vibrations. However, in the excited state the chain structure is not adequately described, which is a major drawback when considering the molecular dynamics. *Ab initio* models have provided a great deal of information regarding the ground state of PDA. An important result is the greater stability of the PDA isomer with respect to the PBT form, even though it was obtained within the Hartree–Fock approximation using a set of crystal orbital wavefunctions.<sup>[21]</sup>

A more rigorous approach has recently been developed,<sup>[22]</sup> which allows a determination of the potential-energy surfaces for the two isomeric conformations PDA and PBT, both in the ground and excited states. The quantum chemical calculations were carried out using complete active space self-consistent field methods (CASSCF, CASPT2). Calculations were performed on the monomer, the linear dimer, and the trimer, as well as on the cyclic trimer for each conformation. The main results obtained using the CASPT2 method, which are summarized in the potential surfaces shown in Figure 18.5, are as follows (note that the abscissa  $\delta$  represents the elongation of the C=C double bond). In the ground state, the PDA con-



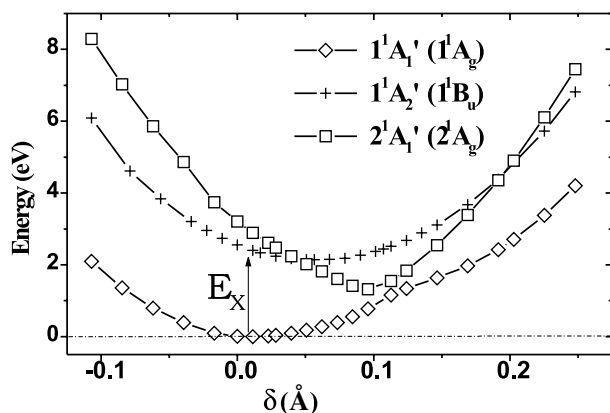


**Fig. 18.5** Potential surfaces of the PDA and PBT conformations in the ground and excited states, calculated using the CASPT2 method.

formation with  $1^1A_g$  symmetry is the most stable. In contrast to the Hartree–Fock calculations,<sup>[21]</sup> the PBT conformation does not exhibit a stationary state with a well-defined potential minimum. This is due to the better description of correlation effects in the present model. In the excited state, the most stable configuration is the  $2^1A_g$  PBT conformation, which has an energy minimum lower than the  $1^1B_u$  PDA conformation.

The potentials shown in Figure 18.5, obtained for the model cyclic trimer representation of the polymer, are very informative with regard to understanding the relaxation dynamics observed in polydiacetylenes. When the polymer is excited with an ultrashort optical pulse, the initial Franck–Condon transition occurs between the  $1^1A_g$  and  $1^1B_u$  states associated with the PDA conformation. The relaxation in the excited state then takes place through an energy transfer from the  $1^1B_u$  PDA to the  $2^1A_g$  PBT conformation. Since this process does not have an associated potential barrier, it can be very fast. A typical time scale is a few vibrational periods of the most active modes of the chain (the two potentials, which, in theory, are orthogonal states, must be coupled through other degrees of freedom, such as torsions of the chain). In this sense, one can attribute the initial step of energy relaxation, which has been found to occur within  $\sim 100$  fs in several polydiacetylenes, to an exciton trapping in the configurational space. The  $1^1B_u$  PDA potential can thus be ascribed to a free exciton and the  $2^1A_g$  PBT potential to a trapped exciton. In our opinion, it is preferable to describe this relaxation process in terms of a geometrical relaxation of the polymer chain between the PDA and PBT conformations. Beyond the semantics, an important aspect is that the coherence of the molecular motion is strongly affected by this energy relaxation. We believe that the damping of the coherent motion seen in Figure 18.3 stems from this internal energy transfer. Recent time-resolved fluorescence measurements, performed on *isolated* chains of the polydiacetylenes 3BCMU and 4BCMU embedded in their monomer matrices, confirm this interpretation.<sup>[16]</sup> A characteristic constant of 135 fs for the exciton lifetime corre-

sponding to the  $1^1B_u \rightarrow 2^1A_g$  internal conversion process has been determined. This lifetime is in good agreement with the rate deduced from our simulations.<sup>[22]</sup>

The ultrafast geometry relaxation in pDCH polymers has an important consequence. Since, for symmetry reasons, the PBT conformation is not optically coupled to the ground state, relaxation occurs through non-radiative processes (internal vibrational relaxation and inter-system crossing). Therefore, the fluorescence is not an efficient process. This is in agreement with pump-probe studies of the *isolated* chains of 4BCMU.<sup>[23]</sup> The authors interpreted the observed ultrafast photo-induced absorption in terms of two vibronic  $A_g$  states. Their interpretation, even if it does not take into consideration configurational space effects, also stresses the important role of non-radiative states in the relaxation process.

### 18.3

#### Femtosecond Gain Dynamics in Phenylene-Vinylene Pentamers

An understanding of the fluorescence quenching in polymers of the *para*-phenylene-vinylene family is of great importance in the context of the fabrication of organic light-emitting devices.<sup>[24–26]</sup> Several mechanisms, such as photoinduced oxidation,<sup>[27,28]</sup> stimulated emission, intra- and intermolecular energy transfer,<sup>[28–30]</sup> and exciton annihilation,<sup>[31,32]</sup> have been reported as being operative when the polymer is in the excited state. Here, attention is focussed on the problem of structural disorder. It is shown that it has a drastic influence on the emission properties of the oriented thin films of conjugated oligomers. Both the process of amplified spontaneous emission and the dynamical gain, as studied by means of femtosecond pump-probe spectroscopy, have been shown to depend on the crystallinity of the films. Our approach has involved study of the oligomer 5-ring *n*-octyloxy-substituted oligo(*p*-phenylene-vinylene) (Ooct-OPV5). In spite of the short oligomer length as compared to polymers, one can still take advantage of the conjugated properties of the electrons since the excitonic delocalization extends over a few monomer units. In addition, by virtue of their excellent molecular orientation, such oligomers can be grown as crystalline thin films.

#### 18.3.1

##### Amplified Spontaneous Emission of Phenylene-Vinylene Pentamers

Thin films of Ooct-OPV5 were prepared from saturated solutions of the oligomer in chloroform by spin-coating on glass substrates. As can be seen in Figure 18.6 (a), large crystalline domains are obtained upon recrystallization of the film from its liquid-crystalline phase.<sup>[33]</sup> The inset in Figure 18.6 (a) shows an electron diffraction pattern recorded from a sample area of 5  $\mu\text{m}$  diameter on a 100 nm thick film. Figure 18.6 (b) shows the (001) face of the crystal and its orthogonal view along the **b** axis. The conjugated backbones of the oligomers point along the growing direction of the crystals and make an angle of  $\sim 20^\circ$  with the substrate. The linear absorption of a 100 nm thick film, measured with a light polarization parallel to the chain, is

shown in Figure 18.6 (c) (curve II). The main resonance at 470 nm corresponds to the first excitonic state. In thick samples ( $> 200$  nm), the electronic diffraction gives rise to a more diffuse pattern characteristic of structural disorder. The corresponding linear absorption is shown in Figure 18.6 (c) (curve I). An additional absorption is present in the spectral region 410–470 nm, which we attribute to a density of localized states associated with the structural disorder observed by electron-diffraction microscopy. In the following, we shall distinguish between these two categories of films by referring to them being either ordered or structurally disordered samples. However, it is important to stress that both types of samples are characterized by a high dichroic ratio. The molecular orientation of the oligomers is therefore excellent (as compared, for instance, to that obtained using quasi-epitaxial growing techniques). Optically, both ordered and disordered samples have an extinction coefficient of  $\sim 2 \times 10^{-3}$  when they are oriented between crossed polarizers. Therefore, the structural disorder under scrutiny here is relatively minor as compared to that reported so far in relation to oriented phenylene-vinylene polymers or oligomers.

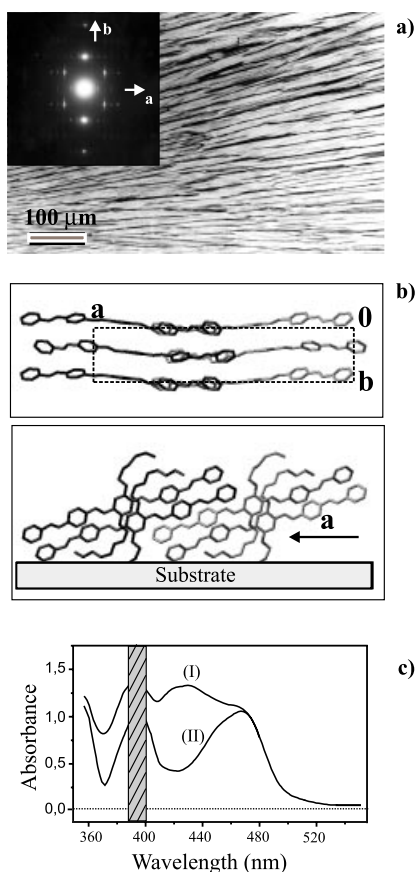


**Fig. 18.6** (a) Polarized light optical micrograph of an Ooct-OPV5 recrystallized thin film, obtained after slow cooling ( $20\text{ }^{\circ}\text{C}/\text{min}$ ) from the liquid-crystalline phase. Inset: electron diffraction pattern recorded from a  $25\text{ }\mu\text{m}^2$  area. (b) Schematic representation of Ooct-OPV5 on a glass substrate after recrystallization: (001) face of the oligomer crystal and its orthogonal view along the *b* axis. (c) Optical density of Ooct-OPV5 samples: (I) 200 nm thick, (II) 100 nm thick.

Figure 18.7 shows the evolution of the time-integrated fluorescence spectrum  $I_F(\lambda)$  for different absorbed energy densities  $I_p$  with a pump polarized parallel to the chain axis, obtained with a thin ordered film. The normalized spectra in Figure 18.7 (a) show the fluorescence spectral narrowing with increasing  $I_p$ . The variations in the fluorescence line widths  $\Delta\lambda$  (diamonds) and amplitudes  $I_F$  (circles) at the wavelength of the fluorescence maximum ( $\lambda = 535$  nm) are illustrated in Figure 18.7 (b). Up to  $\sim 10 \mu\text{J}/\text{cm}^2$ , the variations in  $\Delta\lambda$  and  $I_F$  correspond to the regime of amplified spontaneous emission (ASE). At higher excitation densities, a regime of saturated ASE is encountered, characterized by a broadening of the emission line.

The important point to be emphasized is that in Figure 18.7 the fluorescence and the pump are both polarized parallel to the chain axis. The ASE therefore behaves as expected in an amplifying medium, having a nonlinear gain, which shows a maximum when the chains are excited with a polarization *parallel* to the oligomer chains. However, the ASE behavior is drastically different in the thicker disordered films. In this case, it is obtained for a polarization of the pump *perpendicular* to the chain axis. In addition, the corresponding threshold for stimulation is five times higher than in the case of the thinner ordered samples. These results suggest the operation of a fluorescence-quenching mechanism associated with the structural disorder. In the next section, we discuss this mechanism in the context of the excited-state dynamics.

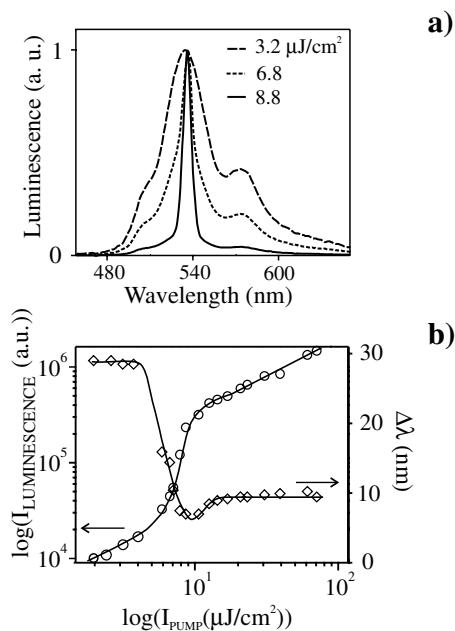


**Fig. 18.7** (a) Time-integrated emission spectra of the Ooct-OPV5 thin film showing the effect of amplified spontaneous emission. (b) Details of the corresponding fluorescence intensity (circles) and line width (diamonds) as a function of the pump-energy density.

## 18.3.2

**The Influence of Structural Disorder on the Femtosecond Gain Dynamics**

Pump-probe experiments were performed on the pentamer films using a tunable Ti:sapphire laser amplified at 5 kHz.<sup>[34]</sup> The beam was split into two parts, one of which was frequency-doubled in a BBO crystal providing pump pulses of 150 fs duration at 400 nm. The other part of the beam was used to generate a broad spectral continuum in a glass plate, which was compensated for the group velocity dispersion by double passes through a pair of gratings and a pair of BK7 prisms. This scheme does not allow for full compensation for the dispersion over the wide spectral range explored in this experiment. The remaining linear chirp was characterized by a cross-correlation between the continuum probe and the pump beams in a CuCl crystal. It was found to be  $\sim 100$  fs in the spectral range 500–700 nm. The probe energy density (integrated in the range 500–600 nm) was less than  $1 \mu\text{J}/\text{cm}^2$ . Conventional synchronous pump-probe detection was used to measure the differential transmittance  $\Delta T/T(\lambda, t)$ .

Figures 18.8 (a) and (b) show the spectral shapes of the pump-probe signals  $\Delta T/T(\lambda)$  for different temporal delays, obtained with an ordered sample (100 nm thick) (a) and a structurally disordered sample (200 nm thick) (b). In both cases, the

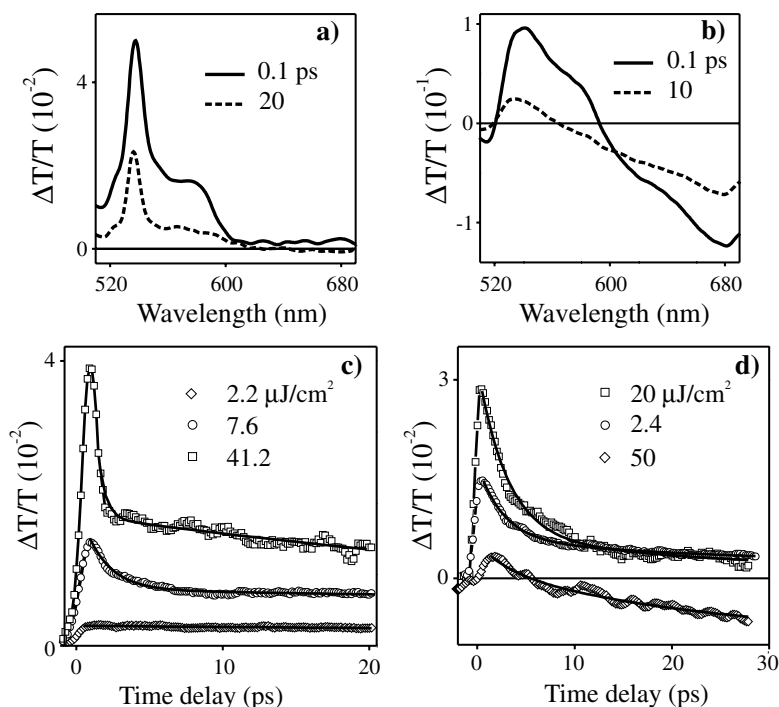


**Fig. 18.8** Differential transmission  $\Delta T/T(\lambda)$  (a,b) and  $\Delta T/T(\lambda = 535 \text{ nm}, \tau)$  (c,d) of Ooct-OPV5 films with thicknesses of 100 nm (a,c)

and 200 nm (b,d). The pump and probe polarizations are parallel to the chains.

pump polarization was set parallel to the chain axis and the absorbed excitation density was comparable ( $I_p \approx 12 \mu\text{J}/\text{cm}^2$ ). For the ordered sample, a large gain was seen over the whole spectral range of the delays (0.1 and 20 ps). For the disordered sample, a large induced absorption was seen above 600 nm. It is this induced absorption that prevents ASE from occurring in the thick films when the pump is polarized parallel to the chains of the oligomer. Figures 18.8 (c) and (d) show the time-dependent gain dynamics for the two different samples obtained by selecting a 15 nm spectral portion of the continuum centered at a wavelength 535 nm, for three different pump-energy densities. For the thin sample, the gain increases with increasing pump intensity, while in the case of the thick disordered sample, it first increases ( $20 \mu\text{J}/\text{cm}^2$ ) and then decreases ( $50 \mu\text{J}/\text{cm}^2$ ).

A detailed study of the gain dynamics was carried out under various conditions of polarization and excitation density.<sup>[35]</sup> All the results show that there is a strong correlation between the presence of structural disorder and the occurrence of fluorescence quenching. An important point to stress is that the structural disorder does not alter the polarization of the emitting species. The latter is always parallel to the chains and can therefore be unambiguously attributed to the excitons. Our proposed mechanism for the fluorescence quenching involves an induced absorption from localized states situated in the spectral range above the excitonic resonance. These have a polarization signature since the ASE process can still be obtained with a pump polarization perpendicular to the chains in the thick disordered films.

Further work will be necessary to characterize the electronic properties of the localized states that contribute to the quenching. The present study has highlighted the importance of molecular orientation in obtaining an efficient gain within conjugated polymer films. We believe that this is a crucial point that needs to be addressed in the context of the optimization of organic light-emitting devices.

## 18.4

### Conclusions

In this review, we have shown that the ultrafast dynamics of conjugated polymers and oligomers is strongly influenced by geometrical factors. The first example concerns the relaxation of a polydiacetylene chain from the acetylenic to the butatrienic conformations in the excited state, which has been investigated using ultrashort optical pulses. Pump-probe studies of pDCH thin films with 9 fs pulses have shown that the coherent motion associated with the stretching vibrations of the polymer chain is damped within the first 150 fs. The wavepacket generated by the pump pulse is seen to oscillate for about ten periods before it is dissipated on the first excited potential surface associated with the excitonic states. Conceptually, one may consider the polymer chain as being represented by a simplified backbone with a reduced number of coordinates in the configurational space. This allows modelling of the ground and excited states of the two PDA and PBT isomers using sophisticated *ab initio* quantum chemistry calculations taking into account the electron correlations at a high level. The structure of the potential surfaces obtained by includ-

ing dynamical correlation effects is consistent with the interpretation of an ultrafast internal energy conversion from the  $1^1B_u$  PDA to the  $2^1A_g$  PBT excited states. These studies have allowed a reinterpretation of the excitonic trapping effect, observed in several polydiacetylenes, in terms of a geometrical relaxation of the backbone conformation in the excited state.

The second example of a geometrical factor influencing the excited-state dynamics is extrinsic. It corresponds to a structural disorder that induces a fluorescence quenching in phenylene-vinylene pentamers. We have shown that it strongly affects the amplified spontaneous emission and gain dynamics of the oligomer octyloxy-OPV5. The dynamical studies have shown that a strong induced absorption is present in the disordered samples and that it considerably reduces the gain. This induced absorption is most likely related to a density of localized states situated above the energy of the excitonic resonance. From a practical point of view, it has been shown that the molecular orientation is a critical parameter that needs to be controlled in order to obtain efficient light-emitting organic materials.

### Acknowledgements

We would like to acknowledge J. Le Moigne and T.-A. Pham of the *Institut de Physique et Chimie des Matériaux de Strasbourg* (IPCMS) for their participation in the sample growth and dynamical measurements performed on pDCH. The *ab initio* calculations on the model PDA system were performed in collaboration with C. Daniel and M. Turki at the *Laboratoire de Chimie Quantique de Strasbourg*. The pentamer films of phenylene vinylene were grown thanks to a collaboration with the group of G. Hadziioannou in the Polymer Chemistry Department at the University of Gröningen. The gain dynamics in this pentamer was measured with the help of T.-A. Pham and L. Guidoni at the IPCMS. We thank them all for their expert contributions to this work.

## References

- 1 A. J. Heeger, S. Kivelson, J. R. Schrieffer, W.-P. Su, *Rev. Mod. Phys.* **1988**, 60, 781–850.
- 2 F. Kajzar, J. Messier, in *Nonlinear Optical Properties of Organic Molecules and Crystals*, Vol. 2 (Eds.: D. S. Chemla, J. Zyss), Academic Press, Orlando, **1987**, 51–83. For a review of the electronic properties of polydiacetylenes, see the article by M. Schott, G. Wegner, in the same book, pp. 3–49.
- 3 W. P. Su, J. R. Schrieffer, A. J. Heeger, *Phys. Rev. Lett.* **1979**, 42, 1698–1701; W. P. Su, J. R. Schrieffer, A. J. Heeger, *Phys. Rev. B* **1980**, 22, 2099–2111.
- 4 T. S. Rose, M. J. Rosker, A. H. Zewail, *J. Chem. Phys.* **1988**, 88, 6672–6673.
- 5 H. L. Fragnito, J.-Y. Bigot, P. C. Becker, C. V. Shank, *Chem. Phys. Lett.* **1989**, 160, 101–104.
- 6 R. Bersohn, A. H. Zewail, *Ber. Bunsenges. Phys. Chem.* **1988**, 92, 373.
- 7 S.-Y. Lee, W. T. Pollard, R. A. Mathies, *J. Chem. Phys.* **1989**, 90, 6146–6150; W. T. Pollard, S.-Y. Lee, R. A. Mathies, *J. Chem. Phys.* **1990**, 92, 4012–4029.
- 8 For a review, see: B. M. Garraway, K.-A. Suominen, *Rep. Prog. Phys.* **1995**, 58, 365–419.
- 9 R. L. Fork, C. H. Brito Cruz, P. C. Becker, C. V. Shank, *Opt. Lett.* **1987**, 12, 483–485.
- 10 J. Le Moigne, F. Kajzar, A. Thierry, *Macromolecules* **1991**, 24, 2622–2628.
- 11 V. da Costa, J. Le Moigne, T.-A. Pham, J.-Y. Bigot, *Synth. Met.* **1996**, 81, 151–154.
- 12 T.-A. Pham, A. Daunois, J.-C. Merle, J. Le Moigne, J.-Y. Bigot, *Phys. Rev. Lett.* **1995**, 74, 904–907.
- 13 B. I. Greene, J. F. Mueller, J. Orenstein, D. H. Rapkine, S. Schmitt-Rink, M. Thakur, *Phys. Rev. Lett.* **1988**, 61, 325–328.
- 14 A. Yasuda, M. Yoshizawa, T. Kobayashi, *Chem. Phys. Lett.* **1993**, 209, 281–286; T. Kobayashi, M. Yoshizawa, U. Stamm, M. Taiji, M. Hasegawa, *J. Opt. Soc. Am. B* **1990**, 7, 1558–1578; M. Yoshizawa, A. Yasuda, T. Kobayashi, *Appl. Phys. B* **1991**, B53, 296–307.
- 15 J.-Y. Bigot, T.-A. Pham, T. Barisien, *Chem. Phys. Lett.* **1996**, 259, 469–474; J.-Y. Bigot, T.-A. Pham, in *Femtochemistry*, Ultrafast Chemical and Physical Processes in Molecular Systems (Ed.: M. Chergui), World Scientific, Singapore, **1996**, 616–622.
- 16 B. Kraabel, M. Joffe, C. Lapersonne-Meyer, M. Schott, *Phys. Rev. B* **1998**, 58, 15777–15788.
- 17 T. Fuji, T. Saito, T. Kobayashi, in *Quantum Electronics and Laser Science Conference*, OSA Technical Digest (Optical Society of America, Washington DC), **2000**, p. 220–221; T. Kobayashi, A. Shirakawa, H. Matsuzawa, H. Nakanishi, *Chem. Phys. Lett.* **2000**, 321, 385–393.
- 18 M. R. Philpott, *Chem. Phys. Lett.* **1977**, 50, 18–21.
- 19 R. Yarkony, *Chem. Phys.* **1978**, 33, 171–178.
- 20 S. Suhai, *Phys. Rev. B* **1984**, 29, 4570–4581.
- 21 A. Karpfen, *J. Phys. C* **1980**, 13, 5673–5689.
- 22 M. Turki, T. Barisien, J.-Y. Bigot, C. Daniel, *J. Chem. Phys.* **2000**, 112, 10526–10537.
- 23 S. Haacke, J. Berrehar, C. Lapersonne-Meyer, M. Schott, *Chem. Phys. Lett.* **1999**, 308, 363–368.
- 24 J. H. Burroughes, D. D. C. Bradley, A. R. Brown, R. N. Marks, K. Mackay, R. H. Friend, P. L. Burns, A. B. Holmes, *Nature* **1990**, 347, 539–541.
- 25 F. Hide, M. A. Diaz-Garcia, B. J. Schwartz, M. R. Andersson, P. Qibing, A. J. Heeger, *Science* **1996**, 273, 1833–1836.
- 26 D. Bradley, *Nature* **1996**, 382, 671.
- 27 N. T. Harrison, G. R. Hayes, R. T. Phillips, R. H. Friend, *Phys. Rev. Lett.* **1996**, 77, 1881–1884.
- 28 L. J. Rothberg, M. Yan, F. Papadimitrakopoulos, M. E. Galvin, E. W. Kwock, T. M. Miller, *Synth. Met.* **1996**, 80, 41–58.
- 29 M. Yan, L. J. Rothberg, F. Papadimitrakopoulos, M. E. Galvin, T. M. Miller, *Phys. Rev. Lett.* **1994**, 72, 1104–1107; M. Yan, L. J. Rothberg, E. W. Kwock, T. M. Miller, *Phys. Rev. Lett.* **1995**, 75, 1992–1995.
- 30 W. Graupner, G. Leising, G. Lanzani, M. Nisoli, S. De Silvestri, U. Scherf, *Phys. Rev. Lett.* **1996**, 76, 847–850.
- 31 V. I. Klimov, D. W. McBranch, N. N. Barashkov, J. P. Ferraris, *Chem. Phys. Lett.* **1997**, 277, 109–117; V. I. Klimov, D. W. McBranch, N. Barashkov, J. Ferraris, *Phys. Rev. B* **1998**, 58, 7654–7662.
- 32 G. J. Denton, N. Tessler, N. T. Harrison, R. H. Friend, *Phys. Rev. Lett.* **1997**, 78, 733–736.



- 33 R. E. Gill, A. Meetsma, G. Hadziioannou, *Adv. Mater.* **1996**, 8, 212–214; R. E. Gill, Ph.D. Thesis, University of Groningen, **1996**.
- 34 T.-A. Pham, T. Barisien, V. Grayer, L. Guidoni, G. Hadziioannou, J.-Y. Bigot, *Chem. Phys. Lett.* **2000**, 318, 459–465.
- 35 T. Barisien, T.-A. Pham, L. Guidoni, V. Grayer, G. Hadziioannou, J.-Y. Bigot, submitted to *Phys. Rev. B*.

## 19

**Excited-State Intramolecular Proton Transfer (ESIPT) and Energy Relaxation Processes in Hydroxyphenylbenzotriazole Derivatives: A Femtosecond Laser Study***Thierry Fournier, Stanislas Pommeret, Jean-Claude Mialocq, and Anré Deflandre***Abstract**

Excited-state intramolecular proton-transfer (ESIPT) is among the most important and fastest unimolecular photoreactions in chemistry. In this contribution, we present the results of a femtosecond absorption experimental study on a so-called TIN derivative [2-(2*H*-benzotriazol-2-yl)-4-methyl-6-(2-methyl-3-{1,3,3,3-tetramethyl-1-[(trimethylsilyl)oxy]disiloxanyl}propyl)phenol] in *n*-heptane, which was photoexcited at 305 and 346 nm in two different absorption transitions. The transient excited states are the  $S_1$  enol state ( $\tau_1 = 50$  fs), the  $S_1$  keto state ( $\tau_2 = 130$  fs), the  $S_0$  keto state ( $\tau_3 = 500$  fs), and the longer-lived hot enol ground state.

**19.1****Introduction**

Organic compounds that have found substantial applications as UV-photostabilizers or screeners<sup>[1–3]</sup> belong to two distinct classes: absorbers for polymers and cosmetic absorbers to filter out light below approximately 320 nm, the latter having higher requirements from a toxicological point of view. Such compounds absorb ultraviolet light and must dissipate the excitation energy in a manner innocuous to the substrate and at a faster rate than any competing chemical reaction. They transform the electronic energy into thermal (i.e. vibrational) energy solely in the singlet manifold through efficient radiationless deactivation pathways. In compounds of this type that have been actively studied over the last thirty years [e.g. salicylic acid, 2-hydroxybenzophenones, 2-hydroxyphenylbenzothiazoles, 2-hydroxyphenyl-*s*-triazines, and 2-(2-hydroxyphenyl)benzotriazoles],<sup>[4–6]</sup> photoprotection is due to the presence of a 2-hydroxy group, which is essential for the formation of a stable intramolecular hydrogen bond in the relevant environments. It is also well-established that bulky groups in the position *ortho* to the hydroxy group lessen the influence of hydrogen-bond-breaking solvents.<sup>[1]</sup> For many of these compounds, the efficient relaxation mechanism first proposed by Otterstedt<sup>[7]</sup> involves the participation of an “enol-keto tautomerism” in the excited state resulting from a fast excited-state intramolecular proton transfer (ESIPT). Since the acidities of phenolic hydroxyl groups and the

basicities of the carbonyl oxygens or the heterocycle nitrogens are raised by about six pK units in the first excited singlet state, the proton transfer becomes more probable.<sup>[3]</sup> The proton transfer is followed by a red fluorescence emission with a very large Stokes shift with respect to the absorption band of the original molecule and a proton back-transfer in the ground state. One of the best known compounds in this context is 2-(2'-hydroxy-5'-methylphenyl)benzotriazole (Tinuvin P or TIN P; trade name of Ciba Geigy Ltd., see Figure 19.1), the optical properties of which have been extensively studied.<sup>[1,7–23]</sup>

In a preliminary paper, we described the excited-state intramolecular proton-transfer (ESIPT) in a hydroxyphenylbenzotriazole derivative substituted by a bulky group possessing three silicon atoms, 2-(2*H*-benzotriazol-2-yl)-4-methyl-6-(2-methyl-3-{1,3,3,3-tetramethyl-1-[(trimethylsilyl)oxy]disiloxanyl}propyl)phenol (TINSi), which was excited at 346 nm in the lower-energy absorption band.<sup>[24]</sup> In the present contribution, we compare the relaxation of the excited states following excitation of TINSi at 346 nm and 305 nm, near the maxima of the two absorption bands, in order to compare the photophysical properties and the photochemical reactivities of the initially photoexcited states of this molecule.

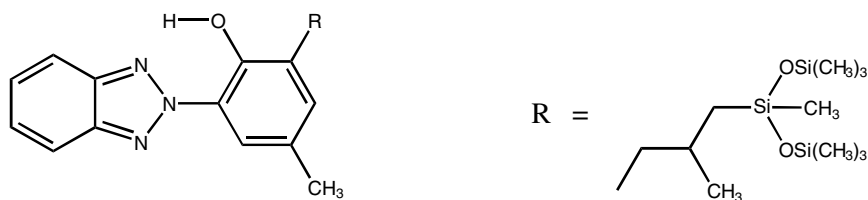


Fig. 19.1 Formula of TINSi molecule (for TIN molecule R = H).

## 19.2

### Experimental Section

#### 19.2.1

##### Chemicals

TINSi, i.e. 2-(2*H*-benzotriazol-2-yl)-4-methyl-6-(2-methyl-3-{1,3,3,3-tetramethyl-1-[(trimethylsilyl)oxy]disiloxanyl}propyl)phenol (CAS number: 155633–54–8, Mexoryl®XL, G4375, batch DG004, 99.9% purity), is a L'Oréal product. TIN, i.e. 2-(2-hydroxy-5-methylphenyl)benzotriazole from Ciba-Geigy Ltd. (trade name Tinuvin P) was recrystallized from methanol/heptane. The chemical structures are shown in Figure 19.1. All solvents used [*n*-heptane, carbon tetrachloride (CCl<sub>4</sub>), methanol (MeOH), ethanol (EtOH), 1-propanol (1-PrOH), 1-butanol (1-BuOH), acetonitrile (MeCN), dimethylacetamide (DMA), dimethyl sulfoxide (DMSO)] were of spectrophotometric grade (Aldrich, Fluka, or Merck UVASOL); their fluorescence spectra were recorded and subtracted where necessary. The laser dye 4-(dicyanomethylene)-

2-methyl-6-[*p*-(dimethylamino)styryl]-4*H*-pyrane (DCM) (Lambdaphysik Lambda-chrome) was used as such for fluorescence quantum yield measurements.

### 19.2.2

#### Steady-State Spectroscopy

UV/vis absorption spectra were recorded with a Varian Cary 3E spectrophotometer. Fluorescence spectra were recorded with a SPEX Fluorolog and were corrected for instrument response over the 375–650 nm spectral range for the emission spectra and over the 250–600 nm range for the excitation spectra.

### 19.2.3

#### Femtosecond Time-Resolved Spectroscopy

The pump-probe time-resolved UV/vis absorption set-up was based on a Ti:sapphire laser system consisting of a mode-locked oscillator and regenerative and multi-pass amplifiers delivering femtosecond pulses of duration 75 fs (FWHM) and energy 1 mJ at 800 nm with a 20 Hz repetition rate. A part of these pulses was passed to a water cell to produce a white-light continuum (WLC), which was dispersed to allow selection of a spectral band at 610 nm prior to its amplification in a four-stage dye (sulforhodamine) amplification system. Femtosecond pump pulses (energy 25  $\mu$ J) were generated at 346 nm by frequency-mixing the outputs of the Ti:sapphire laser system at 800 nm and of the dye amplifier at 610 nm in a 200  $\mu$ m-thick BBO crystal. Pump pulses of energy 20  $\mu$ J were generated at 305 nm by frequency-doubling the output of the dye amplifier in the same BBO crystal. A small part of the 800 nm pulse was focussed in a 1 mm-thick CaF<sub>2</sub> plate to produce a WLC from 350 nm to 800 nm for the probe and reference pulses (see Figure 19.2). The WLC pulse was separated into two beams so as to have a probe and a reference going through the sample and the dispersed transmitted light was detected by a CCD camera. The signal was passed to a PC and averaged over 2500 to 3500 pump pulses per delay-time step. The pump-probe inter-correlation ( $120 \pm 10$  fs and  $220 \pm 20$  fs FWHM for the 346 nm and 305 nm pump pulses, respectively) was measured, as indicated in Figure 19.3, by monitoring the photobleaching of rhodamine 6G in methanol in the 500–515 nm range (where the absorption and gain of the excited species are minimal and do not complicate the signal), as described elsewhere.<sup>[25]</sup> The group velocity dispersion (GVD) correction for the zero time delay *versus* wavelength was realized by a previously described method.<sup>[26]</sup> The TINSi solution was prepared in *n*-heptane and passed through a flow cell (sample thicknesses: 250  $\mu$ m for a 4 mM solution –pumped at 305 nm; 500  $\mu$ m for a 2 mM solution pumped at 346 nm). We checked the steady-state absorption spectrum before and after every experiment to verify that no photodegradation had taken place.

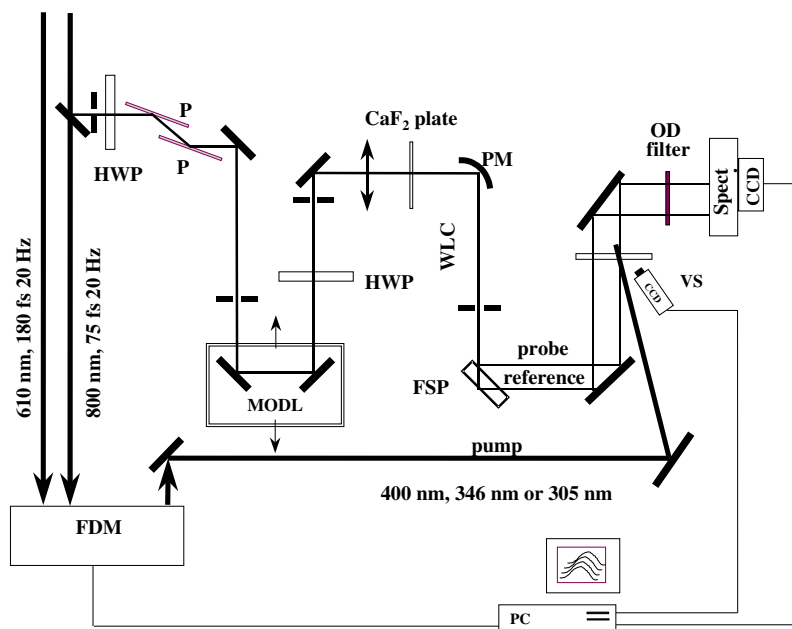


**Fig. 19.2** Schematic of the femtosecond transient absorption experiment. P: reflective polarizer; HWP: half-wave plate; PM: parabolic mirror; MODL: motorized optical delay line;

FSP: thick fused-silica plate; VS: pump-probe overlap visualization system; WLC: white-light continuum; FDM: frequency doubling and mixing; Spect.: spectrometer.

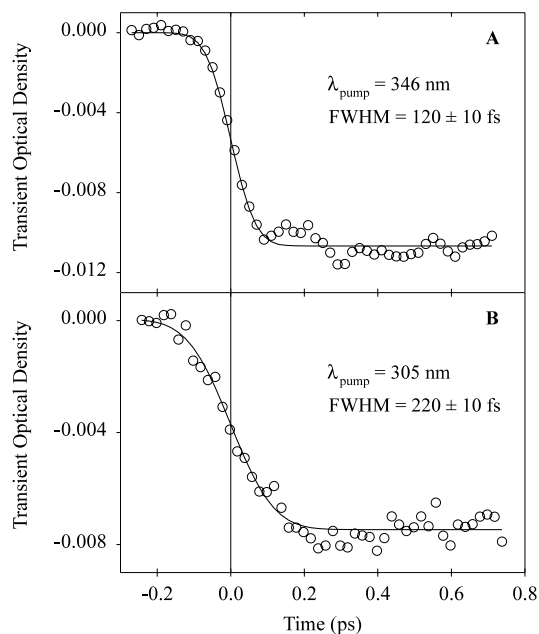


**Fig. 19.3** Photobleaching of Rhodamine 6G in methanolic solution at 505 nm following excitation at 346 nm (A) and 305 nm (B).

### 19.3 Results

#### 19.3.1 Steady-State Spectroscopy

Figure 19.4 shows the UV/vis absorption spectrum and fluorescence emission ( $\lambda_{\text{exc}} = 300 \text{ nm}$  and  $348 \text{ nm}$ ) and excitation ( $\lambda_{\text{em}} = 630 \text{ nm}$ ) spectra of TINSi in *n*-heptane. The absorption spectrum is characterized by two intense bands of similar intensities ( $\epsilon \approx 16000 \text{ cm}^{-1}$ ) at  $305$  and  $348 \text{ nm}$ . Further bands of lower intensities are present below  $260 \text{ nm}$ , along with a shoulder at around  $315 \text{ nm}$ . In *n*-heptane or  $\text{CCl}_4$ , excitation of both TIN and TINSi solutions at  $300 \text{ nm}$  results in a low intensity, broad emission band peaking at around  $410 \text{ nm}$  and extending to over  $600 \text{ nm}$ . On excitation near  $350 \text{ nm}$ , we observe a far less intense emission (10 to 40 times weaker) peaking at  $410 \text{ nm}$ , as well as a band of similar intensity with a maximum at around  $650 \text{ nm}$ . The fluorescence quantum yield of the red emission in *n*-heptane is estimated to be less than  $7 \times 10^{-7}$  by comparison with that of DCM in methanolic solution. The excitation spectrum of the red emission shows two bands at ca.  $300 \text{ nm}$  and  $350 \text{ nm}$ , reminiscent of the two bands observed in the absorption spectrum.

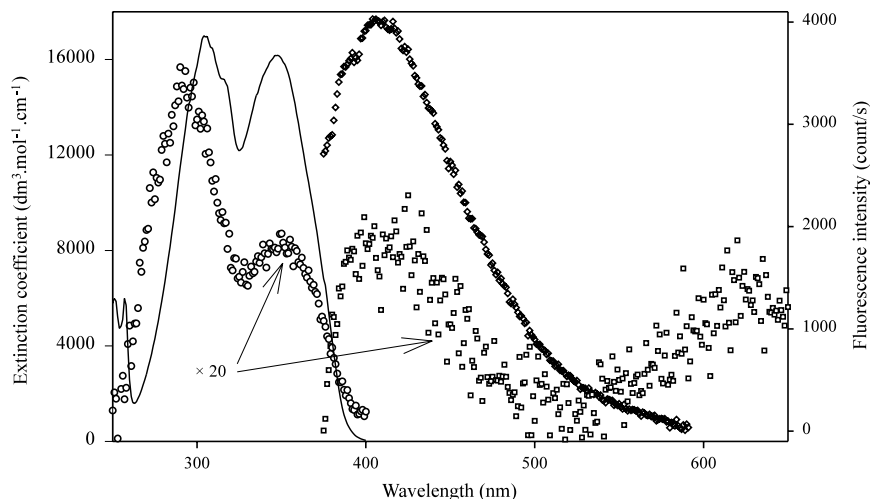


**Fig. 19.4** UV/vis electronic absorption spectrum of TINSi in *n*-heptane (solid line). Fluorescence emission spectra (diamond

symbols: excitation at  $300 \text{ nm}$ ; square symbols: excitation at  $348 \text{ nm}$ ) and excitation spectrum (circle symbols: emission at  $630 \text{ nm}$ ).

## 19.3.2

**Femtosecond UV/vis Absorption and Gain Spectra**

Pump-probe measurements were made over a probing spectral range extending from 380 nm to 720 nm. The pump wavelength was either 346 nm ( $\sim 28900 \text{ cm}^{-1}$ ) or 305 nm ( $\sim 32800 \text{ cm}^{-1}$ ), i.e. near the maxima of the two lowest-energy ground-state absorption bands (see Figure 19.3). Transient spectra measured for time delays between the pump and probe extending over 3 ps in 30 fs increments were recorded as changes in absorbance:

$$\Delta\text{OD} = \log[T_{\text{ref}}(\delta t)/T_{\text{pr}}(\delta t)] - \log[T_{\text{ref}}(\delta t \ll 0)/T_{\text{pr}}(\delta t \ll 0)],$$

where  $T_{\text{ref}}/T_{\text{pr}}$  is the light intensity transmitted at reference/probing positions through the sample and  $\delta t$  is the delay time between pump and probe, so that absorbance increases are positive while bleaching and gain are negative. All the presented data were corrected for group velocity dispersion.<sup>[26]</sup> Each spectrum was obtained by averaging the transmitted intensities over 2500 (346 nm pump) or 3500 (305 nm pump) laser pulses. We chose to have CCD pixels every 0.6 nm, i.e. a slight spectral oversampling for the resolution of ca. 1 nm.

Figure 19.5 shows the temporal evolution of the differential absorption spectrum for excitations at 305 nm (Figure 19.5A) and 346 nm (Figure 19.5B). At early delay times ( $\delta t = 80 \text{ fs}$ ), we observe a strong absorption increase in the blue region with two peaks at ca. 412 nm (A)/403 nm (B) and 433 nm (A)/443 nm (B) for a pump at 305 nm (A)/346 nm (B) and a broad weaker band extending from 500 nm to

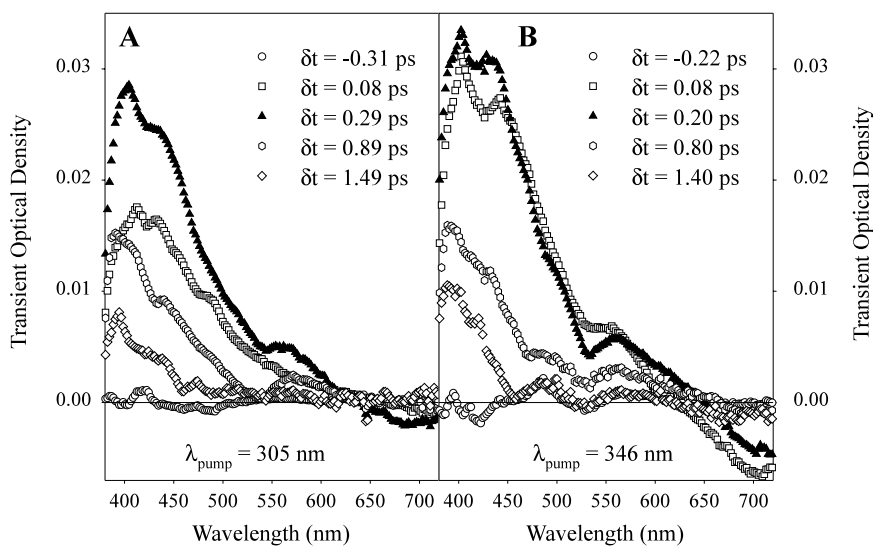


**Fig. 19.5** Experimental GVD-corrected transient absorption spectra (A: excitation at 305 nm; B: excitation at 346 nm).

600 nm, as well as a gain above 600 nm when pumping at 346 nm. This spectrum then changes very rapidly: the double band below 450 nm increases in intensity at  $\delta t = 290$  fs (A)/200 fs (B) following pumping at 305 nm (A)/346 nm (B). The presence of a gain band at around 680 nm at  $\delta t = 290$  fs can be noted on pumping at 305 nm. It is blue-shifted compared to that previously observed for the excitation at 346 nm. Almost half of the absorbance in the blue spectral domain has decayed at  $\delta t = 890$  fs (A)/800 fs (B) with a significant blue-shift of the absorption bands when pumping at 305 nm (A)/346 nm (B); it may also be noted that the gain band then totally disappears for both excitation wavelengths. Finally, all the absorption bands disappear over the next 2 ps except for a small residual absorption below 450 nm with a maximum intensity of about 10 % of that of the original signal. This residual transient absorption is insensitive to the pumping wavelength.

Figure 19.6 shows the kinetics of the absorption and gain for two different probing wavelengths, 408 nm (Figure 19.6A) and 689 nm (Figure 19.6B), obtained by pumping at 305 nm and 346 nm, respectively. The symbols refer to the experimental data, while the solid lines represent the fits. The fits were calculated from a rate

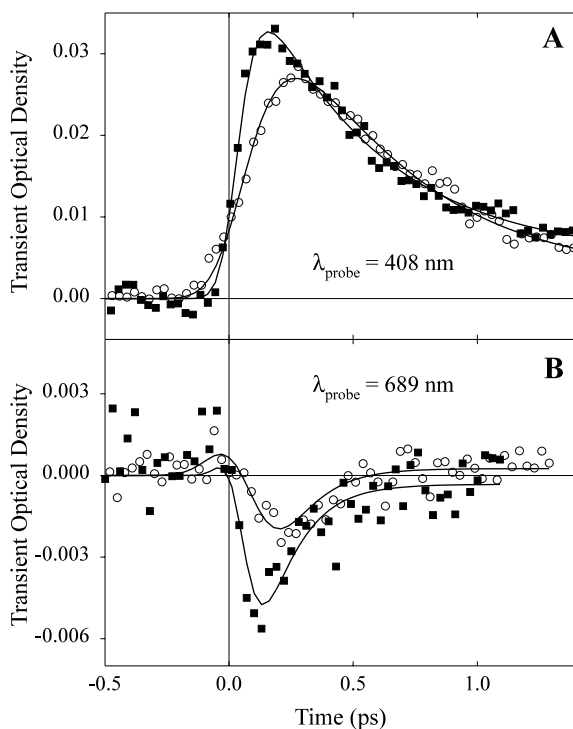


**Fig. 19.6** Experimental transient absorption and gain kinetics at 408 nm (A) and 689 nm (B) following excitation at 305 nm (open circles) and at 346 nm (full squares); (solid lines) fitted kinetics.



equation model comprising four consecutively populated electronic levels (enol excited state, keto excited state, keto ground state, enol “hot” ground state) with the assumption that the last species has a spectrum different from that of the initial ground state and is much longer-lived than the maximum delay time in our experiment; they were simultaneously optimized for 100 wavelengths at regular intervals between 380 nm and 720 nm. For both types of excitation (305 nm and 346 nm), the best fits were obtained with lifetimes of the three intermediate species of 50 fs, 130 fs, and 500 fs. From the amplitudes of the exponential functions at each wavelength, we recalculated the contributions of each transient species relative to the ground state, as indicated in Figure 19.7. The first transient shows a small and ill-defined absorption over the whole visible spectrum (almost no contribution to the kinetics other than above 600 nm). The second transient shows two absorption bands between 400 and 450 nm (peaks at 408 and 452 nm when pumping at 305 nm; at 401 and 445 nm when pumping at 346 nm) and a gain band above 600 nm. The third transient is characterized by two bands between 390 and 425 nm (peaks at 401 and 425 nm when pumping at 305 nm; at 391 and 420 nm when pumping at 346 nm) and a broad, less intense absorption band between 500 and 600 nm. The last species only shows an absorption superior to that of the initial ground state below 450 nm. Interestingly, we observe that the absorption bands of the transients are blue-shifted for pumping at 346 nm compared to that at 305 nm, while at the same time the gain band is red-shifted.

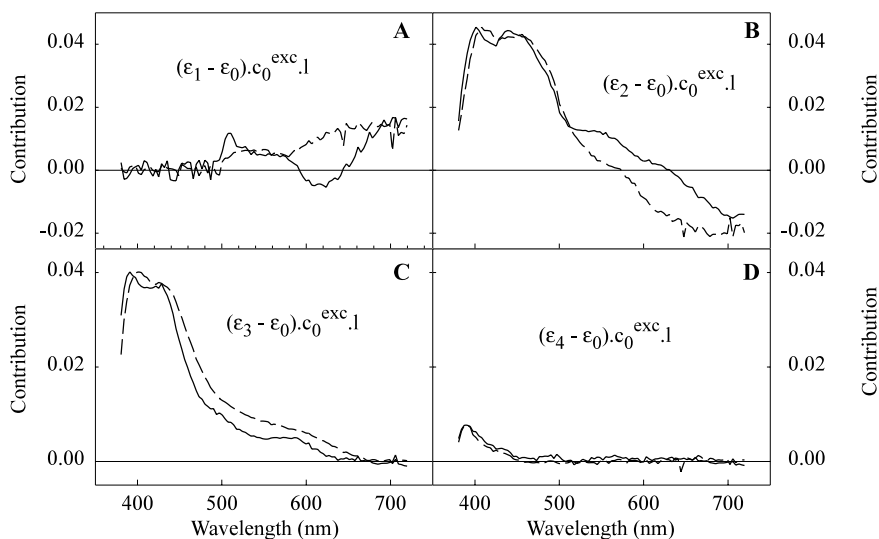


**Fig. 19.7** Contributions to the transient optical density from the four transient species: (A)  $S_1$  enol excited state, (B)  $S_1'$  keto excited

state, (C)  $S_0'$  keto ground state, (D) hot enol ground state. Excitation at 305 nm (dashed line) and 346 nm (solid line).

## 19.4 Discussion

The steady-state UV/vis absorption spectrum of the TINSi molecule is similar to that of the other hydroxyphenylbenzotriazoles (HPBs) bearing bulky groups in the *o*-position relative to the hydroxy group. The red emission observed at room temperature in non-polar solutions of TINSi is comparable to that observed for HPBs at low temperature,<sup>[8,11,12]</sup> in mixed crystals and in pure crystalline form,<sup>[13,19]</sup> in polymers<sup>[27–29]</sup> and, more recently, in solutions at room temperature.<sup>[17,18,30]</sup> It can therefore be attributed to the keto form of TINSi. The feeble fluorescence quantum yield of the red emission ( $< 7 \times 10^{-7}$ ) that we measured in *n*-heptane is even lower than the value of  $10^{-5}$  reported by Wiechman et al.<sup>[17]</sup> for TIN in  $C_2Cl_4$ . The deviation of its excitation spectrum from the steady-state absorption spectrum can be attributed to the fact that the blue emission gives rise to a very broad band with a trailing emission that extends into the red (Figure 19.4); the excitation spectrum is thus the sum of two contributions, one from the species emitting only in the red, and the other from the species emitting in the blue.<sup>[31]</sup>

The model used to fit the data from our femtosecond transient absorption experiments is in effect the classical model proposed more than 25 years ago by Otterstedt<sup>[7]</sup> assuming that the relaxation of the molecule leads ultimately to the “hot” enol ground state. The laser excitation first leads to the formation of the enol  $S_1$  state, which then decays with a time constant  $\tau_1 = (50 \pm 20)$  fs. This state contributes to the kinetics essentially through a small absorption above 600 nm and our data do not permit an unambiguous characterization of its absorption (Figure 19.7A). It disappears upon ESIPT with formation of the keto  $S'_1$  state, which is responsible for the gain spectrum above 600 nm and the initial absorption showing peaks at ca. 440 nm and 400 nm (Figure 19.7B). The presence of this gain was expected from the small emission observed in the steady-state fluorescence experiments in *n*-heptane. In turn,  $S'_1$  relaxes with a lifetime of  $\tau_2 = (130 \pm 30)$  fs to the keto ground state  $S'_0$ , which absorbs more in the blue (Figure 19.7C) than the  $S'_1$  state and is responsible for the observed blue-shift in the time-resolved spectra. Finally, the  $S'_0$  state relaxes to the vibrationally hot enol ground state  $S_0$  with a lifetime  $\tau_3 = (500 \pm 50)$  fs. Observation of the thermalization of the ground state would require much longer delay times than those used in our experiment. The residual increased absorption between 400 and 450 nm is the result of the broadening of the absorption bands of the hot ground state compared to those observed by the steady-state technique. In view of the small contribution to the fit from the first excited state in the aforementioned model, we also tried to fit the experimental data with a model involving only three electronic levels. However, no satisfactory results could be obtained in this way. Both our kinetics and absorption and gain spectra are consistent with the femtosecond measurements at fixed wavelengths reported by Elsässer et al. for the TIN molecule.<sup>[18,30,32–34]</sup> However, our time constants for TINSi in *n*-heptane ( $\tau_1 = 50$  fs,  $\tau_2 = 130$  fs,  $\tau_3 = 500$  fs) are a little smaller than those determined for TIN by Wiechman et al. in  $C_2Cl_4$  ( $\tau_1 = 100$  fs,  $\tau_2 = 150$  fs,  $\tau_3 = 500$  fs)<sup>[18]</sup> and by Chudoba et al. in cyclohexane ( $\tau_1 = 100$  fs,  $\tau_2 = 150$  fs,  $\tau_3 = 600$  fs).<sup>[32]</sup> More-

over, in contrast to the findings of the latter authors,<sup>[30]</sup> we observed no absorption above 600 nm after the disappearance of the gain signal. Interestingly, due to a much better spectral resolution in our experiment at the expense of a decrease in the signal-to-noise ratio in comparison to the data presented by these authors, we observed two well-resolved absorption bands in the 400–500 nm region for both the  $S'_1$  and  $S'_0$  states of the TINSi keto-type molecule.

## 19.5

### Conclusion

We have studied the relaxation processes of a new hydroxyphenylbenzotriazole derivative, TINSi, following excitation in the two lowest absorption bands. At room temperature in non-polar solution, intramolecular proton transfer in the excited and ground states of TINSi was shown to take place on the subpicosecond time scale. The lifetimes of the excited species were found to be independent of the excitation wavelength and the UV/vis absorption spectra of the transients show only differences resulting from the higher energy absorbed when TINSi is excited at a higher energy. Of the two emission bands observed in the blue and red spectral regions, the red one, present as a gain emission in the femtosecond experiments, was assigned to the keto form.

### Acknowledgement

The authors thank O. Gobert, M. Perdrix, and P. Meynadier (CEA/Saclay/DSM/DRECAM) for their help with these experiments

### References

- 1 H. J. Heller, *Eur. Polym. J. Suppl.* **1969**, 105.
- 2 D. L. Williams, A. Heller, *J. Phys. Chem.* **1970**, 74, 4473.
- 3 H. J. Heller, H. R. Blattmann, *Pure Appl. Chem.* **1972**, 30, 145.
- 4 P. F. Barbara, H. P. Tromsdorff (Eds.), Special Issue on Proton Transfer, *Chem. Phys.* **1989**, 136, 153, and references therein.
- 5 S. J. Formosinho, L. G. S. J. Arnaut, *J. Photochem. Photobiol. A: Chem.* **1993**, A75, 21, and references therein.
- 6 A. Douhal, F. Lahmani, A. H. Zewail, *Chem. Phys.* **1996**, 207, 477, and references therein.
- 7 J.-E. A. Otterstedt, *J. Chem. Phys.* **1973**, 58, 5716.
- 8 T. Werner, *J. Phys. Chem.* **1979**, 83, 320.
- 9 S. Y. Hou, W. M. Hetherington III, G. M. Koronowski, K. B. Eisenthal, *Chem. Phys. Lett.* **1979**, 68, 282.
- 10 A. L. Huston, G. W. Scott, A. Gupta, *J. Chem. Phys.* **1982**, 76, 4978.
- 11 S. R. Flom, P. F. Barbara, *Chem. Phys. Lett.* **1983**, 94, 488.
- 12 G. Woessner, G. Goeller, P. Kollat, J. J. Stezowski, M. Hauser, U. K. A. Klein, H. E. A. Kramer, *J. Phys. Chem.* **1984**, 88, 5544.
- 13 G. Woessner, G. Goeller, J. Rieker, H. Hoier, J. J. Stezowski, E. Daltrozzi, M. Neureiter, H. E. A. Kramer, *J. Phys. Chem.* **1985**, 89, 3629.
- 14 K. P. Ghiggino, A. D. Scully, I. H. Leaver, *J. Phys. Chem.* **1986**, 90, 5089.

- 15 M. Lee, J. T. Yardley, R. M. Hochstrasser, *J. Phys. Chem.* **1987**, 91, 4621.
- 16 G. Goeller, J. Rieker, A. Maier, J. J. Stezowski, E. Daltrozzo, M. Neureiter, H. Port, M. Wiechmann, H. E. A. Kramer, *J. Phys. Chem.* **1988**, 92, 1452.
- 17 M. Wiechmann, H. Port, F. Laermer, W. Frey, T. Elsaesser, *Chem. Phys. Lett.* **1990**, 165, 28.
- 18 M. Wiechmann, H. Port, W. Frey, F. Laermer, T. Elsaesser, *J. Phys. Chem.* **1991**, 95, 1918.
- 19 M. Wiechmann, H. Port, *J. Luminescence* **1991**, 48–49, 217.
- 20 J. Rieker, E. Lemmert-Schmitt, G. Goeller, M. Roessler, G. J. Stueber, H. Schettler, H. E. A. Kramer, J. J. Stezowski, H. Hoier, S. Henkel, A. Schmidt, H. Port, M. Wiechmann, J. Rody, G. Rytz, M. Slongo, J.-L. Birbaum, *J. Phys. Chem.* **1992**, 96, 10225.
- 21 J. Catalán, J. C. Del Valle, F. Fabero, N. A. Garcia, *Photochem. Photobiol.* **1995**, 61, 118.
- 22 P. F. McGarry, S. Jockusch, Y. Fujiwara, N. A. Kaprinidis, N. J. Turro, *J. Phys. Chem. A* **1997**, 101, 764.
- 23 J. Catalán, J. L. G. de Paz, M. R. Torres, J. D. Tornero, *J. Chem. Soc., Faraday Trans.* **1997**, 93, 1691.
- 24 T. Fournier, S. Pommeret, J.-C. Mialocq, A. Deflandre, R. Rozot, *Chem. Phys. Lett.* **2000**, 325, 171.
- 25 F. Laermer, W. Israel, T. Elsaesser, *J. Opt. Soc. Am. B* **1990**, 7, 1604.
- 26 S. Pommeret, R. Naskrecki, P. van der Meulen, M. Ménard, G. Vigneron, T. Gustavsson, *Chem. Phys. Lett.* **1998**, 288, 833.
- 27 D. B. O'Connor, G. W. Scott, D. R. Coulter, A. Gupta, S. P. Webb, S. W. Yeh, J. H. Clark, *Chem. Phys. Lett.* **1985**, 121, 417.
- 28 J. Keck, H. E. A. Kramer, H. Port, T. Hirsch, P. Fischer, G. Rytz, *J. Phys. Chem.* **1996**, 100, 14468.
- 29 K. P. Ghiggino, *Pure Appl. Chem.* **1996**, A33, 1541.
- 30 W. Frey, F. Laermer, T. Elsaesser, *J. Phys. Chem.* **1991**, 95, 10391.
- 31 This issue will be discussed at length in a forthcoming paper.
- 32 C. Chudoba, S. Lutgen, T. Jentzsch, E. Riedle, M. Woerner, T. Elsaesser, *Chem. Phys. Lett.* **1995**, 240, 35.
- 33 W. Frey, T. Elsaesser, *Chem. Phys. Lett.* **1992**, 189, 565.
- 34 K. Lenz, M. Pfeiffer, A. Lau, T. Elsaesser, *Chem. Phys. Lett.* **1994**, 229, 340.

## 20

# Direct Detection of the Charge-Shift Reaction in Aromatic Vinyl Polymers by means of Transient Absorption and Dichroism Measurements

*Hiroshi Miyasaka, Takao Moriyama, Sazzadur R. Khan, and Akira Itaya*

### 20.1

#### Introduction

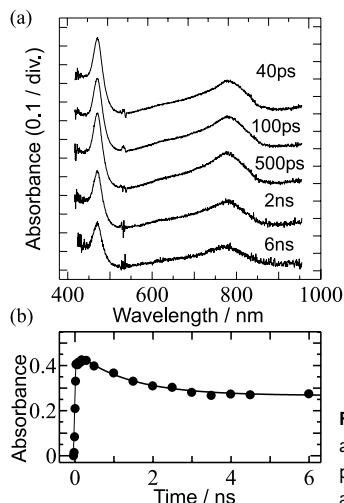
The transport of electrons following photoexcitation is ubiquitous in Nature as well as in artificial systems. Photoconductivity in aromatic vinyl polymers is one of the typical phenomena closely related to this fundamental process, and much attention has been focused on the elucidation of factors regulating the efficiency of charge transport following carrier generation in these systems.<sup>[1–3]</sup> From the viewpoint of photoinduced electron-transfer (ET) processes in condensed phases,<sup>[4–7]</sup> the photoconduction in these polymer systems may be regarded as one of the integral phenomena of “intermolecular” ET processes, since in most of these polymers interactions between the pendant aromatic groups are rather weak and band structures in the electronic states are not plausible. Hence, the application of the general concepts accumulated for ET and its related phenomena may provide deeper insights into the photoconductivity in these systems.

To this end, we have investigated photoprimary processes in typical photoconductive polymers such as poly(*N*-vinylcarbazole) (PVCz) doped with electron acceptors, both in the solid amorphous state and in solution, by transient absorption spectroscopy and dichroism measurements.<sup>[8–13]</sup> The addition of an appropriate electron acceptor to a given aromatic polymer systems leads to the formation of the weak ground-state charge-transfer (CT) complex. Selective excitation of the CT complex enables us to easily determine the time origin of the charge separation and to transfer the “memory” of the polarized excitation (dichroism) onto the charge-separated state. The dichroism time profile provides information concerning the hole migration along the pendant aromatic groups. On the basis of these direct measurements, we discuss the ET dynamics in these polymer systems.

### 20.2

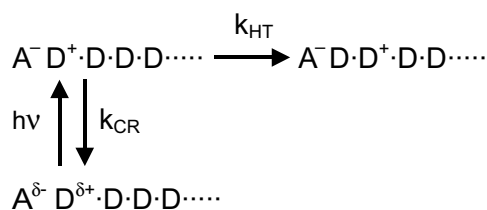
#### Dynamic Behavior in Solid Amorphous Systems

Figure 20.1 (a) shows time-resolved transient absorption spectra of a PVCz solid film doped with 3.0 mol% 1,2,4,5-tetracyanobenzene (TCNB) as an electron accep-



**Fig. 20.1** (a) Time-resolved transient absorption spectra of a PVCz film doped with 3.0 mol% TCNB, excited with a picosecond 532 nm laser pulse; (b) time profile of transient absorbance at 470 nm.

tor, excited with a picosecond 532 nm laser pulse with 15 ps FWHM (for selective excitation of the CT complex). Each spectrum shows two maxima at 470 nm ( $\text{TCNB}^-$ ) and 780 nm ( $\text{Cz}^+$ ), indicating that the excitation of the ground-state CT complex results in rapid charge separation in the excited state. The time profile of the charge-separated state monitored at 470 nm ( $\text{TCNB}^-$ ) over several nanoseconds is shown in Figure 20.1 (b). The absorbance decreases slightly for ca. 3 ns after the excitation and then attains a constant value of 60 % of the intensity of that immediately after the excitation, which persists into the longer time region. To analyze the time profile, we employed the simplified model shown in Scheme 20.1, where the ion pair (IP) undergoes charge recombination (CR) in competition with hole transfer (HT) through the Cz groups. According to this scheme, the time constants for HT and CR were estimated to be  $4.8 \pm 10^8 \text{ s}^{-1}$  and  $3.1 \pm 10^8 \text{ s}^{-1}$ , respectively.



**Scheme 20.1**

In order to elucidate the hole migration process more directly, we measured the transient dichroism of the absorptions due to  $\text{Cz}^+$  and  $\text{TCNB}^-$ . Since hole migration in the Cz moieties in the solid film seems to decrease the “memory” of the polarized excitation (the dichroism signal of the cation), a comparison of the dichroism signals due to the cation and anion may provide direct information on the hole migration processes. For these measurements, the polarization angle between the excitation and monitoring light pulses was set at  $45^\circ$ . The analyzer polarizer perpendicu-

lar to the polarization of the probe light was placed in front of the detector.<sup>[14–17]</sup> In this optical arrangement, the transmitted light intensity falls to zero when the “memory” of the polarized excitation is diminished by HT among the aromatic groups. The actual measurements were performed under heterodyne conditions.

Figure 20.2 shows the time profiles of the transient dichroism signals monitored at around 750 nm ( $\text{Cz}^+$ ) and 470 nm ( $\text{TCNB}^-$ ), respectively. These profiles clearly demonstrate that the “memory” of the polarized excitation in  $\text{Cz}^+$  decreases to the background level, while that in  $\text{TCNB}^-$  extends into the nanosecond time region, from which it can be concluded that HT from the initial  $\text{Cz}^+$  moiety prepared by photoinduced charge separation to the neighboring Cz moieties actually proceeds with a time constant of ca. 2 ns and is thus in competition with the charge-recombination process. On the other hand, a charge-shift reaction among the TCNB moieties cannot take place on this time scale because of their low concentration.

In general, the carrier generation process has been conventionally interpreted in terms of a scheme in which the initial CS state rapidly relaxes during the thermalization process to ion-pair (IP) states with an inter-ionic distance of  $r_0$  prior to the CR process (carrier generation), and then carrier transport ensues under the electric field.<sup>[1,18]</sup> Typical values estimated for  $r_0$  have been ca. 20–30 Å. Since the thermalization in the condensed phase may be regarded as a cooling process (vibrational relaxation), the time constant for this thermal relaxation is estimated to be of the order of a few tens of picoseconds or less. However, if an increase in the inter-ionic distance up to ca. 20 Å (3–5 Cz units) occurred on a time scale of less than a few tens of picoseconds, such “memory” of the polarization of the excitation light over several nanoseconds, as observed in the present results, would not be detected. Although the conventional model based on this  $r_0$  value is not appropriate for a description of the dynamic behavior, it is worth noting here that this model adequately rationalizes the experimental results on the electric field effects on the steady-state fluorescence due to CS states and on the carrier generation yield. The rational interpretation of  $r_0$  from the viewpoint of actual dynamic behavior is very important.<sup>[19]</sup>

The temperature effect on the HT and CR rate constants was investigated for a solid PVCz film doped with *p*-chloranil (CA) as an electron acceptor (Figure 20.3). For analysis of the PVCz–CA system, we employed a continuous hole migration

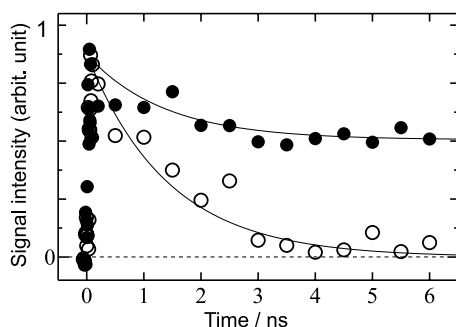


**Fig. 20.2** Time profiles of transient dichroism signals of a PVCz film doped with 3.0 mol% TCNB, excited with a picosecond 532 nm laser pulse, monitored at ca. 750 nm ( $\text{Cz}^+$ , open circles) and at ca. 470 nm ( $\text{TCNB}^-$ , filled circles).

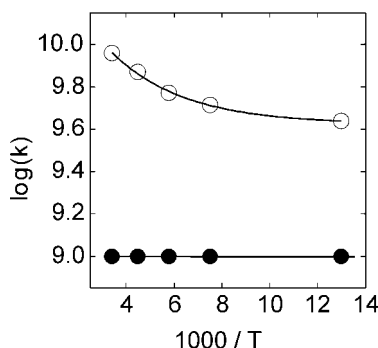


**Fig. 20.3** Temperature dependence of  $k_{HT}$  (open circles) and  $k_{CR}$  (filled circles) in a PVCz film doped with 3.0 mol% CA, excited with a picosecond 532 nm laser pulse. The solid lines are to guide the eye.

model confined to a sphere.<sup>[13]</sup> The CR rate constant,  $k_{CR}$ , was found to decrease with decreasing temperature in the high temperature region and to become less dependent on the temperature below ca. 120 K. It has been reported that the CR rate is mainly regulated by intramolecular high-frequency modes and partly by low-frequency intermolecular (intra-ion pair) vibrations.<sup>[5]</sup> On decreasing the temperature, the contribution from the low-frequency mode diminishes and the rate constant becomes regulated only by the high-frequency modes, as a result of which it does not show any significant temperature dependence. The present result may be interpreted in a similar manner. On the other hand, the hole-transfer rate constant was found to be completely unaffected by the temperature change examined here.

It is well known that for photoconduction in PVCz solid films, the hole mobility decreases on decreasing the temperature.<sup>[1–3]</sup> The discrepancy between the present result in the initial stages after the excitation and the photocurrent measurements may be interpreted as follows. Generally, hole mobility in amorphous bulk polymer films can be divided into two contributing processes: hopping of the hole between the sites and the detrapping process from the trap site, for which the environment is relatively stable for the cation. From measurement of the singlet excitation energy migration in the amorphous PVCz solid film, it was reported that the deep trap sites for the singlet exciton (excimer sites) correspond to ca.  $1/10^3$  of the total number of carbazolyl units.<sup>[20,21]</sup> Provided that the deep trap sites for the cation are similar to those for the singlet exciton, the probability of the cation being trapped immediately after the excitation is very small. Hence, the hole-shift reaction in the present time window may take place prior to the trapping at the deep trap sites. Actually, our preliminary results on the dynamic time profiles over a wide time window showed the temperature effect to be pronounced with an increase in the delay time after the excitation (typically, at or after several tens of nanoseconds following the excitation).

Regarding the effective hole-transfer process in the solid phase, it is worth noting here a theoretical study by Slowik and Chen,<sup>[22]</sup> in which it was pointed out that the transfer integral (the electronic tunneling matrix element) for the charge-shift reaction in solid carbazolyl systems is strongly dependent on the mutual orientations and the distance. In their report, these authors suggested that the thermally activated hindered rotation process of the carbazolyl groups in the solid state, leading to



an increase in the transfer integral, plays an important role in the detrapping of the hole. Although the thermally activated motion is not involved in the hole-shift reaction on the present time scales, a small fluctuation in the orientation of the carbazolyl moiety in the hindered space of the polymer film (zero-point motion) can occur. This motion may modulate the transfer integral and may allow a rapid hole-transfer reaction when there is a favorable mutual orientation of the moieties. Although it is rather difficult to derive a clear-cut conclusion, the contribution of the fluctuation in the electronic interaction is strongly suggested to play an important role in the rapid hole migration in aromatic vinyl polymer systems.

### 20.3

#### Direct Detection of Charge-Shift Reactions in Aromatic Vinyl Polymers in the Solution Phase

Photoinduced charge separation and subsequent charge-shift reactions also take place in aromatic vinyl polymers in the solution phase. Since a number of investigations on electron-transfer processes have been performed in the solution phase, comparison of the dynamic behavior in polymers with that in various systems in the solution phase may provide some important insights. In Figure 20.4, we show the time profile of the charge-separated state of PVCz–TCNB in 1,2-dichloroethane (DCE) solution, excited with a picosecond 532 nm laser pulse and monitored at 465 nm.<sup>[9]</sup> As in the solid films, the ground-state CT complex between TCNB and Cz was selectively excited. The charge-separated state decreases on a subnanosecond time scale and is followed by a much longer-lived component. No such residual absorption signal was detected for the monomer model system, where only a charge recombination with a time constant of 130 ps was observed. The temporal behavior of the polymer system was analyzed on the basis of Scheme 20.2. Here,  $k_{\text{HTi}}$  is the hole-transfer rate constant for transfer between two neighboring Cz moieties. For simplicity, all of the  $k_{\text{HTi}}$  constants were assumed to be the same. In addition, charge recombination was assumed to take place only between  $\text{TCNB}^-$  and  $D_0^+$  (at the initial position of the charge separation). The rate constant for the charge recombination was set as being equal to that for the monomer model system in DCE solution. Hence, the only parameter in the calculation was  $k_{\text{HT}}$ . The result obtained with

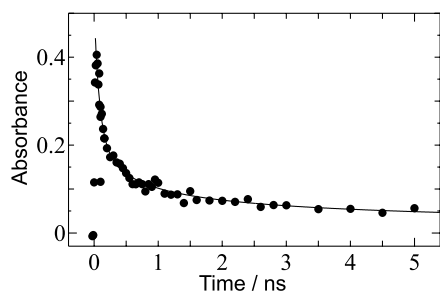
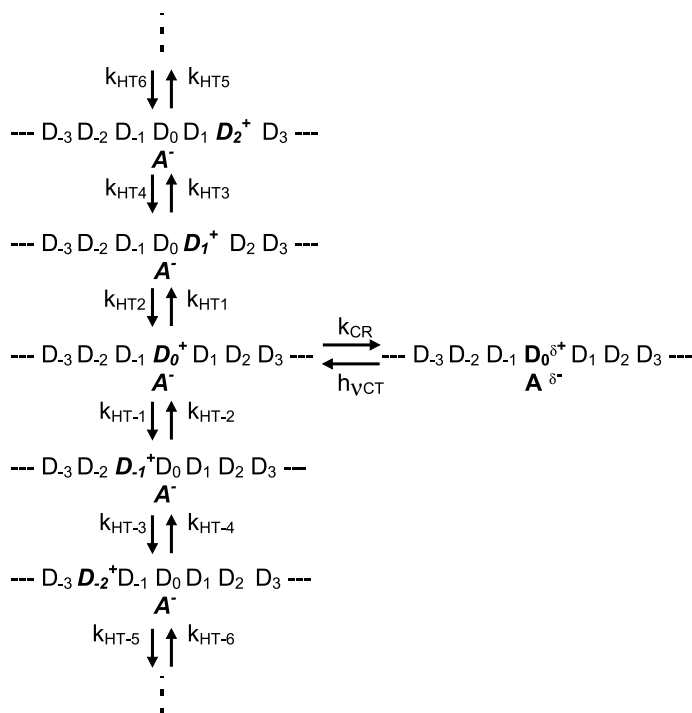


**Fig. 20.4** Time profile of charge-separated state of PVCz–TCNB in 1,2-dichloroethane solution, excited with a picosecond 532 nm laser pulse and monitored at 465 nm.



Scheme 20.2

$k_{\text{HT}} = 2.0 \times 10^9 \text{ s}^{-1}$  is shown as the solid line in Figure 20.4, where the calculated curve reproduces the experimental results fairly well.

For a more direct elucidation of the hole migration process, we measured the transient dichroism of the absorption due to  $\text{Cz}^+$  and  $\text{TCNB}^-$ . As in the solid films, the hole migration in the polymer chain seems to decrease the “memory” of the polarized excitation. Figure 20.5 depicts the time profiles of the transient dichroism monitored at around 780 nm ( $\text{Cz}^+$ ) and 465 nm ( $\text{TCNB}^-$ ), respectively. It can clearly be seen that the “memory” of the polarized excitation in  $\text{Cz}^+$  decreases faster than that in  $\text{TCNB}^-$ . In the monomer model system (*N*-ethylcarbazole and  $\text{TCNB}$ ), the time constants for the dephasing process of the polarized excitation (rotational relaxation) of the cation and anion in the ion pair were found to be identical. The dichroism signal,  $I(t)$ , is given by  $I(t) = P(t) \times R(t)$ . Here,  $P(t)$  is the population decay and  $R(t)$ , in the present case, is the local geometrical change in the orientation of the polymer chain. The solid line for the time profile of  $\text{TCNB}^-$  represents the result calculated assuming  $P(t)$  to be identical to that used for Figure 20.1, and that  $R(t) = \exp(-t/950 \text{ ps})$ , which reproduced the experimental results fairly well. Since the local motions resulting in conformational changes of the pendant aromatic groups take place in the order of subnanoseconds to nanoseconds, the present time constant for  $\text{TCNB}^-$  attached to the  $\text{Cz}$  moiety may be attributable to these local motions.

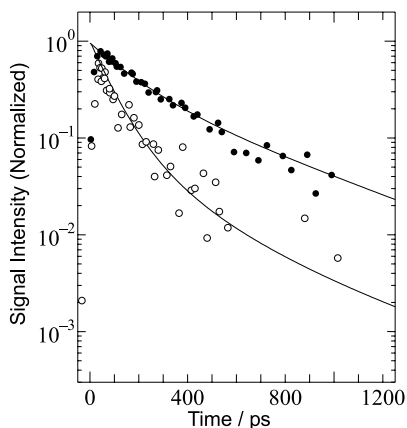


**Fig. 20.5** Time profiles of transient dichroism signals of PVCz–TCNB in 1,2-dichloroethane solution, excited with a picosecond 532 nm laser pulse and monitored at ca. 780 nm (Cz<sup>+</sup>, open circles) and 465nm (TCNB<sup>−</sup>, filled circles).

For the dichroism decay of Cz<sup>+</sup>, we show the time profile of  $D_0^+$  in Scheme 20.2 with the same time constants as used for Figure 20.4 (the solid line), since the hole-shift reaction to neighboring, randomly positioned Cz moieties in the polymer chains seems to diminish this “memory”. The calculated curve reproduces the experimental result for Cz<sup>+</sup> fairly well, like that for TCNB<sup>−</sup>. By integrating the present results, it can be concluded that the Cz<sup>+</sup> initially produced through excitation of the ground-state CT complex actually undergoes hole migration to the neighboring neutral Cz moieties with a time constant of 500 ps, as assumed in Scheme 20.2.

It should be mentioned that the hole-escape reaction is endothermic, since the increase in the inter-ionic distance reduces the Coulombic attractive interaction in the ion pair. For the reaction,  $A^-D_0^+D_1 \rightarrow A^-D_0D_1^+$ , the  $\Delta G^0$  value was estimated to be ca. +0.2 eV in DCE solution, provided that the distances between A and D<sub>0</sub> and between A and D<sub>1</sub> are 3.5 and 7.0 Å, respectively, and  $\Delta G^0$  arises only from the reduction of the Coulombic attraction. On the basis of standard Marcus theory, the activation energy,  $\Delta G^*$ , for the above reaction in DCE solution was estimated to be more than ten times larger than the magnitude of  $k_B T$  at 20 °C. In the framework of non-adiabatic ET theories, it is arduous to interpret such a large hole-migration rate constant of the order of  $10^9 \text{ s}^{-1}$  for a system with  $\Delta G^* \gg 10k_B T$ .

Table 20.1 lists the hole-transfer rate constant of various aromatic polymer systems in 1,2-DCE solution; it can be seen that  $k_{HT}$  increases with an increase in the overlap between the two neighboring aromatic groups. Comparison of the  $k_{HT}$  values between P1VN and P2VN and between P7VBCz and P5VBCz also reveals that the degree of overlap between the neighboring aromatic moieties plays an important role in the hole-transfer process. These results strongly suggest that the rather large electronic interaction between the cation and the neutral group plays an important role in the hole-transfer process.

It should be pointed out here that the stable dimeric cation resulting from large interaction, however, is usually regarded as the trapping site for the hole. In this context, it is noteworthy that effective dimeric cation formation through intermolecular interaction does not occur in 7-ethylbenzo[*c*]carbazole, 5-ethylbenzo[*b*]carba-

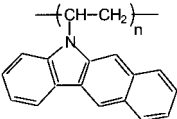
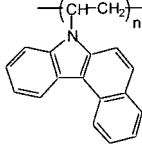
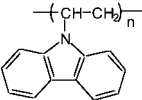
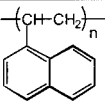
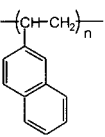
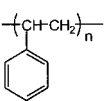
Polymer	$k_{HT} / s$
<b>P5VBCz</b> 	$5.6 \times 10^9$
<b>P7VBCz</b> 	$3.1 \times 10^9$
<b>PVCz</b> 	$2.0 \times 10^9$
<b>P1VNp</b> 	$3.0 \times 10^8$
<b>P2VNp</b> 	$1.3 \times 10^8$
<b>PSt</b> 	$\leq 4 \times 10^7$

Table 20.1

zole, or *N*-ethylcarbazole under standard conditions, while 1-ethylnaphthalene and 2-ethylnaphthalene readily form the intermolecular dimeric radical cations in solution. These results indicate that the carbazolyl and benzocarbazolyl moieties have intrinsically small stabilization energies in dimeric cation formation, leading to effective hole-transfer reactions. In addition, hole-transfer processes in the benzocarbazolyl polymers as well as PVCz were found to be faster than the conformational rearrangement of the local structures in the polymer chain, as indicated by the dichroism decay of the anion. Since stable dimer cation formation requires a conformational rearrangement, migration of the hole prior to stable dimer cation formation can facilitate rapid and effective HT processes in these polymers.

## 20.4

## Summary

We have shown that the application of dichroism measurements has allowed a clear delineation of the primary processes in electron-transfer dynamics in aromatic vinyl polymers, both in the solid state and in solution. This approach has also made it possible to elucidate the elementary processes relating to macroscopic photoconduction from the theoretical viewpoint of electron-transfer reactions on a molecular scale. Several models of the electron-transfer dynamics in these polymer systems<sup>[22]</sup> and their dynamic behavior in the shorter time region<sup>[23]</sup> have also been reported. At the present stage, however, most of the theories on electron-transfer reactions are based on the very weak interactions between the reactants. Further progress in theoretical studies is also required for a comprehensive understanding of the electron-transfer reaction in various phases.

## References

- 1 J. Mort, G. Pfister (Eds.), in *Electronic Properties of Polymers*, Wiley Interscience, New York, 1982, p. 215, and references cited therein.
- 2 M. Van der Auweraer, F. C. De Schryver, P. M. Borsenberger, H. Bässler, *Adv. Materials* **1994**, 3, 199.
- 3 (a) R. C. Penwell, B. N. Ganguly, T. W. Smith, *J. Poly. Sci., Macromolecular Rev.*, **1978**, 13, 63. (b) J. M. Pearson, M. Stolka, *Poly(N-vinylcarbazole)*, Gordon and Breach Science Publishers, New York, **1981**.
- 4 R. A. Marcus, N. Sutin, *Biochim. Biophys. Acta* **1985**, 811, 265.
- 5 (a) N. Mataga, in *Electron Transfer in Inorganic, Organic and Biological Systems* (Eds.: J. R. Bolton, N. Mataga, G. McLenden), Advances in Chemistry Series 228, American Chemical Society, Washington DC, **1991**, Chapter 6. (b) N. Mataga, H. Miyasaka, *Prog. React. Kinetics* **1994**, 19, 317. (c) N. Mataga, H. Miyasaka, *Adv. Chem. Phys.* **1999**, 107, 431.
- 6 I. Rips, J. Klafter, J. Jortner, in *Photochemical Energy Conversion* (Eds.: J. R. Norris, D. Meisel), Elsevier, New York, **1988**, p. 1.
- 7 P. F. Barbara, W. Jarzeba, *Adv. Photochem.* **1990**, 15, 1.
- 8 H. Miyasaka, T. Moriyama, S. Kotani, R. Muneyasu, A. Itaya, *Chem. Phys. Lett.* **1994**, 225, 15.
- 9 H. Miyasaka, T. Moriyama, A. Itaya, *J. Phys. Chem.* **1996**, 100, 12609.
- 10 T. Moriyama, K. Monobe, H. Miyasaka, A. Itaya, *Chem. Phys. Lett.* **1997**, 275, 291.
- 11 A. Itaya, T. Kitagawa, T. Moriyama, T. Matsushita, H. Miyasaka, *J. Phys. Chem.* **1997**, B101, 524.
- 12 H. Miyasaka, T. Moriyama, A. Itaya, *J. Phys. Chem.* **1997**, B101, 10726.
- 13 H. Miyasaka, T. Moriyama, T. Ide, A. Itaya, *Chem. Phys. Lett.* **1998**, 292, 339.
- 14 C. V. Shank, E. P. Ippen, *Appl. Phys. Lett.* **1975**, 26, 62.
- 15 D. Waldeck, A. J. Cross, Jr., D. B. McDonald, G. R. Fleming, *J. Chem. Phys.* **1981**, 74, 3381.
- 16 G. R. Fleming, in *Chemical Applications of Ultrafast Spectroscopy*, Oxford University Press, New York, **1986**, p.72.
- 17 G. L. Easley, M. D. Levenson, W. M. Tolles, *IEEE J. QE.*, **1978**, 14, 192.
- 18 M. Yokoyama, S. Shimokihara, A. Matsubara, H. Mikawa, *J. Chem. Phys.* **1982**, 76, 724.
- 19 H. Miyasaka, S. R. Khan, A. Itaya, in preparation.

- 20 (a) A. Itaya, K. Okamoto, S. Kusabayashi, *Bull. Chem. Soc. Jpn.* **1977**, *50*, 22. (b) A. Itaya, K. Okamoto, S. Kusabayashi, *Bull. Chem. Soc. Jpn.* **1979**, *52*, 3737.
- 21 W. Klöpffer, *Chem. Phys.* **1981**, *57*, 75.
- 22 J. H. Slowik, I. Chen, *J. Appl. Phys.* **1983**, *54*, 4467.
- 23 (a) H. Masuhara, A. Itaya, in *Macromolecular Complexes: Dynamic Interactions and Electronic Processes* (Ed.: E. Tsuchida), VCH, New York, **1991**, pp. 61–92. (b) K. Watanabe, T. Asahi, H. Masuhara, *Chem. Phys. Lett.* **1994**, *233*, 69. (c) K. Watanabe, T. Asahi, H. Masuhara, *J. Phys. Chem.* **1996**, *100*, 18436.
- 24 A. Ruseckas, V. Gulbinas, V. Sundström, A. Undzenas, L. Valkunas, *J. Phys. Chem. B* **1998**, *102*, 7365.

## 21

# Femtosecond Chemical Events of Intramolecular Charge Transfer and Intermolecular Hydrogen Bond Breaking after Electronic Excitation: Structural Dynamics in the Condensed Phase

*Erik T. J. Nibbering and Jens Dreyer*

### 21.1

#### Introduction

Since the invention of flash photolysis in 1949 and the advent of pulsed laser technology in the 1960's, chemical reactions have been studied with continuously improved time resolution. Early experiments on the micro- and nanosecond time-scales were restricted to the examination of kinetic rates and reaction yields, whereas the underlying microscopic processes remained unresolved. The transition into the femtosecond time domain in the 1980's, as a result of major developments in ultrafast dye<sup>[1–5]</sup> and solid-state<sup>[6–11]</sup> laser technology, made it possible to follow chemical reactions in real time and hence detailed studies of microscopic reaction dynamics became feasible.<sup>[12,13]</sup> Fundamental physical processes, such as vibrational relaxation, collisions in liquids, and energy transfer, e.g. in photosynthesis, could be investigated. Nuclear motion became directly observable from vibrationally coherent wavepacket dynamics in ultrafast photoinduced chemical and biochemical reactions. This rapidly expanding field has been named *femtochemistry*<sup>[14]</sup> owing to the fact that the dynamics of breaking or formation of chemical bonds can be followed on the femtosecond time scale.<sup>[15–20]</sup>

In the condensed phase, the static and dynamic properties of the surrounding solvent often have a decisive influence on the reaction dynamics.<sup>[21–23]</sup> With femtosecond spectroscopy it became possible to directly analyze solvent fluctuations and relaxation,<sup>[24–27]</sup> processes which determine dephasing and energy relaxation (solvation dynamics), between ca. 10 fs and several picoseconds.<sup>[13,28–30]</sup>

The elucidation of ultrafast photochemical reaction mechanisms requires an experimental technique with sufficient time resolution as well as the ability to resolve structural changes in the course of the reaction. Electronic spectroscopy probing transmission or emission changes of reactants, intermediates, or products is the most widely used method for condensed-phase investigations. However, due to the inherent delocalized character of electronic transitions, site-specific information about structural changes of the solute or local intermolecular interactions between the solute and the environment is difficult to obtain. In the future, methods such as time-resolved electron diffraction<sup>[31]</sup> and X-ray diffraction<sup>[32–34]</sup> or X-ray spectroscopy<sup>[35,36]</sup> may prove to be most useful for elucidating structurally resolved reac-

tion dynamics. However, at the present time, these rather demanding techniques are still in the development stage as far as (sub)picosecond time resolution is concerned. One thus has to rely on alternative approaches to study structural dynamics.

Decades of stationary vibrational spectroscopy have shown that vibrational modes are usually much more localized than electronic transitions, and thus provide local information about functional groups in the solute or the environment. This is the case, for example, for O–H stretching and bending and C=O stretching modes of hydrogen-donor and -acceptor molecules capable of hydrogen bonding.<sup>[37]</sup> These modes change their characteristics (frequency, transition moment) upon hydrogen bonding and may thus be regarded as “spectators” of the hydrogen bond. If an optical pulse triggers a dynamic process in a hydrogen bond, it is possible to follow the dynamics of this hydrogen bond by inspection of the temporal behavior of these spectator modes (see Figure 21.1). Vibrational modes can be probed by infrared, resonance Raman, or coherent Raman spectroscopy.

We demonstrate herein that the coupling of vibrational mid-infrared spectroscopy with femtosecond time resolution provides a powerful method for exploring excited-state reaction pathways as well as for investigating local interactions between solutes and their environment. Tunable and intense femtosecond mid-infrared pulses can now be generated in the 2–12  $\mu\text{m}$  wavelength range.<sup>[38–41]</sup>

Examples that have been studied by other groups using time-resolved infrared spectroscopy include excited-state intramolecular proton transfer in 2-(2'-hydroxy-phenyl)benzothiazole,<sup>[42,43]</sup> the photodissociation of ICN,<sup>[44]</sup> the photodissociation of metallocarbonyl compounds such as  $(\eta^5\text{-C}_5\text{H}_5)\text{Fe}(\text{CO})_2$ ,<sup>[45]</sup>  $(\eta^5\text{-C}_5\text{H}_5)\text{Co}(\text{CO})_2$ ,<sup>[46]</sup>  $\text{M}(\text{CO})_6$  ( $\text{M} = \text{Cr}, \text{Mo}, \text{W}$ ),<sup>[47]</sup> or  $\text{Mn}_2(\text{CO})_{10}$ ,<sup>[48]</sup> photochemical Si(H bond activation by  $\eta^5\text{-(C}_5\text{H}_5)\text{V}(\text{CO})_4$ ,<sup>[49]</sup> C=O ligand dynamics in the heme pockets of hemoglobin

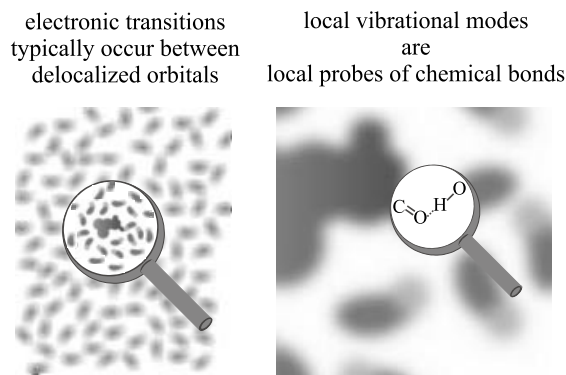


**Fig. 21.1** Schematic representation of the principle of IR spectroscopy as a means of probing structural dynamics. Electronic spectroscopy usually determines the dynamics of a specific probe molecule and the surrounding

solvent shells, and information on a specific reaction coordinate cannot usually be obtained directly. In principle, IR spectroscopy offers information on site-specific dynamics if local modes are probed.



and myoglobin,<sup>[50–53]</sup> and the photoisomerizations of azobenzene<sup>[54]</sup> and all-*trans* retinal.<sup>[55]</sup>

In this contribution, we review our recent transient mid-infrared studies on photoinduced intramolecular charge transfer (ICT) in 4-(dimethylamino)benzonitrile (DMABN),<sup>[56–58]</sup> and on intermolecular hydrogen-bonding in coumarin-102 (C102) in polar solvents and C102–phenol complexes.<sup>[59–64]</sup> We show that the combined approach of ultrafast infrared spectroscopy and high-level *ab initio* quantum chemical calculations allows new insight to be gained into the ICT mechanism in DMABN. In the second part, we demonstrate that O–H and C=O stretching modes involved in intermolecular hydrogen bonds are sensitive probes of hydrogen-bond dynamics. These investigations are supplemented by theoretical studies of infrared absorption line shapes. We conclude with an outline of future perspectives of femto-second infrared spectroscopy as a tool for studying ultrafast dynamics.

## 21.2

### Structural Information on Transient States: Comparison of Vibrational Spectra with *Ab initio* CASSCF Calculations

As a first example, we show in this section how structural information on electronically excited states can be obtained through a combination of experimental transient infrared spectra and *ab initio* quantum chemical calculations. From these calculations, a vibrational analysis in terms of vibrational frequencies and transition moments is obtained for local minima or transition states in the electronic ground state as well as in excited states. Local minima may correspond to observed transient states. In general, many more minima and maxima exist than are relevant for the description of the observed features, and a restriction in the  $3N - 6$  vibrational parameter space should be well premeditated.

The quantum chemical description of electronically excited states requires an approach that adequately accounts for the multi-configurational nature of excited-state wavefunctions. This is realized in the complete active space SCF (CASSCF) method, which has been successfully applied in the investigation of electronic excitation spectra and photochemical reaction mechanisms.<sup>[65,66]</sup> Our strategy is as follows: (a) possible mechanisms for excited-state pathways are selected; (b) CASSCF geometry optimizations and vibrational analyses are performed along each pathway for all appearing intermediates; (c) experimental transient infrared spectra are compared with calculated vibrational patterns to assign the transients. We demonstrate this approach in the case of the ICT reaction in DMABN dissolved in acetonitrile.<sup>[56–58]</sup> We note here that a similar approach has recently been undertaken by Harris and co-workers in a study of photochemical Si–H bond activation by  $\eta^5$ -(C<sub>5</sub>H<sub>5</sub>)V(CO)<sub>4</sub>.<sup>[49]</sup>

The ICT mechanism responsible for the solvent-dependent photoinduced dual fluorescence of DMABN and related donor–acceptor compounds has been a subject of intense debate ever since its discovery almost 40 years ago.<sup>[67]</sup> It has been shown experimentally that normal emission occurs from a moderately polar, locally-excited

(LE) state, whereas the red-shifted anomalous emission can be attributed to a highly-polar charge-transfer (CT) state. The discussion on the structure of this ICT state has recently focussed on three different models (see Figure 21.2). The twisted ICT (TICT) model assumes decoupling of the dimethylamino and benzonitrile moieties as a result of a twisting of the dimethylamino group into a perpendicular position relative to the benzene ring (Figure 21.2 (a)).<sup>[68,69]</sup> In contrast, the solvent-induced pseudo-Jahn–Teller model predicts planarization (PICT) of the initially pyramidalized amino group as being the relevant ICT reaction coordinate (Figure 21.2 (a)). In this model, the LE state is assumed to be still fully or at least partly

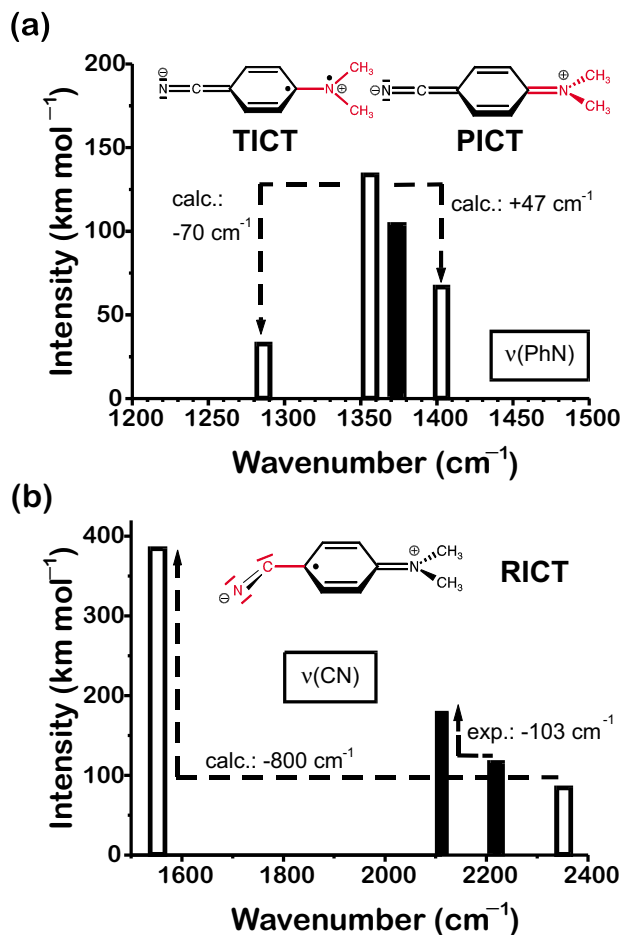


**Fig. 21.2** Calculated (hollow bars) and experimental (filled bars) vibrational frequencies and intensities for the CT state of DMABN. Dashed arrows denote observed and predicted frequency shifts. (a) Results for the  $\nu(\text{PhN})$

mode (*cf.* Figure 21.3). Theoretical data calculated for the TICT and PICT models. (b) Results for the  $\nu(\text{CN})$  mode (*cf.* Figure 21.3). Theoretical data calculated for the RICT model.

pyramidalized, whereas the final CT state exhibits a planar quinoidal structure with significant coupling between the dimethylamino and benzonitrile groups.<sup>[70,71]</sup> Finally, rehybridization (RICT) of the cyano group from a linear to a bent configuration has been suggested as an alternative ICT mechanism based on the results of ab initio calculations (Figure 21.2 (b)).<sup>[72]</sup>

The three different ICT models can be qualitatively distinguished by observing the time development of two distinct vibrational modes that are highly sensitive to the nature of the CT state, namely the cyano  $\nu(\text{CN})$  and the phenyldimethylamino  $\nu(\text{PhN})$  modes (Figure 21.3). The characteristic

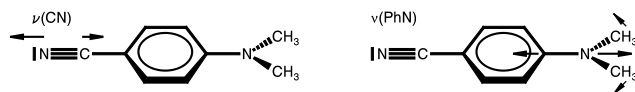


**Fig. 21.3** Schematic representation of the  $\nu(\text{CN})$  and  $\nu(\text{PhN})$  normal modes.

changes in these two modes can also be used to assign the LE state.

Structures having a pyramidal and a planar dimethylamino group have been identified computationally as local minima on the potential-energy surface of the LE state. In the experimental transient infrared spectrum of the LE state that is formed in less than 500 fs, the band intensities of the  $\nu(\text{CN})$  and  $\nu(\text{PhN})$  modes are completely lost, which is in agreement with the calculated pattern for the planar structure. A planar LE state indicates that planarization of the dimethylamino group can not serve as the relevant reaction coordinate in the time-determining step of the ICT mechanism as predicted by the PICT model. For 4-aminobenzonitrile, which does not exhibit dual fluorescence, the transient infrared spectrum shows only minor intensity changes for the  $\nu(\text{CN})$  and  $\nu(\text{PhN})$  modes with respect to the ground state, in accordance with the vibrational pattern calculated for a pyramidal LE state of 4-aminobenzonitrile.

The RICT model can be distinguished from the TICT and PICT models by inspection of the  $\nu(\text{CN})$  mode, which should be red-shifted from the absorption frequency of a triple bond in the ground state ( $2215\text{ cm}^{-1}$  in acetonitrile) to that of a double bond in the CT state (calculated:  $1552\text{ cm}^{-1}$ ) (Figure 21.2 (b)). Experimentally, a new band emerges at  $2112\text{ cm}^{-1}$  with a rise time of  $4.0 \pm 0.5\text{ ps}$ . This band can be assigned to the  $\nu(\text{CN})$  mode in the CT state and hence the time constant represents the conversion rate from the LE to the CT state. As the experimental red-shift of the  $\nu(\text{CN})$  mode of  $103\text{ cm}^{-1}$  differs greatly from the expected value within the assumptions of the RICT model, this model can reliably be excluded. For the TICT and PICT models, shifts of  $110$  and  $36\text{ cm}^{-1}$ , respectively, are calculated for the  $\nu(\text{CN})$  mode, seemingly favoring the TICT model. The calculated intensity increases for both models are in accordance with the experimental results. A qualitative differentiation between these models is possible on the basis of the  $\nu(\text{PhN})$  mode. In the TICT model, decoupling of the dimethylamino and benzonitrile moieties leads to a decrease in conjugation, resulting in a lengthening of the phenyldimethylamino C–

N bond. Consequently, a red-shift of the  $\nu(\text{PhN})$  frequency of  $70\text{ cm}^{-1}$  is predicted with respect to the ground-state frequency, which is found experimentally to be  $1373\text{ cm}^{-1}$  in acetonitrile (Figure 21.2 (a)). In contrast, the PICT model implies the development of partial double-bond character in the phenyldimethylamino C–N bond, leading to a calculated blue shift of  $47\text{ cm}^{-1}$  (Figure 21.2 (a)). Unfortunately, no band corresponding to the  $\nu(\text{PhN})$  mode in the CT state could be assigned in our experiment. This highlights a potential drawback of vibrational spectroscopy, in that vibrational transition moments are typically 2–3 orders of magnitude smaller than those of electronic transitions. However, recent picosecond resonance Raman experiments on natural and isotopically-labeled DMABN have unambiguously identified a mode at  $1281\text{ cm}^{-1}$  in methanol, corresponding to a downshift of  $96\text{ cm}^{-1}$  from its ground-state frequency, as the  $\nu(\text{PhN})$  mode in the CT state.<sup>[73–75]</sup> This finding has been confirmed by a recent picosecond transient IR spectroscopic study with an improved signal-to-noise ratio on DMABN in acetonitrile, in which a new band was observed in the CT state (at  $1276\text{ cm}^{-1}$ ) with the same downshift.<sup>[76]</sup> Thus, the combined results of time-resolved vibrational spectroscopy and CASSCF calculations of excited-state vibrational spectra provide substantial evidence for the TICT model.

### 21.3

#### Structural Information on Hydrogen Bonds after Electronic Excitation: Local Femtosecond Dynamics and Comparison of Vibrational Spectra with Line-Shape Theory

##### 21.3.1

##### Ultrafast Response of Hydrogen-Bonded Complexes after Electronic Excitation of One of the Constituents

In the following, we present an example where femtosecond infrared spectroscopy has been shown to produce results indicating a reorganization of a molecular complex. We have studied the case of the response of an intermolecular hydrogen-bonded complex, of which the acceptor unit is electronically excited to the  $S_1$  state, the hydrogen bond being probed through “spectator” modes. The acceptor unit is the molecule coumarin-102 (C102), a member of the large class of coumarin laser dyes. C102 has a carbonyl group at one end of its  $\pi$ -electronic system, which, by virtue of its high electron density, constitutes an ideal acceptor site for the formation of a hydrogen bond. We have shown that the C=O stretch of C102 is red-shifted when the dye is dissolved in  $\text{CHCl}_3$ , and that upon electronic excitation this band reverts to approximately the position of the C=O stretch of C102 dissolved in  $\text{C}_2\text{Cl}_4$ , where there is no hydrogen-bonding.<sup>[59]</sup> By probing the spectator C=O mode, it was established that a hydrogen bond with the solvent  $\text{CHCl}_3$  is formed when C102 is in the  $S_0$  state, and that within 200 fs (the time resolution of the experiment) this hydrogen bond is cleaved if C102 is promoted to the  $S_1$  state. On a picosecond time scale, solvation dynamics (solvent reorganization) of  $\text{CHCl}_3$  is observed.<sup>[59,63]</sup> We have observed the same features in a study of the dynamics of complexes between

C102 and the phenol monomer or dimer dissolved in the inert solvent  $\text{C}_2\text{Cl}_4$ , where, besides the  $\text{C}=\text{O}$  stretch of C102, the  $\text{O}-\text{H}$  stretch on the hydrogen-donor side can also be studied<sup>[60,61]</sup> (Figure 21.4). We note here that the results of optical experiments (pump-probe, grating scattering, two-pulse photon-echo) on the electronic transition of hydrogen-bonded C102 suggest that the features of hydrogen-bond breaking and subsequent reorganization should also be observable in the dynamics of electronic transitions.<sup>[62]</sup> However, a clear dissection of the signals into contributions from hydrogen-bond cleavage and reorientation dynamics (inertial solvent motion) remains difficult.<sup>[63]</sup>

Interestingly, in the case of the phenol dimer, the hydrogen bond between the two phenol units also contributes to the observed transient vibrational features, since the  $\text{O}-\text{H}$  stretch region shows two contributions from the released phenol dimer: (a) at around  $3610\text{ cm}^{-1}$ , corresponding to the  $\text{O}-\text{H}$  stretching band of the non-H-bonded hydroxyl group, and (b) in the range  $3200\text{--}3550\text{ cm}^{-1}$ , corresponding to the absorption due to the  $\text{O}-\text{H}$  stretch of the hydrogen-bonded hydroxyl group. Case (a) corresponds to the hydroxyl group released from C102 within 200 fs. This signal does not increase at longer time delays, indicating that no additional hydro-

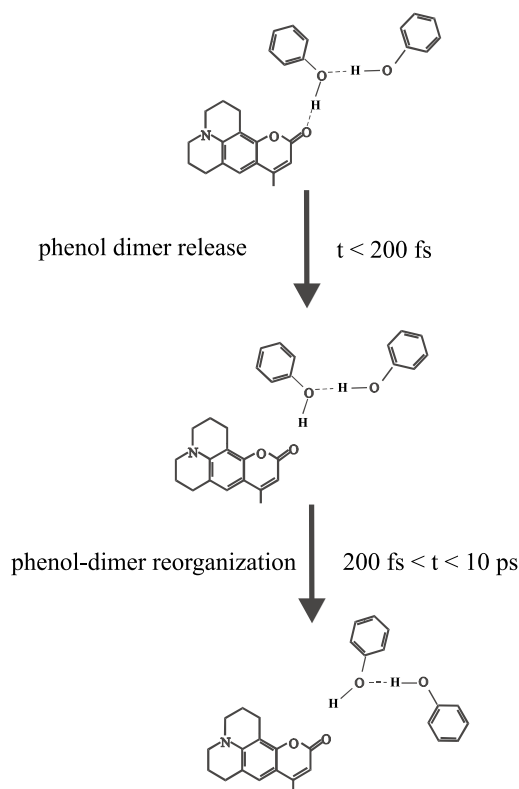


**Fig. 21.4** Schematic representation of the events that occur after electronic excitation of a C102-(phenol)<sub>2</sub> complex. The phenol dimer is released within 200 fs, and subsequent reorganization of this dimer follows with a time constant of 800 fs. The actual structural conformation of the dimer in solution during these processes is not known, hence the presented configurations are merely illustrative.

gen-bond breaking occurs. Case (b) is due to the hydroxyl group involved in the hydrogen bond within the phenol dimer. This band shows additional changes at longer delays with the broad band in the range  $3200\text{--}3550\text{ cm}^{-1}$  being replaced by a smaller and weaker band in the range  $3400\text{--}3550\text{ cm}^{-1}$ . From these observations, it follows that we are indeed observing the *dynamics* of the hydrogen bond of the phenol dimer.<sup>[60,63]</sup>

### 21.3.2

#### Transient IR Spectroscopy of the Phenol Dimer after Release from Optically Excited Coumarin-102: Structural Dynamics

We now discuss the observed transient line shape of the phenol dimer that is released from C102 after cleavage of the hydrogen bond. A broad band centered at  $3350\text{ cm}^{-1}$  is observed 400 fs after electronic excitation of the C102–(phenol)<sub>2</sub> complex (Figure 21.5). This band is then transformed with a time constant of 800 fs to a smaller blue-shifted band at  $3500\text{ cm}^{-1}$ . This implies that after its release the dimer rearranges to a new configuration in which the hydrogen bond is weaker.

The observed transient features may be interpreted with the assumption that the optical pump and infrared probe pulses are separated in time. Figure 21.5 shows the

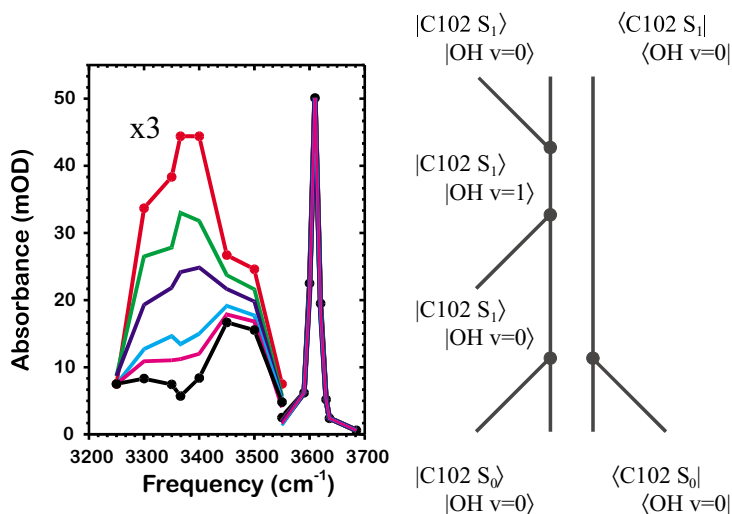


**Fig. 21.5** Dynamics of the O–H stretching band of the released phenol dimer. The narrow band at  $3610\text{ cm}^{-1}$  is due to the free O–H groups of both the phenol monomer and phenol dimer. This band does not change after longer delays. The broad band shows the dynamic rearrangement of the associated O–H group linking the two phenol units in the dimer. The transients were measured at (top-to-bottom):

0.4 ps, 0.7 ps, 1 ps, 1.5 ps, 2 ps, and 5 ps. The double-sided Feynman diagram on the right is identical to diagram A in Figure 4 of ref.<sup>[77]</sup> It describes the dynamics of the released phenol dimer (as well as of the phenol monomer) after its release from C102, assuming that the hydrogen-bond cleavage process and electronic coherences of C102 are much faster than the optical pulse width.

transients at positive pulse delays  $\tau > 200$  fs. We excite the C102–(phenol)<sub>2</sub> complex in the red wing of the electronic absorption spectrum, such that only contributions from the  $v = 0 \rightarrow v = 1$  transition of the O–H stretching mode of the released phenol dimer are responsible for the observed transient infrared absorption signal in the range 3200–3550 cm<sup>−1</sup>. Ground-state contributions of the C102–(phenol)<sub>2</sub> complex due to impulsive stimulated Raman scattering are not seen since we excite with an almost transform-limited optical pump pulse with a duration of 100 fs. We note that the perturbed free-induction decay only contributes at negative time delays.<sup>[77,78]</sup> It thus turns out that the observed transient features can be interpreted as being due to the transient linear absorption spectra of the phenol dimer, as is clear from inspection of the double-sided Feynman diagram (Figure 21.5) indicating the interaction order of the light fields in this pump-probe experiment. An additional diagram describes the ground-state bleaching.<sup>[77]</sup>

In the following, we aim to elucidate the underlying factors responsible for the observed features. To this end, we model the absorption line shape of O–H stretching modes subject to hydrogen bonding using currently existing theories. We focus on the phenol dimer in C<sub>2</sub>Cl<sub>4</sub> at equilibrium and then expand on the case of the phenol dimer after release from the acceptor C102. For this purpose, we first provide a brief introduction to the theories of linear IR spectral line shapes in Section 21.3.3, and then discuss results from the application of these theories on the phenol dimer in Section 21.3.4.

### 21.3.3

#### Theory of Absorption Line Shapes of Vibrational Modes Subject to Hydrogen Bonding

The vibrational absorption line shapes of O–H stretching modes of hydroxyl groups involved in hydrogen bonds exhibit characteristic features, such as large red-shifts proportional to the strength of the hydrogen bond, extreme broadening, and often peculiar substructures.<sup>[37]</sup> It has been suggested that the underlying mechanism for these observed features is strong anharmonic coupling between the high-frequency X–H stretching and other low-frequency modes that modulate the hydrogen bond X–H...Y, such as the X...Y stretching mode. As early as the 1940s, it was suggested by Stepanov that due to the large difference in time scales of the fast X–H mode and the slow X...Y mode, an adiabatic separation can be made leading to effective potential-energy curves for the slow mode defined for every quantum state of the fast mode.<sup>[79]</sup> This can be thought of as being akin to the Born–Oppenheimer approximation, where a separation is made between electronic and nuclear motion. Vibrational transitions are then governed by Franck–Condon factors, indicating the transition moments for excitation of the high-frequency X–H mode accompanied by changes in the quantum state of the low-frequency mode X...Y.<sup>[80]</sup> The effect of anharmonic coupling between a high-frequency and a low-frequency mode can be described in terms of linearly displaced harmonic potential wells for the slow mode:

$$H_{k=0} = \frac{\hbar \cdot \Omega}{2} \cdot [p^2 + q^2], \quad (1a)$$

$$\begin{aligned} H_{k=1} &= \frac{\hbar \cdot \Omega}{2} \cdot [p^2 + (q + \alpha)^2] + \hbar \omega_0 \\ &= \frac{\hbar \cdot \Omega}{2} \cdot [p^2 + q^2] + \hbar \omega_{\text{eff}}(q), \end{aligned} \quad (1b)$$

with:

$$\hbar \cdot \omega_{\text{eff}}(q) = \hbar \cdot \omega_0 + \frac{\hbar \cdot \Omega \cdot \alpha^2}{2} + \hbar \cdot \Omega \cdot \alpha \cdot q. \quad (1c)$$

Here, the coordinates of position  $p$  and momentum  $q$  for the slow mode are dimensionless,  $\Omega$  is the frequency of the slow mode,  $\hbar$  is Planck's constant  $h/2\pi$ ,  $\omega_0$  is the frequency of the fast mode, and  $\alpha$  is a dimensionless anharmonic coupling constant. The indices  $k = 0$  and  $k = 1$  refer to the quantum state of the fast mode. The vibrational transition frequency of the fast mode can thus be considered as being described by a term that is dependent on the positional coordinate of the slow mode. If the surrounding solvent induces fluctuations in the motion of the slow mode, then, through the anharmonic coupling, the motion of the fast mode will also be affected. The damping of vibrational coherence of the fast mode (i.e. dephasing) is thus indirectly induced by the solvent and models taking this into account are denoted as indirect damping mechanisms. On the other hand, if the solvent is directly coupled to the fast mode, direct damping of vibrational coherence of the fast mode is induced by solvent fluctuations.

Several approaches for describing the absorption line shape of the fast mode have been developed during the last three decades. Recently, a thorough comparison of the different models in a unified notation has been given by Henri-Rousseau and Blaise.<sup>[81]</sup> Herein, we use several models described in this paper, namely the indirectly damped semi-classical Robertson–Yarwood model (RY),<sup>[82]</sup> the indirectly damped quantum oscillator model of Henri-Rousseau (HR),<sup>[83]</sup> and the directly damped quantum oscillator model of Rösch and Ratner (RR).<sup>[84]</sup>

#### 21.3.3.1 Semi-Classical Brownian Oscillator Model Based on the Robertson–Yarwood (RY) Approach

In the RY model, the motion of the slow mode is modelled classically as a Brownian oscillator (BO) through the use of a Langevin equation, where the effect of the surrounding solvent is taken into account by a damping parameter and a stochastically fluctuating force. A phenomenological correlation function  $C(t)$  can be defined for the positional coordinate of the slow mode. Using the cumulant expansion explicit expressions for the transition dipole moment correlation function of the fast mode,  $J_{BO}(t)$  can be derived, and, through a Fourier transform of  $J_{BO}(t)$ , the absorption line shape of the fast mode is obtained. This model has successfully been used in the description of linear and nonlinear experiments on electronic transitions of dye molecules in liquid solution<sup>[24,25,27]</sup> based on the well-founded theoretical work on nonlinear spectroscopy developed by Mukamel and co-workers.<sup>[85–88]</sup> We note here that



in the original RY model a classical, even, and real correlation function  $C(t) = C(-t)$  has been used,<sup>[82]</sup> although formally better expressions for a complex correlation function should obey the condition  $C(-t) = C^*(t)$ . We use here Mukamel's formulation<sup>[88]</sup> for  $C(t) = C'(t) + iC''(t)$ , with  $C'(t)$  being the real and  $C''(t)$  the imaginary part of  $C(t)$ :

$$C''(t) = -\frac{S \cdot \Omega^3}{\zeta} \cdot e^{-\gamma \cdot t / 2} \sin(\zeta \cdot t), \quad (2a)$$

$$C'(t) = -\frac{S \cdot \Omega^3}{2\zeta} \cdot \left[ \coth(i \cdot \varphi \cdot \hbar \cdot \beta / 2) \cdot e^{-\varphi \cdot t} - \coth(i \cdot \psi \cdot \hbar \cdot \beta / 2) \cdot e^{-\psi \cdot t} \right] \\ + \frac{4 \cdot S \cdot \Omega^3}{\hbar} \cdot \frac{\gamma}{\beta} \cdot \sum_{n=1}^{\infty} \frac{\nu_n \cdot e^{-\nu_n \cdot t}}{(\Omega^2 + \nu_n^2)^2 - \gamma^2 \cdot \nu_n^2}, \quad (2b)$$

with:

$$\varphi = \frac{\gamma}{2} + i \cdot \zeta, \quad (2c)$$

$$\psi = \frac{\gamma}{2} - i \cdot \zeta, \quad (2d)$$

$$\zeta = \sqrt{\Omega^2 - \frac{\gamma^2}{4}}, \quad (2e)$$

$$\nu_n = \frac{2 \cdot \pi}{\hbar \cdot \beta} \cdot n. \quad (2f)$$

In these equations,  $\gamma$  is the damping constant of the Brownian oscillator,  $\beta = 1/kT$  determines the relative thermal excitation of the low-frequency mode ( $k$  is Boltzmann's constant and  $T$  is the absolute temperature), and the Huang–Rhys factor  $S = \alpha^2/2$  determines the coupling strength between the slow Brownian oscillator and the fast vibrational mode. Depending on the relative magnitude of the damping compared to the frequency of the slow mode, the motion will be underdamped  $\gamma < 2\Omega$ , critically damped  $\gamma = 2\Omega$ , or overdamped  $\gamma > 2\Omega$ . We note that in Mukamel's notation the dimensionless displacement is given by the symbol  $d$ , where  $d = \alpha$ , but an additional time-independent term  $\frac{1}{2}\hbar\Omega \alpha^2$  is present in the excited-state Hamiltonian  $H_{k=1}$ . This extra static term leads to an offset in the transition frequency, which is responsible for the steady-state Stokes shift between the absorption and emission frequencies of electronic transitions. It should be noted that this additional term is not present in the original model due to Robertson and Yarwood.

The transition dipole moment correlation function of the fast mode,  $J_{BO}(t)$ , is given by:

$$J_{BO}(t) = e^{-\left[i \cdot \left(\omega_0 + \frac{\Omega \alpha^2}{2}\right) \cdot t + g_{BO}(t)\right]}, \quad (3a)$$

with the complex line-shape function  $g_{BO}(t)$  defined as:<sup>[88]</sup>

$$g_{BO}(t) = \int_0^t d\tau_1 \int_0^{\tau_1} d\tau_2 \left[ C''(\tau_2) + i \cdot C'''(\tau_2) \right], \quad (3b)$$

The real part of this function is responsible for the broadening of the line shape, whereas the imaginary part takes frequency shifts, such as the dynamic Stokes shift, into account. The absorption line-shape function  $S_{A-BO}(\omega)$  of the fast mode as a function of frequency  $\omega$  is then defined by the Fourier–Laplace transform of  $J_{BO}(t)$ :

$$S_{A-BO}(\omega) = \text{Re} \int_0^\infty J_{BO}(t) \cdot e^{i\omega t} dt. \quad (3c)$$

### 21.3.3.2 Indirectly Damped Quantum Oscillator Model by Henri-Rousseau (HR)

In the indirectly damped quantum oscillator model by Henri-Rousseau and co-workers (HR), the solvent induces changes in the quantum state of the slow mode, and through anharmonic coupling indirectly affects the temporal behavior of the phase coherence of the fast mode. The broadening of the absorption line shape is thus an effect of the indirect damping mechanism. If one derives the linear response of a system composed of a fast and a slow mode in a fully quantum mechanical way, the factor  $\hbar\omega_{\text{eff}}(q)$  contains a quantum operator in the positional coordinate of the slow mode  $q$ . Henri-Rousseau and co-workers have shown that the slow mode becomes a driven mode after excitation of the fast mode. The motion is that of a damped quasi-classical coherent state.<sup>[81]</sup> The transition dipole moment correlation function of the fast mode  $J_{HR}(t)$  is then:

$$J_{HR}(t) = e^{-\left[i \cdot \left(\omega_0 + \frac{\Omega \alpha^2}{2}\right) \cdot t + g_{HR}(t)\right]}, \quad (4a)$$

with the line-shape function  $g_{HR}(t)$ :

$$g_{HR}(t) = -\frac{1}{2} \cdot B^2 \cdot (1 + 2\langle n \rangle) \cdot \left[ 2e^{-\gamma \cdot t / 2} \cdot \cos(\Omega t) - e^{-\gamma \cdot t} - 1 \right] \\ + i \cdot B^2 \cdot \left[ e^{-\gamma \cdot t / 2} \cdot \sin(\Omega t) - \Omega t \right] - i \cdot \alpha^2 \cdot \Omega \cdot t. \quad (4b)$$

Here,  $B$  is the effective anharmonic coupling parameter:

$$B = \frac{\alpha \cdot \sqrt{4\Omega^4 + \gamma^2 \Omega^2}}{2\Omega^2 + \gamma^2 / 2}, \quad (4c)$$

and  $\langle n \rangle$  is the thermal occupation number of the low-frequency mode:

$$\langle n \rangle = \frac{1}{e^{\hbar\Omega / kT} - 1}. \quad (4d)$$

The absorption line shape of the fast mode  $S_{A-HR}(\omega)$  is then given by:

$$S_{A-HR}(\omega) = \text{Re} \int_0^{\infty} J_{HR}(t) \cdot e^{i\omega t} dt. \quad (4e)$$

### 21.3.3.3 Directly Damped Quantum Oscillator Model by Rösch and Ratner (RR)

In the model developed by Rösch and Ratner (RR), the solvent is directly coupled to the fast mode, which is itself anharmonically coupled to a slow mode.<sup>[84]</sup> The solvent is thought to generate a stochastically fluctuating local electric field that couples to the dipole moment operator of the hydrogen bond. Direct damping of the fast mode leads to dephasing and hence to broadening of the absorption line shape. The transition dipole moment correlation function of the fast mode  $J_{RR}(t)$  is defined by:

$$J_{RR}(t) = e^{-\left[ i \cdot \left( \omega_0 + \frac{\Omega \alpha^2}{2} \right) \cdot t + g_{RR}(t) \right]}, \quad (5a)$$

with the line-shape function  $g_{RR}(t)$ :

$$g_{RR}(t) = -\alpha^2 \cdot (1 + 2\langle n \rangle) \cdot [\cos(\Omega t) - 1] + i \cdot \alpha^2 \cdot \sin(\Omega t) - 2i \cdot \alpha^2 \cdot \Omega \cdot t \\ + 2\Delta^2 \int_0^t (t - \tau) \cdot \cos\left(\alpha^2 \cdot \sin(\Omega \tau)\right) \cdot e^{\alpha^2(1+2n)[\cos(\Omega t)-1]} \cdot e^{-i\Omega \tau - \Lambda \tau} d\tau. \quad (5b)$$

Here,  $\Delta$  gives a measure of the coupling strength between the fast mode and the solvent and  $\Lambda$  is the inverse correlation time of the solvent fluctuations. The absorption line shape of the fast mode  $S_{A-RR}(\omega)$  is then given by:

$$S_{A-RR}(\omega) = \text{Re} \int_0^{\infty} J_{RR}(t) \cdot e^{i\omega t} dt. \quad (5c)$$

### 21.3.4

#### Inspection of the O–H Stretch Line Shape of the Phenol Dimer with Line-Shape Theories

##### 21.3.4.1 The O–H Stretch Line Shape of the Phenol Dimer at Equilibrium: Comparison of Gas-Phase and Condensed-Phase Data

The O–H stretching region of the phenol dimer has been studied both in the gas phase and in liquid solution. Felker and co-workers have used ionization-induced stimulated Raman spectroscopy to determine the positions of the O–H vibration of the phenol monomer and of the dimer.<sup>[89]</sup> Ebata *et al.* have reached similar conclusions using IR-UV and stimulated Raman-UV double-resonance spectroscopies.<sup>[90]</sup> In the gas phase, the O–H stretching absorption band of the phenol monomer is found at 3656.7 cm<sup>-1</sup>. In the dimer, the free O–H group has its resonance at almost the same frequency (3654.7 cm<sup>-1</sup>), whereas the O–H stretching band of the hydroxyl group linking the two phenol subunits is located at 3530.3 cm<sup>-1</sup>. This characteristic red-shift is due to weakening of the O–H bond upon formation of the hydrogen

bond. The magnitude of the red-shift of  $126.4\text{ cm}^{-1}$  indicates that only a weak hydrogen bond is formed with an enthalpy of about  $4\text{ kcal/mol}$ .<sup>[91]</sup> Kleinermanns and co-workers have determined the low frequency  $\text{O}\cdots\text{O}$  mode at  $109\text{ cm}^{-1}$  using spectral hole burning and dispersed fluorescence spectroscopy.<sup>[92]</sup> Rotational coherence spectroscopy has been used to show that in the phenol dimer the two phenol units are linked only by a hydrogen bond, and that  $\pi$ -interactions between the aromatic rings are not involved.<sup>[93,94]</sup>

When the phenol dimer is dissolved in  $\text{C}_2\text{Cl}_4$ , a solvent shift is evident from the O–H absorbances (see Figure 21.6). The free O–H band of the phenol monomer is found at  $3610\text{ cm}^{-1}$ , that of the free O–H band of the phenol dimer is located at  $3598\text{ cm}^{-1}$ , and the O–H stretching band of the hydrogen bond in the phenol dimer is found at  $3483\text{ cm}^{-1}$ ; almost the same values have been found in  $\text{CCl}_4$ .<sup>[95]</sup> This means that the red-shift of the O–H stretch upon hydrogen bonding is about the same in the gas phase and in solution, and therefore the strength of the hydrogen bond is not altered upon solvation of the dimer in  $\text{C}_2\text{Cl}_4$ . A tail extending to lower frequencies is present, indicative of species in which the hydrogen bond appears to be stronger. These signals have been attributed to species consisting of more than two phenol units, such as the phenol trimer.<sup>[90,96]</sup> We discard these extra contributions to the IR spectrum, which we estimated to be due to less than 10 % of the total amount of complexes in the solutions of C102 and phenol in  $\text{C}_2\text{Cl}_4$ .<sup>[61]</sup> We will now use the models presented in Section 21.3.2 to simulate the steady-state IR spectrum of associated O–H stretch of the phenol dimer in  $\text{C}_2\text{Cl}_4$ , as shown in Figure 21.6.

We first discuss an analysis of the steady-state IR line shape of the O–H stretching band of the hydrogen-bonded phenol dimer applying the semi-classical RY model. We use the experimental value of  $109\text{ cm}^{-1}$  for the low-frequency mode  $\Omega$ . In Figure 21.7, we show the calculated line shape for three different values of the anharmonic coupling constant  $\alpha$  with varying damping constants  $\gamma$ . This model cannot take into account the red-shift of the O–H stretching mode, the magnitude of which depends

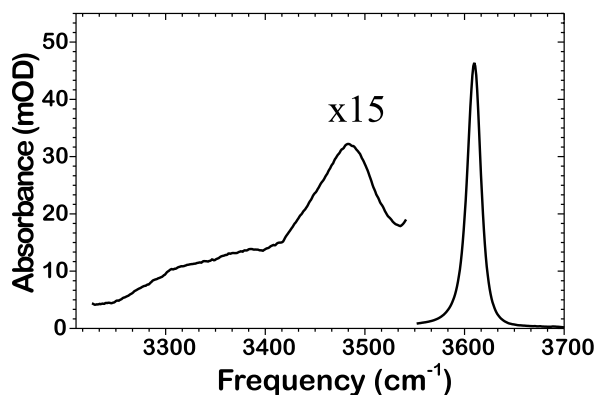


**Fig. 21.6** Infrared spectrum of a 0.035 M solution of phenol in  $\text{C}_2\text{Cl}_4$ . The narrow band at  $3610\text{ cm}^{-1}$  indicates free O–H groups, whereas

the band in the range  $3200\text{--}3550\text{ cm}^{-1}$  is due to associated O–H groups involved in hydrogen bonds between phenol units.

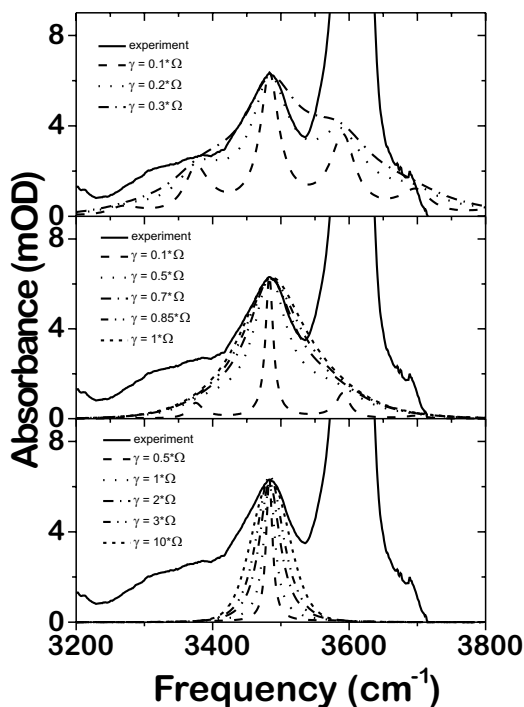


**Fig. 21.7** Calculated line shapes for the associated O–H stretching band of the phenol dimer using the RY model (Eqs. 2–3) for three cases of anharmonic coupling  $\alpha = 0.2$  (bottom);  $\alpha = 0.5$  (middle);  $\alpha = 0.8$  (top). In each case, the value of the damping  $\gamma$  was varied. Other parameters were  $T = 300$  K;  $\omega_0 = 3483$   $\text{cm}^{-1}$ ;  $\Omega = 109$   $\text{cm}^{-1}$ .

on the strength of the hydrogen bond. We thus have to alter the frequency  $\omega_0$  of the O–H high-frequency mode to an appropriate value. It turns out that the static term  $\frac{1}{2}\hbar\Omega\alpha^2$  does not add a significant blue-shift to the calculated line shape, given the magnitude of the anharmonic coupling constant  $\alpha$  that can be expected for this situation. If the line shape is described by the RY model, suitable parameter values span only a narrow range. In the case of  $\alpha = 0.8$ , the calculations even show that a substantial amount of the tail extending into the red may be due to the Franck–Condon progression of the low-frequency mode that is calculated to constitute the overall line shape of the O–H stretch. Even for moderate values of  $\alpha$ , the damping is not so strong that the situation of an overdamped mode ( $\gamma > 2\Omega$ ) should prevail, as is frequently assumed to be the case.

In contrast, the quantum description of an indirectly damped oscillator (HR model) cannot describe the overall line shape, merely due to the fact that no significant line broadening can be invoked with this model (see Figure 21.8). The increase in the value of the damping parameter  $\gamma$  only leads to a collapse of the Franck–Condon progression into a single line, as indicated previously by Blaise et al.<sup>[97]</sup> We also note that for moderate values of  $\alpha$  the evident red-shift is not fully taken into account and an additional adjustment of  $\omega_0$  has to be made.

The directly damped RR model, on the other hand, can take the observed red-shift into account, since not only an increase in the anharmonic coupling constant  $\alpha$  but also in the coupling strength parameter  $\Delta$  leads to a red-shift of the band (see

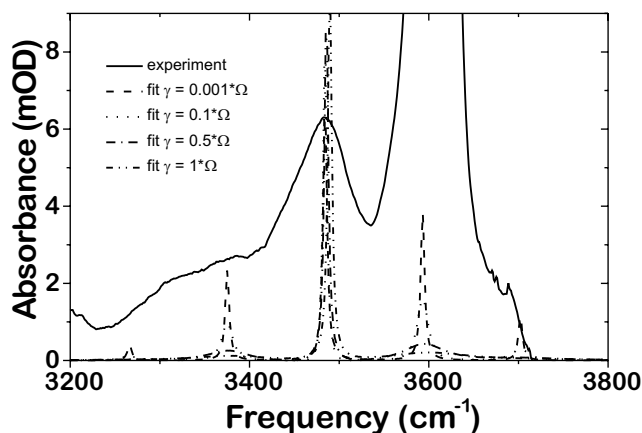


Fig. 21.8. Calculated line shapes for the associated O–H stretching band of the phenol dimer using the HR model (Eqs. 4) for the case

of anharmonic coupling  $\alpha = 0.5$ . The value of the damping  $\gamma$  was varied. Other parameters were  $T = 300$  K;  $\omega_0 = 3525$   $\text{cm}^{-1}$ ;  $\Omega = 109$   $\text{cm}^{-1}$ .

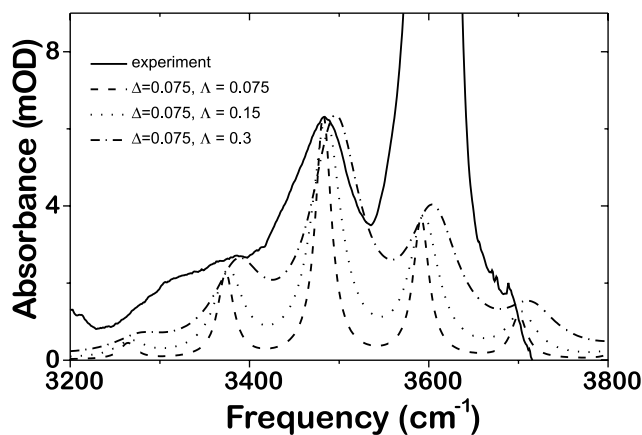


Fig. 21.9. Calculated line shapes for the associated O–H stretching band of the phenol dimer using the RR model (Eqs. 5) for the case of anharmonic coupling  $\alpha = 0.5$  and the solvent

coupling  $\Delta = 0.075$  THz. The value of the solvent fluctuation  $\Delta$  was varied. Other parameters were  $T = 300$  K;  $\omega_0 = 3610$   $\text{cm}^{-1}$ ;  $\Omega = 109$   $\text{cm}^{-1}$ .

Figure 21.9). Broadening, meanwhile, is mainly determined by the magnitude of the inverse correlation time  $\Lambda$ . However, the magnitude of  $\Lambda$  used in the calculations indicates that an extremely short correlation time for solvent fluctuations on the order of a few femtoseconds has to be assumed, and it is difficult to suggest microscopic reasons for such short correlation times.

Overall, none of these methods leads directly to a full description of the line shape of the O–H stretching band of the hydrogen bond in the phenol dimer. In any

case, the models indicate that part of the line shape is due to substructure as dictated by the Franck–Condon progression. On the other hand, in the gas-phase, only a single peak with no substructure has been observed.<sup>[89,90]</sup> Whether these models give a proper description of the solvated phenol dimer thus requires further investigation. We note here that these models imply that all parameters have the same value for each member of the ensemble of dimers. It may well be the case that due to solvent interaction there may be a small variation in, for instance,  $\alpha$ . In addition, the phenol dimer is a rather “floppy” complex, such that variation in the angle between the two phenol units due to solvent motion has to be taken into account. One might, for instance, implement this using the derivation of Abramczyk.<sup>[81,98]</sup> This would lead to additional contributions to the overall line broadening.

#### 21.3.4.2 The O–H Stretching Line Shape of the Rearranging Phenol Dimer

In contrast to the steady-state case, parameters such as  $\alpha(\tau)$ ,  $\gamma(\tau)$ ,  $\Omega(\tau)$ ,  $\Delta(\tau)$ , and  $\Lambda(\tau)$  can also be time-dependent, reflecting the fact that the nature of the slow mode, the coupling between the slow and the fast mode, the coupling of the slow mode with the solvent, or of the fast mode with the solvent may all depend on the reorganization of the phenol dimer. In addition, if part of the excitation energy is deposited in the slow mode of the hydrogen bond, the thermal excitation number parameter  $\langle n(\tau) \rangle$  will also vary with time. This shows that there are many options for a quantitative explanation of the transient data, even more than is the case for the phenol dimer in equilibrium. The fact that the width, strength, and frequency down-shift of the O–H stretching band diminish in magnitude as the dimer reorganizes points to a decrease in the anharmonic coupling strength  $\alpha$ , and thus in the strength of the hydrogen bond. For example, Figure 21.10 depicts the calculated line shapes for the associated O–H stretching band of the phenol dimer 400 fs after initial excitation of the C102–(phenol)<sub>2</sub> complex using the RY model. Comparison of these results with those depicted in Figure 21.7 suggests that both  $\alpha$  and  $\gamma$  diminish slightly when the phenol dimer rearranges.

## 21.4

### Conclusions and Prospects

In this contribution, we have shown that ultrafast chemistry can be studied in a site-specific manner through the use of femtosecond infrared spectroscopy. The transient behavior of infrared transitions (positions, transition moments, line shapes) has the potential to reveal structural dynamics of molecular systems undergoing ultrafast chemical reactions. Comparison between experimental infrared spectra and the results of quantum chemical calculations leads to structural information on transient states, from which reaction mechanisms can be deduced, as illustrated by the example of intramolecular charge-transfer in 4-(dimethylamino)benzonitrile. Hydrogen-bonding dynamics can be studied in detail by virtue of the fact that the line shapes reflect the nature of the hydrogen bond owing to strong anharmonic coupling between the vibrational modes. We have demonstrated that initially present

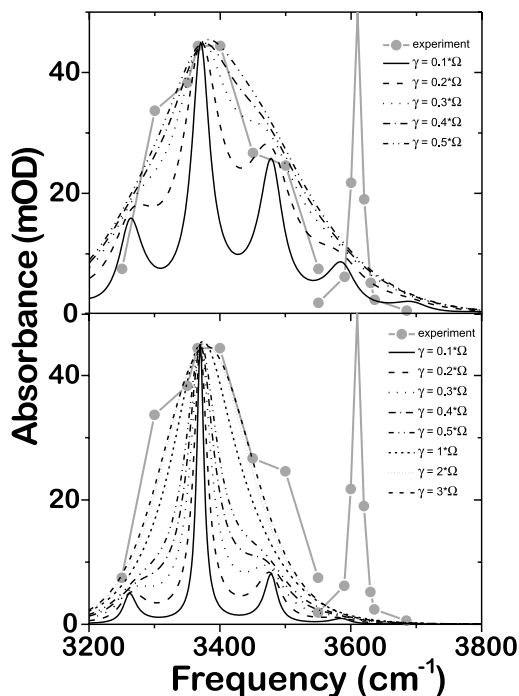


**Fig. 21.10.** Calculated line shapes for the associated O–H stretching band of the phenol dimer 400 fs after initial excitation of the C102–(phenol)<sub>2</sub> complex using the RY model (Eqs. 2–3) for two cases of anharmonic coupling  $\alpha = 0.5$  (bottom);  $\alpha = 0.8$  (top). In each case, the value of the damping  $\gamma$  was varied. Other parameters were  $T = 300$  K;  $\omega_0 = 3370$  cm<sup>−1</sup>;  $\Omega = 109$  cm<sup>−1</sup>.

hydrogen bonds between the coumarin-102 chromophore and hydrogen donors such as chloroform or phenol are cleaved within 200 fs, which is followed by rearrangement of the surroundings on a time scale of 0.5–10 ps. In the case of release of a phenol dimer, we have shown that the broad line shape of the O–H stretching mode due to the hydrogen bond within the dimer rearranges into a blue-shifted smaller band. We have applied line-shape theories of strongly anharmonically coupled vibrations due to hydrogen-bonding to the case of the phenol dimer.

In addition to the studies presented here, we have demonstrated that the observation of coherent vibrational dynamics of a hydrogen bond in the electronic ground state obtained by IR pump-IR probe spectroscopy provides the first experimental evidence for anharmonic coupling of fast and slow vibrational motions in a hydrogen bond.<sup>[99,100]</sup> Even more detailed structural information will become accessible by extension to nonlinear infrared techniques, such as 2D-pump-probe infrared spectroscopy<sup>[101–103]</sup> and IR photon echoes.<sup>[104–109]</sup> The existence of coherent wavepacket oscillations for several picoseconds might allow for optical manipulation of wavepacket motion, i.e. coherent control by repetitive interaction with femtosecond IR pulses, in particular with amplitude- and phase-shaped pulses.<sup>[110,111]</sup>

We are convinced that we are at a crossroads in femtochemistry, where ultrafast structural techniques, such as IR- and X-ray spectroscopy, electron- and X-ray diffraction, will open to new paths leading to exciting new findings.



## Acknowledgements

We thank Christian Chudoba, Frank Tschirschwitz, Andreas Kummrow, and Jens Stenger, without whose experimental work this contribution would not have been possible, Klaas Zachariasse for valuable discussions, and Thomas Elsaesser for continuous support of these projects and valuable discussions. ETJN gratefully acknowledges financial support from the Deutsche Forschungsgemeinschaft through the *Schwerpunktprogramm "Femtosekunden-Spektroskopie elementarer Anregungen in Atomen, Molekülen und Clustern"*. JD gratefully acknowledges financial support from the Deutsche Forschungsgemeinschaft in the form of a fellowship.

## References

- 1 R. L. Fork, B. I. Greene, C. V. Shank, *Appl. Phys. Lett.* **1981**, 38, 671.
- 2 J. A. Valdmanis, R. L. Fork, *IEEE J. Quantum Electron.* **1986**, QE-22, 112.
- 3 A. Migus, C. V. Shank, E. P. Ippen, R. L. Fork, *IEEE J. Quantum Electron.* **1982**, QE-18, 101.
- 4 W. H. Knox, M. C. Downer, R. L. Fork, C. V. Shank, *Opt. Lett.* **1984**, 9, 552.
- 5 W. H. Knox, *IEEE J. Quantum Electron.* **1988**, QE-24, 388.
- 6 D. E. Spence, P. N. Kean, W. Sibbett, *Opt. Lett.* **1991**, 16, 42.
- 7 P. Maine, D. Strickland, P. Bado, M. Pessot, G. Mourou, *IEEE J. Quantum Electron.* **1988**, QE-24, 398.
- 8 J. V. Rudd, G. Korn, S. Kane, J. Squier, G. Mourou, P. Bado, *Opt. Lett.* **1993**, 18, 2044.
- 9 C. Spielmann, P. F. Curley, T. Brabec, F. Krausz, *IEEE J. Quantum Electron.* **1994**, QE-30, 1100.
- 10 S. Backus, C. G. Durfee III, M. M. Murnane, H. C. Kapteyn, *Rev. Sci. Instrum.* **1998**, 69, 1207.
- 11 M. K. Reed, M. K. Steiner-Shepard, M. S. Armas, D. K. Negus, *J. Opt. Soc. Am. B* **1995**, 12, 2229.
- 12 G. R. Fleming, *Chemical Applications of Ultra-fast Spectroscopy*, Oxford University Press, **1986**.
- 13 G. R. Fleming, P. G. Wolynes, *Phys. Today* **1990**, 36 (May issue).
- 14 Press release of the Nobel Foundation, **1999**.
- 15 A. H. Zewail, *Science* **1988**, 242, 1645.
- 16 L. R. Khundkar, A. H. Zewail, *Annu. Rev. Phys. Chem.* **1990**, 41, 15.
- 17 A. H. Zewail, *J. Phys. Chem.* **1993**, 97, 12427.
- 18 A. H. Zewail, in *Femtosecond Chemistry*, vol. 1 (Eds.: J. Manz, L. Wöste), VCH, Weinheim, **1995**, chapter 2, p. 15.
- 19 A. H. Zewail, *J. Phys. Chem.* **1996**, 100, 12701.
- 20 A. H. Zewail, *J. Phys. Chem. A* **2000**, 104, 5660.
- 21 P. F. Barbara, G. C. Walker, T. P. Smith, *Science* **1992**, 256, 975.
- 22 P. F. Barbara, T. J. Meyer, M. A. Ratner, *J. Phys. Chem.* **1996**, 100, 13148.
- 23 G. A. Voth, R. M. Hochstrasser, *J. Phys. Chem.* **1996**, 100, 13034.
- 24 E. T. J. Nibbering, D. A. Wiersma, K. Duppen, *Chem. Phys.* **1994**, 183, 167.
- 25 G. R. Fleming, M. Cho, *Annu. Rev. Phys. Chem.* **1996**, 47, 109.
- 26 R. M. Strat, M. Maroncelli, *J. Phys. Chem.* **1996**, 100, 12981.
- 27 W. P. de Boeij, M. S. Pschenichnikov, D. A. Wiersma, *Annu. Rev. Phys. Chem.* **1998**, 49, 99.
- 28 R. Grote, J. T. Hynes, *J. Chem. Phys.* **1980**, 73, 2715.
- 29 G. van der Zwan, J. T. Hynes, *J. Phys. Chem.* **1985**, 89, 4181.
- 30 W. Jarzeba, G. C. Walker, A. E. Johnson, P. F. Barbara, *Adv. Photochem.* **1990**, 15, 1.
- 31 J. C. Williamson, J. Che, H. Ihee, H. Frey, A. H. Zewail, *Nature* **1997**, 386, 159.
- 32 C. Rischel, A. Rousse, I. Uschmann, P.-A. Albouy, J.-P. Geindre, P. Audebert, J.-C. Gauthier, E. Förster, J.-L. Martin, A. Antonetti, *Nature* **1997**, 390, 490.

- 33 J. Larsson, P. A. Heimann, A. M. Lindenberg, P. J. Schuck, P. H. Bucksbaum, R. W. Lee, H. A. Padmore, J. S. Wark, R. W. Falcone, *Appl. Phys. A* **1998**, 66, 587.
- 34 C. Rose-Petruck, R. Jimenez, T. Guo, A. Cavalleri, C. W. Siders, F. Ráksi, J. A. Squier, B. C. Walker, K. R. Wilson, C. P. J. Barty, *Nature* **1999**, 398, 310.
- 35 R. Haight, *Surf. Sci. Rep.* **1995**, 21, 275.
- 36 F. Raksi, K. R. Wilson, Z. Jiang, A. Ikhlef, C. Y. Côté, J.-C. Kieffer, *J. Chem. Phys.* **1996**, 104, 6066.
- 37 D. Hadzi, S. Bratos, in *The Hydrogen Bond: Recent Developments in Theory and Experiments*, vol. II (Eds.: P. Schuster, G. Zundel, C. Sandorfy), North Holland, Amsterdam, **1976**, chapter 12, p. 565.
- 38 F. Seifert, V. Petrov, M. Woerner, *Opt. Lett.* **1994**, 19, 140.
- 39 P. Hamm, M. Lim, R. M. Hochstrasser, *J. Chem. Phys.* **1997**, 107, 10523.
- 40 R. A. Kaindl, F. Eickemeyer, M. Woerner, T. Elsaesser, *Appl. Phys. Lett.* **1999**, 75, 1060.
- 41 P. Hamm, R. A. Kaindl, J. Stenger, *Opt. Lett.* **2000**, 25, 1798.
- 42 T. Elsaesser, W. Kaiser, *Chem. Phys. Lett.* **1986**, 128, 231.
- 43 T. Elsaesser, in *Femtosecond Chemistry*, vol. 2 (Eds.: J. Manz, L. Wöste), VCH, Weinheim, **1995**, chapter 18, p. 563.
- 44 D. Raftery, E. Gooding, A. Romanovsky, R. M. Hochstrasser, *J. Chem. Phys.* **1994**, 101, 8572.
- 45 P. A. Anfinrud, C.-H. Han, T. Lian, R. M. Hochstrasser, *J. Phys. Chem.* **1991**, 95, 574.
- 46 T. P. Dougherty, E. J. Heilweil, *J. Chem. Phys.* **1994**, 100, 4006.
- 47 T. P. Dougherty, E. J. Heilweil, *Chem. Phys. Lett.* **1994**, 227, 19.
- 48 J. C. Owrrutsky, A. P. Baronavski, *J. Chem. Phys.* **1996**, 105, 9864.
- 49 P. T. Snee, H. Yang, K. T. Kotz, C. K. Payne, C. B. Harris, *J. Phys. Chem. A* **1999**, 103, 10426.
- 50 P. A. Anfinrud, C. Han, R. M. Hochstrasser, *Proc. Natl. Acad. Sci. USA* **1989**, 86, 8387.
- 51 M. Lim, T. A. Jackson, P. A. Anfinrud, *Science* **1995**, 269, 962.
- 52 M. Lim, T. A. Jackson, P. A. Anfinrud, *J. Chem. Phys.* **1995**, 102, 4355.
- 53 M. Lim, T. A. Jackson, P. A. Anfinrud, *Nature Struct. Biol.* **1997**, 4, 209.
- 54 P. Hamm, S. M. Ohline, W. Zinth, *J. Chem. Phys.* **1997**, 106, 519.
- 55 P. Hamm, M. Zurek, T. Röschinger, H. Patzelt, D. Oesterhelt, W. Zinth, *Chem. Phys. Lett.* **1997**, 268, 180.
- 56 C. Chudoba, A. Kummrow, J. Dreyer, J. Stenger, E. T. J. Nibbering, T. Elsaesser, K. A. Zachariasse, *Chem. Phys. Lett.* **1999**, 309, 357.
- 57 J. Dreyer, A. Kummrow, *J. Am. Chem. Soc.* **2000**, 122, 2577.
- 58 A. Kummrow, J. Dreyer, C. Chudoba, J. Stenger, E. T. J. Nibbering, T. Elsaesser, *J. Chin. Chem. Soc.* **2000**, 47, 721.
- 59 C. Chudoba, E. T. J. Nibbering, T. Elsaesser, *Phys. Rev. Lett.* **1998**, 81, 3010.
- 60 C. Chudoba, E. T. J. Nibbering, T. Elsaesser, *J. Phys. Chem. A* **1999**, 103, 5625.
- 61 E. T. J. Nibbering, C. Chudoba, T. Elsaesser, *Isr. J. Chem.* **1999**, 39, 333.
- 62 F. Tschirschwitz, E. T. J. Nibbering, *Chem. Phys. Lett.* **1999**, 312, 169.
- 63 E. T. J. Nibbering, F. Tschirschwitz, C. Chudoba, T. Elsaesser, *J. Phys. Chem. A* **2000**, 104, 4236.
- 64 E. T. J. Nibbering, T. Elsaesser, *Appl. Phys. B* **2000**, 71, 439.
- 65 F. Bernardi, M. Olivucci, M. A. Robb, *Chem. Soc. Rev.* **1996**, 321.
- 66 B. O. Roos, *Acc. Chem. Res.* **1999**, 32, 137.
- 67 E. Lippert, W. Lüder, F. Moll, W. Nägele, H. Boos, H. Prigge, I. Seibold-Blankenstein, *Angew. Chem.* **1961**, 73, 695.
- 68 K. Rotkiewicz, K. H. Grellmann, Z. R. Grabowski, *Chem. Phys. Lett.* **1973**, 19, 315.
- 69 K. Rotkiewicz, K. H. Grellmann, Z. R. Grabowski, *Chem. Phys. Lett.* **1973**, 21, 212.
- 70 U. Leinhos, W. Kühnle, K. A. Zachariasse, *J. Phys. Chem.* **1991**, 95, 2013.
- 71 W. Schuddeboom, S. A. Jonker, J. H. Warman, U. Leinhos, W. Kühnle, K. A. Zachariasse, *J. Phys. Chem.* **1992**, 96, 10809.
- 72 A. Sobolewski, W. Sudholt, W. Domcke, *J. Phys. Chem. A* **1998**, 102, 2716.
- 73 W. M. Kwok, C. Ma, D. Phillips, P. Matousek, A. W. Parker, M. Towrie, *J. Phys. Chem. A* **2000**, 104, 4188.
- 74 W. M. Kwok, C. Ma, P. Matousek, A. W. Parker, D. Phillips, W. T. Toner, M. Towrie, *Chem. Phys. Lett.* **2000**, 322, 395.
- 75 W. M. Kwok, C. Ma, P. Matousek, A. W. Parker, D. Phillips, W. T. Toner, M. Towrie, S. Umapathy, *J. Chem. Phys. A* **2001**, 105, 984.
- 76 H. Okamoto, *J. Phys. Chem. A* **2000**, 104, 4182.

- 77 K. Wynne, R. M. Hochstrasser, *Chem. Phys.* **1995**, 193, 211.
- 78 P. Hamm, *Chem. Phys.* **1995**, 200, 415.
- 79 B. I. Stepanov, *Nature* **1946**, 157, 808.
- 80 Y. Marechal, A. Witkowski, *J. Chem. Phys.* **1968**, 48, 3697.
- 81 O. Henri-Rousseau, P. Blaise, *Adv. Chem. Phys.* **1998**, 103, 1.
- 82 G. N. Robertson, J. Yarwood, *Chem. Phys.* **1978**, 32, 267.
- 83 B. Boulil, J.-L. DeJardin, N. El Ghandour, O. Henri-Rousseau, *J. Mol. Struct. Theochem.* **1994**, 314, 83.
- 84 N. Rösch, M. A. Ratner, *J. Chem. Phys.* **1974**, 61, 3344.
- 85 Y. J. Yan, S. Mukamel, *J. Chem. Phys.* **1988**, 88, 5735.
- 86 Y. J. Yan, S. Mukamel, *J. Chem. Phys.* **1988**, 89, 5160.
- 87 Y. Tanimura, S. Mukamel, *Phys. Rev. E* **1993**, 47, 118.
- 88 S. Mukamel, *Principles of Nonlinear Optical Spectroscopy*, Oxford University Press, Oxford, **1995**, chapter 8.
- 89 G. V. Hartland, B. F. Henson, V. A. Venturo, P. M. Felker, *J. Phys. Chem.* **1992**, 96, 1164.
- 90 T. Ebata, T. Watanabe, N. Mikami, *J. Phys. Chem.* **1995**, 99, 5761.
- 91 G. C. Pimentel, A. L. McClellan, *The Hydrogen Bond*, W. H. Freeman and Co., San Francisco, **1960**.
- 92 M. Schmitt, U. Henrichs, H. Müller, K. Kleiermanns, *J. Chem. Phys.* **1995**, 103, 9918.
- 93 L. L. Connell, S. M. Ohline, P. W. Joireman, T. C. Corcoran, P. M. Felker, *J. Chem. Phys.* **1992**, 96, 2585.
- 94 P. M. Felker, A. H. Zewail, in *Femtosecond Chemistry*, vol. 1 (Eds.: J. Manz, L. Wöste), VCH, Weinheim, **1995**, chapter 5, p. 193.
- 95 L. J. Bellamy, R. J. Pace, *Spectrochim. Acta* **1966**, 22, 525.
- 96 D. Clotman, D. Van Lerberghe, Th. Zeegers-Huyskens, *Spectrochim. Acta A* **1970**, 26A, 1621.
- 97 P. Blaise, O. Henri-Rousseau, A. Grandjean, *Chem. Phys.* **1999**, 244, 405.
- 98 H. Abramczyk, *Chem. Phys.* **1985**, 94, 91.
- 99 J. Stenger, D. Madsen, J. Dreyer, E. T. J. Nibbering, P. Hamm, T. Elsaesser, *J. Phys. Chem A* **2001**, 105, 2929.
- 100 J. Stenger, D. Madsen, J. Dreyer, E. T. J. Nibbering, P. Hamm, T. Elsaesser, *Chem Phys. Lett.* **2001**, in press.
- 101 P. Hamm, M. Lim, R. M. Hochstrasser, *J. Phys. Chem. B* **1998**, 102, 6123.
- 102 P. Hamm, M. Lim, W. F. DeGrade, R. M. Hochstrasser, *Proc. Natl. Acad. Sci. USA* **1999**, 96, 2036.
- 103 P. Hamm, M. Lim, W. F. DeGrade, R. M. Hochstrasser, *J. Chem Phys.* **2000**, 112, 1907.
- 104 D. Zimdars, A. Tokmakoff, S. Chen, S. R. Greenfield, M. D. Fayer, T. L. Smith, H. A. Schwettman, *Phys. Rev. Lett.* **1993**, 70, 2718.
- 105 C. W. Rella, A. Kwok, K. Rector, J. R. Hill, H. A. Schwettman, D. D. Dlott, M. D. Fayer, *Phys. Rev. Lett.* **1996**, 77, 1648.
- 106 K. D. Rector, M. D. Fayer, *J. Chem. Phys.* **1998**, 108, 1794.
- 107 P. Hamm, M. Lim, R. M. Hochstrasser, *Phys. Rev. Lett.* **1998**, 81, 5326.
- 108 M. Lim, P. Hamm, R. M. Hochstrasser, *Proc. Natl. Acad. Sci. USA* **1998**, 95, 15315.
- 109 P. Hamm, M. Lim, W. F. DeGrade, R. M. Hochstrasser, *J. Phys. Chem. A* **1999**, 103, 10049.
- 110 R. A. Kaindl, M. Wurm, K. Reimann, P. Hamm, A. M. Weiner, M. Woerner, *J. Opt. Soc. Am. B* **2000**, 17, 2086.
- 111 F. Eickemeyer, R. A. Kaindl, M. Woerner, T. Elsaesser, A. M. Weiner, *Opt. Lett.* **2000**, 25, 1472.

## 22

### **Vibrational Coherence in Electron Donor–Acceptor Complexes: Assignment of the Oscillatory Mode**

*Igor V. Rubtsov and Keitaro Yoshihara*

#### **Abstract**

The excited-state dynamics of several electron donor–acceptor complexes have been studied by a femtosecond fluorescence up-conversion technique. The spontaneous fluorescence of the complexes exhibits an oscillatory feature, which is superimposed by an ultrafast decay component. For complexes with three different acceptors, namely tetracyanoethylene, chloranil, and fluoranil, the oscillation can be assigned to out-of-plane vibrations of the acceptors. The peak-shift correlation function shows an ultrafast relaxation attributable mainly to the intramolecular vibrational-energy redistribution process, which is superimposed by the oscillatory component, demonstrating the modulation of the transition frequency during the vibration. At the same time, a modulation of the mean transition moment is observed, which gives an indication of a non-Condon transition. Thus, two mechanisms are found to be responsible for the observed oscillations: the modulation of the transition frequency and the modulation of the mean transition moment as a result of the vibrational motion.

#### **22.1**

##### **Introduction**

It is now easy to generate optical pulses of shorter than 50 fs duration in the visible or near-IR regions. As the spectrum of these pulses is broad, vibrations with frequencies smaller than the pulse bandwidth can be excited coherently. In other words, if the excitation pulse duration is shorter than a vibrational period, the vibration coupled to the electronic transition is excited coherently. This coherence can be observed by spectroscopic methods in real time as oscillations (see, for example, refs.<sup>[1–11]</sup>) and specific information can be gained about the dynamics of particular vibrational modes. Coherent spectroscopy is currently a separate spectroscopic method for studying vibrational relaxation, vibrational dephasing, and the contribution of particular vibrations to chemical reactions.

Several methods are available for observing vibrational coherence using short pulses at the frequency of electronic transitions. Coherence in the ground electronic

state can be measured by a time-resolved Raman scattering technique. By a transient absorption method with electronic excitation of the molecular system, coherence can be observed in both the ground and excited electronic states. The advantage of the time-resolved fluorescence method is that it is only sensitive to the excited electronic state. A coherence observed in spontaneous fluorescence is thus caused only by the vibrations in the excited electronic state, which offers a tool for studying the role of particular vibrations in photoreactions. In this contribution, we describe the application of coherent spectroscopy, particularly the time-resolved fluorescence method, to the study of the vibrations coupled to charge separation in electron D–A complexes in solution.

Another approach is to use short IR pulses to detect a particular vibration. Though this method is now being actively developed, even the shortest IR pulses should consist of at least one oscillation period, which makes it impossible to observe coherence in a molecular system having a vibration of the same wavelength as the probe light.

Early reports of vibrational coherence concerned diatomic molecules in the gas phase,<sup>[1]</sup> in which only one vibrational frequency was involved. Later, coherent oscillations were observed in polyatomic molecules in the liquid phase<sup>[2–12]</sup> and even in proteins.<sup>[4–7]</sup> The more complicated is a molecular system, the less clear is the assignment of the coherence to a particular vibrational mode. In the work described herein, the vibrational coherence in systems of medium complexity in the liquid phase has been studied. Specifically, we have examined various electron donor–acceptor (EDA) complexes formed by relatively large organic molecules. Even though such complexes have many inter- and intramolecular vibrational modes, the underdamped oscillations with only one frequency predominate.<sup>[8–11]</sup>

Electronic states having charge-transfer character can be found in many natural molecular systems. For example, in iron porphyrin, which is present in heme proteins such as myoglobin, hemoglobin, cytochromes, etc., relaxation of the electronic excited state passes through several electronic states having charge-transfer (CT) character.<sup>[13]</sup> The photosynthetic reaction center contains a chlorophyll dimer, of which the charge-transfer state is considered to play an important role in the charge separation.<sup>[14]</sup>

Upon photoexcitation of a “weak” EDA complex to the charge-transfer band, an electron is transferred from the HOMO located mainly on the donor to the LUMO located mainly on the acceptor.<sup>[15]</sup> Thus, the absorption of a photon is accompanied by electron transfer from the donor to the acceptor. When a molecular system undergoes a charge-transfer reaction, the equilibrium positions of the nuclei of both reacting components change. After excitation of the EDA complex, the nuclei have to relax to the equilibrium geometry corresponding to the almost ionic state. As a result, various vibrations are excited in the complex. In other words, several intra- and intermolecular vibrations are coupled to the optical transition. Surprisingly, only one oscillating frequency has been observed experimentally in EDA complexes examined to date.<sup>[8–11]</sup> The origin of even this one vibration is not clear yet; its assignment has been one of the goals of the present work.

A particular EDA complex that has recently been studied by several methods is that of hexamethylbenzene (HMB) with tetracyanoethylene (TCNE).<sup>[9–11]</sup> In transient absorption experiments, an oscillation with a frequency of  $162\text{ cm}^{-1}$ , excited by impulsive stimulated Raman scattering, was observed in the bleach recovery signal.<sup>[9]</sup> This oscillation was assigned to vibration in the *ground* electronic state of the complex. A peak at about  $163\text{--}165\text{ cm}^{-1}$  was observed in the resonance Raman spectrum.<sup>[16–18]</sup> Recently, we observed an oscillation in the spontaneous fluorescence of this complex, with a frequency of about  $155\text{ cm}^{-1}$ ,<sup>[11]</sup> attributable to a coherent vibration in the *excited* electronic state. The oscillations observed in these three types of experiment have very similar frequencies. It was suggested that this coherence is due to the *intermolecular* vibrational mode in either the ground or excited electronic states. At the same time, the frequencies of the *intermolecular* vibrations are expected to be vastly different in the ground and excited states due to a large Coulombic attraction in the excited state of EDA complexes, the excited state being ionic and the ground state being almost neutral. This makes the assignment of the observed oscillations to the intermolecular stretching mode questionable.

In this contribution, we present fluorescence data on the ultra-fast time scale for the coherence in EDA complexes and discuss the assignment of the observed oscillations. The structure of the paper is as follows. After a short description of experimental aspects, the evolution of the fluorescence spectrum of TCNE–HMB complex is discussed, which is followed by an analysis of the mechanisms causing oscillations. Finally, various EDA complexes are considered with a view to assigning the oscillatory features to particular vibrations in the complexes.

## 22.2 Experimental

Time-resolved fluorescence measurements were made using a femtosecond fluorescence up-conversion set-up, which has been described in detail elsewhere.<sup>[19]</sup> Briefly, an all-solid-state cavity damped chromium:forsterite laser was used as a source of short light pulses with a wavelength of around  $1270\text{ nm}$  and a pulse duration of  $55\text{ fs}$ . The second harmonic (SH) pulses generated by a  $\beta$ -barium borate crystal were compressed by a prism pair to  $44\text{ fs}$  and used for excitation of the sample. The central wavelength of the laser could be slightly tuned resulting in tuning of the SH central wavelength from  $610$  to  $655\text{ nm}$ . The collected fluorescence was gated by the fundamental pulses and passed through an optical delay line. The up-converted light intensity at the sum frequency was measured by a photomultiplier attached to a monochromator. The instrument response function measured as a time-resolved Raman scattering from a pure solvent was  $75\text{ fs}$  (FWHM). The sample was circulated in a fused silica flow cell with an optical path-length of  $0.5\text{ mm}$  and walls of thickness  $0.7\text{ mm}$ . The experiments were performed at  $23^\circ\text{C}$ . Spectrophotometric grade chemicals were used as received. The donors and acceptors used in this work are illustrated in Figure 22.1. The concentrations of the donor (D) and acceptor (A) were kept such that mostly 1:1 complexes were formed. Since the equilibrium con-

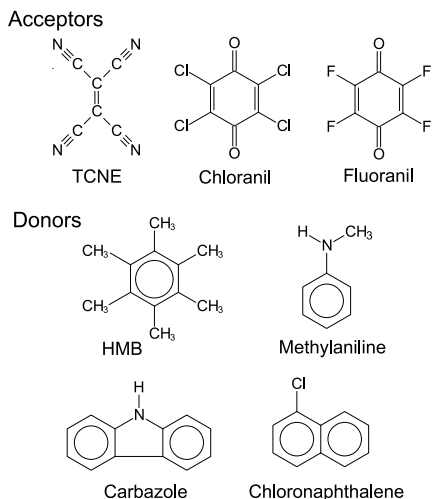


**Fig. 22.1** Donors and acceptors used in this work.

stands for the formation of both D–A and D–A–D complexes are strongly dependent on the solvent used, care was taken in nonpolar solvents to minimize 1:2 complex formation. For complexes of TCNE with HMB in  $\text{CCl}_4$ , experiments were performed with TCNE concentrations of  $\sim 6$  mM and HMB concentrations of  $\sim 30$  mM, which led to about 18% of the 1:2 complex.

## 22.3

### Results and Discussion

#### 22.3.1

##### Oscillations in the TCNE–HMB Complex

The complex that we have studied in greatest detail is that of TCNE with HMB. Upon complexation, a broad absorption band (FWHM  $\sim 5500$   $\text{cm}^{-1}$ ), the so-called CT band, appears with a maximum at 537 nm in  $\text{CCl}_4$ , the position of this maximum being slightly solvent-dependent. The time-integrated fluorescence spectrum is also broad (FWHM  $\sim 4100$   $\text{cm}^{-1}$ ), with a maximum at 917 nm in  $\text{CCl}_4$ ; <sup>[16,18]</sup> this maximum is strongly dependent on the solvent polarity since the excited state of the complex is ionic. The Stokes shift is very large even in nonpolar solvents such as  $\text{CCl}_4$  ( $\sim 7500$   $\text{cm}^{-1}$ ), where it is mainly due to internal reorganization energy. We measured the fluorescence from the complex after photoexcitation in the CT band. On a long time scale, it shows decay with a time constant of about 13 ps, which can be assigned to the excited-state lifetime.

The fluorescence time profiles were measured from 700 nm (at the very “blue” side of the time-integrated fluorescence spectrum) to 970 nm (which is to the red from the fluorescence maximum). Fluorescence decays measured at 774 nm and

907 nm are presented in Figure 22.2 as representative examples. The fluorescence data were fitted by the function  $f(t)$  (Eq. (1)) convoluted with the instrument response function.

$$f(t) = A_1 \exp(-t/\tau_1) + A_2 \exp(-t/\tau_2) + A_3 \cos(2\pi\kappa t + \phi) \exp(-t/\tau_{\text{damp}}) \quad (1)$$

Here,  $\kappa$ ,  $\phi$ , and  $\tau_{\text{damp}}$  are the frequency (in  $\text{cm}^{-1}$ ), the initial phase, and the damping time of the oscillation, respectively. A clear oscillation in the fluorescence intensity can be seen, with a time period of 216 fs, which corresponds to a frequency of  $155 \pm 3 \text{ cm}^{-1}$ . Oscillations with the same frequency were observed for eight wavelengths in the range 700 to 895 nm. At 907 nm, the oscillatory component is observable (Figure 22.2), though it cannot be fitted well with a single sinusoidal function. Another frequency seems to be involved in the initial part of the signal. Generally, at wavelengths near the fluorescence maximum, a twice higher frequency can be expected to be involved as the wavepacket passes the maximum of the fluorescence spectrum twice in one period. However, model calculations show that the amplitude of the oscillations with frequency  $2\omega$  should be very small. The lack of time-resolution is another reason why the oscillations with  $\omega$  frequency  $2\omega$  are not very clear. No oscillations were observed at 970 nm.

A fast exponential decay component is superimposed on the oscillations. It decays with a characteristic time constant of about 100 fs at the “blue” edge of the fluorescence spectrum (Figure 22.2). The amplitude of this component decreases and the characteristic decay time increases on increasing the wavelength of observation from 700 to 970 nm. This causes a shift in the fluorescence spectrum, which can be characterized by a peak-shift correlation function.

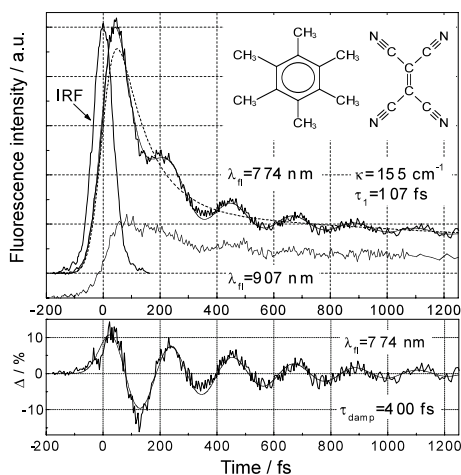


**Fig. 22.2** Fluorescence decays of the TCNE-HMB complex in  $\text{CCl}_4$  at 774 and 907 nm. The best fit of the convolution of the  $f(t)$  function with IRF (85 fs FWHM) is shown. The oscillatory component at 774 nm is shown at the bottom.



## 22.3.2

**Peak-Shift of the Fluorescence Spectrum**

Time-dependent fluorescence spectra were constructed using the fluorescence signals at different wavelengths normalized according to the time-integrated spectrum.<sup>[18]</sup> The spectrum at each time delay was fitted with a Gaussian function and the wavelengths of the spectral peaks were determined from the fits. The peak position of the fluorescence spectrum as a function of time is shown in Figure 22.3.

The spectral change with time can be characterized by the peak-shift correlation function  $C(t)$ .  $C(t) = [\nu(t) - \nu(\infty)]/[\nu(0) - \nu(\infty)]$ , where  $\nu(t)$ ,  $\nu(0)$ , and  $\nu(\infty)$  are the wavenumbers of the peak position of the fluorescence spectrum at times  $t$ , zero, and infinity, respectively. Although the evolution of  $C(t)$  has mainly been used to characterize solvent dynamics,<sup>[20]</sup> it is generally related to all types of spectral relaxation. On a fast time scale, the vibrational relaxation and/or intramolecular vibrational-energy redistribution (IVR) contribute to  $C(t)$ . These processes are expected to be predominant, especially in nonpolar solvents where solvation effects are small.

The  $C(t)$  function is plotted vs. time in Figure 22.3. It consists of an exponential-like relaxation superimposed by an oscillatory component. The relaxation is well fitted by a bi-exponential function (Eq. (1)) with  $\tau_1 = 115 \pm 25$  fs (77%) and  $\tau_2 = 1.4 \pm 0.5$  ps (23%). In EDA complexes, excitation to the CT absorption band causes excitation of several different vibrations, since a strongly polarized state is created. In response to the change in the electronic state, the nuclei start to move in order to reach the equilibrium geometry of the new electronic state. Due to the large change in the electronic state, the internal reorganization energy is very large. A combination of vibrations is excited, including high-frequency vibrations. About  $1800\text{ cm}^{-1}$  of extra energy above the 0-0 transition must be dissipated by relaxation for the TCNE–HMB complex excited by light of wavelength 630 nm. This relaxation can generally be divided into two parts: exchange of the vibrational energy inside the molecule (IVR), and vibrational energy transfer to the solvent (VR). In large organic

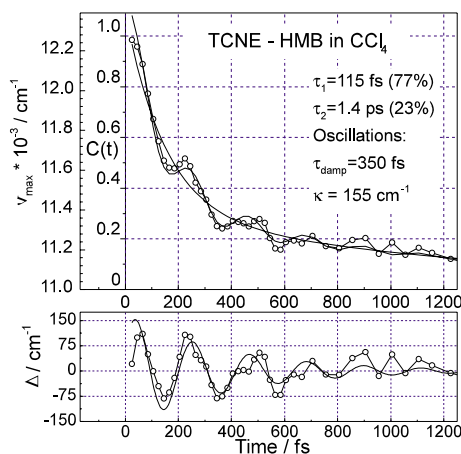


**Fig. 22.3** The  $C(t)$  function vs. time. The oscillating component is shown at the bottom.

molecules, the IVR process is much faster than energy transfer to the solvent. Thus, the main component of 115 fs is assigned mainly to the vibrational-energy redistribution process from the Franck–Condon (FC) active vibrations to inactive “dark” modes,<sup>[11]</sup> while the slow component is likely to consist of different contributions, namely IVR, vibrational energy transfer to the solvent, and solvation. It should be noted that the value of 115 fs must be considered as an upper limit for the IVR process in this complex, as the single wavelength signals were treated without deconvolution for reconstruction of the fluorescence spectra.

The frequency of the oscillations is the same as that observed in the single-wavelength measurements. Thus, the fluorescence spectral position oscillates with time, indicating a wavepacket motion in the excited state of the complex. In other words, the transition frequency between the excited and ground states is modulated by the vibrational mode coherently excited by the short light pulse (Figure 22.4a). Two main factors determine the amplitude of the spectral modulation by vibrational motions. These are the displacement of the ground- and excited-state potential-energy surfaces along the vibrational coordinate that causes the oscillations, and the gradient of the potential-energy surfaces along this coordinate. The larger the displacement and gradient, the greater the modulation of the transition moment during the vibration (Figure 22.4a).

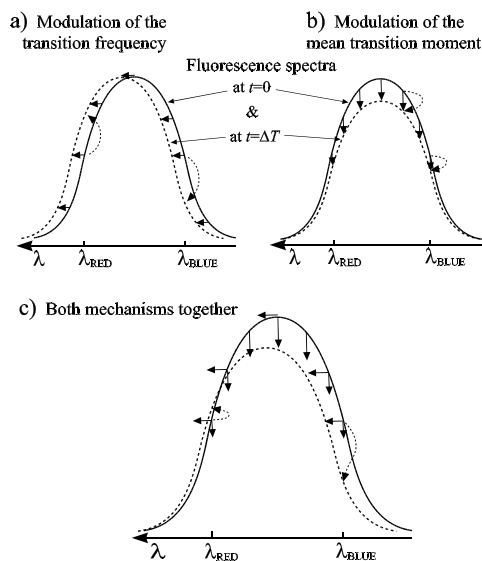


**Fig. 22.4** The effects of the two mechanisms contributing to the oscillation are illustrated separately, (a) and (b), and together, (c). The horizontal and vertical arrows indicate the direction of the initial changes in the fluorescence spectrum induced by the two modulation mechanisms.

## 22.3.3

**Modulation of the Mean Transition Moment by the Vibration**

The mean electronic transition moment ( $\overline{M}_{eg}(t)$ ) can be estimated from the integral over the fluorescence ( $F(\nu, t)$ ) spectrum (Eq. (2)).

$$\overline{M}_{eg}^2(t) \sim S(t) = \int \frac{F(\nu, t)}{\nu^3} d\nu \quad (2)$$

The  $S(t)$  function was constructed by integration of the Gaussian fitting functions for the fluorescence spectra  $F(\nu, t)$  at each time delay  $t$ . The result is shown in Figure 22.5. It can clearly be seen that the mean transition moment oscillates with time. This is clearly indicative of a non-Condon transition.<sup>[21]</sup> The period of the oscillations is 215 fs ( $155 \text{ cm}^{-1}$ ), which shows that they are caused by the same vibration. Thus, the mean transition moment is modulated by the vibrational motion. The transition moment of the charge-transfer transition in EDA complexes is directed approximately along the axis connecting the donor and acceptor centers. To modulate the transition moment, the vibration must modulate the distance between the donor and acceptor and/or the charge on the donor or acceptor in the excited state of the complex. For example, the donor–acceptor stretching mode probably modulates the transition moment.

Thus, it has been shown experimentally that there are two mechanisms contributing to the observed coherent oscillations in fluorescence: modulation of the transition frequency and modulation of the mean transition moment (Figure 22.4). It is interesting to note that the initial phase of oscillations caused by the spectral shift mechanism depends on the observation wavelength. A phase shift of  $\pi$  is expected for oscillations observed to the “red” of the fluorescence maximum compared with those observed to the “blue”, while for wavelengths on the same side of the fluorescence maximum, the initial phase is almost the same (Figure 22.4a) as the absorption/fluorescence bands are very broad. The initial phase of oscillations caused by

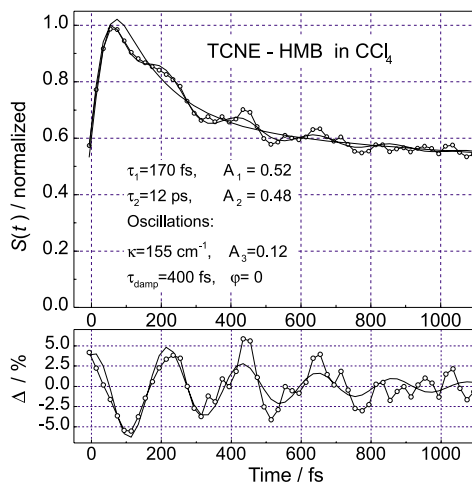


**Fig. 22.5** The  $S(t)$  function vs. time for the HMB–TCNE complex in  $\text{CCl}_4$ . The oscillating component is shown at the bottom.

the mechanism of the transition-moment modulation is independent of the observed wavelength (Figure 22.4b). From Figure 22.4, it can be seen that at the “blue” slope of the fluorescence spectrum, the oscillations caused by both mechanisms are in-phase, while at the “red” slope they are out-of-phase. In this case, large amplitude oscillations can be observed at the “blue” slope, while at the “red” slope the contributions from the two mechanisms partly cancel each other (Figure 22.4c). This is probably the reason why almost no oscillations were observed in the fluorescence of the HMB–TCNE complex at 970 nm.

A fast decay component of the  $S(t)$  function is superimposed by oscillations (Figure 22.5). Fitting by Eq. (1) gives characteristic decay times of 170 fs and 12 ps. The latter value corresponds to the lifetime of the excited state and was fixed in the analysis. The fast decay component (~170 fs) might be assigned to a fast recombination reaction from hot vibrational states as well as to a change in the value of the transition moment during the IVR and VR processes. Another possibility is to assign the fast decay component to a conversion process between two CT excited states, the presence of which was calculated in ref.<sup>[22]</sup>

#### 22.3.4

##### Assignment of the Oscillatory Modes

The origin of the vibration responsible for the oscillations could be either intermolecular or intramolecular. Experiments with different EDA complexes were thus carried out with the aim of identifying this particular vibration. In the following, we first describe complexes in which the donor was varied while the acceptor (TCNE) was kept the same, and then we describe complexes with different acceptors.

##### 22.3.4.1 Complexes of TCNE with Different Donors in Various Solvent

The underdamped oscillations of spontaneous fluorescence were observed in different complexes, namely carbazole–TCNE (Figure 22.6) and chloronaphthalene–TCNE. The frequencies of the oscillations in these complexes ( $153 \pm 4 \text{ cm}^{-1}$  and  $154 \pm 4 \text{ cm}^{-1}$ , respectively) are very similar to that observed in the HMB–TCNE complex, while the damping times and lifetimes of the excited states vary significantly. The oscillation frequency of the HMB–TCNE complex in different solvents, e.g. DCM ( $155 \text{ cm}^{-1}$ ), is the same as that observed in  $\text{CCl}_4$ , while the damping time clearly becomes longer (changing from 350 fs in  $\text{CCl}_4$  to 450 fs in DCM). The longer damping time in DCM is due to a lack of intramolecular solvent modes with frequencies similar to the oscillation frequency, which decreases the dephasing rate in this medium. In the various complexes studied with TCNE, the force constant varies substantially as the equilibrium constant of complex formation changes over about two orders of magnitude, although the frequencies of the oscillations are almost the same. These results suggest that the observed oscillatory frequencies are not due to the intermolecular D–A stretching mode, but to the vibrational mode of the acceptor. In the following section, we consider the intramolecular vibrational modes of TCNE in detail. The vibrational modes of the TCNE anion are also considered, since the excited state of the EDA complexes is ionic. It should be noted that the assign-

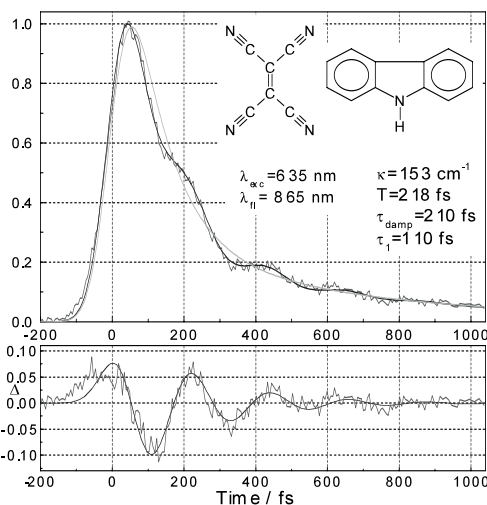


**Fig. 22.6** Fluorescence decay of the TCNE–carbazole complex in chloroform, showing also the best fit of convolution with IRF.

ment of the low-frequency vibrations is not yet certain, hence our semiempirical calculations (PM3 model) are used as well.

#### 22.3.4.2 Vibrations of TCNE and TCNE<sup>−</sup>

Let us analyze the vibrational modes of TCNE with frequencies around  $155\text{ cm}^{-1}$  (the frequency of the oscillations). The molecule has two vibrations with frequencies near the observed oscillatory frequency (Table 22.1). One is the scissoring mode ( $\nu_{12}$ ) having  $b_{1u}$  symmetry ( $D_{2h}$  point group, when the  $z$ -axis is directed along the  $C=C$  bond) and the other is the out-of-plane bending mode ( $\nu_{14}$ ) with  $b_{3u}$  symmetry (Figure 22.7). Both are IR-active modes of TCNE. The IR absorption data suggest that the frequencies of both modes are near to  $160\text{ cm}^{-1}$ , though the assignment is not unequivocal.<sup>[23–25]</sup> Our semiempirical calculations give  $175\text{ cm}^{-1}$  for the  $b_{1u}$  mode and  $167\text{ cm}^{-1}$  for the  $b_{3u}$  mode (Table 22.1). Almost no frequency shift of the  $\nu_{12}$  ( $b_{1u}$ ) mode was found in the anion relative to the neutral molecule (ref.<sup>[26]</sup>/this work), whereas a decrease of ca. 10 % in the  $\nu_{14}$  frequency was calculated for the TCNE anion.

**Tab. 22.1** Frequencies ( $\text{cm}^{-1}$ ) and assignment of the selected vibrations of TCNE and TCNE<sup>−</sup>.

	Experiment		Calculations		Species $D_{2h}$	Description
	TCNE [23–25]	TCNE modes in TCNE-HMB complex [22]	PM3 (this work) TCNE neutral	TCNE- anion		
	125	134	137		$a_g$	(CN)-C-(CN) scissoring
$\nu_{12}$	165	167	175	174	$b_{1u}$	in-plane scissoring
$\nu_{14}$	(180)	170	167	148	$b_{3u}$	out-of-plane (CN)-C-(CN) wag
	278	291 or 305	293		$b_{3g}$	(CN)-C-(CN) rocking

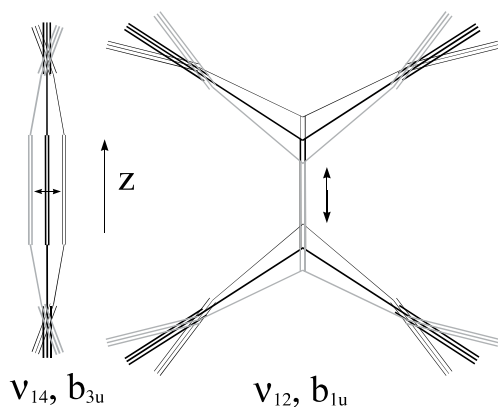


Fig. 22.7 Illustration of the two normal modes of TCNE.

A strong Raman band for the TCNE–HMB complex in solution was observed at about  $165\text{ cm}^{-1}$ .<sup>[17,18,24]</sup> There is no consistency in the assignment of this band. It has been variously assigned to an overtone of the D–A stretching mode ( $2\nu_{\text{DA}}$ ),<sup>[17]</sup> to a fundamental of the stretching D–A mode,<sup>[24]</sup> and to some acceptor mode (a  $b_{1u}$  scissoring mode was suggested) that becomes Raman-active in the complex, the latter having lower symmetry than the acceptor.<sup>[18]</sup>

The data relating to the frequencies of these two TCNE vibrations are summarized as follows. Scissoring mode: (a) the frequency is about  $165\text{ cm}^{-1}$ ; (b) there is no difference in frequency on going from the neutral to the anionic form; (c) it is not totally symmetric in the complex. Out-of-plane bending mode: (a) the frequency is about  $165\text{ cm}^{-1}$  for neutral TCNE; (b) for the anion of TCNE the frequency is about  $15\text{ cm}^{-1}$  less than that for the neutral form; (c) it is a totally symmetric mode in the complex. We believe that the vibrational mode that gives the peak in the Raman spectrum of the complex is also responsible for the oscillations in the transient absorption and fluorescence experiments. We suggest that this is the out-of-plane bending mode. There are three factors in favor of this assignment: (1) the frequency observed in the ground state of the complex [neutral TCNE; transient absorption ( $162\text{ cm}^{-1}$ ) and resonance Raman experiments ( $165\text{ cm}^{-1}$ )] is larger than that observed in the excited state [TCNE<sup>−</sup> anion; fluorescence experiment ( $155\text{ cm}^{-1}$ )]. (2) The small depolarization ratio of 1:3 of the peak of interest observed in the resonance Raman spectrum of the complex<sup>[17]</sup> suggests that the vibration is totally symmetrical. (3) The vibration modulates the size of the transition moment (Figure 22.5); during the out-of-plane vibration, the distance between the central parts of D and A changes. For the scissoring mode, modulation of the direction of the transition moment can be expected, although fluorescence anisotropy does not show any oscillation. Thus, we conclude that the oscillatory component and the Raman peak at  $165\text{ cm}^{-1}$  are caused by the out-of-plane bending mode of TCNE ( $b_{3u}$ ).

Such oscillatory behavior was also observed in several other EDA complexes with different acceptors, namely chloranil and fluoranil.

### 22.3.4.3 Oscillations in the Complexes with Fluoranil and Chloranil as Acceptors

Clear oscillations were observed for the fluoranil–HMB complex in DCM (Figure 22.8). The oscillation period was found to be 157 fs, which corresponds to a frequency of  $212 \pm 7 \text{ cm}^{-1}$ . The amplitude of the oscillations is small, being partly limited by the time resolution.

Finally, underdamped oscillations in the fluorescence were also observed in the chloranil–HMB complex (Figure 22.9), with an oscillation frequency of  $178 \pm 4 \text{ cm}^{-1}$  (period of 188 fs). Oscillations were also observed in the fluorescence from the complex between chloranil and *N*-methylaniline (MAN). The frequency of  $179 \pm 4 \text{ cm}^{-1}$  is similar to that for the chloranil–HMB complex. The oscillations in the fluorescences of both complexes with chloranil as the acceptor have similar features, i.e. the same oscillatory frequency, a similar amplitude of oscillations even though the absorption maxima of the complexes are rather different (520 nm for chloranil–

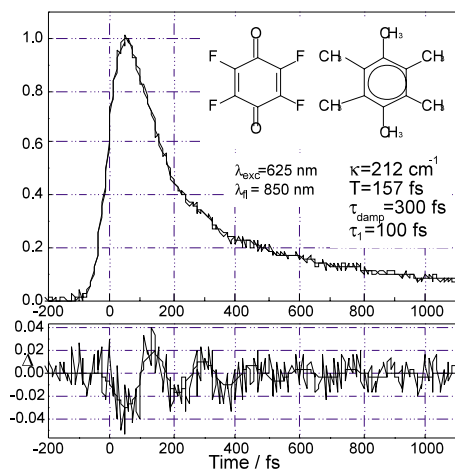


Fig. 22.8 Fluorescence decay of fluoranil–HMB complex in DCM. The extracted oscillatory component is shown below.

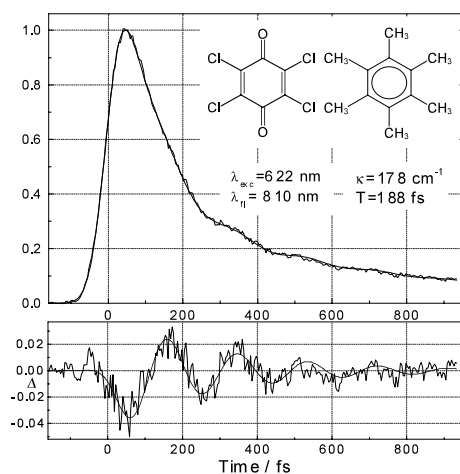


Fig. 22.9 Fluorescence decay of chloranil–HMB complex in  $\text{CCl}_4$ . The extracted oscillatory component is shown below.

HMB; 595 nm for chloranil–MAN). These experiments support the assignment that the oscillations are due to intramolecular vibrations of the acceptors. To confirm this, let us consider the low-frequency vibrations in chloranil and fluoranil.

For fluoranil, a strong IR absorption at about  $217\text{ cm}^{-1}$  was assigned to the out-of-plane bending mode,  $\nu_{29} (b_{3u})$ .<sup>[28]</sup> The scissoring mode,  $\nu_{14} (b_{1u})$ , has a much higher frequency ( $310\text{ cm}^{-1}$ ). We calculate an approximately 2 % decrease in the frequency of the  $\nu_{29}$  mode of the fluoranil anion with respect to the neutral form. If we use this difference of 2 % to estimate the frequency of the anion based on the experimental value for the neutral form, i.e.  $217\text{ cm}^{-1}$ , we obtain a value of  $213\text{ cm}^{-1}$ , which is in good agreement with the experimental oscillatory frequency of  $212 \pm 7\text{ cm}^{-1}$ .

The peak at  $186\text{ cm}^{-1}$  in the IR spectrum of chloranil was assigned to the out-of-plane bending mode,  $\nu_{29} (b_{3u})$ .<sup>[29]</sup> As for fluoranil, a shift of about 2 % to lower frequencies for the  $\nu_{29} (b_{3u})$  mode is expected for the anion of chloranil. A 2 % decrease in the  $186\text{ cm}^{-1}$  experimental value gives a  $\nu_{29}$  frequency of  $182\text{ cm}^{-1}$  for the anion, which is close to the frequency of the observed oscillations ( $179 \pm 5\text{ cm}^{-1}$ ). Thus, we can assign the observed oscillations in the complexes with fluoranil and chloranil to the  $\nu_{29} (b_{3u})$  out-of-plane vibrational mode. In the complexes with the three acceptors studied, the oscillatory component is assigned to the out-of-plane vibrational mode of the  $b_{3u}$ -symmetric acceptors.

In conclusion, the excited-state dynamics of electron donor–acceptor complexes have been studied by means of the femtosecond fluorescence up-conversion technique. Coherent oscillations in the spontaneous fluorescences observed for the various complexes have been assigned to the out-of-plane bending modes of the acceptors. Two mechanisms have been found to be responsible for the oscillations: the modulation of the transition frequency and the modulation of the mean transition moment by the vibrational motion.

## Acknowledgement

We acknowledge financial support through a grant-in-aid (no. 10440170) from the Ministry of Education, Science, Sports and Culture of Japan.



## References

- 1 T. S. Rose, M. J. Rosker, A. H. Zewail, *J. Chem. Phys.* **1988**, *88*, 6672.
- 2 J. Chesnoy, A. Mokhtari, *Phys. Rev. A* **1988**, *38*, 3566.
- 3 L. Zhu, J. T. Sage, P. M. Champion, *Science* **1994**, *266*, 629.
- 4 H. Okamoto, K. Yoshihara, *Chem. Phys. Lett.* **1991**, *177*, 568.
- 5 S. E. Bradforth, R. Jimenez, F. van Mourik, R. van Grondelle, G. R. Fleming, *J. Phys. Chem.* **1995**, *99*, 16179.
- 6 R. J. Stanley, S. G. Boxer, *J. Phys. Chem.* **1995**, *99*, 859.
- 7 M. H. Vos, M. R. Jones, J.-L. Martin, *Chem. Phys.* **1998**, *223*, 179.
- 8 K. Wynne, G. Reid, R. M. Hochstrasser, *J. Chem. Phys.* **1996**, *105*, 2287.
- 9 K. Wynne, C. Galli, R. M. Hochstrasser, *J. Chem. Phys.* **1994**, *100*, 4797.
- 10 I. V. Rubtsov, K. Yoshihara, *J. Phys. Chem. A* **1997**, *101*, 6138.
- 11 I. V. Rubtsov, K. Yoshihara, *J. Phys. Chem. A* **1999**, *103*, 10203.
- 12 P. Vöringer, R. A. Westervelt, T.-S. Yang, D. C. Arnett, M. J. Feldstein, N. F. Scherer, *J. Raman Spectrosc.* **1995**, *26*, 535.
- 13 M. Lim, T. A. Jackson, P. A. Anfinrud, *J. Phys. Chem.* **1996**, *100*, 12043.
- 14 S. Gnanakaran, G. Haran, R. Kumble, R. M. Hochstrasser, *Energy Transfer and Localization: Applications to Photosynthetic Systems*, in *Resonance Energy Transfer* (Eds.: D. L. Andrew, A. A. Demidov), John Wiley & Sons, U.K., **1999**.
- 15 R. S. Mulliken, W. B. Person, *Molecular Complexes*, John Wiley & Sons, New York, **1969**.
- 16 F. Markel, N. S. Ferris, I. R. Gould, A. B. Myers, *J. Am. Chem. Soc.* **1992**, *114*, 6208.
- 17 M. L. Smith, J. L. McHale, *J. Phys. Chem.* **1985**, *89*, 4002.
- 18 K. Kulinowski, I. R. Gould, A. B. Myers, *J. Phys. Chem.* **1995**, *99*, 9017.
- 19 I. V. Rubtsov, H. Shirota, K. Yoshihara, *J. Phys. Chem.* **1999**, *103*, 1801.
- 20 M. Maroncelli, J. MacInnis, G. R. Fleming, *Science* **1988**, *243*, 1674.
- 21 B. D. Fainberg, *Opt. Spectrosc. (USSR)* **1988**, *65*(6), 722.
- 22 M. Hayashi, T.-S. Yang, J. Yu, A. Mebel, S. H. Lin, *J. Phys. Chem. A* **1997**, *101*, 4156.
- 23 K. H. Michaelian, K. E. Rieckhoff, E. M. Voigt, *J. Mol. Spectrosc.* **1982**, *95*, 1.
- 24 M. Rossi, E. Haselbach, *Helv. Chim. Acta* **1979**, *62*(20), 140.
- 25 F. A. Miller, O. Sala, P. Devling, J. Overend, E. Lippert, E. Luder, H. Moser, J. Varchmin, *Spectrochim. Acta* **1964**, *20*, 1233.
- 26 Y. Iida, *Bull. Chem. Soc. Jpn.* **1973**, *46*, 423.
- 27 M. Hayashi, T.-S. Yang, J. Yu, A. Mebel, R. Chang, S. H. Lin, I. V. Rubtsov, K. Yoshihara, *J. Phys. Chem. A* **1998**, *102*, 4256.
- 28 A. Giraldo, C. Pecile, *J. Chem. Soc., Faraday Trans. 2* **1975**, *71*, 689.
- 29 A. Giraldo, C. Pecile, *J. Chem. Soc., Faraday Trans. 2* **1973**, *69*, 1291.

## 23

### Femtosecond Studies of the Initial Events in the Photocycle of Photoactive Yellow Protein (PYP)

Matthew A. Horn, Julie A. Gruetzmacher, Jeongho Kim, Seung-Eng Choi, Spencer M. Anderson, Keith Moffat, and Norbert F. Scherer

#### Abstract

Primary photoinduced chemical events in the photocycle of photoactive yellow protein (PYP), a photoreceptor from the eubacterium *Ectothiorhodospira halophila*, have been probed by femtosecond pump-probe and anisotropy measurements. A transient absorption signal that relaxes with a bi-exponential decay ( $\tau_1 = 760$  fs and  $\tau_2 = 2.8$  ps) has been observed for the first time (400 nm pump and probe), the anisotropy of which remains constant over more than 10 ps. Kinetic modeling of the pump-probe data suggests an inhomogeneous population in the ground and initial photoexcited states. Complementary molecular dynamics simulations have highlighted the importance of hydrogen bond dynamics in the primary isomerization event of the chromophore.

#### 23.1

##### Introduction

Photoreceptors are a class of molecules that have attracted great interest owing to their ability to transform the small structural changes of a photoisomerization event into large structural changes in the entire protein backbone, thereby facilitating cellular processes such as signal transduction.<sup>[1–8]</sup> The challenge is to understand the interactions relevant to function based on a detailed knowledge of the structure, dynamics, and photocycle kinetics. The recent development of a time-resolved X-ray diffraction/structure determination method has enabled a uniquely informative understanding of protein function through the direct connection of structural changes to kinetics.<sup>[9]</sup> At the same time, ultrafast optical spectroscopies provide an approach for elucidating the rate(s) of reactions even on the timescale of vibrational motions. Key issues that can profitably be addressed by these methods are how the dynamics of the chromophore influence the protein structure and motions, and the reciprocal influence of the protein.

One system well-suited for detailed study is photoactive yellow protein (PYP), a small (14 kDa), water-soluble, cytoplasmic photoreceptor found in halophilic phototrophic bacteria.<sup>[10,11]</sup> Action spectra suggest that PYP mediates a negative phototac-

tic response in *Ectothiorhodospira halophila*.<sup>[12]</sup> PYP, which contains a *p*-coumaric acid<sup>[13–15]</sup> chromophore, has a ground-state structure that is known to within an accuracy of 1.4 Å.<sup>[16]</sup> The chromophore is isolated from the surrounding solvent (in the ground state) and is connected to the protein through a thiol ester linkage to cysteine 69. Part of the photo-driven action is a *cis* → *trans* isomerization of the chromophore about its only carbon–carbon double bond.<sup>[14]</sup>

Several factors contribute to making PYP an excellent test case for the study of photoactive proteins.<sup>[17]</sup> The photocycle of PYP involves several kinetically and spectroscopically well-defined intermediates.<sup>[10,18,19]</sup> The ground state  $S_0(\textit{trans})$  exhibits a broad absorption (~60 nm) centered at 446 nm ( $\epsilon = 45 \text{ mM}^{-1}\text{cm}^{-1}$ ).<sup>[10]</sup> The first well-characterized intermediate  $S_0(\textit{cis})$  appears within 10 ns of photoexcitation from  $S_0(\textit{trans})$  to  $S_1(\textit{trans})$  and has an absorption centered at 464 nm, red-shifted relative to the *cis-trans* isomerized ground state.<sup>[20]</sup> The second intermediate, [pB], in which the chromophore is exposed to solvent and is protonated, gives rise to a blue-shifted absorption maximum (355 nm); it appears within 1 ms<sup>[21]</sup> and is very long-lived ( $\tau = 150 \text{ ms}$ ). Furthermore, the [pB] intermediate has been observed by means of time-resolved X-ray crystallography, making PYP unique among the photo-sensory proteins.<sup>[22]</sup> Finally, since only one bond is involved in the isomerization, in contrast to the situation in rhodopsins, the isomerization step of the photocycle is less complicated.<sup>[23]</sup>

## 23.2

### Methods

#### 23.2.1

##### Molecular Dynamics Simulations

The molecular dynamics simulations were performed with a commercial simulation and visualization package (IMPACT, MSI) using the AMBER potential function with chromophore partial charges, angles, and bond lengths parameterized from He et al.<sup>[24]</sup> A complete description of the details of the simulation and the results are given elsewhere.<sup>[25]</sup>

#### 23.2.2

##### Femtosecond Spectroscopy

Femtosecond spectroscopic measurements were made using a home-built regeneratively amplified gain-switched all-acousto-optic Ti:sapphire laser system. The design and performance specifications will be described elsewhere.<sup>[26]</sup> The system produces pulses of energy >100  $\mu\text{J}$  at a repetition rate of 4 kHz and with duration ca. 50 fs. The experimental set-up for pump-probe spectroscopy is described elsewhere.<sup>[25]</sup>

## 23.2.3

**Sample**

PYP apoprotein was cloned from the SL-1 strain of *Ectothiorhodospira halophila*. Although in an earlier publication<sup>[27]</sup> it was reported that the amino acid sequences from the SL-1 and BN9626 strains of PYP were identical, more recent results (S. M. Anderson, K. Moffat, unpublished results) have suggested that this is not the case; the sequences are very similar but not identical. The apoprotein was expressed in *Escherichia coli* and then reconstituted with the chromophore *p*-coumaric acid to create the PYP holoprotein.<sup>[28]</sup> An N-terminal histidine tag was removed by cleavage with TEV protease to leave a residual glycine. The protein was purified by means of ion-exchange and size-exclusion chromatography until the optical purity (absorbance ratio 279 nm/446 nm) was 0.42. The purity was further assessed by mass spectrometry and isoelectric focusing.

The PYP sample was prepared by diluting a concentrated stock solution with a tris-HCl buffer of pH ~ 8.0 to obtain an optical density of 0.3 at 400 nm. The sample was spun (~15 Hz) in a cell to mitigate photobleaching effects by providing a new sample for each laser shot. The sample path length in the cell was 0.5 mm.

## 23.3

**Results**

## 23.3.1

**Pump-Probe Measurements**

Pump-probe measurements were performed for pump-probe delays from -5 ps to 125 ps with a 400 nm pump and probe pulses between 400 nm and 490 nm. These measurements allow the determination of kinetic processes such as excited-state absorption, ground-state bleaching, and photoproduct formation. Short-time data with parallel pump and probe polarizations (400 nm pump and probe) are given in Figure 23.1a.

An excited-state transient absorption (negative signal) is seen at early delay times and rapidly converts to a bleach/stimulated emission signal. The rate of this conversion is wavelength-dependent. To the best of our knowledge, this is the first time that an excited-state absorption has been observed from the  $S_1(\text{trans})$  state of the PYP chromophore. A least-squares fit of the data, as shown in Figure 23.1a, yields a bi-exponential decay of the transient absorption (time constants:  $\tau_1 = 760$  fs and  $\tau_2 = 2.8$  ps) and a bleach component that does not decay within the 125 ps measurement window, in agreement with previous measurements.<sup>[29,30]</sup>

A pump-probe measurement taken from -1 ps to 19 ps following excitation with a 400 nm pump and probing at 490 nm is shown in Figure 23.2. This measurement, in agreement with that at 487 nm in ref. [29], offers a spectral window on the bleach recovery kinetics of the  $S_0$  states.

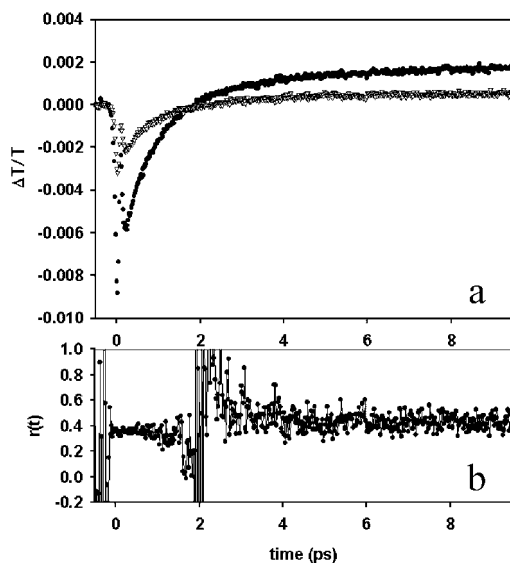


Fig. 23.1 Pump-probe measurements (a) and the calculated transient anisotropy (b) of PYP for 400 nm pump and probe pulses; parallel (●) and perpendicular (▽) polarizations.

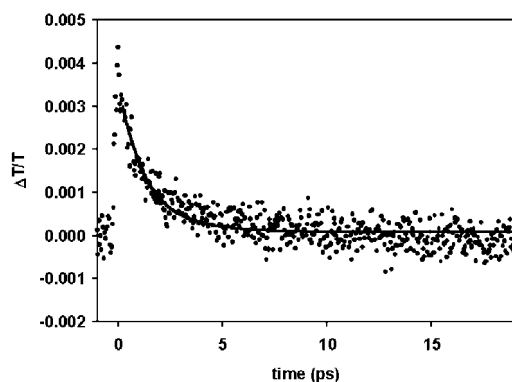


Fig. 23.2 Pump-probe signal of PYP for pump = 400 nm, probe = 490 nm, and the kinetic model fit.

### 23.3.2

#### Anisotropy

The anisotropy,  $r(t)$ , as indicated in Figure 23.1b, was constructed from the results of pump-probe experiments performed with parallel and perpendicular polarizations.<sup>[31]</sup> The derivative-like shape is due to a singularity at a delay of  $\sim 1.8$  ps. Rotational motion makes a negligible contribution to the anisotropy as the protein is too large to rotate on these timescales and the chromophore is locked in its interior. The lack of a decay of the anisotropy indicates that the transition dipole direction of the probed transition does not change with time as detected in the 400 nm window.

## 23.3.3

**Molecular Dynamics Simulations**

Analysis of a series of trajectories lasting ~200 ps revealed unusual H-bond dynamics between the carbonyl oxygen on the *p*-coumaric acid “tail” and a backbone amine, specifically that on tyrosine 92. This bond must be broken for isomerization to occur. An autocorrelation function analysis of the trajectories indicated significant partitioning between the two H-bond conformations (that is, formed *versus* broken), which would be expected to lead to different barriers for isomerization. The time required for H-bond breaking is ~30 ps. By contrast, the autocorrelation function of virtually all other H-bonds lost correlation in less than 1 ps.

## 23.4

**Discussion**

## 23.4.1

**Energetics**

The excited-state transient absorption presented here has not been seen in previous femtosecond experiments on PYP.<sup>[29,30]</sup> In these previous studies, only probe wavelengths between 420 nm and 570 nm were used. The lack of absorption at 420 nm, in contrast to that seen at 400 nm and 410 nm in 400/410 nm pump-probe data (not shown), suggests that the Franck–Condon region for the excited-state absorption is narrow. The excited-state absorption seen here cannot be accounted for in terms of a two-electronic state model; a hitherto unobserved higher-lying state must also be invoked. Transient absorptions have been noted previously in photoisomerization reactions and have been used to probe reaction dynamics.<sup>[32,33]</sup>

The relatively slow dynamics of the transient absorption decay suggests that the  $S_1$ (*trans*) energy surface in the Franck–Condon region is not repulsive but is instead flat or a shallow well. A model developed by Schulten<sup>[34]</sup> to explain similar observations in rhodopsin was invoked by Anfinrud et al.<sup>[35]</sup> to explain their experimental observation that, in bacteriorhodopsin, the energy surface of the photoexcited state cannot be repulsive. Glasbeek and coworkers<sup>[36]</sup> also made reference to this model in explaining their time-resolved fluorescence results for PYP.

## 23.4.2

**Isomerization**

The rapid rate out of the  $S_1$ (*trans*) Franck–Condon region (that is, the initial phase of the isomerization) is in accordance with photoisomerization measurements made on stilbene in solution. The *cis* → *trans* photoisomerization of stilbene has been interpreted as occurring on a potential surface with a very small energy barrier (<1.5 kcal/mol) and to take place within 2 ps.<sup>[37,38]</sup> This rapid photoisomerization of *cis*-stilbene (nearly 100 times faster than the photoisomerization of *trans*-stilbene)

suggests that the *cis*  $\rightarrow$  *trans* stilbene photoisomerization is analogous to *trans*  $\rightarrow$  *cis* photoisomerization of PYP; only a small energy barrier needs to be surmounted in  $S_1$ . Rhodopsins are believed to undergo a rapid photoisomerization very similar to that of PYP,<sup>[4]</sup> hence comparisons can be expected to be quite informative. The rhodopsin *cis*  $\rightarrow$  *trans* photoisomerization occurs on a barrierless energy surface and is complete within 200 fs.<sup>[39,40]</sup> An extremely rapidly decaying excited-state absorption is also observed.<sup>[33,41]</sup>

Although the bi-exponential decay observed here is detected by probing to a higher-lying excited state, bi-exponential kinetics for electronically-excited PYP have been observed previously in time-resolved fluorescence measurements.<sup>[36]</sup> It was concluded that this was due to an inhomogeneous distribution of the protein environments that affect the dynamics of the chromophore in the  $S_1$  state. The excited-state absorption presented in this work is likewise sensitive to an inhomogeneous distribution of chromophore environments in the  $S_1$  state. Furthermore, the bi-stable hydrogen-bond dynamics of the hydrogen on tyrosine 92 with the carbonyl oxygen on the chromophore observed in our molecular dynamics simulations is indicative of the existence of two distinct ground-state populations.<sup>[25]</sup> This is strongly supportive of an inhomogeneous distribution in the  $S_1$  state upon photoexcitation.

The kinetic scheme shown in Figure 23.3 has been used to simulate our data. An initial photoexcited population exists in a pair of states ( $S_{1a/b}(trans)$ ) that differ in the hydrogen-bonding behavior revealed by the molecular dynamics studies. They can only be distinguished spectroscopically from the different absorption decay time constants; their spectra overlap in the probed region. From the  $S_{1a/b}(trans)$  states, PYP proceeds to a species "I", a twisted conformation in  $S_1$  that lies intermediate between *cis* and *trans*. From this well, PYP can proceed to either the *cis* or *trans*  $S_0$  configuration.

Expressions were derived for the time-dependent populations of each state shown in the scheme.<sup>[25]</sup> With this kinetic scheme, the measured time constants, and the constraint that the *cis/trans* quantum yield must be in agreement with that reported in ref. [29], the 400 nm probe data could be fitted by adjusting the inhomogeneous distribution in the  $S_1(trans)$  states, the kinetic time constants, and the absorption coefficients of the states involved. The best fit was achieved with the inhomogeneous distribution of the  $S_1(trans)$  (and hence also the  $S_0(trans)$  ground state) populations of 0.5 each and a quantum yield of  $S_0(cis)$  of 0.6. The fit to the data in Figure 23.1a is excellent. The absorption coefficient of the  $S_1(trans) \rightarrow S_n$  transition was

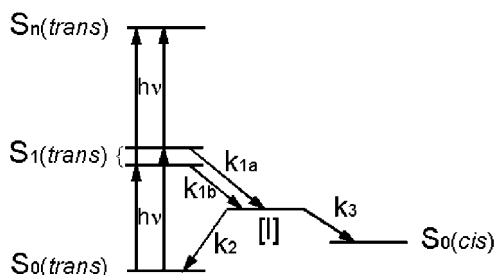


**Fig. 23.3** Proposed mechanism accounting for inhomogeneous kinetics. Arrows indicate the optical transitions and the reaction "pathway".

found to be approximately five times greater than that for the  $S_0(\text{trans}) \rightarrow S_1(\text{trans})$  transition. The absorption coefficient for the  $S_0(\text{cis}) \rightarrow S_1(\text{cis})$  transition proved to be zero, which is consistent with previous work suggesting that the *cis* absorption does not extend to these wavelengths. This kinetic scheme differs from that of Tollin et al.<sup>[29]</sup> in that in their scheme the two  $S_1(\text{trans})$  states (Tollin's  $P^*$  and  $P'^*$ ) decayed to two different intermediates.

The kinetic parameters from the 400 nm fit were used to fit the 490 nm data; only the absorption coefficients were allowed to change. The very good fit of the 490 nm data is shown in Figure 23.2. The time constants for the evolution of the two  $S_1(\text{trans})$  states to I are 1.8 ps and 0.6 ps; for the reversions from I to  $S_0(\text{trans})$  and  $S_0(\text{cis})$  the values are 1.4 ps and 0.9 ps, respectively. The absorption coefficients for the 490 nm data are approximately equal, both being around half of that for the  $S_0(\text{trans}) \rightarrow S_1(\text{trans})$  transition at 400 nm.

### 23.4.3

#### Anisotropy

The transition dipole direction has been measured in a single crystal of PYP.<sup>[43]</sup> The electronic structure of the PYP chromophore in an amino acid environment has been calculated.<sup>[24]</sup> Initial results suggest that the transition dipole of the PYP chromophore from the *trans* ground state to the lowest excited state, in an environment of seven amino acid residues represented by point charges and water molecules to allow hydrogen bonding, is largely contained within the plane of the chromophore. It is also roughly collinear with the axis of the carbon chain. It is assumed that the transition dipole of the *cis* form is rotated with respect to that of the *trans* form.

A transient anisotropy measurement determines the change in direction of the transition dipole vector between the initial *trans* ground to  $S_1$  state absorption and any optical transitions from the various photointermediates. It gives a measure of the angle between the transition dipole of the  $S_0(\text{trans})$  to  $S_1(\text{trans})$  initial excitation at time zero and the same transition moment probed at time  $t$  and the transition moment of  $S_1(\text{trans}) \rightarrow S_n$ . The initial anisotropy is indicative of the excited-state absorption and stimulated emission of the *trans* conformation; the anisotropy of the long-time increased transmission is indicative of the remaining ground-state bleaching that persists due to photoreaction and the transient absorption from the intermediate and  $S_0(\text{cis})$  states that are formed. Thus, the timescale of the decay of the instantaneous anisotropy level to the long-time anisotropy level will be indicative of the formation of the intermediates (I and  $S_0(\text{cis})$ ). Hence, the lack of a change in the anisotropy, as shown in Figure 23.1b, suggests that these intermediates are not detected within this spectral window. Only bleaching and ground-state recovery are observed, which is at variance with other reports.<sup>[42]</sup> However, further anisotropy measurements over a broader range of probe wavelengths are necessary to confirm this tentative conclusion. Such efforts are in progress.



## 23.5

## Conclusions

The results presented here suggest that the photoisomerization reaction of PYP shows a striking similarity to that of rhodopsin. The Franck–Condon region of the ground-state absorption is relatively flat and the chromophore proceeds rapidly from this region. An excited-state absorption is observed, which decays bi-exponentially. This is argued to be the result of an inhomogeneous distribution in the  $S_1$ (*trans*) photointermediate because of two populations in the ground state caused by hydrogen bonding of the chromophore, as observed in molecular dynamics simulations.

The energy level scheme used here is analogous to that proposed by Anfinrud for bacteriorhodopsin.<sup>[35]</sup> This model entails several predictions for spectroscopic measurements. First, no immediate stimulated emission spectral shift to lower energies should be seen (or seen as a Stokes shift in fluorescence up-conversion measurements), as the excited-state population does not immediately slide down an excited-state well to the product conformation. To date, no such shift has been observed.<sup>[29,30,36,44,45]</sup> Second, as the small excited-state energy barrier is surmounted, low-temperature (below the thermal activation barrier) measurements should indicate a population trapped in the excited state. Finally, the stimulated emission spectrum should not match the fluorescence spectrum as an excited-state absorption should cancel some of the emission.

## Acknowledgements

We thank Dr. Zhong Ren for fruitful discussions and Qing Chang for her initial work on PYP. We thank Dr. Z. He and Prof. Karl Freed for sharing the results of electronic structure calculations of the PYP chromophore in a protein environment. The NIH (GM57768) provided financial support for this work. JAG acknowledges the NSF for a predoctoral fellowship. NFS acknowledges the Sloan and Dreyfus Foundations for fellowships.

## References

- 1 G. K. Farber, Sensing Photons, *Nature Struct. Biol.* **1998**, 56, 415–417.
- 2 K. J. Hellingwerf, R. Kort, W. Crielgaard, *Symp. Soc. Gen. Microbiol.* **1998**, 56, 107–123.
- 3 T. E. Meyer, E. Yakali, M. A. Cusanovich, G. Tollin, *Biochemistry* **1987**, 262, 418–423.
- 4 G. G. Kochendoerfer, R. A. Mathies, *Isr. J. Chem.* **1996**, 35, 211–226.
- 5 W. D. Hoff, K.-H. Jung, J. L. Spudich, *Ann. Rev. Biophys. Biomol. Struct.* **1997**, 26, 223–258.
- 6 P. Quail, *BioEssays* **1997**, 19, 571–579.
- 7 D. Oesterhelt, *Curr. Opin. Struct. Biol.* **1998**, 84, 489–500.
- 8 H. Kandori, N. Kinoshita, Y. Yamakazi, A. Maeda, Y. Shichida, R. Needleman, J. K. Lanyi, M. Bizounok, J. Herzfeld, J. Raap, J. Lugtenberg, *Proc. Natl. Acad. Sci. USA* **2000**, 979, 4643–4648.
- 9 V. Srajer, T.-Y. Teng, T. Ursby, C. Pradervand, Z. Ren, S. Adachi, W. Schildkamp, D. Bourgeois, M. Wulff, K. Moffat, *Science* **1996**, 274, 1726–1729.

- 10 T. E. Meyer, *Biochim. Biophys. Acta* **1985**, 806, 175–183.
- 11 M. Koh, G. van Driessche, B. Samyn, W. D. Hoff, T. E. Meyer, M. A. Cusanovich, J. J. van Beeumen, *Biochemistry* **1996**, 35, 2526–2534.
- 12 T. E. Meyer, G. Tollin, J. H. Hazzard, M. A. Cusanovich, *Biophys. J.* **1989**, 56, 559–564.
- 13 M. Baca, G. E. O. Borgstahl, M. Boissinot, P. M. Burke, D. R. Williams, K. A. Slater, E. D. Getzoff, *Biochemistry* **1994**, 33, 14369–14377.
- 14 W. D. Hoff, P. D  x, K. H  rd, B. Devreese, I. M. Nugteren-Roodzant, W. Crielaard, R. Boelens, R. Kaptein, J. Van Beeumen, K. J. Hellingwerf, *Biochemistry* **1994**, 33, 13959–13962.
- 15 M. Kim, R. A. Mathies, W. D. Hoff, K. J. Hellingwerf, *Biochemistry* **1995**, 34, 12669–12672.
- 16 G. E. O. Borgstahl, D. R. Williams, E. D. Getzoff, *Biochemistry* **1995**, 34, 6278–6287.
- 17 The nomenclature in the PYP literature is somewhat confusing and there has been some controversy in the assignment of intermediates.<sup>[29]</sup> We have employed a more standard spectroscopic description in this report. This will be explained more fully in ref. 25. For the long-lived intermediate that is accessed thermally rather than by direct photoexcitation, we use the unspectroscopic [pB] name.
- 18 W. D. Hoff, I. H. M. van Stokkum, H. J. van Ramesdonk, M. E. van Brederode, A. M. Brouwer, J. C. Fitch, T. E. Meyer, R. van Grondelle, K. J. Hellingwerf, *Biophys. J.* **1994**, 67, 1691–1705.
- 19 L. Ujj, S. Devanathan, T. E. Meyer, M. A. Cusanovich, G. Tollin, G. H. Atkinson, *Biophys. J.* **1998**, 75, 406–412.
- 20 U. K. Genick, S. M. Soltis, P. Kuhn, I. L. Canestrelli, E. D. Getzoff, *Nature* **1998**, 392, 206–209.
- 21 U. K. Genick, G. E. O. Borgstahl, K. Ng, Z. Ren, C. Pradervand, P. M. Burke, V. Srajer, T.-Y. Teng, W. Schildkamp, D. E. McRee, K. Moffat, E. Getzoff, *Science* **1997**, 275, 1471–1475.
- 22 B. Perman, V. Srajer, Z. Ren, T.-Y. Teng, C. Pradervand, T. Ursby, D. Bourgeois, F. Schotte, M. Wulff, R. Kort, K. Hellingwerf, K. Moffat, *Science* **1998**, 279, 1946–1950.
- 23 Q. Zhong, S. Ruhman, M. Ottolenghi, M. Sheves, N. Friedman, G. H. Atkinson, J. K. Delaney, in *Ultrafast Phenomena X*, Springer Series in Chemical Physics, vol. 62 (Eds.: P. F. Barbara, J. G. Fujimoto, W. H. Knox, W. Zinth), Springer-Verlag, Germany, **1996**.
- 24 Z. He, C. H. Martin, R. Birge, K. F. Freed, *J. Phys. Chem. A* **2000**, 112, 2939–2952.
- 25 M. A. Horn, S.-E. Choi, J. Kim, J. A. Gruetzmacher, S. M. Anderson, Z. He, K. F. Freed, K. Moffat, N. F. Scherer, manuscript in preparation, **2001**.
- 26 J. A. Gruetzmacher, M. A. Horn, B. N. Flanders, X. Shang, N. F. Scherer, manuscript in preparation, **2001**.
- 27 R. Kort, W. Hoff, M. Van West, A. Kroon, S. Hoffer, K. Vlieg, W. Crielaard, J. Van Beeumen, K. J. Hellingwerf, *EMBO J.* **1996**, 15, 3209–3218.
- 28 Y. Imamoto, T. Ito, M. Kataoka, F. Tokunaga, *FEBS Lett.* **1995**, 374, 157–160.
- 29 S. Devanathan, A. Pacheco, L. Ujj, M. Cusanovich, G. Tollin, S. Lin, N. Woodbury, *Biophys. J.* **1999**, 77, 1017–1023.
- 30 A. Baltuska, I. H. M. van Stokkum, A. Kroon, R. Monshouwer, K. J. Hellingwerf, R. van Grondelle, *Chem. Phys. Lett.* **1997**, 270, 263–266.
- 31 G. R. Fleming, *Chemical Applications of Ultrafast Spectroscopy*, Oxford University Press, New York, **1986**.
- 32 N. F. Scherer, L. R. Khundkar, T. S. Rose, A. H. Zewail, *J. Phys. Chem.* **1987**, 91, 6478–6483.
- 33 G. Haran, K. Wynne, A. Xie, Q. He, M. Chance, R. M. Hochstrasser, *Chem. Phys. Lett.* **1996**, 261, 389–395.
- 34 K. Schulten, W. Humphrey, I. Logunov, M. Sheves, D. Xu, *Isr. J. Chem.* **1995**, 35, 447–464.
- 35 K. C. Hasson, F. Gai, P. A. Anfinrud, *Proc. Natl. Acad. Sci. USA* **1996**, 93, 15124–15129.
- 36 P. Changenet, H. Zhang, M. J. van der Meer, K. J. Hellingwerf, M. Glasbeek, *Chem. Phys. Lett.* **1998**, 282, 276–282.
- 37 R. J. Sension, S. T. Repinec, A. Z. Szarka, R. M. Hochstrasser, *J. Chem. Phys.* **1993**, 98, 6291–6315.
- 38 J. Saltiel, Y.-P. Sun, *J. Phys. Chem.* **1989**, 93, 6246–6250.

- 39 R. W. Schoenlein, L. A. Peteanu, R. A. Mathies, C. V. Shank, *Science* **1991**, 254, 412–415.
- 40 Q. Wang, R. W. Schoenlein, L. A. Peteanu, R. A. Mathies, C. V. Shank, *Science* **1994**, 266, 422–424.
- 41 T. Ye, N. Friedman, Y. Gat, G. H. Atkinson, M. Ottolenghi, S. Ruhman, *J. Phys. Chem. B* **1999**, 103, 5122–5130.
- 42 J. Hendriks, I. H. M. van Stokkum, W. Crie-laard, K. J. Hellingwerf, *FEBS Lett.* **1999**, 458, 252–256.
- 43 K. Ng, E. D. Getzoff, K. Moffat, *Biochemistry* **1995**, 34, 879–890.
- 44 H. Chosrowjan, N. Mataga, N. Nakashima, Y. Imamoto, F. Tokunaga, *Chem. Phys. Lett.* **1997**, 270, 267–272.
- 45 H. Chosrowjan, Y. Shibata, N. Mataga, Y. Imamoto, F. Tokunaga, in *Ultrafast Phenomena XI*, Springer Series in Chemical Physics, vol. 63 (Eds.: T. Elsaesser, J. G. Fujimoto, D. A. Wiersma, W. Zinth), Springer-Verlag, Germany, **1998**.

## 24

### Elementary Reactions in the Condensed Phase: Bond Breaking, Isomerization, and Electron Transfer

*Eva Åkesson, Alexander N. Tarnovsky, Gabor Benkő, Arkady Yartsev, and Villy Sundström*

#### 24.1

##### Introduction

A chemical reaction can be reduced to a number of elementary reactions – breaking and forming of chemical bonds, energy transfer within and between molecules, electron transfer, proton or hydrogen atom transfer, etc. Understanding a chemical reaction at the atomic level not only requires a description of the reactants and products, but also a description of the medium or surroundings in which the reaction takes place, as well as an understanding of the interactions between the reacting system and surroundings. In this contribution, we discuss three elementary chemical reactions in the condensed phase, namely bond breaking, isomerization, and electron transfer, and we show that considerations of the surroundings and system–surrounding interactions are important with regard to understanding the reaction mechanisms.

#### 24.2

##### Bond Breaking and Isomerization in Solution

##### 24.2.1

##### Photodissociation of Dihalomethanes

Despite numerous ultrafast studies<sup>[1]</sup> of chemical reactions, a clear picture of dissociation dynamics in the condensed phase is not yet available. In solution, the task is challenging since additional processes such as geminate recombination, product formation, etc., may be operative. As a result, the overall mechanism of a photodissociation reaction, involving steps such as bond-breaking, geminate recombination and vibrational relaxation of photofragments, and product formation, is far from being adequately understood. We have performed extensive time-resolved studies, covering a wide time scale from 100 fs to 50  $\mu$ s, aimed at exploring the photodissociation dynamics of dihalomethanes ( $\text{CH}_2\text{ICl}$ ,<sup>[2]</sup>  $\text{CH}_2\text{IBr}$ , and  $\text{CH}_2\text{I}_2$ <sup>[3]</sup>) as well as the subsequent reactions involving the photofragments.

In the gas phase,  $\text{CH}_2\text{I}_2$  is known to dissociate when excited to the low-lying excited states (spectral range 245–360 nm), forming the  $\text{CH}_2\text{I}$  radical and an iodine atom in its ground state  $\text{I}(^2\text{P}_{3/2})$  or spin-orbit excited state  $\text{I}^*(^2\text{P}_{1/2})$ . In solution, however, the time scale for the dissociation and the fate of the  $\text{CH}_2\text{I}$  and  $\text{I}$  fragments during the first few picoseconds have remained controversial<sup>[3–5]</sup>. In our recent femtosecond pump-probe study,<sup>[3]</sup> performed over a wide analyzing wavelength range (290–1220 nm), we concluded that the photodissociation of  $\text{CH}_2\text{I}_2$  in acetonitrile (initiated with a 310-nm photon) is followed by the formation of an isomer, namely iso-diiodomethane ( $\text{CH}_2\text{I}-\text{I}$ ). This isomer, as well as the  $\text{CH}_2\text{Br}-\text{I}$  and  $\text{CH}_2\text{Cl}-\text{I}$  isomers of bromoiodomethane and chloroiodomethane, have previously been observed in matrix-isolation studies.<sup>[6]</sup> C–I bond-breaking and formation of the  $\text{CH}_2\text{I}-\text{I}$  photo-product are evident from the temporal evolution of the transient absorption spectrum. An initial ~350 fs decay of the excited state-absorption (at ~700 nm) reflects the bond breaking (Figure 24.1), which is mirrored by the appearance of an absorption band characteristic of the  $\text{CH}_2\text{I}$  fragment (~340 nm).<sup>[3]</sup> The appearance of characteristic product spectra (400–600 nm) indicates the formation of the isomeric product after ~1 ps. The product spectra are initially broad and show a structureless red tail extending into the infrared, indicating that the isomer is vibrationally hot. As the hot  $\text{CH}_2\text{I}-\text{I}$  isomer relaxes by intramolecular vibrational-energy redistribution (IVR) and cooling, the spectrum sharpens and the signal in the NIR region shifts towards shorter wavelengths. Ultimately, we observe the “stable” long-time spectrum of the isomer after 50 ps with two maxima in the UV and visible regions (390 and 560 nm, respectively). The vibrational cooling of the isomer occurs on the 10 ps time scale in acetonitrile, and is somewhat slower in less polar solvents. The

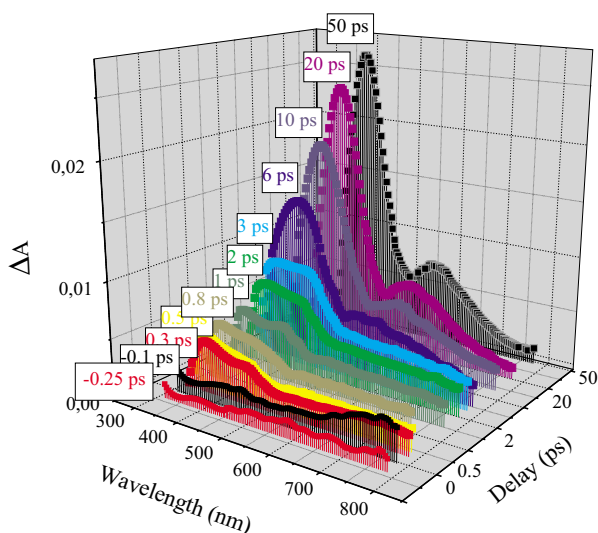


**Fig. 24.1** Time-resolved absorption spectra of  $\text{CH}_2\text{I}_2$  in acetonitrile, excited at 310 nm.

longtime thermal stability of the isomer was studied by means of nanosecond flash photolysis. The experiments revealed a lifetime of the  $\text{CH}_2\text{I-I}$  isomer of 45 ns in acetonitrile and 200 ns in *n*-hexane. Both the UV and visible absorption bands were found to decay with the same rate constant, confirming that these bands are indeed due to the same species. On a time scale of a few microseconds, the transient spectrum is dominated by the well-known  $\text{I}_3^-$  absorption in acetonitrile and by  $\text{I}_2$  absorption in *n*-hexane.

The photodissociations of  $\text{CH}_2\text{ICl}$  and  $\text{CH}_2\text{IBr}$  were initiated by a fs-pulse of light of wavelength 266 nm. For  $\text{CH}_2\text{ICl}$  in acetonitrile, the following characteristic stages of the transient absorption signal could be distinguished: an approximately 200-fs decay, a wavelength-dependent rise (1.5–12 ps), and a slower  $\sim 100$  ps wavelength-independent decay (380–850 nm) or rise (below 380 nm). The general features of the kinetics and spectral evolution are highly reminiscent of these for  $\text{CH}_2\text{I}_2$ . Thus, bond-breaking occurs within 200 fs and the rise time of  $\sim 1.5$  ps suggests that the isomer is formed as a result of in-cage recombination between  $\text{CH}_2\text{Cl}$  and I. After 20 ps, a strong band at 460 nm and one weaker band at 710 nm dominate the spectrum, which resembles that reported in the literature for the isomer.<sup>[6]</sup> The isomer decays with a time constant of 100 ps. Following 266 nm excitation of  $\text{CH}_2\text{IBr}$ , we also observed an intense transient absorption characteristic of the  $\text{CH}_2\text{Br-I}$  isomer, showing peaks at  $\sim 440$  (strong) and 610 nm (weak). The  $\text{CH}_2\text{Br-I}$  lifetime is intermediate ( $\sim 1$  ns) between the lifetimes of the  $\text{CH}_2\text{Cl-I}$  and  $\text{CH}_2\text{I-I}$  isomers.

In summary, UV excitation of the dihalomethanes ( $\text{CH}_2\text{IX}$ ; X = Cl, Br, I) leads to dissociation of the C–I bond within a few hundred femtoseconds, and is followed by the formation of a vibrationally excited isomer ( $\text{CH}_2\text{X-I}$ ). The hot isomer relaxes (IVR and cooling) on a time scale of several picoseconds. The vibrational relaxation time is solvent-dependent and varies for the different isomers. The  $\text{CH}_2\text{X-I}$  isomers have different thermal stabilities; the  $\text{CH}_2\text{Cl-I}$  isomer is the least stable, while  $\text{CH}_2\text{I-I}$  is the most stable.

#### 24.2.2

##### Barrierless Isomerization in Solution

In exploring the influence of a medium on the reaction rate (see, for instance, ref. [7]), *cis-trans* isomerizations have been extensively used as model reactions. In the past, we have studied barrierless isomerizations<sup>[8–10]</sup> and two closely related cyanine dye molecules, 1,1-diethyl-4,4-cyanine<sup>[10–16]</sup> and 1,1-diethyl-2,2-cyanine<sup>[17]</sup> have been particularly useful in establishing the characteristics of this reaction type. By measuring the transient absorption spectrum (including ground-state bleaching, stimulated emission, excited-state absorption, and photoisomer absorption) over a wide wavelength range, we can monitor the complete temporal evolution of the reaction coordinate, from the initially excited-state back to the original ground-state conformation. We illustrate this here by the recent results obtained for 1,1'-diethyl-2,2'-cyanine iodide (1122C).<sup>[17]</sup> The transient absorption spectrum was recorded over the wavelength interval 370–1000 nm and the following typical barrierless character of

isomerization was observed. (i) Stimulated emission (SE) exhibits a large spectral shift from  $\sim 570$  nm to more than 1000 nm (Figure 24.2). (ii) The spectral shift is coupled to a significant decrease in the SE cross-section. This SE spectral evolution reflects the dynamics of all-downhill motion of the excited-state population followed by formation of a quasi-equilibrated distribution at the bottom of the excited state, representing a  $90^\circ$  twisted conformation. Neither a solvation process nor IVR can account for this spectral shift. (iii) The decrease in the SE cross-section is related to a decrease of the  $S_1$ – $S_0$  Franck–Condon overlap as the torsion angle approaches  $90^\circ$ . (iv) We also observe typical kinetics for the ground-state absorption recovery with a pronounced induction period. Ground-state absorption recovery correlates well with the decay of the excited-state absorption, measured in the spectral region where neither SE nor ground-state bleaching can be observed (probe wavelength  $\sim 400$  nm) as well as with a delayed appearance and subsequent decay of the red-most SE. (v) The decays of the excited-state absorption and the red-most SE are very similar, reflecting the overall decay of excited-state population. (vi) The overall ground-state absorption recovery is slightly slower than depopulation of the excited state since an additional process of reverse torsion motion or ground-state isomerization (also barrierless, as expected) must follow the internal conversion to return the molecule to the original ground-state conformation.

It is very interesting to compare the experimentally measured dynamics with that derived from *ab initio* calculations on a model cyanine dye.<sup>[20]</sup> These calculations

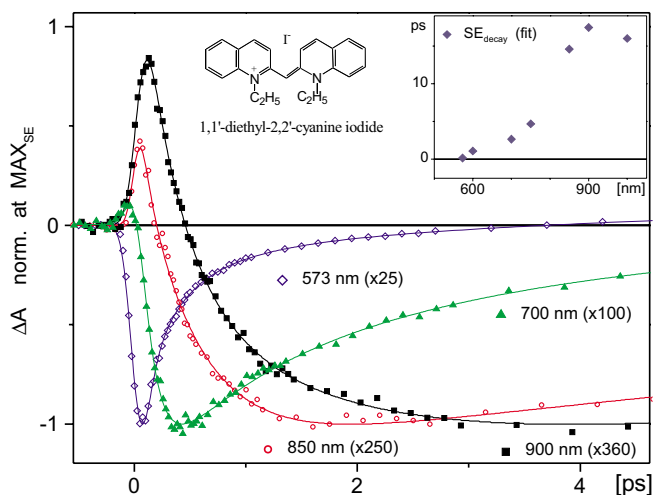


**Fig. 24.2** 1122C in propanol. Normalized kinetics of the SE rise and decay, measured at the wavelengths indicated in the figure. Normalization coefficients are given. The insert shows the spectral dependence of the average decay times.

showed that the reaction coordinate is quite well described by a simple twisting of the C=C bond, and that only at a late stage of the reaction, in the sink region, is bond-stretching involved. This explains why the measured dynamics of barrierless cyanine molecules<sup>[11–15,17]</sup> exhibit the characteristics of a one-dimensional barrierless PES.

Our ability to selectively probe the various steps of the isomerization reaction was also exploited to obtain information on the viscosity dependence of the various stages. The dynamics of the quasi-equilibrated distribution of the population at the bottom of the excited-state determines the decays of the excited-state absorption and the red-most SE, and also determines the rate-limiting step of the ground-state recovery. A similar, almost linear dependence of the time constant on the solvent shear viscosity ( $\eta$ ) was found for all three processes. In contrast, strongly nonlinear dependence on  $\eta$  was found for the dynamics of the short-lived SE signals, which correspond to passage through positions in the reaction coordinate for downhill population motion. The speed of the excited-state motion decreases as the population approaches the bottom of the excited state. This is clear from the slowing down of the SE decays probed at increasingly longer wavelengths (Figure 24.2, insert). Since, in the overdamped regime, the torsional motion of a bulky molecular group is determined by the local friction of the solvent, we conclude that for 1122C in *n*-alcohols the relationship between solvent friction and viscosity depends on the speed of population motion, or in other words, on the gradient of the excited-state potential.

### 24.3

#### Electron-Transfer in Dye-Sensitized Titanium Dioxide

Several different strategies have been suggested for the harvesting of light energy and its conversion to chemical energy or electricity. All these methods employ to some extent the principles and concepts of natural photosynthesis. An array of dye-sensitized TiO<sub>2</sub> nanoparticles in the form of a thin ( $\approx 10\ \mu\text{m}$ ) transparent film positioned between two electrodes has recently been proposed as a material with the potential to directly convert light energy into electricity.<sup>[21]</sup> Light is absorbed by the sensitizing dye, which injects electrons into the conduction band of a wide band gap semiconductor (in this case TiO<sub>2</sub>) and electrons are transported through the thin film material, from particle to particle, until they are coupled out through the back of the electrode into an external circuit. The oxidized sensitizer dye is re-reduced through a redox couple, hence the whole process can be repeated and electrons can be pumped continuously through the external circuit. For the best systems, an overall light-to-electricity efficiency of approximately 10% has been obtained.

The primary light-induced electron injection from the dye to the TiO<sub>2</sub> semiconductor nanoparticles is currently being studied by several groups. In the first time-resolved experiments,<sup>[24–28]</sup> the injection/recombination dynamics were often monitored in the visible and near IR regions of the spectra, where most species (i.e.



excited states, injected electrons, oxidized dye, etc.) involved in the charge-transfer processes absorb light. This made it difficult to find experimental conditions to monitor purely the electron dynamics, leading to some confusion as to the rate of electron injection and the spectral properties of the intermediates.<sup>[29,30]</sup> To resolve these difficulties, it was suggested that monitoring the electron dynamics in the mid-IR spectral range (4–7  $\mu\text{m}$ ) would yield unambiguous information, since this would probe absorption from free carriers and intraband electron transitions.<sup>[31–33]</sup> Experiments probing the dynamics in the mid-IR spectral region<sup>[32–34]</sup> have suggested that the majority of the electron injection occurs with a time constant shorter than 100 fs, while other experiments<sup>[34,35]</sup> have indicated the presence of substantial amplitudes of slower phases (~1–10 ps). The slower injection components have been attributed to heterogeneity in distance and coupling between the dye molecule and the  $\text{TiO}_2$  surface. Back electron transfer (recombination) from the semiconductor to the oxidized dye has also been extensively studied and has been found to be a highly non-exponential process with rate components ranging from picoseconds to microseconds.

In our own work, we have studied the electron injection and recombination dynamics of the laser dye Fluorescein-27 attached to ~3–4 nm sized  $\text{TiO}_2$  nanoparticles, both in colloidal solution<sup>[36,37]</sup> and in thin films.<sup>[38]</sup> The spectral properties of this dye molecule made it possible to unambiguously monitor the electron injection and recombination processes by means of the electron absorption in the near IR, dye-stimulated emission, and absorption by the oxidized dye molecule. For instance, the perfect correlation between the rise time of electron absorption (monitored in the near-IR spectral range) and dye-stimulated emission decay showed that electron injection in this system (in colloidal solution)<sup>[37]</sup> occurs with a characteristic time of ~300 fs. In more recent work<sup>[38]</sup> on the same Fluorescein– $\text{TiO}_2$  system, in this case as a thin film of nanoparticles, we have performed extensive spectral characterization of the system in order to establish the optimal conditions for probing the various processes related to the electron injection. Through judicious choice of the probe conditions, a contribution to the measured signal from excited-state absorption of the dye could be avoided, and the very weak electron signal could thus be observed. From the perfect agreement between dye-stimulated emission decay and electron absorption rise time (see Figure 24.3), it was concluded that electron injection is highly non-exponential and occurs with the time constants < 100 fs, ~1 ps, and ~8 ps.<sup>[38]</sup> From this work, it was also realized that the transient spectral characteristics of the sensitizing dye in solution do *not* give a good control for non-electron injecting conditions since dye– $\text{TiO}_2$  interactions affect the excited-state spectral properties of the sensitizing dye when it is adsorbed on the  $\text{TiO}_2$  surface.

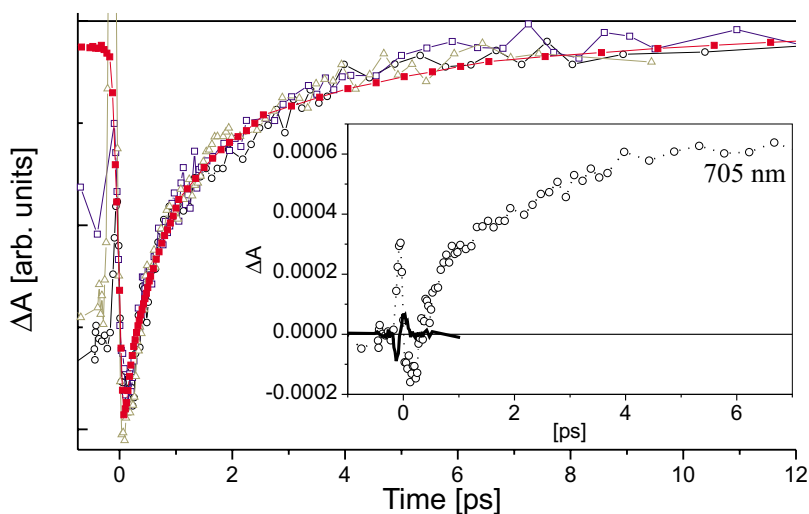


**Fig. 24.3** Comparison of kinetics of dye-stimulated emission and electron absorption. Identical kinetics suggest that all measurements reflect the same process, namely injection of electrons from the excited Fluorescein-27 into

the  $\text{TiO}_2$  semiconductor. Filled symbols – stimulated emission; open symbols – electron absorption at three different wavelengths, 690, 695, 705 nm.

## Acknowledgements

We would like to thank all our collaborators at the Department of Chemical Physics, Lund University for their contributions to this work.

## References

- 1 A. L. Harris, J. K. Brown, C. B. Harris, *Annu. Rev. Phys. Chem.* **1988**, 39, 341–366.
- 2 A. N. Tarnovsky, M. Wall, M. Rasmusson, T. Pascher, E. Åkesson, *J. Chin. Chem. Soc.* **2000**, 47, 1–4.
- 3 A. N. Tarnovsky, J.-L. Alvarez, A. P. Yartsev, V. Sundström, E. Åkesson, *Chem. Phys. Lett.* **1999**, 312, 121–130.
- 4 B. Schwartz, J. C. King, J. Z. Zhang, C. B. Harris, *Chem. Phys. Lett.* **1993**, 203, 503–508.
- 5 K. Saitow, Y. Naitoh, K. Tominaga, K. Yoshihara, *Chem. Phys. Lett.* **1996**, 262, 621–626.
- 6 G. Maier, H. P. Reisenauer, J. Hu, L. J. Schaad, B. A. Hess, Jr., *J. Am. Chem. Soc.* **1990**, 112, 5117–5122.
- 7 G. R. Fleming, P. Hänggi, (Eds.), *Activated Barrier Crossing*, World Scientific, Singapore **1993**.
- 8 V. Sundström, T. Gillbro, H. Bergström, *Chem. Phys.* **1982**, 73, 439–458.
- 9 V. Sundström, T. Gillbro, *J. Chem. Phys.* **1984**, 81, 3463–3474.
- 10 E. Åkesson, H. Bergström, V. Sundström, T. Gillbro, *Chem. Phys. Lett.* **1986**, 126, 385–393.
- 11 U. Åberg, V. Sundström, *Chem. Phys. Lett.* **1991**, 185, 461–467.
- 12 U. Åberg, V. Sundström, *J. Mol. Liq.* **1993**, 57, 149–176.

- 13 U. Åberg, V. Sundström, *Chem. Phys. Lett.* **1993**, 215, 388–394.
- 14 U. Åberg, E. Åkesson, J.-L. Alvarez, I. Fedchenia, V. Sundström, *Chem. Phys.* **1994**, 183, 269–288.
- 15 A. Yartsev, J.-L. Alvarez, U. Åberg, V. Sundström, *Chem. Phys. Lett.* **1995**, 243, 281–289.
- 16 J.-L. Alvarez, A. Yartsev, U. Åberg, E. Åkesson, V. Sundström, *J. Phys. Chem. B* **1998**, 102, 7651–7658.
- 17 A. Yartsev, A. N. Tarnovsky, V. Sundström, *Chem. Phys. Lett.* submitted.
- 18 B. Bagchi, G. R. Fleming, D. W. Oxtoby, *J. Chem. Phys.* **1983**, 78, 7375–7385.
- 19 M. Garavelli, P. Celani, F. Bernardi, M. A. Robb, M. Olivucci, *J. Am. Chem. Soc.* **1997**, 119, 6891–6901.
- 20 A. Sanchez-Galvez, P. Hunt, M. A. Robb, M. Olivucci, T. Vreven, H. B. Schlegel, *J. Am. Chem. Soc.* **2000**, 122, 2911–2924.
- 21 B. O'Regan, M. Grätzel, *Nature*, **1991**, 353, 737–739.
- 22 A. Hagfeldt, M. Grätzel, *Chem. Rev.* **1995**, 95, 49–68.
- 23 A. J. Nozik, R. Memming, *J. Phys. Chem.* **1996**, 100, 13061–13078.
- 24 Y. Tachibana, J. E. Moser, M. Grätzel, D. R. Klug, J. R. Durrant, *J. Phys. Chem.* **1996**, 100, 20056–20062.
- 25 J. M. Rehm, G. L. McLendon, Y. Nagasawa, K. Yoshihara, J. Moser, M. Grätzel, *J. Phys. Chem.* **1996**, 100, 9577–9578.
- 26 I. Martini, J. H. Hodak, G. V. Hartland, P. V. Kamat, *J. Phys. Chem. B* **1997**, 101, 8064–8072.
- 27 R. W. Fessenden, P. V. Kamat, *J. Phys. Chem.* **1995**, 99, 12902–12906.
- 28 T. Hannappel, B. Burfeindt, W. Storck, F. Willig, *J. Phys. Chem. B* **1997**, 101, 6799–6802.
- 29 J. E. Moser, D. Noukakis, U. Bach, Y. Tachibana, D. Klug, J. R. Durrant, R. Humphry-Baker, M. Grätzel, *J. Phys. Chem. B* **1998**, 102, 3649–3650.
- 30 T. Hannappel, C. Zimmermann, B. Meissner, B. Burfeindt, W. Storck, F. Willig, *J. Phys. Chem. B* **1998**, 102, 3651–3652.
- 31 H. N. Ghosh, J. B. Asbury, T. Lian, *J. Phys. Chem. B* **1998**, 102, 6482–6486.
- 32 R. J. Ellingson, J. B. Asbury, S. Ferrere, H. N. Ghosh, T. Lian, A. J. Nozik, *J. Phys. Chem. B* **1998**, 102, 6455–6458.
- 33 J. B. Asbury, R. J. Ellingson, H. N. Ghosh, S. Ferrere, A. J. Nozik, T. Lian, *J. Phys. Chem. B* **1999**, 103, 3110–3119.
- 34 Y. Tachibana, S. A. Haque, I. P. Mercer, J. R. Durrant, D. R. Klug, *J. Phys. Chem. B* **2000**, ASAP article.
- 35 H. N. Ghosh, J. B. Asbury, Y. Weng, T. Lian, *J. Phys. Chem. B*, **1998**, 102, 10208–10215.
- 36 M. Hilgendorff, V. Sundström, *Chem. Phys. Lett.* **1998**, 287, 709–713.
- 37 M. Hilgendorff, V. Sundstrom, *J. Phys. Chem. B* **1998**, 102, 10505–10514.
- 38 G. Benko, A. Yartsev, M. Hilgendorff, V. Sundström, *J. Phys. Chem. B* **2001**, 105, 967–974.

## 25

# Primary Processes in Photosynthesis Studied by Femtosecond Nonlinear Spectroscopy

*Jante M. Salverda and Rien van Grondelle*

### 25.1

#### Introduction

In photosynthesis, the energy of sunlight is very efficiently converted into chemical free energy. The solar photons are absorbed by so-called light-harvesting antennae, which subsequently transfer the excitation energy to a reaction center (RC). There, the energy is stabilized by a transmembrane charge separation. Both the antennae and the RCs are pigment-protein complexes bound to the photosynthetic membrane and their supramolecular organization is a key factor in the observed high efficiency. In plants, two RCs, namely photosystem I (PSI) and photosystem II (PSII), occur in series; PSII is able to oxidize  $\text{H}_2\text{O}$  to form  $\text{O}_2$ , while PSI reduces  $\text{NADP}^+$ . Photosynthetic purple bacteria make do with a single RC, which is incapable of oxidizing  $\text{H}_2\text{O}$ .<sup>[1–4]</sup> In the mid-1980s, the bacterial RC was the first membrane protein to be crystallized, by Michel and Deisenhofer.<sup>[5]</sup> During the last decade, high-resolution structures have become available for the bacterial light-harvesting complex LH2,<sup>[6,7]</sup> the plant light-harvesting complex LHCII,<sup>[8]</sup> and, more recently, the cores (i.e. RC plus surrounding antennae) of PSI<sup>[9]</sup> and PSII.<sup>[10]</sup>

To obtain a quantum efficiency of 90 % or higher for the photosynthetic process, all steps involved have to be extremely fast. After excitation of the first antenna pigment, the RC is reached in about 40–50 ps through several tens of transfer steps, each of which takes only a few 100 fs. The subsequent first electron-transfer step in the RC also occurs within a few ps, and is followed by a sequence of slower (several hundreds of ps up to ms) electron-transfer events. After the charge separation, the “dark” reactions, resulting in NADPH and/or ATP production, proceed on a much slower timescale.

These light-dependent reactions, i.e. the “primary processes”, have only been observable for the last two decades, as first pico- and then femtosecond lasers were developed. The most popular ultrafast techniques applied to their study have been pump-probe (time-dependent absorption difference) spectroscopy and time-resolved fluorescence measurements (for a description of these techniques, see ref.<sup>[11]</sup>). Both have a signal strength that varies linearly with the size of the excited-state population, at least for  $T \gg \tau_{\text{pulse}}$ . Thus, although they are third-order nonlinear techniques, they are usually not grouped with others such as three-pulse photon-echo, which are dis-

cussed here. This linear character makes them easy to understand intuitively. However, their use is limited to certain cases and they are not readily applicable to all processes. For example, the pump-probe technique can only monitor a process if the absorption of the probe light is affected, i.e. either a transition must occur to a state with a frequency other than the probe frequency or the orientation of the transition must change. The same holds for fluorescence, with the additional limitation that the state which we wish to observe must fluoresce appreciably. Therefore, with both techniques, energy transfer between isoenergetic pigments is rather difficult to observe. Anisotropy decay of the signal can sometimes be used for this, but with the pump-probe method the anisotropy is often difficult to calculate since the signal may contain both positive  $\Delta A$  (bleaching and stimulated emission) and negative  $\Delta A$  (excited-state absorption) contributions, each with their own polarization. Moreover, if these contributions exactly cancel each other, the division by zero results in an infinitely large “anisotropy”. Narrowband pulses can be used to selectively excite a subset of pigments within the absorption band, and the time evolution of the spectrum then provides information about the process one wishes to study, although a spectrally narrow pulse is intrinsically long, which limits the time resolution.

The techniques discussed here, i.e. three-pulse echo peak shift (3PEPS) and transient grating (TG), can help to solve some of these problems (for an overview of the background of these femtosecond nonlinear spectroscopies, see the monograph by Mukamel<sup>[12]</sup>). Both methods have been extensively used to probe solvent dynamics using a chromophore.<sup>[13,14]</sup> 3PEPS is specifically suited for monitoring changes in the excitation frequency of a sample within the bandwidth of the excitation pulses rather than for registering removal of population from within this wavelength range. TG is quadratic with respect to the bleaching and/or excited-state absorption, i.e. it is always positive. Therefore, it can be used to calculate anisotropies without zero-crossing problems. Herein, we describe the principle of these techniques and their experimental realization. We demonstrate their utility with three examples of experiments carried out on photosynthetic systems. Specifically, these encompass: (i) the study of energy transfer in the B800 ring of antenna LH2 of purple bacteria,<sup>[15]</sup> (ii) the study of energy transfer in the antenna LH1 of purple bacteria,<sup>[16,17]</sup> and (iii) the study of energy transfer and charge separation in the reaction center (RC) of purple bacteria.<sup>[18]</sup> We show how new and/or clearer information about these processes has been obtained with these nonlinear techniques.

## 25.2

### The Three-Pulse Echo Peak Shift and Transient Grating Methods

We will describe the principle of the 3PEPS experiment using the impulsive limit. The configuration of a 3PEPS experiment is shown in Figure 25.1a. In such an experiment, a sequence of three laser pulses, each with a slightly different direction of propagation,  $\mathbf{k}_1$ ,  $\mathbf{k}_2$ , or  $\mathbf{k}_3$ , is focused onto the sample. A fourth pulse, the photon echo, is emitted in the direction  $\mathbf{k}_3 - \mathbf{k}_2 + \mathbf{k}_1$  at a time  $\tau$  after the third pulse, with  $\tau$  being the delay between the first two pulses. The time-integrated intensity of the

echo is measured as a function of the delay  $\tau$ , with the delay  $T$  between the second and third pulse, also known as the population time, as a parameter. The distance of the maximum of this signal (further referred to as the echo) from  $\tau = 0$ , the peak shift, is then determined as a function of  $T$ . The decay of the peak shift with  $T$  reflects all processes that lead to frequency changes of the excited pigments (described as  $\Delta\omega(t)$ ) within the spectral window of the pulses used, which can be rationalized as follows. Pulses 1 and 2 generate a frequency-dependent modulation of the excited-state population within the laser bandwidth, a so-called frequency grating, which has spacing proportional to  $1/\tau$ . For an example of such a grating, see Figure 25.1b. The manner in which this frequency grating is imprinted on the sample by pulses 1 and 2 can be explained as follows: pulse 1 does not actually excite the sample to an excited state, which would correspond to two interactions between the pulse field and molecule (note that absorption of a photon corresponds to two interactions with an electric field  $\mathbf{E}$  because  $N_{\text{phot}} \sim I \sim E^2$ ). Instead, only one interaction takes place, as a result of which the molecules are put into a coherence, i.e. a superposition of ground and excited states. This superposition, corresponding to off-diagonal elements of the density matrix, has a phase factor  $e^{i\omega_i t}$ , i.e. it oscillates with a transition frequency  $\omega_i$  after the interaction with pulse 1 at  $t = 0$ . Therefore, the phase of each molecule with slightly different  $\omega_i$  will be different for non-zero  $t$ . When pulse 2 interacts with the sample at time  $t = \tau$ , some molecules will have phase  $\omega\tau = 2n\pi$ , while others will have phase  $\omega\tau = (2n+1)\pi$ . After the second interaction, these will be in the excited and ground states, respectively. Hence, the appearance of the frequency grating and the inverse dependence of the grating spacing on  $\tau$ . After the interaction with pulse 3, the reverse takes place: all molecules are again in a coherence, and, at time  $\tau$  after pulse 3, all coherences have the same phase, leading to a macroscopic electric field  $P^{(3)}$ , which can be detected.

During the time  $T$  between pulses 2 and 3, the modulation depth and width of the grating produced by the combined effect of the first two pulses will be affected by changes in the transition frequencies of the pigments within the laser bandwidth, rather like in a transient hole-burning experiment. The amplitude of the grating also decays, due to a loss of population, for instance due to energy transfer to pigments absorbing outside the laser window, but this does not affect the peak shift. Because intra-band frequency changes efface a fine grating more easily, an increasingly widely spaced grating is needed to survive when longer  $T$  values are used. As a more widely spaced grating corresponds to a smaller delay between pulses 1 and 2, this means that the echo intensity maximum gets closer and closer to zero  $\tau$ . Thus, the decay of the peak shift as a function of  $T$  reflects the loss of correlation, averaged over all pigments, between the excitation frequency at the time of pulse 2 and the frequency at the time of pulse 3. We note in passing that in the case of non-zero pulse widths, the overlap of the pulses in time, leading to different time ordering, must be explicitly accounted for in the modeling of these experiments.

The fluctuating frequency  $\omega_i(t)$  of each pigment  $i$  can be described as:

$$\omega_i(t) = \omega_{eg} + \Delta\omega_i(t) + \varepsilon_i \quad (1)$$

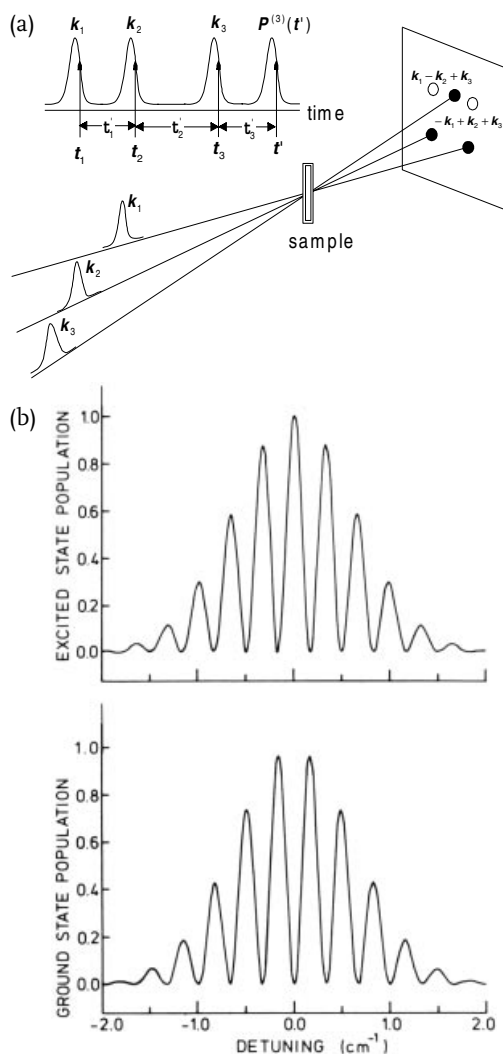


**Fig. 25.1** (a) Pulse sequence and phase-matching diagram for the three-pulse echo. The three pulses, incident on the sample with vectors  $k_1$ ,  $k_2$ , and  $k_3$ , generate two echo signals in the phase-matched directions  $k_3 - k_2 + k_1$  and  $k_3 + k_2 - k_1$ , which are indicated on the screen behind the sample as open circles. The delays between the maxima of the pulses as  $\tau$  between  $k_1$  and  $k_2$ , and  $T$  between  $k_3$  and the last of  $k_1$  and  $k_2$ , respectively. Interactions between the pulse fields and the sample can take place at any realization of the times  $t_1$ ,  $t_2$ , and  $t_3$ , respectively. These times and the interval times

$t_1'$ ,  $t_2'$ , and  $t_3'$  are used in the calculations but are not discussed in detail here.<sup>1</sup> (b) The frequency grating: a modulation of the population in states  $|g\rangle$  and  $|e\rangle$  after application of two pulses. The calculation for this particular graph uses  $\tau = 100$  ps, which yields the detuning given on the horizontal axis. However, the figure should only be taken as qualitative.<sup>2</sup>

1) Figure source: Jimenez *et al.*, 1997, *ref.* [16]

2) Figure source: Duppen and Wiersma, 1986, *ref.* [19]

where  $\omega_{eg}$  is the ensemble average of the transition frequency,  $\Delta\omega_i(t)$  is the fluctuation of the frequency of pigment  $i$ , and  $\varepsilon_i$  is its static deviation from average, i.e. the inhomogeneous broadening. The average frequency correlation of the ensemble is then described by the two-point frequency correlation function:

$$M(t) = \frac{\langle \Delta\omega(0)\Delta\omega(t) \rangle}{\langle \Delta\omega(0)^2 \rangle} \quad (2)$$

From  $M(t)$ , we can derive the line-shape function  $g(t)$ , and with  $g(t)$  we can calculate the third-order response functions  $R(t, \tau, T)$ . The third-order polarization  $P^{(3)}$  can then be calculated by integrating the product of the pulse fields and the response functions over time. All this is described in detail by Mukamel in ref.<sup>[12]</sup>

The transient grating technique is a special case of the three-pulse echo, with the first two pulses set at  $\tau = 0$  and the signal intensity scanned as a function of the population time  $T$ . The first two pulses create a spatial population grating in the sample due to interference between the beams, which intersect at a small angle. The decay of this grating reflects the loss of excited-state population from within the laser spectrum. This spatial grating is, of course, also created in the 3PEPS experiment, but in such experiments the amplitude decay, which is caused by population transfer, is not considered (as mentioned above). Also, at non-zero delay between pulses 1 and 2, the phase of this grating will be different for each frequency, leading to canceling contributions.

It is intuitively clear that energy transfer among more or less identical pigments of an inhomogeneous distribution leads to an increased rate of disappearance of the frequency grating and thus to a faster peak shift decay. In the most commonly used approach, the energy transfer is incorporated by taking  $\omega_i(t)$  (Eq. (1)) to describe a two-level electron-hole system that migrates among the pigments, rather than a fixed pigment. During the migration, the electron-hole pair samples the inhomogeneous distribution, hence the  $\varepsilon_i$  term in Eq. (1) becomes a time-dependent quantity. The diffusive character of energy transfer implies an exponential decay term of  $M(t)$ , which is added to a sum of Brownian oscillators (see 25.4). In fact, the electron-hole system is analogous to a solute in a liquid sampling all possible environments, with the exponential term analogous to an overdamped oscillator.

## 25.3

### The 3PEPS/TG Experiment

A fs laser producing stable  $\sim 30$  fs pulses at a high repetition rate is used as a source. Depending on the system under study, a Ti:Sa oscillator is used either directly (for 800 nm excitation) or as a seed for an amplifier. Cavity dumping is built into either the oscillator or the amplifier so that the repetition rate can be varied. The beam is then split into three and all pulses can be delayed with respect to one another. The polarization of the pulses can be set individually if desired. The three pulses are focused on one sample spot. Pulse 3 is always last, but 1 and 2 can exchange roles, that is, both



echoes with  $k_3 + k_2 - k_1$  and  $k_3 - k_2 + k_1$  are detected. The peak shift is half the separation between the peaks of these echoes. For a typical example, see Figure 25.2. Behind the sample, filters can be put in the detection path so as to obtain frequency-selective echo signals. Fortunately, the pulse lengthening due to the bandwidth limitation by these filters does not affect the time resolution. As the echo is detected in a homodyne, time-integrated fashion, the instrument response is determined solely by the convolution of the three original pulses. Typically, with  $\sim 30$  fs pulses, this gives a time resolution of 50–60 fs. The sample is circulated to avoid local heating damage. A low optical density of  $\sim 0.2$  must be used. The repetition rate is adapted (in the 100 kHz range) to avoid build-up of population in a long-lived product state, such as a triplet.

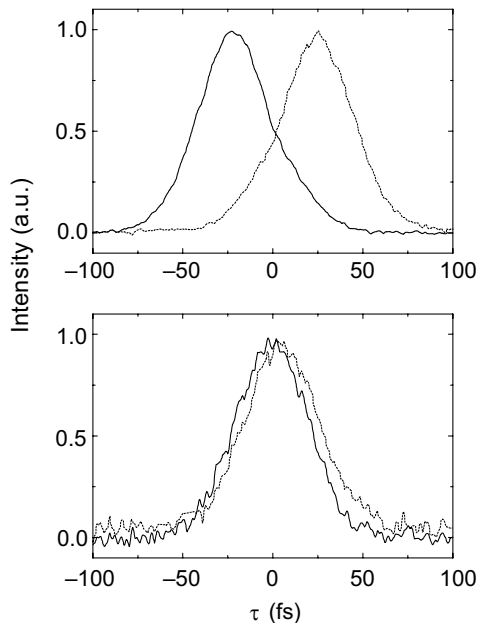


**Fig. 25.2** Three-pulse echo signals (measured on LH1) for two population times  $T = 0$  fs (top) and  $T = 1000$  fs (bottom). Both echoes for the two phase-matched directions are shown. At each  $T$ , the peak shift is half the time difference between the peaks of the two echo signals.<sup>3</sup>

3) Figure source: Jimenez *et al.*, 1997, ref. [16]

#### 25.4 Simulations

All data discussed here were simulated with the Brownian oscillator model.<sup>[20–23]</sup> In this model, a Gaussian term is added to describe the fastest decay component of  $M(t)$ , which is due to electron-phonon coupling. We then get:

$$M(t) = \left\{ \langle \Delta \omega_g^2 \rangle e^{-(t^2/\tau_g^2)} + \sum_i \langle \Delta \omega_{i,e}^2 \rangle e^{-(t^2/\tau_{i,e}^2)} + \sum_j \langle \Delta \omega_{j,o}^2 \rangle e^{-(t^2/\tau_{j,o}^2)} \cos(\omega_j t + \varphi_j) \right\} \frac{1}{\sum_k \langle \Delta \omega_k^2 \rangle} \quad (3)$$

In this equation, the subscripts  $g$ ,  $e$ , and  $o$  denote the Gaussian, exponential, and oscillatory contributions, respectively. The sums over  $i$  and  $j$  are partial sums over

the exponential or oscillatory terms, whereas the sum over  $k$  includes all processes that contribute to  $M(t)$ . The  $\langle \Delta\omega^2 \rangle$  factors describe the ensemble-averaged coupling strength of each process. In Eq. (3), one of the exponentials describes energy transfer with rate  $\tau_{i,e}$ , but additional exponentials may also be used to describe other processes such as overdamped vibrational relaxation of the pigment, or spectral diffusion of the protein. However, in the simulations described below for the energy transfer in the B800 ring of Bacteriochlorophylls (Bchls) of LH2, for instance, only a single exponential was needed for the energy transfer, with rate  $\tau_e$  and coupling strength  $\omega_e$ . In such a case, the latter becomes equal to the inhomogeneous broadening. The (damped) oscillatory terms in Eq. (3) represent specific vibrational modes of the chromophore and/or bath molecules. A non-zero phase-shift  $\phi_j$  can be needed to account for the vibrations being set in motion before  $T = 0$  by the first of the pulses.

The assumption on which the BO model is based, namely that all processes are independent and sample their own frequency space, is obviously an oversimplification. In a proper description, the rate of loss of frequency information through one-pigment relaxation should be added to the rate of transfer of the excitation to a neighboring pigment through energy transfer. To account for energy transfer in this manner, Yang and Fleming<sup>[24]</sup> have developed an approach which describes the system as a two-level donor system and a two-level acceptor system. The donor is described by a monomeric  $M(t)$ , which contributes to the echo signal. The acceptor has an  $M(t)$  too, but one that will only contribute a free-induction decay (FID) signal with zero peak shift. The signals are then multiplied by the population amplitude of donor ( $P_D$ ) and acceptor ( $P_A$ ). We then get:

$$R(t, T, \tau) = [R_{g_D g_D}^0(t, T, \tau) + R_{e_D e_D}^0(t, T, \tau)] P_D(T) + [e^{-g^*(\tau) - g(t)} + e^{-g^*(\tau) - g^*(t)}] P_A(T) \quad (4)$$

Here,  $R_{g_D g_D}^0$  and  $R_{e_D e_D}^0$  are the response functions for the case where all three pulses interact with the donor molecule D. The second term between square brackets describes the FID signal for interaction of pulse 3 with the acceptor A. The population amplitudes  $P_A$  and  $P_D$  are described by rate equations, see ref. [24] for more details. See also Figure 25.3 for the Feynman diagrams describing this model. For

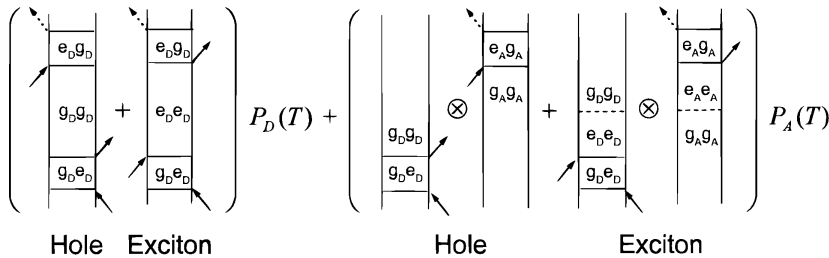


**Fig. 25.3** A simplified picture of the model used to simulate the peak shift in the case of intra- and interband energy transfer. Feynman diagrams are shown for the excitation remaining on the donor during time  $T$  (first diagram) and

for the excitation migrating to an acceptor during  $T$  (second diagram).<sup>4</sup>

4) Figure source: Agarwal *et al.*, 2000, ref. [25]

systems with well-separated timescales for all the different processes, such as the B800 ring of monomeric bacteriochlorophyll molecules in LH2, the model used is not crucial. On the other hand, for systems such as LH1, for which pulse duration, protein relaxation time, and energy transfer time are all of very similar magnitude, a new analysis with the exact model would be advisable.

## 25.5

### The B800 Ring of the Purple Bacterial Antenna LH2

Photosynthetic purple bacteria contain a reaction center (RC) and two types of light-harvesting complexes, a core antenna LH1 that surrounds the RC and a peripheral antenna LH2. The structure of the peripheral antenna LH2 was resolved a few years ago for the species *Rhodopseudomonas (Rps.) acidophila* and *Rhodospirillum (Rs.) rubrum*.<sup>[6,7]</sup> Figure 25.4 depicts the structure of LH2 of *Rps. acidophila*. LH2 consists of two concentric rings of nine  $\alpha$ -helical polypeptides, which bind two rings of pigments: a ring of eighteen closely-packed Bchls absorbing at 850 nm, called B850, and a ring of nine more widely separated Bchls absorbing at 800 nm, called B800. The B850s are at a center-to-center distance of ca. 9 Å from each other and form a strongly coupled system with partly delocalized excitons. The B800 Bchls, on the other hand, are at about 20 Å from each other and 17 Å from the nearest B850 Bchl. As a consequence, excitations on B800 are essentially localized. Apart from the Bchls, a ring of nine carotenoid molecules was also identified in LH2 of *Rps. acidophila*, with their polyene chains more or less perpendicular to the plane of LH2, thus essentially bridging the two rings of Bchls.

The main function of B800 is to enable the bacteria to absorb light at 790–810 nm. The absorbed energy is then transferred to B850 in  $\sim 700$  fs at room temperature;<sup>[26–28]</sup> at low temperature it takes  $\sim 1$  ps.<sup>[29–31]</sup> Whether any energy transfer between B800s occurs prior to B800  $\rightarrow$  B850 transfer is a subject of discussion. At low temperature, pump-probe experiments with narrow-band pulses, which selec-

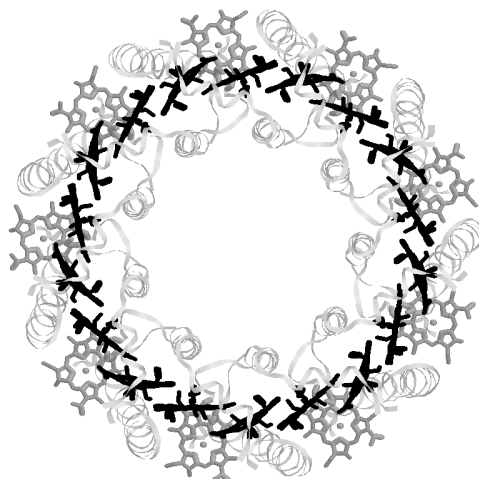
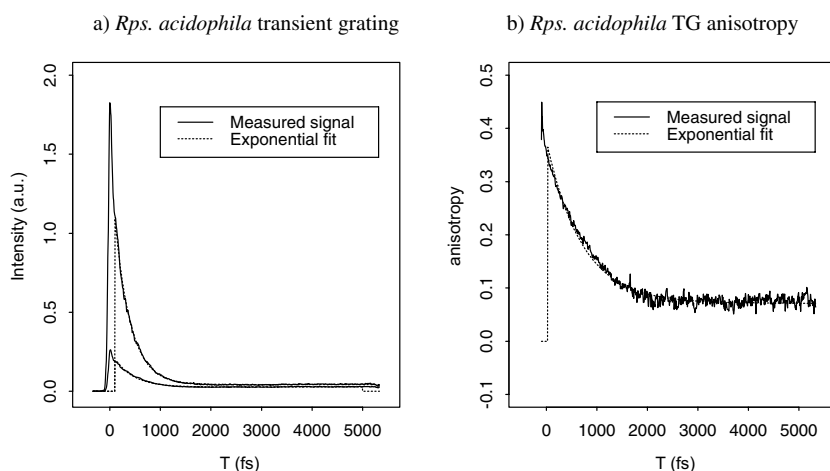


Fig. 25.4 Model of the X-ray structure of the peripheral antenna LH2 of purple bacteria *Rps. acidophila*. The membrane is seen from the top, with the nine B800 Bchls (gray) in its plane and the eighteen B850 Bchls (black) perpendicular to it.<sup>5</sup>

5) Figure source: Brookhaven protein data bank, based on the structure determination by McDermott *et al.*, 1995, ref. [6]

tively excite a subset of B800s, have shown that it does.<sup>[27,30,32,33]</sup> The timescale varies from blue to red throughout the band, from  $\sim 300$  fs to  $\sim 1$  ps. At room temperature, selective excitation is very difficult due to the large homogeneous bandwidth. Also, the B800 population is depleted more rapidly by transfer to B850. Pump-probe anisotropy decay measurements<sup>[32,34,35]</sup> do suggest that  $B800 \leftrightarrow B800$  energy transfer occurs, but at the zero-crossing of the pump probe signal, where the B800 bleaching is equal to the B850 excited-state absorption (ESA), the anisotropy becomes very large. This prevents a precise determination of the transfer timescale. It was estimated to be  $\sim 1$  ps. An earlier 3PEPS measurement on B800 was interpreted as showing only  $B800 \rightarrow B850$  transfer.<sup>[36]</sup>

In the experiments discussed here, Salverda et al.<sup>[15]</sup> measured 3PEPS and TG at room temperature for LH2 of *Rps. acidophila* and *Rs. molischianum*. To search for energy transfer specifically, measurements were carried out with both perpendicular and parallel polarization of the third pulse. Also, frequency-selective detection of the echo signal was applied for *Rs. molischianum* with pulse 3 parallel. In this case, a filter was used with 7 nm bandwidth, at both 790 nm and 810 nm maximum transmission. The results of the TG measurements are shown in Figure 25.5a. The observed decays essentially represent loss of excited B800 due to energy transfer to B850. These traces were fitted with a single exponential, which means that the minimum in the trace due to interference between the B800 bleach and B850 ESA was neglected. Decay times were found to be 300–500 fs, corresponding to times of 600–1000 fs for energy transfer from B800 to B850. For the measurements over the whole bandwidth, with all three pulses parallel, transfer times of 600 fs for *Rps. acidophila* and 700 fs for *Rs. molischianum* were found. With the third pulse perpendicular, the decay time of the TG signal was generally found to be longer than with all



**Fig. 25.5** (a) Transient grating signal of the B800 ring of LH2 of *Rps. acidophila*. Both the parallel polarization signal (large amplitude) and the perpendicular polarization signal (small amplitude) are shown. (b) Anisotropy of the

transient grating of B800 of LH2 of *Rps. acidophila* calculated from the square roots of the two signals in Figure 25.5 (a).<sup>6</sup>

**6)** Figure source: Salverda et al., 2000, ref. [15]

pulses parallel. To study this depolarization more carefully, Salverda et al.<sup>[15]</sup> calculated an anisotropy decay from the square roots of the TG signals. The decays obtained, without a filter, are shown in Figure 25.5b. Exponential fits gave decay times of 700 fs for *Rps. acidophila* and of 900 fs for *Rs. molischianum*. The contribution from the excited-state absorption of B850 was again neglected, its effect expected to be small as no zero-crossing occurs.

Figure 25.6a depicts the peak shift decay curves calculated from the 3PEPS measurements. The peak shift measured with a perpendicular polarization of pulse 3 is lower than that measured with a parallel polarization with the same population time. It also appears to decay more rapidly. This confirms the conclusion from the TG experiments that B800  $\leftrightarrow$  B800 energy transfer occurs. After energy transfer, a population of pigments is established with an orientation different to that of the initially excited pigments. At the same time, the frequency correlation is lost, which leads to a lower peak shift. Colored peak shift decays, see Figure 25.6b, again show the B800  $\leftrightarrow$  B800 energy transfer. The “blue” peak shift does not decay after the initial protein relaxation in  $\sim 80$  fs as only the pigments that are yet to transfer their excitation remain within the probed frequency range. The “red” peak shift decays about twice as rapidly, as excitations arrive within the probed frequency range after energy transfer has occurred. Simulations with the Brownian oscillator model gave the timescales for the processes seen in the peak shift decay. The energy transfer time was found to be 1100 fs for *Rps. acidophila* and 800 fs for *Rs. molischianum*. Other processes observed were electron-phonon coupling leading to relaxation with-

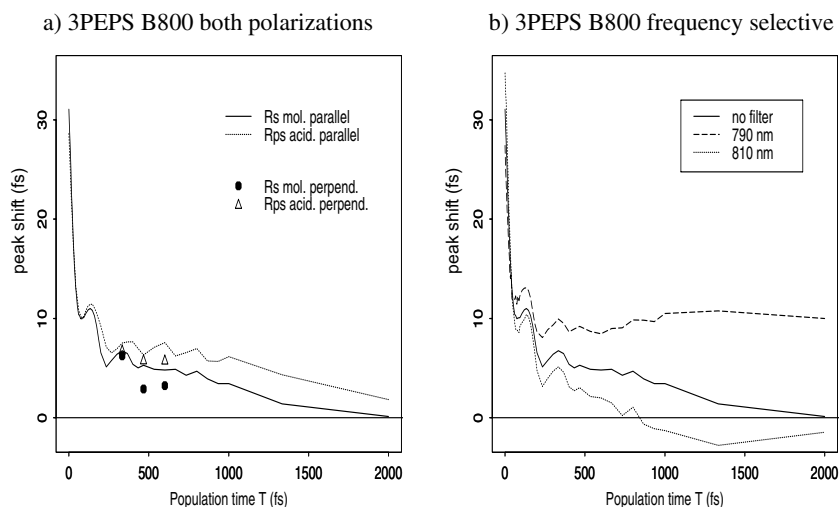


**Fig. 25.6** (a) Peak-shift decay signals measured on B800 of LH2 of *Rps. acidophila* (dotted curve, open triangles) and *Rs. molischianum* (solid curve, filled octagons). Signals measured with both parallel polarization of pulse 3 (curves) and perpendicular polarization of pulse 3 (points) are shown. (b) Peak-shift decays

measured on B800 of LH2 of *Rs. molischianum* at 810 nm (dotted) and 790 nm (dashed), both with parallel polarization of pulse 3. The peak shift decay measured without frequency selection (solid) is shown as a reference.<sup>7</sup>

7) Figure source: Salverda et al., 2000, ref. [15]

in 80 fs, and a strong oscillation of  $\sim 162 \text{ cm}^{-1}$  showing damping in  $\sim 500 \text{ fs}$ . This oscillation is not seen with pump-probe techniques, nor with transient grating. The main conclusion to be drawn from these 3PEPS and TG experiments is that  $\text{B800} \leftrightarrow \text{B800}$  transfer does occur and that the timescale for this process is  $\sim 1 \text{ ps}$ .

## 25.6

### The Bacterial Antenna LH1 and its Dimeric Subunit B820

The core antenna LH1 surrounds the bacterial RC. No high-resolution structure has been determined to date, although electron microscope images with  $\sim 8 \text{ \AA}$  resolution (see Figure 25.7) suggest that it is a ring much like LH2. It consists of 32  $\alpha$ -helical polypeptides arranged in two concentric rings with a closely-packed ring of 32 Bchls sandwiched between them.<sup>[37]</sup> The maximum absorption of the latter appears at 875 nm, hence the LH1 complex is often denoted as B875. When excess detergent is added to the isolated LH1 antenna, it separates into polypeptide-Bchl dimers, absorbing at 820 nm, called B820.<sup>[38]</sup> No energy transfer can be observed in B820.<sup>[39,40]</sup> This suggests that the allowed optical transition at 820 nm originates from strong excitonic interactions involving both Bchls. In LH1, the energy transfer dynamics takes place on a timescale of  $\sim 100 \text{ fs}$ , as was observed by the pump-probe method, pump-probe anisotropy, fluorescence anisotropy, and several other techniques.<sup>[41–44]</sup> However, from these experiments it remained unclear as to whether the exciton was localized on a monomer, on a dimer, or on a larger unit.

To shed more light on this matter, Fleming and co-workers carried out 3PEPS measurements on both the whole LH1 ring and on the subunit B820. The extra information they obtained was largely based on comparisons between these complexes.<sup>[16,17]</sup> Figure 25.8 depicts the 3PEPS signals obtained. The most striking feature is the large difference in decay of the two peak shifts. For LH1, the peak shift decays to almost zero within 200 fs, whereas that for B820 remains at a value of  $\sim 15 \text{ fs}$  after the first sub-100 fs decay. This high value of the B820 peak shift persists up to 100 ps, as can be seen in Figure 25.8b. The observed difference between the two

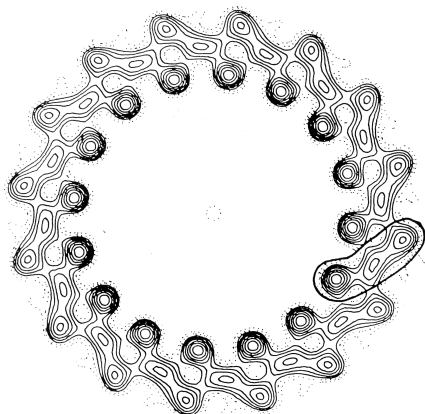


**Fig. 25.7** Model of the  $8 \text{ \AA}$  electron microscopy structure of the core antenna LH1 of purple bacteria *Rs. Rubrum*. A subunit consisting of two polypeptides  $\alpha$  and  $\beta$  (which are probably mostly  $\alpha$ -helical) is encircled. This subunit corresponds to a B820 particle. The polypeptides are separated by  $15\text{--}20 \text{ \AA}$ , hence they are not covalently bound.<sup>8</sup>

8) Figure source: Karrasch *et al.*, 1995, ref. [37]

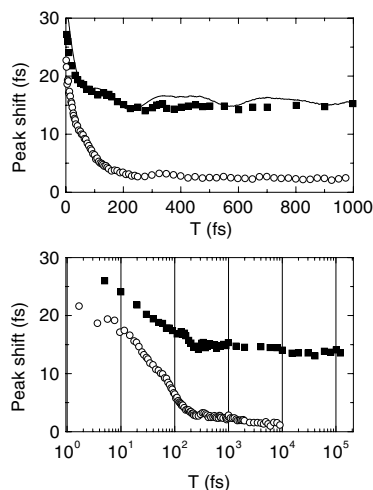


**Fig. 25.8** Peak shift decays measured on LH1 of *Rb. sphaeroides* (open circles) and the B820 subunit from LH1 of *Rb. sphaeroides* (filled squares). The solid line is a simulation of the B820 subunit peak shift decay using parameters taken from the simulation of the LH1 peak shift decay (see text). Both the short time scale with  $T$  from 0–1 ps (a) and the long time scale with  $T$  from 0–140 ps (b) are shown.<sup>9</sup>

9) Figure source: Yu *et al.*, 1997, ref. [17]

signals must be due to the energy transfer among all the dimeric subunits that takes place in the LH1 ring. In addition to the fast decay due to energy transfer, LH1 also shows a further slow ~10 ps decay process that is not present in B820. This is probably related to energy transfer among different LH1 rings. Apart from the two energy transfer processes, the dynamics of both signals are actually quite similar. Both exhibit a large initial peak shift of about 25–30 fs, which then decays to 10–15 fs in less than 100 fs. This first decay must be due to electron-phonon coupling between the pigment and the protein. Moreover, the oscillations superimposed on the peak shift decays are similar in both cases. This suggests that the basic excitonic unit of LH1 is indeed a dimer. A time constant for each process could be estimated from simulations. BO model simulations yielded a value of ~90 fs for the energy transfer. Unfortunately, this time is not much longer than the ~50 fs decay time for the initial Gaussian decay that is present in both LH1 and B820. Moreover, the instrument response of ~50 fs is of the same order of magnitude. This coincidence in time of these events leads to a large degree of uncertainty in the time constants extracted for these two fast processes. However, the ~90 fs time does correspond reasonably well with values found earlier by other authors. From anisotropy decay measurements,<sup>[42]</sup> a depolarization time was obtained that can best be reconciled with the 90 fs transfer time found here if a dimeric exciton is assumed, as argued by Jimenez *et al.*<sup>[16]</sup> The similarity between the B820 and LH1 excited-state properties was confirmed by the simulations as the parameters from the LH1 simulation could be used for B820 without any adaptation, except for omission of the ultrafast energy transfer events. Therefore, it was concluded by Yu *et al.*<sup>[17]</sup> that the exciton in LH1 is really delocalized over 2 Bchls.

## 25.7

## The Accessory Bacteriochlorophylls of the Bacterial Reaction Center

The crystal structure of the bacterial RC was resolved in the 1980s for the purple bacteria *Rhodospseudomonas (Rps.) viridis*<sup>[5]</sup> and *Rhodobacter (Rb.) sphaeroides*.<sup>[45,46]</sup> The structure of the RC of *Rb. sphaeroides*, which is discussed below, is shown in Figure 25.9. Only the pigments are shown for clarity. In total, there are 4 Bchls, 2 Bacteriopheophytins (Bph), and 2 quinones. The two top Bchls are very close together and form the special pair P. The other two Bchls are positioned at either side of this pair, forming the beginning of two nearly symmetric branches A and B. These are the accessory or “voyeur” Bacteriochlorophylls B and to differentiate between the branches they are denoted as B<sub>A</sub> and B<sub>B</sub>. They absorb at ~800 nm, with B<sub>A</sub> absorbing more at the blue side of the absorption band and B<sub>B</sub> more to the red. One function of these accessories is to transfer the absorbed energy to the special pair P, which has a lower-energy excited state, as befits its absorption band at 870 nm. This occurs within a few 100 fs after B is excited.<sup>[47,48]</sup> A second and most important function of B<sub>A</sub> is to accept the electron donated by the excited special pair (P\*) and to transfer this charge to the neighboring Bph (denoted as H<sub>A</sub>). The electron thus follows the path:



with H<sub>A</sub> being the Bph in branch A, Q<sub>A</sub> the quinone in branch A, and Q<sub>B</sub> the quinone in branch B.

Recently, it was concluded by van Brederode et al.,<sup>[49,50]</sup> on the basis of transient absorption difference spectroscopy at 77 K, that B<sub>A</sub><sup>\*</sup> can also donate an electron directly to H<sub>A</sub>, thereby circumventing the excitation (and oxidation) of P. In fact, they observed two new pathways for ultrafast electron transfer

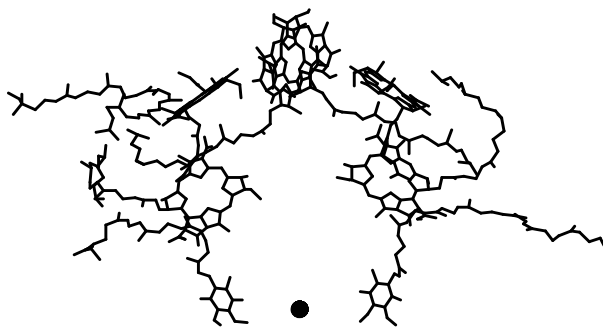
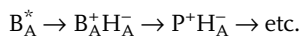


**Fig. 25.9** Model of the X-ray structure of the bacterial reaction center (RC) of *Rb. sphaeroides*. Only the cofactors are shown. The plane of the membrane is perpendicular to the plane of the figure and the normal to the membrane plane is

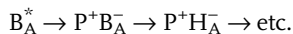
pointing to the top of the page. For a more detailed description, see text.<sup>10</sup>

**10** Figure source: Brookhaven protein data bank, based on the structure determination by Allen *et al.*, 1987, ref. [45]





and



To compete with the energy transfer  $B_A^* \rightarrow P^*$ , the first step of this process must, of course, proceed at a similar rate of a few 100 fs. In order to independently confirm the occurrence of this alternative pathway at room temperature, Groot et al.<sup>[18]</sup> made 3PEPS and TG measurements on the *Rb. sphaeroides* RC (wild type). They excited the accessories of the RC at 800 nm with 30 fs laser pulses. They detected both the whole-band echo signals and frequency-selective echo signals with 10 nm bandwidth filters at 790 nm and 810 nm. In fact, Groot et al.<sup>[18]</sup> were the first to employ this frequency-selective detection of 3PEPS. Figure 25.10 depicts the TG signals for detection at 790 nm and 810 nm. The signal decays faster at the red side than at the blue side. This shows that  $B_B$  transfers its energy to P more rapidly than  $B_A$  does. The decay times evaluated from linear exponential fits were 40 fs and 65 fs, respectively, corresponding to times for the transfer processes of 80 fs and 130 fs.

The non-zero level of the TG on a ps timescale shows that some signal persists at 800 nm. This can either be due to  $P^*$  excited-state absorption or direct  $B_A^{\pm}$  formation via the alternative pathway. At later times, the band shift of B due to the charges of  $P^+ H_A^-$  will also give a grating signal. This is manifested in the slow rise of the TG in the inset of Figure 25.10 (10 ps scale).

From 3PEPS, additional information can be obtained regarding this persisting signal, as shown in Figure 25.11. The peak shift decays for both 810 nm (a) and

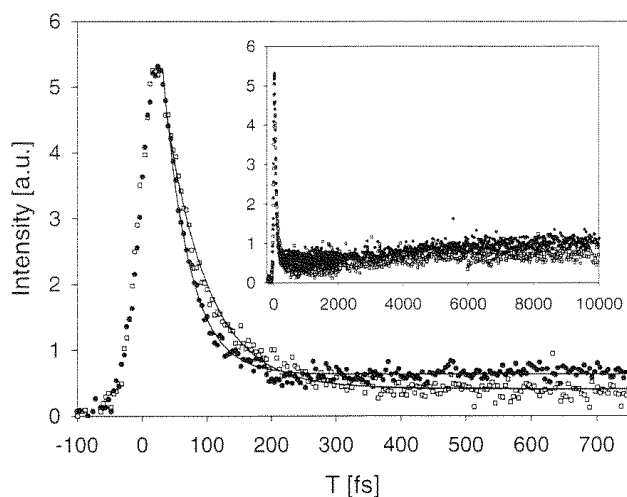


**Fig. 25.10** Transient grating decays measured on the accessory Bchls (B) of the RC of *Rb. sphaeroides*. Signals measured at 810 nm (filled circles) and at 790 nm (open squares) are shown, together with mono-exponential fits

(solid lines) with  $t = 40$  and 65 fs, respectively. The inset shows the signal up to 10 ps.<sup>11</sup>

**11)** Figure source: Groot *et al.*, 1998, ref. [18]

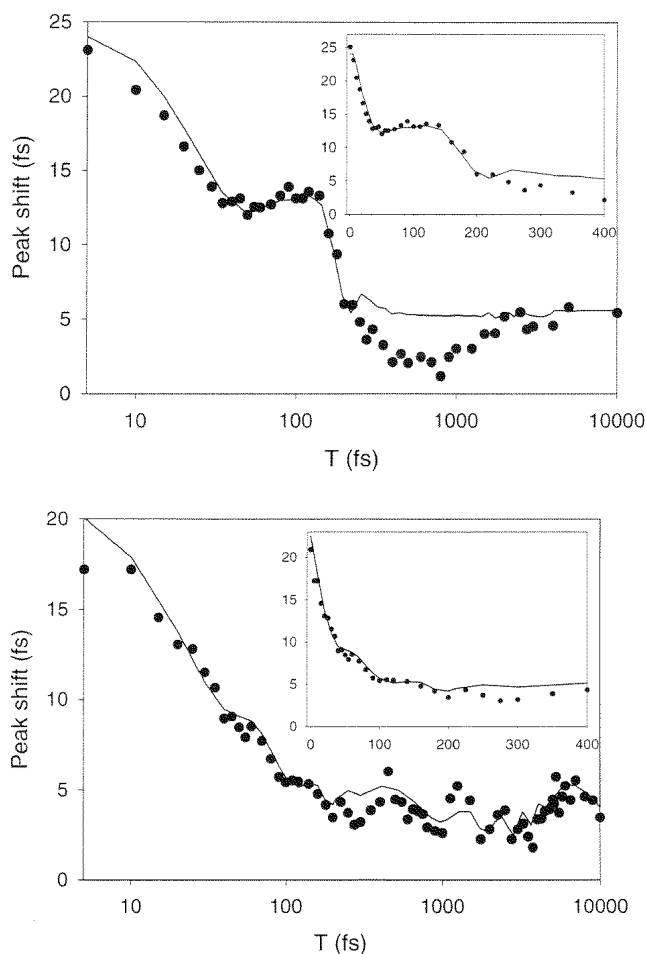


**Fig. 25.11** (a) Peak shift decay at 810 nm on a logarithmic scale. The inset shows the initial part of the decay on a linear scale. The solid line is a simulation; see text. The data points between 100 fs and 4 ps were ignored since they are assumed to arise from  $P^*$  and thus do not contain information on B.<sup>12</sup> (b) Peak shift decay at 790 nm on a logarithmic scale. The inset shows the initial part of the decay on a linear scale. The solid line is a simulation.<sup>13</sup>

<sup>12</sup> Figure source: Groot *et al.*, 1998, ref. [18]

<sup>13</sup> Figure source: Groot *et al.*, 1998, ref. [18]

790 nm (b) detection are presented. The whole-band signal (not shown) looks very similar to the 810 nm signal. Through linear fits, the main lifetimes were extracted from these signals. A long lifetime of 240 fs found for the whole-band signal shows that at least part of the frequency grating persists after the transfer to P has taken place, which takes  $\sim 120$  fs. This could mean that the gratings of  $P^*$  (ESA) and  $B^*$  are correlated, or that direct charge separation from  $B^*$  occurs, leading to a signal from the persisting ground-state grating of B. From the 3PEPS signal detected

through the 810 nm filter, it was concluded that the occurrence of the latter process is the most likely explanation. The  $P^*$  ESA is significantly larger here than when averaged over the whole band, but no difference in the decay of the peak shift is seen. Therefore, this peak shift cannot relate to  $P^*$ . The same is concluded from the blue 3PEPS. At 790 nm, the  $P^*$  ESA should be absent, so that after  $B^* \rightarrow P^*$  transfer in 130 fs all dynamics should be over unless due to B itself. However, the opposite is true: the peak shift in Figure 25.11b shows a remarkable degree of complex oscillatory dynamics extending up to 10 ps. Overall, Groot et al. have indeed presented a very nice independent confirmation of the occurrence of direct charge separation from the accessory Bchl  $B_A$ . Their measurements show for the first time that this charge separation also takes place at room temperature. Moreover, with the good time resolution of the 3PEPS method, the various timescales can be delineated more clearly than with the pump-probe method. Furthermore, the peak shift does not depend on the population amplitude of a certain state. In the pump-probe method, the short-lived  $B_A^+H_A^-$  and  $P^+B_A^-$  states can be identified only with difficulty for the wild-type RC.

## 25.8

### Concluding Remarks

In this chapter, we have discussed two nonlinear spectroscopic techniques, namely three-pulse echo peak shift (3PEPS) and transient grating (TG). We have introduced these techniques by discussing their principles, the experimental methods, and two simulation methods. The goal of the chapter has been to demonstrate the utility of these techniques in studying early events in photosynthesis. For the B800 ring of the purple bacterial antenna LH2, we have discussed the application of 3PEPS with both parallel and perpendicular polarization and with frequency-resolved detection, as well as TG anisotropy measurements. With these techniques, it has been shown unambiguously that energy transfer in the B800 ring of Bchls does occur at room temperature and that the transfer timescale is approximately 1 ps.

Comparison of the 3PEPS measurements on purple bacterial antenna LH1 with the results of experiments on its dimeric subunit B820 has confirmed that the excitation in LH1 is most likely delocalized over a dimer. Hopping of the excitation between dimers is seen to take place in  $\sim 90$  fs.

Electron transfer processes can also be studied with 3PEPS and TG, as has been shown for the purple bacterial RC. 3PEPS and TG measurements were carried out on the accessory Bchls B, with frequency-selective detection to allow the separate study of the dynamics of  $B_B$  and  $B_A$ . The results confirmed that direct charge separation from  $B_A$  ( $B_A^* \rightarrow B_A^+H_A^-$  or  $P^+B_A^-$ ) does occur. The timescale of this process is  $\sim 200$  fs.

In short, 3PEPS and TG are very useful for studying fast (sub-ps) energy transfer and electron transfer processes between (almost) isoenergetic states. We wish to emphasize the fact that identification of the processes observed in 3PEPS is especially efficient when different wavelengths, polarizations, or complexes are compared.

## References

- 1 R. van Grondelle, J. P. Dekker, T. Gillbro, V. Sundström, *Biochim. Biophys. Acta* **1994**, *1187*, 1–65.
- 2 G. R. Fleming, R. van Grondelle, *Phys. Today* **1994**, *47*, 48–55.
- 3 H. van Amerongen, L. Valkunas, R. van Grondelle, *Photosynthetic Excitons*, World Scientific, Singapore, **2000**.
- 4 J. P. Dekker, R. van Grondelle, *Phot. Res.* **2000**, *63*, 195–208.
- 5 J. Deisenhofer, O. Epp, K. Miki, R. Huber, H. Michel, *Nature* **1985**, *318*, 618–624.
- 6 G. McDermott, S. M. Prince, A. A. Freer, A. M. Hawthornthwaite-Lawless, M. Z. Papiz, R. J. Cogdell, N. W. Isaacs, *Nature* **1995**, *374*, 517–521.
- 7 J. Koepke, X. Hu, C. Muenke, K. Schulten, H. Michel, *Structure* **1996**, *4*, 581–597.
- 8 W. Kühlbrandt, D. N. Wang, Y. Fujiyoshi, *Nature* **1994**, *367*, 614–621.
- 9 N. Krauss, W. D. Schubert, O. Klukas, P. Fromme, H. T. Witt, W. Saenger, *Nat. Struct. Biol.* **1996**, *3*, 965–973
- 10 H. T. Witt, personal communication.
- 11 R. Jimenez, G. R. Fleming, Ultrafast Spectroscopy of Photosynthetic Systems, in: *Bio-physical Techniques in Photosynthesis* (Eds.: J. Amesz, A. J. Hoff), Kluwer Academic Publishers, Dordrecht, The Netherlands, **1996**, 63–74.
- 12 S. Mukamel, *Principles of Nonlinear Optical Spectroscopy*, Oxford University Press, New York, **1995**.
- 13 W. P. de Boeij, M. S. Psenichnikov, D. A. Wiersma, *Chem. Phys. Lett.* **1995**, *238*, 1–8.
- 14 T. Joo, Y. Jia, J. Y. Yu, M. J. Lang, G. R. Fleming, *J. Chem. Phys.* **1996**, *104*, 6089–6108.
- 15 J. M. Salverda, F. van Mourik, G. van der Zwan, R. van Grondelle, *J. Phys. Chem. B* **2000**, *104*, 11395–11408.
- 16 R. Jimenez, F. van Mourik, J. Y. Yu, G. R. Fleming, *J. Phys. Chem. B* **1997**, *101*, 7350–7359.
- 17 J. Y. Yu, Y. Nagasawa, R. van Grondelle, G. R. Fleming, *Chem. Phys. Lett.* **1997**, *280*, 404–410.
- 18 M. L. Groot, J. Y. Yu, R. Agarwal, J. R. Norris, G. R. Fleming, *J. Phys. Chem. B* **1998**, *102*, 5923–5931.
- 19 K. Duppen, D. A. Wiersma, *J. Opt. Soc. Am. B* **1986**, *3*, 614–621.
- 20 Y. J. Yan, S. Mukamel, *Phys. Rev. E* **1990**, *41*, 6485–6504.
- 21 W. Bosma, Y. J. Yan, S. Mukamel, *Phys. Rev. E* **1990**, *42*, 6920–6923.
- 22 S. Mukamel, *Annu. Rev. Phys. Chem.* **1990**, *41*, 647–681.
- 23 Y. J. Yan, S. Mukamel, *J. Chem. Phys.* **1991**, *94*, 179–190.
- 24 M. Yang, G. R. Fleming, *J. Chem. Phys.* **1999**, *111*, 27–39.
- 25 R. Agarwal, B. P. Krueger, G. D. Scholes, M. Yang, J. Yom, L. Mets, G. R. Fleming, *J. Phys. Chem. B* **2000**, *104*, 2908–2918.
- 26 A. P. Shreve, J. K. Trautman, H. A. Frank, T. G. Owens, A. C. Albrecht, *Biochim. Biophys. Acta* **1991**, *1058*, 280–288.
- 27 S. Hess, E. Åkesson, R. J. Cogdell, T. Pullerits, V. Sundström, *Biophys. J.* **1995**, *69*, 2211–2225.
- 28 J. T. M. Kennis, A. M. Streltsov, T. J. Aartsma, T. Nozawa, J. Amesz, *J. Phys. Chem.* **1996**, *100*, 2438–2442.
- 29 H. van der Laan, T. Schmidt, R. W. Visschers, K. J. Visscher, R. van Grondelle, S. Völker, *Chem. Phys. Lett.* **1990**, *170*, 231–238.
- 30 R. Monshouwer, I. Ortiz de Zarate, F. van Mourik, R. van Grondelle, *Chem. Phys. Lett.* **1995**, *246*, 341–346.
- 31 T. Pullerits, S. Hess, J. L. Herek, V. Sundström, *J. Phys. Chem. B* **1997**, *101*, 10560–10567
- 32 Y. Z. Ma, R. J. Cogdell, T. Gillbro, *J. Phys. Chem. B* **1997**, *101*, 1087–1095.
- 33 Y. Z. Ma, R. J. Cogdell, T. Gillbro, *J. Phys. Chem. B* **1998**, *102*, 881–887.
- 34 S. Hess, F. Feldchtein, A. Babin, I. Nurgaleev, T. Pullerits, A. Sergeev, V. Sundström, *Chem. Phys. Lett.* **1993**, *216*, 247–257.
- 35 J. T. M. Kennis, A. M. Streltsov, S. I. E. Vulto, T. J. Aartsma, T. Nozawa, J. Amesz, *J. Phys. Chem. B* **1997**, *101*, 7827–7834.
- 36 T. Joo, Y. Jia, J. Y. Yu, D. M. Jonas, G. R. Fleming, *J. Phys. Chem.* **1996**, *100*, 2399–2409.
- 37 S. Karrasch, P. Bullough, R. Ghosh, *EMBO J.* **1995**, *14*, 631–638.

- 38 P. A. Loach, P. S. Parkes, J. F. Miller, S. Hinchigeri, P. M. Callahan, in *Cold Spring Harbor Symposium on Molecular Biology of the Photosynthetic Apparatus* (Eds.: C. Arntzen, L. Bogorad, S. Bonitz, K. Steinback), Cold Spring Harbor Laboratory Press, Cold Spring Harbor, NY, **1985**.
- 39 R. W. Visschers, M. C. Chang, F. van Mourik, P. S. Parkes-Loach, B. A. Heller, P. A. Loach, R. van Grondelle, *Biochemistry* **1991**, *30*, 5734–5742.
- 40 F. van Mourik, C. J. R. van der Oord, K. J. Visscher, P. S. Parkes-Loach, P. A. Loach, R. W. Visschers, R. van Grondelle, *Biochim. Biophys. Acta* **1991**, *1059*, 111–119.
- 41 H. M. Visser, O. J. G. Somsen, F. van Mourik, S. Lin, I. H. M. van Stokkum, R. van Grondelle, *Biophys. J.* **1995**, *69*, 1083–1099.
- 42 S. E. Bradforth, R. Jimenez, F. van Mourik, R. van Grondelle, G. R. Fleming, *J. Phys. Chem.* **1995**, *99*, 16179–16191.
- 43 M. Chachisvilis, O. Kuhn, T. Pullerits, V. Sundström, *J. Phys. Chem. B* **1997**, *101*, 7275–7283.
- 44 R. Monshouwer, A. Baltuška, F. van Mourik, R. van Grondelle, *J. Phys. Chem. B* **1998**, *102*, 4360–4371.
- 45 J. P. Allen, G. Feher, T. O. Yeates, H. Komiya, D. C. Rees, *Proc. Natl. Acad. Sci. USA* **1987**, *84*, 5730–5734.
- 46 J. P. Allen, G. Feher, T. O. Yeates, H. Komiya, D. C. Rees, *Proc. Natl. Acad. Sci. USA* **1987**, *84*, 6162–6166.
- 47 R. J. Stanley, B. King, S. G. Boxer, *J. Phys. Chem.* **1996**, *100*, 12052–12059.
- 48 D. M. Jonas, M. J. Lang, Y. Nagasawa, T. Joo, G. R. Fleming, *J. Phys. Chem.* **1996**, *100*, 12660–12673.
- 49 M. E. van Brederode, M. R. Jones, F. van Mourik, I. H. M. van Stokkum, R. van Grondelle, *Biochemistry* **1997**, *36*, 6855–6861.
- 50 M. E. van Brederode, F. van Mourik, I. H. M. van Stokkum, M. R. Jones, R. van Grondelle, *Proc. Natl. Acad. Sci. USA* **1999**, *96*, 2054–2059.

## 26

### Femtosecond Studies of Intramolecular Bond Twisting in Solution

Max Glasbeek, Hong Zhang, Pascale Chagnenet, Pascal Plaza, Monique M. Martin,  
Wolfgang Rettig

#### Abstract

Femto- and picosecond fluorescence up-conversion and transient absorption studies in solution of the excited-state dynamics of selected organic chromophores containing singly-bonded phenyl groups are presented. For one of the investigated molecules, auramine, i.e. 4,4'-(imidocarbonyl)-bis(*N,N*-dimethylaniline) monohydrochloride, the excited-state dynamics has been investigated as a function of the viscosity of the ethanol solvent. On increasing the viscosity by lowering the temperature ( $300\text{ K} > T > 170\text{ K}$ ), a retardation of the initial picosecond Stokes shift and a concomitant drop in the integrated fluorescence intensity are found. The results are discussed assuming that diffusional torsional motions of the phenyl groups induce relaxation of the population density along the excited-state potential-energy surface. The latter is argued to be characteristic of *two* adiabatically-coupled excited states. These states involve the locally-excited emissive state and a geometry-relaxed weakly emissive ("dark") state. On the basis of the proposed model, the temporal dependence of the band emission, in low- and high-viscosity solutions, can be satisfactorily simulated. In addition, for some unbridged and bridged ionic styryl dyes, the results of (sub)picosecond fluorescence studies are discussed. Typically, for both the bridged and unbridged compounds, the initial dynamics (on a time scale of a few picoseconds) is controlled by the solvation of the solutes in the solvent. We observe a drastic shortening of the lifetime of the styryl dyes, by at least an order of magnitude, when the chromophore contains at least one singly-bonded phenyl group. We propose that for both types of molecule, the relaxed excited state further evolves by the twisting of a singly-bonded phenyl group into a region where the excited-state potential-energy surface has a conical intersection with the potential-energy surface of the ground state.

#### 26.1

##### Introduction

Ultrafast photoinduced conformational changes are of great importance in many processes of chemical and biological interest.<sup>[1,2]</sup> Usually, very high values for the reaction rate (often in excess of  $10^{12}\text{ s}^{-1}$ ) are obtained when the excited-state poten-

tial energy as a function of the reaction coordinate lacks an activation barrier. In the condensed phase, solvent viscosity is then often of great importance to the excited-state dynamics. This has been extensively investigated for photoexcited di- and tri-phenylmethane dye molecules showing twisting dynamics of the phenyl groups.<sup>[3–7]</sup> In this contribution, we report on femto- and picosecond transient absorption and fluorescence up-conversion studies of fast internal reorientational motions for selected fluorescent organic chromophores. More specifically, we discuss time-resolved experiments performed on the diphenylmethane dye molecule auramine (structure 1 in Figure 26.1), for which barrierless relaxation in the excited state due to internal twisting has been examined. In addition, the relaxation dynamics for the bridged and unbridged ionic styryl dye molecules 2–5 in Figure 26.1 has been studied. For the latter systems, it has been found that bridging of various functional groups in the molecule strongly affects the lifetime of the emissive state.

Auramine is a yellow dye that is weakly fluorescent in low-viscosity solvents (e.g., water) and highly fluorescent in viscous solvents, DNA, and polymeric acids.<sup>[8,9]</sup> In their early steady-state spectroscopic investigations, Oster and Nishijima<sup>[10]</sup> concluded that diffusion-controlled twisting motions of the phenyl rings in the molecule play an important role in the relaxation of the locally-excited state. Recently, several studies have provided information concerning the dynamics of the fluorescent excited state of auramine.<sup>[11–14]</sup> In the present chapter, transient absorption and emission spectroscopic results for auramine are presented. The time-resolved spectra are discussed in terms of an adiabatic coupling model involving an emissive locally-excited and a quasi-non-emissive transient excited state. The dynamics of the excited-state relaxation is considered as being controlled by diffusional phenyl group twisting motions.

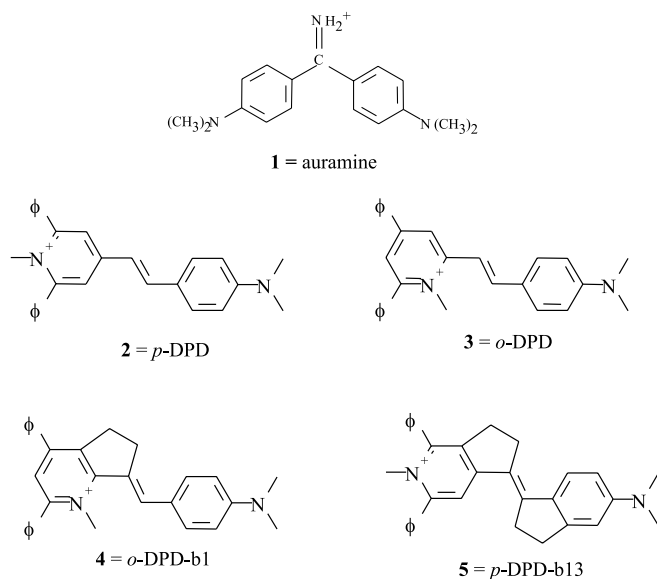


**Fig. 26.1** The structures of auramine (1) and the ionic styryl dyes *p*-DPD (2), *o*-DPD (3), *o*-DPD-b1 (4), and *p*-DPD-b13 (5).

Unbridged and bridged diphenyl derivatives of 1- or 4-(4'-dimethylaminostyryl)pyridinium dyes **2–5** (Figure 26.1) have received widespread interest because of their application as spectral sensitizers,<sup>[15]</sup> laser dyes,<sup>[16]</sup> and biosensors.<sup>[17]</sup> In addition to our results on auramine, we also review our recent (sub)picosecond fluorescence studies<sup>[18]</sup> on **2–5** in various solvents. It is pointed out that following pulsed laser excitation, the early excited-state dynamics is typical of solvation of the solutes in the solvents. Furthermore, it is shown that the presence of unbridged styryl group single bonds (as in **2–4**) allows for an effective non-radiative decay process, thus shortening the lifetime of the excited state. This process is suppressed by double chemical bridging (as in **5**) and most likely involves torsional motions of the singly-bonded phenyl groups.

## 26.2

### Experimental

Auramine was purchased from Aldrich and purified by several sublimations to eliminate a fluorescent impurity. The DPD compounds **2–5** (Figure 26.1) were synthesized as described elsewhere.<sup>[19]</sup> The solvents used were UV-spectrophotometric grade ethanol, 1-decanol, and benzonitrile. The femtosecond fluorescence up-conversion set-up and the time-correlated single-photon counting picosecond set-up have been described previously.<sup>[12]</sup> The instrument response was about 100 fs for the up-conversion experiment and about 16 ps for the time-correlated single-photon counting fluorescence set-up. The fluorescence transients were measured under magic-angle conditions to avoid temporal effects due to rotational diffusion motions of the molecule. Temperature variation of the sample was realized by the use of a home-built liquid nitrogen flow cryostat. The temperature of the sample was measured with a thermocouple attached to the copper cuvette holder. After thermal equilibration, the accuracy of the temperature control was  $\pm 3$  K. Time-resolved transient absorption and gain spectra were measured at room temperature by the pump-probe technique using a 700 fs 20  $\mu$ J pump pulse at 425 nm and a white-light continuum probe according to methods described elsewhere.<sup>[11,12,14]</sup> Measurements were made at the magic angle and accumulated over 500 laser shots. The samples were recirculated in a 1 mm flow cell. The FWHM of the pump-probe cross-correlation function was estimated to be about 1.5 ps. The transient spectra were corrected for the group velocity dispersion of the probe pulse.

## 26.3

### Results and Discussion

#### 26.3.1

##### Auramine

Figure 26.2a shows the steady-state absorption and emission spectra, recorded at room temperature, of auramine dissolved in ethanol and decanol. Figure 26.2b illus-



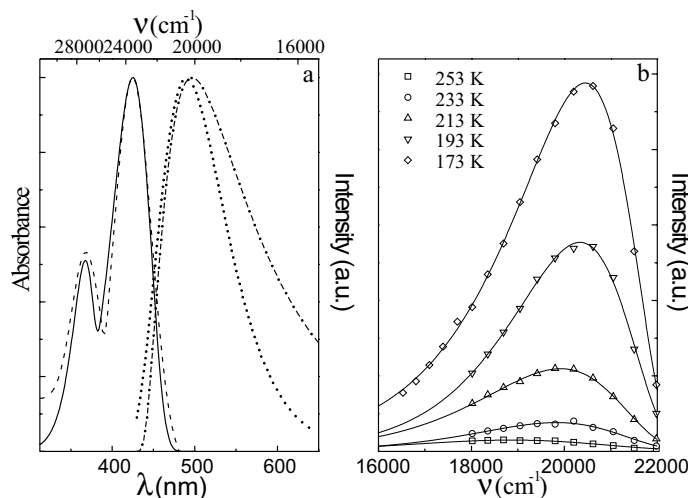


**Fig. 26.2** (a) Steady-state absorption spectrum of auramine in ethanol (solid line) and decanol (dashed line). (b) Steady-state emission spectrum of auramine in ethanol at the temperatures indicated.

trates the main changes in the steady-state emission band of auramine in ethanol as the temperature is lowered. There is a shift of the emission band maximum of about  $800 \text{ cm}^{-1}$  to the blue as the temperature is decreased from 293 K to 173 K. Also, the total fluorescence intensity increases by a factor of about five, in agreement with the quantum yield enhancements reported in refs.<sup>[10]</sup> and <sup>[20]</sup>.

### 26.3.1

#### (a) Transient Absorption

Figure 26.3 shows the differential absorbance ( $\Delta D$ ) spectra of auramine in ethanol, recorded for 1–5.5 ps pump-probe delays in the 360–660 nm wavelength range at room temperature. The stimulated emission band (above 470 nm) rapidly decays and a transient absorption band is observed a few picoseconds after excitation between 470 and 550 nm. A temporary isosbestic point is seen at 459 nm for a non-zero  $\Delta D$  value, indicating the presence of more than two species or states. At longer delays, both the induced absorption and bleaching bands decay. The kinetics of  $\Delta D$  was fitted to a bi-exponential function with components of 1.75 ps and 20 ps at 439 nm in the bleaching band and of 2.75 ps and 32 ps at 479 nm, where the initial gain signal gives way to a transient absorption band. In decanol, the transient spectra exhibit the same dominant features but the kinetics are slower and more complex: a 10 ps lag prior to a single 130 ps exponential decay is found in the bleaching band, and a rough bi-exponential fit at 490 nm in the transient absorption band shows that the shorter component is 19 ps.<sup>[12]</sup> Possible reasons for the difference in the observed solvent viscosity effect on the two components have previously been discussed in detail.<sup>[7]</sup>

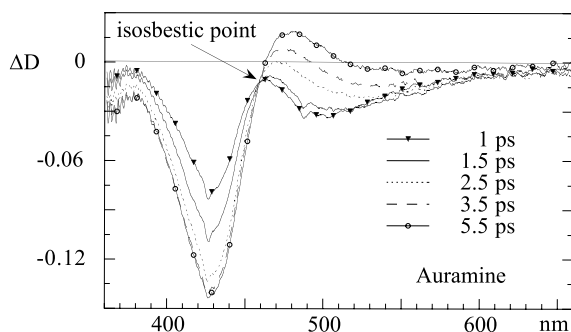


**Fig. 26.3** Time-resolved differential absorption spectra of auramine in ethanol after sub-picosecond excitation at 425 nm for pump-probe delays of 1, 1.5, 2.5, 3.5, and 5.5 ps.

### 26.3.1

#### (b) Fluorescence Up-Conversion

Femtosecond fluorescence up-conversion experiments have been performed for auramine in the solvents ethanol and decanol at room temperature. The influence of a change in the viscosity was examined for the ethanolic auramine solution by changing the temperature. The typical features observed in the fluorescence transients of auramine are illustrated in Figure 26.4. The figure shows fluorescence up-conversion transients for auramine dissolved in ethanol at three detection wavelengths (panel (a)) and three different temperatures (panel (b)). Typically, the fluorescence shows an instantaneous rise followed by a multi-exponential decay with time constants ranging from 500 fs up to a few hundred picoseconds. From the fluorescence transients, after spectral reconstruction, the time-dependent fluorescence spectra could be obtained.<sup>[12,13]</sup> As an example, we show in Figure 26.5 the temporal behavior of the auramine emission band for the solute dissolved in ethanol at 273 K. The spectra reveal a small dynamic Stokes shift of a few hundred wavenumbers (within the first 10 ps), accompanied by a drastic drop in fluorescence intensity to about 10 % of the initial value. The residual fluorescence has a longer decay (about 30 ps). Note how the decay of the initially excited fluorescent state is accompanied by the rise of a new transient absorption band peaking near 480 nm, as mentioned in Section 26.3.1 (a) above. Furthermore, like the 480 nm transient absorption, the lifetime of the residual red-shifted fluorescence is about 30 ps in ethanol and about 130 ps in decanol. The transient absorption at 480 nm has been assigned as being due to a dark state (Figure 26.6).<sup>[11,12]</sup> From the similar time constants for the fluorescence decay and the rise of the transient absorption at 480 nm, it is evident that the emissive locally-excited (LE) state relaxes within about 2 ps to the weakly emissive excited state, which, at room temperature, emits the 30 ps fluorescence component. This state is referred to hereafter as  $S_{\text{relax}}$ .

As already argued in the pioneering work reported in refs.<sup>[10]</sup> and <sup>[20]</sup> as well as in our previous publications,<sup>[11–14]</sup> the rotational motions of the phenyl rings play an

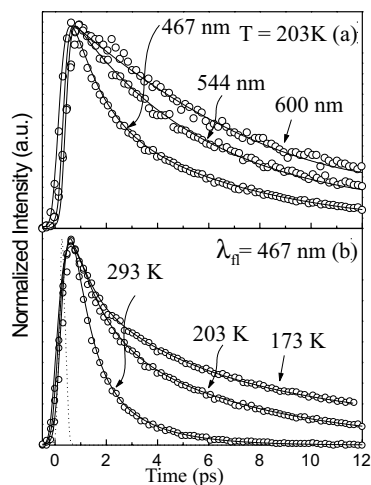


**Fig. 26.4** Fluorescence up-conversion transients for auramine dissolved in ethanol: (a) transients at three different detection wavelengths; (b) transients at three different temperatures.

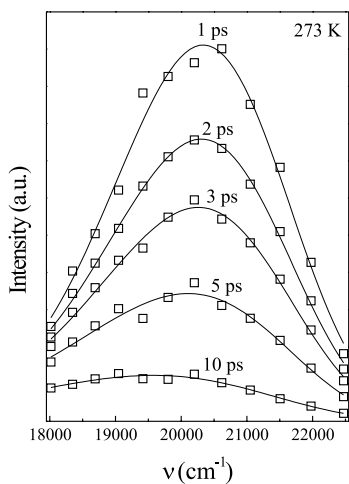


**Fig. 26.5** Temporal dependence of the auramine emission band after spectral reconstruction of the fluorescence transients at 273 K.

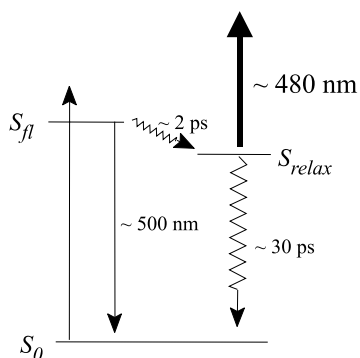


**Fig. 26.6** Simple kinetic scheme for auramine as deduced from transient absorption results.

important role in the relaxation of the excited state of auramine. The influence of temperature on the fluorescent-state decay kinetics (Figure 26.4b) further illustrates this idea. As the viscosity increases on lowering the temperature, the damping of the torsional motions of the phenyl rings is enhanced and thus the relaxation is expected to slow down. Very recently, the retardation of the LE-state-to- $S_{\text{relax}}$ -state relaxation at lower temperatures was examined more quantitatively.<sup>[13]</sup> After spectral reconstruction from the fluorescence up-conversion transients, measured in the temperature range  $300 \text{ K} > T > 170 \text{ K}$ , the variation of the temporal behavior of the auramine emission spectrum with temperature was obtained. In Figure 26.7, typical examples are given for  $T = 273 \text{ K}$ ,  $233 \text{ K}$ , and  $173 \text{ K}$ . It can be seen that, as the temperature is lowered, the dynamics of both the dynamic Stokes shift as well as the drop in the integrated emission intensity slow down.

Bagchi et al.<sup>[21]</sup> have considered the problem of a rapid drop in the integrated fluorescence intensity accompanying a barrierless reaction. The time development of an initial population distribution along an excited-state potential-energy surface was considered on the basis of a modified Smoluchowski diffusion equation that included a non-local sink function term to take into account an enhancement in the non-radiative decay as the reaction proceeded. The fluorescence intensity will show a drop concomitant with the dynamic Stokes shift if the rate of the non-radiative decay caused by the sink function term and the rate of population relaxation along the potential-energy surface are comparable in magnitude. This is what is observed for auramine and thus, in accordance with the approach of Bagchi et al., one would expect the typical lifetime of the relaxed excited state to eventually be determined by

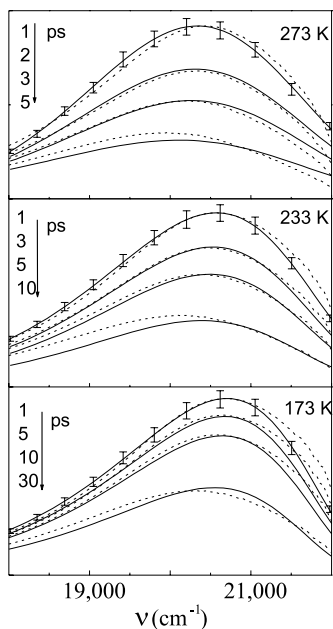


**Fig. 26.7** Temporal dependence of auramine emission at three different temperatures. The drawn curves were obtained after spectral reconstruction of the experimental fluorescence transients. Dashed curves were simulated according to the model described in the text.

the sink function term and thus be comparable to the characteristic time of the dynamic Stokes shift of about 2 ps at room temperature. As mentioned above, however, experimentally a residual lifetime of about 30 ps in ethanol and of about 130 ps in decanol is found for auramine in the excited state.<sup>[12]</sup> We conclude that the model of Bagchi et al.,<sup>[21]</sup> with a non-emissive sink, cannot fully account for our observations.

Alternatively, we explored the possibility that the *radiative* (rather than the *non-radiative*) decay shows a functional dependence on the twisting angle of the phenyl rings. Implicit to this idea is that the nature of the electronic wavefunction varies with the phenyl twisting angle. Such a situation may arise if there is adiabatic coupling between the (emissive) locally-excited state and a dark state.<sup>[12]</sup> Based on this approach, and starting from a Smoluchowski equation that included relaxation along a potential-energy surface resulting from the adiabatic coupling of the two lowest excited states only (the sink function term being omitted), we performed simulations of the temporal evolution of the excited-state population. Details have been published elsewhere.<sup>[13]</sup> Figure 26.7 includes the simulated spectra (dashed curves) that showed the best fit to the experimental spectra (drawn curves). The best-fit results were obtained for a (quasi-)barrierless shape of the excited-state potential,<sup>[13]</sup> this potential giving rise to a dynamic Stokes shift on a (sub)picosecond time scale.

In the simulations of the temporal behavior of the emission spectra at lower temperatures, the diffusion coefficient in the Smoluchowski equation was a variable parameter and its value was varied to obtain the best fit with the experimental data. It appeared<sup>[13]</sup> that the best-fit values for the rotation diffusion coefficient,  $D_r$ , showed a linear dependence on  $T/\eta$ , which conforms to the Debye–Einstein–Stokes relationship for rotational diffusion motion of a sphere,  $D_r = k_B T / 12 V \eta$ . The radius corresponding to this sphere was found to be 1.0 Å, which compares well with the value of 1.2 Å for the effective radius of a twisting phenyl group.

In summary, the drop in the fluorescence intensity on the (sub)picosecond time scale is not due to a rapid population decay from the excited state to the ground state (no sink function). Instead, it may be attributed to the change in the radiative character of the excited state that accompanies the fast (~2 ps in ethanol) relaxation *within* this excited state while the molecule is twisting. This is also illustrated in Figure 26.6, where  $S_{\text{relax}}$  represents the relaxed region of  $S_1$  with strongly reduced emission probability. Especially at early times, the model yields a satisfactory agreement between the simulated and experimental data. At later times, the agreement between the reconstructed and simulated curves is less good since population decay from  $S_{\text{relax}}$  to the ground state (30 ps in ethanol) is neglected in the simulations.

### 26.3.2

#### Ionic Styryl Dyes

The emissive states of the ionic styryl dyes 2–5 shown in Figure 26.1 are charge-transfer states, in which charge has been transferred from the styryl group to the pyridinium acceptor.<sup>[22]</sup> In polar solvents, Stokes shifts typical of the charge-transfer state of about 5,000 cm<sup>-1</sup> have been measured.<sup>[23]</sup> In this section, we review the

results of recent (sub)picosecond fluorescence experiments aimed at delineating the internal twisting dynamics of the ionic styryl dyes in the excited state.<sup>[18]</sup>

Figure 26.8 depicts the steady-state emission spectra of the DPD compounds 2–5, dissolved in ethanol, decanol, and benzonitrile. For all the compounds, a broad band emission (maximum near 660 nm; FWHM about  $2,500\text{ cm}^{-1}$ ) is observed. In the highly polar solvent benzonitrile, the DPD cation emissions are red-shifted compared to those from the ethanol and decanol solutions, as expected for emission from a charge-transfer state.

Figure 26.9 shows fluorescence up-conversion transients for *p*-DPD (2) in ethanol (a) and benzonitrile (b), at some selected detection wavelengths. As can be seen in Figure 26.9a, when detection is in the blue part of the emission band ( $\lambda < 610\text{ nm}$ ), the fluorescence shows an instantaneous rise (within 100 fs), which is followed by a decay component on the picosecond time scale. At higher detection wavelengths ( $\lambda > 620\text{ nm}$ ), the transients show picosecond rise components with time constants similar to those for the decay components measured on the blue emission side. Similar results were obtained for *p*-DPD dissolved in decanol. The time span was expanded in the SPC measurements. As can be seen in Figure 26.9c, for *p*-DPD in benzonitrile the ps rise components when  $\lambda > 620\text{ nm}$  are missing due to the limited instrument time response (16 ps) and only the decay components remain. However, in the more viscous decanol solution, all the kinetics are slowed and the phenomenology of rise and decay components, as seen in the femtosecond up-conversion experiments, becomes resolved once more (Figure 26.9d). The femto- and picosecond transients, as obtained at detection wavelengths between 530 nm and

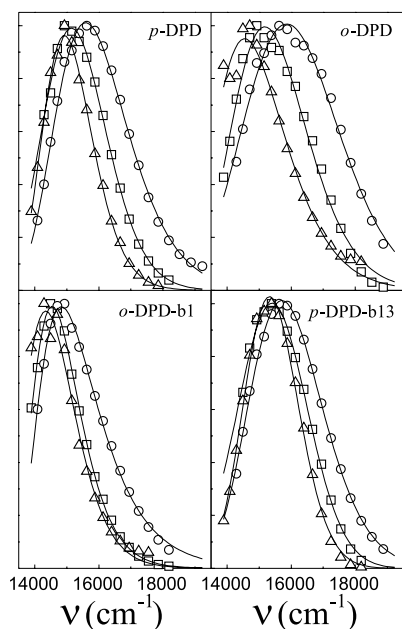


**Fig. 26.8** Steady-state emission spectra of the styryl dyes 2–5 dissolved in ethanol ( $\square$ ), decanol ( $\circ$ ), and benzonitrile ( $\triangle$ ). Solid lines are best fits to log-normal line-shape functions.

700 nm, could all be fitted to a two- or three-exponential function convoluted with the instrument response function. The drawn curves in Figure 26.9 depict the multi-exponential best fits.

From the best-fit fluorescence transients, the time dependence of the emission spectrum could be reconstructed.<sup>[18]</sup> The results show that for *p*-DPD in ethanol the dynamic Stokes shift (DSS) is approximately  $1600\text{ cm}^{-1}$  in about 20 ps, in benzonitrile it is about  $1000\text{ cm}^{-1}$  in less than 10 ps, while in decanol it is about  $1600\text{ cm}^{-1}$  in more than 500 ps. The excited-state population decay to the ground state is much slower than the dynamic Stokes shift. The variation in the lifetime of *p*-DPD in the three solvents is given in Table 26.1.

**Tab. 26.1** Lifetimes (in ps) for ionic styryl dyes 2–5 in various solvents.

	<i>Ethanol</i>	<i>Benzonitrile</i>	<i>Decanol</i>
<i>p</i> -DPD	80	215	900
<i>o</i> -DPD	40	85	400
<i>o</i> -DPD-b1	65	230	500
<i>p</i> -DPD-b13	1400	2000	2400

Analogous dynamic Stokes shifts were obtained from the fluorescence transients measured for **3** (*o*-DPD) and **4** (*o*-DPD-b1). After spectral reconstruction, temporal behavior of the emission spectra of **3** and **4** in the various solvents similar to that seen for **2** was obtained. For the doubly-bridged compound *p*-DPD-b13 (Figure

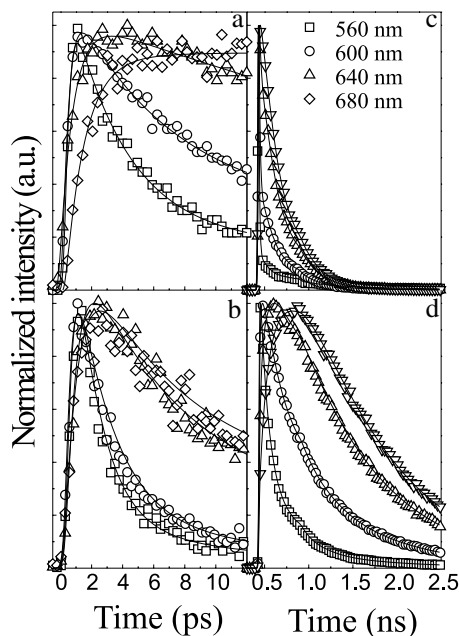


**Fig. 26.9** Fluorescence up-conversion transients (time window: 12 ps) of *p*-DPD dissolved in ethanol (a) and benzonitrile (b). Fluorescence transients (time window: 2.5 ns) of *p*-DPD dissolved in benzonitrile (c) and decanol (d). Detection wavelengths are as indicated. Solid lines are best fits to a multi-exponential function.

26.1), experiments similar to those on 2–4 were performed. The signal-to-noise ratios for the fluorescence transients were comparable to those achieved for *p*-DPD. In the case of *p*-DPD-b13, a strong solvent dependence of its fluorescence kinetics was also measured. This is reflected in the temporal dependence of the first moment of the emission bands of 2–5, as shown in Figure 26.10.

Several possible causes of the dynamic Stokes shift may be considered. As a first possibility, by analogy with di- and triphenylmethane dye molecules<sup>[3–7]</sup> and the results discussed in Section 26.3.1 for auramine, a twisting motion involving one or more of the functional groups in the styryl compounds is considered. A characteristic feature of the DPD compounds, however, is that bridging of *both* single bonds of the styryl dye has no significant influence on the rate of its dynamic Stokes shift (compare, e.g., the spectral dynamics of 2 and 5 in Figure 26.10). This result cannot be reconciled with the idea that the rate of the Stokes shift of styryl dyes is determined by twisting about a single styryl bond.

Alternatively, since for the ionic styryl dyes 2–5 the Stokes shift dynamics is seen to vary with the nature of the solvent, and considering also that the probed molecules are chemically inert with respect to the solvents ethanol, benzonitrile, and decanol, it is very likely that the observed dynamic Stokes shift is due to solvation. The time dependences of the first moment of the emission bands of 2–5 are in agreement with this interpretation. The time constants and relative amplitudes characterizing the bi-exponential time dependences are given in Table 26.2. The table includes the average solvation times known for the various polar solvents used.<sup>[24]</sup> The weighted average times for the dynamic Stokes shifts of the styryl dye emission bands as discerned from experiment and the known average solvation times of the solvents are consistent to within a factor of about three. This prompts us to propose that the dynamic Stokes shift is mainly due to solvation dynamics in the excited state.

We now consider the lifetime results for the DPD derivatives as presented in Table 26.1. It can be seen that, if the styryl dye has at least one unbridged single bond adjacent to the styryl group double bond (compounds 2–4), the lifetimes of the corresponding compounds in a given solvent are comparable. If, however, both single bonds are bridged, as in 5, the excited-state lifetime is lengthened significantly

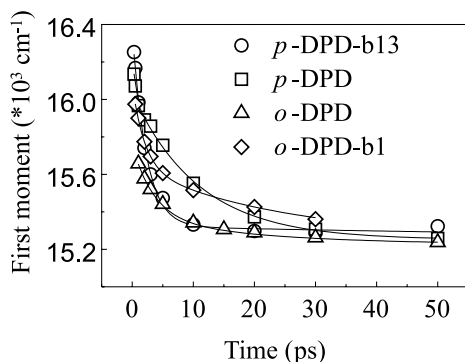


**Fig. 26.10** Time dependence of the first moments of the emission spectra of 2–5 in ethanol. Solid lines are best fits to bi-exponential decay functions.



(by a factor of at least ten when the solvent is ethanol). We propose that the enhanced non-radiative decay of compounds 2–4 is related to the flexibility (torsional or bending) of functional groups that are linked by a single bond to the remainder of the molecule. The presence of singly-bonded flexible groups can thus be viewed as leading to increased coupling of the excited state to the dense manifold of vibrational levels of the ground state, thereby facilitating effective radiationless decay (“loose bolt theory”<sup>[25]</sup>). The motions of the flexible groups also depend on the viscosity of the solvent. As the viscosity of the solvent increases, the torsional or bending motions slow down and this will reduce the rate of the radiationless decay process. This is indeed corroborated by the changes in the excited-state lifetimes of each of the styryl dyes with the viscosity of the solvent: in more viscous solutions, longer lifetimes are found.

**Table 26.2.** Characteristic times (in ps) of the dynamic Stokes shift of the DPD emission bands. Relative intensities are given in brackets.

	<i>Ethanol</i>			<i>Benzonitrile</i>			<i>Decanol</i>		
	$\tau_1$	$\tau_2$	$\tau_{av}$	$\tau_1$	$\tau_2$	$\tau_{av}$	$\tau_1$	$\tau_2$	$\tau_{av}$
<i>p</i> -DPD	0.2 (0.3)	10 (0.7)	7.1	0.8 (0.4)	19 (0.6)	11.7	53 (0.3)	330 (0.7)	233
<i>o</i> -DPD	3.5 (0.7)	19 (0.3)	8.2				45 (0.6)	460 (0.4)	211
<i>o</i> -DPD-b1	1.9 (0.6)	24 (0.4)	10.7				45 (0.4)	210 (0.6)	136
<i>p</i> -DPD-b13	1.8 (0.8)	5.8 (0.2)	2.6	9.5 (0.5)	17.7 (0.5)	13.6	82 (0.5)	550 (0.5)	339
$\tau_S$ (Ref. <sup>[24]</sup> )			16			5.1			245

Figure 26.11 schematically depicts a model for the processes in the fluorescent excited state, consisting of initial solvation (yielding the DSS, with a time constant of approximately 7 ps in ethanol) and the viscosity-dependent population decay (~80 ps in ethanol) to a dark state by bond twisting. Recent quantum chemical calculations on related dyes<sup>[26,27]</sup> suggest that a conical intersection (a funnel between the  $S_1$  and  $S_0$  hypersurfaces<sup>[28,29]</sup>) is situated close to single- and double-bond-twisted conformations. If this were to be identified with  $S_{\text{dark}}$ , it could explain the absence of emission from  $S_{\text{dark}}$  and its ultrafast non-radiative deactivation in the case of *p*-DPD. The determined fluorescence decay rate would then be given by the rate of access to  $S_{\text{dark}}$ , which may be considerably slower than solvent relaxation (Tables 26.1 and 26.2). A possible reason for this is that  $S_{\text{dark}}$  may be higher in energy, or may be reached by tunneling from the solvent-relaxed state  $S_{\text{relax}}$ . The model shown in Figure 26.11 yields a mechanistic basis for the loose bolt theory<sup>[25]</sup> and is an extension of the simplified model in Figure 26.6. It may also be invoked to elaborate on the results for auramine. Whereas for the DPD dyes, the fluorescence transition moments of  $S_{\text{fl}}$  and  $S_{\text{relax}}$  all seem to be of comparable magnitude, a marked drop is seen in the emissive transition rate for the relaxed state ( $S_{\text{relax}}$ ) in auramine. This gives a further indication that this state already involves bond twisting, in contrast to the case of DPD. As for the  $S_{\text{relax}}$ -to- $S_{\text{dark}}$  step, large amplitude motion on the

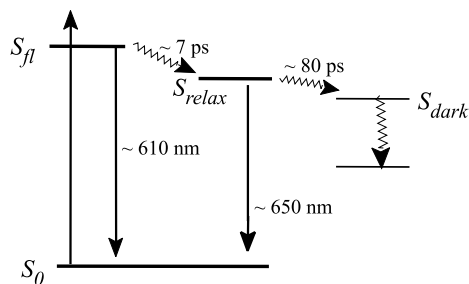


**Fig. 26.11** Kinetic scheme for the excited-state relaxation of *p*-DPD and related dyes. The values of the characteristic times given are those for *p*-DPD in ethanol (Tables 26.1 and 26.2). The coordinate leading to  $S_{relax}$  involves mainly solvent relaxation but may also contain bond twisting (as in the case of auramine). The reaction coordinate leading to  $S_{dark}$  involves a single bond twisting coordinate for *p*-DPD (see text). A probable candidate for the nature of  $S_{dark}$  is a conical intersection of the excited-state and ground-state surfaces, as indicated by their narrowed energy gap leading to ultrafast depopulation.

excited-state potential surface, involving torsion of the other phenyl ring, and relaxation to the ground state through a conical intersection between the  $S_1$  and  $S_0$  hypersurfaces, have previously been proposed for TPM dyes.<sup>[7]</sup> The observed viscosity effects on the relaxation time of the twisted  $S_{relax}$  state of auramine give a strong indication of a similar relaxation pathway for this compound.<sup>[14]</sup> The comparisons with DPD molecules reinforce this conclusion.

## 26.4 Conclusion

To study the excited-state dynamics in liquid solution of organic dye molecules containing singly-bonded phenyl groups, femto- and picosecond transient absorption and fluorescence up-conversion experiments have been performed. For auramine (1), it has been shown that upon pulsed laser excitation a rapid (~2 ps) relaxation from the initially excited fluorescent Franck–Condon state to a weakly emissive twisted relaxed excited state takes place in ethanol at room temperature. Starting from a model in which the excited state is considered as an adiabatic mixture of the fluorescent state and a non-emissive state, the initial kinetics could be simulated quantitatively. Additionally, time-resolved fluorescence experiments have been described for selected DPD dye molecules (2–5). Following fs pulsed optical excitation, solvation dynamics dominates at first, but subsequently, in the case of molecules 2–4 with non-bridged phenyl groups, twisting dynamics of these groups takes over. This twisting most probably involves conversion to the ground state in a conical intersection region of the hypersurfaces of the excited and ground states. Comparison of the results obtained for auramine and the DPD dye molecules offers a clue as to the nature of the relaxed excited state opening the way for ultrafast relaxation to the ground state: in both cases, this state is characterized by bond twisting and probably corresponds to a region of the excited-state surface lying close to a conical intersection with the electronic ground-state surface.

## References

- 1 B. Bagchi, R. Biswas, *Adv. Chem. Phys.* **1999**, 109, 207.
- 2 A. H. Zewail, *J. Phys. Chem.* **1996**, 100, 12701.
- 3 V. Sundström, T. Gillbro, *J. Chem. Phys.* **1984**, 81, 3463.
- 4 F. W. Wise, M. J. Rosker, C. Tang, *J. Chem. Phys.* **1987**, 86, 2827.
- 5 D. Ben-Amotz, R. Jeanloz, C. B. Harris, *J. Chem. Phys.* **1987**, 86, 6119.
- 6 M. M. Martin, P. Plaza, Y. H. Meyer, *J. Phys. Chem.* **1991**, 95, 9310.
- 7 M. Jurczok, P. Plaza, M. M. Martin, W. Rettig, *J. Phys. Chem. A* **1999**, 103, 3372.
- 8 R. H. Conrad, J. R. Heitz, L. Brand, *Biochemistry* **1970**, 9, 1540.
- 9 R. F. Steiner, S. Albaugh, E. Nenortas, L. Norris, *Biopolymers* **1992**, 32, 73.
- 10 G. Oster, Y. Nishijima, *J. Am. Chem. Soc.* **1956**, 78, 1581.
- 11 M. M. Martin, P. Plaza, P. Changenet, Y. H. Meyer, *J. Photochem. Photobiol.* **1997**, A105, 197.
- 12 P. Changenet, H. Zhang, M. J. van der Meer, M. Glasbeek, P. Plaza, M. M. Martin, *J. Phys. Chem. A* **1998**, 102, 6716.
- 13 M. J. van der Meer, H. Zhang, M. Glasbeek, *J. Chem. Phys.* **2000**, 112, 2878.
- 14 P. Changenet, H. Zhang, M. J. van der Meer, M. Glasbeek, P. Plaza, M. M. Martin, *J. Fluoresc.* **2000**, 10, 155.
- 15 J. Fabian, H. Nakazumi, M. Matsuoka, *Chem. Rev.* **1992**, 92, 1197.
- 16 U. Brackmann, *Lambdachrome Laser Dyes*, 2<sup>nd</sup> ed., Lambda Physik, Göttingen, **1994**.
- 17 P. Fromherz, K. H. Dambacher, H. Ephardt, A. Lambacher, C. O. Müller, R. Neigle, H. Schaden, O. Schenk, T. Vetter, *Ber. Bunsenges. Phys. Chem.* **1991**, 95, 1333.
- 18 M. J. van der Meer, H. Zhang, W. Rettig, M. Glasbeek, *Chem. Phys. Lett.* **2000**, 320, 673.
- 19 M. Szczepan, W. Rettig, V. V. Kurdyukov, A. I. Tolmachev, *to be published*.
- 20 T. Förster, G. J. Hoffmann, *Z. Phys. Chem. (Munich)* **1971**, 75, 63.
- 21 B. Bagchi, G. R. Fleming, D. W. Oxtoby, *J. Chem. Phys.* **1983**, 78, 7375.
- 22 W. Rettig, K. Rurack, M. Szczepan, in *Proceedings of the International Conference on Methods and Applications of Fluorescence Spectroscopy* (Paris, 1999) (Eds.: B. Valeur, J. C. Brochon), Springer, Berlin, **2000**.
- 23 U. Narang, C. F. Zhao, J. D. Bhawalkar, F. V. Bright, P. N. Prasad, *J. Phys. Chem.* **1996**, 100, 4521.
- 24 M. L. Horng, J. A. Gardecki, A. Papazyan, M. Maroncelli, *J. Phys. Chem.* **1995**, 99, 17311.
- 25 G. N. Lewis, M. Calvin, *Chem. Rev.* **1939**, 25, 273.
- 26 M. Dekhtyar, W. Rettig, V. Rozenbaum, *J. Photochem. Photobiol. A: Chem.* **1999**, 120, 75.
- 27 M. Dekhtyar, W. Rettig, M. Szczepan, *Phys. Chem. Chem. Phys.* **2000**, 2, 1129.
- 28 M. Klessinger, J. Michl, *Excited States and Photochemistry of Organic Molecules*, VCH Publishers, New York, **1995**.
- 29 F. Bernardi, M. Olivucci, M. A. Robb, *Chem. Soc. Rev.* **1996**, 25, 1321.